Chrome-spinel geochemistry of the northern Oman-United Arab Emirates ophiolite

Sarah Anne Sophia Dare

Submitted in partial fulfilment of the requirements for the degree
of Ph.D.

Cardiff University

September 2007

ProQuest LLC
789 East Eisenhower Parkway
P.O. Box 1346
Ann Arbor, MI 48106-1346

Form: PGR_Submission_200701

NOTICE OF SUBMISSION OF THESIS FORM:
POSTGRADUATE RESEARCH

CARDIFF
UNIVERSITY
PRIFYSGOL
CAERDYDD

APPENDIX 1:
Specimen layout for Thesis Summary and Declaration/Statements page to be included in a Thesis

DECLARATION

This work has not previously been accepted in substance for any degree and is not concurrently submitted in candidature for any degree.

Signed .... (candidate) Date ..28/9/2007....

STATEMENT 1

This thesis is being submitted in partial fulfillment of the requirements for the degree of Ph.D.

Signed .... (candidate) Date ....28/9/2007..

STATEMENT 2

This thesis is the result of my own independent work/investigation, except where otherwise stated. Other sources are acknowledged by explicit references.

Signed .... (candidate) Date ...28/9/2007...

STATEMENT 3

I hereby give consent for my thesis, if accepted, to be available for photocopying and for inter-library loan, and for the title and summary to be made available to outside organisations.

Signed .... (candidate) Date ...28/9/2007...

STATEMENT 4: PREVIOUSLY APPROVED BAR ON ACCESS

I hereby give consent for my thesis, if accepted, to be available for photocopying and for inter-library loans **after expiry of a bar on access previously approved by the Graduate Development Committee.**

Signed .... (candidate) Date ....

Abstract

The Oman ophiolite is the largest and best preserved ophiolite in the world and records a switch from mid-ocean ridge (MOR) to supra-subduction zone (SSZ) setting. This study investigates the geochemical variability of chrome-spinel in the mantle sequence of the poorly known United Arab Emirates (U.A.E.) part of the northern Oman-U.A.E. ophiolite. Extensive field work was carried out and 260 samples collected for petrogenetic studies and geochemical mapping of the U.A.E. mantle. Chrome-spinel geochemistry provides valuable information on both the residual mantle and on the nature and extent of melt-rock reaction. In particular, it is used to fingerprint the compositions of the magmas that interacted with the mantle lithosphere. This study also develops a new method to analyse gallium in chrome-spinel by Laser Ablation-ICP-MS, and successfully uses it to improve the tectonic discrimination of chrome-spinel.

The results show that the U.A.E. mantle lithosphere formed at a MOR-type setting and was modified by melt-rock reaction with MORB-type and SSZ-type melts. This history of melt infiltration strongly resembles the magmatic history of the crustal sequence in each of the Aswad and Khawr Fakkan Blocks. Geochemical mapping illustrates a strong spatial control on the pattern of melt infiltration in the mantle and constrains the proximity of each mantle domain with respect to the subduction zone. The Khawr Fakkan mantle extensively interacted with boninitic melts during subduction initiation. Thus, it was closer to the subduction zone than the Aswad mantle which predominantly interacted with island-arc tholeiite melts. Importantly, this work demonstrates for the first time that the Dibba Zone peridotites originate from pre-existing 'true' MOR mantle lithosphere between the trench and the main body of the ophiolite.

A further important conclusion is that the mantle lithosphere of the northern Oman-U.A.E. ophiolite was not the source region for the SSZ magmatism. Previous workers proposed that the plane of detachment and the subduction zone were the same, which implies that the mantle of the ophiolite was the source of the SSZ magmatism. Instead, this study proposes that detachment of the ophiolite took place at a shallower level than the plane of the subduction zone and thus provides strong evidence for a subduction zone at a still deeper level. During detachment, the ophiolite incorporated slices of ultramafic rock near the trench (i.e. the Dibba Zone peridotites) as it bulldozed its way over the underlying plate and onto the continental margin of Arabia.

Acknowledgements

Firstly, thanks must go to Prof. Julian Pearce and Dr. Chris MacLeod for devising this project in collaboration with the British Geological Survey. I would like to thank Julian Pearce very much for his time, guidance and support over the four years. The project has benefited a great deal from the BGS both in the field and for the use of their electron microprobe. I would like to thank Dr. Mike Styles (mapping project leader and co-supervisor) enormously for his assistance in the field, on the probe and his valuable input on the petrographical side of this project. I would also like to thank all the BGS team members for their excellent company and helpful discussions in the field. Special thanks go to Emrys Phillips for his discussions about the Dibba Zone and his wonderful cooking, and to Bob Thomas for his insights on the MTZ geology! Also I would like to thank my long-suffering field assistant, Omar, for carrying all my rocks and keeping me company in the field.

Big thanks also go to Dr. Iain McDonald for his assistance and patience with the ICP and Laser Ablation analyses here at Cardiff University. I would also like to thank Eveline De Vos, Pete Fisher and the rest of the technical staff for their assistance. I would also like to thank Dr. Hazel Prichard for bouncing ideas off each other while on field trips and for many enjoyable hours demonstrating with her. Thanks also to Alun Rogers for his assistance with GIS. I would like to thank Prof. Paul Robinson and Dr. Andrew Kerr for being my examiners and for their useful suggestions for the thesis. I am also grateful to Gren Turner and Kath Oakely for their support and assistance and to Mike & Olivia for their evening meals and good company, during my visits to the BGS.

Many, many thanks to all the Ph.D. students at Cardiff University (past and present) for their friendship and laughter over the years, and especially for their support during the final months of writing up. Thanks also to my wonderful housemates, past and present (Lizanne, Cat, Helena, Freddie, Kath, Jenny and last, but not least, the 'nuns' at 180!).

And lastly a huge thanks to my wonderful parents, and Zac and Zöe, for their love, support and belief in me.

For

My Parents

Glossary

Geological abbreviations

MOR – Mid-Ocean Ridge
SSZ – Supra-Subduction Zone
MORB –Mid-Ocean Ridge Basalt
IAT – Island Arc Tholeiite
BON – Boninite
HZ – Harzburgite
LHZ – Lherzolite
DU – Dunite
fO_2 – Oxygen fugacity
LREE – Light Rare Earth Elements
MREE – Middle Rare Earth Elements
HREE – Heavy Rare Earth Elements
REE - Rare Earth Elements

List of Contents

Chapter 7: Conclusions 312

Appendix A – Sample description and locality

Appendix B – Petrography

Appendix C – Whole rock analyses

Appendix E – Analysis of Ga in chrome-spinel by LA-ICP-MS

Chapter 1: The Oman-U.A.E. ophiolite

The Oman-United Arab Emirates (U.A.E) ophiolite (Semail or Samail ophiolite) is the largest and arguably best-preserved ophiolite in the world. The Oman-U.A.E. ophiolite is located on the NE coast of the Arabian Peninsula (Figure 1.1) and dominates the geology of the Oman Mountains (Hajar Mountains). The Oman section of the Oman-U.A.E. ophiolite has been studied extensively over the last 30 years and used as a natural laboratory in studying oceanic lithosphere and guiding ideas of modern oceanic spreading centres. In contrast, the U.A.E. section of the Oman-U.A.E. ophiolite has received relatively little attention (see Chapter 2). Recent geological mapping of the U.A.E. by the British Geological Survey (2002 – 2006) provided the opportunity for two complementary research projects on the crustal sequence (Lilly, 2006) and the mantle sequence (this study).

The tectonic setting of the Oman-U.A.E. ophiolite remains controversial. Geological evidence indicates that it formed at a mid-ocean ridge (MOR) and as such has influenced ideas on oceanic crustal accretion (e.g. Nicolas et al., 1988; Boudier et al., 1996; Kelemen et al., 1997a; MacLeod and Yaouancq, 2000) and segmentation at fast-spreading centres (e.g. Nicolas et al., 2000a; LeMée et al., 2004; Monnier et al., 2006). However, geochemical evidence from the crustal sequence in the north of Oman provides evidence for a supra-subduction zone (SSZ) setting, in which sea-floor spreading occurred above a young subduction zone (e.g. Pearce et al., 1981; Alabaster et al., 1982; Lippard et al., 1986). The U.A.E. contains the two northernmost, and least well known, blocks of the ophiolite (Aswad and Khawr Fakkan). A recent study of the crustal sequence in the U.A.E. provides strong evidence for a SSZ setting origin with an evolution from MORB-like magmas to arc-like magmas (island arc tholeiites and boninities) (Lilly, 2006). This research project investigates the geochemical variability of the U.A.E. mantle sequence associated with a switch in tectonic setting from MOR to SSZ.

1.1 Regional setting of the ophiolite

The Oman Mountains represent a continent-ocean collision boundary of Late Cretaceous age. The Oman Mountains are part of the Atlas-Alpine-Himalayan orogenic belt that extends from the western Mediterranean to the Far East (Figure 1.1). Over thirty ophiolite complexes, of late Jurassic to late Cretaceous in age, can be found within this vast mountain belt. The Oman-U.A.E. ophiolite is the largest and least deformed member because it crops out southward of the orogenic belt and has yet to suffer continent-continent collision.

The Atlas-Alpine-Himalayan orogenic belt formed when the African, Arabian and Indian Plates (Gondwana) migrated northward and collided with the Eurasian Plate (Laurasia), closing the Tethys Ocean (Figures 1.2 and 1.3).

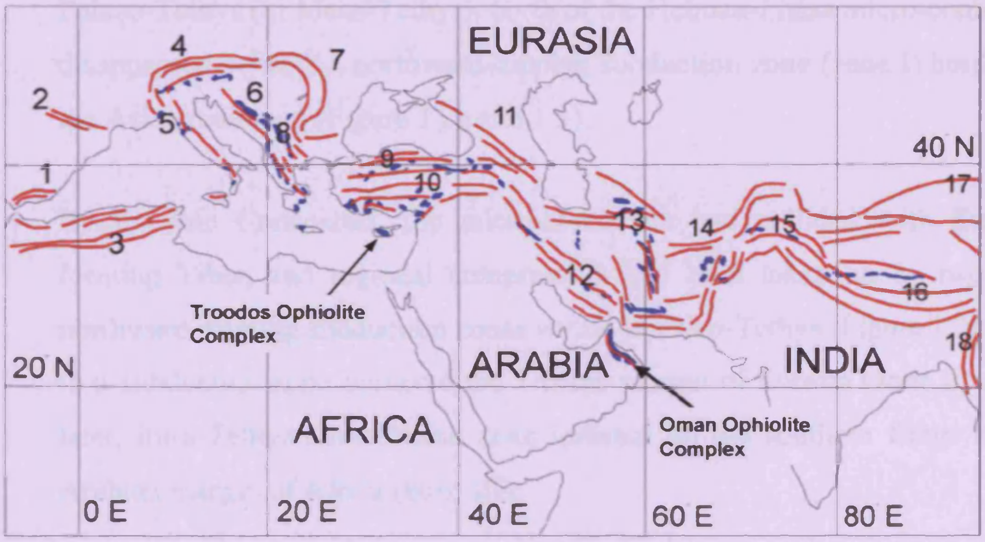

Figure 1.1: Regional setting of the Oman-U.A.E. Ophiolite Complex in relation to other ophiolite complexes (shown in blue) within the Atlas-Apline Himalayan Mountain Belt (shown in red). 1. = Beltic Cordillera 2. = Pyrenees 3. = Atlas 4. = Alps 5. = Apennines 6. = Dinarides 7. = Carpathians 8. = Hellenides 9. = Pontides 10. = Taurides 11. = Caucasus 12. = Zagros 13. = Alborz 14. = Hindukush 15. = Karakorum 16. = Himalayas 17. = Kunlun 18. = Indo-Burma Ranges. Figure modified after Lippard et al., 1986, figs. 1.2 & 1.4. Taken from Grantham et al., 2003 (CGS mapping report).

The Arabian Peninsula was located on the southern margin of the Neo-Tethys during the Mesozoic (Figure 1.2). The Arabian margin formed in the late Palaeozoic when the micro-continent of Halmand-Lhasa (Figure 1.2) rifted from NE Gondwana in the Mid-Permian. The geology of the Oman Mountains (Section 1.2) was initially interpreted as a passive margin (Glennie et al., 1974). However, calc-alkaline magmatism of the 'Podataksasi arc' in nearby Iran led to an alternative model that the Neo-Tethys opened as a back-arc basin above a Palaeo-Tethys continental margin magmatic arc (Şengör, 1990). Şengör (1990) has interpreted the geology of the Oman Mountains as similar to the margin and basin sequence of present day rifting within the back-arc basin of the Tyrrhenian Sea. By the end of the Mesozoic, regional compression was accommodated by three northward-dipping subduction zones which closed the Tethys Ocean in the following way (Van der Voo et al., 1999 and references within).

- During the late Jurassic, the Neo-Tethys Ocean grew larger while an older Palaeo-Tethys (or Meso-Tethys), north of the Helman-Lhasa micro-continent, disappeared beneath a northward-dipping subduction zone (zone I) bordering the Asian mainland (Figure 1.2a and 1.3).

- By the late Cretaceous, the micro-continents had collided with Eurasia, forming Tibet, and regional compression had been taken up by two new northward-dipping subduction zones within the Neo-Tethys (Figure 1.2b) The first subduction zone bordered the Tibetan margin of Eurasia (zone II) and a later, intra-Tethyan subduction zone initiated on the southern fringe of the Arabian margin of Africa (zone III).

- This southern marginal basin (south of zone III) closed at the end of the Cretaceous, obducting ophiolites onto both the Arabian and Indian margins. The Neo-Tethys continued to close until India collided with Asia in the Tertiary forming the Himalayas.

Fossil slabs, interpreted as the three Mesozoic Tethyan subduction zones described above, have been tomographically imaged beneath the Indian Ocean (Van der Voo et al., 1999) (Figure 1.3b). The presence of the southernmost of three deep fossil slabs (zone III) supports the idea that an intra-Neo-Tethys subduction zone existed to the north of India and Arabia during the late Cretaceous. Subduction zone III was the likely location for the supra-subduction zone setting of the Oman-U.A.E. ophiolite (pink circle in Figure 1.2b and 1.3) within a southern marginal basin of the Neo-Tethys.

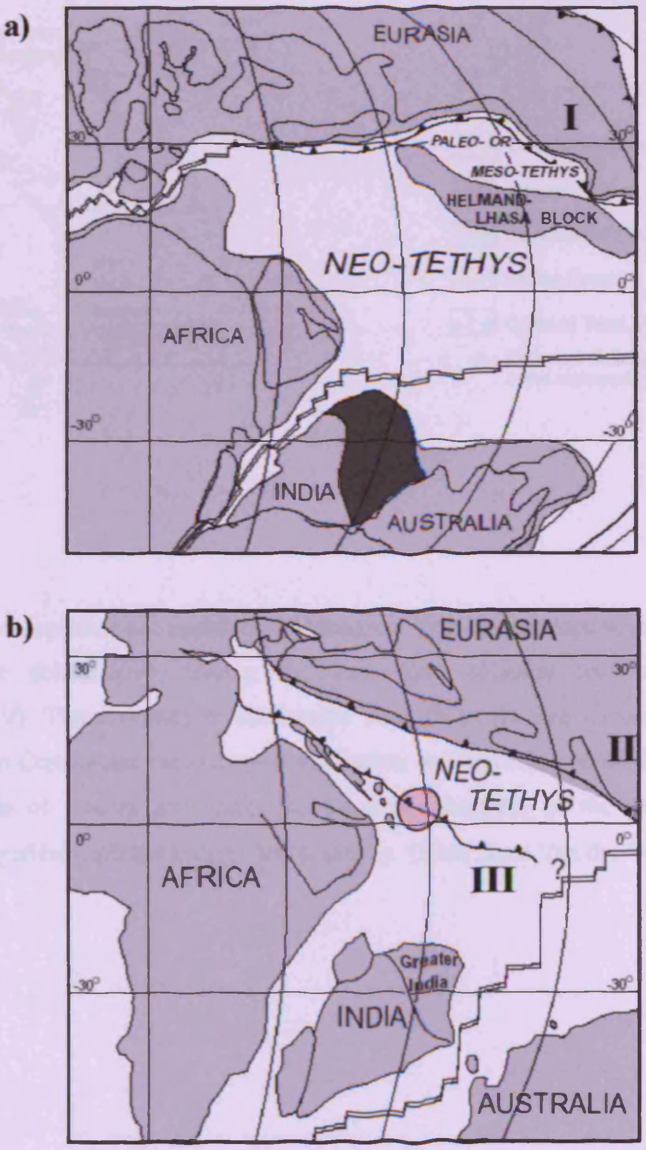

Figure 1.2 Palaegeographic map of a) Late Jurassic (150Ma) and b) Late Cretaceous (84 Ma). Northward dipping subduction zones marked I – III whereas the hashed are marks the likely location of the supra-subduction zone setting for the Oman-U.A.E. ophiolite. Taken from Van der Voo et al., (1999).

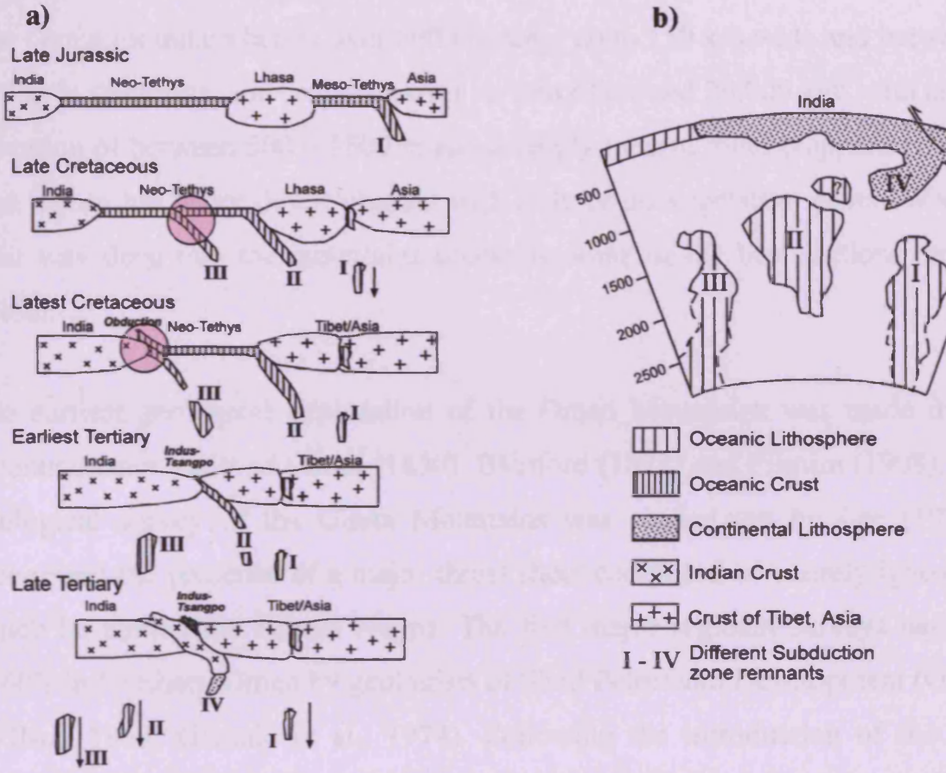

Figure 1.3: a) Cartoon depicting the evolution of Mesozoic Tethyan subduction zones (I, II, III) and the Tertiary lithospheric delamination during the India-Asia collision and continued north-south convergence (zone IV). The existence of subduction zone III in the late Cretaceous is inferred from evidence for mid-late Cretaceous intra-oceanic subduction and ophiolite obduction (pink circles) onto the northern margins of Arabia and India. B) Summary diagram of the remnant Tethyan slabs tomographically imaged beneath the Indian Ocean mantle. Taken from Van der Voo et al., (1999).

1.2 Geological setting of the ophiolite

The Oman mountain belt is over 600 km long, up to 150 km wide and between 5 and 10 km in thickness, and crops out over an area of around 20,000 km^2 with an average elevation of between 500 – 1500 m and a deeply incised relief (Lippard et al., 1986). The region has a dry desert climate with little or no vegetation cover. Wadis carve their way deep into the mountains accessing some of the best sections through the ophiolite.

The earliest geological exploration of the Oman Mountains was made during the reconnaissance visits of Carter (1850), Blanford (1872) and Pilgrim (1908). The first geological survey of the Oman Mountains was carried out by Lee (1928), who recognised the presence of a major thrust sheet composed of entirely igneous rocks, which he named the Semail Nappe. The first major regional surveys began in the 1960's in Northern Oman by geologists of Shell Petroleum Development (Oman) Ltd (Wilson 1969; Glennie et al., 1974). Following the introduction of the ophiolite concept (Coleman, 1971; Penrose Conference Participants, 1972), described in Section 1.3.1, it was recognised that the igneous rocks of Oman and the U.A.E. represent an ophiolite (Reinhardt, 1969; Allemann and Peters, 1972) and it was named the 'Semail ophiolite'. The geological map (scale 1: 500 000) and memoir produced by the Shell team (Glennie et al., 1974) has become the classic study of the Oman Mountains and formed the basis for all subsequent research (see Section 1.4).

Glennie et al., (1974) concluded that the Oman Mountains were formed by the deformation of a NE-facing Late Palaeozoic and Mesozoic continental margin by the obduction of oceanic rocks from the Neo-Tethys Ocean in the Late Cretaceous The obduction event produced a complex series of nappes thrust over the paraauthocthonous units of the Arabian margin. The allochthonous units consisted of deep ocean sedimentary rocks and ocean floor rocks with the Oman-U.A.E. ophiolite forming the uppermost unit. The allochthonous units formed a thrust sequence that propagated within a foreland basin during obduction, with distal-deepwater units overlying proximal-slope units and a mélange unit formed of mixed components, reworked from the units below and the ophiolite above, as the ophiolite bulldozed its way over the continental margin towards the Arabian platform.

The obduction of the Oman-U.A.E. ophiolite has a two part history. The first stage was detachment from the ocean floor very shortly after it was formed creating its metamorphic sole during south-westward intra-oceanic thrusting (Searle and Malpas, 1980; Tilton et al., 1981). The metamorphic sole describes the thin (up to 300-m-thick), fault-bounded sheets of highly strained, high-grade metamorphic rocks that occur structurally beneath the Oman-U.A.E. ophiolite. The metamorphic sole shows inverted metamorphic field gradients from granulite/upper amphibolite to lower greenschist facies in a structurally descending order (see review in Searle and Cox, 1999, for details). The metamorphic fabric is parallel to the banding and microstructure texture in the lowermost peridotites of the Mantle Sequence, indicating that the fabric within this Banded Unit is also related to emplacement (Boudier and Coleman, 1981; Searle and Cox, 1999).

Paleomagnetic studies have shown that the crust underwent a 145° clockwise rotation (Perrin et al., 1994 and 2000) while it was still magmatically active during intra-oceanic obduction in response to oblique collision oriented NW-SE along the Zagros Mountains.

The second stage was the emplacement of the ophiolite onto the Arabian continental margin as a crescent-shaped thrust sheet along the coast of the Sultanate of Oman and the United Arab Emirates. Granite and leucogranite dykes in the lowermost part of the mantle of the Khawr Fakkan Block (U.A.E) commonly contain muscovite, biotite, tourmaline, garnet, andalusite and cordierite (Searle and Cox, 1999). These granites are classified as "S-type" granites because of their peraluminous nature and derive from a metasedimentary source. Subduction of the leading edge of the Arabian continental crust resulted in crustal melting beneath the Oman-U.A.E. ophiolite (Figure 1.4), and formation and intrusion of these granites into the overlying mantle sequence (Searle and Cox, 1999). During this second stage of obduction, the ophiolite was faulted into twelve large tectonic Blocks (Figure 1.6).

Apart from gravitational collapse and gentle folding and up-lift in the late Tertiary there has been minimal post-emplacement deformation.

The Oman ophiolite was emplaced over the Arabian continental margin within less than 5 m.y. after the initiation of subduction beneath it (Hacker et al., 1996). Precise radiometric and isotopic dating of the sole rocks from various ophiolites and their metamorphic soles indicate that detachment from their oceanic settings and emplacement onto continental margins commonly took place within 5-10 m.y. (Wakabayashi and Dilek, 2000). Various obduction models have been proposed for ophiolites and depend on the preferred model for tectonic setting of the ophiolite. These are discussed in Section 1.3.

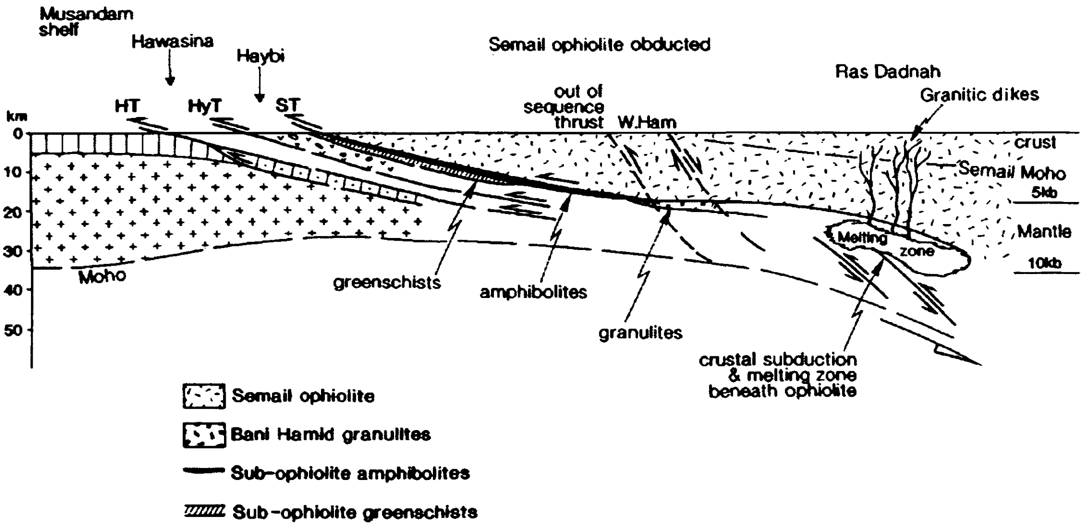

Figure 1.4: Emplacement of ophiolite into Arabian continental margin and partial melting of sedimentary rocks beneath to form the S-type granite dykes intruding the ophiolite above. Taken from Searle and Cox, (1999).

1.3 Stratigraphy of the Ophiolite

1.3.1 The Ophiolite concept

The internal structure of the Oman-U.A.E. ophiolite corresponds with that of the classic GSA Penrose Conference Participants (1972) definition of an ophiolite (Figure 1.5) which refers to a distinctive assemblage of mafic to ultramafic rocks. In a completely developed ophiolite, the rock types form the following stratigraphy, starting from the bottom and working up:

- **Ultramafic complex**, consisting of variable proportions of harzburgite, lherzolite, and dunite, usually with a metamorphic tectonic fabric (more or less serpentinized);

- **Gabbroic complex**, ordinarily with cumulus textures commonly containing cumulus peridotites and pyroxenites and usually less deformed than the ultramafic complex;

- **Mafic sheeted dyke complex**; wall-to-wall intrusion of dolerite dikes;

- **Mafic volcanic complex**, commonly pillowed;

- **Associated rock types** include (1) an overlying sedimentary section typically including ribbon cherts, thin shale interbeds and minor limestones; (2) podiform bodies of chromite generally associated with dunite; and (3) sodic felsic intrusive and extrusive rocks.

An ophiolite may be incomplete, dismembered, or metamorphosed. Faulted contacts between mappable units are common. The Penrose definition of ophiolites does not include any statement about emplacement mechanism(s) of ophiolites or its tectonic setting of its igneous origin.

The concept that ophiolites were fragments of ocean floor (Hess, 1965) was developed alongside plate tectonic theory with the following four main conclusions:

1. Wall-to-wall intrusion of dolerite dykes of the sheeted dyke complex within ophiolites signified their extensional, seafloor spreading origin. This was first identified in the Troodos ophiolite (Gass, 1968).

2. Ophiolites are slices of fossil oceanic lithosphere composed of oceanic crust and uppermost mantle. Tectonized harzburgites represent depleted refractory mantle deformed by convective flow beneath the spreading axis (Nicolas, 1989). Pyroxenites and gabbros constitute intrusive crustal bodies derived from partial melting of this mantle. The discovery of a mantle unit in ophiolites (de Roever, 1957; Gass and Masson-Smith, 1963) was a formal recognition of the fact that crustal units and mantle rocks in ophiolites were not the products of a single, comagmatic event as first proposed by Steinmann (1927).

3. Plutonic sequences represent solidified, fossil magma chambers (Gass, 1968). Ophiolite magma chamber models (reviewed in Thy and Dilek, 2003) are applied to the oceans because their magma chambers can not be directly observed (e.g. MacLeod and Yaouanq, 2000).

4. Ophiolites are fragments of fossil oceanic lithosphere that have been thrust over or "obducted" (Coleman, 1971) into continental margins at consuming plate boundaries (Dewey and Bird, 1971; Dewey, 1976).

The "Penrose-type" ophiolite model became an ideal analogue to explain the seismic velocity structure of modern oceanic lithosphere developed at fast-spreading, non-rifted ridges e.g. Pacific Ocean crust (Dilek et al., 1998). In contrast, the oceanic lithosphere of slow-spreading ridges has a different internal stratigraphy to that of the "Penrose-type" as it consists of mainly serpentinized peridotites capped by lavas and/or thin gabbroic rocks e.g. "Hess-type" crust (Hess, 1955; Cannat et al., 1995).

1.3.2 The Oman-U.A.E. Ophiolite

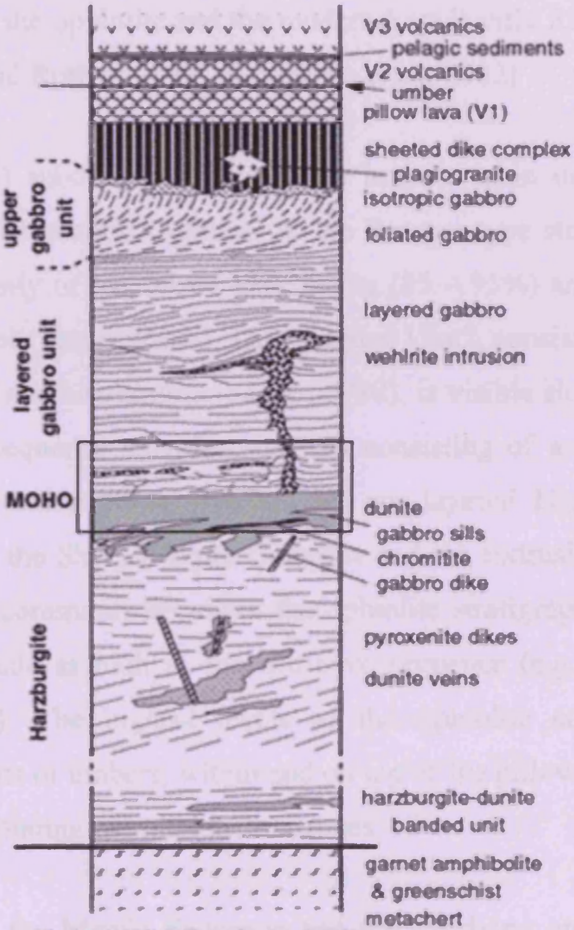

Nicolas (1989) & Ernewin et a. (1989)

Figure 1.5: An idealised stratigraphic cross-section through the Oman-U.A.E. ophiolite (not to scale). Taken from Nicolas (1989) after Ernewein et al., (1989).

The Oman-U.A.E ophiolite formed in the Neo-Tethys Ocean during the middle to late Cretaceous (Figure 1.2b). U/Pb zircon ages from plagiogranites in the crust dated by Tilton et al., (1981) range from ~97 and 93.5 Ma, with a mean age of 94.8 Ma. These dates are in agreement with hornblende $^{40}Ar/^{39}Ar$ ages of plagiogranites and gabbros for the crystallization of the crust between 95.4 – 94.5 Ma (Hacker et al., 1996).

All the stratigraphic components of the ophiolite as defined by the Penrose Conference Participants (1972) are present throughout the Oman-U.A.E ophiolite (Figure 1.5). The Oman-U.A.E. ophiolite formed by sea-floor spreading, leading to comparisons between the ophiolite and the modern East Pacific Rise (e.g. Lippard et al., 1986; MacLeod and Rothery, 1992; Girardeau et al., 2002)

Lippard et al., (1986) subdivided the ophiolite into its main units as follows. A mantle sequence (or Ultramafic Complex of the Penrose-type stratigraphy, Section 1.3.1), consisting mainly of tectonized harzburgite (85 – 95%) and dunite (5-15%), all of which are variably serpentinized. The "Banded Unit", consisting of metre-thick alternations of dunite and harzburgite (Searle, 1980), is visible along the base of the mantle. The crustal sequence was described as consisting of a Layered Series of cumulate peridotites and gabbros, overlain by non-layered High Level gabbros, which passed up into the Sheeted Dyke Complex and the Extrusive Sequence. Late Intrusive Complexes commonly cross-cut the ophiolite stratigraphy in the northern Blocks, and can intrude as high as the extrusive sequence (e.g. Browning, 1982; Umino et al., 1990). The highest levels of the ophiolite contain Fe-Mn-rich metalliferous sediments or umbers, within and on top of the pillow lavas, overlain by pelagic sediments, including radiolarian mudstones.

The contact between the Mantle Sequence and the overlying crustal layers of the ophiolite is a marked structural and petrological boundary between tectonized harzburgites below and overlying cumulate peridotites and gabbros that represents the sub-oceanic "Petrological Moho" (e.g. Greenbaum, 1972). The petrological Moho, marked on Figure 1.5, is not a simple boundary but rather a gradual passage from mantle to crust, hence the term Moho Transition Zone (MTZ) (Benn et al., 1988). Detailed observations from the Oman-U.A.E. ophiolite have demonstrated the complexity of the MTZ which displays large lateral variations in thickness and composition of ultramafic (dunites, wehrlites, and pyroxenites) and mafic (troctolites and gabbros) assemblages (Benn et al., 1988; Boudier and Nicolas, 1995; Korenaga and Kelemen, 1997; Jousselin and Nicolas, 2000a).

The extrusive sequence of lavas (or mafic volcanic complex) consists of up to 2 km of pillow lavas and scarce massive lava flows. In northern Oman, it has been subdivided into five major units on the basis of field appearance, petrography and geochemistry, each separated from the other by a more or less continuous layer of pelagic sediments (Pearce et al., 1981; Alabaster et al., 1982, Lippard et al., 1986). In stratigraphic order, starting with the oldest, they are: Geotimes, Lasail, Alley, Clinopyroxene-phyric and Salahi Units.

The late plutonic complexes represent high-level, magma chambers feeding the upper lava units (e.g. Browning, 1982). The Lasail Unit lavas are associated with localised cone-sheets and dyke swarms and the Late Intrusive Gabbro Bodies (clinopyroxene-series of differentiated gabbro to plagiogranite) and were interpreted as 'seamount'-type volcanism (Pearce et al., 1981; Alabaster et al., 1982; Lippard et al., 1986). The lavas of the Alley and the Clinopyroxene-phyric Units are associated with the development of graben structures and the Late Intrusive Gabbro Bodies (orthopyroxene-series of wehrlite to gabbro) following the 'seamount' eruptions.

The Oman-U.A.E. ophiolite reaches a maximum estimated thickness of 16-20 km. It comprises a 8-12-km-thick section of mantle peridotite overlain by a crustal section that includes gabbro (0.5 – 6.5 km thick), sheeted dykes (1 – 1.5 km thick), and extrusive rocks (0.5 – 2 km thick) (Boudier and Coleman, 1981; Pallister and Hopson, 1981; Lippard et al., 1986). The stratigraphy of each Block in the Oman-U.A.E. ophiolite is relatively consistent, although the thickness of individual units can vary considerably between locations (e.g. Nicolas et al., 1996). The volcanic stratigraphy is also spatially variable in thickness between Blocks and some sections do not include all the volcanic Units (Alabaster et al., 1982). The Lasail, Alley and Clinopyroxene-phyric lava Units only outcrop in northern Oman. Often the top part of the ophiolite sequence (the sheeted dykes and lavas) is incomplete or absent as is the case in Khawr Fakkan, Bahla, Sumail and Wadi Tayin Blocks (Figure 1.6).

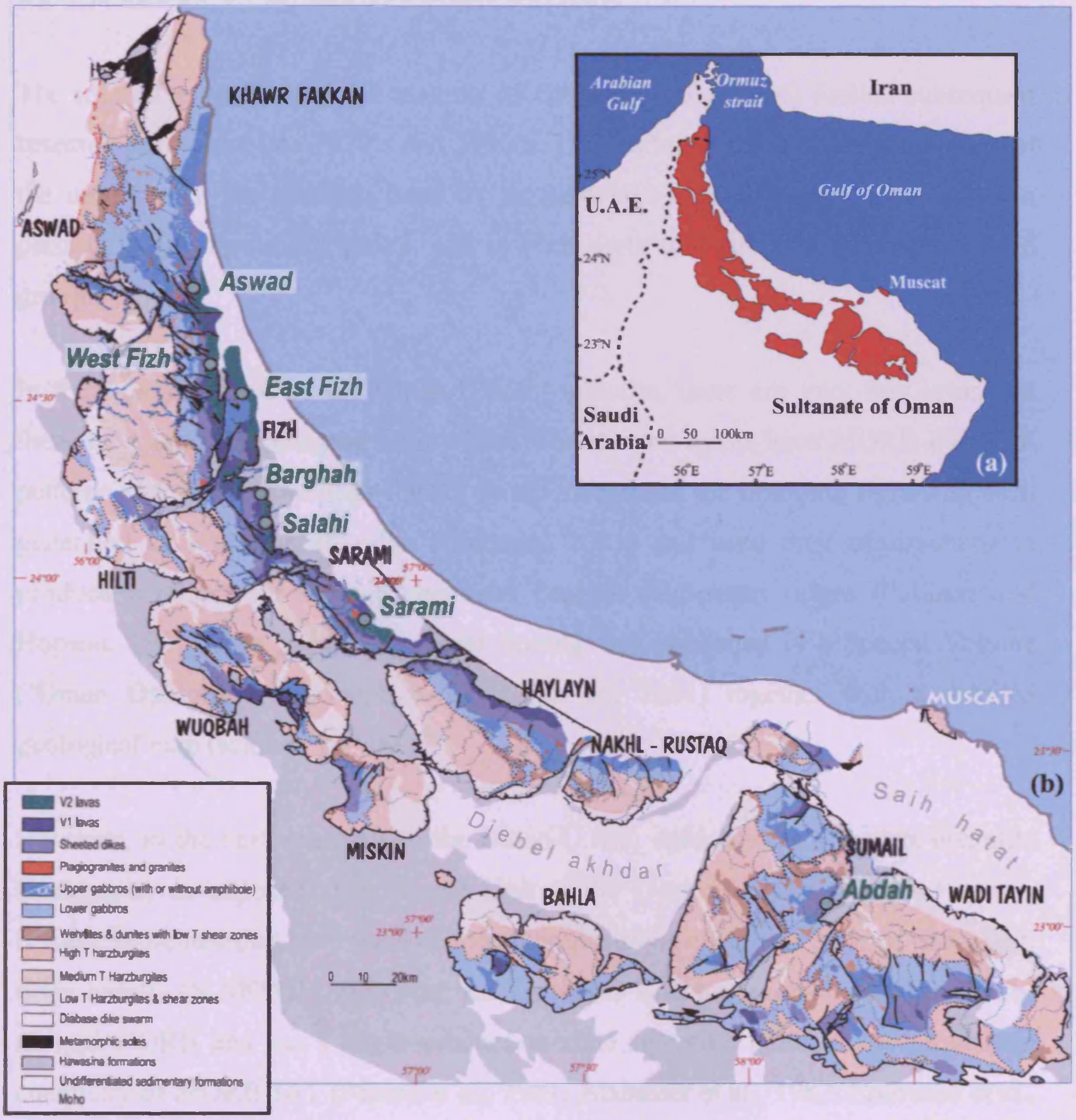

Figure 1.6: Geological map of the Oman-U.A.E. ophiolite (Taken from Godard et al., (2003) after Nicolas et al., (2000a); geographical map inset with ophiolite in red. Structural Blocks are labelled in black whilst town localities are in green. The mantle sequence is coloured brown and crust sequence is blue to purple).

1.4 Debate over the tectonic setting

The interest generated by the memoir of Glennie et al., (1974) fuelled subsequent research during the late 1970's and 1980's. This included more detailed mapping of the ophiolite in the southern parts by an American-funded group, in the northern parts by a British-funded group, and in both north and south by a French-funded group.

In the southern parts of the Oman-U.A.E. ophiolite, there are very few lavas and these have not been assigned to any Unit. The sheeted dykes have MORB-like REE patterns and so the American-funded group interpreted the ophiolite as having been generated at a mid-ocean ridge (Coleman, 1981) and used their observations to produce a model for magma chambers beneath mid-ocean ridges (Pallister and Hopson, 1981). The group's principal findings are published in a Special Volume ('Oman Ophiolite', J. Geophys. Res., vol. 86, 1981) together with a detailed geological map (scale 1: 100 000).

However, in the northern parts of the Oman-U.A.E. ophiolite the complete ophiolite stratigraphy is exposed. The lowest Unit is the Geotimes Unit which comprises basaltic tholeiites that have trace element compositions closest to those of mid-ocean ridge basalts (N-MORB). However, the Geotimes Unit has anomalously low Cr for normal MORB and has a slight subduction zone signature indicating a transitional chemistry of MORB-IAT (Pearce et al., 1981; Alabaster et al., 1982; Ernewein et al., 1988; Godard et al., 2003). The eruption of this Unit during accretion at a spreading centre is dated at 95.4 – 94.5 Ma from hornblende $^{40}Ar/^{39}Ar$ ages of plagiogranites and gabbros (Hacker et al., 1996).

The upper volcanic rocks of Lasail, Alley, and Clinopyroxene-phyric Units erupted shortly after (< 2Ma) the first Geotimes volcanic episode (Hacker et al., 1996). Their geochemistry reveals a strong island arc affinity, with variable enrichments in elements highly mobile in fluids. From these results, the British-funded group concluded that the ophiolite formed in a supra-subduction zone setting (Pearce et al., 1981; Alabaster et al., 1982; Lippard et al., 1986).

These two different interpretations for the origin of the Oman-U.A.E. ophiolite, mid-ocean ridge vs. supra-subduction zone setting, are still debated today, over 20 years later. The French-funded group has continued the structural mapping of the entire ophiolite for the last twenty years, developing a better understanding of magma chamber dynamics, mantle diapirs (see Section 1.2.2.) and ridge segmentation of a spreading centre. Their work is summarised in the special volume 'The Ophiolite of Oman' (Tectonophysics, vol. 151, 1988) and in Marine Geophysical Researches, vol.21 (2000). They still firmly believe the ophiolite formed at a mid-ocean ridge (e.g. Boudier et al., 1988, 2000; Juteau et al., 1988; Nicolas et al., 1988; 2000a; Godard et al., 2000; Le Mée et al., 2004; Monnier et al., 2006; Godard et al., 2006).

Interest in the northern blocks of Oman has continued to provide further evidence for a supra-subduction zone setting (e.g. Matsukage et al., 2001; Ishikawa et al., 2002, 2005; Ahmed and Arai, 2003; Kanke and Takazawa, 2005, 2006; Tamura and Arai, 2006; Arai et al., 2006). For example, boninites (primitive high-MgO andesites) are documented in the Alley Unit of the Fizh Block (Ishikawa et al., 2002). The Ph.D. project run in parallel with this thesis confirms the strong SSZ signature in the crust in the northern Oman-U.A.E. ophiolite (Lilly, 2006). This is discussed in more detail in Chapter 6.

At present, all of those concerned agree that the geochemical signature of the upper lavas originated from fluid-enhanced melting of depleted mantle, possibly incorporating the mantle residue after Geotimes (MORB) extraction (e.g. Pearce et al., 1981; Moores et al., 2000; Godard et al., 2003, 2006). The abundance of wehrlite and gabbronorites intruding the crustal sequence of the Oman-U.A.E. ophiolite also provides evidence for the involvement of water/fluids and enhanced degrees of melting (Ernewein et al., 1988; Browning, 1982; Boudier, et al., 2000; Nonnotte et al., 2005; Koepke et al., 2005; Feig et al., 2006).

However, it is the tectonic setting in which this fluid-enhanced melting occurred that is still contentious. Those in favour of the supra-subduction zone setting propose that the fluids derived from the slab of an immature, hot, shallow subduction zone (Pearce et al., 1981; Ishikawa et al., 2005). In contrast, those in favour of the mid-ocean ridge setting suggest that the fluids derived from seawater contamination, either at a mid-ocean ridge (e.g. Godard et al., 2003, 2006) or during obduction (e.g. Boudier and Coleman, 1981). Moores et al., (2000) tries to combine the two models by proposing that the mantle source under the mid-ocean ridge was abnormal, e.g. Indian Ocean MORB, and so preserved older slab-derived signatures.

1.4.1 Supra-Subduction Zone (SSZ) Model

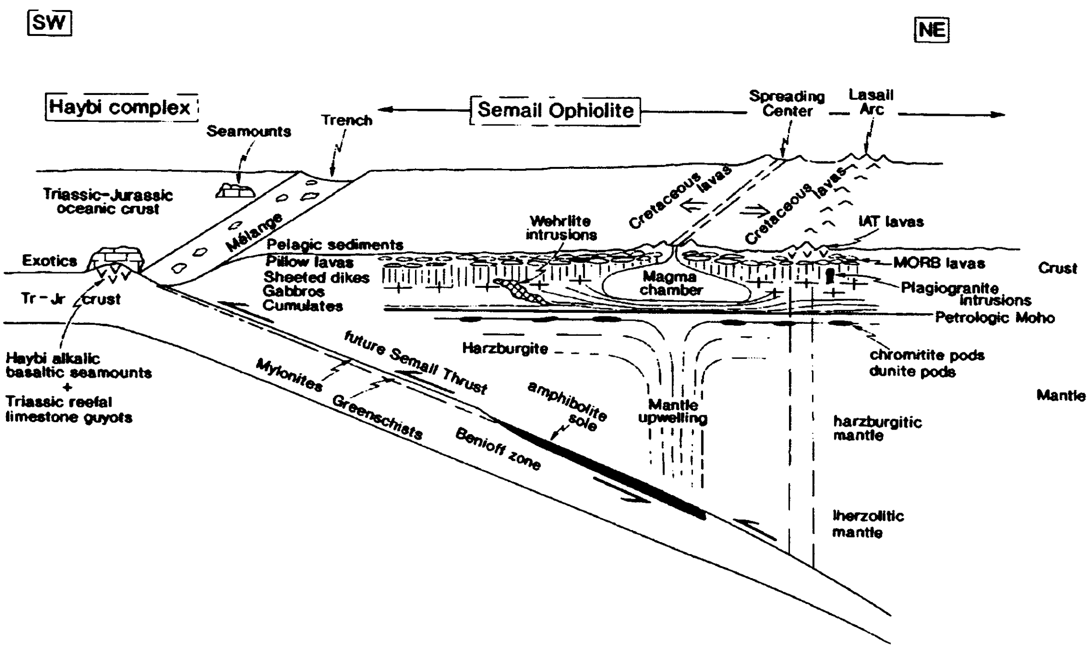

Figure 1.7: Reconstruction of the Oman-U.A.E. ophiolite immediately prior to emplacement, according to the supra-subduction zone setting model presented by Searle and Cox (1999), after the models of Searle and Malpas (1980, 1982), Pearce et al., (1981) and Lippard et al., (1986).

The supra-subduction zone setting was defined to explain ophiolites which have geochemical characteristics of immature island arcs but the structure of oceanic crust with no associated mature arc structure (Pearce et al., 1984) (Figure 1.7). SSZ-type ophiolites are characterized by tectonized harzburgite, dunite and podiform chromitite in the mantle, pyroxenites, wehrlites, norites and gabbronorites in the crust and lavas with subduction signatures (Pearce et al., 1984).

In the SSZ model, the fluid-enhanced melting was attributed to fluid derived from the slab of an immature, hot, shallow subduction zone (e.g. Pearce et al., 1981; Alabaster et al., 1982; Lippard et al., 1986). Ishikawa et al., (2005) demonstrated that boninite lavas from the Alley Unit of the Fizh Block, documented by Ishikawa et al., (2002), have trace element characteristics (such as LREE-enriched signatures) that require melt or fluid derived from dehydration of amphibolites of the metamorphic sole of the ophiolite. Ishikawa et al., (2005) proposed that these fluids triggered hydrous remelting of the shallow mantle, residual after MORB extraction. There is also evidence in the mantle of northern Oman to support the SSZ model. Tamura and Arai, (2006) found clinopyroxenes in orthopyroxenite mantle dykes that could be linked geochemically to the boninite lavas in the crust (Ishikawa et al., 2002). In addition, they proposed that the highly depleted harzburgites (high Cr# spinels >0.6) surrounding the orthopyroxenite dykes formed by fluid-enhanced re-melting of the mantle and that this melt formed the orthopyroxenite dykes. Fluids that were derived from the metamorphic sole and migrated along a mid-mantle shear zone may also have caused re-melting of the mantle to form highly depleted harzburgites of the Fizh Block (Matsukage et al., 2001; Kanke and Takazawa, 2005, 2006). Arai et al., (2006) demonstrated that late, discordant dunites and surrounding modified harzburgites exclusively contain high Cr# spinels (0.6 – 0.8) that formed by reaction of the mantle, residual after MORB extraction, with a depleted island-arc melt. Ahmed and Arai (2002) also proposed that boninitic magma formed a late, discordant chromitite pod in Wadi Hilti which is Cr-rich and PGE-rich.

Extensive geochemical work on chromitites from the Oman-U.A.E. ophiolite (e.g. Augé, 1987, Brown, 1980, 1982, Al-Aabed, 2000, Ahmed and Arai, 2002; Rollinson, 2005) demonstrated that the majority of chromitites, including Maqsad diapir, are of Al-rich, PGE-poor type. These were attributed to the involvement of MORB-type melts (Leblanc and Ceuleneer, 1992). Yet the role of water in the formation of chromitite (Edwards et al., 2000) and the abundant hydrous silicate inclusions present (Leblanc and Ceuleneer, 1992) actually favours a SSZ-type melt (Edwards et al., 2000). Schiano et al., (1997b) showed that, even though melt inclusions from Maqsad chromitite have trace element characteristics of MORB, they have an arc-like negative Nb anomaly and high Ba concentrations atypical of N-MORB. To counter this, Nicolas and Al Azri (1991) argued that seawater contamination could drive chromitite formation in a mid-ocean ridge environment. However, chromitite pods have never been found at a mid-ocean ridge, except for a micro-chromitite pod (< 3cm) from Hess Deep which does not contain primary hydrous silicate inclusions and formed from almost anhydrous primary MORB (Matsukage and Arai, 1998).

The rapid obduction of the ophiolite, < 5 m.y. after its formation, may explain the lack of volcanic arc edifices in SSZ-type ophiolites because of short-lived subduction and sudden “death” (e.g. Shervais, 2001). Petrological studies and thermal modelling of the “metamorphic soles” of ophiolites have shown that their accretion at the base of ophiolite likely took place at the inception of an oceanic subduction (Figure 1.7). This would have meant that inverted metamorphic field gradients developed at the top of the descending slab as it came into contact with progressively hotter, hanging-wall rocks (Hacker, 1990 and references therein). The amphibolites of the metamorphic sole of the Oman-U.A.E. ophiolite are geochemically dissimilar to the Cenomanian ophiolite volcanic rocks and are closest to the Haybi tholeiitic volcanic rocks of Triassic or Jurassic age (Searle, 1980; Searle and Malpas, 1982; Searle and Cox, 1999). This supports the model that a subduction zone existed underneath the Oman-U.A.E. ophiolite with older and colder volcanic rocks subducted along the footwall of the Semail Thrust. In this model, obduction initiated at the trench along the Semail Thrust welding the amphibolites of older origin to the sole of the ophiolite.

Suggested tectonic settings where SSZ-type ophiolites could be found at present include the forearc region (e.g. the Izu-Bonin-Mariana and South Sandwich forearcs: Parkinson and Pearce, 1998; Pearce et al., 2000; Ishiwatari et al., 2006), the back arc region (e.g. Lau and East Scotia back-arc basins: Dilek, 2003), and subduction-influenced mantle melting beneath oceanic spreading centres (e.g. Woodlark Basin and the Chile Ridge spreading centres: Dilek, 2003). These settings either recorded (as in the forearc and back arc cases) or are recording ("proto-ophiolites" such as the Woodlark Basin/ Chile Ridge spreading centres) the initiation of intra-oceanic subduction beneath ocean ridges to form an infant arc.

1.4.2 Mid-Ocean Ridge (MOR) Model

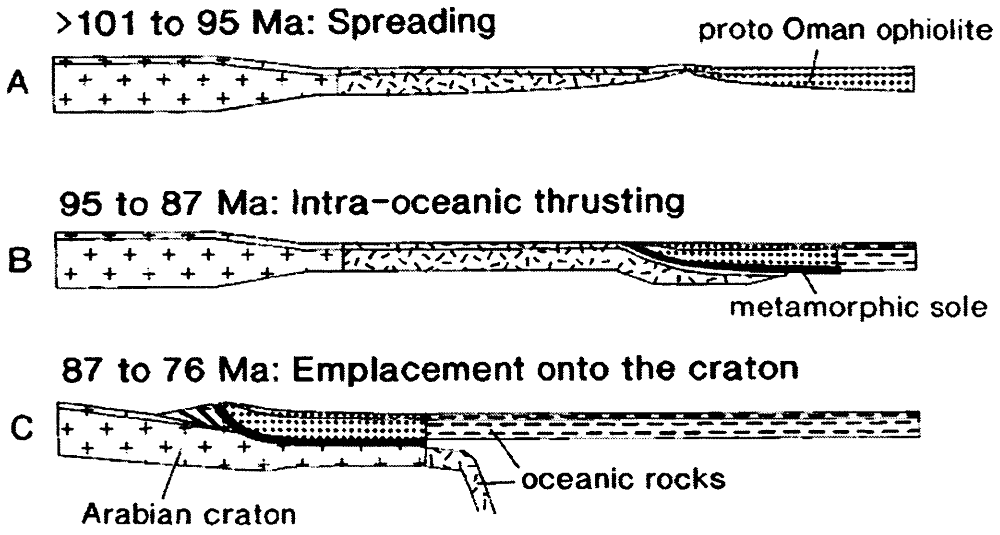

Figure 1.8: The mid-ocean ridge model for the formation and emplacement of the Oman-U.A.E. ophiolite, after Hopson et al., 1981; Pallister and Hopson, 1981; Boudier et al., 1985; Nicolas et al., 1988; Boudier and Nicolas, 1995; Hacker, 1991, 1994. Taken from Searle and Cox, 1999.

In the mid-ocean ridge model (Figure 1.8) there was no subduction zone present before obduction, but the oceanic lithosphere could not have been emplaced on the continent without some influence of a subduction zone. Boudier et al., (1981, 1988) and Boudier and Coleman (1981) proposed that the origin of the subduction signature was caused by seawater transported along lithospheric scale thrust faults into the shallow mantle at the onset of intra-oceanic thrusting of the ophiolite close to the ridge.

Another proposed mechanism for fluid-enhanced melting at a mid-ocean ridge prior to obduction is by the introduction of seawater into the shallow mantle at the ridge itself (e.g. Benoit et al., 1999; Boudier et al., 2000; Godard et al., 2003, 2006; Nonnotte et al., 2005). There is some evidence for this happening at modern-day mid-ocean ridges. For example, the Sr isotope signature of depleted gabbronorite cumulates drilled at DSDP Site 334 (Mid-Atlantic Ridge off the FAMOUS area) revealed that seawater introduction into residual peridotite at shallow depth beneath mid-ocean ridges resulted in hydrous partial melting to form the gabbronorites (Nonnotte et al., 2005). Nonnotte et al., (2005) and Koepke and Feig (2005) proposed that this mechanism could produce depleted melts, such as boninitic-andesitic magmas, which are classically attributed to subduction zones environments. As yet, no such magmas are documented from mid-ocean ridges.

In the Oman-U.A.E. ophiolite, clinopyroxenes in depleted gabbronorites (e.g. Benoit et al., 1999; Boudier et al., 2000) and some wehrlites (Koga et al., 2001) have the same trace element signature as MORB-like melts. Benoit et al. (1999) also demonstrated that the Oman gabbronorites have seawater isotopic signatures. These results imply, in this view, that some gabbronorites and wehrlites are related to the MORB-like spreading ridge rather than a SSZ setting. However, Adachi and Miyashita (2003) demonstrated that wehrlites and gabbronorites in Oman formed throughout all the magmatic episodes. Therefore, maybe both the influx of seawater from above and slab-fluids from below play a role in the formation of wehrlites and gabbronorites in the Oman-U.A.E. ophiolite.

A mechanism for seawater to reach the shallow mantle at a mid-ocean ridge setting requires a special type of hydrothermal circulation operating at very high temperatures. Boudier et al., (2000) proposed that this could take place as a tectonically active propagating ridge segments rotates, as identified in Oman. The hydrothermally-altered peridotite at mid-ocean ridges could then remelt by a hot intruding mantle diapir (Benoit et al., 1999).

Figure 1.8 displays the mid-ocean ridge model for the initiation of obduction at the ridge (Hopson et al., 1981; Pallister and Hopson, 1981; Boudier et al., 1985; Nicolas et al., 1988; Boudier and Nicolas, 1995; Hacker, 1991, 1994). Searle and Cox (1999) argued that, if the site of the initiation of the Semail thrust was at the actual ridge, the footwall (protoamphibolites of the metamorphic sole) would have to be the same age and composition as the ophiolite volcanic rocks above. Searle (1980) and Searle and Malpas (1982) demonstrated that the timing of metamorphism in the amphibolite facies sole was older than, and the composition different to, the ophiolite rocks. Thus obduction of the Oman-U.A.E ophiolite could not have initiated at a mid-ocean ridge.

Information on modern analogues comes from ocean drilling and ocean dredging. However, this restricts our knowledge of the lower crust and mantle to certain areas such as fracture zones. Hess Deep on the fast spreading East Pacific Rise is a good analogy for the Oman-U.A.E. ophiolite (Nicolas et al., 1988; Girardeau et al., 2002), and mantle has been sampled in that location (e.g. Dick and Natland, 1996; Arai and Matsukage, 1996). Macquarie Island ophiolite, Southern Ocean, is a very rare occurrence (comparable to Hess Deep) of young (9 Ma) ocean crust and mantle, exposed above sea level. Macquarie Island provides an important example of an ophiolite which represents young ocean floor that unequivocally had no influence from a supra-subduction zone setting (Varne et al., 2000).

For those who support the mid-ocean ridge model, the Oman-U.A.E. ophiolite has guided ideas on sea-floor spreading at mid-ocean ridges for the last 30 years. With regards to the mantle, these ideas include a better understanding of the kinematics of mantle flow beneath a spreading axis (e.g. Nicolas, 1986; Ceuleneer et al., 1988; Nicolas et al., 1988), ridge segmentation (e.g. e.g. Nicolas et al., 1988; Nicolas and Boudier, 1995, 2000; Nicolas et al., 2000a; Le Mée et al., 2004; Monnier et al., 2006) and melt flow and extraction of MORB in dunite channels (e.g. Kelemen et al., 1995, 1997b, 2000; Braun and Kelemen, 2002; Hirschmann, 1995).

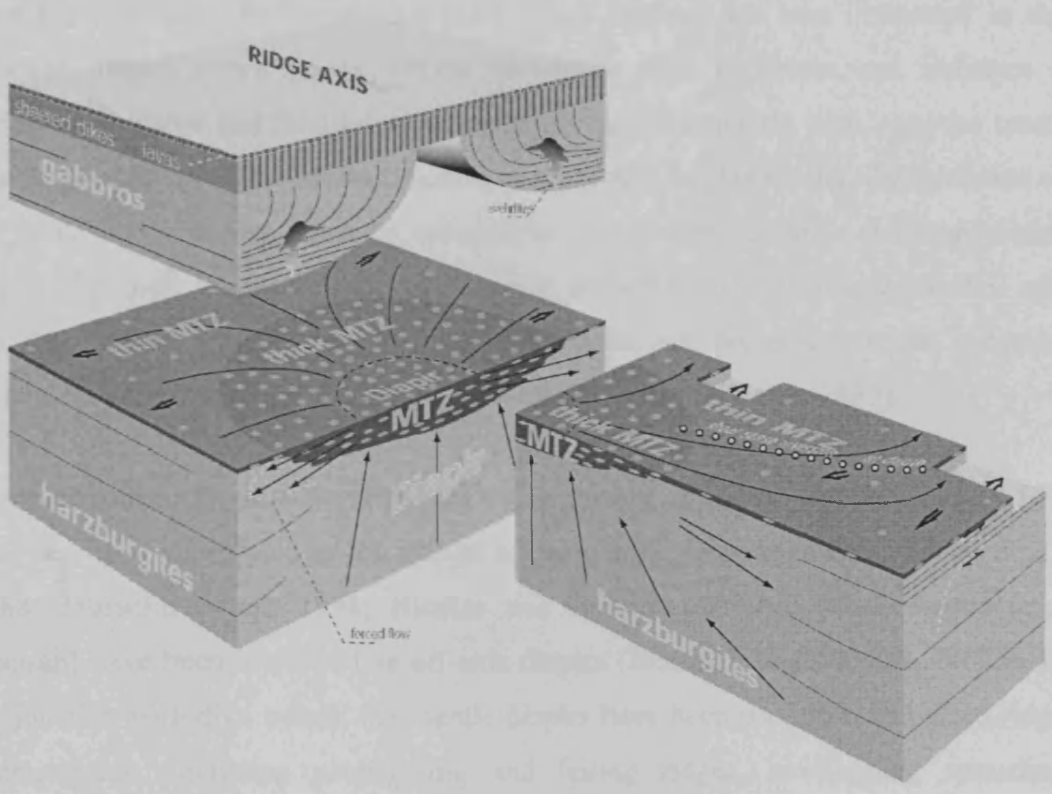

Figure 1.9: Sketch of a spreading ridge from the kinematic and structural analysis of the Oman-U.A.E. ophiolite. The mantle illustrates the contrast between a diapiric head covered by a thick MTZ and the surrounding areas associated with a thin MTZ, intrusions of wehrlite and a shear sense inversion at ~ 1km below the Moho. Taken from Nicolas et al., 2000a.

Figure 1.9 summarises the main findings from the Oman-U.A.E. ophiolite for the proposed kinematics of mantle flow beneath a spreading axis. The dominant mantle flow fabric is sub-parallel to the Moho with flow direction perpendicular to paleo-spreading axis, as determined from the sheeted dyke strike. Shear sense inversion is observed within this mantle fabric (e.g. Ceuleneer et al., 1988) and is explained by an actively uprising mantle and the subsequent forceful horizontal flow immediately below the Moho producing a large plastic strain. However, in some regions the mantle flow fabric is near-vertical, preserving an irregular cylinder 10-20 km wide perpendicular to the Moho. This vertical structure is ascribed to an uprising of focused flow inside a mantle diapir (e.g. Ceuleneer et al., 1988; Nicolas et al., 1988; Bartholomew, 1993; Nicolas and Boudier, 1995, 2000; Jousselin and Nicolas, 2000a). Mantle diapirs are associated with thick MTZ magmatic impregnations, and abundant wehrlites and chromitite pods. Such features are best illustrated in the Maqsad diapir, which is the richest chromitite area in Oman and indicates a particularly active and focused melt discharge from the mantle with vigorous crust-mantle interaction at the Moho (Nicolas et al., 1988). In this model, the thickness of the MTZ above a diapir can be reduced in thickness by tectonic thinning, which expels the melt mush into the lower crust as wehrlite intrusions (Jousselin and Nicolas, 2000a) (see Figure 1.9). Mantle diapirs are preserved in the ophiolite because it was frozen in situ during oceanic detachment (Nicolas, 1989).

Mapping of the ophiolite has identified the alignment of mantle diapirs (Figure 1.10). This has been interpreted as the axis of a propagating ridge segment (Nicolas et al., 1988; Jousselin et al., 1998; Nicolas and Boudier, 2000a). Other diapirs (e.g. Mansah) have been identified as off-axis diapirs (Jousselin and Nicolas, 2000b). In conjunction with dike trends, the mantle diapirs have been used to map palaeo-ridge segmentation, including propagating and failing ridges, overlapping spreading centres, and transform faults interpreted as resulting from spreading at a mid-ocean ridge (e.g. Jousselin and Nicolas, 2000b; Nicolas and Boudier, 2000a, Girardeau et al., 2002). However, there is no structural evidence to oppose the idea that they could be related to a supra-subduction zone setting.

The majority of harzburgites from Oman, except those mentioned already in Section 1.3.1, have compositions compatible with abyssal peridotites from mid-ocean ridges (i.e. Cr# spinel < 0.6 and low oxygen fugacity) (Monnier et al., 2006). High resolution sampling of harzburgites along the palaeo-ridge axis for the entire length of the ophiolite revealed a periodicity in Cr# of spinel which LeMeé et al., (2004) and Monnier et al., 2006) attributed to the spatial variation in partial melting associated with ridge segmentation. This periodicity matched diapiric upwellings mapped in the mantle by Nicolas et al., (2000a). The chemistry of the basal lherzolites in the northern Fizh Block was also attributed to processes at a failing ridge and to detachment of the ophiolite at a mid-ocean ridge (Takazawa et al., 2003).

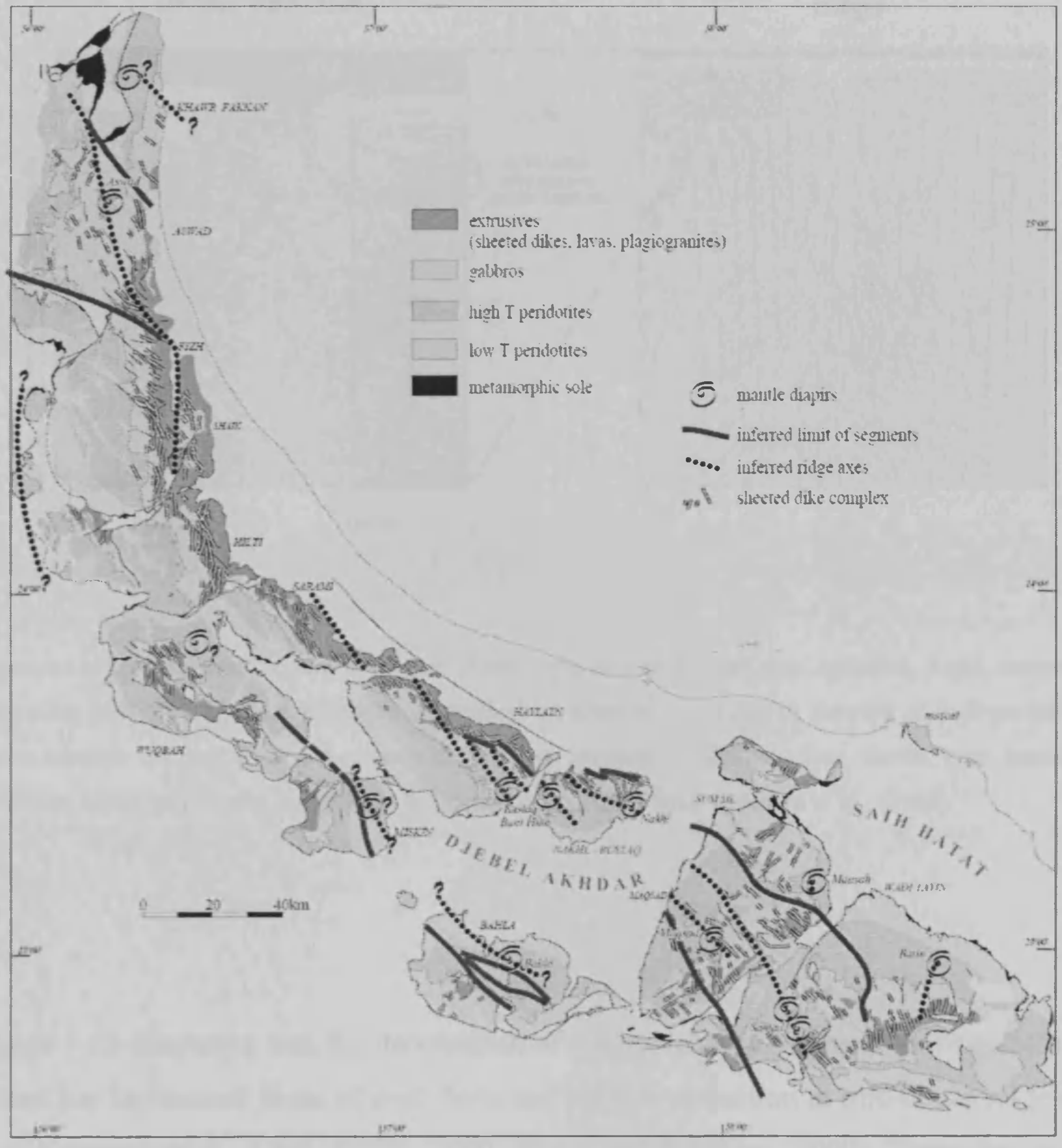

Figure 1.10: Map of the Oman-U.A.E. ophiolite illustrating the present state of understanding of the ridge system. Taken from Nicolas et al., (2000b).

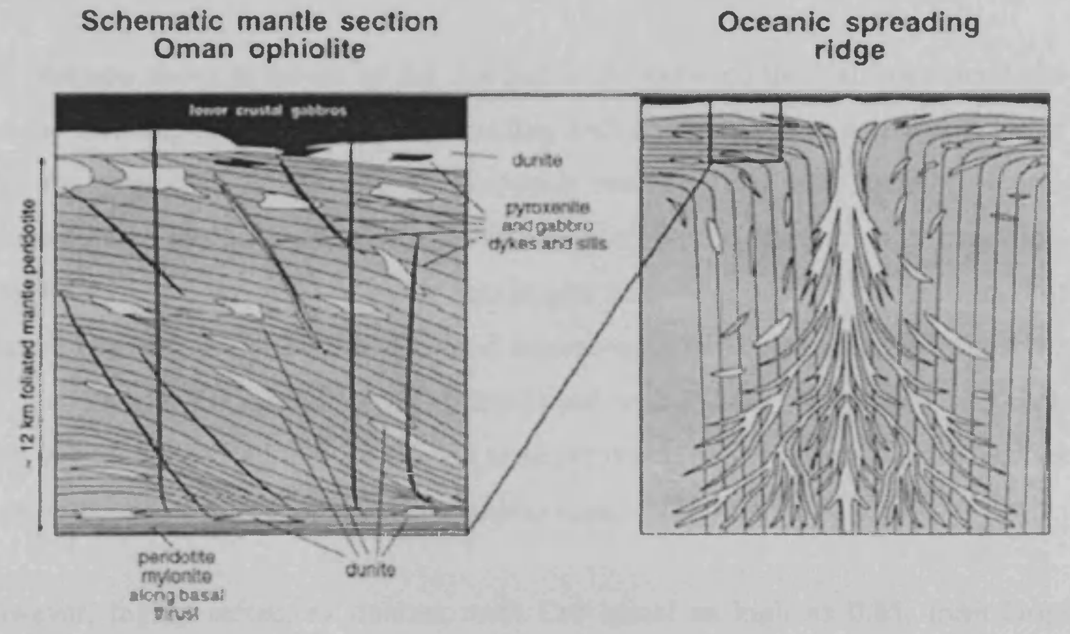
Schematic mantle section Oman ophiolite

Oceanic spreading ridge

Figure 1.11: Left, schematic cross-section of Wadi Tayin section of the Oman ophiolite. Right, cartoon illustrating possible ridge-axis geometry of residual harzburgite, a coalescing network of high-porosity dunite conduits for melt flow and oceanic lower crust. Shading as follows: white, dunite; grey, mantle peridotite; blank, pyroxenite and gabbro dykes and sills. Taken from Kelemen et al., (1995).

Figure 1.11 illustrates that the distribution of dunite veins in the mantle of southern Oman has influenced ideas of melt flow and MORB extraction at mid-ocean ridges (e.g. Kelemen et al., 1995, 1997b, 2000; Braun and Kelemen, 2002). These dunites have spinel Cr# similar to that of MORB spinels (<0.6).

The composition of mid-ocean ridge basalts requires that migrating melts were isolated from reaction with the uppermost mantle. Kelemen et al., (1990) proposed that this was achieved by chemically-isolated transport through dunite conduits. In this model, dunite formed by in situ replacement of the residual harzburgite by the following melt-rock reaction:

Orthopyroxene + Melt (1) = Olivine+ Chrome-spinel + Melt (2)

The reaction above is driven by the disequilibrium between the wall-rock peridotite and the invading melt (melt-1). The invading melt originated from a greater pressure than the peridotite at the site of melt-rock reaction, and was therefore silica-undersaturated (Jacques and Green, 1980) resulting in the dissolution of the silica-rich phase (orthopyroxene) from the harzburgite wall-rock, and the crystallization of relatively silica-poor phases (olivine and chrome-spinel). This reaction increased the silica content of the ascending melt (melt-2) and replaced the surrounding wall-rock with dunite, which includes little or no orthopyroxene, and required focused, porous flow of the reactive melt on an inter-granular scale.

However, highly refractory dunites, with Cr# spinel as high as 0.85, form large dunite bodies (up to 30m) in the lower mantle of the Haylayn Block and demonstrate that not all dunites represent the melt circulation that was responsible for the accretion of the crust and that 'true' MORB conduits were highly focused (Suhr, 2003). This affects the Kelemen et al., (1995) model for melt flow under a mid-ocean ridge which assumed that the dunites are all related to the same generation of MORB melt.

1.5 Aims and content of thesis

This thesis focuses on the mantle section of the U.A.E. and will complement the work of Lilly (2006) on the corresponding crustal sequence, thereby providing a complete picture for the tectonic evolution of the northern Oman-U.A.E. ophiolite. Therefore this study aims to do the following:

1) Investigate, using chrome-spinel geochemistry, the mantle processes associated with a switch in tectonic setting from mid-ocean ridge spreading to a supra-subduction zone setting.

2) Relate the mantle sequence to the corresponding crustal sequence in order to investigate whether melt infiltration in the upper mantle is representative of the magmatism in the crust as documented by Lilly (2006) for the U.A.E.

This thesis comprises a further 6 chapters:

Chapter 2: Geology of the U.A.E. mantle and MTZ. Geology of the study area, field observations of the ultramafic units and the sampling strategy are described.

Chapter 3: Characterisation of the U.A.E. ultramafic rocks. Classification of the ultramafic rocks into rock types, microstructure types and spinel types using both petrography and some whole rock geochemistry. GIS is used to illustrate the spatial distribution of the petrographical features.

Chapter 4: Tectonic discrimination of the U.A.E. peridotites. Chrome-spinel geochemistry is used to determine the petrogenetic and tectonic history of the peridotites.

Chapter 5: New developments in the tectonic discrimination of chrome-spinel: analysis of gallium by Laser Ablation-ICP-MS. A new method for the analysis of Ga in chrome-spinel by LA-ICP-MS is applied to peridotites from both modern-day oceanic settings and the U.A.E. ophiolite in order to develop a new discrimination diagram.

Chapter 6: Tectonic evolution of the northern Oman-U.A.E. ophiolite. Comparisons are made between the mantle sequence and the crustal sequence and the evolution of the ophiolite in time and space is discussed.

Chapter 7: Conclusions. Summary of each Chapter and concluding with key advances and future recommendations for research.

Chapter 2: Geology of the U.A.E. mantle and MTZ

The United Arab Emirates hosts the three most northerly blocks of the Oman-U.A.E. ophiolite (Figure 2.1); from the south working northwards they are Fizh (largely in Oman), Aswad (largely in U.A.E) and Khawr Fakkan (entirely U.A.E.). The Khawr Fakkan Block (also spelt Khor Fakkan or Khor Faqqan), is 50 km long and 35 km wide with an area of approximately 870 km^2 (Lippard et al., 1986). The Aswad Block is one of the largest massifs in the entire ophiolite belt, covering over 2000 km^2 (Nicolas et al., 2000b). It is approximately 75 km long and up 40 km wide, although it extends another 15 km westward under the Quaternary sands. The Fizh Block exposed in the U.A.E. is only 60km^2 in area.

Compared to the detailed research taken place in Oman during the last thirty years, the ophiolite blocks in the U.A.E. have remained largely unstudied, apart from some structural mapping (Ceuleneer et al., 1988; Nicolas et al., 2000a, b), small isolated studies on chromitites (Al-Aabed, 2003) and the granitoid intrusions of the Dadnah region (Peters and Kamber, 1994; Cox et al., 1999; Searle and Cox, 1999). More recently, the Emirate of Fujairah was surveyed, and maps published at 1: 50 000 scale, by the Council for Geoscience (South Africa) (Grantham et al., 2003). However, recent geological mapping, by the British Geological Survey (2002 – 2006), represents the first detailed study of the entire outcrop of the ophiolite within the U.A.E. and has resulted in 14 published maps at 1:25 000, 1:50 000 and 1: 100 000 scales with associated map sheet explanations and a detailed Geological Report (Styles et al., 2006).

Figure 2.1: Geological map of the Oman-U.A.E. ophiolite (Taken from Godard et al., 2003 after Nicolas et al., 2000a); geographical map inset (a) with ophiolite in red. Structural massifs labelled in black whilst town localities in green. Mantle (brown) and crust (blue-purple). U.A.E. field area (dashed box) hosts the three most northerly Blocks.

2.1 Geology of the U.A.E.

The BGS mapping project divided the geology of the Emirates into five main components (Figure 2.2): (1) a middle Permian to lower Cretaceous passive margin with carbonate platform sequence (Hajar Supergroup) forming the Musandam Peninsula; (2) a deformed sequence of limestones and associated deepwater sedimentary rocks, with minor volcanic rocks, which crops out in the Dibba and Hatta Zones; (3) a polydeformed sequence of metamorphic rocks, seen in Masafi-Ismah and Bani Hamid areas; (4) a **Late Cretaceous Oman-U.A.E. ophiolite**; and (5) an upper Cretaceous to Neogene foreland basin cover sequence. The following geological description of each mapping component is summarised from the BGS report (Styles et al., 2006).

2.1.1 Musandam Peninsula

The Musandam Peninsula lies at the northernmost part of the study area (Figure 2.2) and is truncated to the south by a high angle brittle fault of the Dibba Zone (see Section 2.1.2). The geology of the Musandam Peninsula is dominated by the Hajar Supergroup, which describes a carbonate platform sequence that was deposited on the Arabian continental passive margin of the Neotethys Ocean between the middle Permian and early Cretaceous (Lees, 1928; Glennie et al., 1974; Robertson and Searle, 1990; Robertson et al., 1990a, b). The succeeding late Cretaceous succession of the Aruma Group includes tectonically-active deposition following uplift and erosion of the carbonate platform associated with initiation of the foreland basin during ophiolite obduction.

2.1.2 The Dibba and Hatta Zones

The Dibba and Hatta Zones comprise folded and faulted Late Triassic to Upper Cretaceous sedimentary and volcanic rocks deposited in the deeper parts of the Neotethys Ocean. The deep water sedimentary sequence includes turbiditic limestone, pelagic lime-mudstones, siliceous mudstones and cherts. Deposition within the Neotethys was punctuated by localised volcanism leading to the eruption of the Dibba and Hatta volcanic formations, both mid-late Cretaceous in age (see review Styles et al., 2006). These sedimentary and igneous rocks were deformed during the north-west propagating obduction of the Oman-U.A.E. ophiolite resulting in a complex imbricate thrust stack (Glennie et al., 1974; Lippard et al., 1982; Searle et al., 1983; Searle, 1985). A number of regional scale olistostrome units were generated in response to active faulting during the break up of the platform margin and obduction of the Oman-U.A.E. ophiolite during the Upper Cretaceous.

The **Dibba Zone** truncates the northernmost limit of the ophiolite belt along the Wadi Sidr Fault system (Figure 2.2). The Dibba Zone forms a 10 – 15 km wide NE-SW trending belt, bounded by high angle brittle faults. Serpentinites and relatively fresh ultramafic rocks are found within several units of the Dibba Zone, often marking major faults at a relatively low structural level within the imbricate thrust stack (see Section 2.2). The largest outcrop of ultramafic rocks in the Dibba Zone, known as the Jebal As Sudah ultramafic body, was presumed to be an infolded and thrusted fragment of the ophiolite (Lippard et al., 1982; Robertson et al., 1990a). However, the BGS mapping found no overturning associated with regional scale nappes and interpreted it as a separate slice of mantle incorporated into the thrust stack ahead of the advancing obducting ophiolite.

The **Hatta Zone** is a WNW-ESE trending belt bounded by high angle faults (e.g. Wadi Hatta), which, at 3 to 10km wide, separates the Aswad Block in the north from the Fizh Block in the south forming a window through the ophiolite into the deep-water sedimentary and volcanic rocks below. The Hatta Zone also has low-medium grade metamorphic rocks, such as quartz schist, quartzite, meta-mafic schist and calc silicates, restricted to narrow, fault bounded slices along the contact with the ophiolite, as a result of ophiolite emplacement.

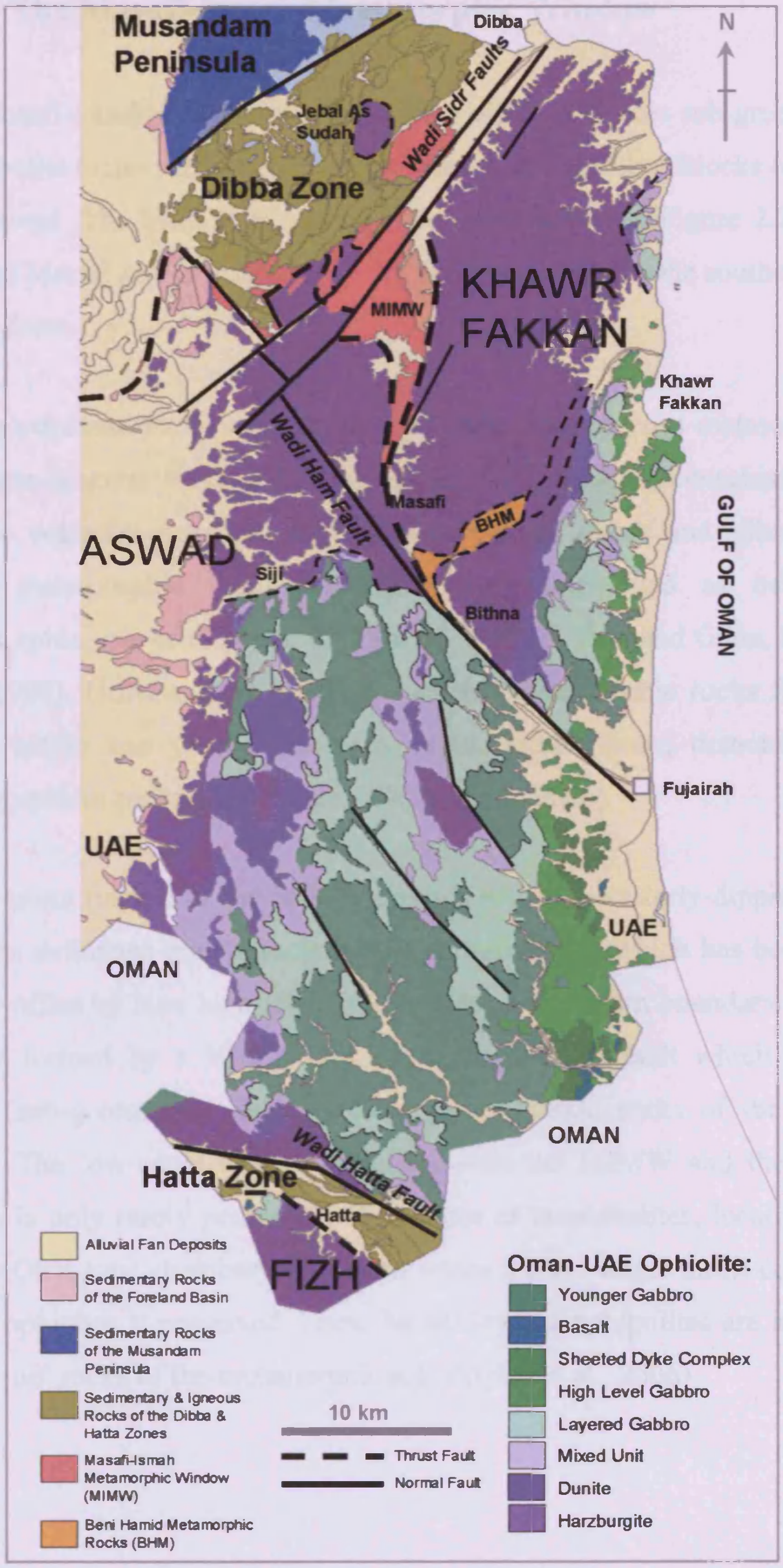

Figure 2.2: Geological Map of the United Arab Emirates. Modified from the BGS geological map at scale 1: 250 000. For location see Figure 2.1.

2.1.3 The Masafi-Ismah Metamorphic Window

The Masafi-Ismah Metamorphic Window (MIMW) reveals sub-greenschist to upper amphibolite facies metamorphic rocks beneath the ophiolite Blocks of Khawr Fakkan and Aswad. The MIMW is a triangular-shaped window (Figure 2.2) which widens north of Masafi and is truncated by the Wadi Sidr faults at the southern margin of the Dibba Zone.

The polydeformed rocks of the MIMW comprise quartzose metasedimentary rocks and meta-igneous rocks (MORB-type) as well as sub-greenschist facies alkaline basaltic volcanic rocks and associated deep-water cherts and siliceous mudstones. These metamorphic rocks were previously interpreted as belonging to the metamorphic sole of the ophiolite (Searle, 1980; Hacker and Gnos, 1997; Searle and Cox, 1999). However, the BGS showed that metamorphic rocks from MIMW are found within one of the mélanges of the Dibba Zone, demonstrating that the metamorphism predated obduction (Styles et al., 2006).

The western margin of the MIMW has a low-angle, westerly-dipping thrust contact with the deformed mantle rocks of the Aswad Block, which has been modified and locally offset by later high-angle brittle faults. The eastern boundary of the MIMW is largely formed by a NNE-SSW-trending high-angle fault which juxtaposes low-grade (sub-greenschist facies) rocks against mantle rocks of the Khawr Fakkan Block. The low-angle thrust contact between the MIMW and the Khawr Fakkan mantle is only rarely preserved. Thin slices of amphibolites, locally garnet-bearing with MORB-type chemistry, are found where the low-angle thrust contact at the base of the ophiolite is preserved. These MORB-type amphibolites are interpreted as the only 'true' rocks of the metamorphic sole (Styles et al., 2006).

2.1.4 The Beni Hamid Metamorphics

The Beni Hamid Metamorphics (BHM) consists of high-grade metamorphic rocks that form a series of tectonic slivers within the ophiolite Block of Khawr Fakkan (Figure 2.2). The polydeformed rocks of the BHM comprises of quartzites, calc-silicates, marbles and metamafic rocks (Gnos and Nicolas, 1996; Searle and Cox, 1999; Styles et al., 2006). The SW-NE trending bounding thrusts dip moderately steeply SE and converge to the east to form a single, subvertical ductile shear zone enclosing a thin 'tail' of mylonitized metasedimentary rocks. Serpentinite mylonite is found up to 5 – 10m from the contact with the surrounding mantle indicating that a sliver of Beni Hamid metamorphic rocks was emplaced into the peridotites as a high temperature shear zone within the mantle of Khawr Fakkan.

The Beni Hamid Metamorphics have previously been interpreted as the highest-grade rocks found from the metamorphic sole of the Oman-U.A.E. ophiolite (Gnos, 1992; Searle and Cox, 1999). However, the BGS propose that the metamorphism was pre-ophiolite in age and was part of the continental basement, incorporated into the mantle shear zone of Khawr Fakkan upon obduction (Styles et al., 2006).

2.1.5 The Oman-U.A.E. ophiolite

2.1.5.1 Stratigraphy

The recent mapping by the BGS divided the ophiolite into three main components: the **mantle section**, an **early crustal section** and a **later magmatic suite**, which can be recognised in all three Blocks of the U.A.E. The ophiolite stratigraphy, using the Moho Transition Zone as a palaeo-horizontal marker, is almost horizontal in the Aswad Block compared to a moderately steep easterly dip in the Fizh and Khawr Fakkan Blocks to the south and north, respectively.

The mantle and early crustal sections represent the classic 'Penrose-type' ophiolite stratigraphy (Chapter 1). The **mantle section** consists of mainly harzburgite with subordinate dunite and chromitite. The mantle rocks pass up into the crustal succession via a very complex zone known as the Moho Transition Zone (MTZ), which was subdivided by the BGS into two components (massive dunite and the 'Mixed Unit'). The **early crustal section** consists of massive dunite, layered gabbros and high-level (Mirbah and Kalba) gabbros, passing up into the Sheeted Dyke Complex and the pillow basalts.

The **later magmatic suite** is made up of intrusive bodies and dykes that cut the mantle section and the early crustal section. It comprises a very heterogeneous assemblage of rocks, including pyroxenites, peridotites (mainly wehrlites), gabbros and microgabbros, tonalites and mixed intrusions. The members of this sequence often exhibit complex, mutually-intrusive relationships, showing that they are part of a polyphase suite. Large amounts of these later magmatic rocks are present in the MTZ, in an assemblage the BGS mapped as the "Mixed Unit" (MU). The MU includes a variety of mafic and ultramafic rocks with very complex field relationships (see Section 2.3.4). At slightly higher levels in the crustal section, voluminous wehrlite bodies intrude the layered gabbros. Gabbroic complexes (the Fujairah and Bithnah gabbros), with associated felsic intrusions, also represent the younger magmatic event within the higher levels of the crustal sequence. Mafic dykes of varying ages are found throughout the ophiolite sequence. Among the youngest intrusions are a series of granite sheets that are chiefly intruded into rocks of the mantle section and the lower crustal section in the Khawr Fakkan Block.

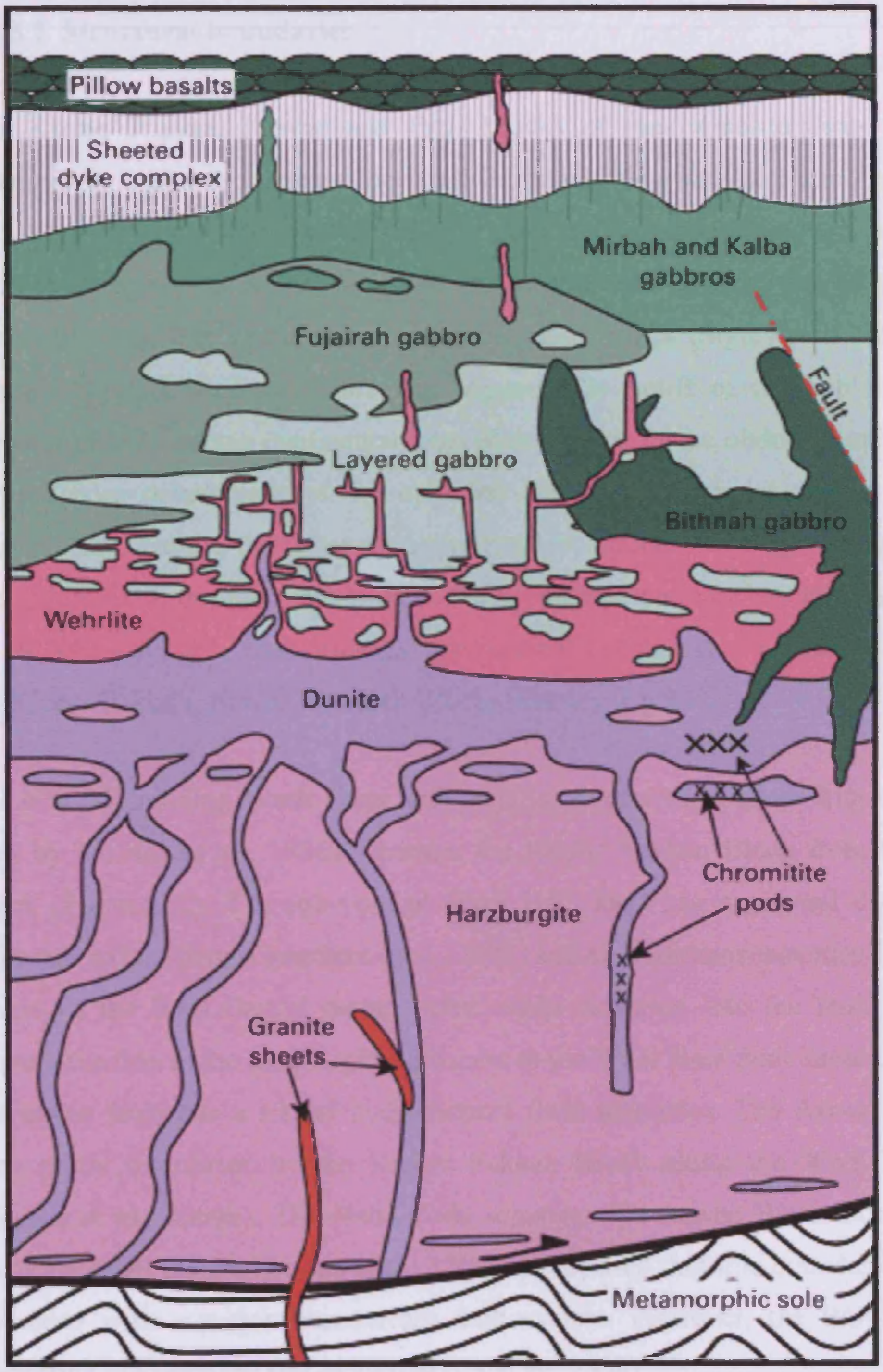

Figure 2.3: Schematic diagram illustrating the generalised ophiolite sequence as identified by the BGS mapping project. Copyright: U.A.E. Ministry Report (Styles et al., 2006).

2.1.5.2 Structural boundaries

The Khawr Fakkan, Aswad and Fizh Blocks of the ophiolite thrust sheet are separated by major fault zones: the Wadi Ham fault zone and the Hatta Zone (Figure 2.2). These faults were originally ductile shear zones, initiated at high temperature close to the spreading ridge system, but have been reactivated by late brittle faulting commonly resulting in magnesite veins and fault rocks (Styles et al., 2006). The brittle reactivation of the faults was triggered by uplift of the ophiolite due to rebound of the Arabian continental crust after loading of the obducted ophiolite slab and offshore detachment of the ophiolite from the remainder of the Neotethys oceanic slab. Unlike the other ophiolite massifs, which broke up during and after obduction, these three Blocks in the U.A.E. remained more or less intact (Nicolas et al., 2000b), with only post-orogenic gravitational collapse causing variable tilting of the Khawr Fakkan, Aswad and Fizh Blocks (Section 2.1.5.1).

The NW-SE trending **Wadi Ham** fault zone (also referred to as the Masafi-Fujairah fault by Nicolas et al., 1988) separates the Khawr Fakkan Block from the Aswad Block (Figure 2.2). The sub-vertical Wadi Ham fault has a sinistral displacement estimated to be 50km (Grantham et al., 2003) and also contains tectonically-bounded slivers of the Bani Hamid metamorphic rocks deflected into the fault. Extensive serpentinization in the harzburgites adjacent to the Wadi Ham fault demonstrates that this major fault was a site of hydrothermal fluid migration. The Aswad Block has been partly overthrust by the Khawr Fakkan Block along the Wadi Ham fault (Nicolas et al., 2000b). The Hatta Zone separates the Aswad Block from the Fizh Block (Section 2.1.2). Nicolas et al., (2000b) proposed that this boundary originally coincided with a major transcurrent fault system. However, the BGS found no supporting evidence for this model (Styles et al., 2006).

The BGS mapping of the ophiolite in the U.A.E. identified, for the first time, significant structures within the Khawr Fakkan and Aswad Blocks, dividing them further (Figure 2.2) (Styles et al., 2006). Within the Khawr Fakkan Block, a major ductile shear zone (Beni Hamid Shear Zone, Section 2.1.4) extends north-north-east from Beni Hamid window, dividing the Block into two domains (Khawr Fakkan North and South). Similarly, in the Aswad Block, a low-angle shear zone (Siji-Bithna Shear Zone) trending west from Bithna separates the Aswad North from Aswad South (Figure 2.4).

2.1.6 Post Cretaceous Deposits

Obduction resulted in the loading of the Arabian Platform, leading to the development of a foreland basin which occupied a depression between the ophiolite and the emergent peripheral swell. This basin was filled by a late Cretaceous to Palaeogene cover sequence of fluctuating marine and terrestrial deposits with weathering and erosion of the emergent ophiolite. The post-Cretaceous deposits are exposed largely along the western edge of the Hajar Mountains and in outliers in the desert west of the mountains. Where the western edge of the ophiolite is covered by Quaternary deposits and the encroaching desert sand, the serpentinised harzburgite shows a dramatic upward increase in the abundance of Mg-carbonate and silica veins forming silicified serpentinite (Styles et al., 2006). The carbonated and silicified serpentinite are thought to have been formed by tropical weathering and groundwater alteration following the uplift of the mountains during the Miocene to recent time.

The most recent geological component of the U.A.E. is the undeformed Quaternary to Recent aeolian and alluvial superficial deposits. During the Quaternary, the complex interplay between fluvial, aeolian and marine processes was driven principally by climatic changes associated with high latitude glaciations (Styles et al., 2006). Alluvial fan deposits emanate from the mouths of the wadis draining the mountains. In the west, where the mountains give way to the wide desert plains, the extensive alluvial fan deposits composed of ophiolite-derived gravel are partially overridden by aoelian sand dunes. In the mountains, the wadis are floored with alluvium and dissected older terrace deposits, with screes and alluvial fans on the mountain slopes.

2.2 The Study Area: Ultramafic Domains

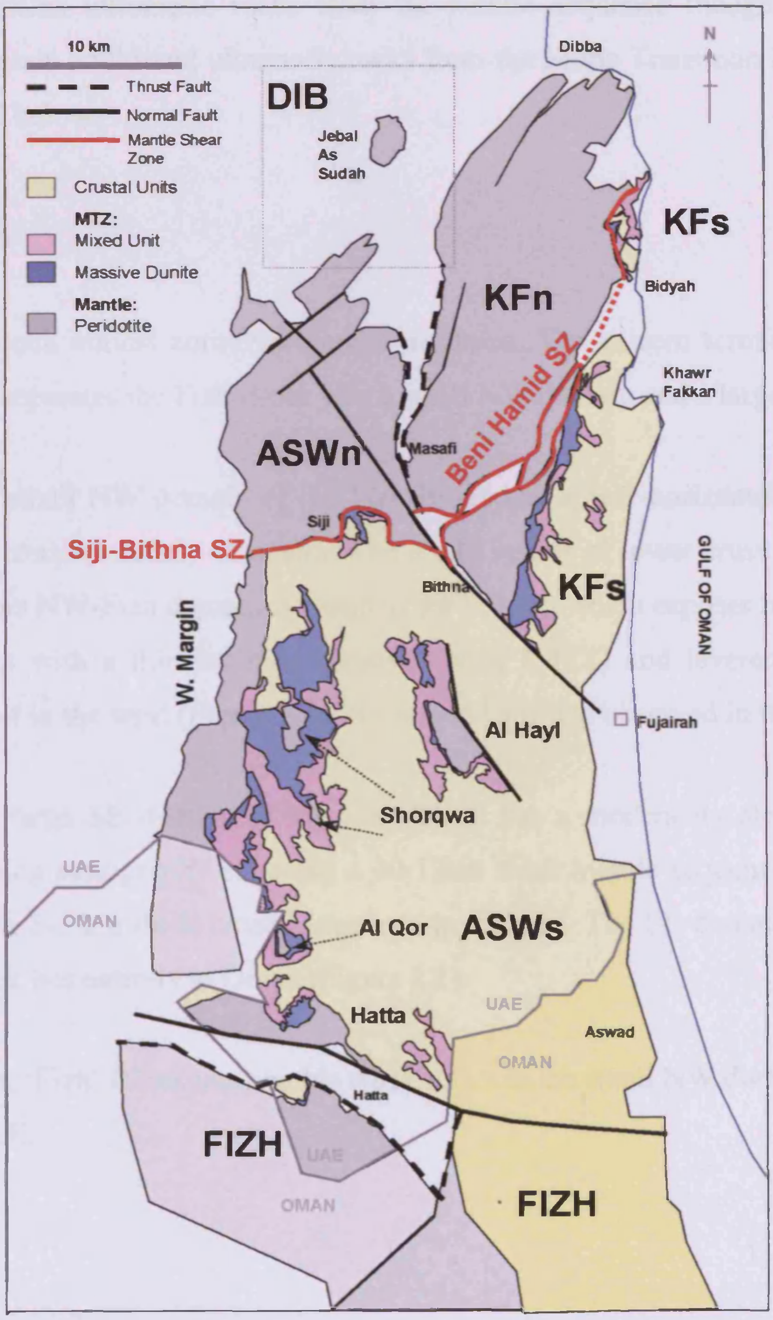

Figure 2.4: Simplified geological map of the ultramafic units and the ophiolite domains assigned in this study. Modified from the BGS map. Details of Inset box around DIB shown in Figure 2.5

Ultramafic rocks from the U.A.E. part of the ophiolite and the Dibba Zone are the subject of this study. The study area is divided, by structural features (discussed in Section 2.1.5.2) into the following domains; Fizh, Aswad South, Aswad North, Khawr Fakkan South, Khawr Fakkan North and Dibba (Figure 2.4 and 2.5). Each domain contains ultramafic rocks from the mantle sequence though only a few domains contain additional ultramafic rocks from the Moho Transition Zone (MTZ), as described below.

2.2.1 Fizh

The Fizh Block almost entirely outcrops in Oman. The eastern termination of the Hatta Zone separates the Fizh Block into a small NW domain and a large SE domain.

1. The small NW domain of the Fizh Block has a near-horizontal stratigraphy and consists mainly of mantle with a thin veneer of lower crust. A small part of this NW-Fizh domain is found in the U.A.E., which exposes mostly mantle rocks with a thin layer of massive dunite (MTZ) and layered gabbro and basalt in the west (Figure 2.4). No Mixed Unit was observed in the MTZ.

2. The large SE domain of the Fizh Block has a moderately steep eastward-dipping stratigraphy exposing a 10-12km thick mantle sequence in the west and a 3-5 km thick crustal sequence in the east. The SE domain of the Fizh Block lies entirely in Oman (Figure 2.1).

The term 'Fizh' Block used in this study refers to the small NW domain hosted in the U.A.E.

2.2.2 Aswad South

Aswad South (ASW-s) hosts the complete ophiolite stratigraphy, with almost every unit of the mantle, early crustal and later magmatic suites represented (Figure 2.2). The Aswad Block has a very shallow eastward dip, exposing the complete ophiolite sequence from the mantle section in the west, bordering the desert, to extrusive pillow basalts in the coastal outcrops. The vast majority of Aswad-south lies in the U.A.E. with only the southernmost corners of mantle and upper crust lying across the border in Oman (Figure 2.4).

The ultramafic units outcropping in Aswad South consist of sub-Moho mantle (< 500m below the palaeo-Moho) and a continuous sequence of MTZ units. The near-horizontal attitude of the Moho leads to a mainly topographically-controlled outcropping pattern of the ultramafic units (Figure 2.4). Mantle is exposed for a continuous length of 30 kilometres along the western margin (20 km in U.A.E. and 10 km in Oman) and along the southern margin at Hatta. Small windows into the shallow mantle are topographically exposed within the MTZ units of the western margin at Al Qor and Shorqwa (Shokah). The only window of mantle exposed further to the east is an up-faulted block of Al Hayl (5km x 2km in size), with the stratigraphy dipping shallowly (~ 10 - 15°) west.

The mantle peridotites of the Aswad Block extend 15km westward under the Quaternary sands where they constitute small, serpentinized ridges covered with Maastrichtian limestones. Peridotites from these ridges were exposed on the seafloor as deduced from their presence in a sedimentary breccia belonging to the basal level of the Maastrichtian limestones (Nicolas et al., 2000b).

Both the massive dunite and Mixed Unit components of the MTZ are common throughout Aswad South, except that massive dunite is noticeably absent around the Al Hayl mantle window (Figure 2.4). The massive dunite component of the MTZ is typically a few hundred metres thick in the western margin. A small area of MTZ dunite and Mixed Unit is found along the north-bounding shear zone at Siji.

The crustal part of the Aswad South Block has three major, NW-SE striking crustal-scale faults on 5-10km scale (Figure 2.2). These normal, extensional faults form horst and graben features along which large volumes of younger gabbro intruded. These NW-SE features overprint an earlier N-S system of extensional faults on scales of 1-3km which affect the highest stratigraphic unit in the east.

2.2.3 Aswad North

Aswad North (ASW-n) consists of entirely mantle rocks from the base of the ophiolite. The basal thrust of the ophiolite is exposed along its NE margin where amphibolites from the metamorphic sole are preserved along the contact with the Masafi-Ismah Metamorphic Window (MIMW) (Section 2.1.3). The upper boundary of the mantle domain is defined by the Siji-Bithna Shear Zone (Section 2.1.5.2), which juxtaposes Aswad North mantle in the north and Aswad South crust in the south (Figure 2.2). Aswad North is the very thin (<1km thick), leading edge of the ophiolite (Styles pers. comm.) the stratigraphic position of which is uncertain, but probably sub-Moho.

The Wadi Ham fault trends NW through Aswad-north and is offset by the NE-SW trending Wadi Sidr Fault system of the Dibba Zone (Figure 2.2). The northern tip of Aswad North is tectonically incorporated into the MIMW.

2.2.4 Khawr Fakkan South

Khawr Fakkan South (KF-s) constitutes a wedge of sub-Moho mantle, MTZ and crustal units exposed along the eastern coast above a moderate (30°- 40°) E-dipping, NNW-SSE trending palaeo-Moho (Figure 2.4). The base of the Khawr Fakkan South domain is the Beni Hamid Shear Zone (Section 1.1.3). The Khawr Fakkan South domain outcrops in two parts (Figure 2.4).

1. A continuous sequence from sub-Moho mantle to crust is exposed from Fujairah to Khawr Fakkan. The mantle sequence reaches a maximum thickness of 3km in the south, by Bithna, and pinches out to negligible thickness within the shear zone at Khawr Fakkan. The MTZ is characterised by the ubiquitous presence of massive dunite, ranging in thickness from a few hundred metres up to 1-2 kms (Figure 2.4). The Mixed Unit is not always present resulting in dunite in direct contact with layered gabbro. The upper part of the crustal sequence, which includes the upper part of the sheeted dyke complex and extrusive rocks, has been removed by uplift and erosion. Small late intrusions of gabbro are frequently found (Figure 2.2).

2. Only a thin part of the MTZ and lower crustal units are preserved east of the shear zone north of Bidyah, in direct contact with underlying mantle of Khawr Fakkan North to the west.

2.2.5 Khawr Fakkan North

Khawr Fakkan North (KF-n) consists entirely of mantle rocks from the deeper parts of the ophiolite. The upper margin of this mantle domain is bounded to the east by the Beni Hamid Shear Zone (Section 2.1.4), which juxtaposes deeper mantle of Khawr Fakkan North in the west with very shallow mantle of Khawr Fakkan South in the east just south of the town of Khawr Fakkan (Figure 2.4). The western margin exposes the base of the ophiolite at approximately 5-7 km depth from the Beni Hamid Shear Zone. The basal thrust of the ophiolite, including amphibolites from the metamorphic sole, is only preserved in its SW part, around Masafi. A number of NE-SW trending brittle faults form parallel to the base faults.

2.2.6 Dibba

The Dibba domain (DIB) consists of ultramafic rocks from various units of unknown age and origin within the Dibba Zone (Section 2.1.2) (Figure 2.5). They are referred to as Dibba Zone peridotites in later Sections.

1. Fault bound lenses of highly deformed serpentinite, up to a few hundred metres thick, form along the major thrust faults in the Dibba Zone (**Serpentinite Thrust Slices** of Figure 2.5). The serpentinite acts as a lubricant for the thrust planes. The tectonized serpentinite possesses a distinctive anastomosing foliation, which wraps around lenses of more massive serpentinite with relict cores of relatively fresh peridotite.

2. A large elliptical body (5 x 2 km) of relatively fresh ultramafic rocks at **Jebal As Sudah** has a pressure shadow-like envelope of serpentinite and a serpentinite mélange surrounding it.

3. Serpentinite also forms clasts within the **Wadi Sanah Mélange formation,** which predominantly crops out to the SE of Jebal As Sudah ultramafic body. This is a tectonic sedimentary mélange of oceanic origin containing clasts of serpentinite, chert, limestone and volcanic rocks in a silicified mudstone matrix.

The NE-SW trending imbricate thrust stack of the Dibba Zone (Figure 2.5) has structurally higher units on the SE side of each thrust fault. Therefore, the structural level of each ultramafic unit within the Dibba Zone is in the following decreasing order below the Oman-U.A.E. ophiolite (Khawr Fakkan North); Wadi Sanah Mélange, Jebal As Sudah ultramafic body, and the Serpentinite Thrust Slices.

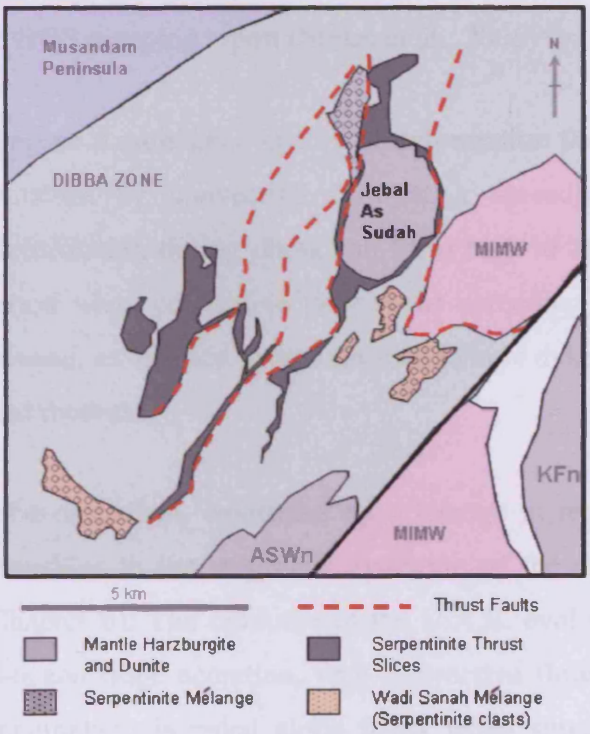

Figure 2.5: Detailed map of the Ultramafic Units in the Dibba domain of the Dibba Zone. Structurally higher units are found to the SE of each thrust.

2.3 Geology of the Ultramafic Units

This study concentrated on the following units of ultramafic rocks in order of decreasing priority of importance: harzburgite unit, dunites and chromitites in both the mantle and MTZ, mixed unit of the MTZ, wehrlite intrusions and mantle dykes. This Section summarises the geological characteristics of each unit, first by summarising the previous work in Oman and then introducing observations on the U.A.E. study area made by the author and the BGS. The description of the MTZ is summarised from the BGS mapping report (Styles et al., 2006) for ease of reference.

The mantle has undergone a multistage history of deformation that can be observed in the field: deformation by convective flow at a spreading ridge at high temperatures; then deformation during obduction from high to lower temperatures. There was also a period when convective flow at the spreading centre ceased and magmatism still continued, as testified by undeformed mantle dykes cross-cutting the mantle harzburgite and dunites.

A change in style of magmatism, controlled by a change in tectonic setting, was linked via age relationships to the magmatic evolution of the crust in the U.A.E. (Lilly, 2006) (See Chapter 6). The ophiolite in the U.A.E. evolved from a steady-state system of mid-ocean ridge accretion, with convective flow in the mantle, to localised plutonic magmatism intruded along faults when spreading stopped and supra-subduction zone magmatism got under way, before and during ophiolite obduction. The effect that the change from spreading to a non-spreading system would have had on the mantle structures will be explored in this Section to try to date the generation of dunites and chromitites and link them to different phases of magmatism in Chapter 6. The hypothesis which will be tested is that in the mantle distal to obduction-related deformation, early MORB dunites and chromitite were deformed by convective flow at a spreading centre whereas later SSZ dunites and chromitite formed after spreading stopped and would therefore be undeformed.

2.3.1 Harzburgites

Harzburgites, with pods and veins of dunite (described in Section 2.3.2), constitute the main part of the ophiolite mantle section. All orthopyroxene-bearing peridotites from the study area were initially classed as harzburgites as it was impossible to estimate the presence or absence of clinopyroxene (cpx) in the field. The harzburgite samples were later reclassified upon petrographic examination into cpx-harzburgites and lherzolites (Chapter 3). The harzburgite has an orange-brown weathering crust which masks the internal features at outcrop, so that the rock appears rather massive. It is only the water-washed surfaces in the wadis that show up the primary features clearly.

The harzburgites are coarse-grained, with light-green orthopyroxene grains, typically 5mm, standing out from the brown-weathered olivine matrix. The coarse-grained harzburgites display a pervasive tectonic fabric (foliation) resulting from convective flow at a spreading ridge (Nicolas, 1989). This can be seen in outcrop as a planar alignment of orthopyroxene and spinel grains and also compositional banding on a centimetre scale (Figure 2.6) resulting from metamorphic segregation (e.g. Browning, 1982). Elongate spinel grains also define a weak lineation in the plane of the tectonite foliation, although this is very difficult to see in outcrop. Harzburgite fabrics are only locally developed and not always visible to measure.

Fine-grained harzburgites, with orthopyroxene crystals up to 1 mm in size, formed along the base of the ophiolite and within mantle shear zones, e.g. the Beni Hamid shear zone and the Siji-Bithna shear zone (Section 2.1.5.2). These fine-grained harzburgites are categorised as **recrystallized harzburgites** because they have undergone recrystallization at high temperatures in shear zones. The small size of the orthopyroxene crystals means that recrystallized harzburgite can resemble dunite in the field; their accurate spatial distribution was determined from petrographic examination (Chapter 3).

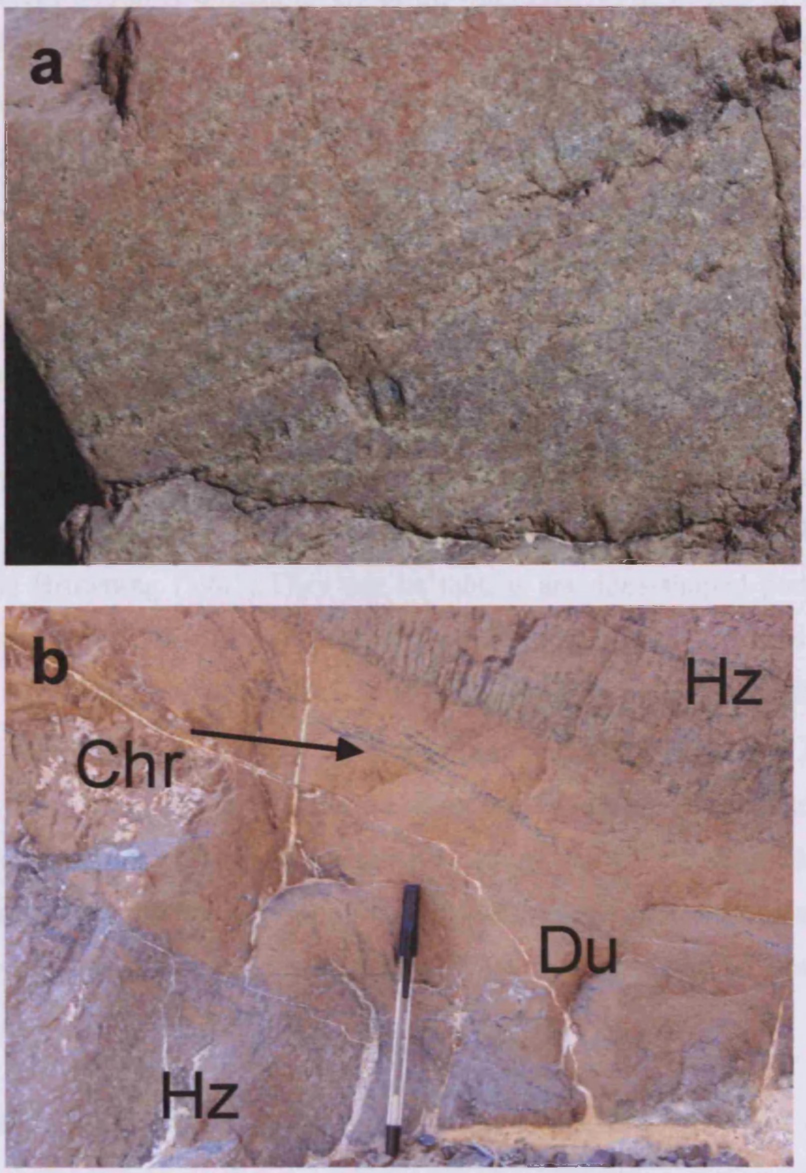

Figure 2.6: a) Water-washed surface of coarse-grained harzburgite showing light-green orthopyroxene (opx) crystals, up to 5 mm long, standing out from brown-weathered olivine (ol) -rich groundmass. Harzburgite fabric formed from elongate and aligned opx as well as compositional banding of opx-rich layers and ol-rich layers. b) Thin dunite (du) vein with chromitite trail (chr) parallel to margin within harzburgite (hz). Photos taken by author in the U.A.E. field area.

2.3.2 Dunites

Dunites form within two main levels of the ophiolite: 1) as bodies of varying shape and size occurring sporadically within the mantle section; and 2) within the Moho Transition Zone (MTZ). Dunites are easily distinguishable from harzburgites and pyroxenites in the field by the lack of pyroxene, resulting in a smooth, brown-weathered rock. The dunites always have sharp contacts with the surrounding harzburgite, often with a gradual decrease in orthopyroxene from the harzburgite host to the dunite vein. The dunites contain accessory chrome-spinel which often congregates in trails subparallel to the orientation of the dunite vein (Figure 2.6a).

The shape and size of dunite bodies in the mantle vary widely, as previously documented in Oman by, for example, Boudier and Coleman (1981), Brown (1980, 1982) and Browning (1982).They can be tabular and lens-shaped pods or irregular and anastomosing channels between a few centimetres to tens of metres thick. Dunite veins in the mantle are attributed to melt circulation into peridotites above or at the solidus (1250 - 1200°C) (e.g. Kelemen et al., 1995; Nicolas et al., 2000c). Their shape is directly related to the amount of deformation they experienced from high-temperature convective flow at the spreading ridge. When undeformed the veins are discordant to the harzburgite foliation and are typically pod-like or anastomosing. Progressive deformation makes them elongate, tabular and concordant to the foliation (Bartholomew, 1983).

Intense deformation associated with obduction in the lowermost part of the mantle section, above the basal thrust contact with the underlying metamorphic rocks, is characterised by a **Banded Unit** of interlayered harzburgite and parallel bands of dunite concordant to the harzburgite foliation (Figure 2.8). This unit has been previously documented from several localities in Oman (Lippard et al., 1986; Jousselin and Nicolas, 2000a) and the deformation strengthens the visual contrast between the metre-thick alternations of dunite and harzburgite.

The top of the mantle is characterised by a more or less continual layer of dunite, marking the base of the Moho Transition Zone (MTZ). The transition from mantle harzburgite to dunite of the MTZ is commonly through an irregular network of dunite veins. The thickness of dunite from the MTZ can vary from 10m to 700m along the length of the Oman-U.A.E. ophiolite (Nicolas and Boudier, 2000). The thickness reflects the amount of melt influx below the ridge of origin. Areas with thick dunite and copious wehrlitic intrusions (cf. Section 2.3.4) in the overlying crust have been used as an indicator of focused melt delivery to the crust (Figure 2.7) that is related to mantle diapirism and upwelling below the palaeoridge (Nicolas and Boudier, 2000).

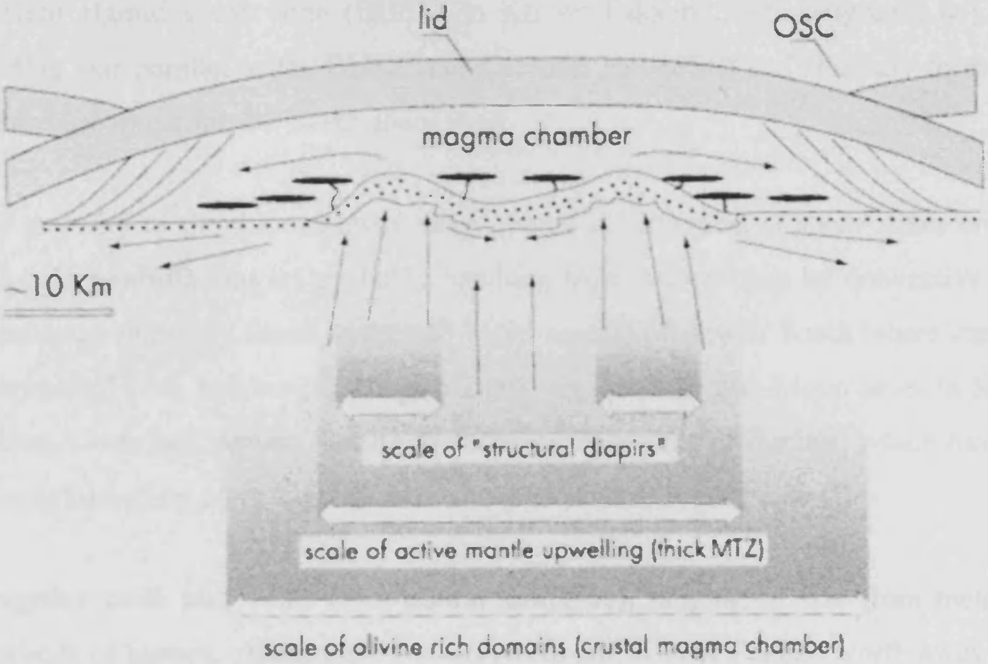

Figure 2.7: Model of mantle upwellings beneath the Oman-U.A.E. ophiolite related to variations in crustal thickness (Nicolas and Boudier, 2000). Dots, MTZ dunite; black lenses, wehrlite intrusions; OSC, overlapping spreading centre. Taken from Nicolas and Boudier (2000).

2.3.2.1 Mantle dunites

Dunites in the mantle of the U.A.E. were observed to have the following characteristics in order of decreasing degree of deformation. The **Banded Unit** (Figure 2.8a-b) is well developed around the basal margins of Aswad north and Khawr Fakkan North domains as well as the eastern edge of Jebel As Sudah, Dibba (Figure 2.9). Dunite bands can reach up to 20m in thickness up to a few hundred metres above the basal contact of the ophiolite. Closer to the contact, only thinner bands, up to a few tens of centimetres across, are found; this may be due to greater deformation close to the contact (Styles et al., 2006). Amphibolites of the metamorphic sole are restricted to the contact with the ophiolite in the region of the Banded Unit. Thinly banded dunite-harzburgite was observed on the southern margin of Beni Hamid shear zone (BHSZ) in Khawr Fakkan South (Figure 2.8c). This banding was parallel to the BHSZ (dip direction 160/40SE) and similarly formed by intense deformation near to the shear zone.

The majority of the dunites away from intense deformation of shear zones are thin (0.1 – 5m) **tabular layers** probably resulting from deformation by convective flow. These are commonly found in the sub-Moho mantle of Aswad South where dunite is interlayered with harzburgite (Figure 2.8d). At the same sub-Moho level in Khawr Fakkan South and Aswad South anastomosing networks of dunites, which have not been deformed by convective flow are also preserved (Figure 2.8e-f).

Irregular pods and veins (non-planar margins), ranging in size from metres to hundreds of metres, characterise Aswad North and Khawr Fakkan North away from the basal contact. In Aswad North, dunites never exceed 20m in thickness and often form an irregular interconnecting network (e.g. Marbad), in contrast to the planar layering of the Banded Unit at its base. In Khawr Fakkan North, large dunite pods, from 20m x 100m and up to a few kilometres in thickness, were observed on the eastern side of the domain, between Wadi Wadishi and Wadi Zikt (Figure 2.9) together with smaller veins including anastomosing networks.

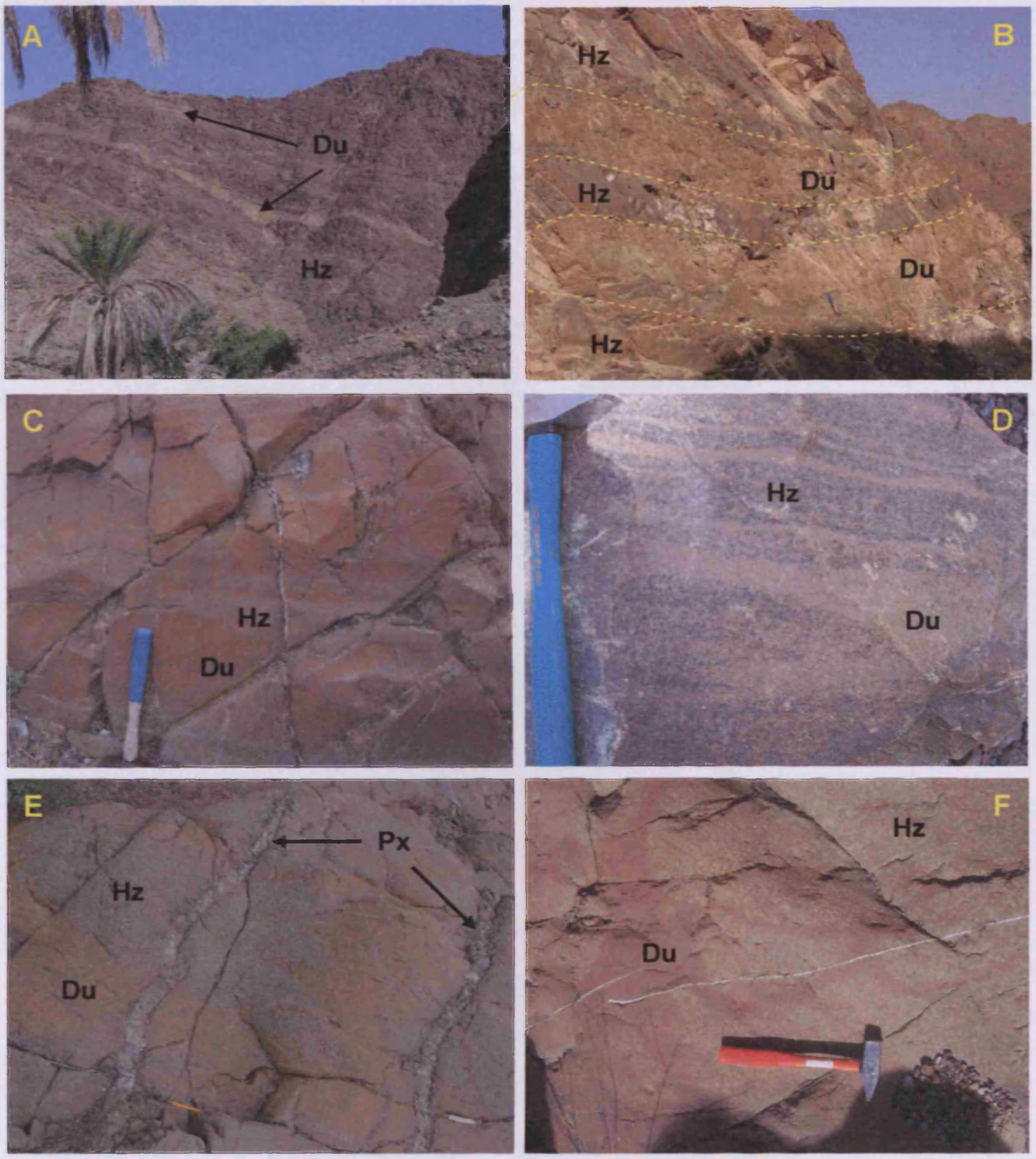

Figure 2.8: Characteristics of dunite (du) within harzburgite (hz) in the field. Distal (A) and close up views (B) of the Banded Unit (inter-layered dunite and harzburgite) at the base of the ophiolite in U.A.E. (C) Thinly banded dunite-harzburgite intensely deformed by the Beni Hamid Shear Zone. (D) Thin layers of dunite in harzburgite deformed by convective flow at Al Hayl cr mine (Iceberg). (E) Anastomosing network of undeformed, thin dunite veins within sub-Moho (<100m) mantle in Khawr Fakkan-south (E) and Al Hayl, Aswad-south (F). Hammer for scale is 30cm long, pencil is 15cm long.

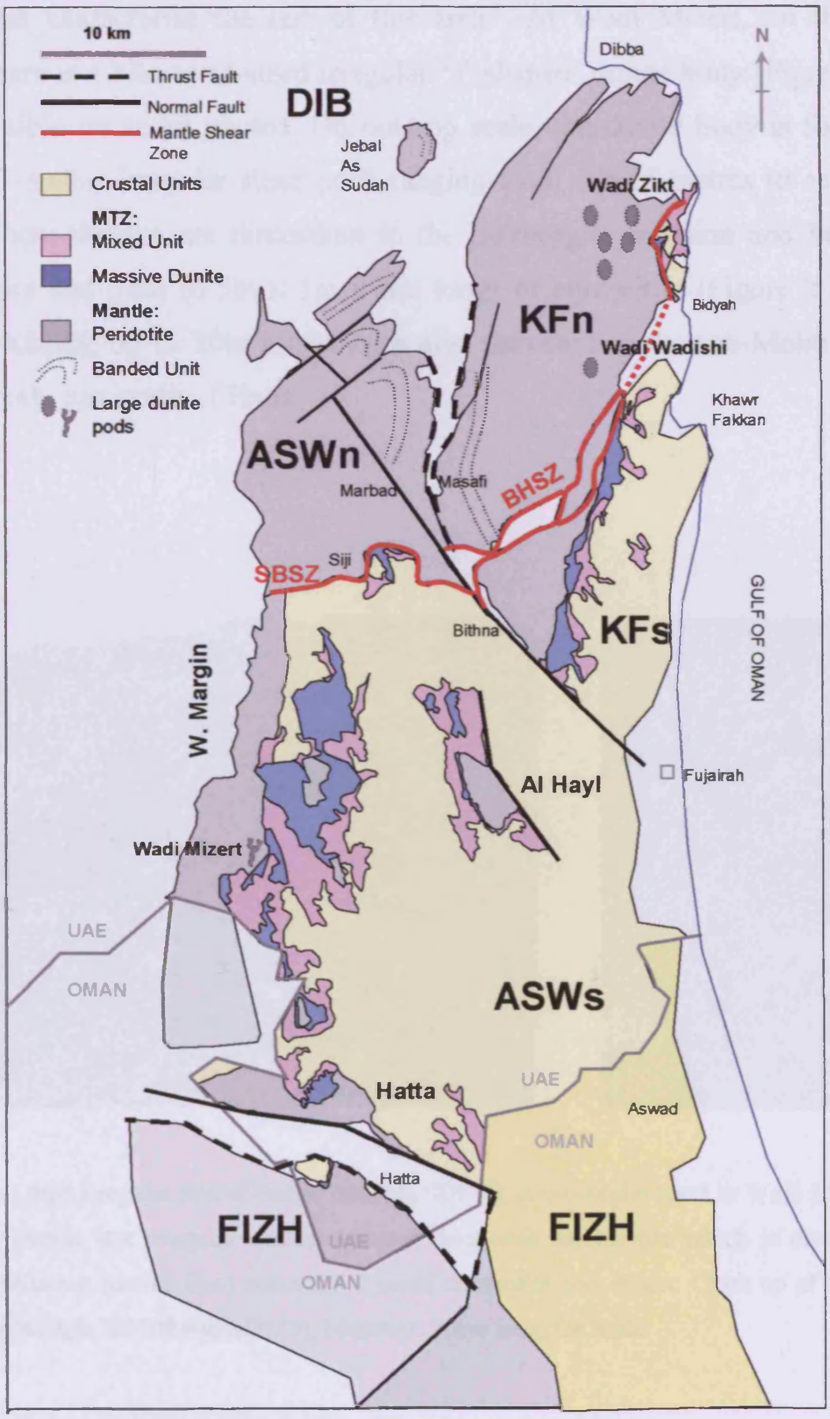

Figure 2.9: Simplified map of the ultramafic domains showing the distribution of dunite features such as the Banded Unit and other large, undeformed dunite pods. BHSZ-Beni Hamid Shear Zone; SBSZ- Siji-Bithna Shear Zone.

Large irregular pods of dunite also occupy a few localities in the sub-Moho mantle of Aswad South. These stand out from the usual thinly layered and anastomosing dunites that characterise the rest of this area. At Wadi Mizert, on the western margin, there is a kilometre-sized irregular 'Y-shaped' dunite body (Figure 2.9) that is even visible on aerial photos. On outcrop scale, the dunite body is formed by a cluster of smaller irregular sized pods ranging from 10s of metres to several 100s metres. These dunites are discordant to the harzburgite foliation and host several small lenses and pods (0.5m x 1m x 5m long) of chromitite (Figure 2.10). Large irregular dunites, up to 20m in size, are also abundant in the sub-Moho mantle of Aswad South, just north of Hatta.

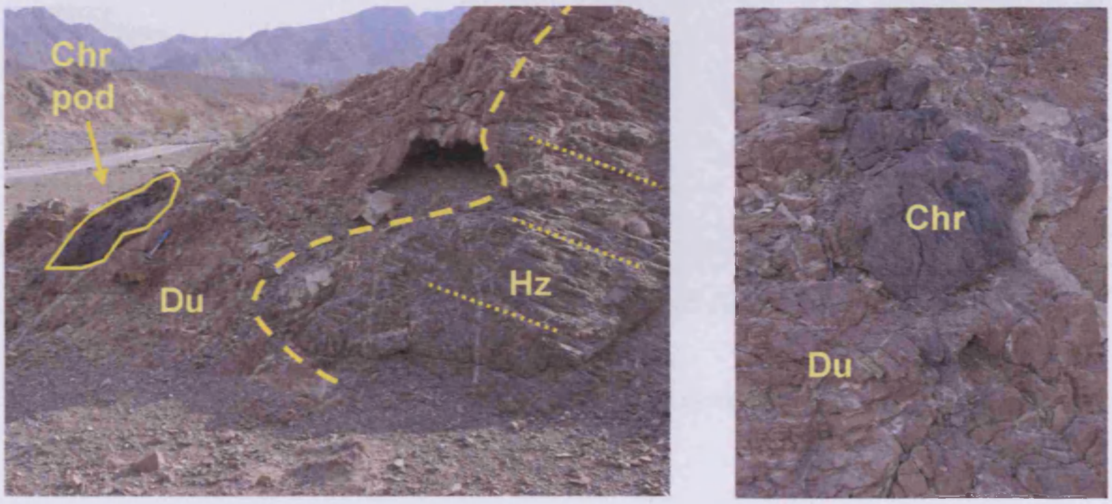

Figure 2.10: Large irregular pod of dunite (sample SD110) at sub-Moho level in Wadi Mizert, Aswad-south. Left: Dunite has irregular contact (dashed line) with harzburgite which is discordant to the harzburgite foliation (dotted line) and hosts a small chromitite pod. Right: Close up of the chromitite pod 1m long (sample SD109 and SD345). Hammer, 30cm long, for scale.

2.3.2.2 MTZ dunites

The top of the mantle section, and the lowest part of the MTZ, is marked by a discontinuous zone of dunite that was mapped by the BGS as ‘massive dunite’ unit. It can locally attain a thickness of several hundreds of metres with large lateral variations in thickness over short distances of no more than a few kilometres. Xenoliths of harzburgite (e.g. UAE323) are present in places within the massive dunite, and at Hatta (Aswad South) a sill-like interlayering of dunite and harzburgite is found, with harzburgite lenses ranging from a few tens of centimetres up to several metres in thickness (Figure 2.11).

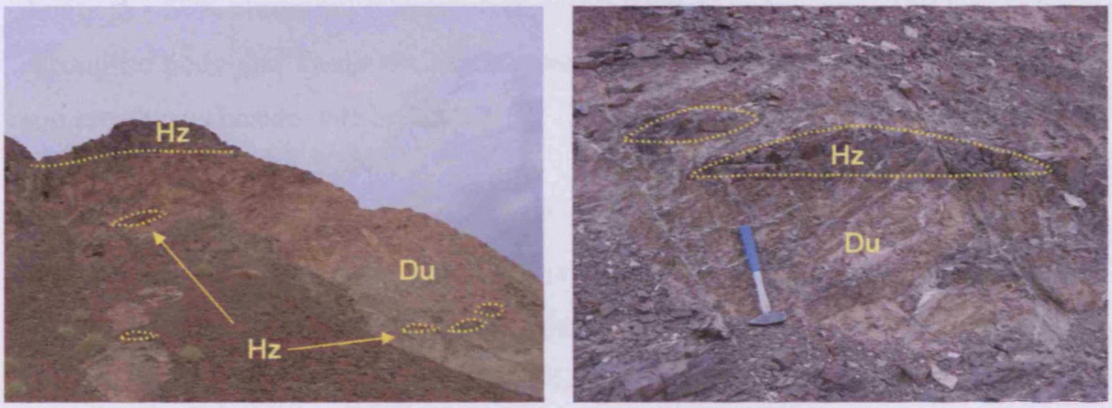

Figure 2.11: Xenoliths of harzburgite forming sill-like lenses in massive dunite of the MTZ at Hatta, Aswad-south (location 2SD-14) (close up right).

Massive dunite is associated with both phases of early and late magmatic suites, however, age relations of dunite intruding dunite are invisible in the field and must rely on geochemistry to distinguish between early and late dunites (Chapter 4). Dunites are also found higher up in the MTZ within the mixed unit, where some are clearly intrusive (see Section 2.3.4).

2.3.3 Chromitites

2.3.3.1 Chromitites in Oman

The chromitiferous rocks of the Oman-U.A.E. ophiolite range from disseminations and minor segregations of chromite in dunite to massive ore bodies of economic importance. Dunites can host layers and pods of chromitite (**podiform-type**) at different stratigraphic heights within the mantle as well as in the Moho Transition Zone (**stratiform-type**). However, the majority of dunite bodies in the U.A.E. and Oman are barren. The composition of chromitite can range from massive chromitite (> 90% chromite) through olivine-chromitite (51 – 90% chromite) to chromitiferous dunite (5 - 50% chromite) (Greenbaum, 1977; Roberts and Neary, 1993). In outcrop, chromitite pods and veins are characterised by dark grey-black, metallic chromite and are always hosted within dunite.

The morphology of the chromitite ore bodies, just like that of the barren dunites (Section 2.3.2), is directly related to the amount of deformation they experienced by convective flow beneath a spreading axis. When undeformed, the chromitite veins are discordant to the harzburgite foliation and preserve primary magmatic crystallisation textures, such as nodular, orbicular, occluded, or chain textures, and host silicate mineral inclusions (Lorand and Ceuleneer, 1989). Progressive deformation by asthenospheric flow transposes the discordant pods into subconcordant and concordant pods (Figure 2.12) (Cassard, et al., 1981). The resulting concordant ore bodies are mainly disseminated or massive and display deformed textures, such as pull-apart textures. The silicate mineral inclusions are absent in the deformed chromitite bodies due to expulsion during strain-induced recrystallisation (Lorand and Ceuleneer, 1989).

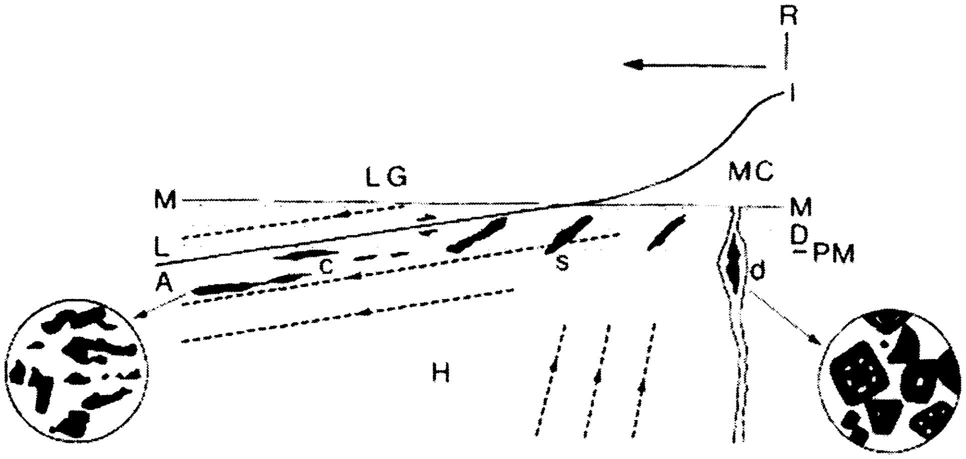

Figure 2.12: Simplified diagram of the position of podiform chromitites (black) that are discordant (d), subconcordant (s) and concordant (c) with respect to mantle foliation flow lines (dashed arrows) in the uppermost mantle beneath an active spreading ridge (adapted from Lago et al., 1982 and Nicolas, 1989 by Edwards et al., 2000). Microtextures of discordant and concordant chromitite pods are shown to demonstrate the differences in morphology of their chrome-spinel and the presence and absence, respectively, of silicate inclusions in this spinel. The 1000°C isotherm (1) marks the top of the magma chamber (MC) and the boundary between lithosphere (L) and asthenosphere (A). Dunitic rocks (D) of the transition zone lie between the Moho (M) and the petrological Moho (PM). These are predominantly underlain by harzburgite (H) and overlain by layered gabbro (GB). Taken from Edwards et al., 2000.

In Oman, most chromitite bodies are located within a few kilometres below the Moho Transition Zone (Nicolas and Al Azri, 1991) where some of the largest deposits can be found, reaching up to 15m in thickness and 40 – 50m in length (Brown, 1982). A chromitite deposit in Wadi Hilti in northern Oman (Figure 2.13) is unusually deep at > 5km below the Moho (Ahmed and Arai, 2002). It is possible that the deeper chromitite bodies are under-represented simply because topography makes the deeper section of the mantle inaccessible (Rollinson, 2006). Chromitites are also found in MTZ and, in one unique case, in the Fizh Block, higher in the layered gabbros (Arai et al., 2004).

The distribution of chromitite deposits is concentrated in two main areas (Figure 2.13): the Maqsad area (Semail Massif) in the south and the Wadi Rajmi area

(Fizh Block) in the north. Although chromitite pods are relatively small (few deposits are greater than 30 000 tons) chromitite is currently mined in Wadi Rajmi and Wadi Fizh in northern Oman. The majority of chromitite ore deposits in Oman are concordant to subconcordant to the foliation as a result of this deformation. Two notable exceptions are the undeformed discordant bodies in the Maqsad area (Leblanc and Ceuleneer, 1989) and the deep pod (>5km below the Moho) in Wadi Hilti (Ahmed and Arai, 2002).

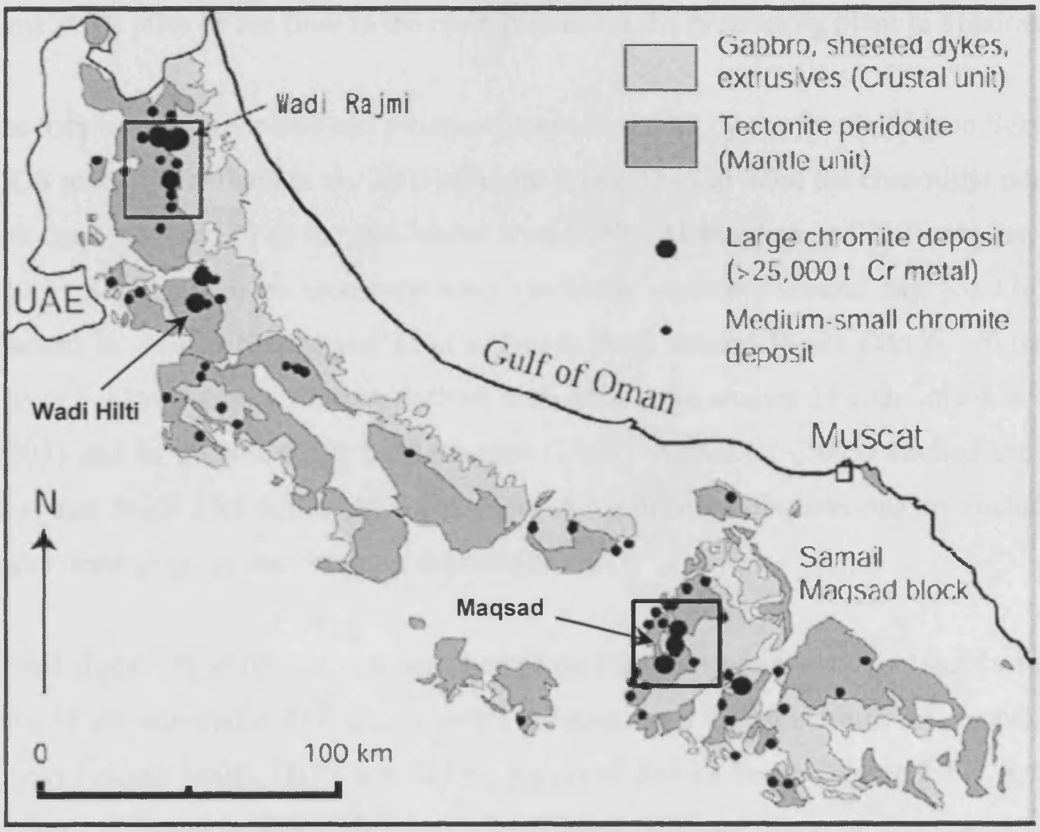

Figure 2.13: Distribution of chromitite deposits in the Oman section of the ophiolite. Location and size classification of chromitite deposits are from Michel (1993). Modified from Ogasawara et al., (2002).

2.3.3.2 Distribution of chromitite in the U.A.E.

Chromitite bodies in the U.A.E. are much smaller than those described above from Oman. The largest bodies, up to 3m thick, form economic ore deposits which were prospected and mined during the late 1990's by Derwent Mining Ltd. They annually exported some 46 000 tons of chromite from 30 mined ore deposits. Another 14 deposits were prospected but never mined as they were considered too small to be economically viable. All the deposits with economic potential have been exhausted (Grantham et al., 2003). By 2001, Derwent Mining Ltd closed its operations, leaving some stock piles of ore float in the open-pits and at the processing plant in Fujairah.

The locations of the mines and prospects were surveyed by the South African Survey (CGS report, Grantham et al., 2003) (Figure 2.14). They divided the chromitite mines into three regions: 1) at the sub-Moho level in the **Al Hayl** (or Al'Hel) window of Aswad South; 2) at an unknown level (probably shallow) around **Siji** (or Friday Market) in Aswad North; and 3) at a deeper level around **Wadi Zikt** (or Siqt) in Khawr Fakkan North. Chromitites from each mine were analysed by Grantham et al., (2003) and in greater detail by Al-Aabed (2003). Al-Aabed (2003) studied the Al Hayl and Wadi Zikt mines only, and some of his detailed observations are included in the description of the chromite deposits below.

In this study, chromitite ore has also been found as float within several wadis within most of the ultramafic domains although the host seam was seldom found, including Khawr Fakkan South, Hatta and Al Qor region of Aswad South (Figure 2.14). Small outcrops of massive chromitite ore (0.3m wide x 5m) and chromite float were also found by the South African mapping in the serpentinite carapace north and south of the **Jebal As Sudah** outlier of the Dibba Zone (Figure 2.14), although none was found in the harzburgite outlier itself (Grantham et al., 2003). From several traverses in this area, the author and BGS did not find any chromitite either.

Small chromitite pods and veins, in situ but unmined due to no economical importance, were observed at **Wadi Mizert** (ASW-s) and **Wadi Sahana** (KF-s) (Figure 2.14). A small massive chromitite pod was observed within the large discordant dunite pod at sub-Moho levels in Wadi Mizert (Figure 2.9). Widespread stringers and layers of chromitite and dunitic-chromitite up to a few centimetres in thickness were found within both mantle dunites and massive dunite (see below). In Wadi Sahana (Khawr Fakkan South/North), chromitite layers can reach over a few metres in size (Figure 2.21).

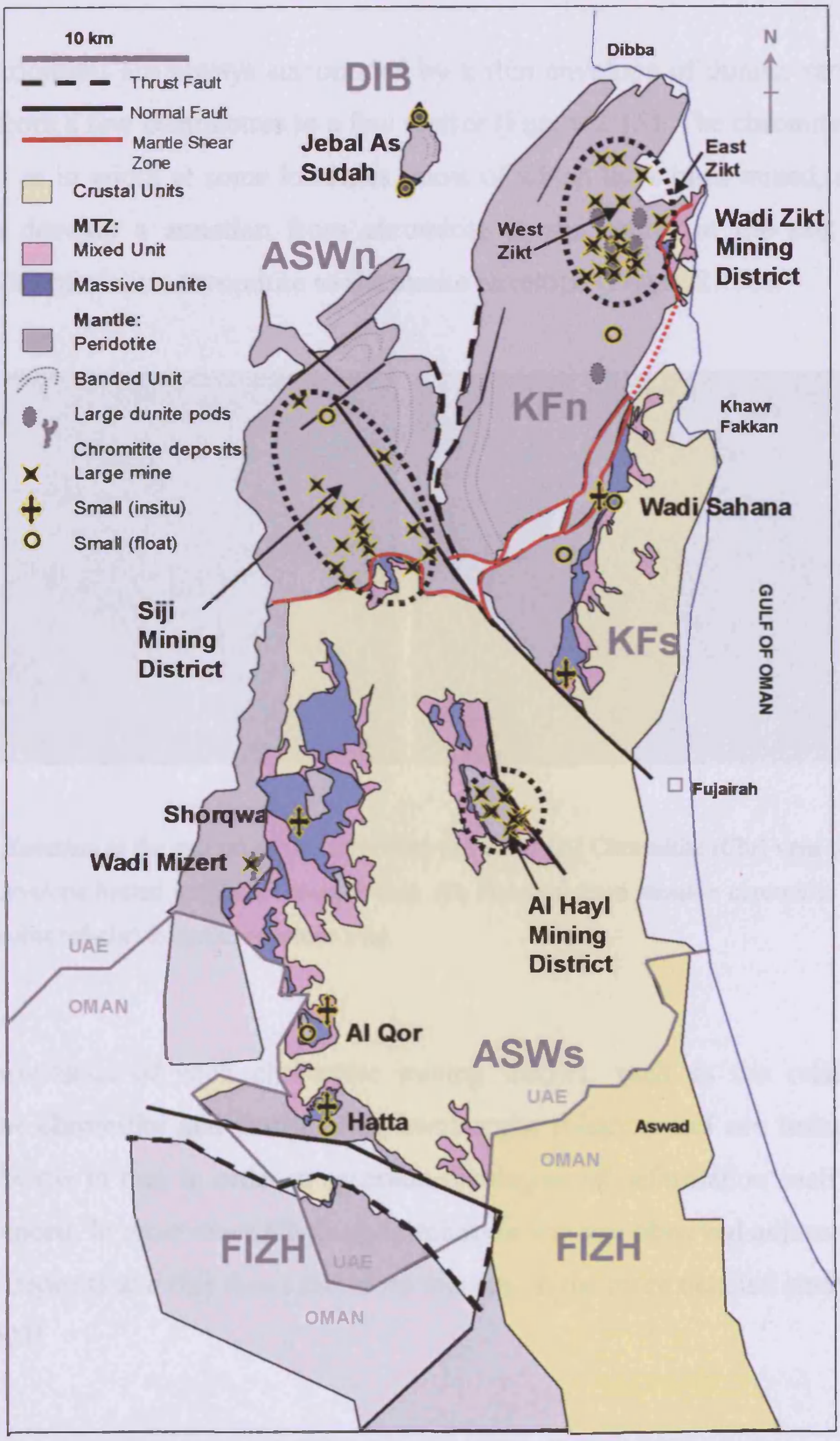

Figure 2.14: Distribution of chromitite deposits in the U.A.E. Locations of the chromitite mines (stars) from the three mining districts are plotted from the CGS Report (Grantham et al., 2003). Additional sites are chromitite float (open circles) and *in situ* small deposits (crosses) discovered during this study.

2.3.3.3 Mantle Chromitites

Mantle chromitites are always surrounded by a thin envelope of dunite, ranging in thickness from a few centimetres to a few metres (Figure 2.15). The chromitite veins are up to 3 m in width at some localities, most of which have been mined, and can sometimes develop a zonation from chromitite in the centre of the ore deposit through a rim of olivine-chromitite to the dunite envelope (Figure 2.15b).

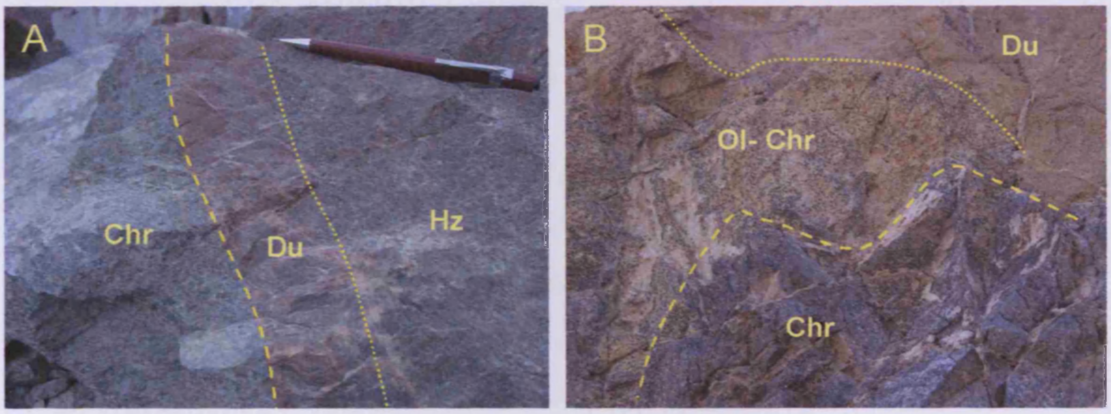

Figure 2.15: Zonation at the margin of the chromitite ore body: (A) Chromitite (Chr) vein with thin dunite (du) envelope hosted within harzburgite (hz). (B) Zonation from massive chromitite (chr) to olivine-chromitite (ol-chr) to dunite envelope (du).

The characteristics of each chromitite mining district, such as the relationship between the chromitite and surrounding harzburgite foliation and ore textures, are described below in turn in order to ascertain the degree of deformation each deposit has experienced. In most cases harzburgite foliation was not observed adjacent to the chromitite deposits and this thesis therefore focuses on the more detailed study of Al-Aabed (2003).

The **Al Hayl district,** in Aswad South, hosts around 10 chromitite mines which are located within the sub-Moho mantle, a few hundred metres below the MTZ. The MTZ surrounding the Al Hayl mantle window has a thin MTZ, composed almost entirely of Mixed Unit and lacking a massive dunite component (Figure 2.4). The Moho is near-horizontal (Nicolas et al., 2000b) and shallowly-dips west by 10-15° in the region of Al Hayl (Styles et al., 2006). The flat-lying foliation in the mantle harzburgites locally steepens downward, as reported by Nicolas et al., (2000). The chromitite deposits are tabular structures which are concordant to sub-concordant to the harzburgite foliation where observed by the author and Al-Aabed (2003). Therefore, the majority of open-pit trenches of the chromitite mines are near horizontal and sub-parallel to the Moho in this area (Figure 2.16 a and b).

The tabular chromitite deposits consist of massive and disseminated chromitite, often with thinly banded sheets (1cm to 30 cm in thickness) and elongate lenses that can extend discontinuously to several tens of metres (Figure 2.16 c and d). Al-Aabed (2003) described the lateral terminations of the Al Hayl chromitite bodies as having tongue-shaped small fold terminations with axial planar foliation. All of the field observations demonstrate that the Al Hayl chromitites were deformed by high temperature spreading flow in the shallow upper mantle (Al-Aabed, 2003). Only a few rare chromitite samples in this area show undeformed and magmatic textures, e.g. antinodular (Figure 2.16e) and nodular ore.

The **Wadi Mizert Chromitite Pod** was the only other chromitite deposit discovered in Aswad-south (Figure 2.14). It crops out in the mantle of the western margin in a kilometre-sized irregular dunite body, previously described in Section 2.3.2.1. The dunite hosts several small lenses and pods (0.5m x 1m x 5m long) of massive chromitite (Figure 2.9) which is discordant to the flat-lying harzburgite foliation in this area. Chromitite float from Al Qor and Hatta in Aswad-south has massive textures, which will require petrographic examination to determine whether they are magmatic or undeformed (Chapter 3).

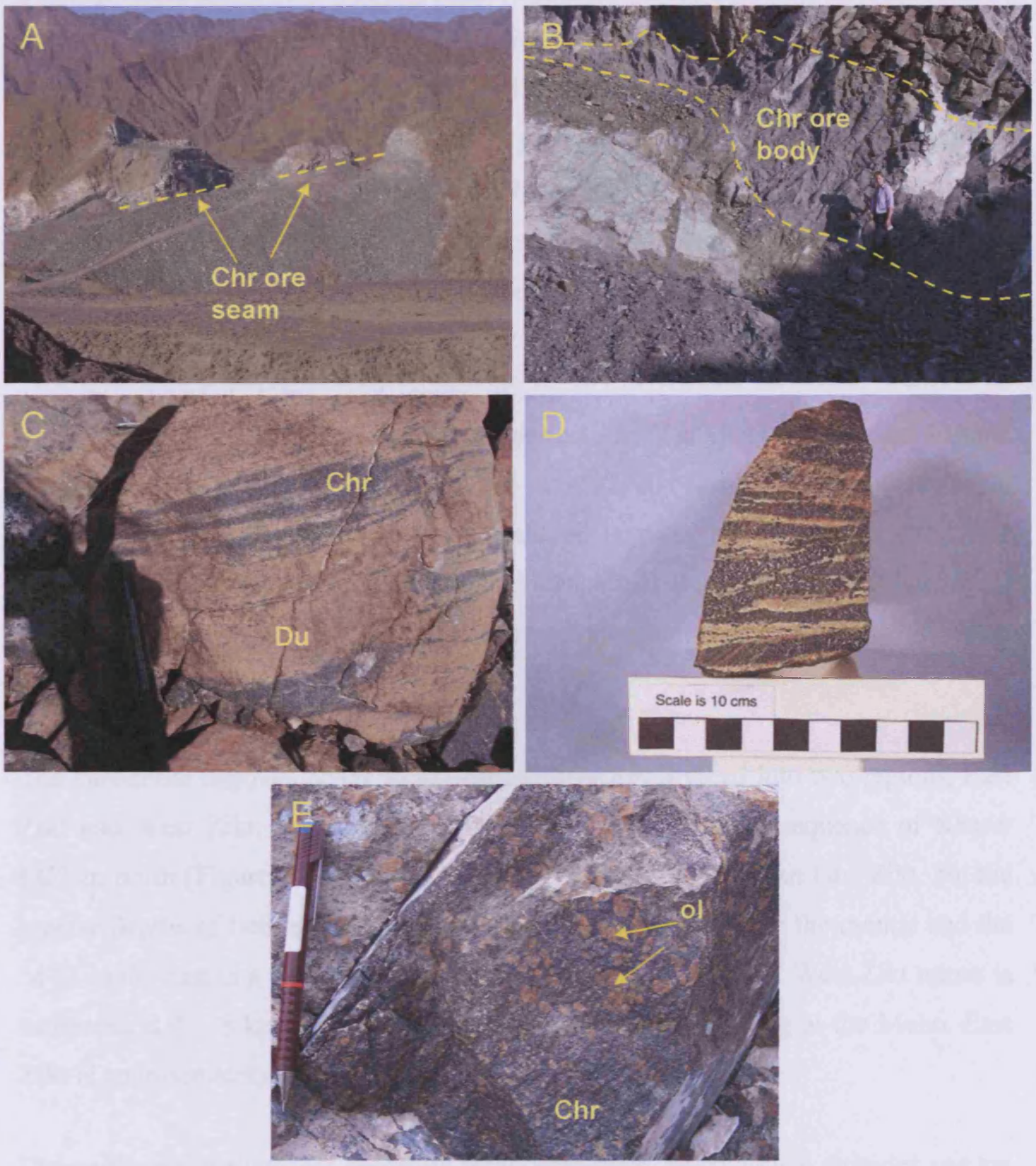

Figure 2.16: Al Hayl district of chromitite mines. (A) and (B); The sub- horizontal nature of the chromitite seam, up to 3m thick, in both mines. (C) and (D); Elongate lenses and banded chromitite in dunite resulting from deformation by convective flow. (E) Antinodular texture, olivine grains surrounded by a network of chromitite, formed by magmatic processes preserved from deformation.

The **Siji Mining District** hosts around 13 chromitite mines in the sub-Moho mantle of Aswad North and one mine within dunite of the MTZ (Siji area of Aswad South) (Figure 2.14). The author and the BGS only visited a few of these sites as they were difficult to locate amidst the current activity of road-stone quarrying. The harzburgite foliation around the area of the mining is horizontal- to moderately- dipping (< 30°) (Nicolas et al., 2000b), whereas the chromitite veins, where located, have a slightly steeper dip (~50°). Therefore, the Siji chromitite deposits can be described as subconcordant to the harzburgite foliation.

The Siji chromitite deposits form thin tabular bodies, displaying massive and banded textures. Al-Aabed (2003) describes one body (LM117) situated in a shear zone, with chromitite showing banded and occluded textures and pillow bands. These limited field observations provide some evidence that the Siji mining district hosts chromitites that have experienced some deformation from convective flow at spreading centre.

The chromitite deposits of the **Wadi Zikt district** are divided into two regions, East Zikt and West Zikt, according to their position in the mantle sequence of Khawr Fakkan-north (Figure 2.14). West Zikt is deeper in the mantle than East Zikt, but the precise depths of both are unknown because the contact between the mantle and the MTZ in the east is a tectonic shear zone. The minimum depth of West Zikt mines is estimated at 4 – 8 km depth below the Moho, assuming shearing at the Moho. East Zikt is approximately 1 km beneath the Moho.

Chromitite excavations are generally small with steep, near vertical attitudes and are therefore mined in narrow opencast trenches (Figure 2.17c). The stratigraphy of the Khawr Fakkan Block is tilted 40° to the east, therefore, the Wadi Zikt chromitite veins were intruded discordant to the Moho by approximately 50°. Granite dykes commonly cut the chromitite deposits in this district.

East Zikt district hosts just one mine (Palace), which is an ellipsoidal pit measuring 36 m x 60 m. The harzburgite foliation in this region is near-vertical, generally striking NW-SE, and concordant to sub-concordant with the chromitite seams (Al-Aabed, 2003).

The chromitite forms non-planar bodies with irregular margins and intricate branching network within the dunite envelope (Figure 2.17b). Magmatic textures, e.g. chromite net, chain and nodular, dominate the outer zone between the core of massive ore and the rim of dunite. Most nodules are small (< 5mm), irregular chromite fragments in a matrix of olivine. However, large (1cm x 2.5cm) regular (ellipsoidal) chromite nodules in highly altered olivine matrix are common (Figure 2.17a). These magmatic textures show no high-temperature deformation from convective flow at the spreading ridge.

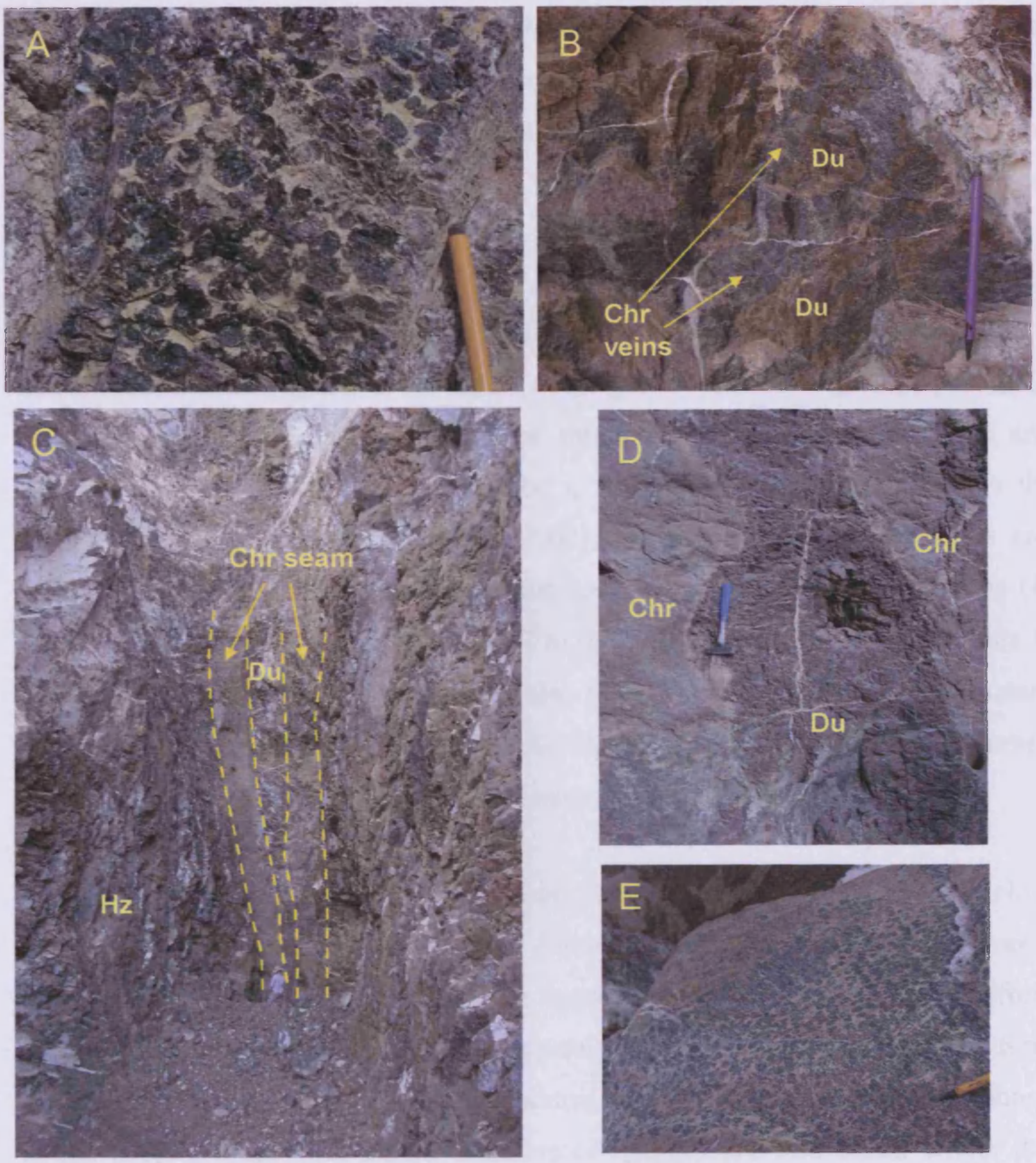

Figure 2.17: Magmatic textures of chromitite ore from the Wadi Zikt mining district. (A) Large 'grapeshot' nodular ore and (B) intricate branching network of chromitite veins in dunite envelope of the main ore body, from East Zikt Mine. (C) Vertical chromitite excavations showing two parallel chromitite seams, (D) close up of the chromitite seams and their irregular margins with dunite envelope and (E) large nodular chromitite ore, from West Zikt Mines.

West Zikt district hosts around 17 chromitite deposits deeper in the mantle of Khawr Fakkan North (Figure 2.14). The harzburgite foliation in this region is near-vertical but the strike varies considerably whereas the chromitite deposits are also near vertical striking between NW-SE and NE-SW. Al-Aabed (2003) described the chromitite deposits and their internal features as sub-concordant to the host harzburgite foliation.

The chromitite deposits are near vertical and have irregular margins (Figure 2.17c-d) and are characterised by a nodular texture ranging from small to large ("grapeshots"), ring- to oval-shaped (Figure 2.17e). The round nodules form in the centre and become elliptical at the edges of the bod y, with their long axes parallel to the margins (Al-Aabed, 2003). Al-Aabed (2003) also described rhythmic layers and bands of massive, disseminated chromitite and dunite with varying thickness (1-30cm) in semi-parallel form, sub-parallel to the dominant foliation. This texture is typical of magmatic processes and was also found in chromitite float downstream south of this chromitite mine (Figure 2.18). Therefore, West Zikt hosts undeformed chromitite deposits that preserve original magmatic textures.

Wadi Sahana hosts two chromitite-bearing dunite bodies in the mantle in close proximity of the Beni Hamid Shear Zone that separates Khawr Fakkan South from – North (Figure 2.14). A large dunite body, approximately 30m wide, hosts stratiform layers of chromitite (sample SD106a), typical of magmatic processes in stratiform chromitites (Figure 2.19a and b). Such textures are similar to chromitite layers found in the MTZ (Figure 2.2). Large, undeformed nodules are also found within this deposit and show no effects of deformation (Figure 2.19).

Figure 2.18: Magmatic texture; banded chromitite float from a wadi downstream from a mine in West Zikt, KF-n (sample U.A.E.94).

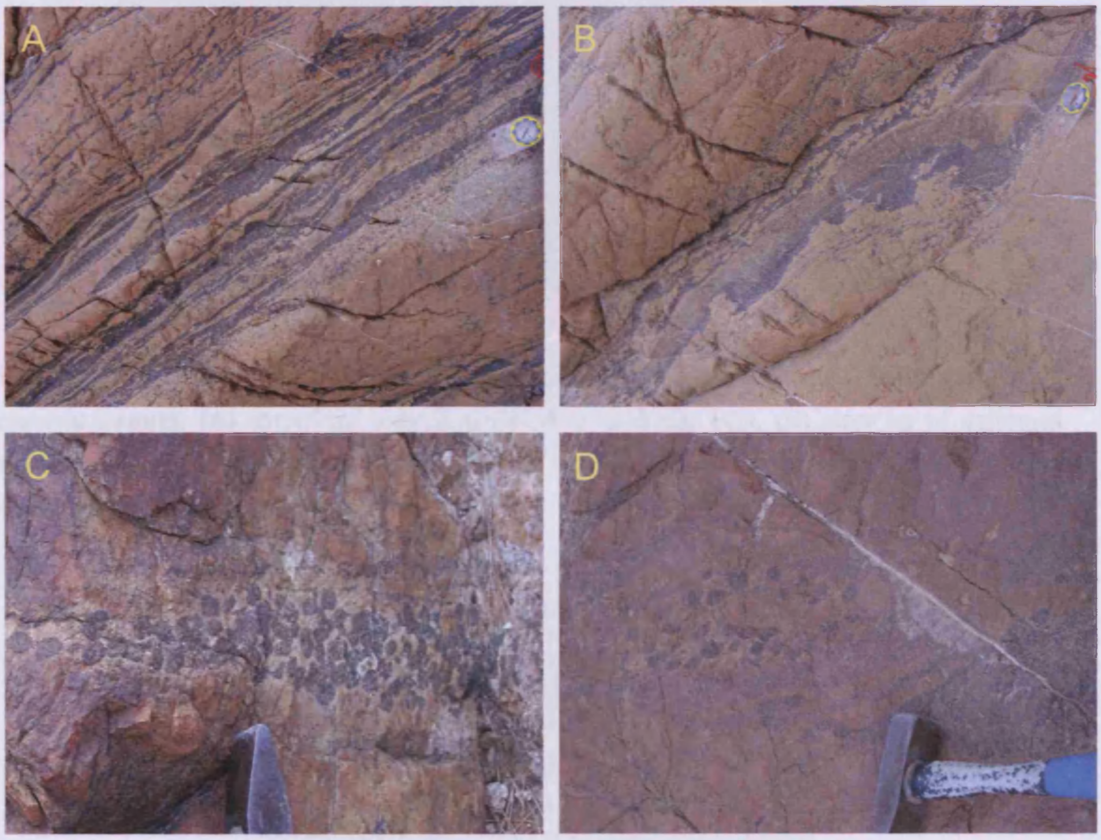

Figure 2.19: Chromitite from a 30m wide dunite body in Wadi Sahana (sample SD106a) displaying magmatic textures. (A) layers (10 cm – 1 m wide), (B) intricate flame structures, (C) large nodular ore and (D) nodules wrapped by thin wispy layers of chromitites.

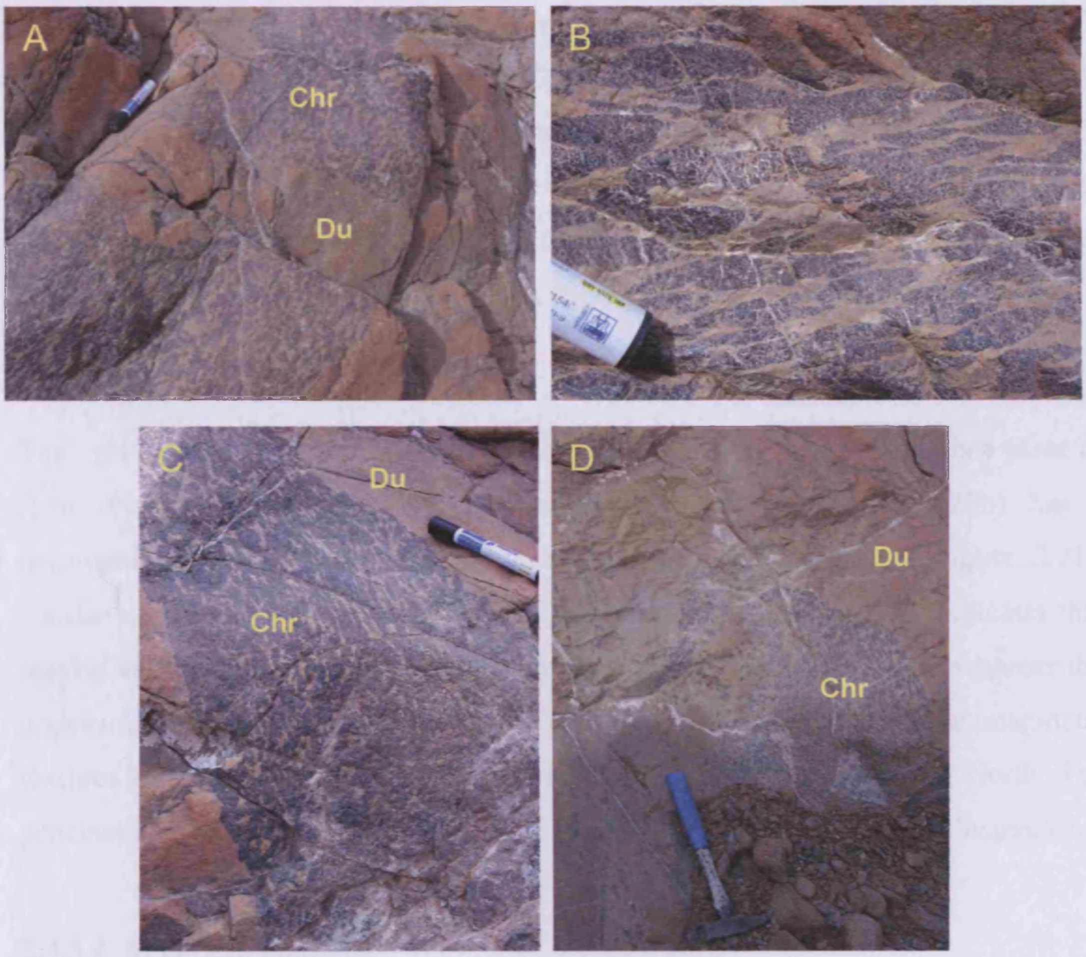

Figure 2.20: Chromitite from a 10m wide dunite body in Wadi Sahana (sample SD102a) displaying deformed textures. (A) chromitite body is cross-cut by a dunite vein, (B) close up of deformed elongated nodules (pillow bands), (C) lineation of elongate nodules and (D) less deformed patch with wispy margins and rings of chromite.

Figure 2.21: Deformed texture; olivine and chromitite pillow bands in disseminated chromitite from KF-s (sample U.A.E.120b).

However, only a kilometre away from the 'stratiform-type' chromitite in the mantle of Wadi Sahana a smaller dunite vein, 10 m wide, bears a more deformed chromitite deposit (sample SD102a). The chromitite displays elongate nodules (pillow bands) that describe a lineation (Figure 2.20). This is typical of deformation from high temperature convective flow, although there are patches which are less deformed (Figure 2.20d). This deformed chromitite deposit is cross-cut by a later vein of dunite (Figure 2.20a).

The only other mantle chromitite originating from Khawr Fakkan South is a piece of float (Figure 2.14). This olivine-chromitite float (sample U.A.E.120b) has a deformed texture of pillow banded olivine and chromitite grains (Figure 2.21), similar to the deformed chromitite (SD102a) from Wadi Sahana. This indicates that maybe the deformed chromitite originated from Khawr Fakkan South, whereas the undeformed chromitite (SD106a) from Wadi Sahana, which has similar magmatic textures to chromitites from West Zikt, originated from Khawr Fakkan North. The geochemistry of these chromitites will be used to assess this possibility (Chapter 6).

2.3.3.4 MTZ Chromitites

There are commonly thin layers and stringers of chromitite within the dunitic components of the MTZ; in both the **massive dunite** and the **Mixed Unit** (see Figure 2.14 for locations). The chromitite layers define a layering structure in the dunite (Figure 2.22) similar to magmatic layering found in the mantle of Wadi Sahana (see above). Most chromitite deposits in the MTZ are small, less than a few metres in width. However, there is a chromitite mine, approximately 100m long, within the massive dunite/mixed unit of the Siji area (sample SD497).

Clinopyroxene is commonly associated with chromitite cropping out in the Mixed Unit; either as the host rock, e.g. clinopyroxene-bearing dunite (U.A.E.65) and wehrlite (SD262), or co-precipitated as part of the chromite net texture (Figure 2.22c-d), e.g. chromitiferous- clinopyroxene-dunite (U.A.E.3996, U.A.E.4056).

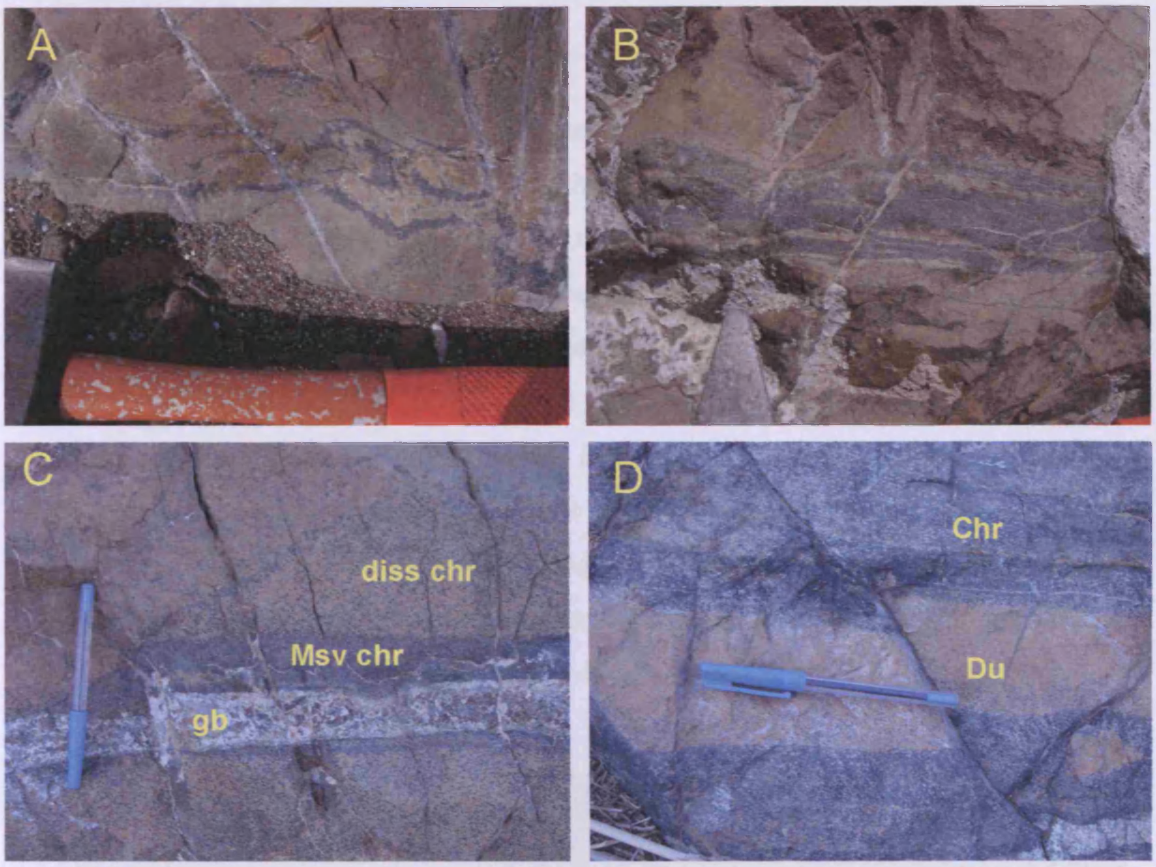

Figure 2.22: Chromitite textures from the MTZ ultramafic rocks; massive dunite unit (a and b) and within dunite from the Mixed Unit (c and d). A) Chromitite net structure within wispy layers of massive chromitite (SD459, KF-s). B) Layers of chromitite in dunite (SD409, Hatta Asw-s). C) chromitite layers (massive and disseminated) in dunite-dominated part of Mixed Unit, cut by gabbro pegmatite dyke (U.A.E.3996, Al Qor, Asw-w). Chromite net texture associated with crystallization of clinopyroxene (chr-wehrlite). D) Massive chromitite layers with dunite xenolith (U.A.E.3996 , Al Qor, Asw-S).

2.3.4 Mixed Unit of the MTZ

The Mixed Unit (MU) is a complex zone of gabbro, wehrlite, dunite and pyroxenite that typically lies above the massive dunite at the top of the mantle section and below the layered gabbro unit of the early crustal section (Figure 2.23). There are many variations on this basic stratigraphy: either the massive dunite or the Mixed Unit may be absent (but not both); the MU may contain massive dunite bodies; or areas of MU may pass laterally as well as up-section into layered gabbros. Areas of Mixed Unit also form as intrusions at higher levels in the layered gabbro section. Much of the Mixed Unit consists of intrusions of the later magmatic suite, with enclaves of the earlier mantle and crustal sections. The Mixed Unit and the massive dunite below are together equivalent to the transition zone as described originally by Benn et al. (1988), and the Moho Transition Zone (MTZ) of Boudier and Nicolas (1995).

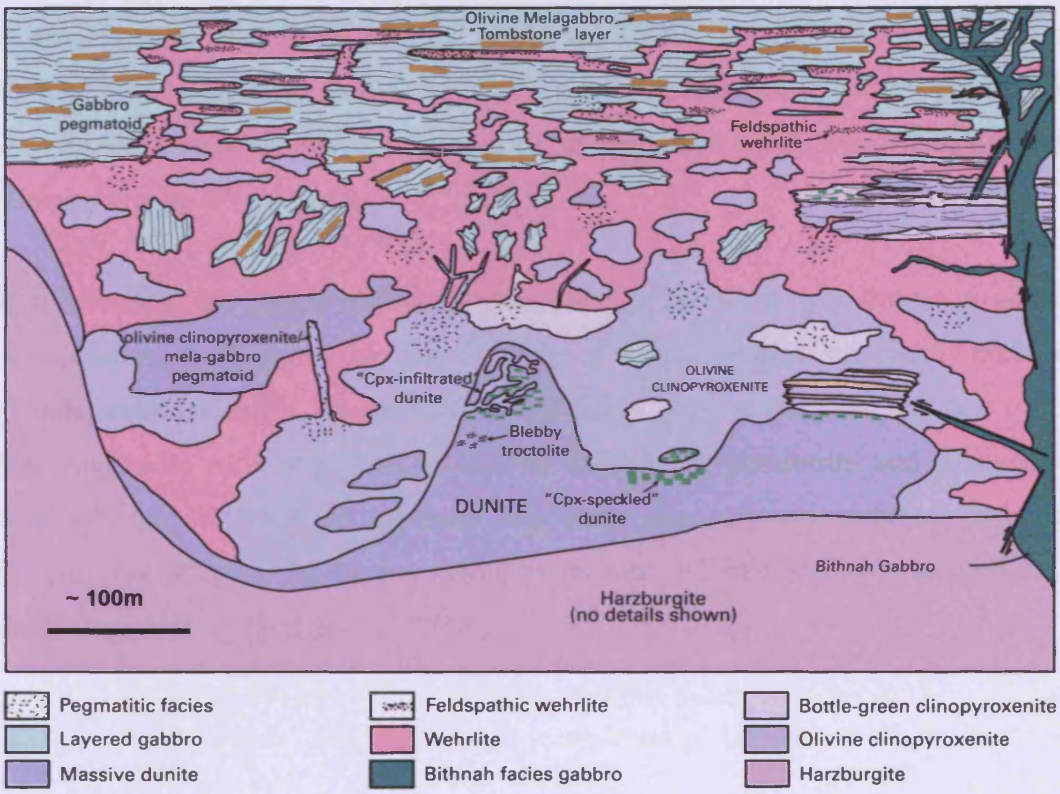

Figure 2.23: Schematic diagram illustrating the Mixed Unit sequence. Copyright U.A.E. ministry report (Styles et al., 2006).

The thickness of the Mixed Unit, in its normal stratigraphical position, varies from a few metres up to 1000m. The base of the Mixed Unit is typically taken at the point where patchy areas rich in coarse grains of clinopyroxene and/or plagioclase feldspar begin to appear at the top of the massive dunite (Figure 2.24a). These areas of 'impregnated dunite' (Benn et al., 1998) pass upwards into the main part of the Mixed Unit, which is rich in coarse-grained wehrlite and olivine clinopyroxenite, together with dunites (Figure 2.24b and c), pyroxenites and at least two generations of gabbroic rocks (Figure 2.24a and b).

Over most of the study area, a crude stratigraphy was recognised within the Mixed Unit (Figure 2.23) by the BGS (Styles et al., 2006). Whereas all the constituent lithologies can be found throughout dunite is generally most common towards the base and decreases upwards in abundance, pyroxenites tend to be most abundant in the middle, and wehrlites and gabbros tend to be more abundant towards the top. The plagioclase content of wehrlite also increases upwards, leading to the appearance of melagabbros in the upper parts of the Mixed Unit. The internal structure of the Mixed Unit is generally chaotic, though the basal part can locally be strongly banded, with several tens of metres of a metre-scale alternation of dunite, wehrlite and olivine clinopyroxenite (Figure 2.24e).

Dunites within the Mixed Unit form pods or larger areas cut by wehrlites or olivine clinopyroxenites (Figure 2.24c and d). Some of the dunite areas are clearly enclaves of older rocks from the mantle section, but others may be intrusive and part of the later magmatic suite (e.g. U.A.E.33). The majority of peridotites and pyroxenites within the Mixed Unit likely represent parts of the later magmatic sequence, although the presence of cross-cutting pegmatitic pyroxenite and amphibolite veins indicate a multi-stage history (Styles et al., 2006).

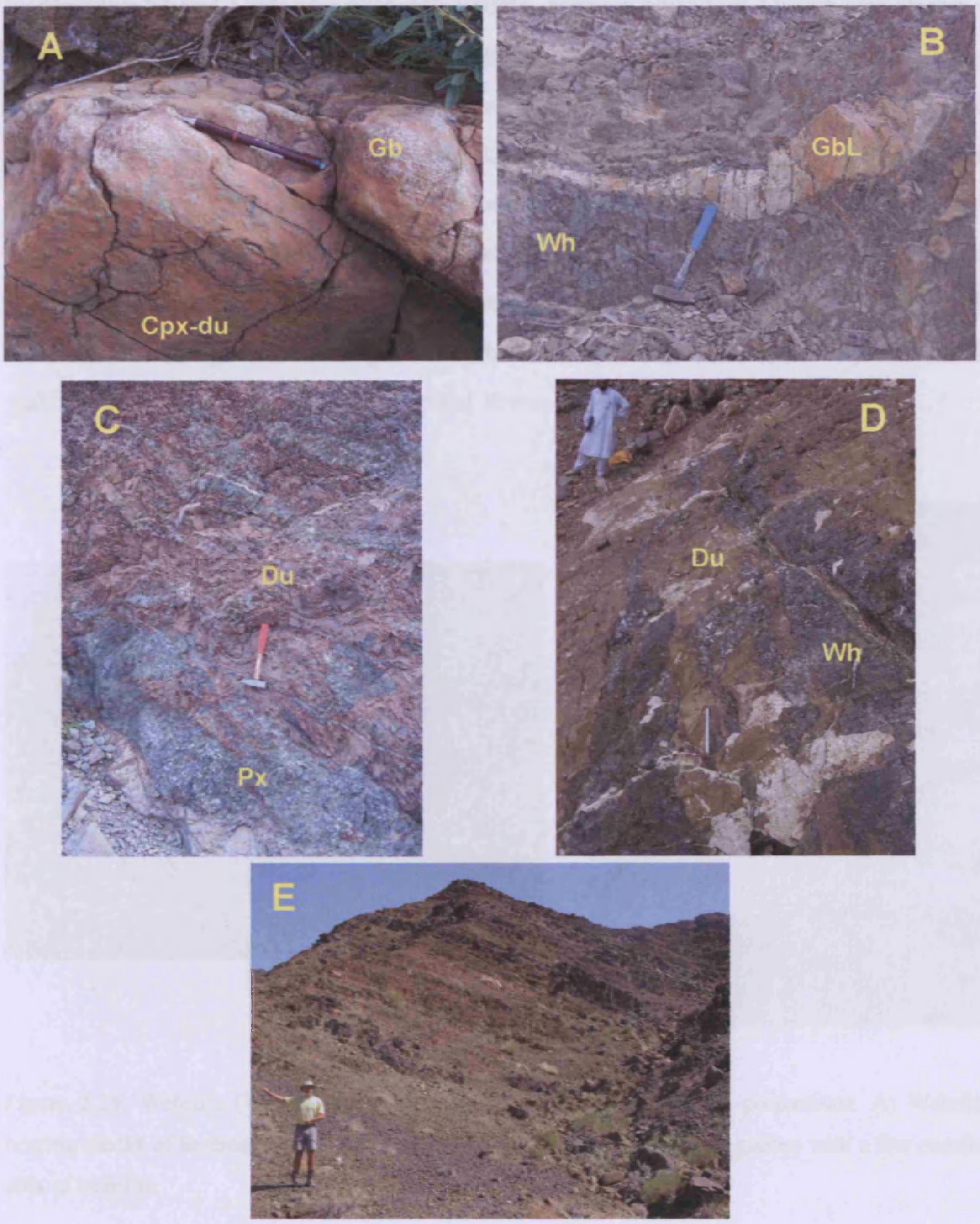

Figure 2.24: Compilation of photos from the main Mixed Unit lithologies: A) Impregnated dunite, rich in clinopyroxene, at the base of the Mixed Unit, along with patches of gabbro intrusion (Gb) B) Wehrlite enclosing lens of layered gabbro. C) Clinopyroxenite intruding dunite. D) Wehrlite intruding dunite. E) Banded ultramafic rocks at the base of the Mixed Unit: alternating dunite, wehrlite and clinopyroxenite.

Within the Mixed Unit, the ultramafic rocks enclose abundant blocks and sheets of layered gabbro (Figure 2.24b). These gabbro bodies can range in size from a few centimetres in thickness, up to many tens of metres. In many outcrops of the Mixed Unit, the gabbros and the ultramafic rocks appear interlayered (Figure 2.25) and this led previous workers in Oman to describe the gabbro sheets as sills, cutting residual peridotites at the top of the mantle section (Boudier and Nicolas, 1995; Korenga and Kelemen, 1997). However, at many localities in the U.A.E., it is clear that the ultramafic rocks post-date the gabbros; the ultramafic rocks cross-cut layering in the gabbros and enclose xenoliths of typical lower crustal layered gabbros.

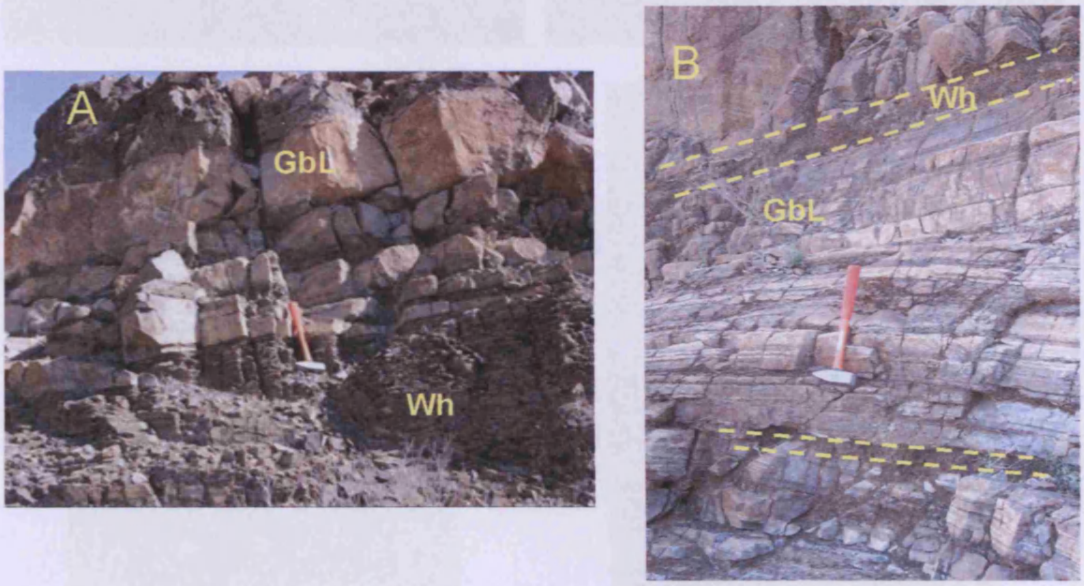

Figure 2.25: Wehrlite (Wh) intruding layered gabbro (GbL) in varying proportions. A) Wehrlite hosting blocks of layered gabbro at the top of the Mixed Unit. B) Layered gabbro with a few parallel sills of wehrlite.

In places the contacts between the ultramafic rocks and the gabbro xenoliths are marked by a gradational zone of troctolites of plagioclase-rich wehrlite, locally with "ghost" layering that appears to have formed through assimilation of the gabbros. Up-sequence the xenoliths become more slab-like and are arranged sub-parallel to the base of the overlying layered gabbro intruded by multiple wehrlite sills (Figure

2.25a). Within this gradational contact, the mapped base of the lower crustal layered gabbro is taken at the approximate position where the layered gabbro becomes the most dominant rock type in outcrop (Figure 2.25b).

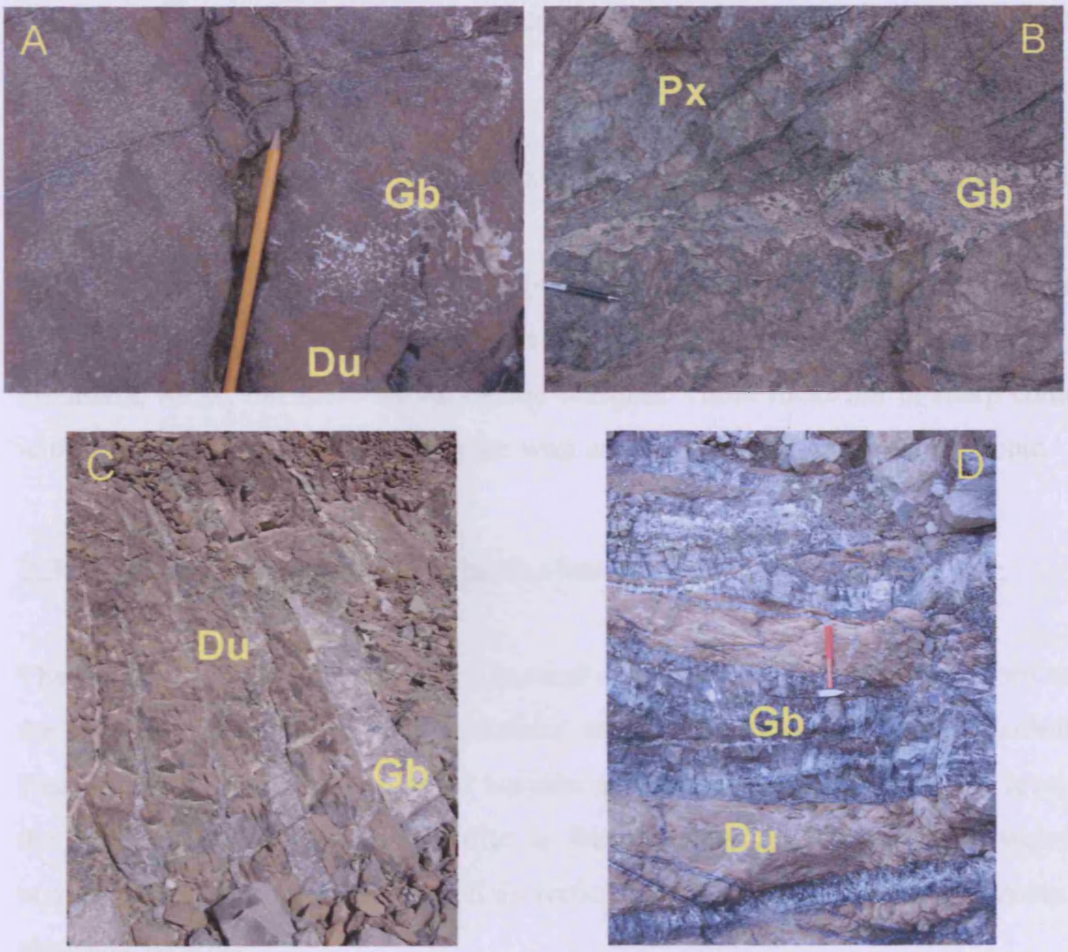

Figure 2.26: Gabbroic intrusions in the MTZ: A) patchy network of gabbro impregnating massive dunite, B) sheared gabbro vein in pyroxenite, C) swarm of parallel-sided gabbro pegmatite dykes intruding massive dunite and D) multiple injections of gabbro pegmatite into the dunitic part of the Mixed Unit.

A second gabbro-type in the Mixed Unit includes veins, dykes, sheets and irregular bodies of gabbro and pegmatitic gabbro, which range from a few centimetres to several metres in width, and cut the ultramafic rocks (Figure 2.26). These clearly represent later intrusive bodies. Thus, it appears that there are two distinct types of gabbro within the Mixed Unit. The tabular xenoliths of partially-assimilated layered gabbro represent the base of the early crustal section, which has subsequently been intruded and disrupted by the voluminous wehrlites and clinopyroxenites. These are distinct from the clearly intrusive gabbro and gabbro pegmatite sheets that relate to a later phase of magmatism, possibly genetically associated with the wehrlites and clinopyroxenites of the Mixed Unit.

There is an unusual variant of the Mixed Unit in the northern part of the Khawr Fakkan South Block, near the village of Bidyah. The rocks in this area include pyroxenites, olivine pyroxenites, wehrlites and dunites; but gabbro sheets are not present. Fairly sharp, irregular contacts are seen between these different types of ultramafic rocks, but there are no chilled margins. These rocks are in sharp contact with layered gabbros on the hills to the west and, in many places may be tectonic.

2.3.5 Wehrlite intrusions into the lower crust

The top of the Mixed Unit grades structurally upwards into the layered gabbro unit, the base of which is somewhat arbitrarily taken at 50:50 layered gabbro: wehrlite. Passing upwards, the proportion of wehrlite sills decreases, such that at the level of the Kalba gabbro, intrusive wehrlite is fairly scarce. This variation in wehrlite concentration may be lateral as well as vertical, giving rise to geographical zones of abundant wehrlite.

2.3.6 Mantle dykes

2.3.6.1 Introduction

During the melting-related upwelling of mantle peridotite at a spreading ridge, melt can be extracted by dykes at progressively decreasing temperatures, from asthenospheric conditions down to 400°C, in the enclosing mantle peridotites (Nicolas, 1989; Nicolas et al., 2000c). Peridotites have a weak mechanical anisotropy and, therefore, dyke orientation is controlled by the local stress field (Nicolas and Jackson, 1982).

Numerous but volumetrically insignificant **mafic and ultramafic dykes** cut the tectonized Mantle Sequence. The dykes vary in size from a few centimetres to 1.5 m wide and are generally undeformed (Lippard et al., 1986). The composition of the mantle dykes varies considerably (e.g. Boudier and Coleman, 1981; Brown, 1982; Browning, 1982; Lippard et al., 1986; Nicolas et al., 2000c; Python and Ceuleneer, 2003).

Felsic dykes intrude the upper part of the Mantle Sequence and the lower Crustal Sequence in the northern part of the ophiolite, particularly in the Khawr Fakkan Block (Peters and Kambers, 1994). The granite dykes are irregular and often anastomosing up to 5 m in width and 100 m in length. The granites are related to ophiolite emplacement (see Section 1.2) and show a wide variation in composition, which include biotite granite, andalusite + cordierite + biotite granite, and garnet + tourmaline leucogranite (Searle and Cox, 1999).

The most comprehensive study to date on mantle dykes by Python and Ceuleneer (2003) identified 36 rock types which can be grouped into two main magma suites, ranging from primitive to evolved lithologies, contrasted in terms of structural and textural characteristics, modal composition, order of crystallization, and phase chemistry, as described below.

The **troctolite suite** has olivine and plagioclase crystallizing early and lithologies range from primitive troctolites to evolved olivine gabbros, opx-poor gabbronorites, and oxide gabbros.

The troctolite dykes are generally rather thick (one to a few metres) and commonly have diffuse boundaries, implying intrusion at asthenospheric conditions (~1280°C) within the ductile-brittle transition (Ceuleneer et al., 1996). The olivine gabbros are thin (few decimetres) sub-vertical dykes with fine to medium grained texture. They form dyke swarms with a strike parallel to the sheeted dyke complex, supporting the view that the troctolite suite (troctolite and olivine gabbro families) were injected in a stress field dominated by the regional extension of seafloor spreading (Python and Ceuleneer, 2003).

On the other hand the **pyroxenite suite** has olivine and pyroxene crystallizing early and lithologies range from primitive pyroxenites (websterites, clinopyroxenites, and orthopyroxenites) and wehrlites to evolved opx-rich gabbronorites, diorites, and tonalite-trondhjemites. However, most of the pyroxenites are devoid of olivine and therefore, wehrlites are uncommon.

Dykes of the pyroxenite suite (pyroxenite and gabbronorite families) have sharp walls and were emplaced into the peridotites well below the solidus. They have variable thicknesses (few centimetres to tens of metres) and textures (from coarse-grained to pegmatitic). Harrisitic growth on the inner dyke walls frequently results in dykes that are coarse grained on their margins and fine grained in their centre. The gabbro pegmatitites previously described from Oman and the U.A.E. (e.g. Browning, 1982; Lippard et al., 1986; Gnos and Nicolas, 1996; Nicolas et al, 2000c) belong not to the olivine-gabbro dyke swarm of the troctolite suite, but to gabbronorites of the pyroxenite suite (Python and Ceuleneer, 2003).

The pyroxenite suite of dykes was intruded at much colder conditions (600 – 1100°C) and fluids were important in the development of these textures, as implied by the ubiquitous association of amphiboles with the last stage of crystallization of the pegmatites (Python and Ceuleneer, 2003). The dykes of the pyroxenite suite are not transposed by high-temperature plastic flow but commonly exhibit mylonitic deformation along shear zones. Their orientation is random with two preferred conjugate orientations, showing that the pyroxenite suite of dykes was not emplaced in an extensional stress field related to spreading but was intruded by hydrofracture.

2.3.6.2 Distribution of mantle dykes in Oman

Mantle dykes display a very irregular distribution. Large parts of the mantle in Oman are devoid of any dyke intrusions and display only a few dunite veins. In contrast, other parts, such as the diapiric areas identified by Nicolas et al., (2000) and shear zones, can be very rich in dykes (Nicolas et al., 2000c). An absence of dykes is observed in the lowest 1 – 2 km of mantle where the large plastic strain associated with detachment-related low temperature deformation has transposed all dykes into the foliation plane (Gnos and Nicolas, 1996; Nicolas et al., 2000c).

The distribution of the two magmatic suites, described above, is displayed on a geological map of the Oman section of the ophiolite (Figure 2.27). Python and Ceuleneer (2003) demonstrated that more than 75% of the mantle dykes belong to the pyroxenite suite, which is distributed fairly evenly over the ophiolite. However, the troctolite suite is restricted to the southern parts of the ophiolite, where it dominates the Semail and Wadi Tayin Blocks. The main troctolite zone is centred on the Maqsad area, which also has the largest chromitite deposits in the south; these dip disconcordant to the harzburgite foliation (Nicolas and Al Azri, 1999) (Figure 2.27).

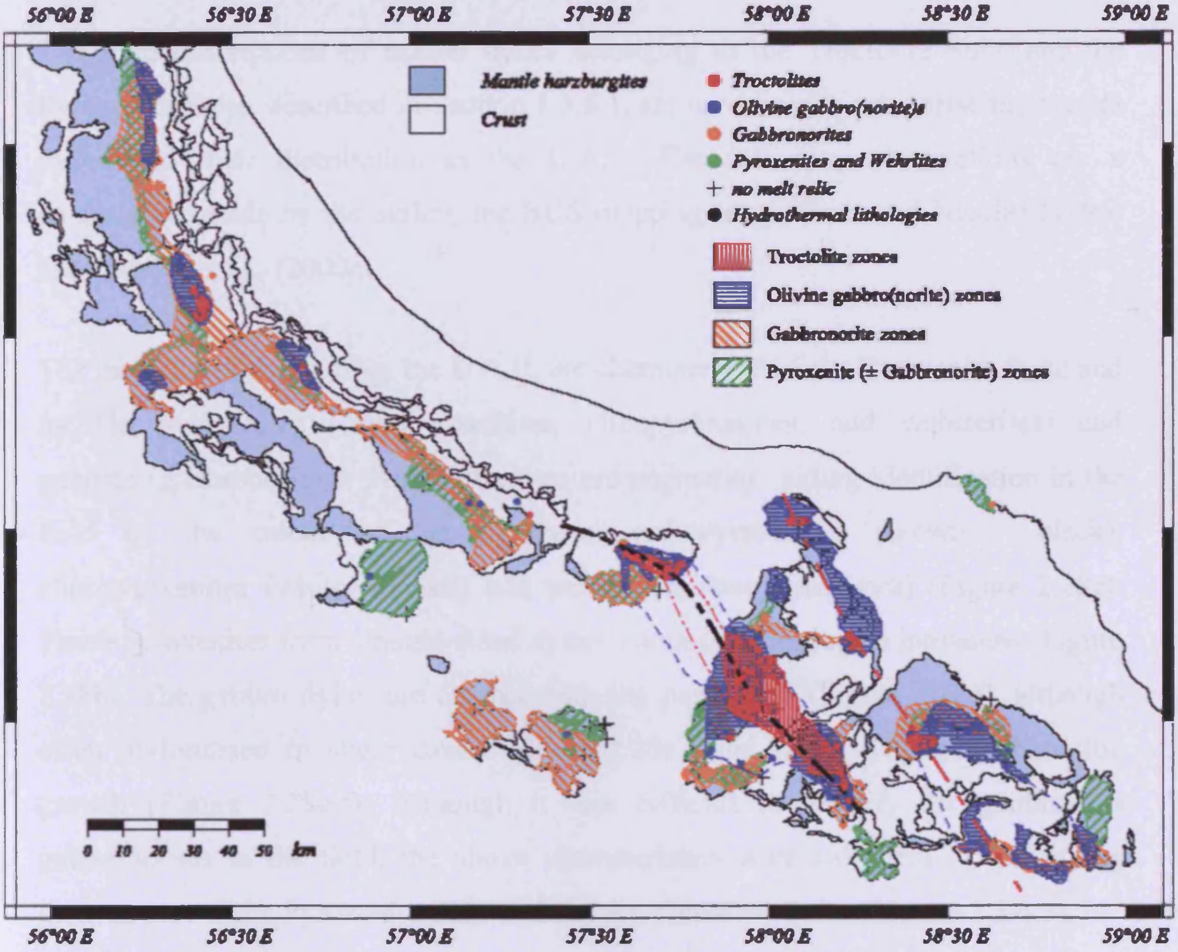

Figure 2.27: Simplified geological map of the ophiolite of Oman showing the location of each mantle dyke sampled and the distribution of the main lithological families inferred from these data. The troctolite suite includes the troctolite zones (red) and olivine gabbro-(norite) zones (blue). The pyroxenites suite includes the pyroxenites zones (green) and the gabbronorite zones (orange

2.3.6.3 Distribution of mantle dykes in the U.A.E.

The field descriptions of mantle dykes belonging to the Troctolite Suite and the Pyroxenite Suite, described in Section 1.3.6.1, are used here to categorise the mantle dykes and their distribution in the U.A.E. The following observations are a compilation made by the author, the BGS mapping team, Gnos and Nicolas (1996) and Nicolas et al., (2000c).

The majority of dykes from the U.A.E. are characteristic of the Pyroxenite Suite and include pyroxenites (orthopyroxenites, clinopyroxenites, and websterites) and gabbros (gabbronorites). The pyroxenites are pegmatitic, aiding identification in the field by the colour of the pyroxene: orthopyroxenites (brown – black), clinopyroxenites (white – green) and websterites (two pyroxenes) (Figure 2.28c). These pyroxenites form straight-sided dykes, commonly conjugate intrusions (Figure 2.28b). The gabbro dykes are characteristically pegmatitic (Figure 2.28d), although often mylonitised in shear zones (Figure 2.28e), and rarely displaying harrisitic growth (Figure 2.28e-f). Although it was difficult to identify the gabbros as gabbronorites in the field, the above characteristics were sufficient in identifying them as part of the Pyroxenite Suite and not the Troctolite Suite (Section 2.3.6.1).

In terms of regional distribution, clinopyroxenites and websterites are commonly sparse throughout all of the mantle domains. Orthopyroxenites are only found in the north around Wadi Zikt and Wadi Wurrayah. The gabbro and gabbronorite dykes are generally restricted to the uppermost level of the peridotite near the Moho in Khawr Fakkan South and Aswad South. Tonalite and composite dykes (most evolved member of pyroxenite suite) are also in Khawr Fakkan North, together with S-type granite. Khawr Fakkan South also has S-type granites but no tonalites (Styles et al., 2006).

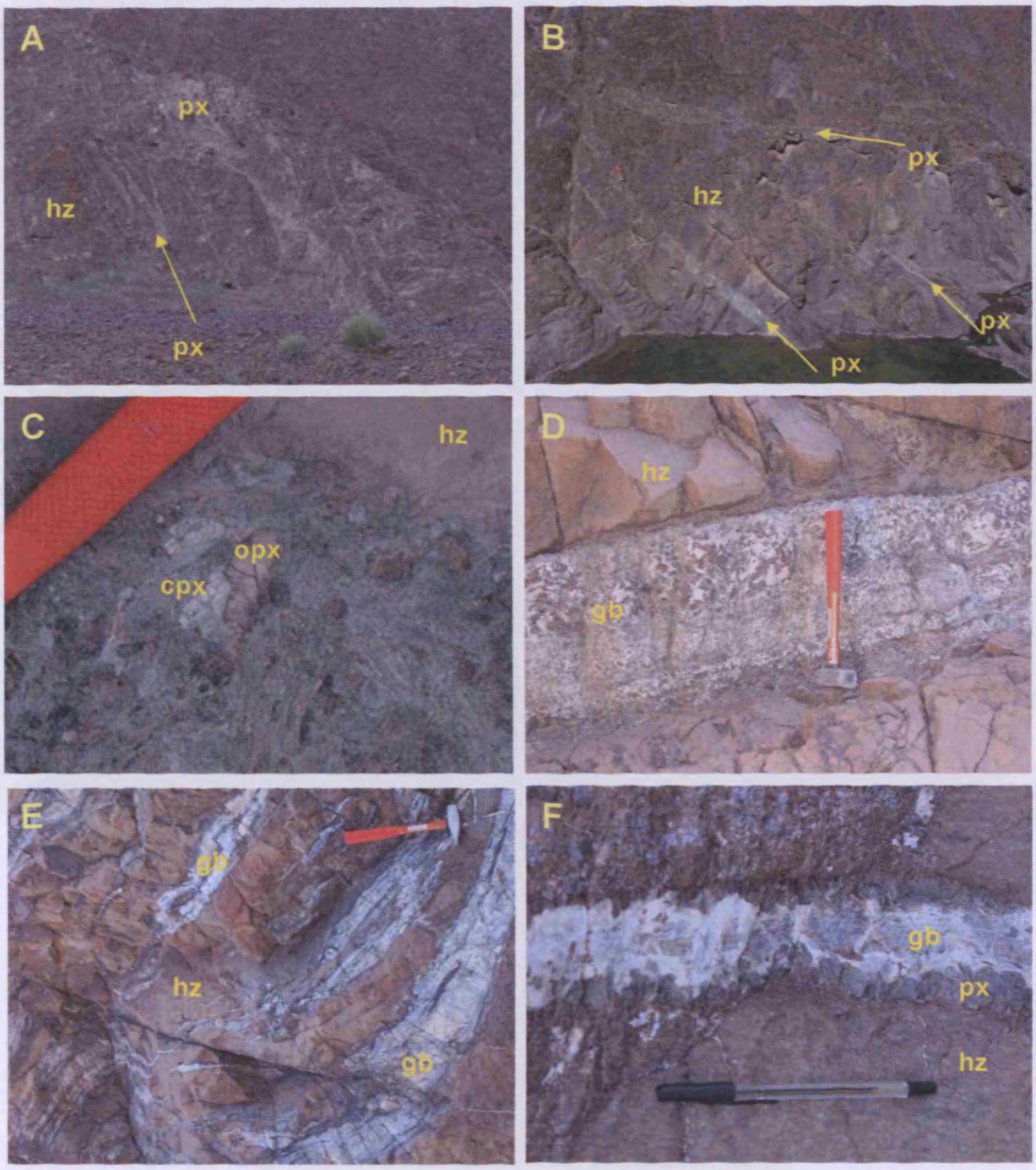

Figure 2.28: Typical field characteristics of pyroxenite (A – C) and gabbro (D – F) dykes in the mantle: (A) swarm of pyroxenite pegmatite dykes in Khawr Fakkan North, (B) conjugate dykes, highlighted by arrows, (C) close up of pyroxenite pegmatite: clinopyroxene (green) and orthopyroxene (brown), (D) gabbro dyke varying in grain-size from coarse to pegmatitic , (E) gabbro mylonite dykes from within a shear zone and (F) harrisitic growth of gabbro pegmatite with pegmatitic pyroxene on margin and medium- grained gabbro in centre.

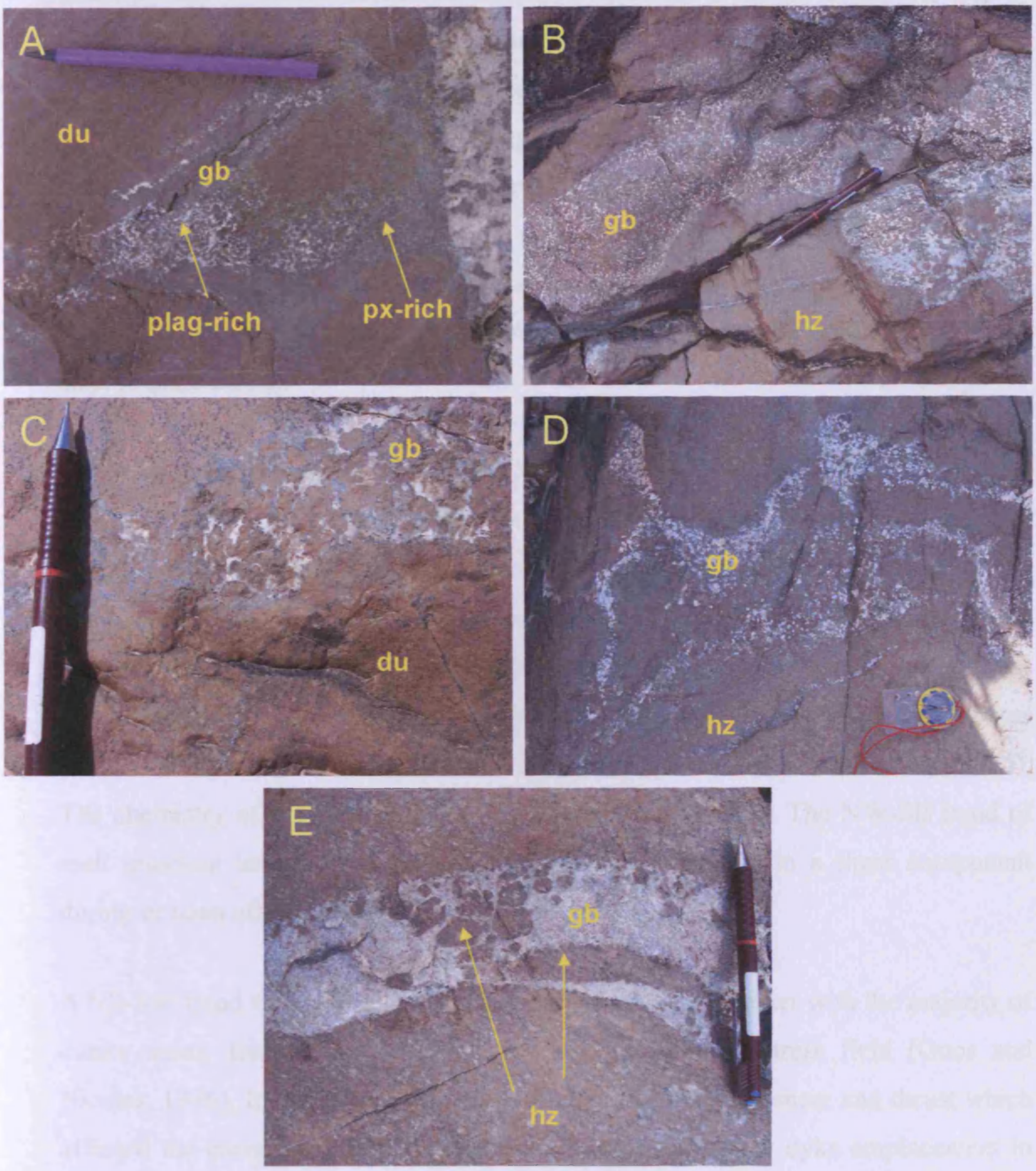

Figure 2.29: Typical field characteristics of 'hot' gabbroic intrusions in the mantle of Al Hayl; irregular veins of coarse-grained to pegmatitic gabbro forming a network around olivine from dunite of harzburgite. (A) gabbroic intrusion in mantle dunite varies from cpx-rich to plag-rich over a few centimetres. Cut by straight-sided gabbro pegmatite dyke. (B) variability of grain-size in gabbroic network, from coarse-grained to pegmatitic, in harzburgite. (C) close up of gabbroic network around coarse olivine grains in mantle dunite. (D) veins of gabbro forming an irregular network in harzburgite, and (E) gabbro forming a network around xenoliths of harzburgite. Pencil, 15cm long, for scale.

The majority of mantle dykes at Al-Hayl and Al-Qor, in Aswad South, display different characteristics to the Pyroxenite Suite of dykes described above. They have diffuse margins with the host harzburgite or mantle dunite, and form irregular networks (Figure 2.29). In this way, they are similar to the hotter 'diffuse' intrusions of the troctolite suite of Python and Ceuleneer (2003), but mineralogically they are not troctolites. They commonly form a net texture of clinopyroxenite or gabbro around olivine grains in the harzburgite or dunite, resulting in an impregnated texture (Figure 2.29c). They are cut by later straight-sided, 'colder' dykes of the pyroxenite suite (Figure 2.29a).

The **orientation** of mantle dykes from the U.A.E. has been measured by Gnos and Nicolas (1996) and Nicolas et al., (2000c), and generally agree with observations from the BGS and the author. The pyroxenite suite of dykes follows a N-S trend and a NW-SE trend in both Aswad and Khawr Fakkan. The N-S trend is parallel to the sheeted dykes in both blocks (Lilly, 2006). The NW-SE trend is parallel to the small NW-SE trending faults, intruded by younger gabbro, and a late suite of dykes associated with supra-subduction zone magmatism in the upper crust (Lilly, 2006). The chemistry of the crustal dykes is discussed in Chapter 6. The NW-SE trend of melt injection into the mantle and crust has been ascribed to a shear component during or soon after accretion (Nicolas et al., 2000c).

A NE-SW trend was also documented for mantle dykes, together with the majority of dunite veins, from Khawr Fakkan, reflecting a different stress field (Gnos and Nicolas, 1996). It cannot be ascribed to the NW-SE, sinistral shear and thrust which affected the massif soon after accretion as that should favour dyke emplacement in the E-W to WNW-SSE direction (Gnos and Nicolas, 1996; Nicolas et al., 2000c).

2.3.7 Summary of the field geology

- Deformed dunites (tabular, concordant layers) are found in close proximity to the basal thrust (Banded Unit) and the Beni Hamid Shear Zone.

- Deformed dunites (tabular, concordant layers) close to the Moho in Aswad South and Aswad North result from high-temperature plastic flow at the spreading ridge.

- Deformed chromitites (tabular, concordant veins) characterise the mantle at Al Hayl, Aswad South. However, in this area there are also undeformed dunites (anastomosing networks) and chromitites with magmatic textures, demonstrating that magmatism in this area continued after spreading stopped.

- Undeformed dunites (large, discordant pods) host small chromitite pods in Aswad South.

- Undeformed dunites (large, irregular network of veins and pods) are characteristic of the mantle in Aswad North and Khawr Fakkan North away from the Banded Unit.

- The chromitites of Wadi Zikt (Khawr Fakkan North) are also undeformed, and display magmatic textures. However, the Wadi Zikt chromitites are only subconcordant to the foliation and not discordant, as expected from the model of deformation at a spreading ridge (Cassard, et al., 1981, Figure 2.12). There was insufficient field evidence to ascertain the degree of deformation experienced by the Siji chromitites in Aswad North.

- The MTZ is a complex zone of rocks from the early magmatic phase at the spreading ridge (massive dunite and layered gabbro) and the later magmatic phase (wehrlites, pyroxenites and gabbros of the Mixed Unit).

- Mantle dykes in the U.A.E. display characteristics of the pyroxenite suite of dykes described by Python and Ceuleneer (2003). No dykes of the troctolite suite were observed. 'Hot' intrusions of the pyroxenite suite were common in the mantle of Al Hayl and could therefore be interpreted as a frozen asthenospheric window of a mantle diapir (Python and Ceuleneer, 2003).

- The hypothesis which will be tested using geochemical data in the following chapter is that the deformed dunites and chromitites originate from magmatism at a spreading ridge whereas the undeformed dunites and chromitites originate from a later magmatic episode in a supra-subduction zone setting.

2.4 Sampling Strategy

2.4.1 Logistics

The author conducted extensive fieldwork (winters 2003 and 2005) and sample collection of ultramafic rocks from the mantle section and the Moho Transition Zone (MTZ) alongside the BGS geological mapping and sampling (2002-2005). The mantle section forms distinctive dark mountains that are very jagged, covered with loose scree material and dissected by steep-sided valleys. This makes access to the mountains difficult and dangerous, and in consequence the harzburgite has been largely studied from the wadis (valleys), with few traverses across the mountains. The central part of Khawr Fakkan North was inaccessible, as a result of its double watershed, and therefore not visited by the BGS or author. The harzburgite along the western margin adjacent to the desert and the MTZ outcrops forms low rounded hills that were easily traversed.

The BGS field base was a villa in the town of Fujairah, situated half way along the U.A.E. coastline. Fieldwork was carried out using a 4 x 4 jeep and a hired, local field-assistant. A vast network of roads and local tracks made it possible to drive to the entrance of every wadi, from where the remainder of the wadi could be traversed on foot. The Council for Geoscience South Africa (CGS) survey map (Grantham et al., 2003) was used to locate the chromitite mines/prospects in this study. The GPS location of each sample collected was catalogued in a GIS system and superimposed on to the topographical and geological maps. This system aided collection of a vast sample base, around 1000 ultramafic samples, collected by the author (prefix-SD), Richard Lilly (prefix-03UR) and by five members of the BGS mapping team (prefix-U.A.E.).

Sampling was restricted solely to within the U.A.E. as the border control was strict and time-consuming for daily trips. It was not considered necessary to collect samples from the small part of Aswad across the border in Oman, as this region had already been sampled for harzburgites (LeMée et al, 2004; Monnier et al., 2006)

2.4.2 Aims

The aim of sampling was to determine the regional variation in the geochemistry of ultramafic rocks, focussing in particular on chrome-spinel, for the entire mantle section, and to a lesser extent the MTZ, of the five domains introduced in Section 2.2. GIS was used to select samples for analysis, based on their geographical location, to produce an even, spatial distribution of samples over the study area in order to produce **geochemical maps** of mantle terrane, the first of their kind (e.g. Chapter 6).

With over 1000 ultramafic rocks to choose from, there was only time for 259 rock samples to be analysed in this study. Table 2.1 displays the number of rock samples analysed from each domain and the spatial distribution of the samples are shown in Figures 2.30, 2.31 and 2.32. Details of the location and field observations for each sample analysed are reported in Appendix A.

Sampling and analysis mainly concentrated on the domains of Aswad and Khawr Fakkan, of which only the western margin of Aswad South had been sampled intensively for harzburgites before (Figure 2.30), while Aswad North and Khawr Fakkan were virgin territory (Le Mée, 2004; Monnier et al., 2006). Only a few samples were analysed from Fizh to compare with the extensive work already carried out in the Fizh Block (e.g. Brown, 1980; Matsukage et al., 2001; Takazawa et al., 2003; Kanke and Takazawa, 2005, 2006; Arai et al., 2006). Samples were taken from the Dibba Zone in high density, for its relatively small size, in order to establish for the first time the origin of the Dibba Zone peridotites and its relation to the ophiolite.

<table>
<tr><th>Rock Samples</th><th>Harzburgites</th><th>Mantle Dunites</th><th>MTZ Dunites</th><th>Mantle Chromitites</th><th>MTZ Chromitites</th><th>Wehrlites</th><th>Pyroxenites</th><th>Gabbros</th></tr>
<tr><td>DIB</td><td>10</td><td>10</td><td>-</td><td>-</td><td>-</td><td>-</td><td>-</td><td>-</td></tr>
<tr><td>KF-n</td><td>41</td><td>21</td><td>-</td><td>10</td><td>-</td><td>-</td><td>2</td><td>-</td></tr>
<tr><td>KF-s</td><td>12</td><td>8</td><td>14</td><td>2</td><td>-</td><td>1</td><td>4</td><td>6</td></tr>
<tr><td>ASW-n</td><td>25</td><td>15</td><td>-</td><td>4</td><td>-</td><td>-</td><td>1</td><td>-</td></tr>
<tr><td>ASW-s</td><td>18</td><td>15</td><td>17</td><td>6</td><td>1</td><td>2</td><td>3</td><td>6</td></tr>
<tr><td>FIZH</td><td>2</td><td>2</td><td>1</td><td>-</td><td>-</td><td>-</td><td>-</td><td>-</td></tr>
<tr><td rowspan="3">Totals</td><td>108</td><td>71</td><td>32</td><td>22</td><td>1</td><td>3</td><td>10</td><td>12</td></tr>
<tr><td>108</td><td colspan="2">103</td><td colspan="2">23</td><td colspan="3">25</td></tr>
<tr><td colspan="8">259</td></tr>
</table>

Table 2.1: Table displaying the number of rock samples collected from each domain for analysis in the following chapters. Ultramafic domains are: DIB - Dibba Zone; KF-n - Khawr Fakkan North; KF-s – Khawr Fakkan South; ASW-n – Aswad North; ASW-s – Aswad South and FIZH – Fizh.

The objectives of the sampling strategy, in order of decreasing priority, were as follows:

- To determine the nature of the residual mantle (harzburgites, n= 108).
- To characterise the type of melt/s percolating through, and reacting with, the mantle (dunites, n= 71 and chromitites, n= 22).
- To characterise the type of melt/s that collected in the MTZ at the base of the crust (dunites, n= 32 and some pyroxenites, n= 6, wehrlites, n= 3 and gabbros, n=14).
- To characterise the type of melt/s that formed dykes in the mantle dykes (very few pyroxenites, n= 4).

The main criterion for the selection of samples for analysis was based on their location. Harzburgites were selected by visual best fit to produce a grid with a distance of < 3km between adjacent samples (Figures 2.30) where possible. Pairs of harzburgites and dunites, collected from the same outcrop, were selected where possible, otherwise dunites were selected to give a good regional distribution in closest proximity to the harzburgites analysed.

Only a few representative samples of chromitites from each of the three mining districts were analysed in this study, along with the host harzburgite and dunite envelope. A more detailed study of the chromitite deposits was beyond the scope of this project and had already been carried out by Al-Aabed (2003) and Grantham et al., (2003).

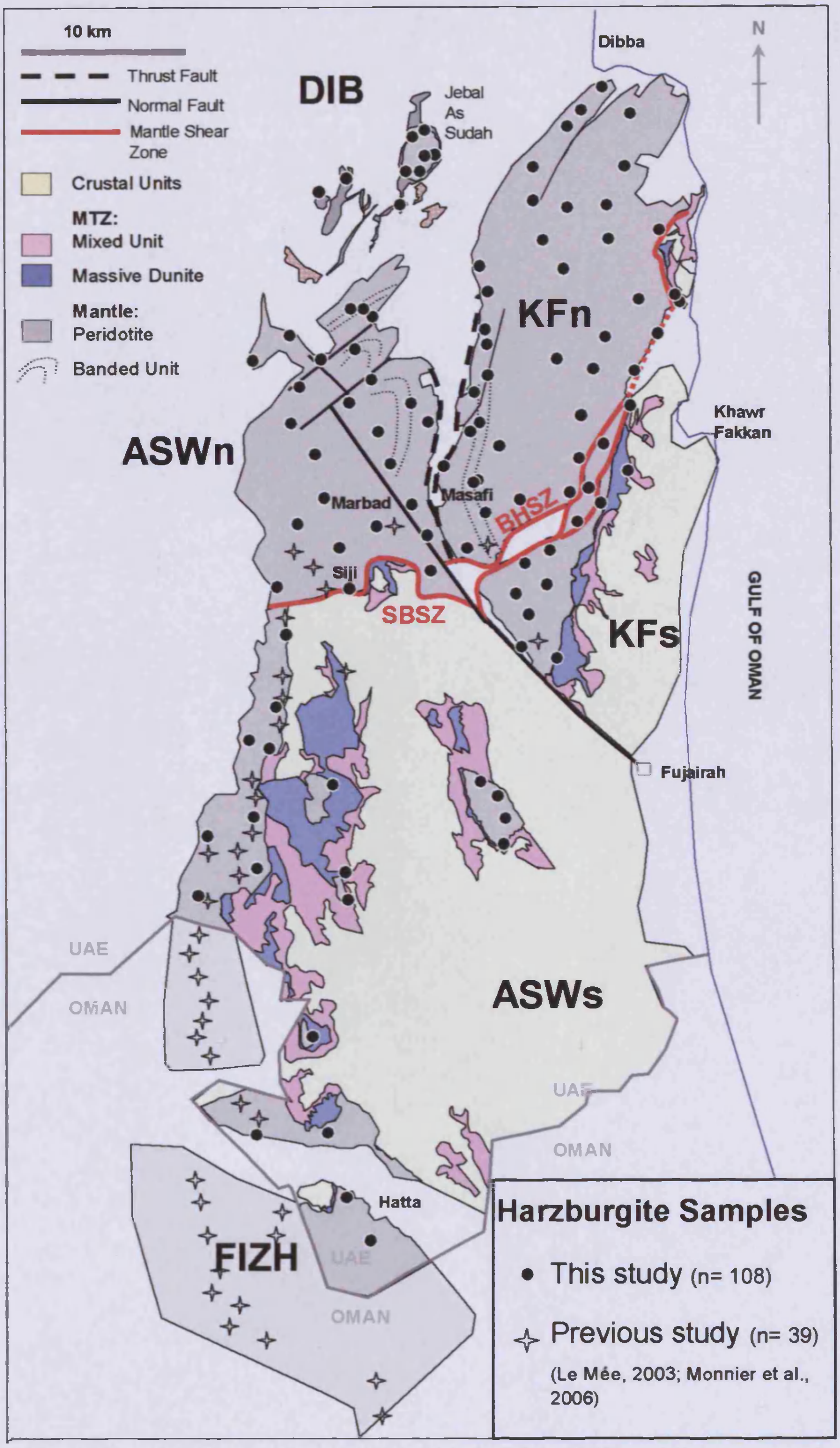

Figure 2.30: Map of the study area displaying the spatial distribution of the harzburgite samples analysed in this study (circles), was well as the harzburgites previously analysed by Le Mée (2003) and Monnier et al., (2006) (crosses).

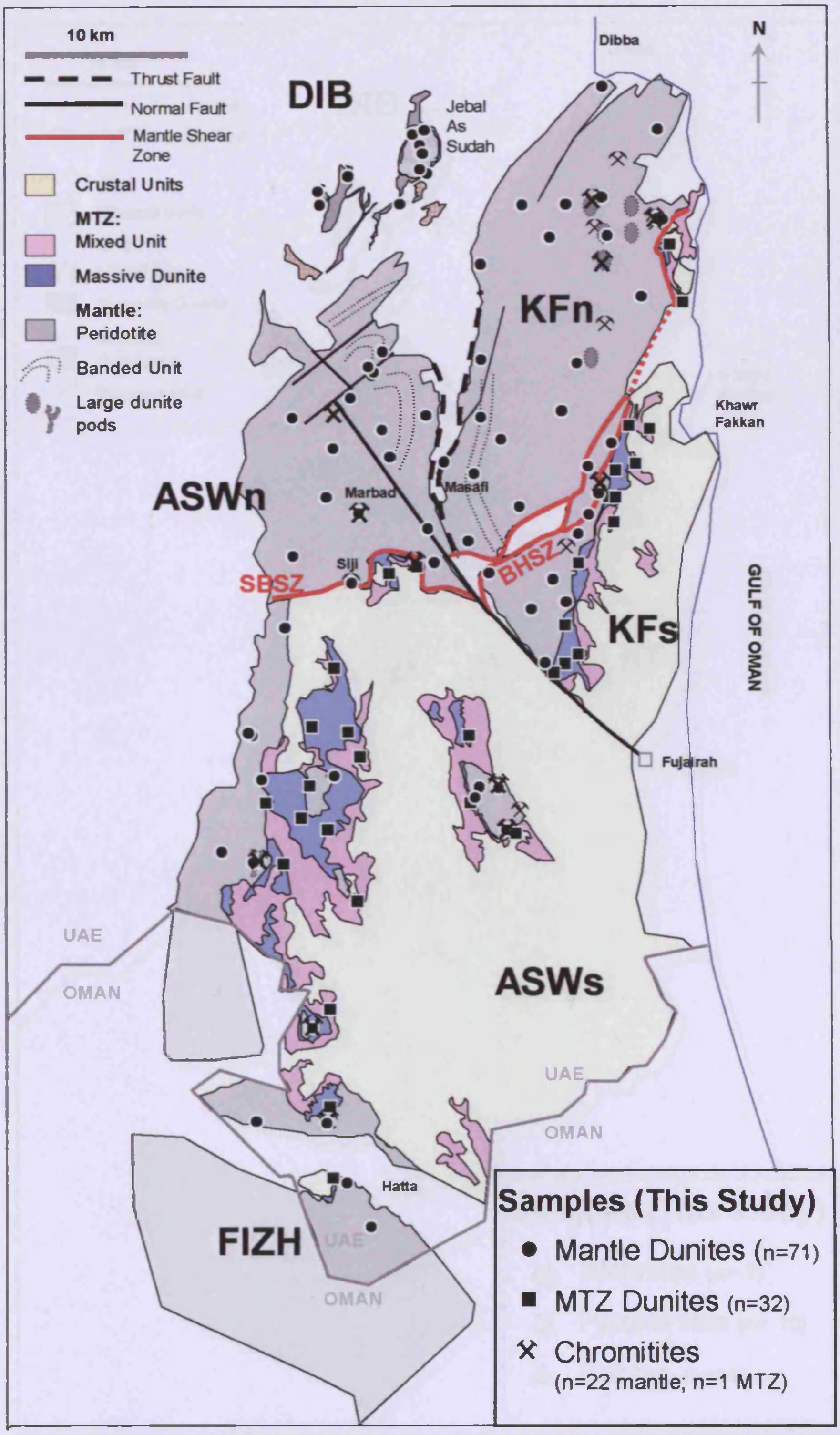

Figure 2.31: Map of the study area displaying the spatial distribution of the dunite samples from the mantle (circles), MTZ (squares) and chromitites (crossed hammers).

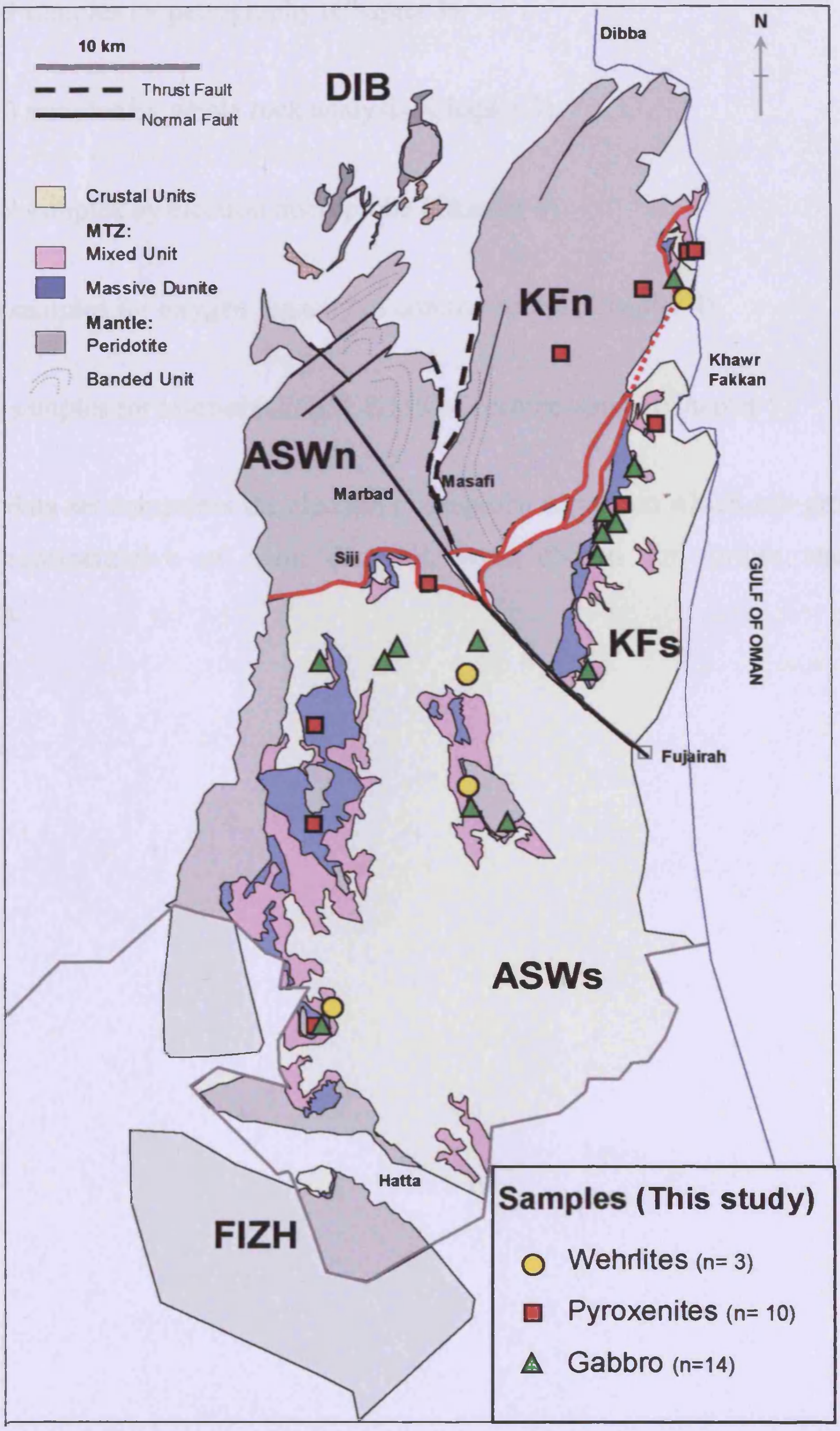

Figure 2.32: Map of the study area displaying the spatial distribution of the wehrlite (yellow circles), pyroxenites (red squares) and gabbros (green triangles) samples.

The rock samples were analysed using the following techniques:

- 259 samples by petrography (Chapter 3)
- 150 samples by whole rock analysis (Chapter 3)
- 259 samples by electron microprobe (Chapter 4)
- 60 samples for oxygen fugacity of chrome-spinel (Chapter 4)
- 41 samples for laser-ablation ICP-MS of chrome-spinel (Chapter 5)

The main data set comprises the electron microprobe data from which sub-groups of samples, representative of main data set, were chosen for further analytical procedures.

Chapter 3: Characterisation of the U.A.E. ultramafic rocks

This Chapter describes the classification and the spatial distribution of the U.A.E peridotites. The U.A.E. ultramafic rocks are classified into rock types, microstructure types and spinel types using petrography. This information is plotted on to the geological map of the U.A.E, using G.I.S, to illustrate the spatial distribution of the peridotites and their petrographic features. The classification of rock types and spinel types are the basis for geochemical grouping in the following chapters.

The main focus of this thesis is on the geochemistry of chrome-spinel because it provides important information on the petrogenesis of the peridotites and the tectonic setting of the U.A.E. ophiolite as presented in the following Chapters. Whole rock geochemistry of peridotites is not so useful and is only used in this Chapter to aid rock classification.

3.1 Rock classification

This Section describes the classification of the U.A.E. ultramafic rocks into rock types, microstructure types and spinel types. This is achieved mostly by petrography and the results of the classification are presented in Appendix B. In addition, whole rock analyses of the U.A.E. peridotites are included in this Section to confirm the subclassification of harzburgites and lherzolites proposed below. Whole rock analyses were carried out on a subset of representative peridotites by solution ICP-OES and solution ICP-MS. The method, quality of data and results for these whole rock analyses are presented in Appendix C.

3.1.1 Petrographic classification of rock types

Rock classification for ultramafic and mafic (Figure 3.1) rocks follows the BGS Rock Classification Scheme (Gillespie & Styles, 1999). Rock types are classified using mineral proportions of olivine (ol), orthopyroxene (opx), clinopyroxene (cpx) and plagioclase (plag).

In this study, mineral proportions are determined by visual estimation of thin sections under the optical microscope. Despite the often high degree of alteration of the peridotites, it was still possible to determine the primary modal mineral proportions from the characteristic pseudomorphs after the primary phases, even when little or no relict primary minerals remain (Appendix B). Clinopyroxene is often difficult to distinguish from olivine in the fine-grained matrix under the optical microscope, but back-scattered imaging on the SEM and during electron microprobe analyses confirmed the modal proportions of clinopyroxene estimated by optical microscope. Detailed SEM image mapping was carried out on a representative clinopyroxene-rich harzburgite (U.A.E.327) and lherzolite (U.A.E.2065) to illustrate the relatively high proportion of clinopyroxene in some of the U.A.E peridotites (Figure 3.2).

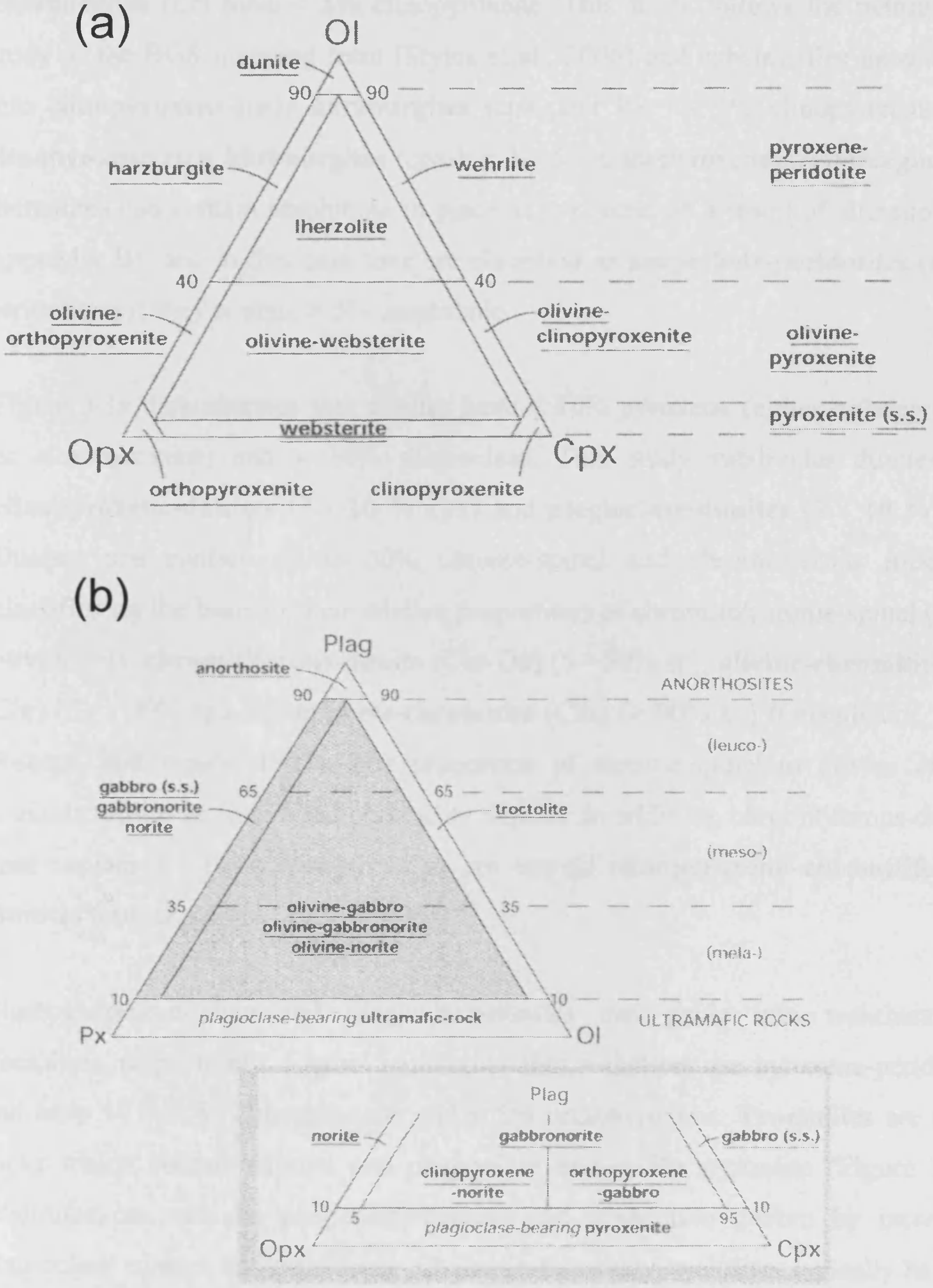

Figure 3.1: BGS classification Scheme (Gillespie and Styles, 1999) for (a) ultramafic rocks and (b) mafic rocks.

Figure 3.1a illustrates that **lherzolites** (lhz) have >5% clinopyroxene and **harzburgites** (hz) have < 5% clinopyroxene. This study follows the petrographic study of the BGS mapping team (Styles et al., 2006) and subclassifies harzburgites into **clinopyroxene-poor harzburgites** (cpx-poor hz: << 1% clinopyroxene) and **clinopyoxene-rich harzburgites** (cpx-hz: 3 - 5% clinopyroxene). Harzburgites and lherzolites can contain amphibole in place of pyroxene, as a result of alteration (see Appendix B), and in this case they are classified as **amphibole-peridotites** (amph-peridotites) if they contain > 5% amphibole.

Figure 3.1a demonstrates that dunites have < 10% pyroxene (either orthopyroxene or clinopyroxene) and < 10% plagioclase. This study subdivides dunites into **clinopyroxene-dunites** (3 - 10 % cpx) and **plagioclase-dunites** (3 - 10 % cpx). Dunites can contain up to 50% chrome-spinel and chromitiferous rocks are classified on the basis of their relative proportions of chromite/chrome-spinel (sp) to olivine (ol): **chromitiferous-dunite** (Chr-Du) (5 - 50% sp), **olivine-chromitite** (Ol-Chr) (51 - 90% sp) and **massive-chromitite** (Chr) (> 90% sp) (Greenbaum, 1977; Roberts and Neary, 1993). The proportion of chrome-spinel to olivine can be variable within an individual chromitite deposit. In addition, chromitiferous-dunites that contain 3 - 10% clinopyroxene are termed **clinopyroxene–chromitiferous-dunites** (cpx-chr-du).

Clinopyroxene-dunites and plagioclase-dunites can grade into wehrlites and troctolites, respectively. Figure 3.1a shows that **wehrlites** are pyroxene-peridotites and have 10 – 60% clinopyroxene and < 5% orthopyroxene. **Troctolites** are mafic rocks which contain olivine and plagioclase and < 5% pyroxene (Figure 3.1b). Wehrlites can also be plagioclase-bearing and grade into gabbro by increasing plagioclase content and decreasing olivine. In this study, wehrlites typically have 20 - 40% clinopyroxene and contain no plagioclase and troctolites typically have 15 - 40% plagioclase and up to 5% clinopyroxene.

Troctolites grade into olivine gabbro and gabbros, whereas wehrlites grade into olivine-pyroxenites and pyroxenites (Figure 3.1). The **olivine gabbros** that are analysed for spinel in this study contain 35 - 70% olivine. **Pyroxenites** are classified into **orthopyroxenites**, **clinopyroxenites** and **websterites**, using Figure 3.1, with the aid of imaging by the SEM.

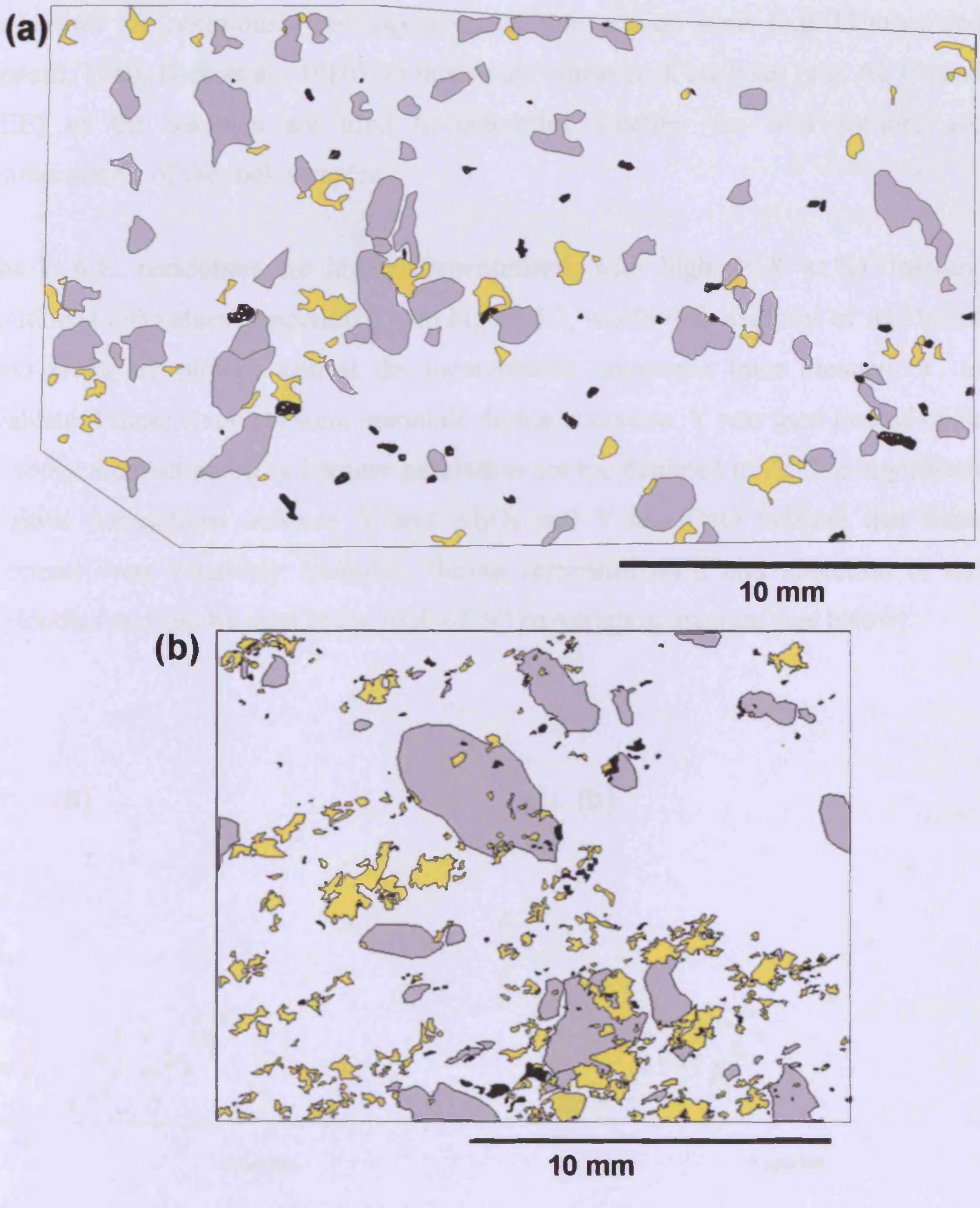

Figure 3.2: SEM image mapping of (a) **clinopyroxene-rich harzburgite** (U.A.E.327) and (b) **lherzolite** (U.A.E.2065). Orthopyroxene (grey), clinopyroxene (yellow), spinel (black) and olivine (white). The proportion of clinopyroxene is estimated as 4% in (a) and 13% in (b).

3.1.2 Checking peridotite rock types with whole rock analyses

The modal proportion of clinopyroxene is critical in the classification of harzburgites and lherzolites, as described above. However, the proportions of clinopyroxene in peridotites are notoriously heterogeneous on thin section scale (e.g. Hamlyn and Bonatti, 1980; Dick et al., 1980). In this study, whole rock analyses (e.g. Al, Ca and REE) of the samples are used to determine whether the thin sections are representative of the rock samples.

The U.A.E. peridotites are highly serpentinized, with high (> 8 wt %) loss-on-ignition (LOI) values (Appendix C). In Figure 3.3, whole rock analyses of Al_2O_3 and CaO wt.% are plotted against the incompatible, immobile trace element, Y, to evaluate if these elements were immobile during alteration. Y was used instead of Zr to verify element mobility because peridotites are too depleted in Zr. The significant positive correlations between Y and Al_2O_3 and Y and CaO indicate that these elements were relatively immobile during serpentinization and alteration of the peridotites and can be used in the Al_2O_3-CaO co-variation diagram (see below).

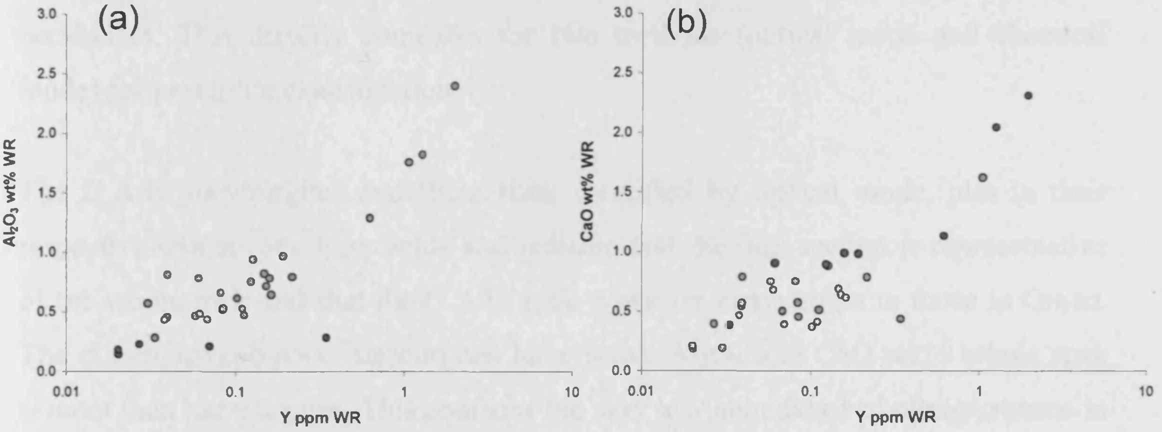

Figure 3.3: Covariations diagrams for the whole rock analysis of immobile element Y plotted against for (a) Al_2O_3 and (a) CaO in peridotites. The correlation between Y and Al_2O_3 and Y and CaO indicates that these elements were relatively immobile during alteration.

3.1.2.1 Al_2O_3-CaO covariation diagram

Al_2O_3 wt.% (whole rock) is plotted against CaO wt.% (whole rock) on Figure 3.4 for peridotites from Oman (Figure 3.4a) and the U.A.E. (Figure 3.4b). The mineral proportions of clinopyroxene in the Oman peridotites were calculated from a mass balance of the whole rock and mineral compositions (i.e. chemical mode) (Takazawa et al., 2000; Godard et al., 2003). In contrast, the mineral proportions of clinopyroxene in the U.A.E. peridotites were estimated by visual estimation of clinopyroxene (i.e. optical mode) as described in Section 3.2. Both data sets are classified as lherzolites, clinopyroxene-rich harzburgites, harzburgites, clinopyroxene-poor harzburgites and dunites using the classification scheme described in Section 3.2.1.

In Figure 3.4a, the Oman peridotites (classified using chemical mode) form distinct compositional fields for lherzolites, clinopyroxene-rich harzburgites, harzburgites and dunites. The Al_2O_3 and CaO wt.% in the whole rock decreases as the proportion of clinopyroxene, and to some extent orthopyroxene, decreases from the lherzolite field to the harzburgite field. The U.A.E. peridotites are plotted on the Al_2O_3-CaO wt.% diagram in Figure 3.4b along with the reference fields for lherzolites, clinopyroxene-rich harzburgites, harzburgites and dunites defined by the Oman peridotites. This directly compares the two methods (optical mode and chemical mode) for peridotite classification.

The U.A.E. harzburgites and lherzolites, classified by optical mode, plot in their respective Oman rock type fields and indicate that the thin section is representative of the whole rock and that the U.A.E. rock types are comparable to those in Oman. The clinopyroxene-poor harzburgites have lower Al_2O_3 and CaO wt.% whole rock content than harzburgites. This confirms the very low abundance of clinopyroxene in these clinopyroxene-poor harzburgites which are uncommon in Oman.

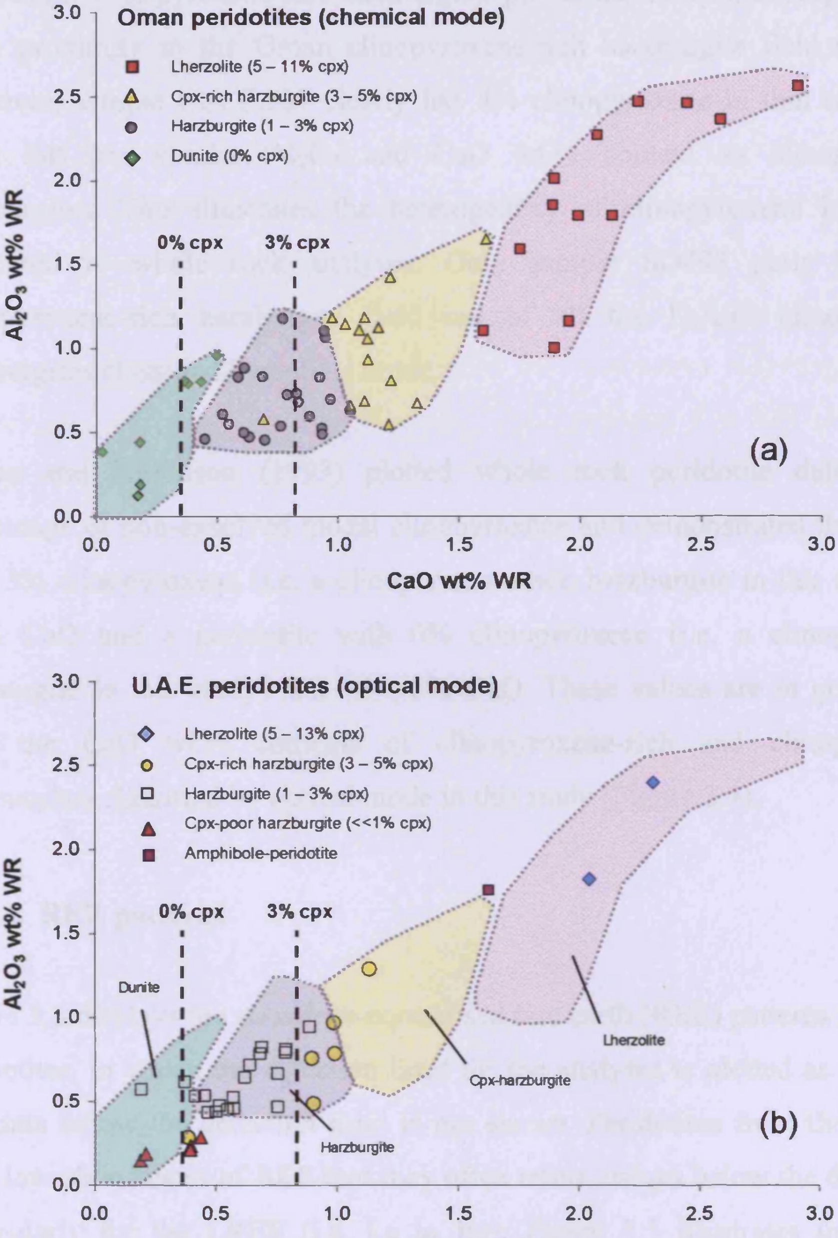

Figure 3.4: Al_2O_3 vs. CaO covariation diagrams for peridotites from (a) Oman (Takazawa et al., 2002; Godard et al., 2000) and (b) U.A.E (this study). The Oman peridotites are classified using chemical mode and the U.A.E. peridotites are classified using optical mode proportions of clinopyroxene. The Oman peridotites define fields in (a) for lherzolites, cpx-harzburgites, harzburgites and dunites that are compared to the U.A.E. peridotites in (b). Pearce and Parkinson (1993) illustrated that peridotites with <0.3 wt.% CaO have 0% clinopyroxene and that peridotites with 0.8 wt.% CaO have 3% clinopyroxene. In (b) the CaO wt.% contents of clinopyroxene-poor harzburgites and clinopyroxene-rich harzburgites classified by optical mode in this study agree with the work of Pearce and Parkinson (1993).

Most of the clinopyroxene-rich harzburgites plot in the Oman harzburgite field but in close proximity to the Oman clinopyroxene-rich harzburgite field (Figure 3.1b). However, sample U.A.E.327 clearly has 4% clinopyroxene in thin section (Figure 3.2a) but has similar Al_2O_3 and CaO wt.% content as clinopyroxene-poor harzburgites. This illustrates the heterogeneity of clinopyroxene in thin section compared to whole rock analyses. Only sample SD493 plots in the Oman clinopyroxene-rich harzburgite field out of all the U.A.E. clinopyroxene-rich harzburgites classified by optical mode.

Pearce and Parkinson (1993) plotted whole rock peridotite data against the percentage of non-exsolved modal clinopyroxene and demonstrated that a peridotite with 3% clinopyroxene (i.e. a clinopyroxene-rich harzburgite in this study) has 0.8 wt.% CaO and a peridotite with 0% clinopyroxene (i.e. a clinopyroxene-poor harzburgite in this study) has 0.3 wt.% CaO. These values are in good agreement with the CaO wt.% contents of clinopyroxene-rich and clinopyroxene-poor harzburgites classified by optical mode in this study (Figure 3.4).

3.1.2.2 REE patterns

Figure 3.5 displays the chondrite-normalised rare earth (REE) patterns for the U.A.E. peridotites, in which the detection limit for the analyses is plotted as a dashed line, and data below the detection limit is not shown. Peridotites from the U.A.E. have such low abundances of REE that they often return values below the detection limit, particularly for the LREE (i.e. La to Eu). Figure 3.5 illustrates that lherzolites, harzburgites and clinopyroxene-poor harzburgites have different REE patterns whereas clinopyroxene-rich harzburgites have similar patterns to harzburgites. In detail, lherzolites have higher abundances of HREE (e.g. $0.8 < \text{Yb} < 1.3$) than harzburgites (e.g. $0.08 < \text{Yb} < 0.2$) and clinopyroxene-poor harzburgites have the lowest abundances of HREE (e.g. $0.01 < \text{Yb} < 0.05$). The highest-abundances are in samples with the greatest clinopyroxene abundances because clinopyroxene is commonly the dominant host of HREE in peridotites. The clinopyroxene-rich harzburgites have similar HREE abundances to harzburgites, except for SD493 which has similar abundances to those of the lherzolites (Figure 3.5a) and was the only clinopyroxene-rich harzburgite to plot in the correct field in Figure 3.4b.

In summary, whole rock analyses of Al, Ca and REE confirm that the visual estimates of clinopyroxene from thin sections are largely representative of the rock sample and that the grouping of the U.A.E peridotites into lherzolites, harzburgites and clinopyroxene-poor harzburgites is valid. However, samples classified in thin section as clinopyroxene-rich harzburgites are sometimes indistinguishable from harzburgites using whole rock analyses. This indicates that the classification of clinopyroxene-rich harzburgite is not always representative of the rock sample. Therefore, whole rock analyses cannot provide further information on how these clinopyroxene-rich harzburgites formed and instead this study relies on petrography and mineral chemistry for answers.

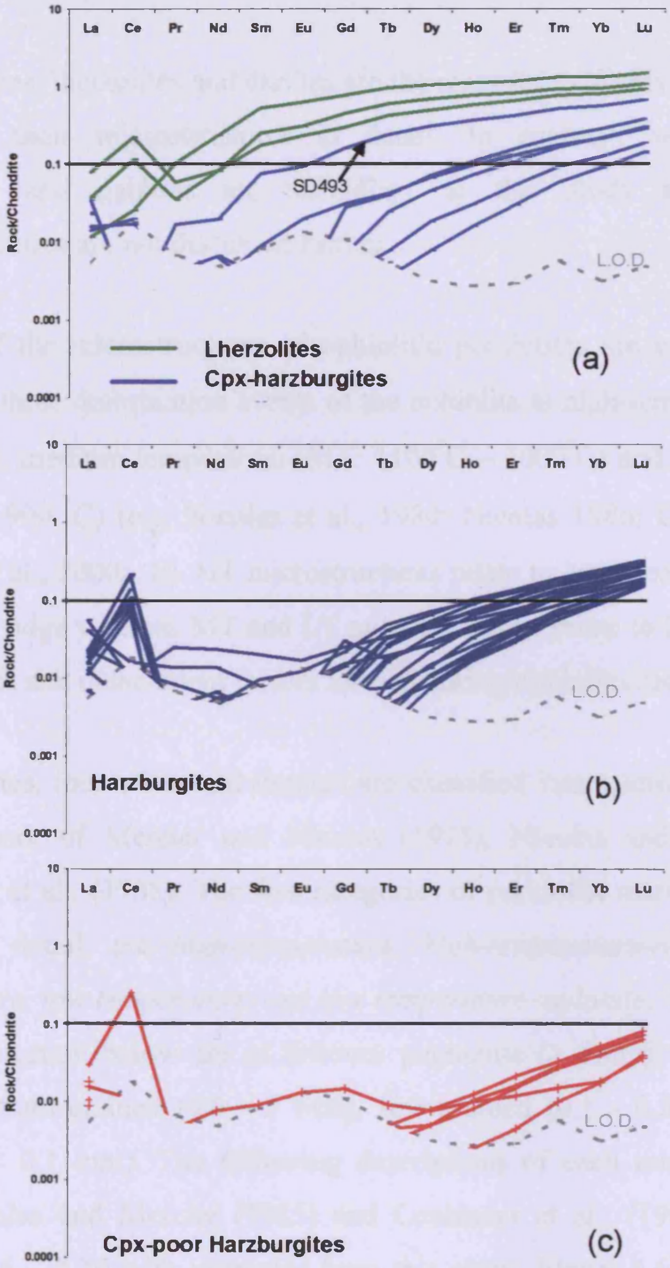

Figure 3.5: Chondrite-normalised REE patterns of the U.A.E. peridotites: (a) Lherzolites and cpx-harzburgites, (b) harzburgites and (c) cpx-poor harzburgites. The limits of detection are marked by a dashed line and data below this is not plotted. Solid line at 0.1 is for reference between diagrams. The lherzolites have higher REE abundances than the harzburgites and the cpx-poor harzburgites have the lowest abundances of REE. Cpx-harzburgites have similar patterns to harzburgites except SD493 which is similar to the pattern for lherzolites. These REE patterns confirm the rock classification proposed by petrography. All samples are normalised to Sun and McDonough (1999).

3.1.3 Microstructure types

Harzburgites, lherzolites and dunites are the main focus of this study and this Section describes their microstructures in detail. In contrast, wehrlites, pyroxenites, troctolites and gabbros are subsidiary to this study and details of their microstructures are not discussed further.

Studies of the microstructures of ophiolitic peridotites are extensive and they are related to three deformation events of the ophiolite at high-temperature (HT: 1200°C – 1250°C), medium-temperature (MT: 1100°C – 1000°C) and low-temperature (LT: 1000°C – 900 °C) (e.g. Nicolas et al., 1980; Nicolas 1986; Ceuleneer et al., 1988, Nicolas et al., 2000a, b). HT microstructures relate to asthenospheric flow below the spreading ridge whereas MT and LT microstructures relate to localised motion along shear zones and detachment thrusts formed during ophiolite obduction.

Harzburgites, lherzolites and dunites are classified into microstructural types based on the work of Mercier and Nicolas (1975); Nicolas and Mercier (1985) and Ceuleneer et al., (1988). The five categories of peridotite microstructures, described below in detail, are *high-temperature, high-temperature-recrystallized, medium temperature, low temperature,* and *low temperature-mylonite*. The grain sizes used in the classification below are as follows: pegmatite (> 5mm), coarse-grained (1 - 4 mm), medium-grained (0.5 - 1 mm), fine-grained (0.1 - 0.5 mm) and very fine-grained (< 0.1 mm). The following descriptions of each microstructure are taken from Nicolas and Mercier (1985) and Ceuleneer et al., (1988) and illustrated in Figures 3.6 – 3.10 with examples from this study. Figure 3.6 displays the range in grain sizes (coarse- to fine-grained) in harzburgites that have HT, MT and LT textures. These textures are illustrated in further detail in Figure 3.7 (HT) and Figure 3.8 (MT/LT). Figure 3.9 shows the wide range in grain sizes (pegmatite- to fine-grained) in dunites with HT and MT textures. Finally, Figure 10 displays the HT, MT and LT textures of dunites in detail.

High-temperature (HT):

High-temperature microstructures display a **granular** texture with sharp grain boundaries and common, well-equilibrated, 120° triple-junctions, demonstrating good recovery at high-temperatures (e.g. Figure 3.7). Grain sizes range from pegmatitic to medium-grained although coarse-grained is the most common (e.g. Figures 3.6a-b, Figures 3.7a-d and Figures 3.9a-c). The grain size in dunites can be pegmatitic (e.g. 3.9a) because of the lack of impingement with other phases (Nicolas and Prinzhofer, 1983). Figure 3.9a illustrates that the pegmatite-grained (HT-peg) microstructure in dunites have irregular, wavy margins which are not recovered and thus show minimal or no deformation from HT plastic flow. Talkington and Malpas (1980) describe similar dunites with pegmatite grain sizes (6 mm) from undeformed dunites that are discordant to the tectonic fabric in the White Hills peridotite.

The grain size distribution of coarse-grained granular fabrics can be unimodal ('equigranular' e.g. Figure 3.6b) or bimodal ('porphyroclastic' e.g. Figure 3.6a) and depends on the amount of asthenospheric shear strain. High shear strain is recovered at high-temperatures by syntectonic recrystallisation (annealing) and olivine can recrystallize in nearly equant (e.g. Figure 3.10a) or tabular (e.g. 3.10b) grains. This results in an **equigranular** texture that can mimic a cumulate texture for dunites (Jackson, 1961). Dunites are more homogeneous than harzburgites, because the former lack orthopyroxene, and therefore recover and recrystallize more easily than harzburgites.

High-temperature-recrystallized (HT-rc):

Increasing deformation at high-temperature results in the formation of closely-spaced sub-grains and dynamic grain size-reduction, commonly followed by recovery, resulting in **fine-grained equigranular** texture (e.g. Figure 3.6c, Figures 3.7e-f and Figure 3.9e).

Medium-temperature (MT):

Coarse-grained porphyroclastic texture consists of coarse-grained porphyroclasts in a fine-grained matrix (Figures 3.6D-E). Porphyroclasts are coarse, strained crystals, predominantly orthopyroxene which is often heavily kinked, with undulose extinction and often with recrystallized rims (e.g. Figures 3.8a-b). Porphyroclasts represent a relict of the original rock which has escaped crushing and recrystallisation during the deformation process. They are generally flattened and elongate, and define a moderate foliation and lineation within the rock. The fine-grained matrix consists of recrystallized, strain-free grains (neoblasts) of predominantly olivine (e.g. 3.10 d-e).

The coarse-grained porphyroclastic texture (MT) is transitional from a coarse-granular texture (HT) with the appearance of porphyroclasts. A transitional HT/MT texture has porphyroclasts with fine grains along the grain boundaries, but lacks a fine-grained matrix (e.g. Figure 3.6d and Figure 3.8b). Figure 3.9f illustrates a transitional HT/MT texture in a dunite with a pegmatite-grain size. In this case the olivine porphyroclasts are elongate forming ribbons and fine-grained olivines form along the margins.

Low-temperature (LT):

Fine-grained porphyroclastic microstructure is transitional from coarse-grained porphyroclastic and is characterised by a reduction in the abundance of, and a decrease in the grain size of, the porphyroclasts and matrix grains (e.g. Figure 3.6f). The orthopyroxene porphyroclasts are significantly more flattened and elongate than those of coarse-grained porphyroclasts (e.g. Figures 3.8c-d).

Fine-grained LT textures in dunites typically have elongate olivines with rounded edges (e.g. Figure 3.10f) and are termed **fine-grained granoblastic**, after Talkington and Malpas (1980).

Low-temperature-mylonite (LT-myl):

A **mylonite** microstructure is transitional from a fine-grained porphyroclastic structure and possesses a strong foliation and lineation defined by elongate pyroxene porphyroclasts (e.g. Figure 3.6f). This texture is characterised by pervasive recrystallisation and a very fine matrix grain size (e.g. Figure 3.8e-f). Olivine and clinopyroxene are normally completely recrystallised into fine-grained neoblasts, which have a heterogeneous grain size distribution (Nicolas et al., 1980).

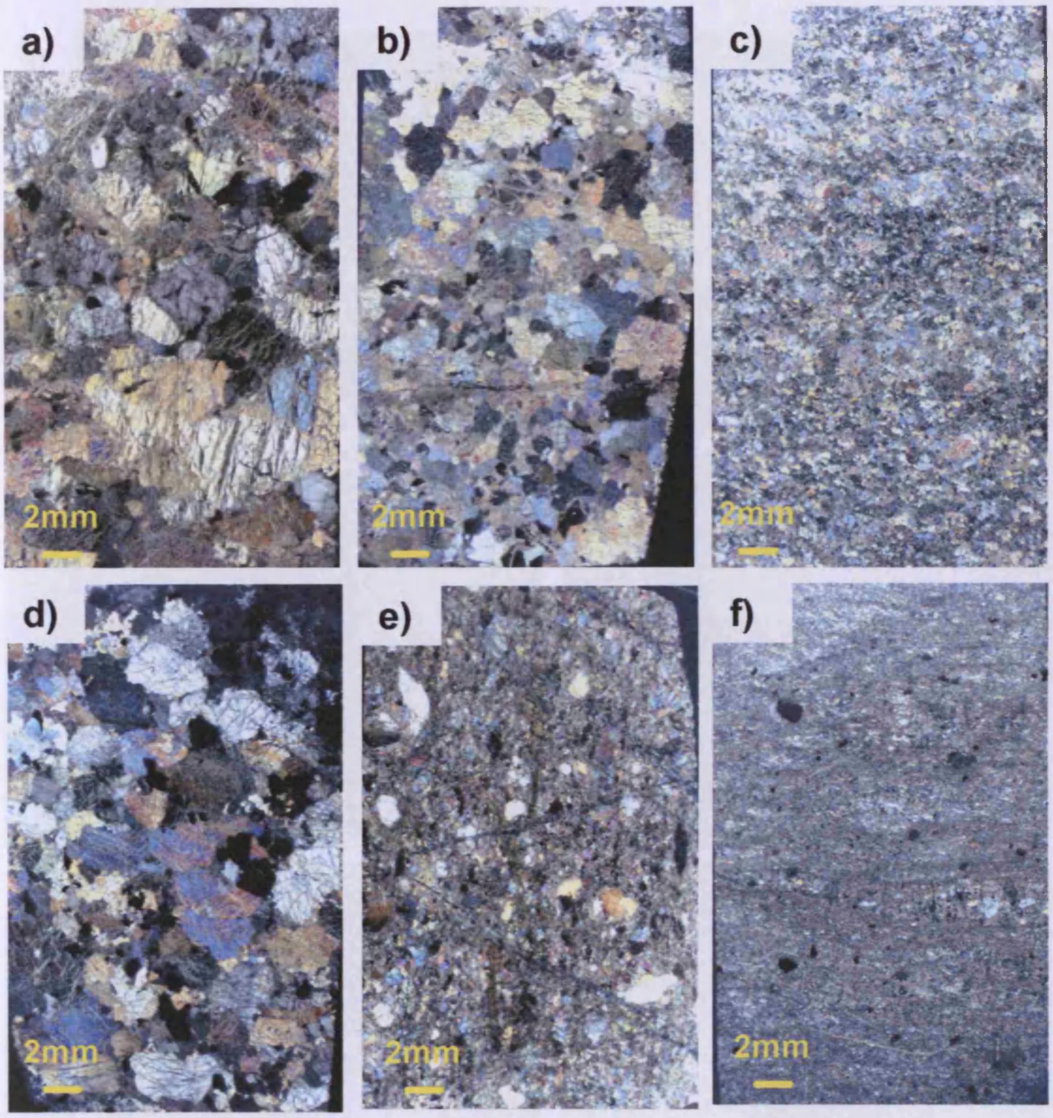

Figure 3.6: Classification of microstructures in harzburgites and lherzolites showing a wide range in grain-sizes: (a) 'bimodal' coarse-grained granular (HT) (U.A.E.86), (b) 'equigranular' coarse-grained to medium-grained granular (HT) (U.A.E.316), (c) fine-grained granular (U.A.E.2167), (d) coarse-grained porphyroclastic (HT/MT) (U.A.E. 312), (e) coarse-grained porphyroclastic (MT) (U.A.E.2035) and (f) fine-grained mylonite (LT) (U.A.E. 432). See text for further explanation. Photos are taken of the entire thin section in crossed-polarised light.

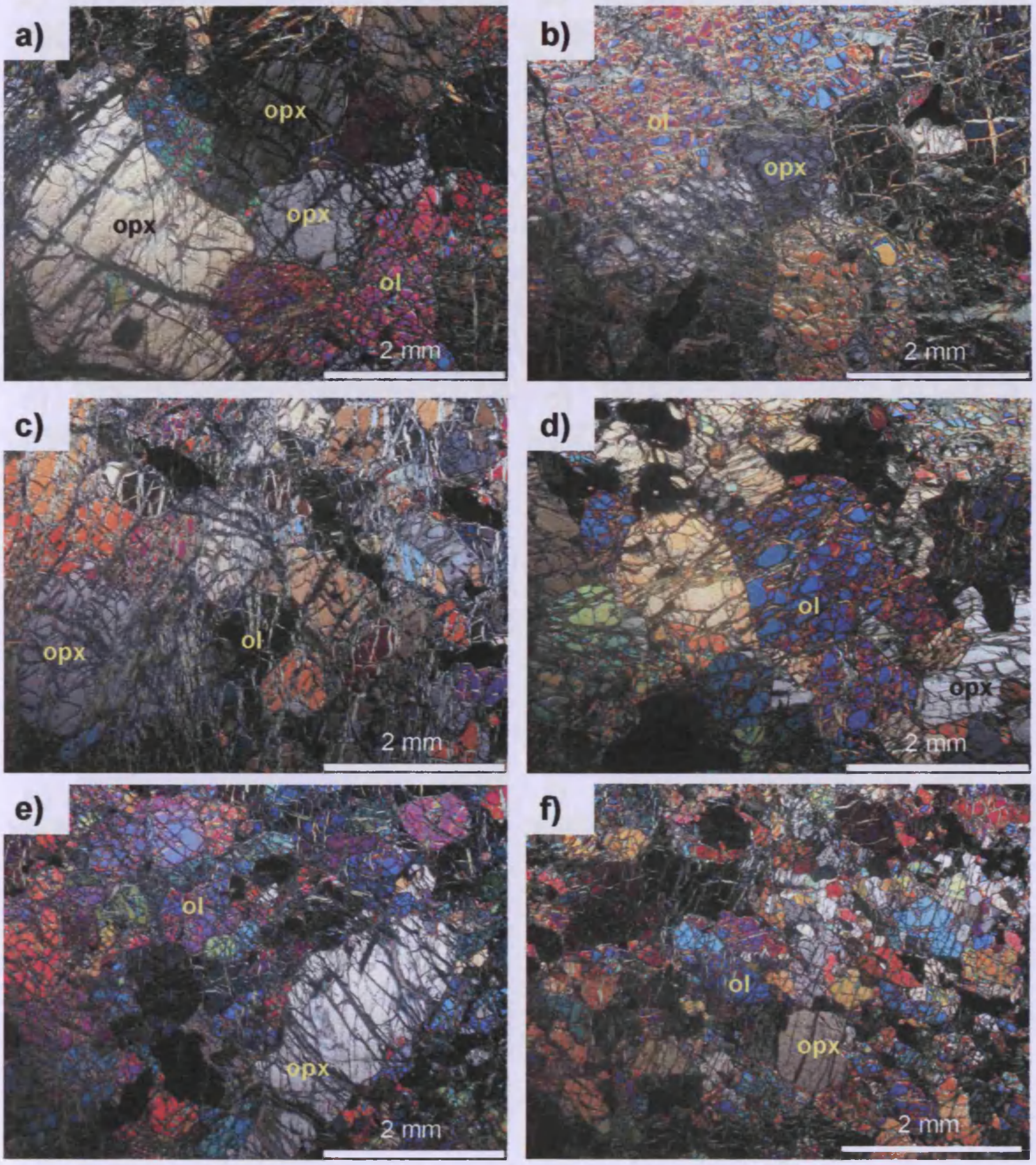

Figure 3.7: HT granular textures in harzburgites: (a) and (b) coarse-grained HT texture (e.g. U.A.E.2087) with opx-rich patch in (a) and ol-rich patch in (b); (c) and (d) medium-grained HT texture; (e-f) HT-recrystallized harzburgite from the Banded Unit (e.g. U.A.E. 2080) with grain size varying from medium in (e) to fine grained in (f). Orthopyroxene grains are marked opx and the remaining high birefringence minerals are olivine (ol) with serpentine cracks.

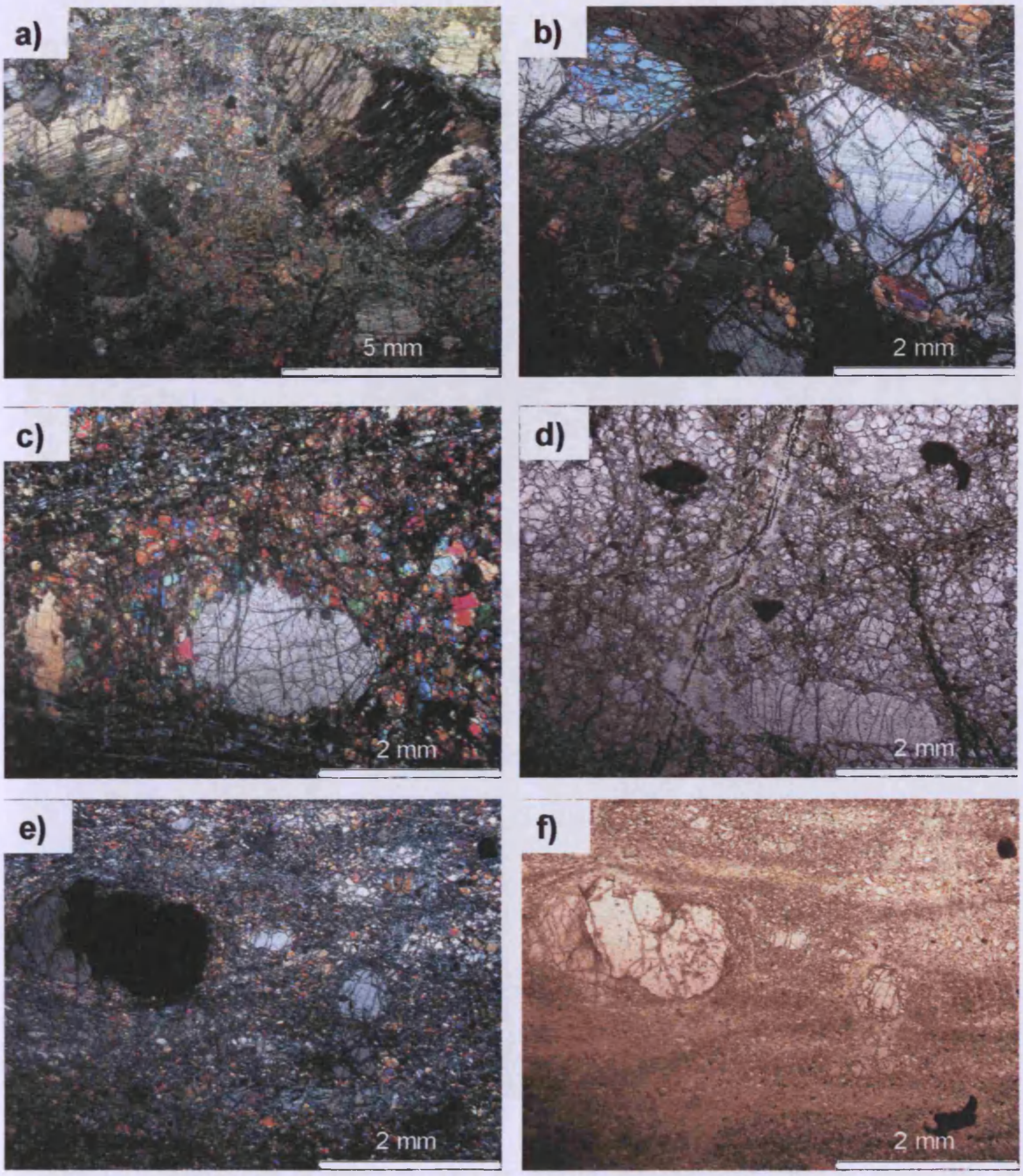

Figure 3.8: MT and LT porphyroclastic textures in harzburgites: (a) and (b) coarse-grained porphyroclastic texture (MT) (e.g. U.A.E.2058); (c) and (d) fine-grained porphyroclastic texture (LT) (e.g. U.A.E.2032); (e) and (f) fine-grained mylonite (LT) (e.g. U.A.E.432). Orthopyroxene grains are marked opx and the remaining high birefringence minerals are olivine with serpentine cracks.

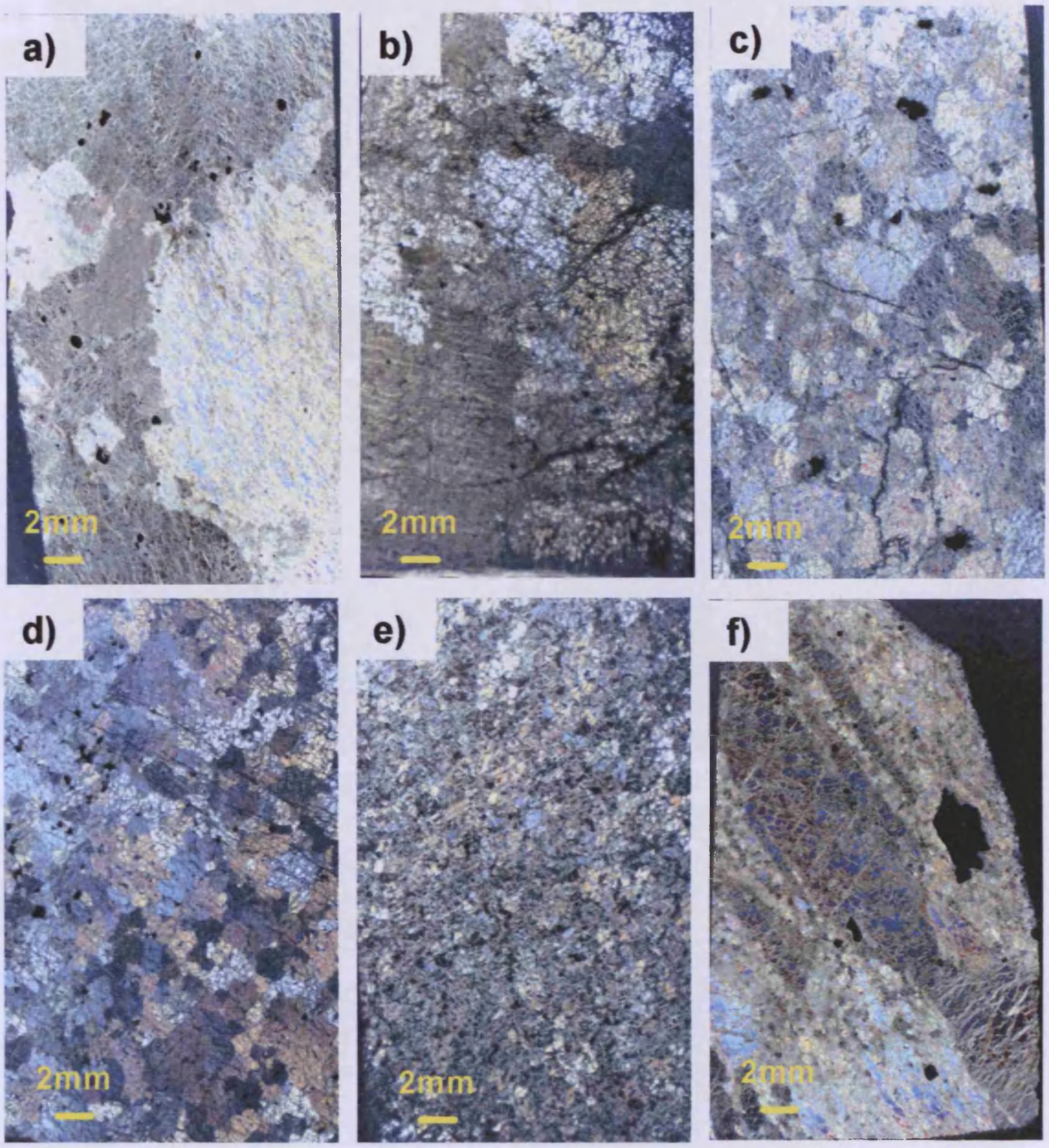

Figure 3.9 Classification of microstructures in dunites showing wide range in grain-sizes: (a) pegmatite-grained granular (HT) (U.A.E. 2222-mantle), (b) coarse-grained granular (HT) (SD 18-mantle), (c) coarse-grained to medium-grained granular (HT) (SD36-mantle), (d) medium- grained 'equigranular' (HT) (U.A.E.2832-MTZ), (e) fine-grained granular (HT-rc) (U.A.E. 2808-MTZ) and (f) pegmatite-grained porphyroclastic (HT/MT) (U.A.E. 299-mantle).

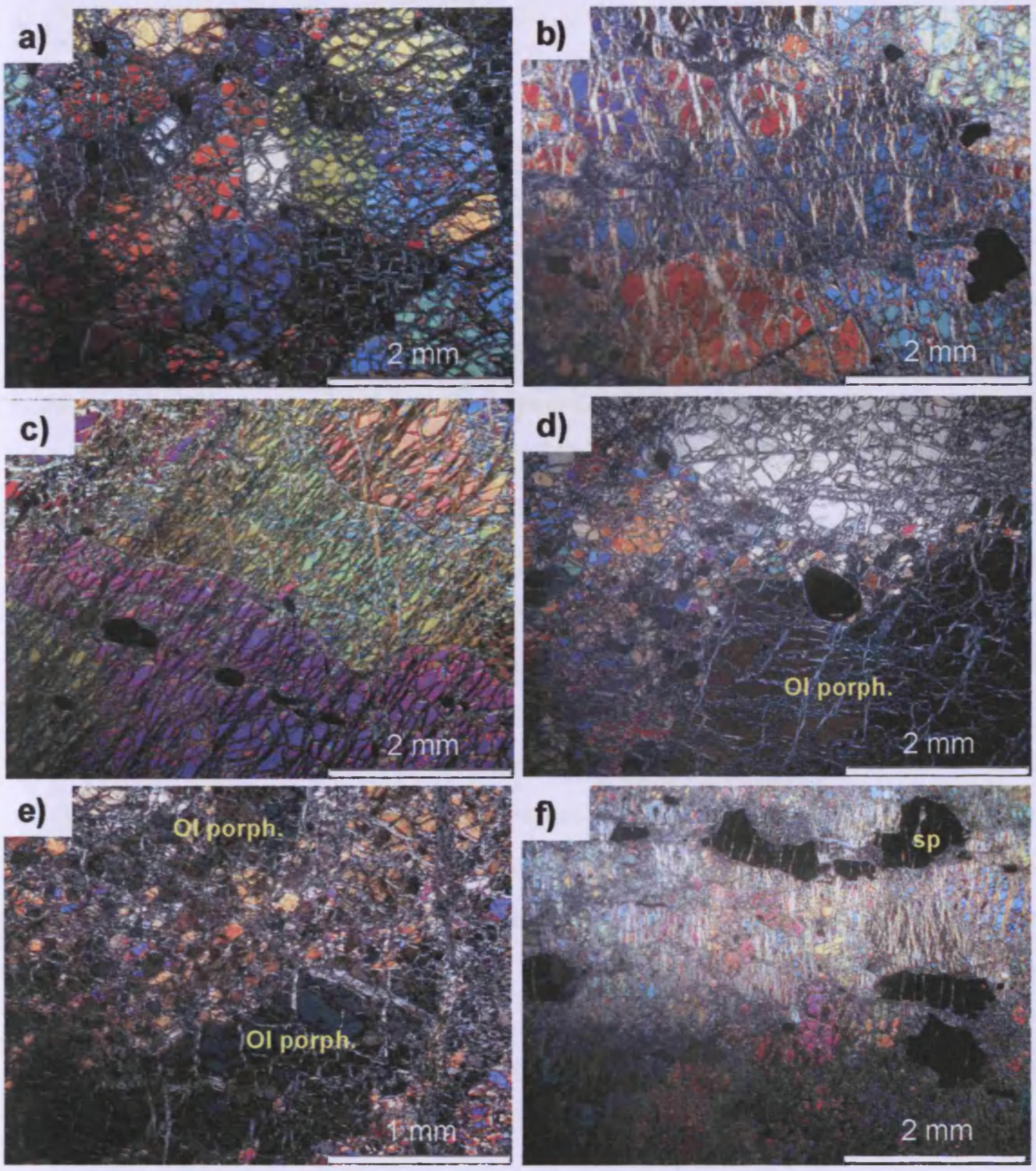

Figure 3.10: HT, MT and LT textures in dunites from the mantle and MTZ : (a) 'equigranular' texture of recrystallized (HT-rc) olivine (U.A.E.535-MTZ), (b) tabular fabric of HT-rc olivine (U.A.E.353-MTZ), (c) elongate olivine with irregular and concave grain boundaries forming a fabric parallel to spinel trail (HT) (U.A.E.615-mantle), (d) pegmatite-grained porphyroclastic (porph.) texture (MT) (U.A.E.138-mantle), (e) coarse-grained porphyroclastic (MT) in dunite of the Banded Unit (SD490-mantle) and (f) medium- to fine-grained granoblastic (MT/LT), elongate olivine fabric is parallel to the leaf spinel (sp) fabric (U.A.E.543 chr-dunite in mantle).

3.1.4 Spinel types

3.1.4.1 Classification

There are three main types of spinel textures described in the literature that are appropriate for the classification of spinels in ophiolites. This study uses the terminology of Type 1 and Type 2 spinels introduced by Augé (1982) to distinguish between the different types of spinels in peridotites from the Oman-U.A.E. ophiolite (e.g. Roberts, 1982; Augé and Roberts, 1982; Roberts, 1986; Le Mée et al., 2004; Monnier et al., 2006). Type 3 is introduced in this study to extend spinel classification. The three spinel types are described below and illustrated with optical photographs (Figures 3.11 – 3.14) taken of spinels from the U.A.E. peridotites and chromitites. Figures 3.11 – 3.14 demonstrates that there are a wide variety of spinel textures.

1. **Type 1: Holly-leaf (HL)** (e.g. Figure 3.11a-d). These are small (< 1 mm) anhedral spinels that are interstitial and have scalloped edges (Mercier 1972, Mercier and Nicolas, 1975, Augé, 1982).They are also commonly described as amoeboid.

2. **Type 2: Subidiomorphic (SI)** (e.g. Figure 3.12a-d). These are subhedral grains that are commonly rounded (Augé, 1982).

3. **Type 3: Euhedral (EU)** (e.g. Figure 3.12e-f). These are euhedral grains that form octahedrons and commonly referred to as idiomorphic (Nielson Pike and Schwarzman, 1976; Dick, 1977; LeBlanc et al., 1980).

These three spinel types are the basis for the classification of spinel types from the U.A.E. This study subclassifies the spinel types further to describe the complete range of spinel textures observed in the U.A.E.

1. **Type 1b: Holly-leaf/Subidiomorphic (HL/SI).** This texture describes peridotites that contain both Type 1 (HL) and Type 2 (SI) spinels.

2. **Type 2a: Subidiomorphic/Euhedral (SI/EU).** This texture describes peridotites that contain both Type 2 (SI) and Type 3 (EU) spinels. There can be a transition from Type 2 to Type 3 as well.

3. **Type 2b: Subidiomorphic/cuspate (SI/cusp).** This texture describes spinels that have irregular, cuspate embayments which partially encloses pre-existing silicate grains (e.g. Figures 3.13c, e and Figures 3.14a-b).

In addition, spinels can form a fabric in the ultramafic rock. Poikiltic textures (e.g. Figures 3.13 and 3.14) are also typical of Type 2 and Type 3 spinels. The poikilitic spinels host silicate inclusions (usually olivine) that range in size from approximately <50 μm (which are typical of chromitites e.g. Figure 3.14f) to 750 μm.

3.1.4.1 Origin of the spinel types

Type 1 (HL) spinel is residual from partial melting of a peridotite (Mercier and Nicolas, 1975; Type 1 of Augé, 1982; Le Mée et al., 2004; Monnier et al., 2006). Spinel recrystallizes during post-kinematic growth, in the absence of a melt, into 'holly-leaf' shaped grains as a result of mantle deformation (Mercier and Nicolas, 1975). They commonly align into trails sub-parallel to the foliation in the rock.

Type 2 (SI) and Type 3 (EU) spinels form either by (i) free growth in a melt during magmatic crystallization (e.g. Nielson Pike and Schwarzman, 1976) or (ii) by reaction between a pre-existing spinel and a percolating melt (Nielson Pike and Schwarzman, 1976; Dick, 1977; LeBlanc et al., 1980; Nicolas and Prinzhofer, 1983). Therefore, Type 2 and Type 3 spinels probably reflect equilibrium between a crystal and a melt/fluid (e.g. Pike and Schwarzman, 1976) and form during recrystallization of the peridotite in the presence of a melt.

The poikilitic textures of spinels (e.g. Figures 3.13. and 3.14) indicate growth of the spinel around pre-existing silicate grains in the presence of a melt. Silicate inclusions in spinels commonly form in chromitites (e.g. Figure 3.14f) during magmatic crystallization and/or melt rock reaction (e.g. Augé, 1982; Roberts, 1982; Lorand and Ceuleeer, 1992). The incomplete poikilitic textures (e.g. Figures 3.14a-b) that Type 2b (SI/cusp) spinels often display probably result from incomplete growth of spinel possibly caused by lower melt/rock ratio.

This section demonstrates that the shape of spinel in harzburgite is potentially a useful indicator for determining the petrogenesis of the peridotite: a residual origin (Type 1) or modification by melt-rock interaction (Type 2 and 3). This hypothesis is tested in Chapter 4. However, Type 1 may not only be residual because Type 2 and Type 3 spinels can corrode into Type 1 by mechanical breakdown and form porphyroclastic textures during MT deformation (e.g. Nielson Pike and Schwarzman, 1976; Talkington and Malpas, 1980). Thus, knowledge of the microstructure of the rock and its deformation history is important in interpreting spinel morphology.

There is no clear reason for the difference between Type 2 and Type 3 spinels. Ohara and Ishii (1998) proposed that Type 2 spinels in amphibole-peridotites from the South Mariana Forearc formed by corrosion of Type 1 spinels with a melt/fluid whereas Type 3 spinels formed by reaction with melt/fluid. Regardless of the mechanism both type of spinels record interaction between peridotite and melt/fluid.

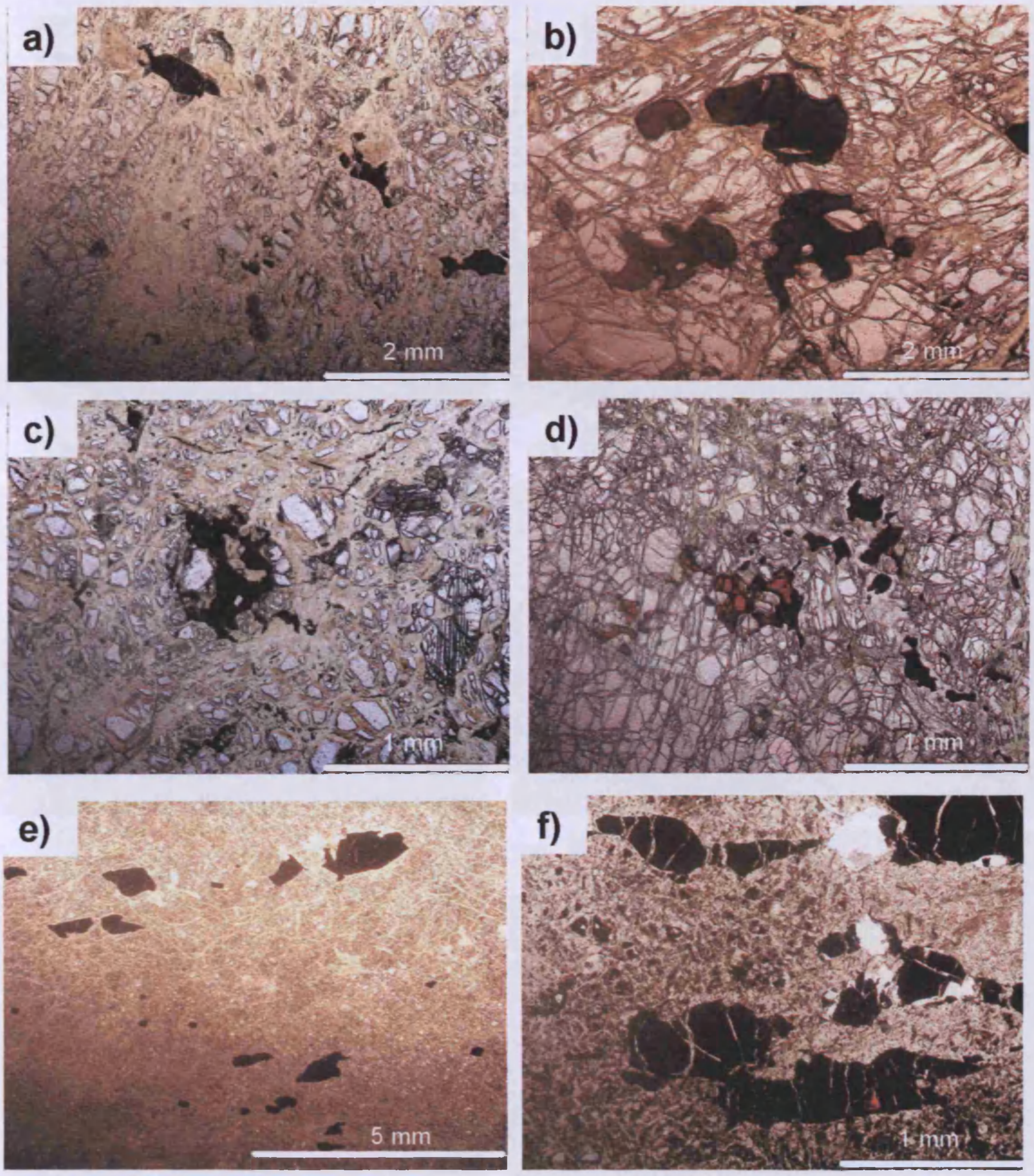

Figure 3.11: Spinel types (dark minerals) in peridotites: Type 1 (holly-leaf) spinels in (a-d) harzburgites (e-f) dunites from the Banded Unit which were deformed during LT emplacement of the ophiolite.

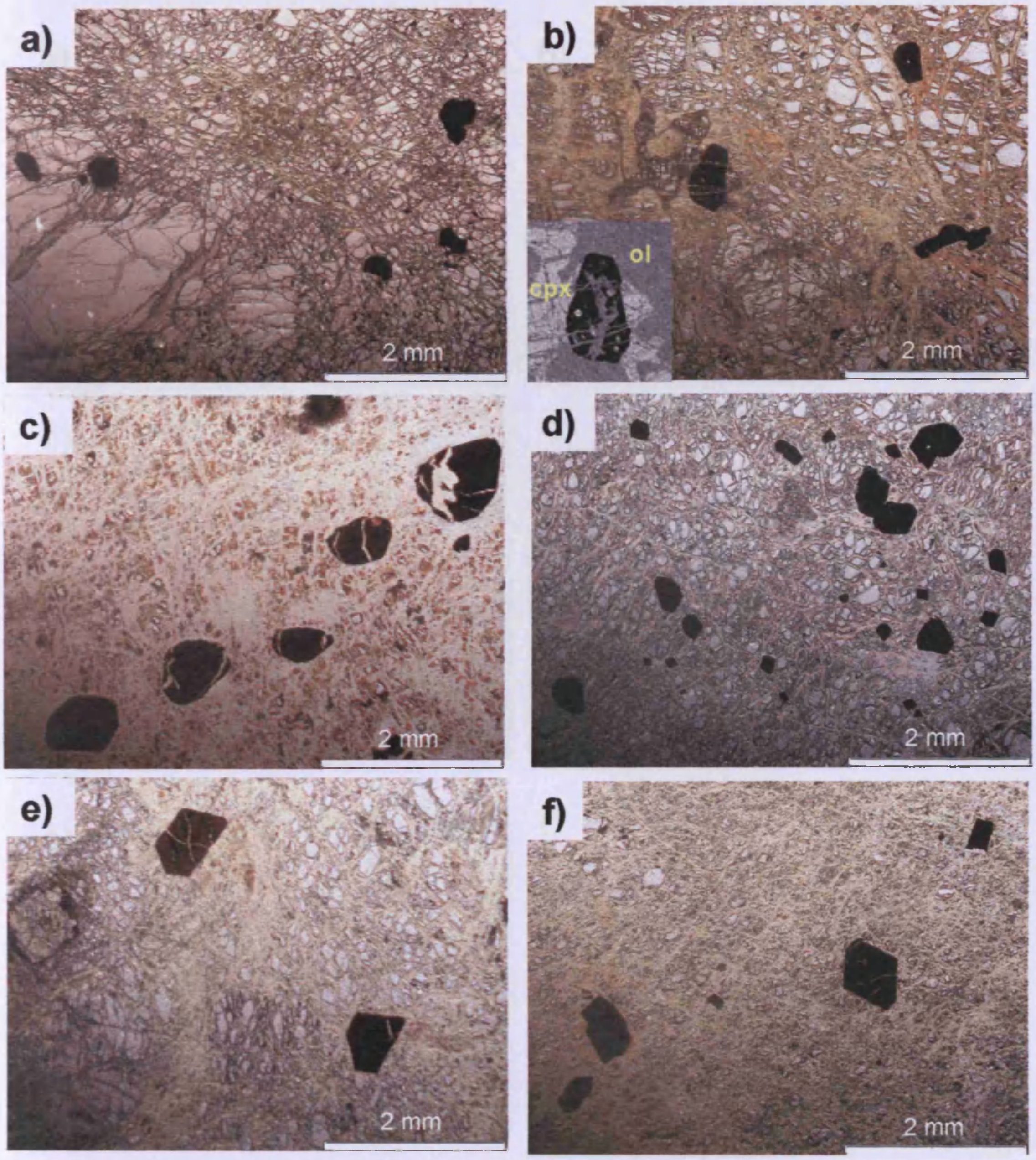

Figure 3.12: Type 2 (subidiomorphic) spinels in (a-b) harzburgites and (c) mantle dunite and (d) MTZ dunite. Type 3 (euhedral) spinels in (e) harzburgites and (f) mantle dunites. These photos illustrate the similarity between Type 2 and Type 2 spinels in harzburgites and dunites.

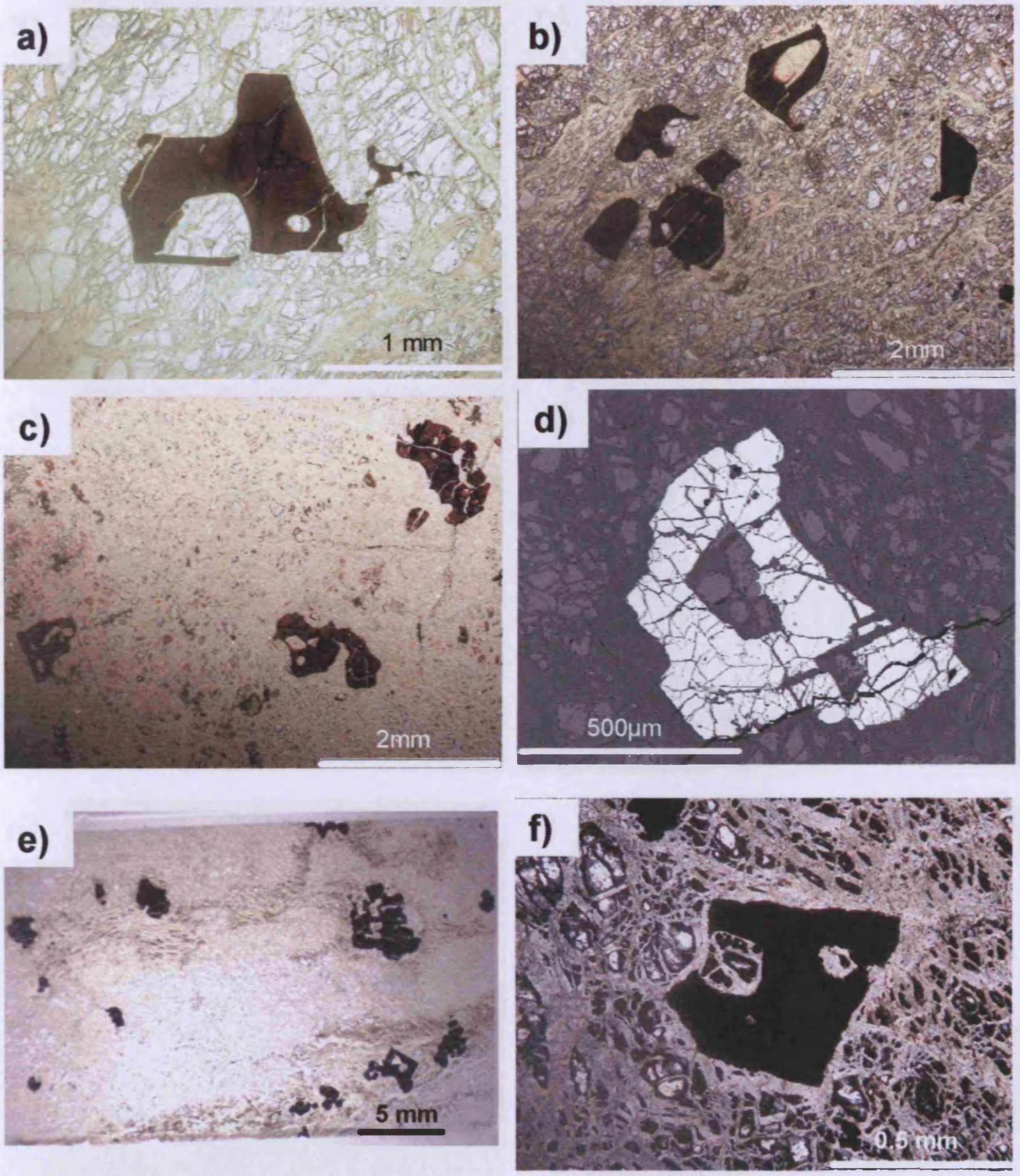

Figure 3.13: Poikilitic growth of Type 2 and Type 3 spinels in (a-d) harzburgites and (e-f) dunites. The spinel grows around olivine grains and completely (as in d) or partly (as in a and f) includes them. Back-scattered image of spinel (white) in (d).

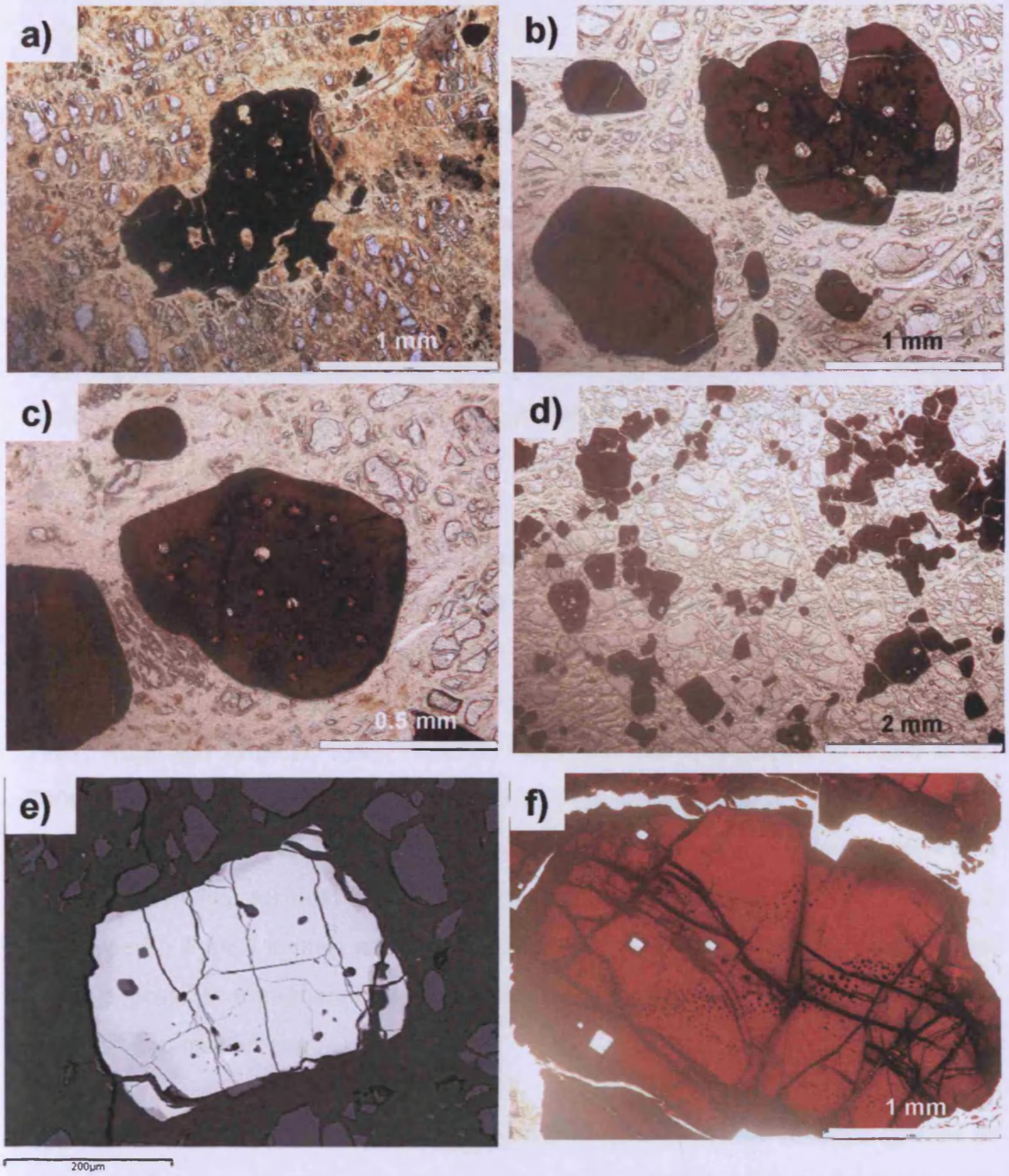

Figure 3.14: Silicate inclusions and poikilitic growth in Type 2 and Type 3 spinels in chromitiferous-dunites: (a-b) Type 2b (SI/cuspate) spinels in SD436 (dunite envelope of mantle chromitite), (c-d) Type 2a (SI/EU) spinels in SD71a (chr-dunite envelope of mantle chromitite), (e) silicate inclusions in Type 3 (EU) spinel in harzburgite and (f) silicate inclusions in chromitite (UAE138).

3.1.4.2 U.A.E. peridotites

Spinels in the U.A.E. peridotites are classified using the proposed scheme in Section 3.1.4.1. The results are presented in Table 1 of Appendix B. Type 1 (HL) spinel is characteristic of harzburgites, regardless of microstructure type, and implies that these Type 1 spinels are residual in origin (e.g. Monnier et al., 2006). In contrast, Type 2 (SI) and Type 3 (EU) spinels are characteristic of dunites from the mantle and the MTZ in the U.A.E. (this study) and Oman (LeBlanc et al., 1980; Augé, 1982). This supports the hypothesis that Type 2 and Type 3 spinels form by melt-rock reaction because dunites are the product of melt-rock interaction in the mantle (e.g Kelemen et al., 1997b).

However, there are exceptions to the above associations between spinel type and rock type. For example, some harzburgites in the U.A.E. have Type 2 and Type 3 spinels (Figure 3.12a-b, e). Harzburgites from Oman commonly have Type 2 spinels where they are considered 'secondary' in origin (Type 2 of Augé, 1982; Roberts, 1982; Augé and Roberts, 1982; Roberts, 1986; Le Mée et al., 2004; Monnier et al., 2006). This study proposes that Type 2 and Type 3 spinels in harzburgites are the result of melt-rock reaction similar to that in dunites and that they represent a transition between residual harzburgite (i.e. Type 1 spinel) and dunite (i.e. Type 2 and Type 3). Type 3 spinels are associated with clinopyroxene-poor harzburgites and imply a possible transitional stage between harzburgite and dunite that involves a decrease in clinopyroxene.

Type 2 and 3 spinels in harzburgites commonly have poikilitic textures (partial or complete) hosting silicate inclusions (e.g. Figures 3.13a-d and Figure 3.14e) that are similar to spinels from chromitiferous dunites and chromitites (e.g. Figures 3.13e-f and Figure 3.14). This texture probably results from spinel growth from a melt in a pre-existing solid matrix and provides further evidence for melt-rock interaction in the harzburgite.

Another exception to the association between dunites and Type 2 and Type 3 spinels is that a very few dunites have anhedral spinels (Figure 3.11e-f) similar to Type 1 spinels in harzburgites. These Type 1 spinels are from dunites with MT-LT microstructures and are related to high strain deformation recorded in the Banded Unit and serpentinite thrust slices in the Dibba Zone. Such late stage deformation probably happened in the absence of a melt for the spinel not to maintain its euhedral shape during post-kinematic growth. Late stage, amagmatic deformation may also have destroyed any evidence for melt-rock reaction in the harzburgites from the Banded Unit by deforming any Type 2 or Type 3 spinels back into Type 1 spinels. Chemistry should distinguish further between a residual petrogenesis and melt infiltration origin for the peridotites in these cases.

Dunites in the mantle have different morphologies according to the amount of deformation they experienced (Chapter 2): early small veins typically deformed into concordant layers by HT deformation near the Moho and late, undeformed, large dunites (100's metres) discordant to the mantle HT fabric (e.g. in Khawr Fakkan north and Wadi Mizert). Spinel morphology of mantle dunites does not distinguish early from late bodies because they all have Type 2 and Type 3 spinels. This indicates that during HT to MT deformation the dunites contained melt to feed the growth of euhedral spinel during deformation.

3.1.4.3 U.A.E. chromitites

Chromitites can display a wide variety of textures which have been described extensively in the literature for Oman chromitites: magmatic cumulate textures include chain textures and nodular textures whereas deformed textures include elongate nodules and gneissic banding (e.g. Brown, 1980; Augé and Roberts, 1982; LeBlanc and Ceuleneer, 1992; Al-Abed, 2003). Both magmatic and deformed textures of mantle chromitites were observed in the field and Chapter 2 defined two generations of chromitites. The earlier chromitites were sheared into bands at sub-Moho levels during asthenospheric flow under the spreading ridge whereas the later chromitites preserved undeformed magmatic textures (e.g. nodular textures).

However, all chromitites display Type 2 and Type 3 spinels, commonly with silicate inclusions. Therefore, early and late chromitites bodies cannot be distinguished using petrography. This implies that the early chromitites were deformed syn-magmatically so that the spinel could recrystallize during the deformation because of the presence of the melt, even though the overall ore body is deformed.

3.2 Spatial distribution of the U.A.E. peridotites

The peridotites classified into rock types, microstructure types and spinel types in Section 3.1 are plotted on maps of the study area using GIS (Arcview 3.2) to illustrate their regional distribution.

3.2.1 Regional variation in microstructure types

The peridotites are classified into microstructure types (see Section 3.1.3) in Table 1 of Appendix B and plotted onto the base map of the field area in Figure 3.15 for harzburgites and lherzolites and in Figure 3.16 for dunites.

3.2.1.1 Harzburgites and lherzolites

Many peridotites in the U.A.E. have microstructures that preserve HT deformation (59% of samples) but some have been overprinted by later MT and LT deformation (41% of samples). Chapter 2 identified shear zones in the mantle: the basal thrust zones in Aswad North and Khawr Fakkan North; and the shear zones in the middle of the mantle that divide Aswad North from South (along the Siji-Bithna SZ) and divide Khawr Fakkan North from South (along the Beni Hamid SZ) (see inset Figure 3.15). The regional distribution of the peridotite microstructures displayed in Figure 3.15 confirms the mantle shear zones as explained below.

Recrystallized textures (HT-rc) are closely associated with the shear zones identified in Section 2.1.5.2, e.g. Beni Hamid shear zone and the basal thrust. There are a few HT-rc peridotites in the sub-Moho mantle of Al Hayl, in Aswad South, indicating a possible small shear zone at the Moho. This indicates that these internal shear zones were active during the HT conditions near the spreading ridge. The absence of recrystallized peridotites along the Wadi Ham Fault indicates that it was not active at these high-temperatures.

Harzburgites and lherzolites with porphyroclastic microstructures formed by MT and LT deformation during emplacement of the ophiolite are characteristic of the base of the mantle. LT textures are restricted to a narrow plane of the basal thrust, marked by HT-rc, and demonstrate that there was reactivation of the earlier HT shear zone during LT emplacement. Harzburgites commonly have MT textures up to 2km above the basal thrust, corresponding to the Banded Unit and above in Khawr Fakkan North and Aswad North. The degree of MT deformation decreases away from the base to become transitional with HT-cg texture. This transitional MT texture was characteristic along the north-western margin of Khawr Fakkan North where no Banded Unit was present.

In contrast, there are no MT/LT microstructures from the internal mantle shear zones of Beni Hamid and Siji-Bithna which implies that these shear zones were not reactivated during emplacement. MT microstructures are common in peridotites juxtaposed with the underlying rocks of the Hatta Zone and Dibba Zone during obduction. LT deformation along the Wadi Ham fault formed mylonitic peridotites and initiated during late-stages of emplacement.

3.2.1.2 Dunites

The majority of dunites in the U.A.E. have microstructures that formed by HT deformation (78% of samples) with some overprinting by MT/LT deformation (22% of samples). 22% of all the samples were too serpentinized to assign a microstructure. The spatial distribution of HT and MT/LT microstructures of dunites (Figure 3.16) shows a similar pattern to that of harzburgites and lherzolites (Figure 3.15) because porphyroclastic microstructures, acquired from MT and LT deformation of dunites during emplacement of the ophiolite, are restricted to the base of the ophiolite in Aswad North and Khawr Fakkan North. Only dunites from the Banded Unit of Aswad North and Khawr Fakkan North have LT textures.

Dunites from the MTZ and the sub-Moho mantle of Khawr Fakkan South and Aswad South commonly have recrystallization (HT-rc) microstructures with an equigranular texture. The recrystallized grain size (medium-grained) in dunites is coarser than in recrystallized harzburgites (fine-grained) because of the lack of impingement with other phases in dunites. Recrystallized harzburgites are closely associated with intense, localised deformation in shear zones, whereas most recrystallized dunites are not associated with shear zones. This is because dunites recrystallize more easily than harzburgites and the forceful horizontal flow beneath the Moho produces a large plastic strain (e.g. Ildefonse et al., 1995) that causes a reduction in grain size by recrystallization. However, intense deformation at a shear zone results in further reduction in grain-size of olivine and a fine-grained HT-rc texture.

Dunites in the deeper mantle of Khawr Fakkan North (Figure 3.16) commonly have pegmatite-grained microstructures characteristic of undeformed, discordant dunites (e.g. Talkington and Malpas, 1980). This provides further evidence that these dunites in Khawr Fakkan North are late, undeformed, discordant dunites, which post-date the HT plastic flow of the spreading ridge that created the harzburgite fabric. This agrees with the general field observations that large, discordant pods are common in this area (Chapter 2). MT deformation starts to break down the pegmatite structure in Khawr Fakkan North and demonstrates that the late, undeformed dunites were affected only by deformation during emplacement.

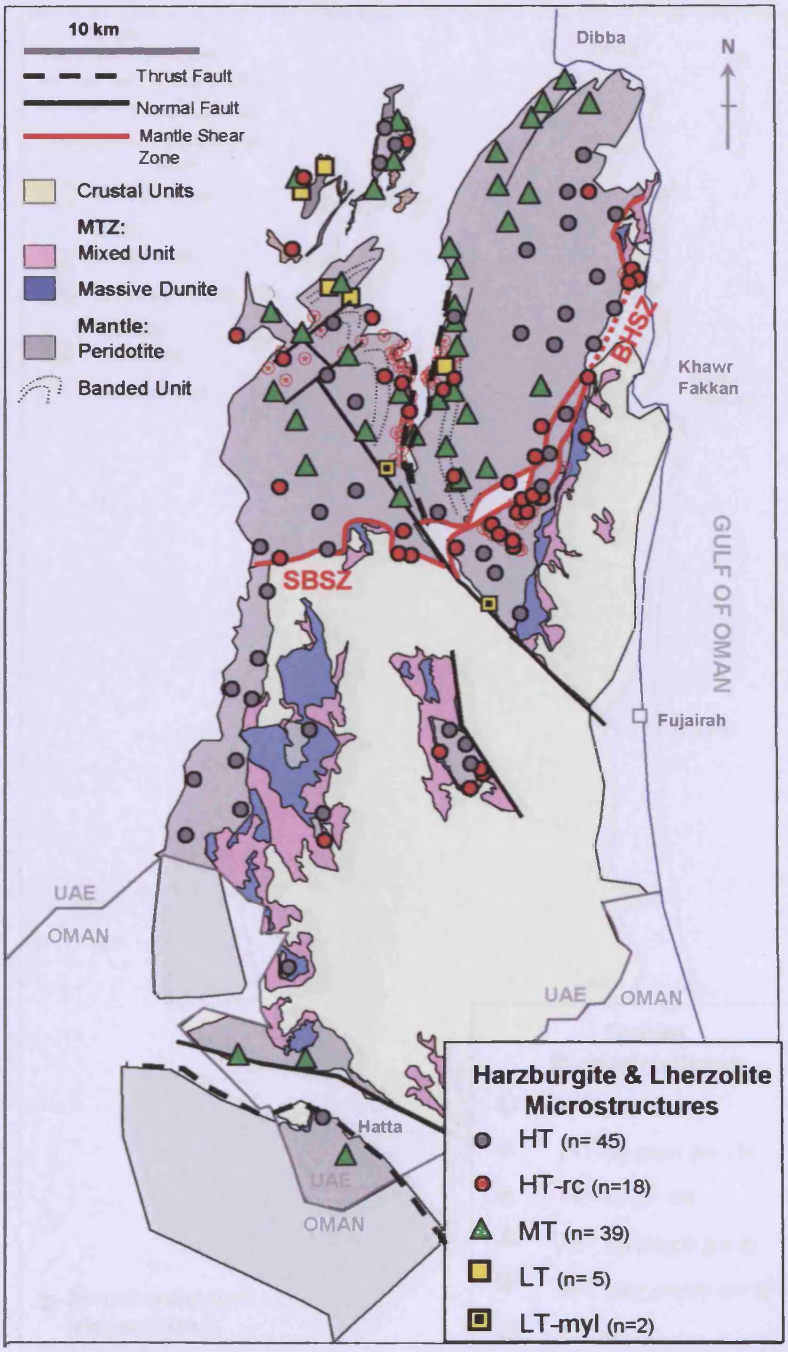

Figure 3.15: Map of harzburgites and lherzolites plotted as microstructure types. Recrystallised harzburgites (HT-rc), which are observed in the field (BGS -open red circles) and in the petrographic study (this work and BGS-large red solid circles), formed at high-temperature shear zones in the mantle, along the basal thrust and the Beni Hamid shear zone (BHSZ). MT and LT microstructures are restricted to the base of the ophiolite.

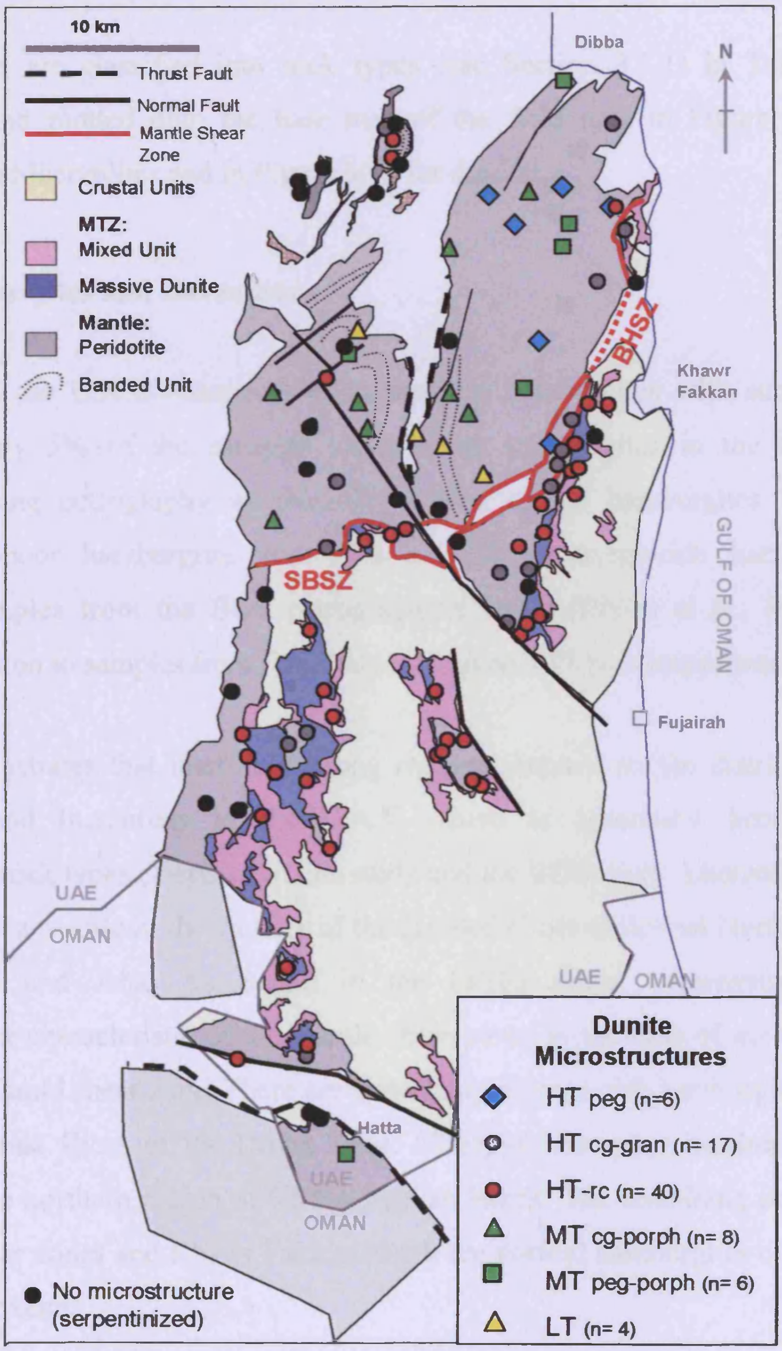

Figure 3.16: Map of dunites plotted as microstructure types. Recrystallised harzburgites (HT-c) are common in the MTZ and sub-Moho and are not associated with shear zones (cf. Figure 3.15). Undeformed dunites with HT-pegmatite structures are restricted to Khawr Fakkan North.

3.2.2 Regional variation of peridotite rock types

The peridotites are classified into rock types (see Section 3.1.1) in Table 1 of Appendix B and plotted onto the base map of the field area in Figure 3.17 for harzburgites and lherzolites and in Figure 3.18 for dunites.

3.2.2.1 Harzburgites and lherzolites

The mantle of the U.A.E comprises predominantly harzburgites with subordinate lherzolites (only 5% of the samples collected as harzburgites in the field are reclassified using petrography as lherzolites). Out of the harzburgites 16% are clinopyroxene-poor harzburgites and 17% are clinopyroxene-rich harzburgites. Additional samples from the BGS petrographical study (Styles et al., 2006) are plotted in addition to samples from this study on Figure 3.17 for comparison.

Figure 3.17 illustrates that there is a strong regional control on the distribution of harzburgites and lherzolites in the U.A.E. There is agreement between the distribution of rock types classified in this study and the BGS study. Lherzolites form at the base of the mantle in the vicinity of the Banded Units of Aswad North, Khawr Fakkan North and Jebal As Sudah in the Dibba Zone. Clinopyroxene-rich harzburgites are characteristic of the mantle shear zones at the base of the ophiolite and the Beni Hamid shear zone. There are also clinopyroxene-rich harzburgites in the serpentinite thrust slices of the Dibba Zone. Clinopyroxene-poor harzburgites are restricted to the northern region of Khawr Fakkan North. The remaining peridotites away from shear zones and Khawr Fakkan North are normal harzburgites containing 1-3% clinopyroxene.

There is also a relationship between spinel colour and rock type: clinopyroxene-poor harzburgites of Khawr Fakkan North have red spinels (typical of Cr-rich chrome-spinel/chromite e.g. Evans and Frost, 1977) whereas basal lherzolites have yellow or brown spinels (typical of Al-rich chrome-spinel).

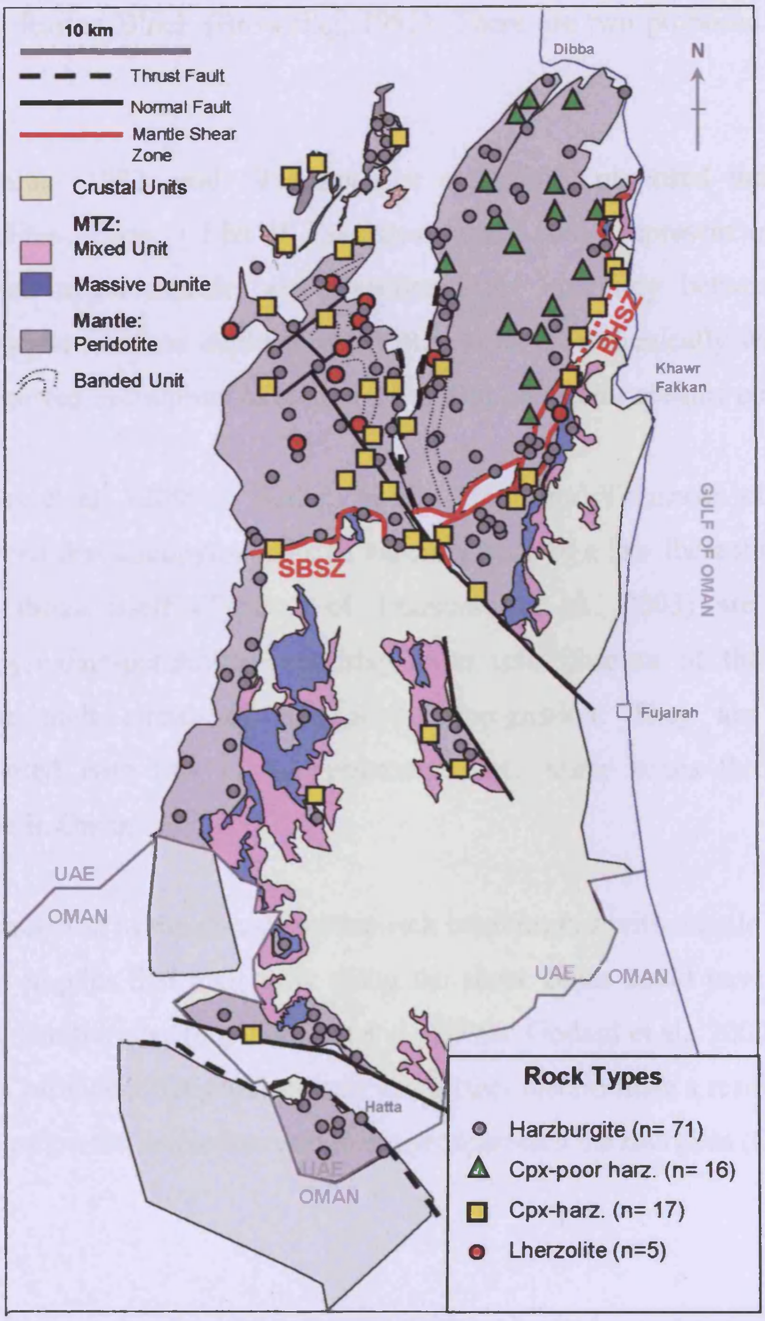

Figure 3.17: Map of peridotites plotted as rock types (harzburgite, clinopyroxene-poor harzburgite, clinopyroxene-rich harzburgite and lherzolite) from this work and the BGS study. Lherzolites form at the base of the mantle in the vicinity of the Banded Unit. Cpx-harzburgites are found mainly along shear zones of Beni Hamid (BHSZ) and those within Aswad North Block. Cpx-poor harzburgites are restricted to a large domain of Khawr Fakkan North.

In Oman, lherzolites and clinopyroxene-rich harzburgites are characteristic of the basal part of the mantle sequence (Browning, 1982; Lippard et al., 1986, Godard et al., 2000, Takazawa et al., 2003) as well as a 2 km thick band in the middle of the mantle of the Rustaq Block (Browning, 1982). There are two proposed models for their origin.

1) Browning (1982) and Takazawa et al., (2003) proposed that the basal lherzolites (Type I Lhz of Takazawa et al., 2003) represent only slightly depleted upper mantle, and considered the boundary between depleted harzburgite and less depleted lherzolites to be a mechanically weak horizon that assisted decoupling of the ophiolite from its in situ oceanic position.

2) Nicolas et al., (2000a), Godard et al., (2000) and Takazawa et al., (2003) proposed that clinopyroxene-rich harzburgites and a few lherzolites from the basal thrust itself (Type 2 of Takazawa et al., 2003) are ‘secondary clinopyroxene-peridotites’ resulting from refertilisation of the mantle by diffuse melt circulation and melt impregnation. They are commonly associated with low to medium-temperature shear zones throughout the mantle in Oman.

The close association of the clinopyroxene-rich harzburgites with mantle shear zones in the U.A.E. implies that melt flow along the shear zones could have refertilised some of these harzburgites (e.g. Nicolas et al., 2000a; Godard et al., 2000; Takazawa et al., 2003). Chrome-spinel geochemistry can further discriminate a residual or melt-rock reaction origin for lherzolites and clinopyroxene-rich harzburgites (Chapter 4).

3.2.2.2 Dunites

Dunites which are classified by their mineral proportions of clinopyroxene, amphibole and plagioclase, are plotted on the map of the U.A.E. in Figure 3.18 to illustrate their spatial distribution. Figure 3.18 demonstrates that dunites from the MTZ commonly contain 3 – 10% clinopyroxene whereas the vast majority of dunites in the mantle have no clinopyroxene except for a few locations (see below). Plagioclase-dunites are restricted to the MTZ. Dunites in the mantle that contain 2 - 3 % clinopyroxene come from the sub-Moho region of Khawr Fakkan South and from the shear zones of Beni Hamid and the Banded Unit of Aswad North. Figure 3.18 illustrates that dunites from the northern region of Khawr Fakkan North, in the vicinity of the late, discordant dunites, commonly contain up to 3% clinopyroxene and/or amphibole which are typically intergrown with spinel (Figures 3.19a-b). This is characteristic of a melt impregnation texture similar to impregnated dunites from the mantle of Hess Deep, East Pacific Rise (Edwards and Malpas, 1996).

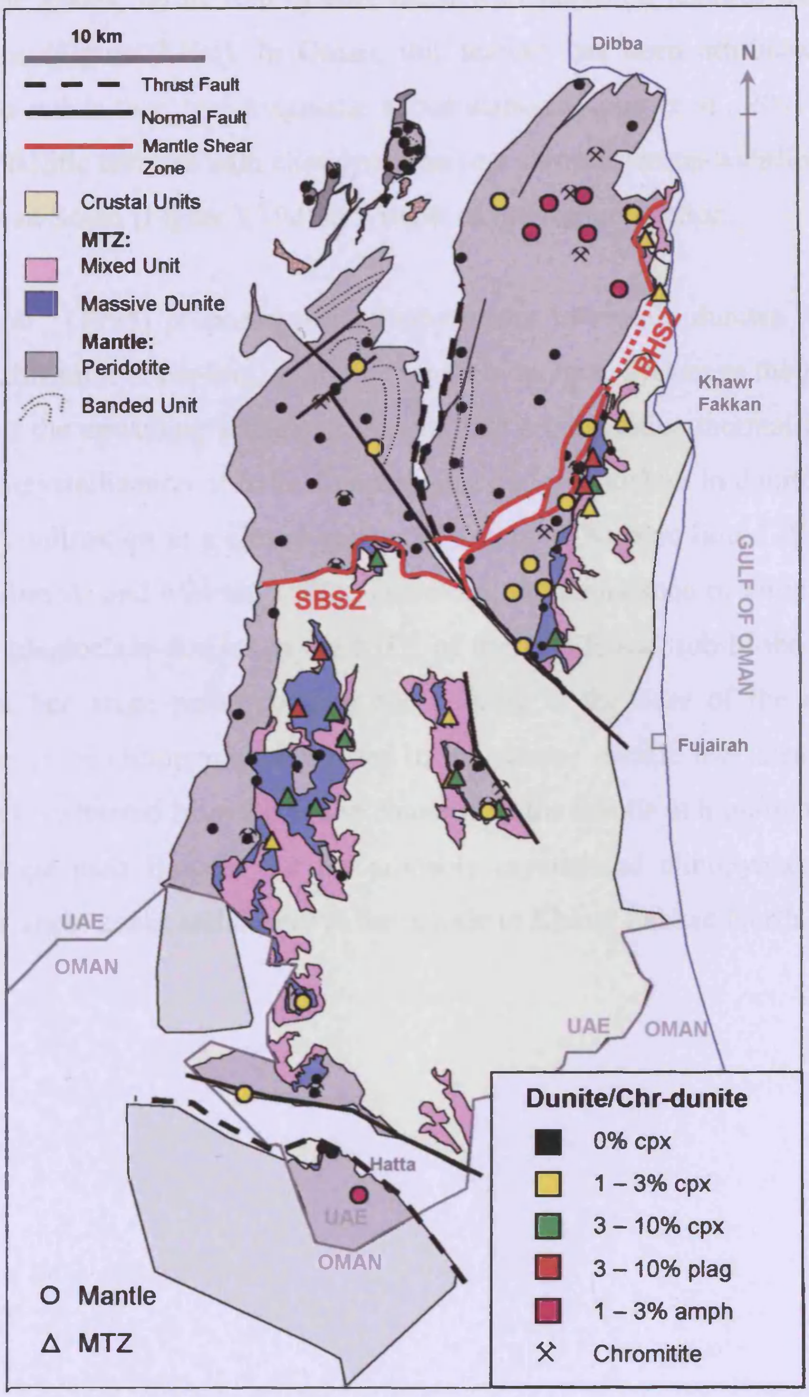

Figure 3.18: Map of dunites and chromitiferous dunites plotted as rock types as classified by clinopyroxene (cpx) plagioclase (plag) and amphibole (amph) content (Section 3.1). Clinopyroxene is common in dunites from the sub-Moho mantle and MTZ but uncommon in dunites from the mantle, apart from the Beni Hamid shear zone (BHSZ) and the Banded Unit. Amphibole and/or clinopyroxene is characteristic of dunites in Khawr Fakkan North.

In the MTZ of the U.A.E. clinopyroxene-dunites and wehrlites typically have large clinopyroxene grains, up to 1cm in size, often with poikilitic textures that enclose olivine grains (Figure 3.19c). In Oman, this texture has been attributed to melt impregnation rather than true magmatic accumulation (Koga et al., 2001). Spinels also form poikilitic textures with clinopyroxene in a chromitiferous-wehrlite from the MTZ in Aswad South (Figure 3.19d) as a result of melt impregnation.

Kelemen et al., (1995) proposed that clinopyroxene in mantle dunites formed by partial crystallization of cooling, migrating liquid in an open system as the peridotites moved out of the upwelling asthenosphere and into a conductive thermal regime. In contrast, the crystallization of both clinopyroxene and plagioclase in dunite indicates complete crystallization in a closed system of a trapped basaltic liquid (Kelemen et al., 1995; Edwards and Malpas, 1996). Therefore, the abundance of clinopyroxene-dunites and plagioclase-dunites in the MTZ of the U.A.E and sub-Moho mantle is indicative of late stage melts ponding and cooling at the base of the crust. The general absence of clinopyroxene-dunites in the deeper mantle indicates that melt was efficiently extracted from the dunite channels in the mantle at high-temperatures. Only late stage melt flow in dunites probably crystallized clinopyroxene in the mantle along shear zones and deeper in the mantle in Khawr Fakkan North.

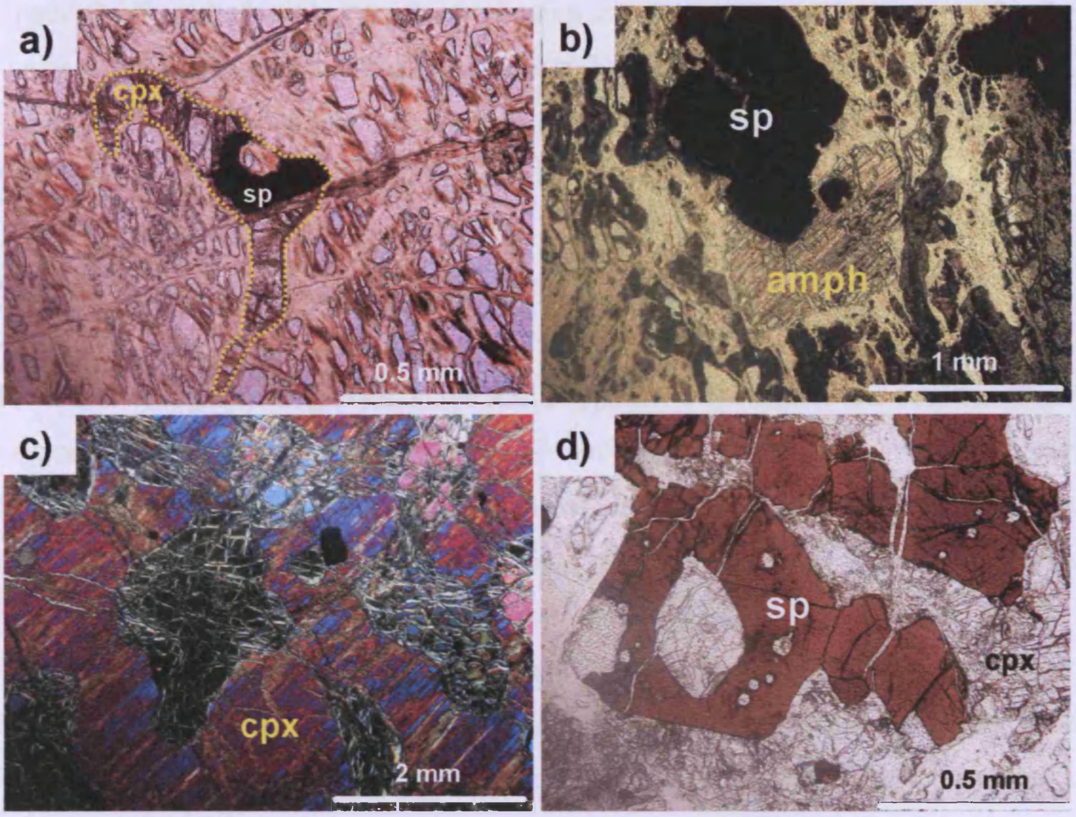

Figure 3.19: Melt impregnation textures of spinels and clinopyroxene in dunites and chromitites: (a) impregnation texture of intergranular cpx and associated euhedral spinel showing poikilitic growth with the cpx in the sub-Moho mantle (U.A.E.615), (b) euhedral amphibole grain associated with euhedral spinel grains in the deep mantle of Khawr Fakkan North (U.A.E. 143), (c) poikilitic clinopyroxene (pegmatite grain size ~ 1cm) and Type 2 spinel in cpx-dunite from MTZ (U.A.E.503) and (d) intergrowth of brown spinel and clinopyroxene poikilitically including each other within in a chr-wehrlite in the MTZ (U.A.E.3996).

3.2.3 Regional variation of spinel types

The peridotites are classified into spinel types (see Section 3.1.4) in Table 1 of Appendix B and plotted onto the base map of the field area in Figure 3.20 for harzburgites and lherzolites. The regional distribution of spinel types in dunites is not shown because they form no obvious pattern. All dunites have either Type 2 or Type 3 spinels and the reason for this difference is not understood.

3.2.3.1 Harzburgites and lherzolites

There is a strong spatial control on the spinel types in harzburgites and dunites. Type 1 spinels are the dominant type in the sub-Moho mantle of Aswad South and Khawr Fakkan South and they often form a fabric parallel to the HT microstructure. Harzburgites and clinopyroxene-rich harzburgites from the basal shear zone of the Banded Unit and the Beni Hamid shear zone commonly have Type 1b and 2 spinels. A few harzburgites along the Wadi Ham fault, including a mylonite, also have Type 1b spinels. The association between Type 2 spinels and shear zones implies that melt flowed along these shear zone and reacted with the harzburgites to form Type 2 spinels and possibly 'refertilised' the mantle to form clinopyroxene-rich harzburgites (e.g. Nicolas et al., 2000a; Godard et al., 2000).

Type 3 spinels are restricted to a large region of mantle in Khawr Fakkan North (Figure 3.20) and indicate that this region experienced pervasive melt-rock reaction. Clinopyroxene-poor harzburgites are only found in this same region (Figure. 3.17) and this implies that the absence of clinopyroxene in harzburgite is probably associated with melt-rock reaction.

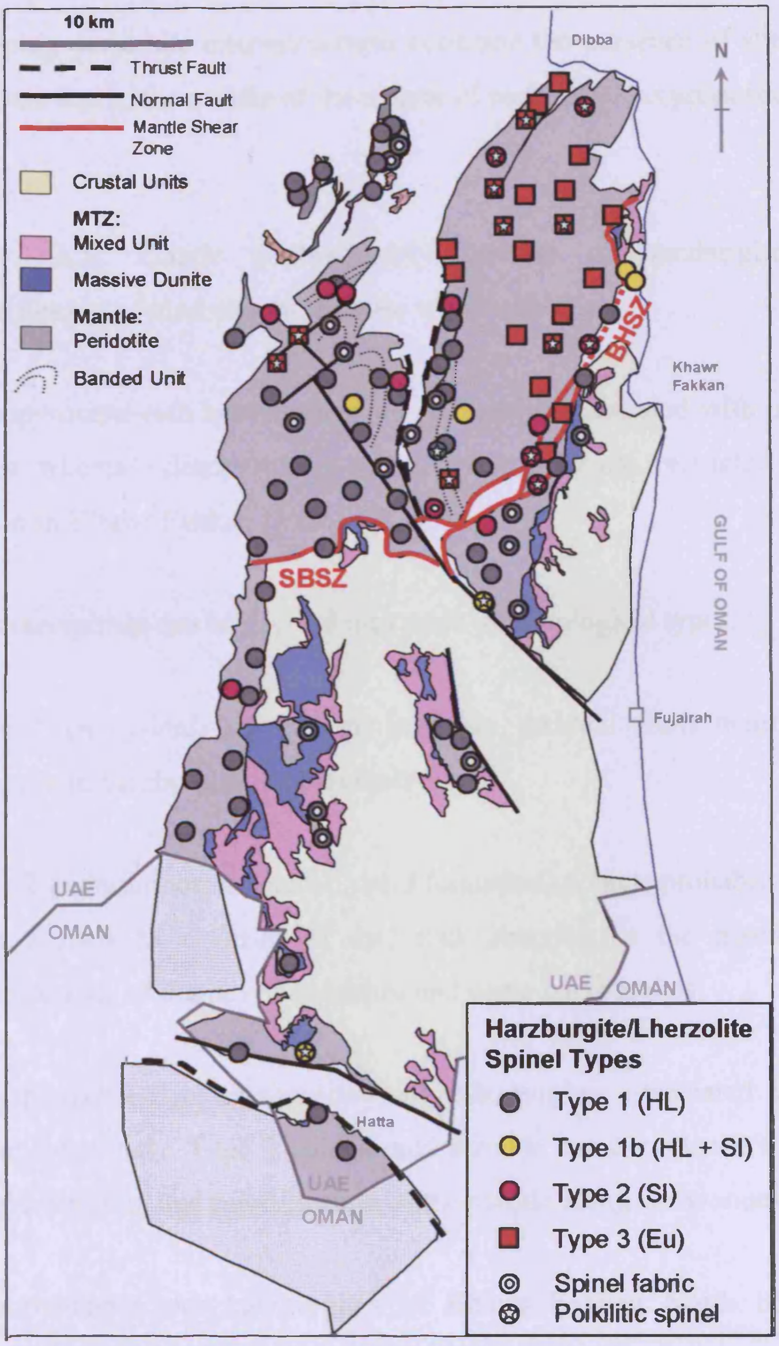

Figure 3.20: Map of harzburgites and lherzolites plotted as spinel types. See text for description of each spinel type. Type 1b and Type 2 (SI) are mainly restricted to mantle shear zones, such as the basal thrusts and Beni Hamid (BHSZ), where clinopyroxene-rich harzburgites also form (Figure 3.17). Type 3 (euhedral, commonly poikilitic) occupy a large domain in Khawr Fakkan North, which also hosts clinopyroxene-poor harzburgites (Figure 3.17).

3.3 Conclusions

- Mapping peridotite microstructures confirms the presence of shear zones at the base and in the middle of the mantle of each Block as proposed in Chapter 2.

- The U.A.E. mantle predominantly consists of harzburgites whereas lherzolites are found only at the base of the ophiolite.

- Clinopyroxene-rich harzburgites are commonly associated with mantle shear zones whereas clinopyroxene-poor harzburgites are restricted to a large region in Khawr Fakkan North.

- Chrome-spinels can be divided into three morphological types.

- Type 1 (holly-leaf) spinels are probably residual from melting and are common in harzburgites and lherzolites.

- Type 2 (subidiomorphic) and Type 3 (euhedral) spinels probably equilibrated with a melt as a result of melt-rock reaction in the mantle, and are characteristic of dunites, chromitites and some harzburgites.

- Clinopyroxene-rich harzburgites and harzburgites associated with mantle shear zones have Type 2 spinels and provide some evidence for late stage melt infiltration and refertilisation of the mantle along shear zones.

- Clinopyroxene-poor harzburgites of Khawr Fakkan North have Type 3 spinels as a result of extensive melt-rock reaction.

- Type 2 and Type 3 spinels are preserved in peridotites and chromitites during HT to MT deformation, because melt was present in the mantle during this time and therefore spinel morphology cannot distinguish between late and early dunites or chromitites identified by field observations in Chapter 2.

- Undeformed olivine microstructures of dunites from Khawr Fakkan North confirm field observations that the dunites in this area were late.

- Only spinels in dunites from the Banded Unit were deformed to anhedral shapes during LT deformation because melt was absent in these dunite channels during ophiolite emplacement.

- U.A.E. peridotites show petrographic evidence that melt infiltration and melt-rock reaction in harzburgites was common in specific regions of the mantle, such as along shear zones and in a large area of Khawr Fakkan North.

- Geochemistry will be used in the following chapters to test the above hypothesis.

Chapter 4: Tectonic discrimination of the U.A.E. peridotites using chrome-spinel

The extrusive sequence of the Oman-U.A.E ophiolite displays a chemical evolution from MORB magmas to arc-like magmas (island arc tholeiites [IAT] and boninites [BON]) (Alabaster et al., 1982; Ishikawa et al., 2001; Lilly, 2006). This provides evidence for a transition in tectonic setting from a mid-ocean ridge (MOR) to a supra-subduction zone setting (SSZ) and thus records the transient stage of subduction initiation. This chapter uses chrome-spinel for the tectonic discrimination of ultramafic rocks (in particular peridotites) from the mantle and MTZ in the U.A.E. study area in order to understand the mantle processes associated with this switch in tectonic setting.

Chrome-spinel is sensitive to petrogenetic conditions in the mantle and has widely been used for the tectonic discrimination of mafic and ultramafic rocks (e.g. Dick and Bullen 1984, Michael and Bonatti, 1985, Barnes and Roeder, 2001, Hellebrand et al., 2001; Parkinson and Pearce, 1998; Pearce et al., 2000). Chrome-spinel is a residual phase in mantle peridotites, but it will also react with, or crystallise from, percolating melts to form new spinel compositions. Therefore, the geochemistry of chrome spinel in mantle peridotites provides information on both the residual mantle, such as its degree of melting and condition of melting, and on the nature and extent of melt/rock interaction (e.g. Zhou et al., 1994; Kelemen et al., 1995). From this information it is possible to discriminate between a MOR setting and a SSZ origin for the mantle sequence and to recognise spinels that owe their origin to more than one tectonic setting (e.g. Parkinson and Pearce, 1998; Pearce et al., 2000).

There are two principal aims of this chapter.

1. To characterise the chemical composition of chrome-spinels in ultramafic rocks in order to establish their petrogenesis.

2. To use chrome-spinel to discriminate between a MOR and a SSZ setting for the mantle sequence of the U.A.E.

4.1 Analytical Techniques

Chrome-spinels and co-existing silicates from 259 ultramafic rocks were analysed by the electron microprobe (EMP) at the British Geological Survey using two procedures. The first was the standard EMP procedure (Section 4.1.1) and was applied to each of the 259 samples for rapid analysis to produce a large reconnaissance data set that covered the entire study area in detail (see Section 2.4.2, Chapter 2). From this, a subset of 60 samples, representing the range of chrome-spinel compositions in these rocks, as analysed in more detail using a second procedure (Section 4.1.2) in order to determine accurate ferric iron for an oxygen fugacity investigation.

A total of 2028 spinels, 815 olivines, 352 orthopyroxenes, 582 clinopyroxenes and 38 amphiboles were analysed. The mean compositions for chrome-spinels and the Fo content of their co-existing olivines are reported in Appendix D. The values for oxygen fugacity calculated from spinel (see Section 4.1.2) are also included with these results in Appendix D. For the subset of samples analysed by both procedures very similar results were obtained for all elements, except Fe^{3+} (see Section 4.1.2). For consistency the main data set for chrome-spinel for the subset preferentially includes analyses from the detailed procedure over the rapid procedure. This data set is used to characterise the chrome-spinels in Section 4.2.

4.1.1 Rapid procedure: Standard EMP

The 259 ultramafic rocks were analysed for major and minor elements of spinel, olivine, pyroxene and amphibole by a wavelength dispersive electron microprobe on the three – spectrometer CAMECA SX50 at the BGS, Keyworth. Samples were analysed with a 15kV accelerating voltage, 20nA beam current and a fixed beam size (approximately 1μm). Calibration was carried out on metals (Cr, Fe, Ti, V, Mn, Ni and Zn), synthetic oxides (Cr_2O_3, Fe_2O_3, and Al_2O_3) and natural materials (forsterite, wollastonite). Counting times for the analysis of chrome-spinel were 10 – 20s for Si, Fe, Mg, Al, Cr, Ni, Mn and Zn. Particular attention was paid to the analysis of key minor elements in chromite spinel using long count times for Ti (120s) and V (40s) with detection limits of 0.02 and 0.04 wt.%, respectively. PAP ϕ - ρ - Z corrections were used in the data reduction (Pouchou and Pichoir, 1991). FeO and Fe_2O_3 in spinels were calculated by charge balance and stoichiometry (Carmichael, 1967).

This standard EMP procedure was carried out on 4 spinels, 3 olivines and 3 pyroxenes per sample to rapidly produce a large reconnaissance data set. The minerals are homogeneous and the mean values measured from this rapid procedure are the same as those measured from the detailed EMP procedure (Section 4.1.2). This reconnaissance data set resulted from eight week-long EMP sessions spanning a two year period. Standards used in the calibration were monitored at the start of every weekly session to ensure that data is comparable between analytical sessions.

One problem encountered near the start was low totals (e.g. 97 – 99) for the analysis of chrome-spinel, yet measurement of each standard (e.g. Cr metal and Fe metal) was good. This problem was solved, before starting the oxygen fugacity study, by using an oxide rather than a metal standard for Cr and Fe. This new calibration resulted in good totals (i.e. 100 ± 1.5) for the analysis of chrome-spinel. The reconnaissance data set is a compilation of both calibration types (old calibration = metal; new calibration = oxide) which are marked alongside the chrome-spinel analyses Table 1 of Appendix D. Chrome-spinels measured by both calibrations yield remarkably similar Cr# values (= Cr/(Cr + Al)) (Figure 4.1). Therefore, it is valid to use data from both calibrations in the reconnaissance data to characterise Cr# in these rocks. However, the old (metal) calibration is not reliably accurate enough to measure ferric iron for the oxygen fugacity study and thus oxygen fugacity was measured only using the new (oxide) calibration. Counting times for Fe and Al were increased to 30 and 40s, respectively, because oxygen fugacity calculations are sensitive to errors of these elements in spinel analyses (Section 4.1.2).

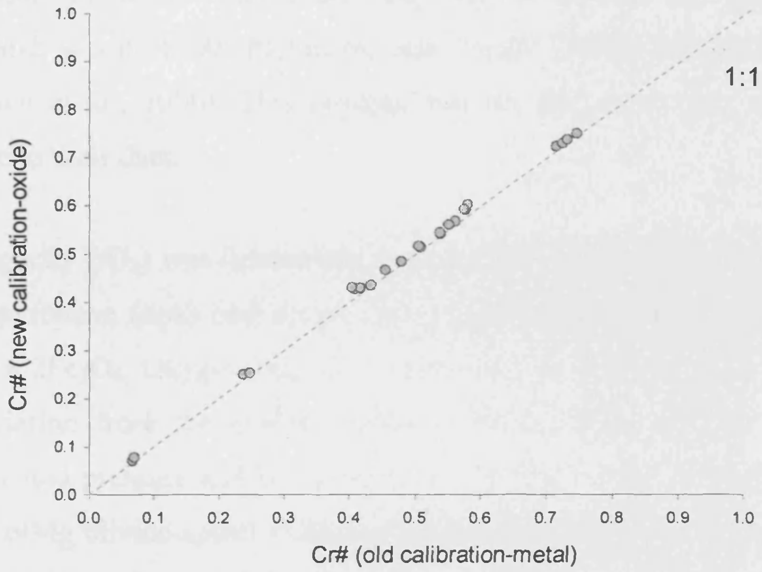

Figure 4.1: Plot of Cr# spinel determined using the new calibration (Cr oxide) for the EMP plotted against Cr# spinel determined by the old calibration (Cr metal). This illustrates that there is a 1:1 relationship (dashed line) between the two calibrations for Cr# spinel despite the poorer totals for the analysis of spinel using the old calibration (see text for further details).

4.1.2 Oxygen fugacity: detailed procedure for accurate ferric iron

The method for determining oxygen fugacity (fO_2) from chrome-spinel in this study follows the procedure employed by the authors whose data are used to define the discrimination fields for MOR, arc and SSZ peridotites in Section 4.3.4 (i.e. Bryndzia and Wood, 1990; Parkinson and Pearce, 1998; Parkinson and Arculus, 1999; Pearce et al., 2000). This ensures that the data from this study is directly comparable to their data.

Oxygen fugacity (fO_2) was determined from the Fe^{2+}-Fe^{3+} equilibria between olivine (ol), orthopyroxene (opx) and spinel (sp) based on the reaction $6Fe_2SiO_4 + O_2 = 3Fe_2Si_2O_6 + 2Fe_3O_4$. Oxygen fugacity is presented as $\Delta logfO_2$ (QFM), which refers to the deviation from the quartz-fayalite-magnetite (QFM) buffer at a specified temperature and pressure and is expressed in log units. Temperatures are calculated using the Fe-Mg olivine-spinel exchange thermometer of Ballhaus et al., (1991). The lack of a suitable barometer for spinel peridotites means that 1GPa was used in the calculation following Parkinson and Pearce (1998) and Parkinson and Arculus (1999). Calibrations using ol-opx-sp equilibria (Nell and Wood, 1991) and ol-sp equilibria (Ballhaus et al., 1991) give fO_2 values within 0.2 – 0.3 log units of each other (Parkinson and Arculus, 1999). The calibration of Ballhaus et al., (1991) was used in this study so that it could be applied to both harzburgites and dunites.

Accurate and precise determination of ferric iron content of chrome-spinel is required to calculate oxygen fugacity. This was achieved using the method of Wood and Virgo (1989) which is based on spinel standards that have well characterised $Fe^{3+}/\Sigma Fe$ ratios (by Mössbauer spectroscopy) to correct the EMP data. Wood and Virgo (1989) argue that ferric iron concentrations calculated by EMP analysis using charge balance and assuming spinel stoichiometry is not accurate enough for oxygen fugacity calculations because they are very sensitive to errors in Al_2O_3 in the spinel analyses. Wood and Virgo (1989) utilise the systematic errors imparted by Al_2O_3 on the calculated $Fe^{3+}/\Sigma Fe$ ratios as the basis for a correction scheme for EMP analyses. The difference between $Fe^{3+}/\Sigma Fe$ measured by Mössbauer and $Fe^{3+}/\Sigma Fe$

measured by the electron microprobe is proportional to the Cr# of spinel for a series of standards in the form of the following linear relationship:

$$Fe^{3+}/\Sigma Fe_{\text{Möss}} - Fe^{3+}/\Sigma Fe_{\text{Probe}} = A + B\ [Cr\#]$$

where A and B are constants. Thus, using secondary standards (analysed by Mössbauer) allows an effective correction of the spinel ferric iron contents and results in a consistent data set of spinel analyses (e.g. Wood and Virgo, 1989; Parkinson and Arculus, 1999).

This detailed procedure for oxygen fugacity of chrome-spinel acquired 24 - 40 analyses of spinels and 12 analyses of olivines per sample for precise determination of ferric iron using the new (oxide) calibration described in Section 4.1.1 with counting times for Ti and V reduced to 50 and 30s, respectively, to speed up analysis time. The resulting data set was corrected using the following secondary standards: DB8803.3, KLB8316, MBR8306, and VI314.5 (Wood and Virgo, 1989) and two additional samples (04-18 and 04-19) from a Cr-rich chromitite from Oman which also have ferric iron determined by Mössbauer (pers. comm. Hugh Rollinson). The Cr-rich standards plot on the same trend as that defined by the Wood and Virgo (1989) standards. These six standards were analysed 10 times each at the start of each day in order to correct the EMP data from that analytical session.

Parkinson and Arculus (1999) investigated the potential errors in fO_2 calculations by propagating the effect of ± 1.5% error in the R_2O_3 content of the spinels on model fO_2 values calculated for spinels in equilibria with Fo_{90} olivine at 1200°C and 1GPa. The results are reproduced in Figure 4.2a as a plot of $\Delta \log fO_2$ (FMQ) vs. $Fe^{3+}/\Sigma Fe$ ratio in spinel. They demonstrated that a constant relative error in R_2O_3 propagates to a wide range in errors in calculated fO_2 (Figure 4.2a). Propagated errors are large at reducing fO_2 (e.g. $\pm > 1$ log unit at FMQ -2 log units) but become insignificant at oxidising fO_2, i.e. less than the error of ± 0.5 log units estimated from inherent error in the calibrations and error in determining compositions of the silicate phases (see Wood et al., 1990). Therefore, Parkinson and Arculus (1999) propose that uncorrected EMP ferric iron data from the literature can be used with some confidence to calculate oxygen fugacity but only for more oxidised spinels.

Peridotites from the South Sandwich forearc were analysed for accurate ferric iron in spinel using secondary standards to correct EMP data (Wood and Virgo, 1989) by Pearce et al., (2000) and this study. The Fe^{3+}/ Total Fe spinel ratios are plotted on Figure 4.2b for direct comparison between the two studies in order to ensure that the secondary EMP calibrations for Fe^{3+} are comparable. The Fe^{3+}/ Total Fe ratios are an average of several spinel grains within the thin section and may not be the exact same grains analysed in both studies. Figure 4.2b illustrates that there is a broad 1:1 trend for ferric iron content in spinels analysed in both studies. Deviation from the 1:1 trend greater than 10% relative error is probably caused by small heterogeneities of ferric iron in spinels within each sample.

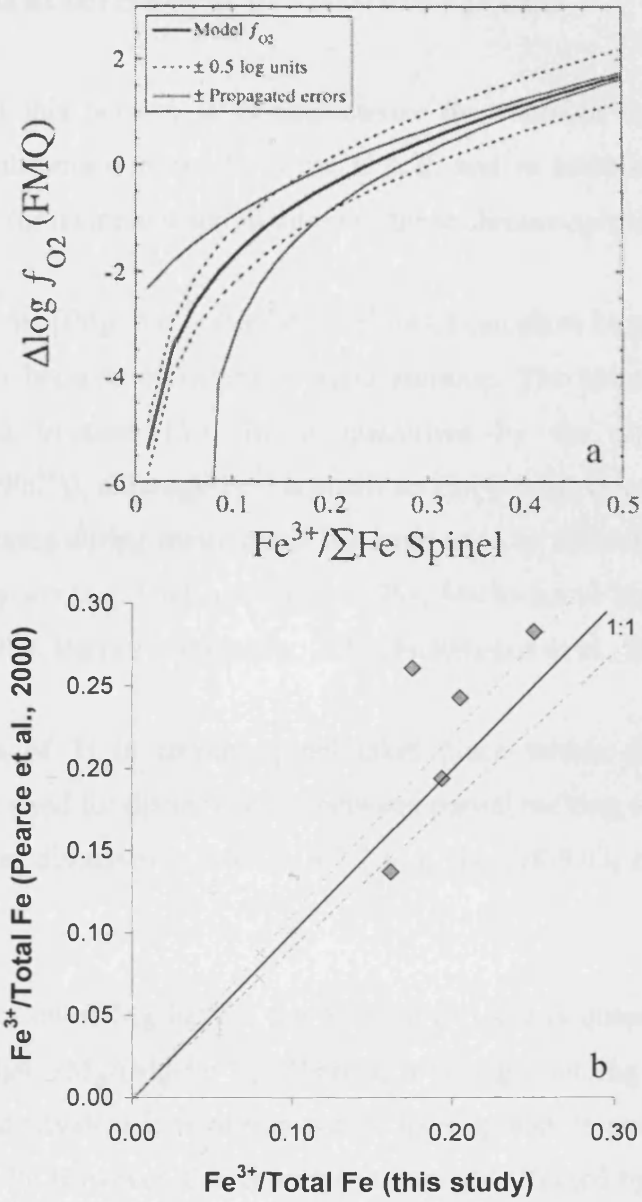

Figure 4.2: (a) Plot of Δ log fO_2 (FMQ) vs. $Fe^{3+}/\ \Sigma Fe$ ratio in spinel taken from Parkinson and Arculus (1999). Model fO_2 values calculated for spinels in equilibria with Fo_{90} olivine at 1200°C and 1 GPa. Model fO_2 values is bound by an error curve which represents the propagated effect of a ± 1.5% error in R_2O_3 content of spinels on calculated fO_2. Errors are large at reduced oxygen fugacities and insignificant at oxidised oxygen fugacities. (b) Plot of Fe^{3+}/ Total Fe ratio in spinel analysed by Pearce et al., (2000) vs. Fe^{3+}/ Total Fe analysed in this study for the same peridotite samples from the South Sandwich forearc. Both studies used secondary standards to correct EMP ferric iron data (Wood and Virgo, 1989). The solid line marks the 1:1 relationship and dotted line marks 10% relative error. There is a broad 1:1 trend for ferric iron analysed in both studies and deviation from the 1:1 trend is probably from the heterogeneity of spinel ferric iron within each sample.

4.2 Characterisation of chrome-spinels

The aim of this Section is to characterise the chemical composition of chrome-spinels in ultramafic rocks from the U.A.E. and to establish their petrogenesis in preparation for tectonic discrimination of these chrome-spinels in Section 4.3.

Chrome-spinel [$(Mg^{2+}Fe^{2+})(Cr^{3+}Al^{3+}Fe^{3+})_2O_4$] can show large variations in chemical composition because of extensive solid solution. The substitution between Cr-Al-Fe^{3+} in the trivalent (Y) site is quantified by the chrome number (Cr# = $Cr/(Cr+Al+Fe^{3+})$), although Fe^{3+} is small so Cr/(Cr+Al) is used in this study. Cr# of spinel increases during melting and has been used an indicator of partial melting for the last 40 years (e.g. Dick and Bullen 1984, Michael and Bonatti, 1985, Bonatti and Michael, 1989; Barnes and Roeder, 2001, Hellebrand et al., 2001).

Substitution of Ti in chrome-spinel takes place within the trivalent site and is particularly good for distinguishing between partial melting and melt-rock reaction in peridotites as discussed in Section 4.2.2 (e.g. the Cr#-TiO_2 diagram of Pearce et al., 2000).

The substitution of Mg-Fe^{2+} in the divalent (X) site is quantified by the magnesian number (Mg# =$Mg/(Mg-Fe^{+2})$). There is a strong coupling behaviour between the divalent and trivalent ions during partial melting and crystallization (see Cr#-Mg#, Section 4.2.1). However, this coupling is strongly affected by Mg and Fe^{2+} exchange between spinel and silicates, such as olivine, during subsolidus re-equilibration. The degree of Mg-Fe^{2+} exchange depends on the ratio of chrome-spinel: olivine and on the cooling period and is the basis for thermobarometry (e.g. Fabries, 1979; Ballhaus et al., 1991). The Mg# is also decoupled from Cr# by alteration to ferritchromit (Evans & Frost, 1985).

Chrome-spinels from the different rock types, classified in Chapter 3, are characterised using the diagrams of Cr#-Fo (e.g. Arai, 1994a, b), Cr#-TiO_2 of spinel (e.g. Pearce et al., 2000) and Cr#-Mg# of spinels (e.g. Dick and Bullen, 1984).

These diagrams are useful for evaluating the relative contributions of partial melting, melt/rock interaction, fractional crystallization, sub-solidus re-equilibration and alteration on spinel composition and thus for establishing the petrogenesis of the ultramafic rocks.

4.2.1 Cr#-Fo diagram: petrogenesis

Cr# of spinel is plotted against the forsterite content (Fo = Mg# = Mg/ (Mg + Fe^{2+})) of co-existing olivine on the Cr#-Fo diagram of Arai (1994 a,b) for the U.A.E. ultramafic rocks in Figure 4.3 (harzburgites and lherzolites) and Figure 4.4 (dunites, chromitites, wehrlites, troctolites, pyroxenites and gabbros). The Cr#-Fo diagram is effective for distinguishing between residual mantle peridotites and peridotites formed by fractional crystallization (Arai, 1994a,b). The interpretation of this diagram for the U.A.E ultramafic rocks is presented in the Sections that follow. But first, the following features that are marked on each Cr#-Fo diagram in Figure 4.3 and Figure 4.4 are described. Both Cr# of spinel and Fo content of olivine increase during partial melting and form the Olivine-Spinel Mantle Array (OSMA) (see Figure 4.3) within which residual peridotites predominantly plot (Arai, 1994a). In contrast, spinels from lavas have lower Fo and so plot to the right of the OSMA trend (fractional melting trend is marked on Figure 4.3). This is because the Fo content of olivine decreases during fractional crystallisation (Arai, 1994b). The Cr#-Fo fractionation trend is dependent on the phases co-crystallising with spinel: Cr# decreases upon crystallisation of chrome-spinel with olivine and pyroxene but Cr# increases upon crystallisation of chrome-spinel with plagioclase (Arai, 1994b). Extrapolation of the Cr#-Fo fractionation line back to the OSMA trend enables the compositions of the mantle residue in equilibrium with the primary magma to be estimated (Arai, 1994b).

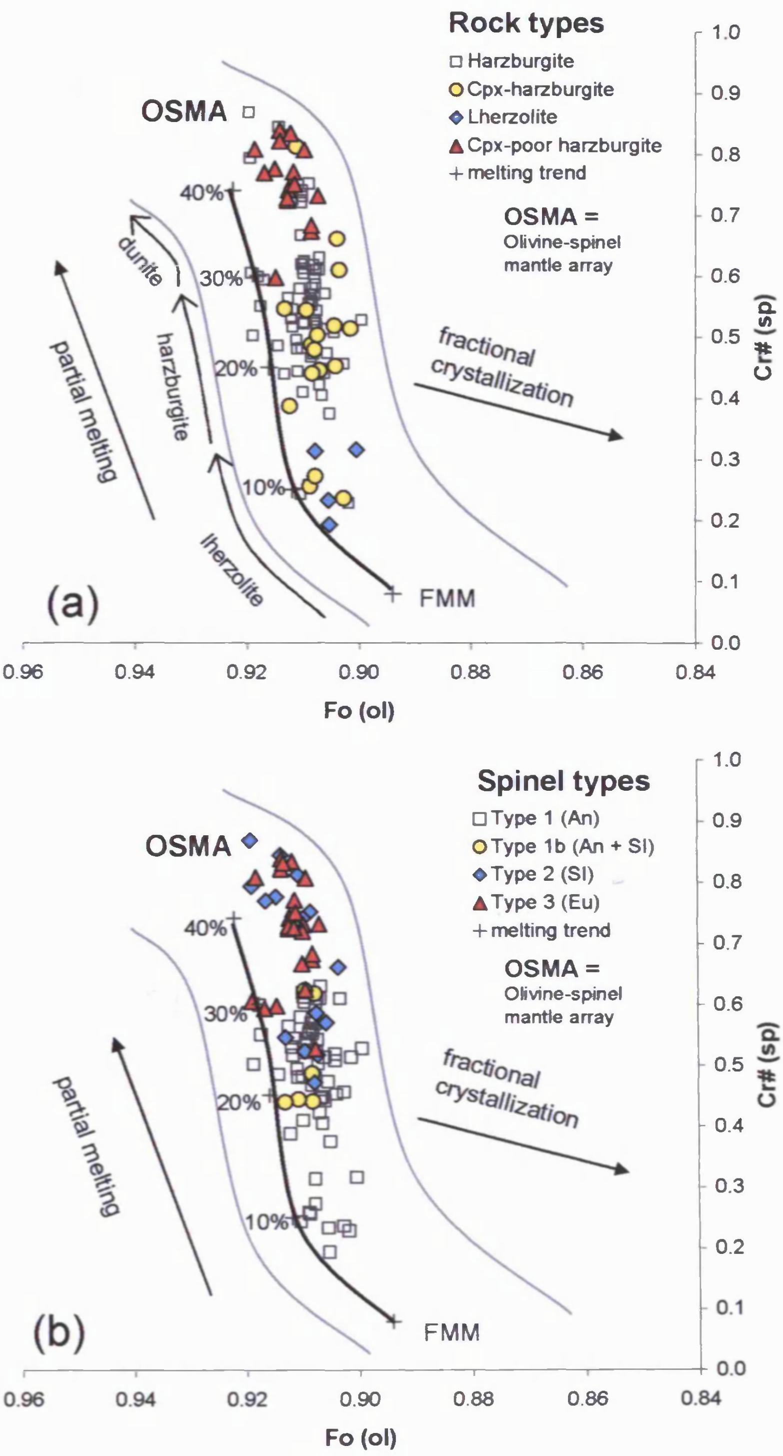

Figure 4.3: Cr#-Fo diagram: plot of Cr# spinel against olivine Fo content for U.A.E. harzburgites and lherzolites classified by (a) rock types and (b) spinel types. The diagram shows the olivine-spinel mantle array (OSMA) and melting trend (annotated by % melting) of Arai (1994a) (FMM Fertile MORB mantle) and the fractional crystallization trend to lower Fo (Arai, 1994b). The U.A.E. peridotites plot within the OSMA array. See text for further explanation.

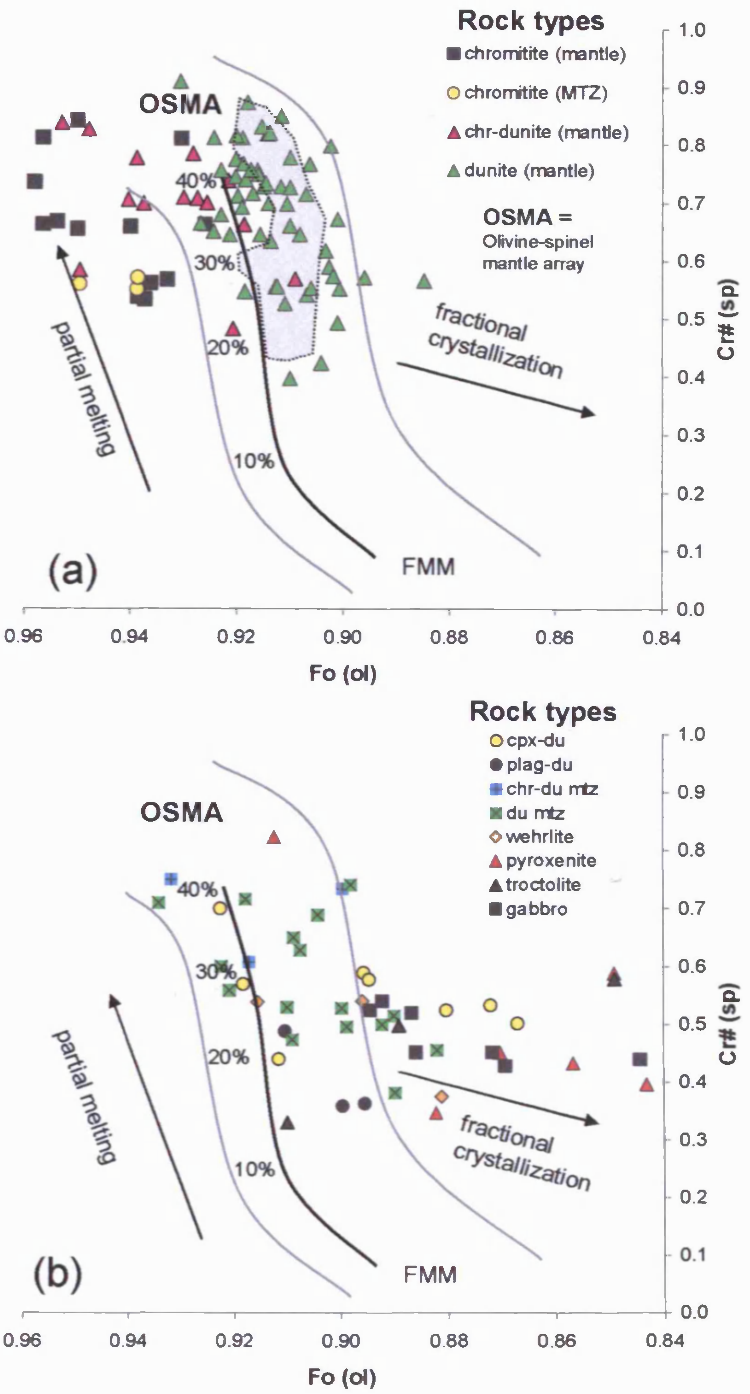

Figure 4.4: Cr#-Fo diagram: plot of Cr# spinel against olivine Fo content for (a) U.A.E. dunites and chromitites and (b) ultramafics from the MTZ. The diagram shows the olivine-spinel mantle array (OSMA) and melting trend (annotated by % melting) of Arai (1994a) (FMM Fertile MORB mantle) and the fractional crystallization trend to lower Fo (Arai, 1994b). In (a) the U.A.E. dunites mostly plot within the OSMA array and chromitites plot at higher Fo values. In (b) many ultramafics from the MTZ follow the fractional crystallization trend. See text for further explanation.

4.2.1.1 Harzburgites and lherzolites

Harzburgites (including clinopyroxene-poor and clinopyroxene-rich harzburgites) and lherzolites all plot within the olivine-spinel mantle array (OSMA) of Arai (1994a, b) in Figure 4.3a and indicate that these peridotites are residual. There is a large variation in Cr# compositions from 0.19 - 0.87 and Fo content in olivine ranges from 0.90 – 0.92 (Figure 4.3a). This variation in Cr# could correspond to 10 – 40% partial melting according to the theoretical melting curve of Arai (1994a). However, if this is the case then residual lherzolites should have a maximum Cr# of 0.3 (~ 10% melting), residual harzburgites should have maximum Cr# of 0.6 (30% melting) and residual dunites should have Cr# between 0.6 - 0.75 after 30 - 40% melting (Figure 4.3a).

Lherzolites from the U.A.E. have low Cr# compositions (0.19 - 0.31) which correspond to ~ 10% melting in Figure 4.3a and probably do represent relatively fertile residue (see Section 4.2.2). Clinopyroxene-rich harzburgites and harzburgites have a wide range in Cr# compositions (0.2 - 0.87). They cannot result from a variation in partial melting from 10 – 40% because such varied melting would form lherzolites, harzburgites and dunites and not just harzburgites. Clinopyroxene-poor harzburgites have high Cr# compositions (0.6 - 0.85), which theoretically correspond to 30 – 40% melting (Figure 4.3a). Again, at such high degrees of melting the residue should be dunite with Cr# > 0.6 and not harzburgite. Therefore, processes other than partial melting probably caused harzburgites to have Cr# compositions above 0.6 (see below).

The Cr#-Fo diagram in Figure 4.3b demonstrates that the spinel morphology has a strong control on the Cr# of spinel in harzburgites and lherzolites. Type 1 (holly-leaf) and Type 1b (holly-leaf + subidiomorphic) spinels are limited to maximum Cr# of 0.63 (e.g. Cr# 0.19 - 0.63 and 0.44 - 0.62 respectively). Holly-leaf spinels were interpreted as residual in origin in Chapter 3. This limited range in Cr# (< 0.63) corresponds to the maximum degree of melting that can form a harzburgite and supports a residual petrogenesis for Type 1 spinels.

Type 2 (subidiomorphic) and Type 3 (euhedral) spinels in harzburgites have a limited range of Cr# from 0.47 - 0.87 (Figure 4.3b). These types of spinels were interpreted as having equilibrated with a melt, probably during melt-rock reaction and/or melt impregnation (Chapter 3). It is easier to explain Cr# > 0.6 in harzburgites by reaction with highly depleted melts than by high degrees of partial melting. This hypothesis will be tested throughout this section.

4.2.1.2 Dunites and chromitites

Dunites and chromitiferous dunites from the U.A.E. mantle and chromitites from the mantle and MTZ are plotted on the Cr#-Fo diagram in Figure 4.4a. One mantle dunite has lower Fo, outside the OSMA array, which is typical of cumulate dunite (Arai, 1994a, b; Kelemen et al., 1995, 1997b). However, the majority of mantle dunites plot within the OSMA array of Arai (1994a). Kelemen et al., (1995, 1997b) argues that this demonstrates that the mantle dunites are not of cumulate origin but form by melt-rock reaction between residual peridotite and olivine-saturated melt. This results in the dissolution of pyroxene and the concomitant precipitation of olivine and spinel to form dunite by porous flow of a melt in mantle lithosphere (Kelemen et al., 1995, 1997b).

If the mantle dunite originated from high degrees of melting (e.g. 30 - 40%), olivine in residual dunite should have higher Mg# than olivine in residual mantle peridotite (Arai, 1994; Kelemen et al., 1995, 1997b) and chrome-spinels in these dunites should have corresponding Cr# between 0.6-0.8 (Figure 4.4a). Mantle dunites from the U.A.E. have a much larger variation in Cr# from 0.4 - 0.9 with the Fo content of olivine between 0.89 and 0.93 (Figure 4.4a). This provides evidence against a residual origin for their petrogenesis. The wide range of Cr# composition (e.g. 0.4 - 0.9) for dunites also provides supporting evidence for the hypothesis that Type 2 and Type 3 spinels in harzburgites formed by melt-rock reaction because they have a similar range of Cr# compositions (e.g. 0.47 – 0.87) as the mantle dunites.

Chromitiferous dunites and chromitites have higher Fo and so lie outside the OSMA array in Figure 4.4a. This high Fo may be an artefact of Mg-Fe^{2+} exchange between olivine and spinel in cases where the modal abundance of olivine: spinel is low. In peridotites, the Mg# content of olivine is buffered by its large proportion of olivine and the Fo value is unaffected by subsolidus re-equilibration with spinel. However, the lower proportion of olivine in chromitite is more sensitive to subsolidus re-equilibration with spinel and results in higher Fo content in olivine in chromitite.

Not all chromitites, especially massive ores (i.e. > 90% chr), contain fresh olivine that could be analysed. Hence the following characterisation of Cr# composition described below is supplemented by data from Table 1 in Appendix D. Chromitites from the U.A.E. mantle have a large variation in Cr# from 0.53 - 0.84 and a Fo range of 0.91 - 0.95. This variation in chrome-spinel composition is similar to that in the mantle dunites. Chromitites from the MTZ have a more limited range of Cr# composition from 0.55 - 0.74 and Fo range of 0.94 – 0.95.

Dunites from the MTZ are plotted on the Cr#-Fo diagram in Figure 4.4b. Dunites, chromitiferous-dunites, clinopyroxene-dunites and plagioclase-dunites that plot in the OSMA array indicate a role for melt-rock reaction similar to that in mantle dunites. The dunites and clinopyroxene-dunites that have lower Fo and lie off the OSMA array could have formed by fractional crystallization (Arai, 1994a, b) or reacted with an evolved, Fe-rich melt (Dick and Bullen, 1984).

Dunites and chromitiferous-dunites from the MTZ have a Cr# range of 0.38 - 0.75 and a Fo range of 0.88 - 0.93; clinopyroxene -dunites have a Cr# range of 0.43 - 0.69 and a Fo range of 0.87-0.92; and plagioclase-dunites have a smaller Cr# range of 0.36 - 0.54 and a Fo range of 0.90 – 0.91 (Figure 4.4b). The range of Cr# composition in the MTZ is more limited than that of mantle dunites and chromitites because high Cr# compositions, e.g. 0.75 - 0.9, are absent from the MTZ.

4.2.1.3 Wehrlites, pyroxenites, troctolites and gabbros

Wehrlites, pyroxenites, troctolites and gabbros are also plotted on the Cr#-Fo diagram in Figure 4.4b. Not all of the samples have olivine and so the Cr# compositions are supplemented by the Table 1 in Appendix D. For those samples that do contain olivine, the majority have low Fo and plot outside of the OSMA trend probably as a result of fractional crystallization. Only one troctolite, one wehrlite and one orthopyroxenite plot within the OSMA array (Figure 4.4b). These three samples probably either crystallised from a primitive melt in equilibrium with the mantle residue or formed by melt impregnation.

Wehrlites have Cr# compositions of 0.37 - 0.53 and a Fo range of 0.88 – 0.92. There is a larger variation in Cr# compositions of pyroxenites (e.g. 0.4-0.85) and Cr# increases with the proportion of orthopyroxene as follows: clinopyroxenites (Cr# 0.38-0.45), websterite (Cr# 0.58-0.59) and orthopyroxenites (Cr# 0.66-0.86). The Fo content of olivine in pyroxenites ranges 0.84 - 0.91.

Troctolites and gabbros have a limited range of Cr# from 0.3 - 0.55, and the Fo content of olivine ranges 0.85 – 0.91 for troctolites and 0.84-0.89 for gabbros. The spinel chemistry of the troctolites and gabbros is affected by the presence of an additional aluminous phase, i.e. plagioclase, which competes with spinel for Al from the magma. Therefore, spinels from troctolites and gabbros are not used in the discrimination of melt compositions in Section 4.3.

4.2.2 Cr#-TiO_2 diagram: melt-rock reaction

The U.A.E. ultramafic rocks are plotted on the Cr#-TiO_2 diagram (Figure 4.5) to characterise the Ti content of chrome-spinel and to distinguish between partial melting and melt-rock interaction (e.g. Pearce et al., 2000). This will test the following hypotheses proposed in Chapter 3 and supported by Cr#-Fo compositions in Section 4.2.1:

1. Type 2 (subidiomorphic) and Type 3 (euhedral) spinels in some harzburgites and all dunites and chromitites equilibrated with a melt during melt-rock reaction.

2. Type 1 (anhedral) spinels in harzburgites are residual in origin.

Pearce et al., (2000) modelled compositions of Ti in spinels during fractional melting in which the Ti content of spinels rapidly decreases as the degree of melting increases and Cr# increases and the resulting melting curve is plotted on Figure 4.5. Fertile MORB mantle has spinels with about 0.08 wt.% TiO_2 before reaction rising immediately to 0.18 wt.% TiO_2 with equilibration during melting. Peridotites which lie close to the melting curve are residual and have undergone relatively little reaction with melt.

Spinels in peridotites that are displaced significantly to the right of the melting curve are Ti-rich because they have equilibrated with melt through reaction or melt impregnation (Kelemen et al., 1995; Edwards and Malpas, 1996; Pearce et al., 2000). Pearce et al., (2000) argues that the interacting melt must be more Ti-rich than the last instantaneous melt extracted from the residual mantle, having pooled with earlier melt fractions and evolved by fractional crystallization. This is evident from compositions of spinels from primitive lavas that predominantly plot to the right of the melting trend and have higher Ti contents (0.2 – 1 wt.%) than residual peridotites (Pearce et al., 2000).

Interaction between Ti-depleted peridotite and the Ti-rich melt enriches the TiO_2 content of the spinel in the peridotite to an extent that depends on the composition of the melt and the degree of reaction (Pearce et al., 2000). In this way, the Cr#-TiO_2 diagram can fingerprint the composition of the melt that interacted with the residual mantle via reaction trends between harzburgites and dunites. This technique is used in the tectonic discrimination of chrome-spinel in Section 4.3.3.

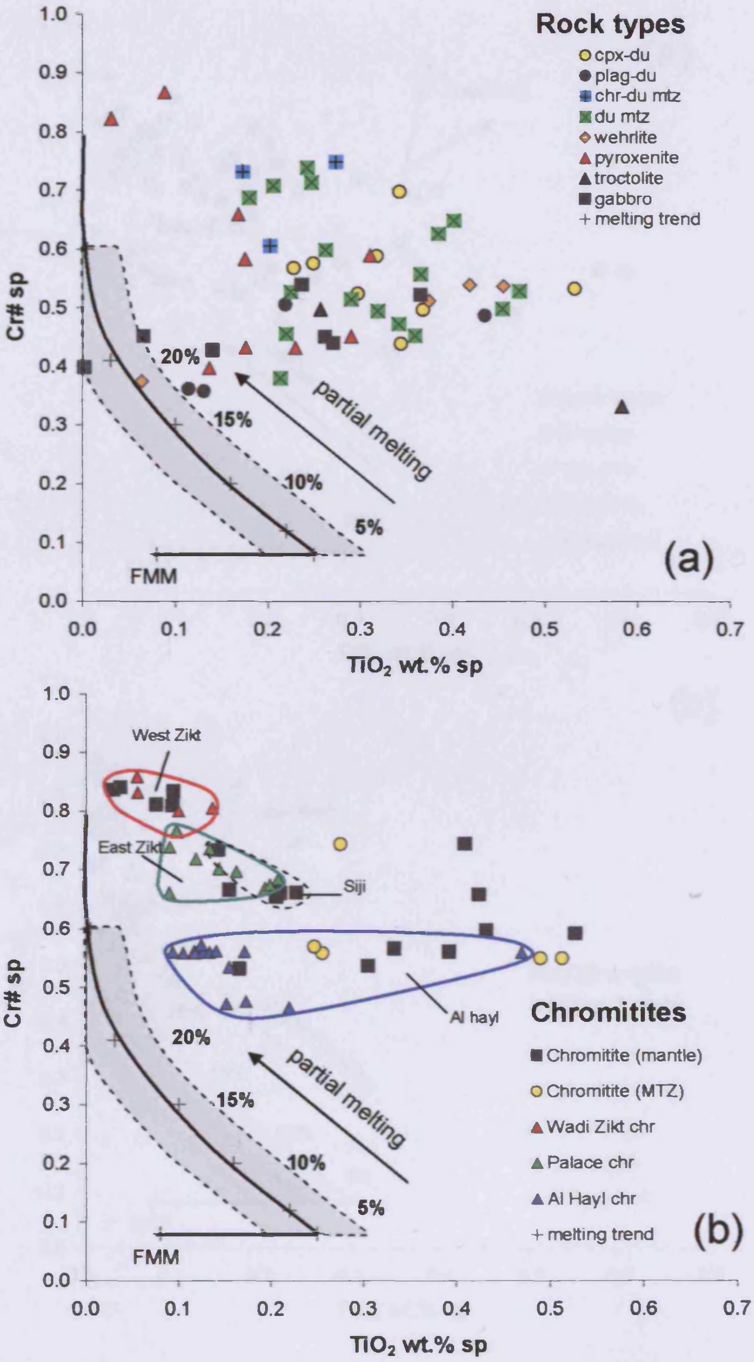

Figure 4.5: Plot of Cr# against TiO$_2$ wt.% of spinel after Pearce et al., (2000) for (a) rock types from the MTZ and (b) chromitites from the mantle and MTZ in the U.A.E. The diagrams discriminate between partial melting trends and melt-rock reaction. Melting trend modelled by Pearce et al., (2000) from Fertile MORB mantle (FMM) and annotated according to degree of melting. Peridotites which lie close to melting trend (i.e. ± 0.05 wt% TiO2 [grey area]) are residual. The MTZ ultramafic rocks and chromitites are significantly displaced from the melting curve because they were enriched in Ti either from fractional crystallization from a melt or from melt-rock reaction.

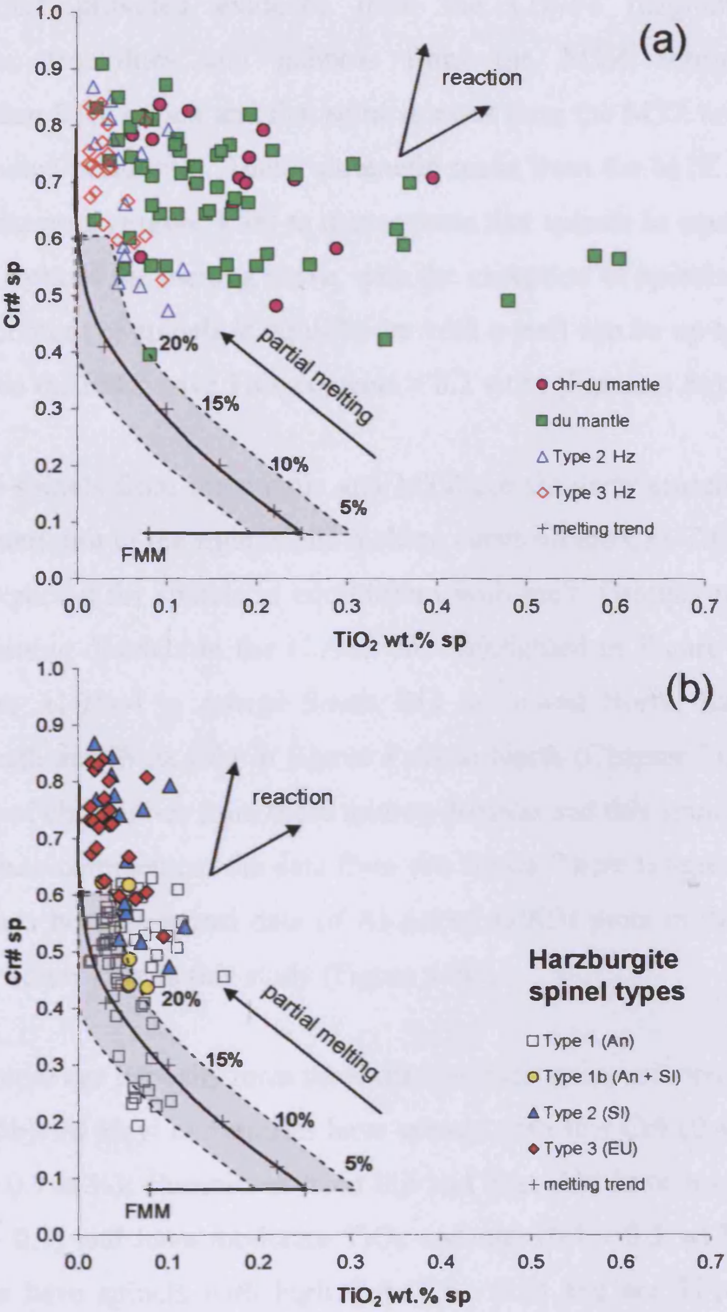

Figure 4.6: Plot of Cr# against TiO$_2$ for spinel after Pearce et al., (2000) for (a) mantle dunites and harzburgites with Type 3 and Type 3 spinels (b) all harzburgites classified as spinel types from the U.A.E. The diagrams discriminate between partial melting trends and melt-rock reaction. Melting trend modelled by Pearce et al., (2000) from Fertile MORB mantle (FMM) and annotated according to degree of melting. Peridotites which lie close to melting trend (i.e. ± 0.05 wt% TiO2 [grey area]) are residual. In (a) the peridotites are significantly displaced from the melting curve as a result of melt-rock reaction. In (b) some harzburgites with Type 1 spinels plot on or near the melting curve and are residual whereas those with Type 2 and Type 3 spinels and some Type 1 spinels are displaced from the curve a similar amount as some mantle dunites.

Section 4.2.1 provided evidence from the Cr#-Fo diagram that wehrlites, pyroxenites, troctolites and gabbros from the MTZ formed by fractional crystallisation from a melt and that some dunites from the MTZ are either cumulates or impregnated peridotites. These ultramafic rocks from the MTZ are plotted on the Cr#-TiO_2 diagram (Figure 4.5a) to demonstrate that spinels in equilibrium with melt plot to the right of the melting curve, with the exception of spinels in a few gabbros. The TiO_2 content of spinels in equilibrium with a melt can be up to 0.6 wt.% and all dunites from the MTZ have TiO_2 contents > 0.2 wt.% (Figure 4.5a).

Chromitite spinels from the mantle and MTZ are similarly enriched in TiO_2 (up to 0.7 wt.%) and plot to the right of the melting curve on the Cr#-TiO_2 diagram (Figure 4.5b) as expected for spinels in equilibrium with melt. Groups of chromitites from the four mining districts in the U.A.E. are highlighted in Figure 4.5b. The mining districts are Al Hayl in Aswad South, Siji in Aswad North, East Zikt in Khawr Fakkan North and West Zikt in Khawr Fakkan North (Chapter 2). Al-Aabed (2003) also analysed chromitites from these mining districts and this spinel data is plotted on Figure 4.5b to complement the data from this thesis. There is agreement between the two data sets because spinel data of Al-Aabed (2003) plots in the chromitite fields defined by spinel data in this study (Figure 4.5b).

The chromitite ore deposits form three discrete melt compositions in Cr#-TiO_2 space (Figure 4.5b): Al Hayl chromitites have spinels with low Cr# (0.4 - 0.6) and are Ti-rich (0.1 - 0.7wt.%); chromitites from Siji and East Zikt have spinels with moderate Cr# (0.6 - 0.7) and have moderate TiO_2 contents (0.1 - 0.3 wt.%); and West Zikt chromitites have spinels with high Cr# (0.8 - 0.9) and are Ti-poor (< 0.2 wt.%). These ore deposits provide some evidence for the involvement of three distinct magma compositions of varying depletion. Identification of the melt responsible for these spinel compositions is discussed in Section 4.3.2 in relation to tectonic discrimination.

Dunite spinels from the mantle are plotted on the Cr#-TiO_2 diagram in Figure 4.6a and are significantly displaced to the right of the melting curve. This confirms that dunites are not depleted residues but the products of reaction with Ti-rich melt (e.g. Kelemen et al., 1995; Edwards and Malpas, 1996; Pearce et al., 2000). The range of Cr# and TiO_2 in dunite spinels is similar to that in chromitites. In addition, mantle dunite spinels can have lower TiO_2 values (< 0.1 wt.%) than chromitites (Figure 4.6a). These Ti-poor dunites have similar spinel compositions to those in Type 2 and Type 3 harzburgites, which are plotted in Figure 4.6a for comparison.

Spinels in harzburgites and lherzolites have low-Ti contents (typically < 0.1 wt.%) and some, but not all, plot within ± 0.05 wt.% TiO_2 of the melting curve in Figure 4.6b. Lherzolites, which have low Cr# (0.2 - 0.3) and low TiO_2 contents (0.05 - 0.1 wt.%), plot near the melting curve (Figure 4.6b) and represent relatively fertile mantle after 10 - 15% melting. This conclusion is in agreement with that of Takazawa et al., (2003) for lherzolites from the Banded Unit (Type I lherzolites) in northern Oman. Some harzburgites with Type 1 spinels plot within ± 0.05 wt.% TiO_2 of the melting curve between 20 - 30% melting. However, other Type 1 spinels in harzburgites have up to 0.1 wt.% higher TiO_2 than that expected for spinels in residual harzburgites with Cr# 0.4 - 0.6 (Figure 4.6b). Type 2 and Type 3 spinels in harzburgites are by also displaced a similar amount from the melting curve and have similar spinel compositions to those Ti-poor dunites from the mantle as noted above. Moreover, harzburgites with TiO_2 values of 0.1 wt.% at Cr# 0.7 - 0.8 can not be residual in origin because Ti would be completely exhausted from spinels at such high degrees of melting. Therefore, spinels in harzburgites displaced by over 0.05 wt.% TiO_2 from the melting curve probably re-equilibrated (e.g. Type 1 spinels) or formed by melt-rock reaction (Type 2 and 3 spinels) to a similar extent to Ti-poor dunites in the mantle.

In summary, the Cr#-TiO_2 diagram demonstrates that a large proportion of spinels in harzburgites have interacted with melt to some degree and supports petrological evidence, from Chapter 3, that Type 2 and Type 3 spinels in harzburgites formed by melt-rock reaction in the mantle.

4.2.3 Cr#-Mg# spinel diagram: subsolidus re-equilibration

U.A.E. ultramafic rocks are plotted on the Cr#-Mg# spinel diagram in Figure 4.7 to evaluate subsolidus re-equilibration and alteration. Harzburgites and lherzolites (Figure 4.7a) and mantle dunites (Figure 4.7b) plot on the linear trend of decreasing Mg# with increasing Cr# (Figure 4.7). This is typical of harzburgites from the Oman ophiolite (e.g. Monnier et al., 2006) and their spinel compositions are drawn as a compositional field in Figure 4.7a. This reflects the strong apparent coupling between divalent and trivalent ions during partial melting, already defined for ophiolitic and abyssal peridotites (e.g. Dick and Bullen, 1984). Chromitiferous dunites (Figure 4.7b) and chromitites (Figure 4.7c) form a parallel trend displaced to higher Mg# because the higher spinel: olivine ratio in these rocks limits the effects of subsolidus exchange.

Most of the ultramafic and mafic rocks from the MTZ, such as wehrlites, pyroxenites, troctolites, gabbros, and some dunites, plagioclase-dunites and clinopyroxene-dunites plot off the peridotite trend to lower Mg# (Figure 4.7d). These rocks have similar spinel: olivine ratios to harzburgites and therefore could not have equilibrated at lower temperatures than harzburgites. Thus, the ultramafic rocks that have lower Mg# either result from fractional crystallisation or equilibrated/reacted with more Fe-rich melts than the surrounding harzburgites (Dick and Bullen, 1984). This is confirmed by the fractional crystallisation trends for these rocks on the Cr#-Fo diagram (Figure 4.4b).

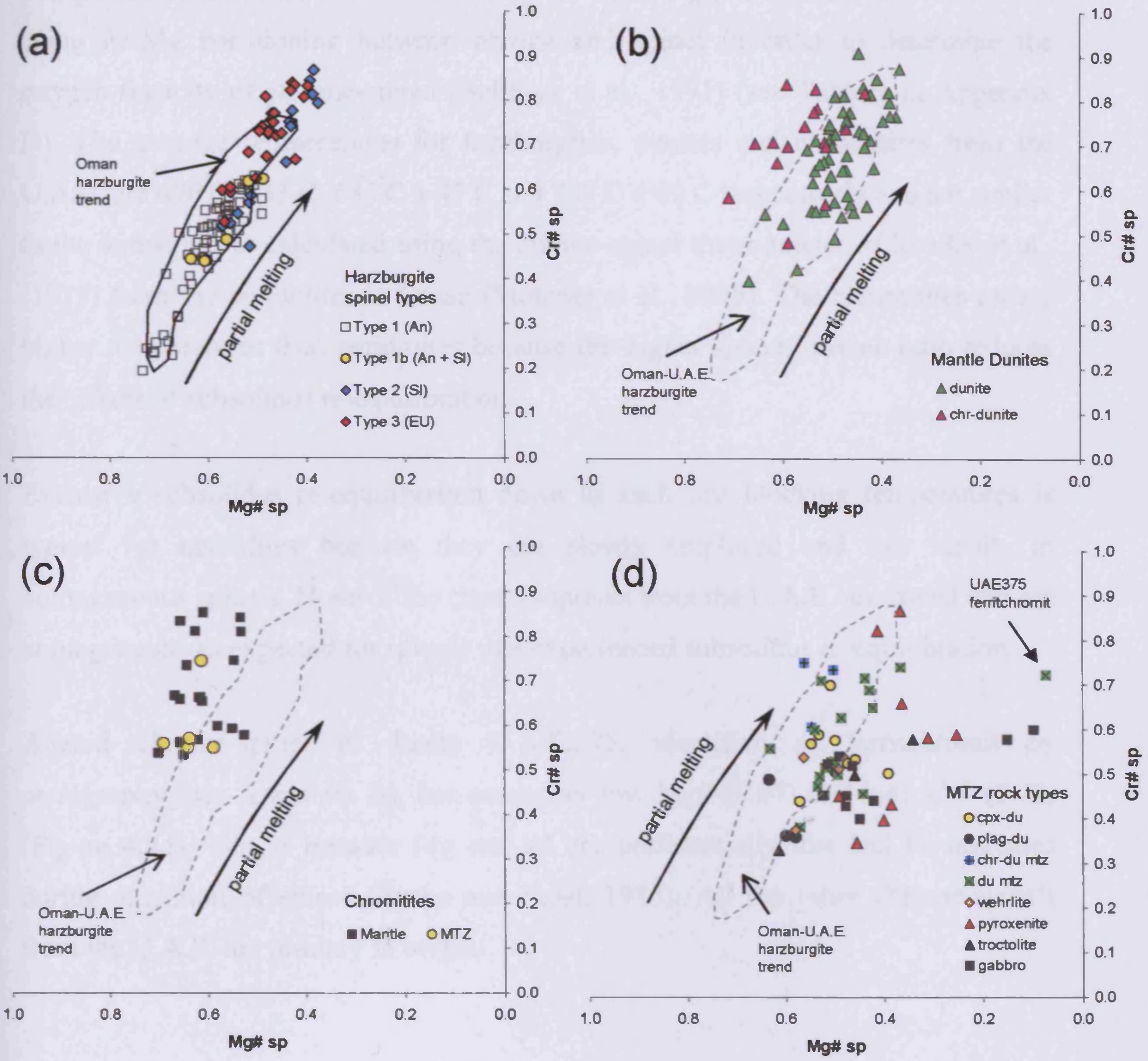

Figure 4.7: Plots of Cr# against Mg# in spinel for (a) harzburgite spinel types, (b) mantle dunites, (c) chromitites and (d) ultramafic rock types from the MTZ of the U.A.E. The compositional field for harzburgite spinels from Monnier et al., (2006) is plotted in (a) and used to display possible partial melting trend. The compositional field for harzburgites from Oman and the U.A.E. is plotted for reference in (b-d). Chromitiferous rocks have higher Mg# values than mantle peridotites and ultramafic rocks from the MTZ commonly have lower Mg# than the U.A.E. peridotites. Spinel altered to ferritchromit has very low Mg#. See text for further explanation.

Temperatures are calculated in this study for harzburgites, dunites and chromitites using Fe-Mg partitioning between olivine and spinel in order to determine the oxygen fugacity of chrome-spinel (Ballhaus et al., 1991) (see Table 1 in Appendix D). The average temperatures for harzburgites, dunites and chromitites from the U.A.E. are 670°C ± 33°C, 685°C ± 47°C and 708°C ± 40°C respectively and are similar to the temperatures calculated using the olivine-spinel thermometer of Roeder et al., (1979) from the peridotites in Oman (Monnier et al., 2006). The chromitites record higher temperatures than peridotites because the higher spinel: olivine ratio reduces the effects of subsolidus re-equilibration.

Extensive subsolidus re-equilibration down to such low-blocking temperatures is typical for ophiolites because they are slowly emplaced and this results in homogeneous spinels. None of the chrome-spinels from the U.A.E. are zoned and are homogeneous as expected for spinels that experienced subsolidus re-equilibration.

Altered chrome-spinel in dunite U.A.E.375, identified as ferritchromit by petrography (see Appendix B), has extremely low Mg# (0.07) and high Cr# (0.72) (Figure 4.7d). This is because Mg and Al are preferentially lost and Fe increases during alteration of spinel (Evans and Frost, 1985). All the other chrome-spinels from the U.A.E. are primary in origin.

4.2.4 Cr# spinel vs. whole rock

Monnier et al., (2006) argued that Cr# in Type 1 spinels that displayed no obvious petrographical or chemical evidence for melt-rock reaction, in Oman harzburgites were excellent indicators for partial melting. They plotted Cr# against selected whole rock elements that are depleted during partial melting, such as Al_2O_3, Yb and Er, and found good correlations between these elements and Cr#. These residual trends formed by the Oman harzburgites are drawn on the diagrams of Yb against Cr# (Figure 4.8a) and Yb/Er against Cr# (Figure 4.8b). These data illustrate that Yb decreases and Yb/Er and Cr# increase during melting and are used to draw possible melting trends on Figure 4.8. Monnier et al., (2006) considered the HREE concentrations and HREE/MREE ratios to be excellent indicators of the degree of melting (cf. Bodinier et al., 1990; Parkinson et al., 1992) and used this as his main argument for using Cr# as reliable partial melting indices.

This assumption has been tested with the U.A.E. peridotites for which there is evidence for melt-rock reaction (Section 4.2.2). The U.A.E. harzburgites, lherzolites and dunites are plotted on the Cr# vs. selected whole rock diagrams in Figure 4.8. The lherzolites and harzburgites that typically have Type 1 spinels plot on the 'partial melting' trends defined by Monnier et al., (2007). The clinopyroxene-poor harzburgites plot at the depleted end of the melting trend of Yb-Cr# diagram (Figure 4.8a) which implies that they could represent highly depleted residues. However, clinopyroxene-poor harzburgites have Type 3 spinels which imply that they have experienced melt-rock reaction. Furthermore, mantle dunites also plot at the end of these trends but Section 4.2.2 provided strong evidence that they are not residual in origin but formed by melt-rock interaction. This implies that Yb is possibly mobile during melt-rock reaction and reaction with highly depleted melts results in higher Cr# and lower Yb in the whole rock peridotite than reaction with less depleted melts. Therefore, the HREE cannot easily distinguish between a residual peridotite and a peridotite that has experienced melt-rock reaction i.e. a 'reacted' peridotite. As a result it is not conclusive from the HREE data if the clinopyroxene-poor harzburgites are residual or reacted.

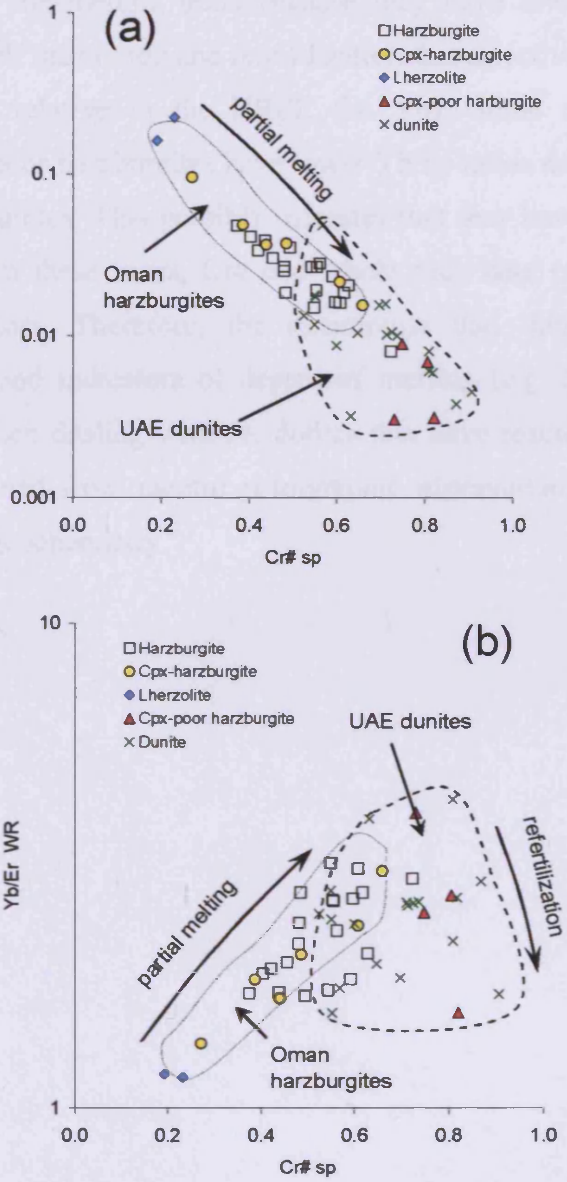

Figure 4.8: Cr# spinel plotted against selected whole rock elements that are depleted during melting such as (a) Yb and (b) Yb/Er ratio. Spinels from Oman harzburgites form a residual trend (dotted field) as a result of variable degrees of partial melting (Monnier et al., 2006) from which a possible partial melting trend is drawn. The U.A.E. peridotites are plotted on these diagrams for comparison and a dashed field drawn around the dunite samples. In (a) Cr# spinel increases and Yb decreases during melting and dunites and clinopyroxenes both plot at the depleted end of this trend. In (b) Cr# spinel increases and Yb/Er increases during partial melting but not all of the dunites and clinopyroxene-rich harzburgites plot on this trend. Yb/Er ratio probably decreases as a result of melt infiltration and melt-rock reaction and a possible refertilization trend is drawn. See text for further explanations.

The effect of melt-rock reaction on the whole rock data is evident when dunites are plotted on the Yb/Er-Cr# diagram in Figure 4.8b. This is because most of the dunites do not plot on the melting trend because they have lower Yb/Er ratios. This is indicative of melt infiltration and refertilization that selectively enriches the dunite in MREE (i.e.Er) relative to the HREE (i.e Yb). Some of the harzburgites and clinopyroxene-poor harzburgites have lower Yb/Er ratios and plot below the melting trend like the dunites. This possibly indicates that they have also experienced melt-rock reaction. In these cases, Cr# and whole rock data cannot be used as partial melting indicators. Therefore, the assumption that these selected whole rock elements are good indicators of degree of melting (e.g. Monnier et al., 2006) is questionable when dealing with peridotites that have reacted with melts. The latter can be determined from careful petrographic observations (i.e. spinel types) and chrome-spinel geochemistry.

4.3 Tectonic discrimination of the U.A.E. peridotites

4.3.1 Introduction

Section 4.2 showed that chrome-spinels in the U.A.E. peridotites provide information on both the degree of melting and the nature and extent of melt/rock interaction. This information is now used to discriminate between a mid-ocean ridge (MOR) and supra-subduction zone (SSZ) setting for the mantle sequence of the ophiolite in the U.A.E. and to recognise spinels that owe their origin to more than one tectonic setting (e.g. Parkinson and Pearce, 1998; Pearce et al., 2000).

The chemical composition of chrome-spinel is a useful indicator of petrogenetic conditions in the mantle. Cr# is highly sensitive to the degree of partial melting in mantle peridotites (e.g. Dick and Bullen, 1984; Arai, 1994a); TiO_2 is sensitive to melt-rock reaction and can fingerprint melt composition (e.g. Pearce et al., 2000); and the Fe^{3+}-Fe^{2+} ratio in spinel is a function of oxygen fugacity (fO_2) (e.g. Wood and Virgo, 1989). The Ti content of chrome-spinel is a reliable indicator of magma chemistry because the diffusivity of Ti^{4+} in olivine is low (Scowen et al., 1991).

Suites of peridotites from the U.A.E. are grouped into those from the main ophiolite body (which are subdivided into 5 mantle domains, as in Chapter 2) and those from the Dibba Zone. Each suite of peridotites is plotted separately in the following tectonic discrimination diagrams. The origin of the Dibba Zone peridotites is unknown and this study aims to reveal their setting of formation and their relation to the main ophiolite. There are several hypotheses for the setting of formation of the peridotites in the Dibba Zone: passive continental margin (PCM), normal MOR of the Hawasina basin, or part of the ophiolite. These hypotheses are discussed further in Section 6.4.

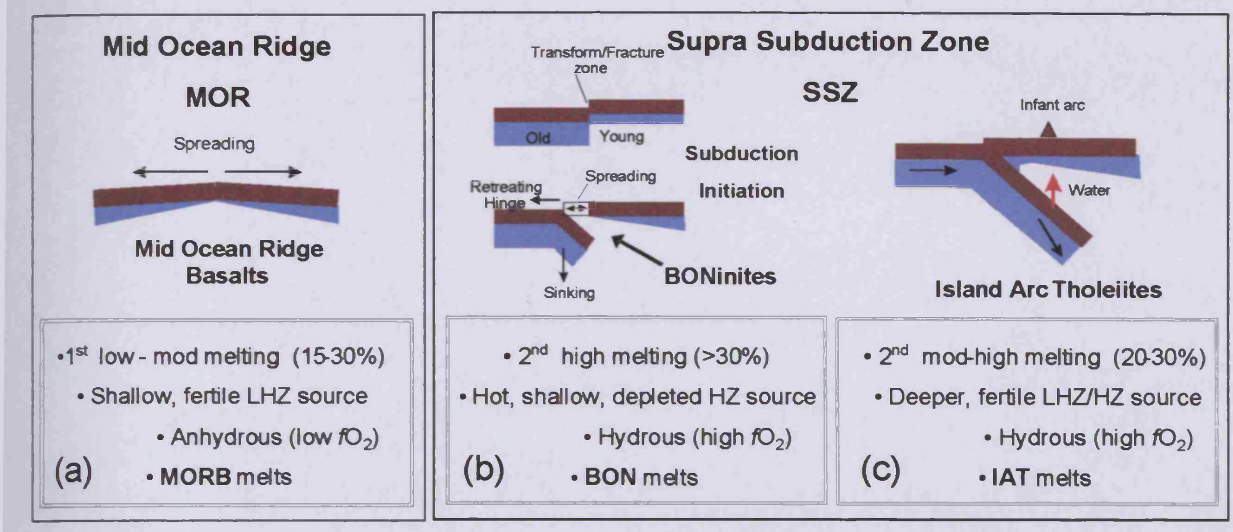

Figure 4.9: Cartoons illustrating the different mantle conditions and resulting melts at (a) a mid-ocean ridge (MOR) and (b-c) a supra-subduction zone (SSZ) setting. In (a) melting at a MOR setting involves low to moderate degrees of melting of a shallow, fertile lherzolite (LHZ) source under anhydrous conditions (i.e. low oxygen fugacity [fO_2]) to form MORB melts. In (b) second stage melting of a hot, shallow and depleted harzburgite (HZ) source under hydrous conditions (i.e. high fO_2) results in high degrees of melting and forms boninites (BON). BON are associated with subduction initiation. For example, Stern et al., (1992) proposed that old dense lithosphere could sink at a transform fault and subduct beneath a young, hot ridge. Subsequent roll back of the sinking slab causes spreading near the trench and remelting of the shallow lithosphere to form BON. In (c) hydrous melting of a deeper, fertile LHZ source or second stage melting of a depleted HZ source above the slab results in island-arc tholeiite (IAT) melts of a young arc.

Mantle conditions, such as degree of partial melting, mantle source and oxygen fugacity, are different for MOR and SSZ settings (e.g. Figure 4.9). These conditions impart distinctive chemical signatures to the residual peridotites and melt which can be used to discriminate the tectonic setting of the ophiolite. In particular, anhydrous melting at a MOR setting produces mid-ocean ridge basalt (MORB) whereas hydrous melting at a SSZ setting produces more depleted magmas such as island-arc tholeiite (IAT) and boninites (BON). Boninites are highly depleted melts which form by re-melting of hot, shallow and depleted mantle lithosphere upon subduction initiation (see Crawford, 1989 and papers within).

Chrome-spinels from peridotites and lavas from MOR, SSZ and PCM settings are well characterised and have been used to establish compositional fields on tectonic discrimination diagrams (e.g. Dick and Bullen, 1989; Michael and Bonatti, 1985; Wood and Virgo, 1989; Bryndzia and Wood, 1991; Ballhaus et al., 1991; Parkinson and Pearce, 1998; Parkinson and Arculus, 1999; Pearce et al., 2000; Barnes and Roeder, 2001; Kamenetsky et al., 2001).

Abyssal peridotites from mid-ocean ridges are relatively easy to sample from slow-spreading ridges, either by drilling or dredging, but peridotites are only available from fast-spreading ridges at Hess Deep and Garrett Transform Fault, EPR. There are extensive published spinel data from abyssal peridotites and MORB lavas (e.g. Barnes and Roeder, 2001). MOR peridotites are monogenetic and typically involve interaction between MORB magma and MOR residual mantle.

The mantle wedge beneath subduction zones is more difficult to sample than MOR peridotites. Spinels from mantle wedge peridotites are characterised from a few arc xenoliths (Parkinson and Arculus, 1999) and forearc peridotites. Two key studies of forearc peridotites are from Izu-Bonin-Mariana forearc seamounts (e.g. Ishii et al., 1992; Parkinson and Pearce, 1998), the South Sandwich forearc and the South Sandwich Trench-Fracture-Zone-Intersection (TFI) (Pearce et al., 2000). Peridotites from these two present-day forearcs, which formed originally in a SSZ setting, emphasise the potential significance of peridotite geochemistry for unravelling the complex tectonic histories of forearcs past and present. SSZ peridotites may be (i) polygenetic (e.g. South Sandwich forearc, South Sandwich TFI and Conical Seamount, Mariana forearc) and involve interaction between SSZ magma and pre-existing mantle lithosphere of different provenance, or (ii) monogenetic (e.g. Torishima Seamount, Izu-Bonin forearc) and involve interaction between SSZ magma and SSZ residual mantle.

In particular, Cr#, TiO_2 and fO_2 of spinel are most useful for the tectonic discrimination of MOR and SSZ setting peridotites. The diagrams of Cr#-Fo (e.g. Arai, 1994a, b), Cr#-TiO_2 (e.g. Pearce et al., 2000) and Cr#-fO_2 (e.g. Wood and Virgo, 1989) will be used in this study to determine the tectonic setting from the mantle peridotites of the U.A.E. ophiolite. There are no chromitites from modern-day oceanic lithosphere, except a small micro-pod from Hess Deep (Maksukage and

Arai, 1996), to establish discrimination fields for chromitites. Therefore, podiform chromitites from the U.A.E. are compared to the discrimination fields of dunites, because they both form by melt-rock reaction (Zhou et al., 1994).

4.3.2 Cr#-Fo discrimination diagram

Section 4.2.1 showed that the Cr#-Fo diagram effectively distinguishes between residual mantle peridotites (olivine-spinel mantle array) and peridotites formed by fractional crystallization (e.g. Arai, 1994a). It also showed that dunites from the U.A.E. mantle plotted within the OSMA array (Figure 4.4a) and are not cumulates but formed by melt-rock reaction of residual peridotites.

In this Section, the Cr#-Fo diagram introduced in Figures 4.3 and 4.4 is reproduced in Figure 4.10 for the purpose of tectonic discrimination. This is because Cr# and Fo in peridotites reflect the degree of melting in the mantle and both increase progressively from passive ocean margins (Cr# 0.05-0.37) to MOR (Cr# 0.1-0.6) to oceanic SSZ settings (Cr# 0.35-0.8) (Dick and Bullen, 1984; Bonatti and Michael, 1989; Arai, 1994a; Pearce et al., 2000). These discrimination fields for peridotites are represented as ellipses on Figure 4.10 and plot within the OSMA array (Arai, 1994a; Pearce et al., 2000). Therefore, the Cr#-Fo discrimination diagram is effective only for U.A.E. peridotites that plot in the OSMA array.

However, the Cr#-Fo diagram is not fully diagnostic for the tectonic discrimination of peridotites because there is considerable overlap in Cr# compositions of spinels from different tectonic settings. For example, passive margin peridotites overlap abyssal peridotites from Cr# 0.1 -0.4 and SSZ peridotites overlap abyssal peridotites from Cr# 0.4-0.6 (Figure 4.10) (Dick and Bullen, 1984; Bonatti and Michael, 1989; Arai, 1994a; Pearce et al., 2000).

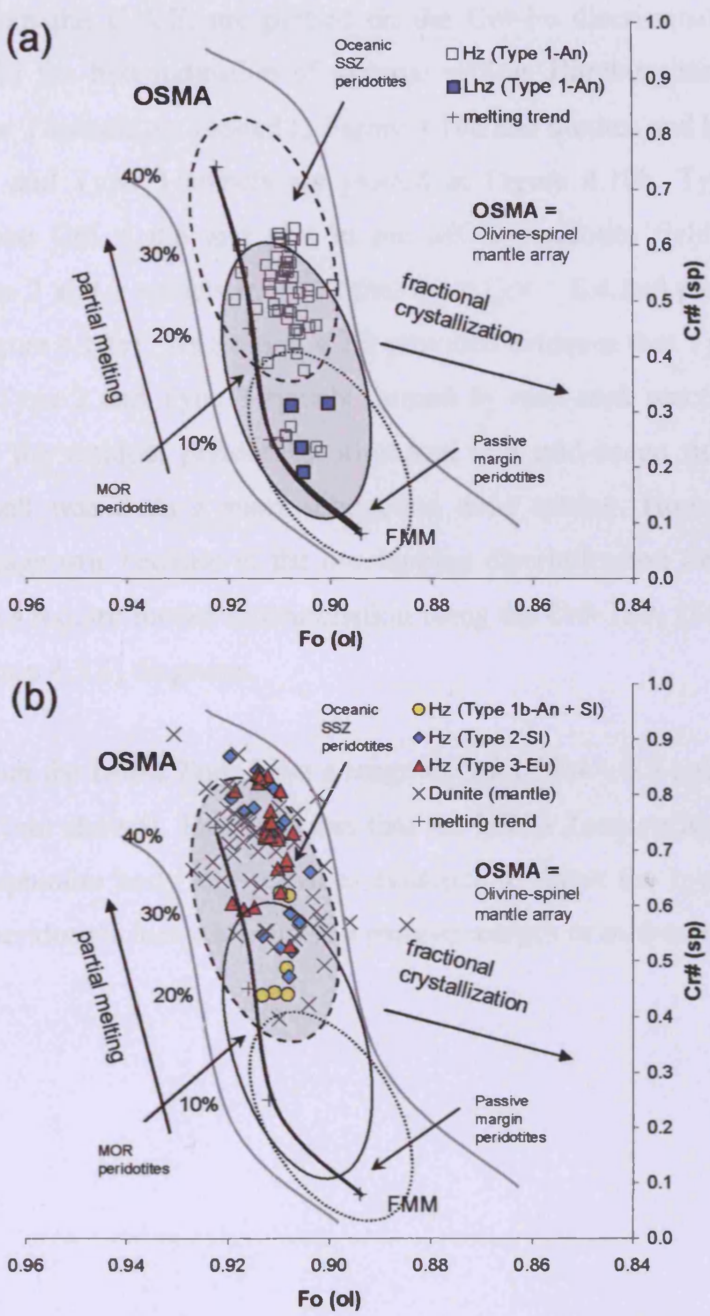

Figure 4.10: Plot of Cr# spinel against olivine Fo content for (a) U.A.E. harzburgites and lherzolites with Type 1 spinels and (b) U.A.E. dunites and harzburgites with Type 2 and Type 3 spinels. The diagram shows the olivine-spinel mantle array (OSMA) and melting trend (annotated by % melting) of Arai (1994) (FMM Fertile MORB mantle) and elliptical tectonic fields for passive continental margin peridotites, MOR peridotites (after Dick and Bullen, 1984) and oceanic SSZ peridotites (after Parkinson and Pearce, 1998 and Pearce et al., 2000). In (a) the Type 1 spinels plot in the MOR field and with some overlap with SSZ and PCM fields whereas in (b) the Type 2 and Type 3 spinels plot in the SSZ field with some overlap with the MOR field.

Peridotites from the U.A.E. are plotted on the Cr#-Fo discrimination diagram in Figure 4.10 for the first indication of tectonic setting. Harzburgites and lherzolites that have Type 1 spinels are plotted in Figure 4.10a and dunites and harzburgites that have Type 2 and Type 3 spinels are plotted in Figure 4.10b. Type 1 spinels in peridotites have Cr# < 0.6 and plot in the MOR peridotite field (Figure 4.10a) whereas Types 2 and 3 spinels in peridotites have Cr# > 0.4 and plot in the oceanic SSZ field (Figure 4.10b). As Section 4.2.2 provided evidence that Type 1 spinels are residual and Type 2 and Type 3 spinels formed by melt-rock reaction, Figure 4.10 indicates that the residual peridotites originated at a mid-ocean ridge and that the interacting melt was from a supra-subduction zone setting. However, this is not completely diagnostic because of the overlapping discrimination fields. The U.A.E. peridotites thus require further discrimination using the Cr#-TiO_2 (Section 4.3.3) and Cr#-fO_2 (Section 4.3.4) diagrams.

Peridotites from the Dibba Zone have a range in Cr# of 0.4 – 0.8 and plot in the SSZ oceanic field (not shown). This indicates that the Dibba Zone peridotites are similar to the main ophiolite body and provides evidence to reject the hypotheses that the Dibba Zone peridotites formed in either a passive margin or mid-ocean ridge setting.

4.3.3 Cr#-TiO_2 discrimination diagram

Section 4.2.2 showed that the Cr#-TiO_2 diagram is effective for distinguishing between partial melting and melt-rock reaction. The Cr#-TiO_2 diagram introduced in Figure 4.5 and 4.6 is reproduced in Figure 4.11 to fingerprint the composition of the melt that interacted with the residual mantle, and thus identify the tectonic setting of the peridotites (e.g. Pearce et al., 2000). This is because reactions between residual mantle and different melt compositions - such as MORB, IAT and BON - form different spinel reaction trends in Cr#-TiO_2 space (e.g. Figure 4.11). Extrapolation of a peridotite trend back to a modelled melting curve predicts the composition of the residual mantle that reacted with the melt (Pearce et al., 2000). Tectonic discrimination using the Cr#- TiO_2 diagram is illustrated in Figure 4.11 by suites of modern-day peridotites that experienced melt-rock reaction at polygenetic (Figure 4.11a) and monogenetic (Figure 4.11b) settings. Polygenetic peridotites are peridotites that formed in more than one tectonic setting, such as SSZ peridotites that formed at a MOR setting and interacted with SSZ melts (Section 4.3.3.1). Monogenetic peridotites are peridotites that formed entirely within one tectonic setting, such as MOR peridotites and some SSZ peridotites (e.g. Torishima Seamount, Izu-Bonin forearc) (Section 4.3.3.2).

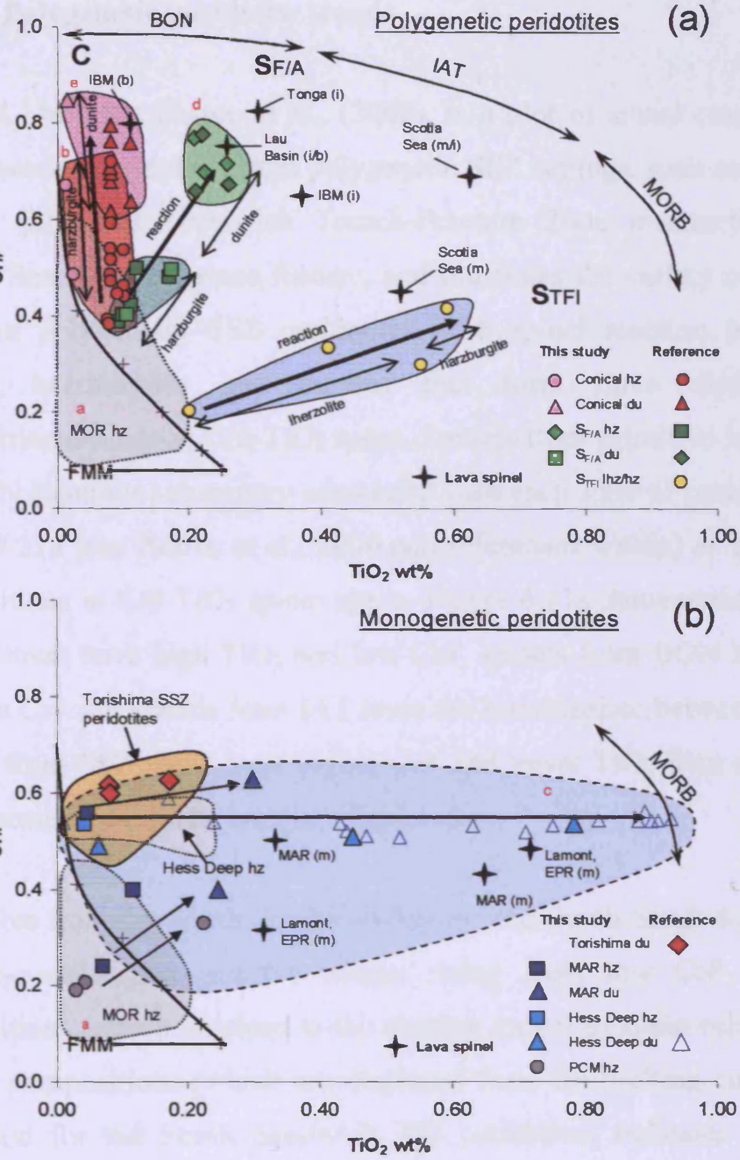

Figure 4.11: Cr#-TiO_2 discrimination diagram after Pearce et al., (2000) for (a) polygenetic SSZ peridotites and (b) monogenetic SSZ and MOR peridotites from modern-day samples of known tectonic settings. Melting curve (black curve) modelled by Pearce et al., (2000) is reproduced from Figure 4.5. Individual modern-day samples are plotted from this study (see Chapter 5) and from published reference data (see key and text for details). These samples define tectonic fields and spinel melt-rock reaction trends: a-MOR hz, b-Conical forearc hz, c-MOR du, d-South Sandwich IAT du, e-Conical BON du. In (a) diagonal reaction trends for peridotites from Conical Seamount (C) [IBM – Izu-Bonin-Mariana], South Sandwich forearc ($S_{F/A}$) and South Sandwich TFI (S_{TFI}) illustrate interaction of MOR mantle lithosphere with SSZ melts. Subscripts m, i and b refer to the MORB, IAT, and BON chemistries, respectively, of the arc-basin spinel lava reference data (see Pearce et al., 2000). In (b) SSZ peridotites from Torishima Seamount, Izu-Bonin forearc have spinel compositions indistinguishable from MOR peridotites (MAR-Mid-Atlantic ridge; EPR – East Pacific Rise).

4.3.3.1 Polygenetic peridotite trends

Figure 4.11a, after Pearce et al., (2000), is a plot of spinel reaction trends in Cr#-TiO_2 space for peridotites from polygenetic SSZ settings, such as (i) South Sandwich forearc, (ii) South Sandwich Trench-Fracture Zone intersection (TFI) and (iii) Conical Seamount, Mariana forearc, and illustrates the variety of melt-rock reaction trends in polygenetic SSZ peridotites. The spinel reaction trends comprise co-existing harzburgites and dunites that form three distinct chrome-spinel compositional fields in Cr#-TiO_2 space. Spinels from primitive lavas of MORB, IAT and BON (boninite) chemistry associated with each suite of peridotites are plotted in Figure 4.11a (see Pearce et al., 2000 and references within) as a guide to their melt compositions in Cr#-TiO_2 spinel space. Figure 4.11a demonstrates that spinels from MORB lavas have high TiO_2 and low Cr#, spinels from BON lavas have low TiO_2 and high Cr# and spinels from IAT lavas are intermediate between MORB and BON. Spinels from SSZ melts have higher Cr# and lower TiO_2 than spinels from MORB melts because SSZ melts are more depleted.

Peridotites from the South Sandwich forearc and South Sandwich TFI form separate but sub-parallel and positive trends: rising from low Cr# and low Ti spinel compositions (which lie close to the melting curve) to attain relatively high Cr# and high Ti compositions (which are displaced from the melting curve) (Figure 4.11a). The trend for the South Sandwich TFI peridotites indicates reaction between a relatively undepleted abyssal peridotite (after < 10% melting) and magma of a MORB composition similar to that from the East Scotia Sea (Pearce et al., 2000). The South Sandwich forearc peridotite trend indicates reaction between a harzburgite residual mantle, after 15-20% melting, and magma of depleted IAT that is transitional to BON, such as lavas from the Lau-Tonga system (Pearce et al., 2000).

Peridotites from Conical Seamount, Izu-Bonin forearc, form a trend from low Cr# and low Ti spinel compositions (which lie close to the melting curve) to high Cr# but low Ti compositions, which are marginally displaced from the melting curve (Figure 4.11b). This trend indicates reaction between a harzburgite residual mantle, after 15-20% melting, and magma of depleted BON composition similar to the BON sample from IBM (Parkinson and Pearce, 1998). In this case, the Ti content of spinel does not increase during melt-rock reaction because the BON melt is highly depleted in Ti; thus the reaction trend is recorded by a large increase in Cr# only (Figure 4.11b).

The Cr#-TiO_2 diagram trends also indicate that SSZ peridotites from the South Sandwich and Izu-Bonin forearcs formed by interaction between pre-existing MOR lithosphere and depleted SSZ magmas (IAT and/or BON), which were not co-genetic with the host peridotites (Pearce et al., 2000).

The above three sets of peridotite trends from SSZ settings (Figure 4.11b) demonstrate that the Cr#-TiO_2 composition of the spinel in peridotite is determined not only by the composition of the interacting melt but also by the extent of reaction. The latter is gradational from (a) lherzolite to harzburgite in the South Sandwich TFI peridotites, (b) from harzburgite to transitional harzburgites to dunite in the South Sandwich Forearc peridotites (Pearce et al., 2000) and (c) from harzburgites to dunites in Conical seamount forearc peridotites in which the harzburgite and dunite compositional fields for spinel overlap (Parkinson and Pearce, 1998). As the Cr#-TiO_2 composition of spinels is dependent on both the extent of reaction and the composition of the interacting melt it is preferable to plot trends of peridotites, rather than isolated dunite or harzburgite samples, in order to identify correctly the true nature of the melt interacting with the peridotite.

The Cr#-TiO_2 plot cannot determine whether the residual mantle and infiltrating low-Cr melt is from dry melting (e.g. MOR setting) or wet melting (e.g. SSZ setting). For example, the pre-existing residual mantles for the Sandwich and Izu-Bonin forearc peridotites are identical in Cr#-TiO_2 space (e.g. Figure 4.11b). However, discrimination using the Cr#-fO_2 diagram (Section 4.3.4.2) provides some evidence that the residual mantle peridotites from South Sandwich forearc formed under more oxidising conditions than those from Izu-Bonin forearc. Therefore, the Cr#-TiO_2 plot is the first step in tectonic discrimination of peridotites, and the discrimination can be finely tuned using the Cr#-fO_2 diagram.

4.3.3.2 Monogenetic peridotite trends

Figure 4.11b is a plot of spinel reaction trends in Cr#-TiO_2 space for monogenetic peridotites from (i) a variety of mid-ocean ridge settings and (ii) Torishima Seamount, Izu-Bonin forearc (see Section 4.3.1). Spinels from MOR harzburgites (dotted grey fields: Barnes and Roeder, 2001) and MOR dunites (dashed blue field): Barnes and Roeder, 2001) are plotted in Figure 4.11b and show that they have similar ranges in Cr# (0.2 – 0.6) but MOR dunites commonly have higher TiO_2 (up to 1 wt.%). The MOR dunites have a similar range in Cr-TiO_2 space as spinels from MORB lavas that are also plotted on Figure 4.11b. Spinels in SSZ harzburgites and dunites from Torishima Seamount, Izu-Bonin forearc are also plotted in Figure 4.11b and demonstrate that they have similar ranges in Cr# and TiO_2 to each other and to MOR peridotites. Therefore, some monogenetic SSZ peridotites cannot be distinguished from MOR peridotites using Cr#-TiO_2. Arai (1992) observed that some SSZ lavas have spinels with Cr# range the same as MORB lava spinels (i.e. 0.3 – 0.6). Although interaction between peridotites and either MORB or some SSZ melts cannot be distinguished in Cr#-TiO_2 space, they can be distinguished by the Cr#-fO_2 diagram (Section 4.3.4). This is because SSZ magmas and SSZ peridotites have higher oxygen fugacity than MORB magmas and MOR peridotites, a result of augmented water in the mantle wedge (Parkinson and Pearce, 1998; Parkinson and Arculus, 1999).

The composition of MORB spinels varies as shown by the Lamont basalts plotted in Figure 4.11a. This variation is a function of fractional crystallization, pressure and temperature of crystallization, and magma mixing (Allan et al., 1988). Therefore, depending on the MORB composition the spinel reaction trend for co-existing harzburgites and dunites could either be (i) increasing TiO_2 content and increasing Cr# or (ii) increasing TiO_2 content of spinel at near constant Cr#, e.g. Hess Deep.

4.3.3.3 U.A.E. peridotite trends

Spinels from harzburgites, dunites and chromitites from each mantle domain in the U.A.E are plotted on a series of Cr#-TiO_2 diagrams to identify melt-rock reaction trends (Figures 4.12 – 4.18) in order to constrain the tectonic setting of the ophiolite. The mantle domains plotted in each Cr#-TiO_2 diagram are (i) the sub-Moho mantle and MTZ of Aswad South and Fizh North (Figure 4.12), (ii) the mid-mantle of Aswad North (Figure 4.13), (iii) the Banded Unit of Aswad North (Figure 4.14), (iv) the sub-Moho mantle and MTZ of Khawr Fakkan South (Figure 4.15), (v) the mid-mantle of Khawr Fakkan North (Figure 4.16), (vi) the Banded Unit of Khawr Fakkan North (Figure 4.17) and (vii) the peridotites from the Dibba Zone (Figure 4.18).

Figures 4.12 – 4.18 each comprise two Cr#-TiO_2 diagrams: the first illustrates the spinel reaction trends in detail and the second is simplified to summarise the main trends. The detailed diagram is reproduced from Figure 4.11a on which individual samples are plotted and co-existing harzburgite and dunite pairs marked to demonstrate the general reaction trends. In these detailed Cr#-TiO_2 diagrams the compositional tectonic fields for peridotites and lavas from MOR and SSZ settings are used to interpret the U.A.E. peridotite trends. This is because there are no spinels in lavas from the U.A.E. crustal sequence of the ophiolite from which to identify the composition of the interacting melt in the U.A.E. peridotites.

However, there are published spinels compositions from the lava Units of Geotimes (MORB/IAT chemistry) and Alley (BON chemistry) in northern Oman (Umino et al., 1991; Ishikawa et al., 2001). These spinels are plotted on the Cr#-TiO_2 diagrams (e.g. Figure 4.12a). Spinels from the Geotimes Unit represent the composition of spinel in equilibrium with a MORB/IAT melt. They have Cr# 0.6 – 0.65 (no Ti data available) and plot near the boundary of MORB and IAT compositions of lava spinels. They are similar to those spinels in the Scotia Sea transitional (MORB/IAT) basalts also shown on Figure 4.12a. Spinels from the Alley Unit have Cr# 0.75 – 0.85 and TiO_2 content of 0.1 – 0.2 wt.% and represent the composition of spinel in equilibrium with a BON melt from northern Oman.

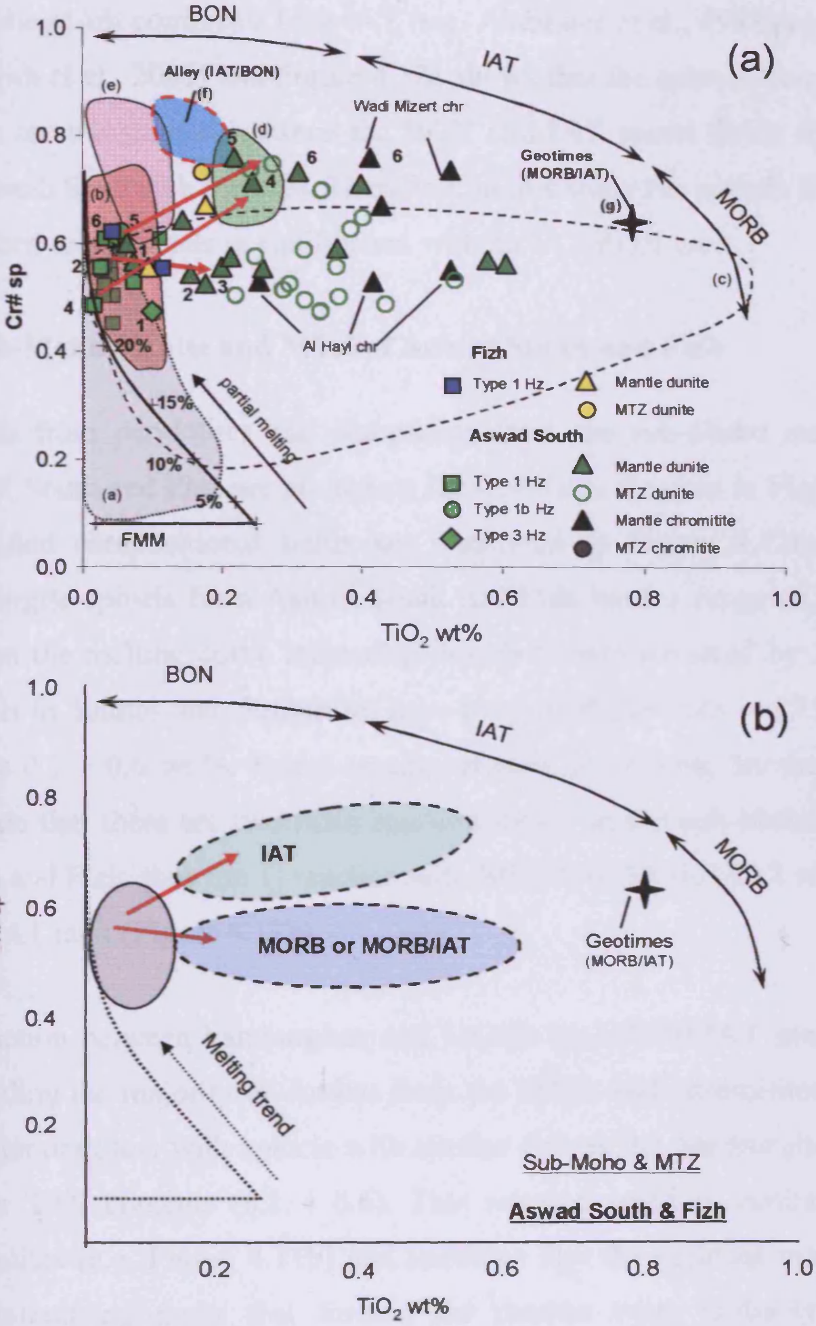

Figure 4.12: Cr#-TiO$_2$ discrimination diagram for peridotites from the sub-Moho mantle and MTZ of Aswad South and Fizh to illustrate spinel reaction trends in (a) detail and (b) summarised format. In (a) individual samples are plotted (see key) and harzburgite-dunite pairs numbered to illustrate the general trends for reaction (red arrows). Tectonic fields and melting trend are taken from Figure 4.11b: a-MOR hz, b-Conical forearc hz, c-MOR du, d-South Sandwich IAT du, e-Conical BON du, f- IAT/BON lava (Alley Unit, Oman) and g-MORB/IAT lava (Geotimes Unit). In (b) elliptical fields approximate the U.A.E. harzburgites (grey) and dunites (dashed) to summarise the two main reaction trends (red arrows) between peridotite and MORB or MORB/IAT melt (blue ellipse) and between peridotite and IAT melt (green ellipse).

The Alley Unit comprises both IAT (e.g. Alabaster et al., 1982) and BON lavas (e.g. Ishikawa et al., 2001) and Figure 4.12a shows that the spinels from the Alley Unit of Oman are transitional between the BON and IAT spinel fields from the Izu-Bonin and South Sandwich forearcs. Therefore, in this study the spinels from the Alley Unit are taken to be spinels in equilibrium with an IAT/BON melt.

(i) sub-Moho mantle and MTZ of Aswad South and Fizh

Spinels from peridotites and chromitites from the sub-Moho mantle and MTZ of Aswad South and Fizh are plotted on the Cr#-TiO_2 diagram in Figure 4.12a and their simplified compositional fields are illustrated in Figure 4.12b. The majority of harzburgite spinels from Aswad South and Fizh have a range of Cr# 0.4 – 0.6 and plot on the melting curve indicating that they were depleted by 20 - 30% melting. Spinels in dunites and chromitites have a range of Cr# 0.45 – 0.75 and TiO_2 content ranges 0.1 – 0.6 wt.%. Spinel trends between co-existing harzburgites and dunites indicate that there are two main reaction trends in the sub-Moho mantle of Aswad South and Fizh: they are 1) reaction with MORB or MORB/IAT melt and 2) reaction with IAT melt (Figure 4.12b).

Interaction between harzburgites and MORB or MORB/IAT melts formed dunites (including the majority of dunites from the MTZ) and chromitites (including the Al Hayl chromitites) with spinels with similar Cr# as the harzburgites (0.45 – 0.6) but higher TiO_2 contents (0.1 – 0.6). This reaction trend is similar to that in MOR peridotites (e.g. Figure 4.11b) and indicates that the residual mantle (harzburgites) and interacting melts that formed the dunites were probably monogenetic. In contrast, interaction between harzburgites and IAT melts formed dunites (including a few in the MTZ) and chromitites (e.g. Wadi Mizert pod, pair 6 in Figure 4.12a) with spinels with higher Cr# (0.65 – 0.75) and higher TiO_2 contents (0.2 – 0.6). This reaction trend is similar to that in SSZ peridotites from the South Sandwich forearc (e.g. Figure 4.11a) and indicates that the residual mantle (harzburgites) and interacting melts that formed the dunites were probably polygenetic i.e. the harzburgite residue was not the source region for the IAT melt.

(ii) mid-mantle of Aswad North

Spinels from peridotites and chromitites from the mid-mantle of Aswad North are plotted on the Cr#-TiO_2 diagram in Figure 4.13a and their simplified compositional fields are illustrated in Figure 4.13b. The majority of harzburgite spinels from this region in Aswad North have a range of Cr# 0.4 – 0.6 and plot on the melting curve indicating that they were depleted by 20 - 30% melting. Spinels in dunites and chromitites have a range of Cr# 0.6 – 0.75 and the TiO_2 content ranges 0.1 – 0.4 wt.%. Spinel trends between co-existing harzburgites and dunites indicate that there are two main reaction trends in the mid-mantle of Aswad North: they are 1) reaction with IAT melt and 2) reaction with IAT/BON melt (Figure 4.13b).

Interaction between harzburgites and IAT melts formed dunites and chromitites (e.g. the Siji mining district) with spinels with higher Cr# (0.6 – 0.7) and higher TiO_2 contents (0.2 – 0.4 wt.%). This reaction trend is similar to that in SSZ peridotites from the South Sandwich forearc (e.g. Figure 4.11a) and indicates that the residual mantle (harzburgites) and interacting melts that formed the dunites were probably polygenetic i.e. the harzburgite residue was not the source region for the IAT melt. In addition, interaction between harzburgites and IAT/BON melts formed dunites with spinels with high Cr# (0.6 - 0.8) and low TiO_2 contents (0.1 - 0.2 wt.%). This reaction trend is similar to that in SSZ peridotites but intermediate to the IAT melt-rock interaction at the South Sandwich forearc and the BON melt-rock interaction at Conical Seamount, Mariana forearc (e.g. Figure 4.11a). This indicates that in Aswad North the residual mantle (harzburgites) and interacting melts that formed the dunites were polygenetic i.e. the harzburgite residue was not the source region for the IAT/BON melt.

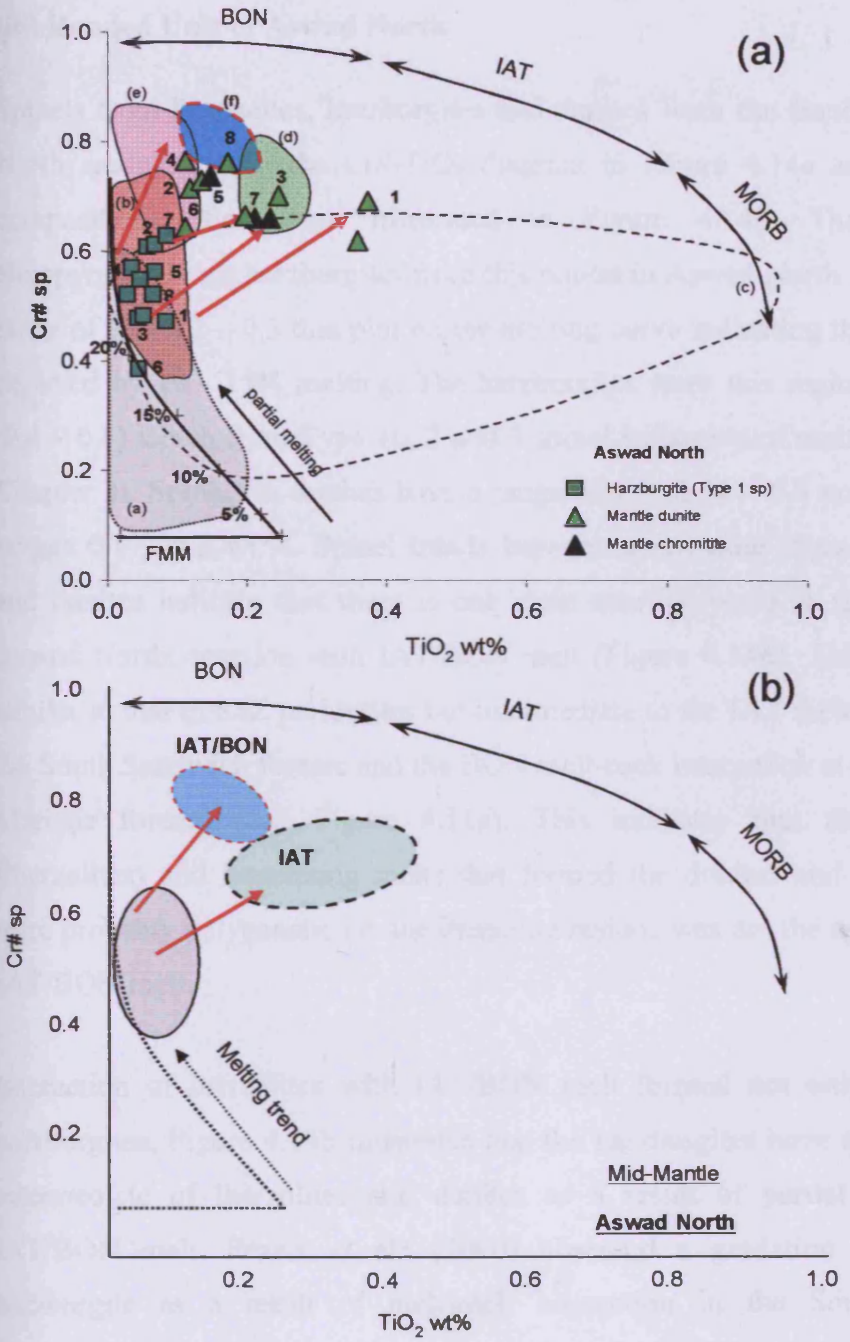

Figure 4.13: Cr#-TiO$_2$ discrimination diagram for peridotites from the mid-mantle of Aswad North to illustrate spinel reaction trends in (a) detail and (b) summarised format. In (a) individual samples are plotted (see key) and harzburgite-dunite pairs numbered to illustrate the general trends for reaction (red arrows). Tectonic fields and melting trend are taken from Figure 4.11b: a-MOR hz, b-Conical forearc hz, c-MOR du, d-South Sandwich IAT du, e-Conical BON du, f- IAT/BON lava (Alley Unit, Oman). In (b) elliptical fields approximate the U.A.E. harzburgites (grey) and dunites (dashed) to summarise the two main reaction trends (red arrows) between peridotite and IAT melt (green ellipse) and between peridotite and IAT/BON melt (blue ellipse).

(iii) Banded Unit of Aswad North

Spinels from lherzolites, harzburgites and dunites from the Banded Unit of Aswad North are plotted on the Cr#-TiO_2 diagram in Figure 4.14a and their simplified compositional fields are illustrated in Figure 4.14b. The lherzolites and clinopyroxene-rich harzburgites from this region in Aswad North have spinels with a range of Cr# 0.2 – 0.3 that plot on the melting curve indicating that peridotites were depleted by 10 - 15% melting. The harzburgites from this region have higher Cr# (0.4 – 0.8) which form Type 1b, 2 and 3 spinel indicative of melt-rock reaction (see Chapter 3). Spinels in dunites have a range of Cr# 0.55 – 0.9 and the TiO_2 content ranges 0.1 – 0.2 wt.%. Spinel trends between co-existing lherzolites, harzburgites and dunites indicate that there is one main reaction trend in the Banded Unit of Aswad North: reaction with IAT/BON melt (Figure 4.14b). This reaction trend is similar to that in SSZ peridotites but intermediate to the IAT melt-rock interaction at the South Sandwich forearc and the BON melt-rock interaction at Conical Seamount, Mariana forearc (e.g. Figure 4.11a). This indicates that the residual mantle (lherzolites) and interacting melts that formed the dunites and some harzburgites were probably polygenetic i.e. the lherzolite residue was not the source region for the IAT/BON melt.

Interaction of lherzolites with IAT/BON melt formed not only dunites but also harzburgites. Figure 4.14b illustrates that the harzburgites have spinel compositions intermediate of lherzolites and dunites as a result of partial reaction with the IAT/BON melt. Pearce et al., (2000) observed a gradation from lherzolite to harzburgite as a result of melt-rock interaction in the South Sandwich TFI peridotites. This provides some evidence that clinopyroxene can be consumed during melt-rock reaction. Therefore, in the basal shear zone (i.e. Banded Unit) of Aswad North reaction between mantle and IAT/BON melt was not restricted to dunite melt-channels but melt also infiltrated and reacted with the host lherzolites to form harzburgites.

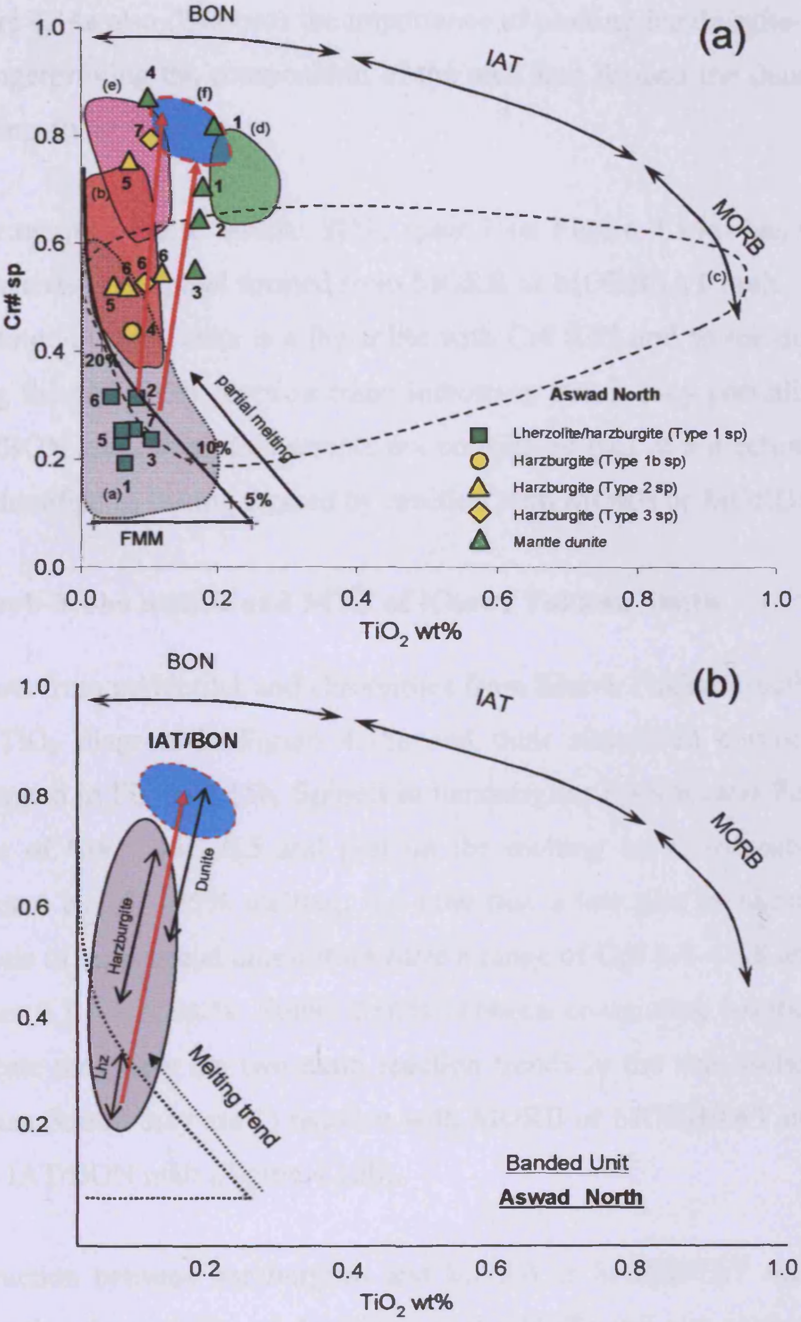

Figure 4.14: Cr#-TiO_2 discrimination diagram for peridotites from the Banded Unit of Aswad North to illustrate spinel reaction trends in (a) detail and (b) summarised format. In (a) individual samples are plotted (see key) and harzburgite-dunite pairs numbered to illustrate the general trends for reaction (red arrows). Tectonic fields and melting trend are taken from Figure 4.11b: a-MOR hz, b-Conical forearc hz, c-MOR du, d-South Sandwich IAT du, e-Conical BON du, f- IAT/BON lava (Alley Unit, Oman). In (b) elliptical fields approximate the U.A.E. harzburgites (grey) and dunites (dashed) to summarise the main reaction trend (red arrow) between peridotite and IAT/BON melt (blue ellipse). There is a gradation from lhz to hz to du during increasing extent of melt-rock reaction.

Figure 4.14a also illustrates the importance of plotting harzburgite-dunite spinel pairs in fingerprinting the composition of the melt that formed the dunite rather than just plotting dunite spinels.

For example, dunite sample SD33 (pair 3 on Figure 4.14a) has Cr# 0.55 which is characteristic of spinel formed from MORB or MORB/IAT melt. However, the host peridotite of this dunite is a lherzolite with Cr# 0.25 and so the dunite plots midway along the IAT/BON reaction trend indicating that it only partially reacted with the IAT/BON melt. Were this sample not considered part of a reaction trend, it could be misclassified as having formed by reaction with MORB or MORB/IAT melt.

(iv) sub-Moho mantle and MTZ of Khawr Fakkan South

Spinels from peridotites and chromitites from Khawr Fakkan South are plotted on the Cr#-TiO_2 diagram in Figure 4.15a and their simplified compositional fields are illustrated in Figure 4.15b. Spinels in harzburgites from Khawr Fakkan South have a range of Cr# 0.35 - 0.5 and plot on the melting curve indicating that they were depleted by 15 - 25% melting; but note that a few plot to higher Cr# (up to 0.7). Spinels in dunites and chromitites have a range of Cr# 0.4 – 0.8 and the TiO_2 content ranges 0.1 – 0.5 wt.%. Spinel trends between co-existing harzburgites and dunites indicate that there are two main reaction trends in the sub-Moho mantle of Khawr Fakkan South: they are 1) reaction with MORB or MORB/IAT melt and 2) reaction with IAT/BON melt (Figure 4.15b).

Interaction between harzburgites and MORB or MORB/IAT melts formed dunites (including the majority of dunites from the MTZ) and chromitites with spinels with similar Cr# as the harzburgites (0.40 – 0.6) but higher TiO_2 contents (0.2 – 0.6). As in Aswad South, this reaction trend is similar to that in MOR peridotites (e.g. Figure 4.11b) and indicates that the residual mantle (harzburgites) and interacting melts that formed the dunites were probably monogenetic.

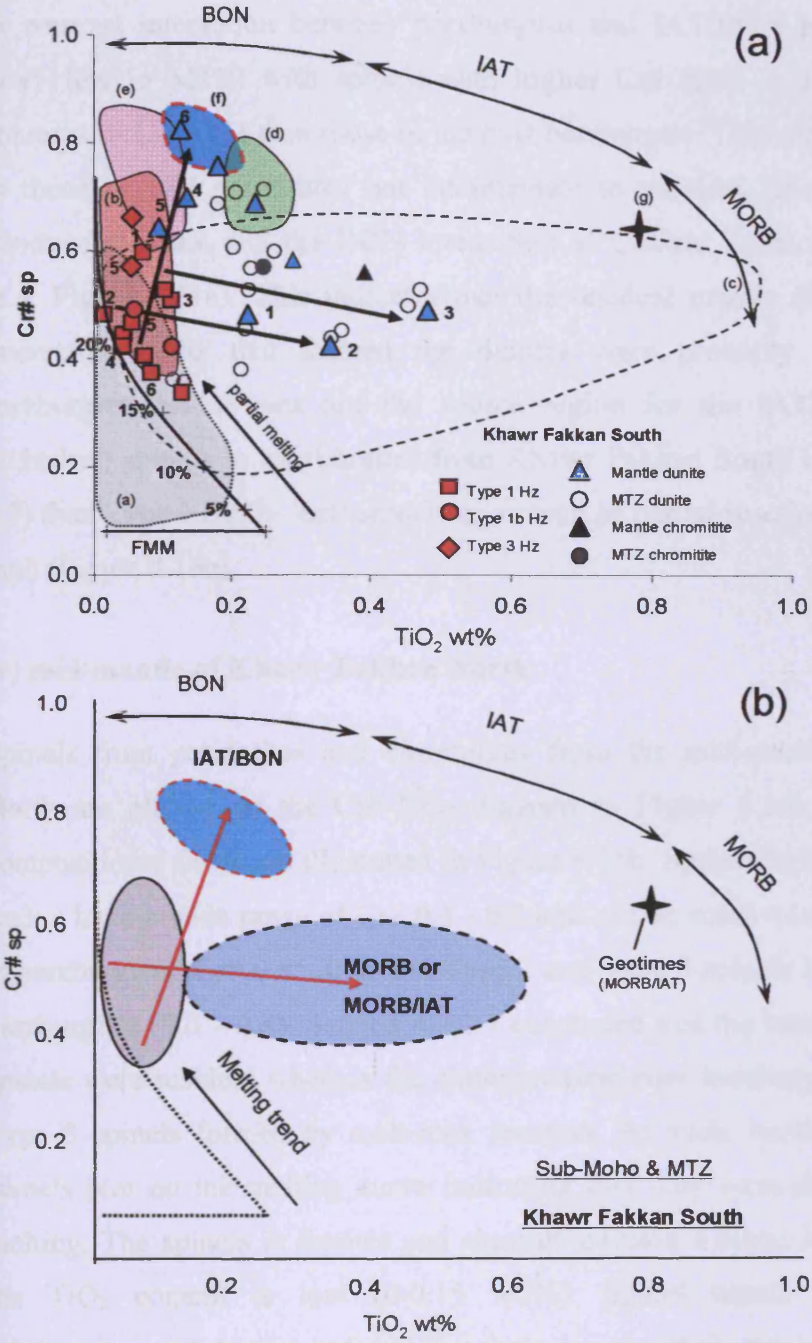

Figure 4.15: Cr#-TiO$_2$ discrimination diagram for peridotites from the sub-Moho mantle and MTZ of Khawr Fakkan South to illustrate spinel reaction trends in (a) detail and (b) summarised format. In (a) individual samples are plotted (see key) and harzburgite-dunite pairs numbered to illustrate the general trends for reaction (red arrows). Tectonic fields and melting trend are taken from Figure 4.11b: a-MOR hz, b-Conical forearc hz, c-MOR du, d-South Sandwich IAT du, e-Conical BON du, f- IAT/BON lava (Alley Unit, Oman) and g- MORB/IAT lava (Geotimes Unit, Oman). In (b) elliptical fields approximate the U.A.E. harzburgites (grey) and dunites (dashed) to summarise the two main reaction trends (red arrows) between peridotite and MORB or MORB/IAT melt (dark blue ellipse) and IAT/BON melt (light blue ellipse).

In contrast interaction between harzburgites and IAT/BON melts formed dunites (very few in MTZ) with spinels with higher Cr# (0.65 – 0.8) and higher TiO_2 contents (0.1 – 0.25) than those in the host harzburgite. This reaction trend is similar to those in SSZ peridotites but intermediate to the IAT interaction at the South Sandwich forearc and the BON interaction at Conical Seamount, Mariana forearc (e.g. Figure 4.11a). This indicates that the residual mantle (harzburgites) and the interacting melts that formed the dunites were probably polygenetic i.e. the harzburgite residue was not the source region for the IAT/BON melt. Type 3 (euhedral) spinels in harzburgites from Khawr Fakkan South have higher Cr# (0.6-0.7) than Type 1 (holly-leaf) spinels as a result of partial reaction with this IAT/BON melt (Figure 4.15a).

(v) mid-mantle of Khawr Fakkan North

Spinels from peridotites and chromitites from the mid-mantle of Khawr Fakkan North are plotted on the Cr#-TiO_2 diagram in Figure 4.16a and their simplified compositional fields are illustrated in Figure 4.16b. Spinels in harzburgites from this region have a wide range of Cr# 0.4 - 0.8 and can be subdivided into Type 1 spinels in harzburgites (Cr# 0.4 – 0.6) and Type 2 and Type 3 spinels in clinopyroxene-poor harzburgites (0.6 – 0.8). Section 4.2.1.1 concluded that the harzburgites with Type 1 spinels were residual whereas the clinopyroxene-poor harzburgites with Type 2 and Type 3 spinels formed by melt-rock reaction. As such, harzburgites with Type 1 spinels plot on the melting curve indicating that they were depleted by 20 - 30% melting. The spinels in dunites and chromitites have a range of Cr# 0.65 – 0.9 and the TiO_2 content is low (0-0.15 wt.%). Spinel trends between co-existing harzburgites and dunites indicate that there are two main reaction trends in the mid-mantle of Khawr Fakkan North: they are 1) reaction with BON melt and 2) reaction with IAT/BON melt (Figure 4.16b).

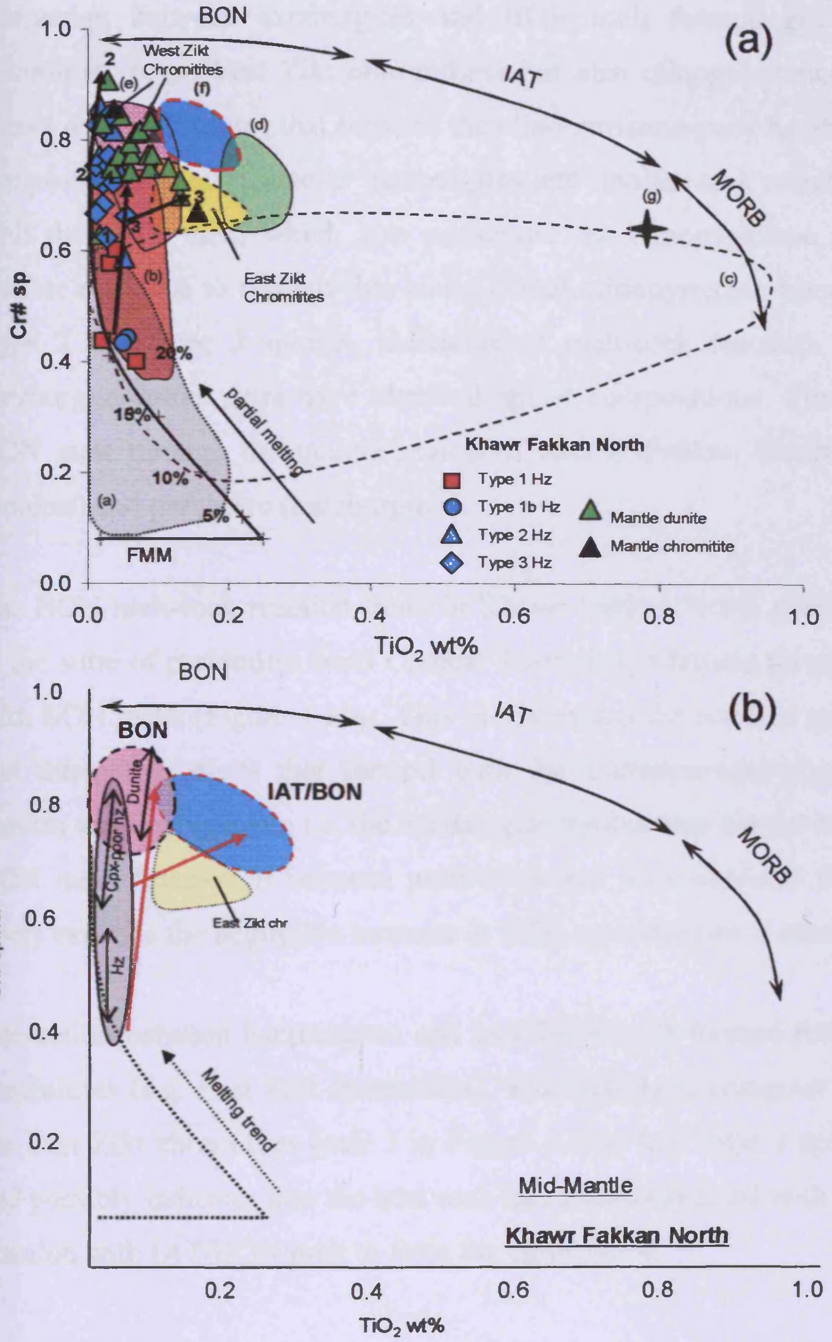

Figure 4.16: Cr#-TiO_2 discrimination diagrams for peridotites from the mid-mantle Khawr Fakkan North to illustrate spinel reaction trends in (a) detail and (b) summarised format. In (a) individual samples are plotted (see key) and harzburgite-dunite pairs numbered to illustrate the general trends for reaction (red arrows). Tectonic fields and melting trend are taken from Figure 4.11b: a-MOR hz, b-Conical forearc hz, c-MOR du, d-South Sandwich IAT du, e-Conical BON du, f- IAT/BON lava (Alley Unit, Oman). In (b) elliptical fields approximate the U.A.E. harzburgites (grey) and dunites (dashed) to summarise the two main reaction trends (red arrows) between peridotite and BON melt(pink ellipse), e.g. West Zikt chromitites, and between peridotite and IAT/BON melt (light blue ellipse), e.g. East Zikt chromitites (yellow field). There is a gradation from hz to cpx-poor hz to du during increasing extent of melt-rock reaction with BON melt.

Interaction between harzburgites and BON melt formed not only dunites and chromitites (e.g. West Zikt chromitites) but also clinopyroxene-poor harzburgites. Figure 4.16b illustrates that some of the clinopyroxene-poor harzburgites have spinel compositions intermediate to harzburgites and dunites as a result of partial reaction with the BON melt, which also consumed the clinopyroxene in the harzburgite. Further evidence to support this claim is that clinopyroxene-poor harzburgites have Type 2 and Type 3 spinels, indicative of melt-rock reaction. In addition, many harzburgite-dunite pairs have identical spinel compositions. Therefore, the flow of BON melt through the mantle region of Khawr Fakkan North was both focused (dunites) and pervasive (harzburgites).

The BON melt-rock reaction trend in Khawr Fakkan North peridotites is analogous to the suite of peridotites from Conical Seamount, Mariana forearc that also reacted with BON melts (Figure 4.11a). This indicates that the residual mantle (harzburgites) and interacting melts that formed both the clinopyroxene-poor harzburgites and dunites were polygenetic i.e. the harzburgite residue was not the source region for the BON melt. Interaction between peridotites and ultra-depleted BON melts (i.e. Ti-poor) explains the negligible increase in TiO_2 upon melt-rock reaction.

Interaction between harzburgites and IAT/BON melt formed few dunites and some chromitites (e.g. East Zikt chromitites). The clinopyroxene-poor harzburgite host to the East Zikt chromitites (pair 3 in Figure 4.16a) has Type 3 spinels with Cr# 0.65 and possibly indicates that the host rock had already reacted with a BON melt before reaction with IAT/BON melt to form the chromitites

(vi) Banded Unit of Khawr Fakkan North

Spinels from lherzolites, harzburgites and dunites from the Banded Unit of Khawr Fakkan North are plotted on the Cr#-TiO_2 diagram in Figure 4.17a and their simplified compositional fields are illustrated in Figure 4.17b. The peridotite spinels from the Banded Unit of Khawr Fakkan North are very similar to those from the Banded Unit of Aswad North (see Figure 4.14 for comparison). Spinels in lherzolites and clinopyroxene-rich harzburgites from this region in Khawr Fakkan North have a range of Cr# 0.2 – 0.3 and plot on the melting curve indicating that they were depleted by 10 - 15% melting. Harzburgites with Type 1 spinels have higher Cr# (0.4 – 0.6) and are residual after 20 - 30% melting. These harzburgites are from the top end of the Banded Unit in Khawr Fakkan North where there is a change from relatively fertile lherzolites at the base to depleted harzburgite above. However, harzburgites with Type 1b, 2 and 3 spinels, indicative of melt-rock reaction (see Chapter 3), have higher Cr# (0.6 – 0.7). The dunites have a range of Cr# 0.65 – 0.8 and the TiO_2 content of spinel ranges 0.1 – 0.2 wt.%.

As in the Banded Unit of Aswad North, spinel trends between co-existing lherzolites, harzburgites and dunites from the Banded Unit of Khawr Fakkan North indicate that there was only reaction with IAT/BON melt (Figure 4.17b). This reaction trend is similar to that in SSZ peridotites but intermediate to the IAT melt-rock interaction at the South Sandwich forearc and the BON melt-rock interaction at Conical Seamount, Mariana forearc (e.g. Figure 4.11a). This provides evidence that the residual mantle (lherzolites) and the interacting melts that formed both dunites and harzburgites were polygenetic i.e. the lherzolite and harzburgite residues were not the source region for the IAT/BON melt.

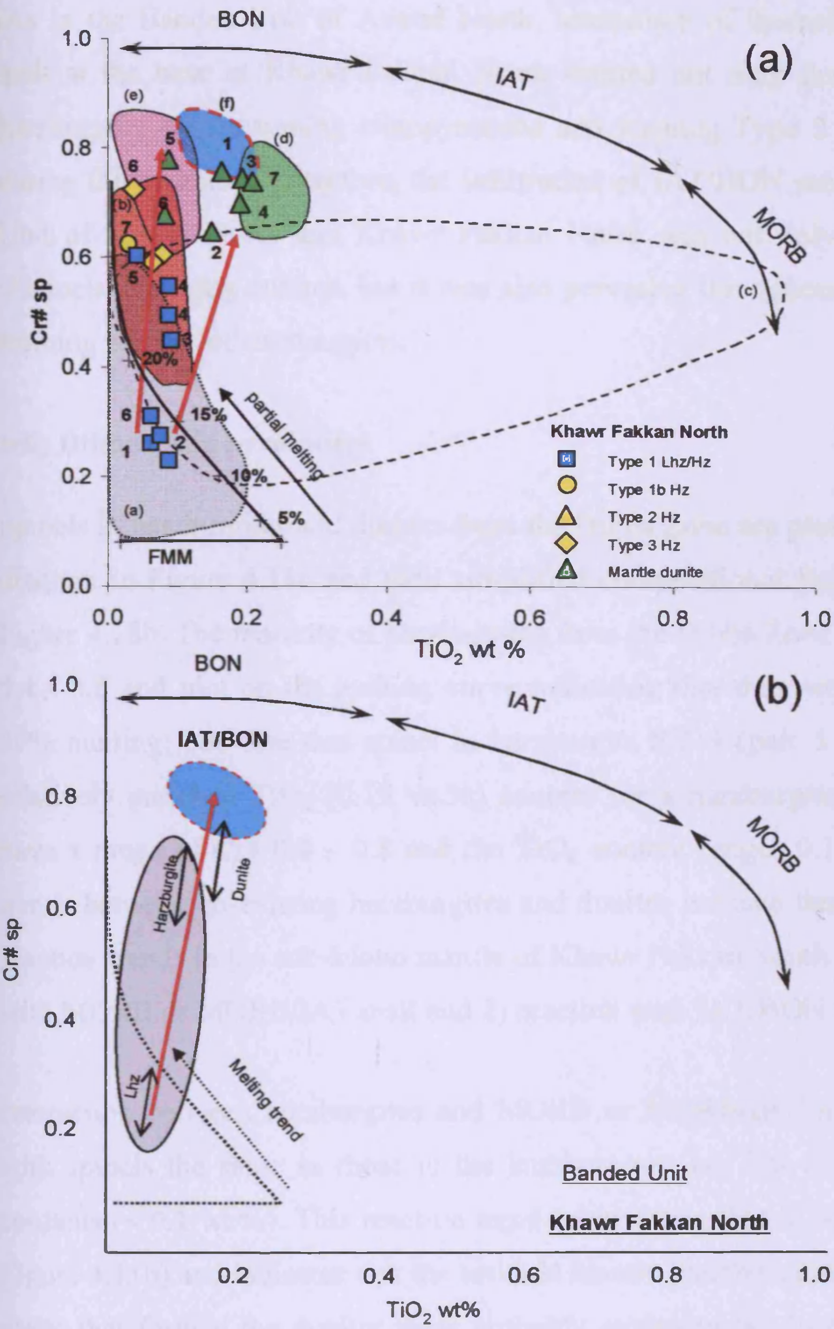

Figure 4.17: Cr#-TiO_2 discrimination diagram for peridotites from the Banded Unit of Khawr Fakkan North to illustrate spinel reaction trends in (a) detail and (b) summarised format. In (a) individual samples are plotted (see key) and harzburgite-dunite pairs numbered to illustrate the general trends for reaction (red arrows). The tectonic fields and melting trend are taken from Figure 4.11b: a-MOR hz, b-Conical forearc hz, c-MOR du, d-South Sandwich IAT du, e-Conical BON du, f- IAT/BON lava (Alley Unit, Oman). In (b) elliptical fields approximate the U.A.E. harzburgites (grey) and dunites (dashed) to summarise the main reaction trend (red arrows) between peridotite and IAT/BON melt (light blue ellipse). There is a gradation from lhz to hz to du during increasing extent of melt-rock reaction.

As in the Banded Unit of Aswad North, interaction of lherzolites with IAT/BON melt at the base of Khawr Fakkan North formed not only dunites but also some harzburgites by consuming clinopyroxene and forming Type 2 and Type 3 spinels during this reaction. Therefore, the infiltration of IAT/BON melt along the Banded Unit of Aswad North and Khawr Fakkan North was not only focused into melt-channels, (forming dunites, but it was also pervasive throughout the host lherzolite, forming patches of harzburgites.

(vii) Dibba Zone peridotites

Spinels in harzburgites and dunites from the Dibba Zone are plotted on the Cr#-TiO_2 diagram in Figure 4.18a and their simplified compositional fields are illustrated in Figure 4.18b. The majority of harzburgites from the Dibba Zone have a range of Cr# 0.4 - 0.6 and plot on the melting curve indicating that they were depleted by 20 - 30% melting; but note that spinel in harzburgite SD19 (pair 5 Figure 4.18a) has a relatively enriched TiO_2 (0.19 wt.%) content for a harzburgite. Spinels in dunites have a range of Cr# 0.4 – 0.8 and the TiO_2 content ranges 0.1 – 0.2 wt.%. Spinel trends between co-existing harzburgites and dunites indicate that there are two main reaction trends in the sub-Moho mantle of Khawr Fakkan South: they are 1) reaction with MORB or MORB/IAT melt and 2) reaction with IAT/BON melt (Figure 4.18b).

Interaction between harzburgites and MORB or MORB/IAT melts formed dunites with spinels the same as those in the harzburgites, i.e. Cr# (0.40 – 0.6) and TiO_2 contents (< 0.1 wt.%). This reaction trend is similar to that in MOR peridotites (e.g. Figure 4.11b) and indicates that the residual mantle (harzburgites) and the interacting melts that formed the dunites were probably monogenetic. In addition, harzburgite sample SD19 (pair 5 in Figure 4.18a) probably reacted with MORB or MORB/IAT melt to enrich the spinel in TiO_2 as is common in Hess Deep harzburgites (Figure 4.11b).

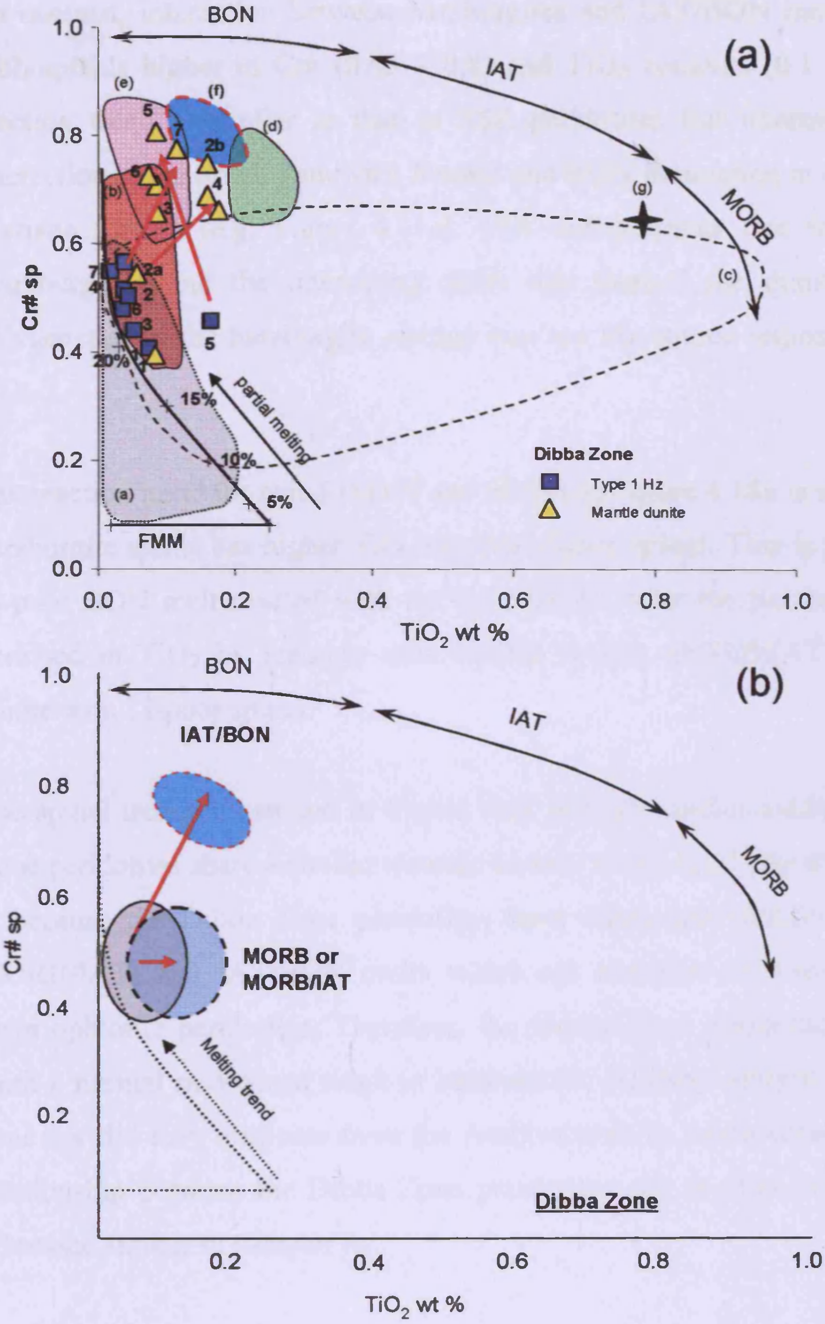

Figure 4.18: Cr#-TiO_2 discrimination diagram for peridotites from the Dibba Zone to illustrate spinel reaction trends in (a) detail and (b) summarised format. In (a) individual samples are plotted (see key) and harzburgite-dunite pairs numbered to illustrate the general trends for reaction (red arrows). Tectonic fields and melting trend are from Figure 4.11b: a-MOR hz, b-Conical forearc hz, c-MOR du, d-South Sandwich IAT du, e-Conical BON du, f-IAT/BON lava (Alley Unit, Oman) and g- MORB/IAT lava (Geotimes Unit, Oman). In (b) elliptical fields approximate the U.A.E. harzburgites (grey) and dunites (dashed) to summarise the main reaction trends (red arrows) between peridotite and MORB or MORB/IAT melt (dark blue ellipse) and between peridotite and IAT/BON melt (light blue ellipse).

In contrast, interaction between harzburgites and IAT/BON melts formed dunites with spinels higher in Cr# (0.65 – 0.8) and TiO_2 contents (0.1 – 0.2 wt.%). This reaction trend is similar to that in SSZ peridotites but intermediate to the IAT interaction at the South Sandwich forearc and BON interaction at Conical Seamount, Mariana forearc (e.g. Figure 4.11a). This demonstrates that the residual mantle (harzburgites) and the interacting melts that formed the dunites were probably polygenetic i.e. the harzburgite residue was not the source region for the IAT/BON melt.

The reaction trend for pair 5 (SD19 and SD18) in Figure 4.18a is unusual because the harzburgite spinel has higher TiO_2 than the dunite spinel. This is probably because a Ti-poor BON melt reacted with the harzburgite, after the harzburgite spinels were enriched in TiO_2 by reaction with MORB and/or MORB/IAT melt, and formed dunite with Ti-poor spinel.

The spinel trends illustrated in Figure 4.18 provide further evidence that the Dibba Zone peridotites share a similar tectonic history to the main part of the ophiolite. This is because the Dibba Zone peridotites have interacted with both MORB (and/or MORB/IAT) and IAT/BON melts which are common melt-rock reactions in the main ophiolite peridotites. Therefore, the Dibba Zone peridotites did not originate from a normal mid-ocean ridge in between the Arabian margin and the subduction zone nor did they originate from the Arabian passive continental margin. The exact relationship between the Dibba Zone peridotites and the Oman-U.A.E. ophiolite is discussed further in Chapter 6.

4.3.4 Cr#-fO_2 discrimination diagram

Section 4.3.3 demonstrated that the Cr#-TiO_2 diagram is successful in discriminating melt-rock reaction between MOR peridotites and SSZ melts. However, the Cr#-TiO_2 diagram does not establish the true nature of the peridotites with low Cr# spinels (0.4 - 0.6) because both MOR and some SSZ peridotites can have similar Cr#-TiO_2 spinel compositions (e.g. Figure 4.11b). Oxygen fugacity (fO_2) can further discriminate peridotites from MOR and SSZ settings (e.g. Parkinson and Pearce, 1998; Pearce et al., 2000). This is because spinels in both peridotites and lavas from SSZ environments are more oxidised and hence have higher fO_2 (i.e. more iron is oxidised to Fe^{+3}) than spinels from MOR environments (e.g. Ballhaus et al., 1991; Parkinson and Pearce, 1998; Pearce et al., 2000; Parkinson and Arculus, 1999; Elburg and Kamenetsky, 2007).

Oxygen fugacity was measured in spinel using the method described in Section 4.1.2. The oxygen fugacity of spinel is plotted as $\Delta \log fO_2$ (QFM), which refers to the deviation from the QFM buffer expressed in log units. $\Delta \log fO_2$ (QFM) is plotted against Cr#, after Wood and Virgo (1989), and termed the Cr#-fO_2 diagram hereafter. The discrimination fields for MOR and SSZ peridotites on the Cr#-fO_2 diagram (Figure 4.19) are defined by plotting spinels from peridotite samples of known tectonic setting and the fields are numbered as follows to aid tectonic discrimination of the U.A.E. peridotites in Section 4.3.4.3. The Cr#-fO_2 discrimination fields are compiled from the literature and the fields for MOR peridotites were improved by additional samples analysed in this study (Table 2, Appendix E).

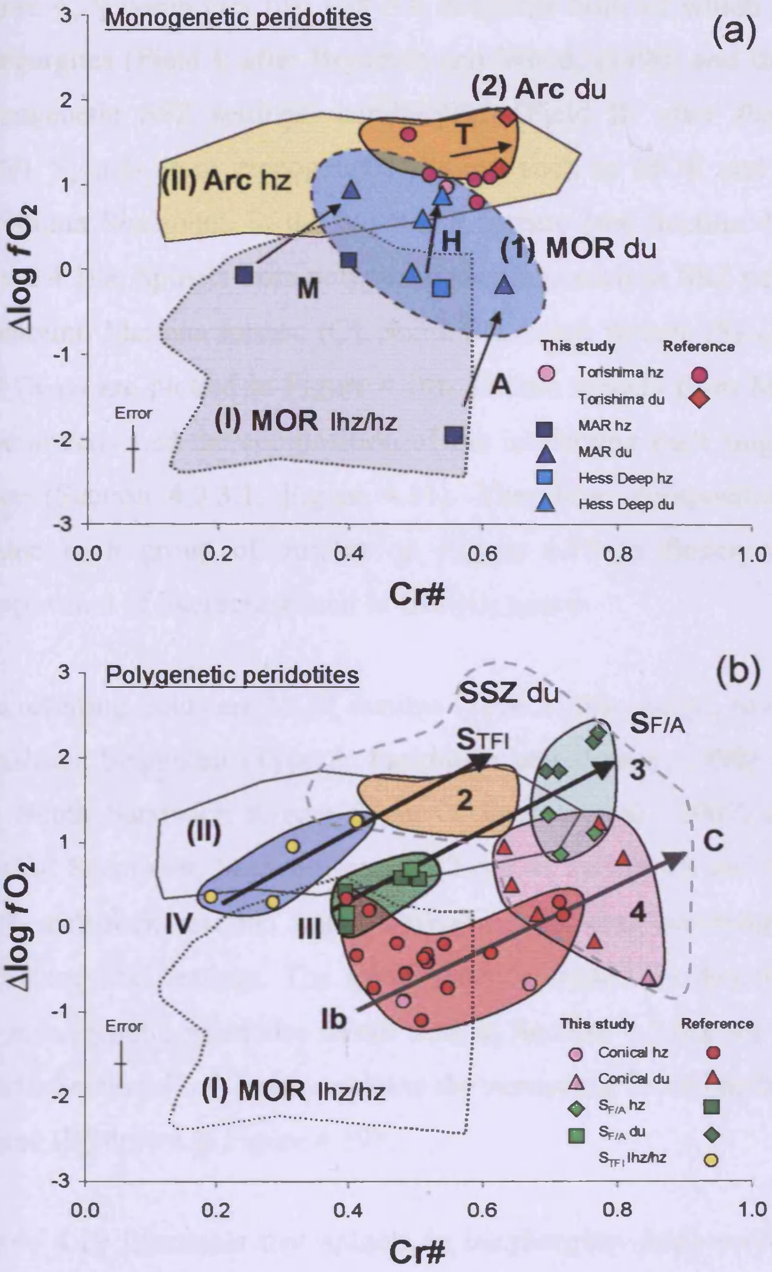

Figure 4.19: Cr#-fO_2 discrimination diagram for (a) monogenetic SSZ (Arc) and MOR peridotites and (b) polygenetic SSZ peridotites from modern-day samples of known tectonic settings. Individual modern-day samples are plotted from this study and from published reference data (see key and text for details) and define tectonic fields: I-MOR hz, II- monogenetic SSZ (arc) hz, 1-MORB du, 2- low Cr# SSZ du, III-transitional SSZ hz, IV-South Sandwich TFI lhz reacted with low Cr# SSZ melt, 3-IAT dunite and 4- BON du and Ib-Conical hz reacted with BON (4). In (b) diagonal reaction trends for peridotites from Conical Seamount (C), South Sandwich forearc ($S_{F/A}$) and South Sandwich TFI (S_{TFI}) illustrate interaction of MOR mantle lithosphere with SSZ melts. The dashed field marked SSZ dunite encompasses all of the SSZ dunites (Fields 2 – 4) and spinels from primitive SSZ lavas (Ballhaus et al., 1991; Kamperman et al., 1996). Error bars representative of 1 s.d. for analysis of fO_2 and Cr#.

Figure 4.19 comprises two Cr#-fO_2 diagrams both of which have fields for MOR harzburgites (Field I: after Bryndzia and Wood, (1990) and this study) and arc (i.e. monogenetic SSZ settings) harzburgites (Field II: after Parkinson and Arculus, 1999). Spinels from monogenetic settings such as MOR and SSZ peridotites from Torishima Seamount, in the Izu-Bonin forearc (see Section 4.3.3.2), are plotted in Figure 4.19a. Spinels from polygenetic settings such as SSZ peridotites from Conical Seamount, Mariana forearc (C), South Sandwich forearc ($S_{F/A}$) and South Sandwich TFI (S_{TFI}) are plotted in Figure 4.19b. Dunite spinels from MOR and SSZ settings have already had the composition of the interacting melt fingerprinted in Cr#-TiO_2 space (Section 4.3.3.1, Figure 4.11). Therefore, compositional fields are drawn around each group of dunites on Figure 4.19 to fingerprint the corresponding composition of interacting melt in Cr#-fO_2 space.

The resulting fields are MOR dunites (Type 1: this study), low Cr# SSZ dunites e.g. Torishima Seamount (Type 2: Parkinson and Pearce, 1998), depleted IAT dunites e.g. South Sandwich forearc (Type 3: Pearce et al., 2000) and BON dunites e.g. Conical Seamount, Mariana forearc (Type 4: Parkinson and Pearce, 1998). Arrows mark melt-rock reaction trends between coexisting harzburgites and dunites from MOR and SSZ settings. The spinel reaction trends are described in Section 4.3.4.1 for monogenetic peridotite trends and in Section 4.3.4.2 for polygenetic peridotite trends. Section 4.3.4.2 also explains the remaining three harzburgite fields (Type Ib, III and IV) drawn in Figure 4.19b.

Figure 4.19 illustrates that spinels in harzburgites from monogenetic SSZ settings (Field II) (i.e. Torishima Seamount) have higher fO_2 ($+0.25 < QFM < +1.75$) than those from MOR settings (Field I: $-2.5 < QFM < +0.5$). This demonstrates that the Cr#-fO_2 diagram is particularly useful at discriminating between harzburgite spinels with similar Cr# composition from different tectonic settings. Field I represents residue from anhydrous melting at a mid-ocean ridge and Field II represents residue from hydrous melting in the mantle wedge. Similarly, low Cr# spinels (i.e. 0.4 – 0.6) in dunites from SSZ settings have higher fO_2 (Field 2: $+1 < QFM < +2$) than those from MOR settings (Field 1: $-0.2 < QFM < +1$). Again, this demonstrates that the

Cr#-fO_2 diagram is particularly useful at discriminating between dunite spinels with similar Cr# composition from different tectonic settings.

4.3.4.1 Monogenetic peridotite trends

Peridotites from the Torishima Forearc Seamount, in the Izu-Bonin forearc, formed entirely within oxidised conditions of a single supra-subduction zone setting (Parkinson and Pearce, 1998). Spinels in these harzburgites and dunites plot within Field II and Field 2 respectively in Figure 4.19a. Spinel reaction trends between coexisting harzburgites and dunites involves a small increase in Cr# and a negligible increase in fO_2 during interaction between peridotite and a low Cr# SSZ melt. This is because the mantle residue and interacting melt are co-genetic and, under hydrous conditions, there is probably little difference between fO_2 in the residue and the infiltrating primitive melt. However, Fe^{3+} and fO_2 can increase during magmatic differentiation and the spinels in arc lavas can vary from QFM+2 to QFM+4 (Ballhaus et al., 1991; Elburg and Kamenetsky, 2007).

In contrast, Figure 4.19a shows that spinels in dunites from MOR settings (Field 1) commonly have higher fO_2 than those in harzburgite residues (Field I). This is illustrated by reaction trends for harzburgite-dunite pairs from a variety of MOR locations (Figure 4.19a). Peridotites from near the Azores hotspot on the Mid Atlantic ridge (A), MAR Site 670 (M, away from Azores) and Hess Deep (H) illustrate that melt-rock reactions commonly result in a larger increase in fO_2 than in Cr#. This is probably because mantle residue and interacting magma are monogenetic and, under anhydrous conditions, Fe^{3+} is depleted in the residue but relatively enriched in the melt. Spinels in MORB lavas typically do not exceed QFM+1 (Ballhaus et al., 1991; Elburg and Kamenetsky, 2007).

4.3.4.2 Polygenetic peridotite trends

Spinel reaction trends for harzburgite-dunite pairs from polygenetic SSZ settings (e.g. Conical Seamount, in the Mariana forearc (C), South Sandwich forearc ($S_{F/A}$) and South Sandwich TFI (S_{TFI})) are plotted in Figure 4.19b. They form three parallel diagonal trends from harzburgites that plot in the upper end of the MOR field (low fO_2 and moderate Cr#) to dunites that plot in the SSZ dunite field, having higher fO_2 and high Cr#. These diagonal trends for SSZ peridotites on the Cr#-fO_2 diagram provide evidence for interaction between pre-existing MOR lithosphere (Field I) and SSZ melts (Fields 2 - 4) (e.g. Parkinson and Pearce, 1998; Pearce et al., 2000).

The trends are displaced from one another in Figure 4.19b because the reaction trends depend on the end-members of the mantle lithosphere and the interacting magma composition. They may reflect the difference between the nature of subduction initiation in the two forearcs and illustrates the wide variety of end-member types of mantle lithosphere and interacting melt in supra-subduction zone peridotites (Pearce et al., 2000).

For example, the reaction trend for $S_{F/A}$ peridotites is parallel to the peridotite trend C but displaced to lower Cr# and/or higher fO_2 (Figure 4.19). The mantle lithosphere end-member of the peridotite trend C has a lower fO_2 typical of normal oceanic lithosphere (i.e. Field I), whereas the end-member of the peridotite trend $S_{F/A}$ has a higher fO_2 (i.e. Field III). Field III probably derives from the slight SSZ character of the East Scotia Sea spreading ridge, i.e. a back-arc setting with augmented water content (Pearce et al., 2000). Transitional harzburgites (Field III), such as those from peridotite trend $S_{F/A}$ (which have impregnation textures and euhedral spinels as a result of melt-rock reaction), lie outside the MOR field towards dunite compositions. They thus represent intermediate products of interaction with SSZ melts (Pearce et al., 2000). Similarly, harzburgites from the peridotite trend C lie outside the MOR field (Field 1b) towards dunite compositions because of partial reaction with BON melt.

The displacement to higher Cr# for the peridotite trend C may also reflect the different SSZ magma end-members: boninite in peridotite trend C (i.e. Field 4) and a depleted island arc tholeiite in the peridotite trend $S_{F/A}$ (i.e. Field 3). Moreover, spinels from boninites commonly have lower fO_2 (0 < QFM < +2) than spinels from depleted island arc tholeiites (+2 < QFM < +4) (Elburg and Kamenetsky, 2007).

The reaction trend for S_{TFI} peridotites is parallel to the $S_{F/A}$ peridotite trend but displaced to lower Cr# and/or higher fO_2 (Figure 4.19b). The mantle lithosphere end-member of the S_{TFI} peridotite trend has a lower Cr# because it was less depleted (Field IV) and interacted with low Cr# SSZ magma (i.e. Field 2), such as back arc basin basalt from the Scotia Sea (Pearce et al., 2000).

4.3.4.3 U.A.E. peridotites and chromitites

The U.A.E. peridotites are plotted on a series of Cr#-fO_2 diagrams (Figures 4.20-4.27) in order to further discriminate the tectonic setting of the U.A.E. peridotites already established using Cr#-TiO_2. In Section 4.3.3.3 the Cr#-TiO_2 diagram could not distinguish between reaction with MORB or MORB/IAT melt for the origin of low Cr# (0.4 – 0.6) spinels in dunites and chromitites. However, there are two pieces of evidence to indicate that these low Cr# spinels may be of SSZ origin rather than of MOR origin: 1) Spinels from the Geotimes Unit have Cr# 0.6 – 0.65 (Umino et al., 1991) and are from lavas of MORB/IAT and not MORB chemistry and 2) many chromitites have Cr# 0.4 – 0.6 and provides some evidence that the melts that formed them may have been more water-rich, i.e. MORB/IAT, than 'true' MORB because water/hydrous melts are required for the formation of chromitite deposits (e.g. Edwards et al., 2000). This hypothesis is tested on the U.A.E. dunites and chromitites using the Cr#-fO_2 diagram in Figure 4.20.

The Cr#-fO_2 diagram in Figure 4.20 is reproduced from Figure 4.19 and includes the tectonic reference fields for MOR harzburgite (Field I), MOR dunite (Field 1) and SSZ dunites (Fields 2 – 4). Spinels from the U.A.E. mantle and MTZ dunites from the main ophiolite and the Dibba Zone are plotted in Figure 4.20a and spinels from the U.A.E. chromitites are plotted in Figure 4.20b.

Figure 4.20a demonstrates that the vast majority of dunites, both from the mantle and MTZ, are SSZ dunites and plot in all of the three fields of SSZ dunites (i.e. Field 2: low Cr# SSZ, Field 3: depleted IAT and Field 4: BON). Thus, the Cr#-fO_2 diagram in Figure 4.20a establishes that the majority of low Cr# dunites (0.4 – 0.6) from the main ophiolite are of SSZ origin ($+1 < \text{QFM} < +2.5$) because their spinels plot in Field 2 and are thus classified as having reacted with MORB/IAT and not MORB melts (Field 1: $-1 < \text{QFM} < +1$). This confirms the hypothesis above that the low Cr# U.A.E. dunites resulted from melt-rock reaction with MORB/IAT melt corresponding to the Geotimes Unit. A few dunites from the main ophiolite plot ambiguously on the narrow overlap between the fields for SSZ dunite and MOR dunite field and are further discriminated in Chapter 5. Only one dunite from the Dibba Zone (+0.3 QFM) plots clearly within the MOR dunite field (Field 1).

Figure 4.20b illustrates that the chromitite spinels from the mantle and MTZ of the main ophiolite plot within the dunite Fields 2 – 4 and thus formed from SSZ melts of similar composition to the SSZ melts that formed the U.A.E. dunites. The low Cr# chromitites (0.4 – 0.6) are of SSZ origin ($+1 < \text{QFM} < +1.5$) and supports the hypothesis that they formed from a melt more water-rich than 'true' MORB (i.e. MORB/IAT chemistry of the Geotimes Unit).

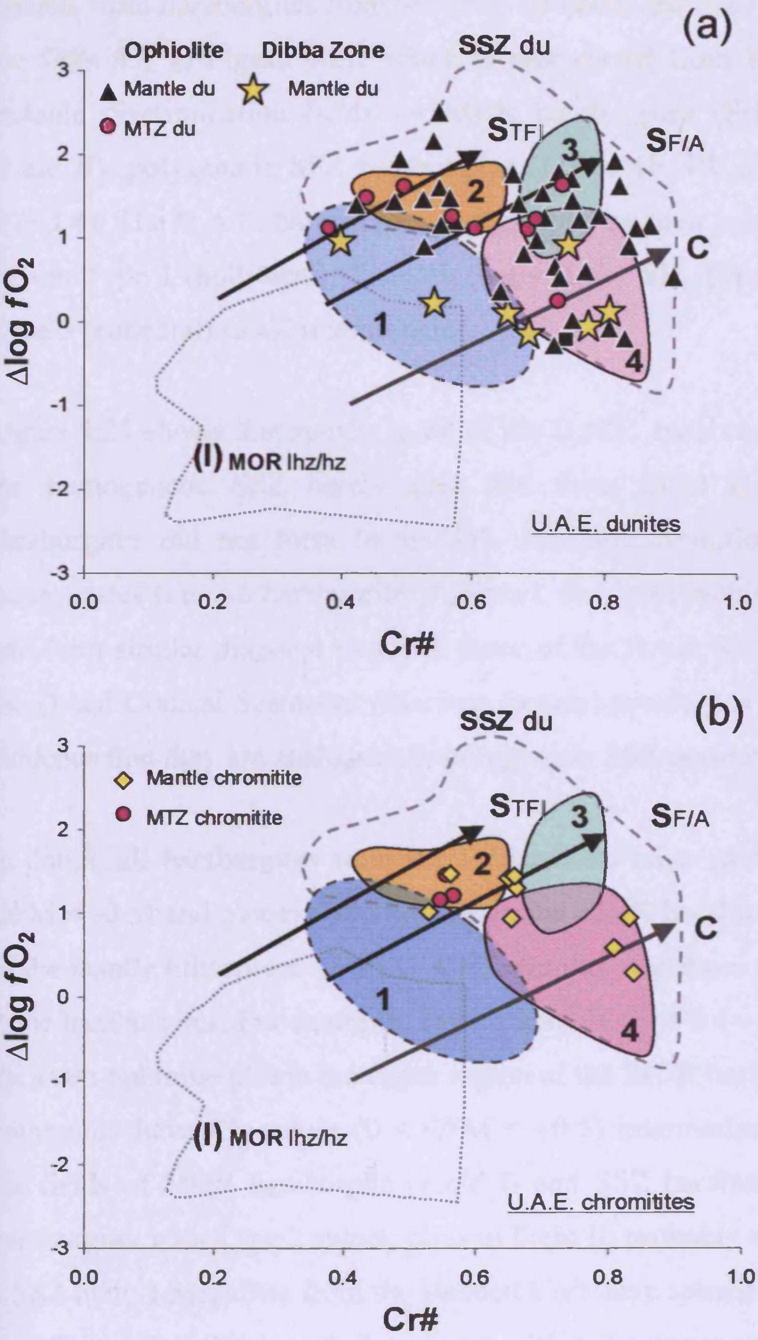

Figure 4.20: Cr#-fO_2 discrimination diagram for (a) U.A.E. dunites from the main ophiolite and the Dibba Zone and (b) U.A.E. chromitites from the main ophiolite. Individual samples are plotted (see key). Error bars representative of 1 s.d. The tectonic fields and diagonal reaction trends are taken from Figure 4.19: 1-MORB du, 2- low Cr# SSZ du, 3-IAT dunite and 4- BON du. All of the ophiolite dunites and chromitites plot within the SSZ dunite field (i.e. Fields 2 – 4). Only some dunites from the Dibba Zone plot in the MORB field.

Spinels from harzburgites from the main ophiolite and the Dibba zone are plotted on the Cr#- fO_2 in Figure 4.21, which is reproduced from Figure 4.19 and includes tectonic discrimination fields for MOR harzburgites (Field I), SSZ harzburgites (Field II), polygenetic SSZ harzburgites (Fields 1b, III and IV) and BON dunites (Field 4). The U.A.E. harzburgites are grouped by their spinel morphology (Chapter 3) into Type 1 (holly-leaf), Type 1b (holly leaf + SI), Type 2 (subidiomorphic) and Type 3 (euhedral) to aid interpretation.

Figure 4.21 shows that spinels in all of the U.A.E. harzburgites have lower fO_2 than the monogenetic SSZ harzburgites that form Field II. Therefore, the U.A.E. harzburgites did not form in as high oxidising conditions as monogenetic SSZ harzburgites (i.e. arc harzburgites). Instead, they plot within the MOR field (Field I) and form similar diagonal trends to those of the South Sandwich forearc peridotites ($S_{F/A}$) and Conical Seamount (Mariana forearc) peridotites (C). This provides some evidence that they are analogous to polygenetic SSZ peridotites.

In detail, all harzburgites from the Dibba Zone have spinels with low fO_2 ($-1.8 < \text{QFM} < -0.5$) and plot exclusively within the MOR harzburgite field (Field I). Much of the mantle lithosphere of the U.A.E. ophiolite was more oxidised than these Dibba Zone harzburgites. For example, Type 1 spinels (Cr# 0.4 – 0.7) in harzburgites from the main ophiolite plot in the upper region of the MOR harzburgite field (Field I) and commonly have fO_2 values ($0 < \text{QFM} < +0.5$) intermediate (i.e. Field III) between the fields of MOR harzburgite (Field I) and SSZ harzburgite (Field II). Only one harzburgite, with Type 2 spinel, plots in Field II, probably as a result of reaction with a SSZ melt. Lherzolites from the Banded Unit have spinels with low Cr# (< 0.3) and low fO_2 ($-0.5 < \text{QFM} < +0.5$) and plot within the upper region of MOR field (Field I).

Only harzburgites (i.e. clinopyroxene-poor harzburgites) from the U.A.E. ophiolite have Type 2 and 3 spinels, commonly with Cr# > 0.7, and they plot within Field 1b and Field 4 (characteristic of Conical Seamount harzburgites and dunites). This provides some evidence that they formed by extensive reaction with boninitic magma to form euhedral spinels with compositions identical to those in BON-type dunites (i.e. Field 4).

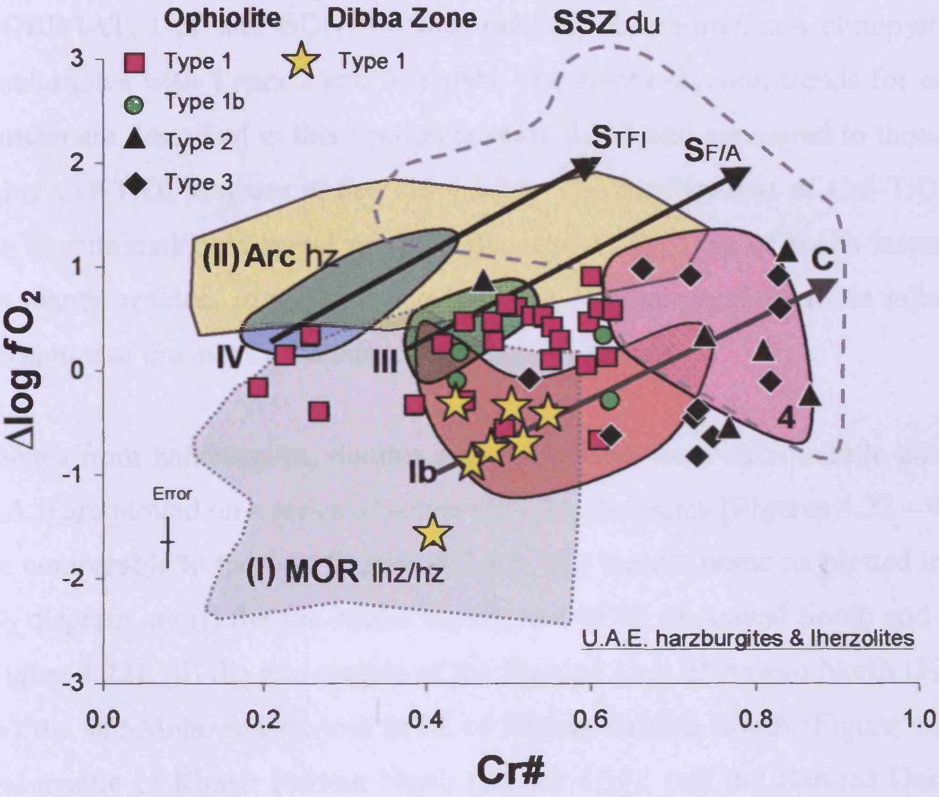

Figure 4.21: Cr#-fO_2 discrimination diagram for the U.A.E. harzburgites and lherzolites from the main ophiolite and from the Dibba Zone. Individual samples are plotted as spinel types (see key). Error bars representative of 1 s.d. The tectonic fields and diagonal reaction trends are taken from Figure 4.19: I-MOR hz, Ib-Conical hz reacted with BON, II- monogenetic SSZ hz, III-transitional SSZ hz, IV-South Sandwich TFI lhz reacted with low Cr# SSZ melt and 4-Conical BON du. The ophiolite harzburgites plot in the upper region of the MOR field and form a diagonal trend towards the BON dunite field similar to Conical Seamount peridotite trend (C). Harzburgites with Type 3 spinels plot within the BON dunite field as a result of melt-rock interaction. Dibba Zone harzburgites plot only in the MOR field.

4.3.4.4 U.A.E. peridotite trends

Section 4.3.4.3 demonstrated that the Cr#- fO_2 diagrams in Figures 4.20 and 4.21 provide strong evidence that the U.A.E peridotites began as MOR-type mantle lithosphere (i.e. harzburgites) and interacted with a variety of SSZ melts (i.e. MORB/IAT, IAT and BON) to form dunites, chromitites and clinopyroxene-poor harzburgites with Types 2 and 3 spinels. The spinel reaction trends for each mantle domain are described in this Section in more detail and compared to those identified using Cr#-TiO_2 diagram in Section 4.3.3.3. The combination of Cr#-TiO_2 and Cr#-fO_2 discrimination of spinel robustly fingerprints the type of melts interacting with the mantle residue. In addition, the Cr#- fO_2 diagram provides more information on the nature of the mantle residue in each mantle domain.

Spinels from harzburgites, dunites and chromitites from each mantle domain in the U.A.E are plotted on a series of seven Cr#- fO_2 diagrams (Figures 4.22 – 4.27) which are comparable to those in Section 4.3.3.3. The mantle domains plotted in each Cr#-fO_2 diagram are (i) the sub-Moho mantle and MTZ of Aswad South and Fizh North (Figure 4.22), (ii) the mid-mantle of the Banded Unit of Aswad North (Figure 4.23), (iv) the sub-Moho mantle and MTZ of Khawr Fakkan South (Figure 4.24), (v) the mid-mantle of Khawr Fakkan North (Figure 4.25), (vi) the Banded Unit of Khawr Fakkan North (Figure 4.26) and (vii) the peridotites from the Dibba Zone (Figure 4.27).

Figures 4.22 – 4.27 each comprise two Cr#-fO_2 diagrams: the first illustrates the spinel reaction trends in detail and the second is simplified to summarise the main trends. The detailed diagram is reproduced from Figure 4.19b in which individual samples from this study are plotted and co-existing harzburgite and dunite pairs marked to demonstrate the general reaction trends. Additional spinel data from harzburgites in the U.A.E. (Nasir, 1997; Monnier et al., 2006) were calculated for oxygen fugacity and plotted on the relevant diagrams for comparison.

(i) sub-Moho mantle and MTZ of Aswad South and Fizh

Spinels from peridotites and chromitites from Aswad South and Fizh are plotted on the Cr#-fO_2 diagram in Figure 4.22a and their simplified compositional fields are illustrated in Figure 4.22b. Section 4.3.3.3 identified two main reaction trends, using the Cr#-TiO_2 diagram, in the sub-Moho mantle of Aswad South and Fizh: they are 1) reaction with MORB or MORB/IAT melt and 2) reaction with IAT melt (Figure 4.12b). The Cr#-fO_2 diagram in Figure 4.22 demonstrates that the reacting melt was MORB/IAT rather than MORB because the dunites have high fO_2 (> +1 QFM) and plot in Field 2. Figure 4.22 also confirms that the second reaction involved depleted IAT melts, similar to the reaction trend for peridotites from South Sandwich forearc. Dunites from the MTZ also plot within the MORB/IAT and IAT dunite fields (not shown).

Spinels in harzburgites from Aswad South have relatively high fO_2 ($-0.5 < QFM < +1$) for the ophiolite (Figure 4.21) and plot from the upper region of the MOR field (Field I) to just below the SSZ dunite field (Field 2). These values are equivalent to Field III harzburgites from the South Sandwich forearc which represent transitional lithosphere formed from hydrous melting at a transitional MORB/IAT spreading centre. This implies that the Aswad South harzburgites could be transitional lithosphere and thus monogenetic with the MORB/IAT melt that formed the dunites in Field 2. However, spinels in harzburgites from Aswad North (Figure 4.23) have lower fO_2 ($-1.5 < QFM < +0.3$) than those from Aswad South and plot within Field I. This indicates that at depth the mantle of Aswad was more reduced and more typical of 'dry' MOR lithosphere (see below). Therefore, the most likely origin for the more oxidised harzburgites of Aswad South is that the MORB/IAT melt partially interacted with MOR lithosphere. In contrast, the harzburgites in Aswad North remained reduced because there was negligible interaction between peridotite and MORB/IAT melt as evidenced by the lack of MORB/IAT-type dunites in this region (see below).

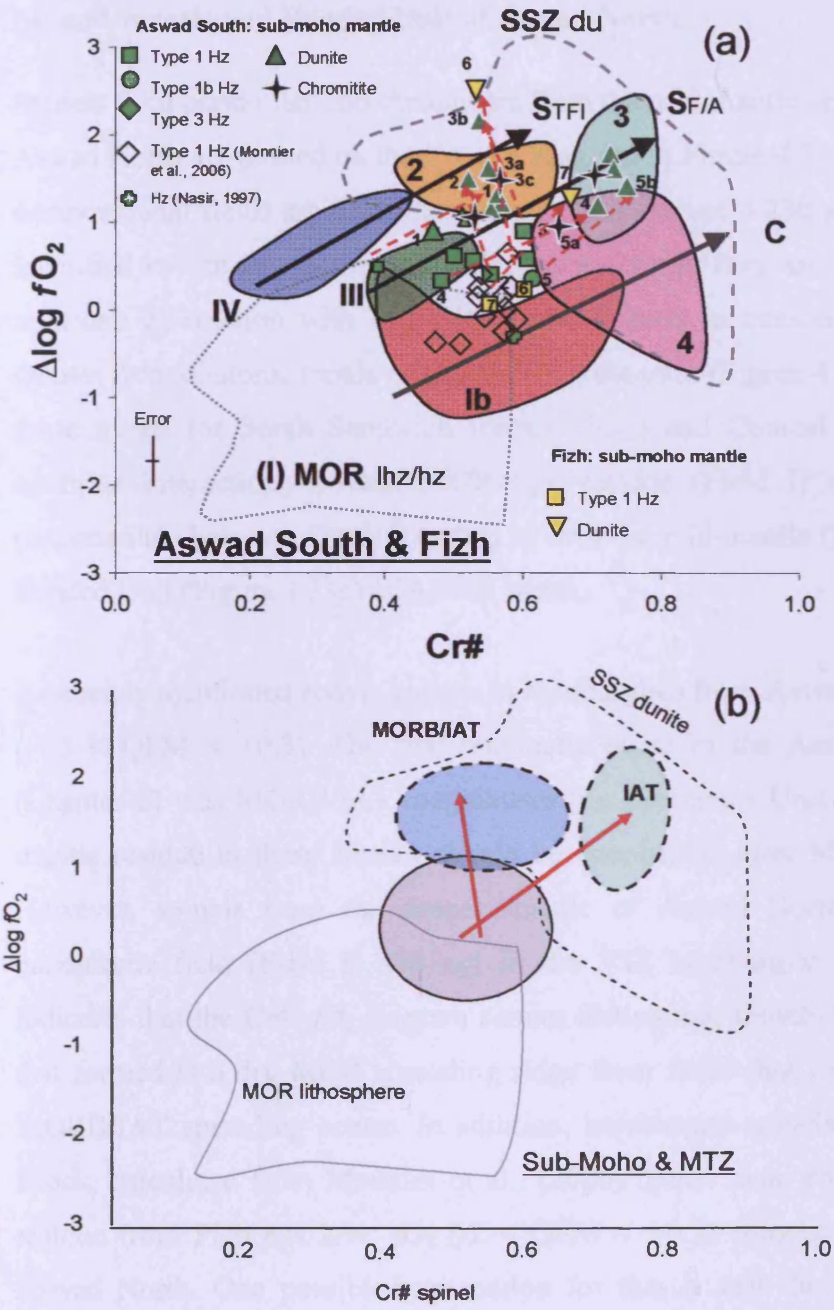

Figure 4.22: Cr#-fO_2 discrimination diagram for peridotites from the sub-Moho mantle of Aswad South and Fizh to illustrate spinel reaction trends in (a) detail and (b) summarised format. In (a) individual samples are plotted (see key) and harzburgite-dunite pairs numbered to illustrate the general trends for reaction (red arrows). Error bars representative of 1 s.d. The tectonic fields and diagonal reaction trends are taken from Figure 4.19: I-MOR hz, Ib-Conical hz reacted with BON, III-transitional SSZ hz, 2-low Cr# SSZ du, 3- South Sandwich forearc IAT du and 4-Conical BON du. In (b) the grey elliptical field approximates the U.A.E. harzburgites and the main reaction trends (red arrows) between peridotite and MORB/IAT melt (blue ellipse) and between peridotite and IAT melt (green ellipse) are shown.

(ii) mid-mantle and Banded Unit of Aswad North

Spinels from peridotites and chromitites from the mid-mantle and the Banded Unit of Aswad North are plotted on the Cr#-fO_2 diagram in Figure 4.23a and their simplified compositional fields are illustrated separately in Figure 4.23b and c. Section 4.3.3.3 identified two main reaction trends in Aswad North: they are 1) reaction with IAT melt and 2) reaction with IAT/BON melt. Spinels in coexisting harzburgites and dunites form diagonal trends on the Cr#- fO_2 diagram (Figure 4.23a) that lie between those trends for South Sandwich forearc ($S_{F/A}$) and Conical Seamount (C). This confirms interaction between MOR-type residue (Field I) and IAT/BON melts (intermediate between Fields 3 and 4) in both the mid-mantle (Figure 4.23b) and the Banded Unit (Figure 4.23c) of Aswad North.

As already mentioned above, spinels in harzburgites from Aswad North have low fO_2 ($-1.5 < QFM < +0.3$). The first magmatic event in the Aswad and Fizh Blocks (Chapter 6) was MORB/IAT magmatism (i.e. Geotimes Unit) and implies that the mantle residue in these Blocks should be transitional after MORB/IAT extraction. However, spinels from the deeper mantle of Aswad North plots in the MOR harzburgite field (Field I) and not in the SSZ harzburgite field (Field II). This indicates that the Cr#- fO_2 diagram cannot distinguish spinels in harzburgite residue that formed at a dry MOR spreading ridge from those that formed at a transitional MORB/IAT spreading centre. In addition, harzburgite spinels from the entire Fizh Block, calculated from Monnier et al., (2006) spinel data, confirm that the mantle residue from Fizh has low fO_2 ($-2 < QFM < +0.3$) spinels similar to those from Aswad North. One possible explanation for this is that the SSZ influence of the transitional MORB/IAT spreading ridge had a negligible affect on the fO_2 of spinel in the mantle residue. Instead, the fO_2 values of spinel in mantle peridotites were increased through melt-rock reaction with oxidising MORB/IAT melts.

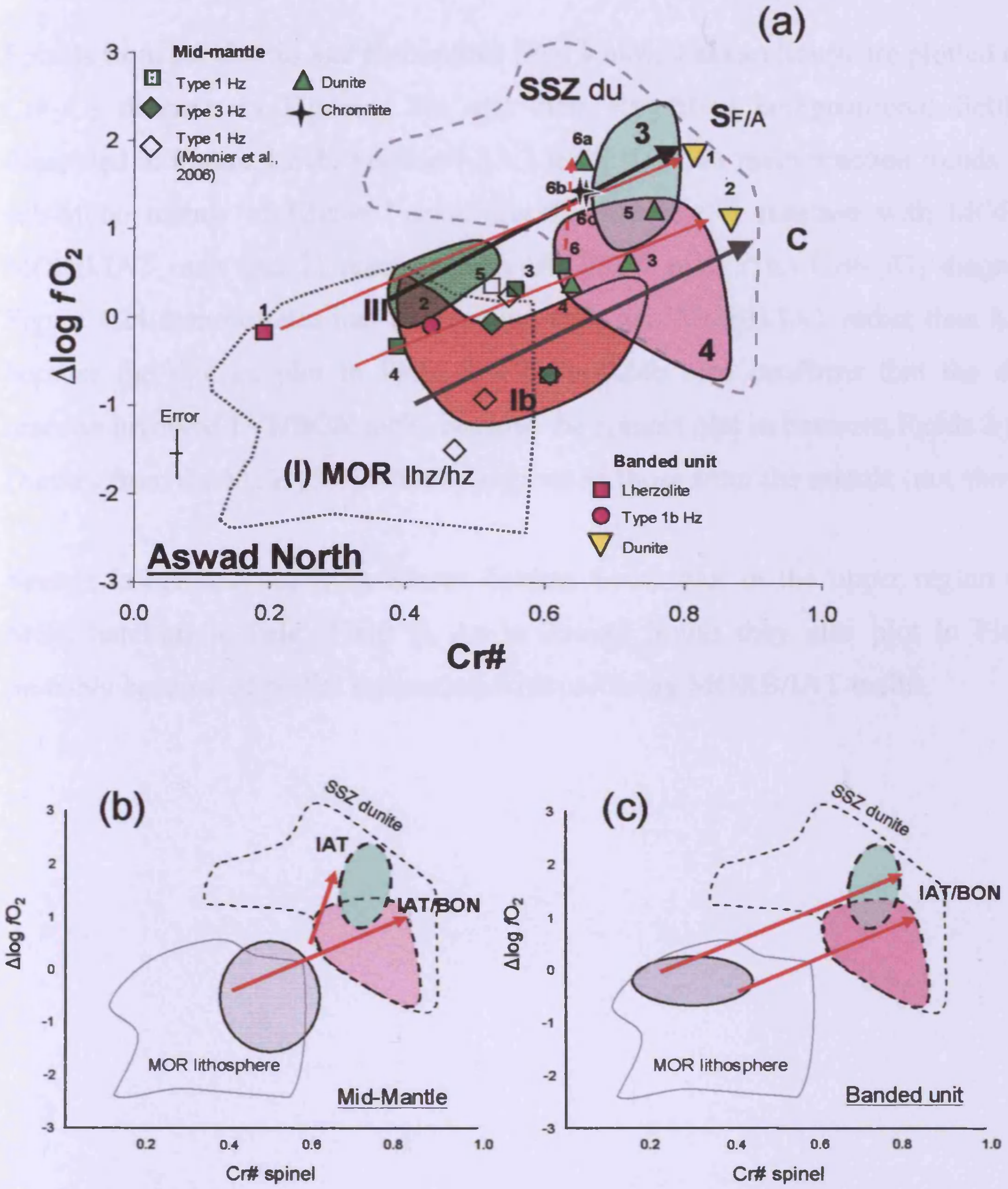

Figure 4.23: Cr#-fO_2 discrimination diagram for peridotites from the Banded Unit and mid-mantle of Aswad North to illustrate spinel reaction trends in (a) detail and (b and c) summarised format. In (a) individual samples are plotted (see key) and harzburgite-dunite pairs numbered to illustrate the general trends for reaction (red arrows). Error bars representative of 1 s.d. The tectonic fields and diagonal reaction trends are taken from Figure 4.19: I-MOR hz, Ib-Conical hz reacted with BON, III-transitional SSZ hz, 3- South Sandwich forearc IAT du and 4-Conical BON du. In (b and c) the grey elliptical field approximates the U.A.E. harzburgites and the main reaction trends (red arrows) between peridotite and and IAT melt (green ellipse) in the mid-mantle in (b) and between peridotite and IAT/BON melt (intermediate of IAT-green ellipse and BON) both in the mid-mantle (b) and in the Banded Unit (c).

(iv) sub-Moho mantle and MTZ of Khawr Fakkan South

Spinels from peridotites and chromitites from Khawr Fakkan South are plotted on the Cr#-fO_2 diagram in Figure 4.24a and their simplified compositional fields are illustrated in Figure 4.24b. Section 4.3.3.3 identified two main reaction trends in the sub-Moho mantle of Khawr Fakkan South: they are 1) reaction with MORB or MORB/IAT melt and 2) reaction with IAT/BON melt. The Cr#- fO_2 diagram in Figure 4.24 demonstrates that the reacting melt was MORB/IAT rather than MORB because the dunites plot in Field 2. Figure 4.24b also confirms that the second reaction involved IAT/BON melts because the spinels plot in between Fields 3 and 4. Dunites from the MTZ plot in similar regions as those from the mantle (not shown).

Spinels in harzburgites from Khawr Fakkan South plot in the upper region of the MOR harzburgite field (Field I). As in Aswad South they also plot in Field III probably because of partial interaction with oxidising MORB/IAT melts.

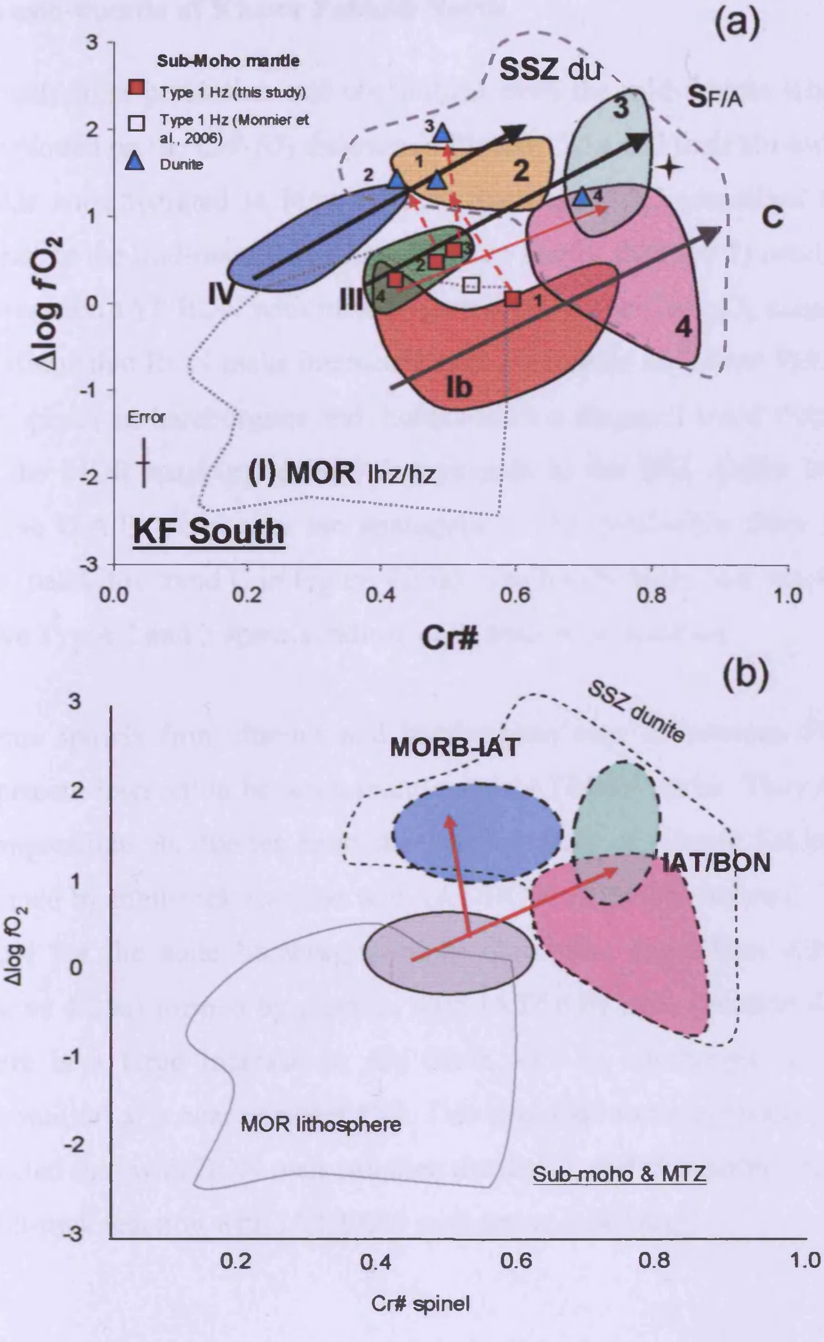

Figure 4.24: Cr#-fO_2 discrimination diagram for peridotites from the sub-Moho mantle of Khawr Fakkan South to illustrate spinel reaction trends in (a) detail and (b) summarised format. In (a) individual samples are plotted (see key) and harzburgite-dunite pairs numbered to illustrate the general trends for reaction (red arrows). Error bars representative of 1 s.d. The tectonic fields and diagonal reaction trends are taken from Figure 4.19: I-MOR hz, Ib-Conical hz reacted with BON, III-transitional SSZ hz, 2-low Cr# SSZ du, 3- South Sandwich forearc IAT du and 4-Conical BON du. In (b) the grey elliptical field approximates the U.A.E. harzburgites and the main reaction trends (red arrows) between peridotite and and MORB/IAT melt (blue ellipse) and between peridotite IAT/BON melt (intermediate of IAT-green ellipse and BON) are shown.

(v) mid-mantle of Khawr Fakkan North

Spinels from peridotites and chromitites from the mid-mantle Khawr Fakkan North are plotted on the Cr#-fO_2 diagram in Figure 4.25a and their simplified compositional fields are illustrated in Figure 4.25b. Section 4.3.3.3 identified two main reaction trends in the mid-mantle of Khawr Fakkan North: they are 1) reaction BON melt and 2) reaction IAT/BON with melt (Figure 4.16b). The Cr#- fO_2 diagram in Figure 4.25 confirms that BON melts interacted with the mantle in Khawr Fakkan North because the spinels in harzburgites and dunites form a diagonal trend from the upper region of the MOR harzburgite field that extends to the SSZ dunite Field 4 (i.e. BON). These U.A.E. peridotites are analogous to the peridotites from Conical Seamount (i.e. peridotite trend C in Figure 4.25a). The harzburgites that reacted with BON melt have Types 2 and 3 spinels indicative of melt-rock reaction.

Some spinels from dunites and harzburgites plot in between Fields 3 and 4 and represent interaction between mantle and IAT/BON melts. They have similar spinel compositions as dunites from the Banded Unit of Khawr Fakkan North that also formed by melt-rock reaction with IAT/BON melts (see below). The spinel reaction trend for the suite harzburgite-dunite-chromitite from East Zikt (numbered 6 in Figure 4.25a) formed by reaction with IAT/BON melt (Section 4.3.3.3). As a result there is a large increase in fO_2 (from -0.5 in harzburgite to +1 in dunite and chromitite) at a near constant Cr#. This provides some evidence that the harzburgite reacted first with BON melt and then the dunite and chromitite formed by subsequent melt-rock reaction with IAT/BON melt (more oxidising).

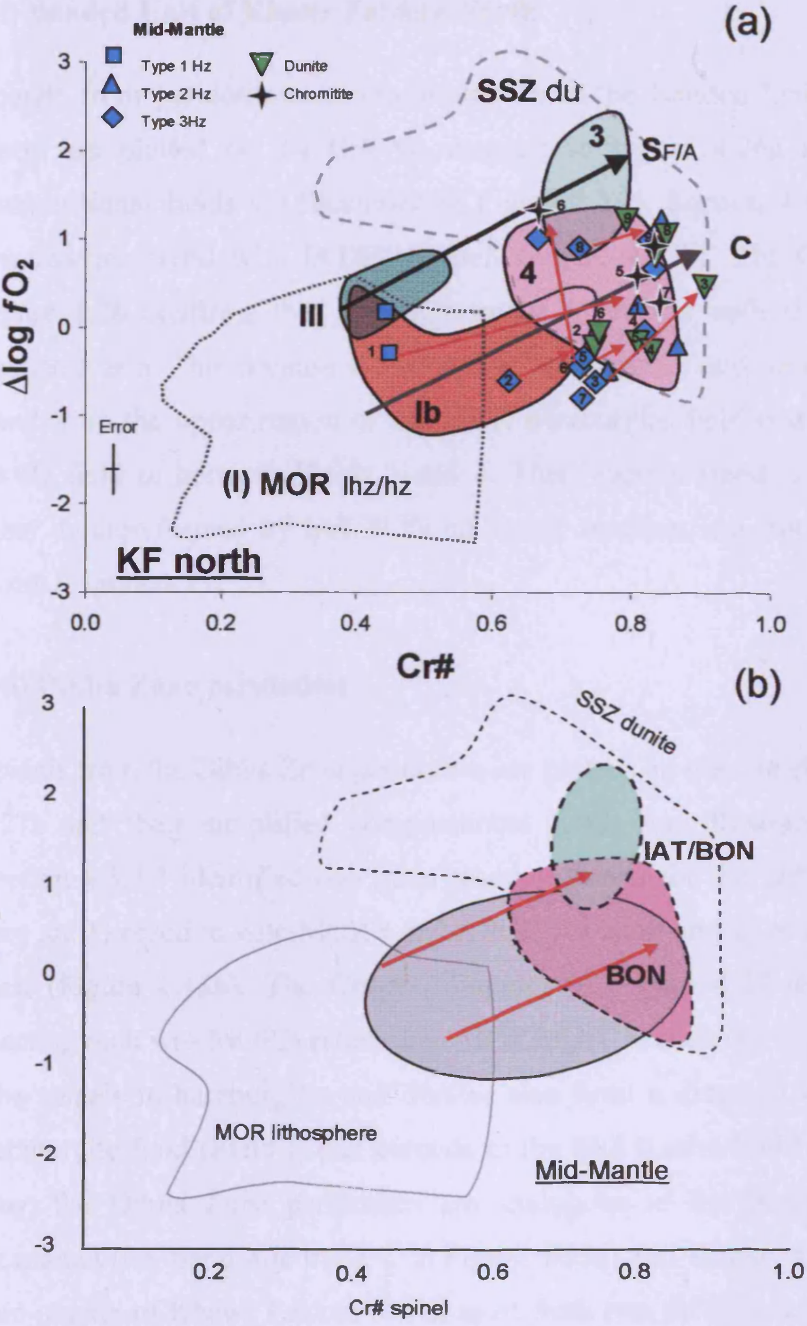

Figure 4.25: Cr#-fO_2 discrimination diagram for peridotites from the mid-mantle of Khawr Fakkan North to illustrate spinel reaction trends in (a) detail and (b) summarised format. In (a) individual samples are plotted (see key) and harzburgite-dunite pairs numbered to illustrate the general trends for reaction (red arrows). Error bars representative of 1 s.d. The tectonic fields and diagonal reaction trends are taken from Figure 4.19: I-MOR hz, Ib-Conical hz reacted with BON, III-transitional SSZ hz, 3-South Sandwich forearc IAT du and 4-Conical BON du. In (b) the grey elliptical field approximates the U.A.E. harzburgites and the main reaction trends (red arrows) between peridotite and and BON melt (pink ellipse) and between peridotite and IAT/BON (intermediate of IAT-green ellipse- and BON)

(vi) Banded Unit of Khawr Fakkan North

Spinels from peridotites and chromitites from the Banded Unit of Khawr Fakkan North are plotted on the Cr#-fO_2 diagram in Figure 4.26a and their simplified compositional fields are illustrated in Figure 4.26b. Section 4.3.3.3 identified only one reaction trend with IAT/BON melt (Figure 4.17b). The Cr#- fO_2 diagram in Figure 4.26 confirms that IAT/BON melts interacted with the mantle in Khawr Fakkan North. This because the spinels in harzburgites and dunites form a diagonal trend from the upper region of the MOR harzburgite field that extends to the SSZ dunite field in between Fields 3 and 4. This reaction trend is characteristic of all other dunites formed by IAT/BON melt-rock reaction, e.g. Banded Unit in Aswad North (Figure 4.23).

(vii) Dibba Zone peridotites

Spinels from the Dibba Zone peridotites are plotted on the Cr#-fO_2 diagram in Figure 4.27a and their simplified compositional fields are illustrated in Figure 4.27b. Section 4.3.3.3 identified two main reaction trends for the Dibba Zone peridotites: they are 1) reaction with MORB or MORB/IAT melt and 2) reaction with IAT/BON melt (Figure 4.15b). The Cr#-fO_2 diagram in Figure 4.27 demonstrates that the reacting melt was MORB rather than MORB/IAT because the dunites plot in Field 1. The spinels in harzburgites and dunites also form a diagonal trend from the MOR harzburgite field (Field I) that extends to the SSZ dunite Field 4 (i.e. BON). In this way, the Dibba Zone peridotites are analogous to the peridotites from Conical Seamount (i.e. peridotite trend C in Figure 4.25a) and similar to peridotites from the mid-mantle of Khawr Fakkan North apart from two differences. The first is that the harzburgites in the Dibba Zone have not reacted with the SSZ melt, unlike the harzburgites in Khawr Fakkan and Conical Seamount that demonstrate extensive reaction with BON melt. The second is that despite that the Dibba Zone dunites and the Khawr Fakkan North dunites both plot in Field 4 (i.e. BON) the melt that formed the Dibba Zone dunites was identified as IAT/BON and not BON using Cr#-TiO_2 discrimination (Section 4.333). This illustrates that it is best to use both Cr#-TiO_2 and Cr#-fO_2 diagrams to fingerprint melts that reacted with mantle peridotites.

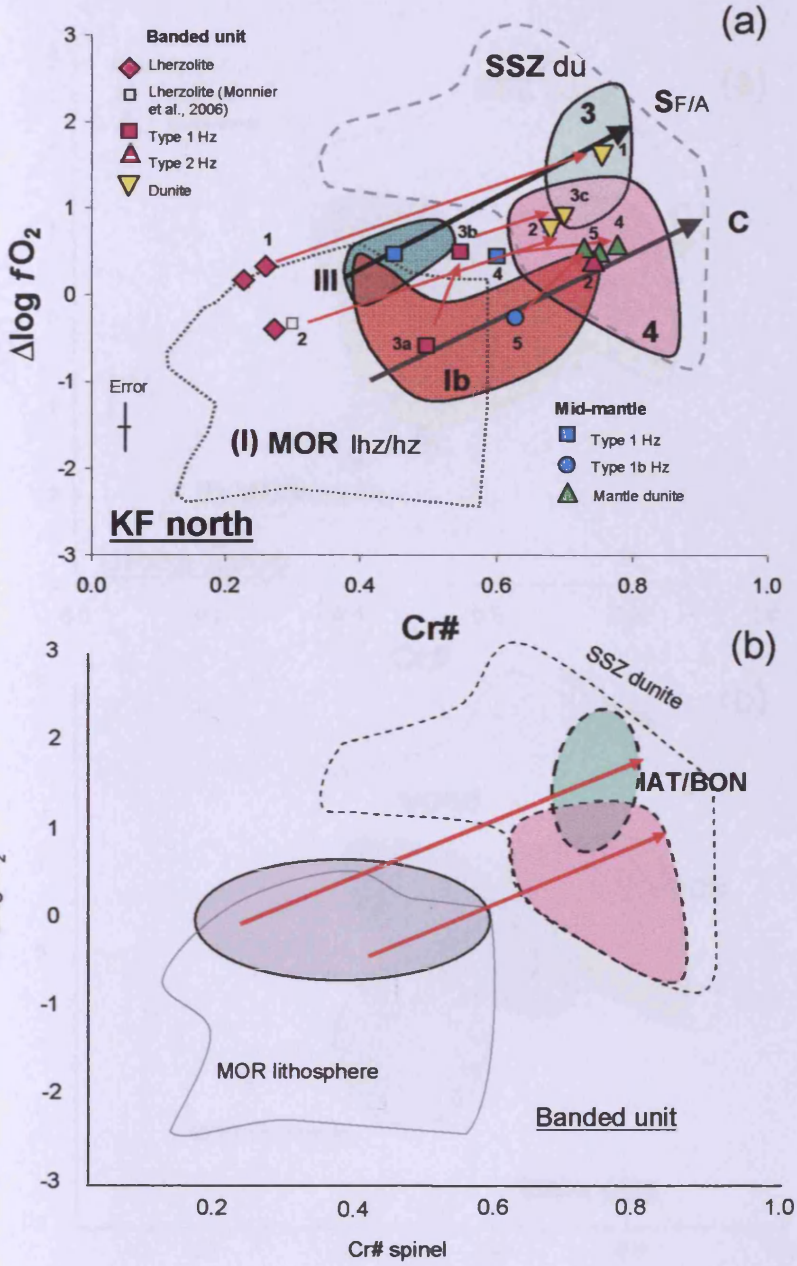

Figure 4.26: Cr#-fO_2 discrimination diagram for peridotites from the Banded Unit and adjacent mid-mantle of Khawr Fakkan North to illustrate spinel reaction trends in (a) detail and (b) summarised format. In (a) individual samples are plotted (see key) and harzburgite-dunite pairs numbered to illustrate the general trends for reaction (red arrows). Error bars representative of 1 s.d. The tectonic fields and diagonal reaction trends are taken from Figure 4.19: I-MOR hz, Ib-Conical hz reacted with BON, II-transitional SSZ hz, 3- South Sandwich forearc IAT du and 4-Conical BON du. In (b) the grey elliptical field approximates the U.A.E. harzburgites and the main reaction trends (red arrows) between peridotite and IAT/BON melt (intermediate of IAT-green ellipse- and BON -pink ellipse) are shown.

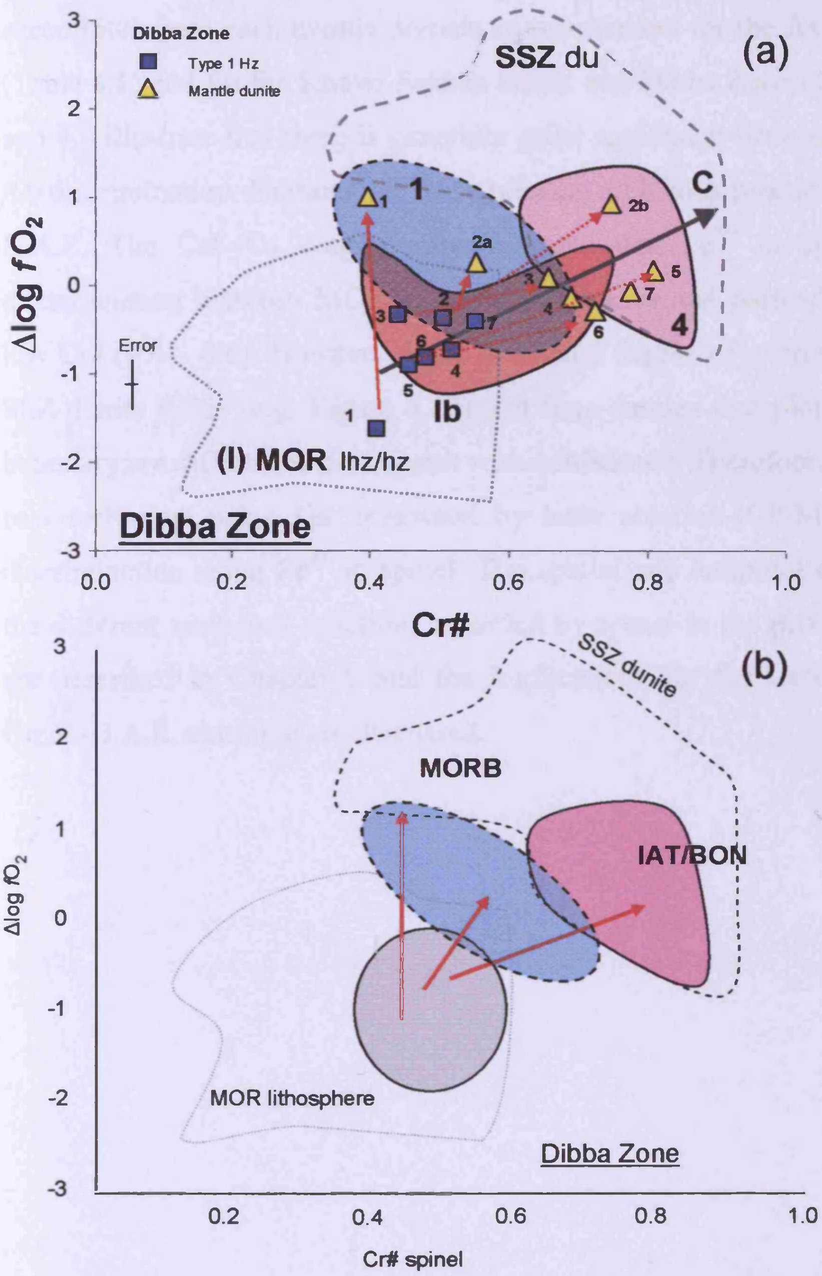

Figure 4.27: Cr#-fO_2 discrimination diagram for peridotites from the Dibba Zone to illustrate spinel reaction trends in (a) detail and (b) summarised format. In (a) individual samples are plotted (see key) and harzburgite-dunite pairs numbered to illustrate the general trends for reaction (red arrows). Error bars representative of 1 s.d. The tectonic fields and diagonal reaction trends are taken from Figure 4.19: I-MOR hz, Ib-Conical hz reacted with BON, 1-MORB du and 4-Conical BON du. In (b) grey elliptical field approximates the U.A.E. harzburgites and the main reaction trends (red arrows) between peridotite and MORB (dark blue ellipse) and between peridotite and IAT/BON melt (pink ellipse) are shown

Spinel data (Cr#, TiO_2 and fO_2), and its interpretation, for the U.A.E. peridotites and chromitites from each mantle domain is summarised for the Aswad and Fizh Blocks (Table 4.1) and for the Khawr Fakkan Block and Dibba Zone (Table 4.2). Tables 4.1 and 4.2 illustrate that there is generally good agreement between Cr#-TiO_2 and Cr#-fO_2 discrimination diagrams for fingerprinting melt-rock reaction of peridotites in the U.A.E. The Cr#-fO_2 diagram demonstrates that Fe^{3+} in spinel is effective in discriminating between MOR and SSZ peridotites and particularly for spinels with low Cr# (0.4 – 0.6). However, there is a small degree of overlap between MOR and SSZ dunite fields (e.g. Figure 4.20) and thus dunites that plot near this MOR/SSZ boundary are difficult to distinguish with confidence. Therefore, Chapter 5 explores a new technique using Ga, measured by laser ablation-ICP-MS, to refine tectonic discrimination using Fe^{3+} in spinel. The spatial and temporal relationships between the different melt-rock reactions recorded by spinel in the different mantle domains are described in Chapter 6 and the implications for the tectonic evolution of the Oman-U.A.E. ophiolite are discussed.

Table 4.1: Summary of spinel data (Cr#, TiO_2 and fO_2), and its interpretation, for peridotites and chromitites from the mantle domains of the Aswad and Fizh Blocks.

Aswad and Fizh Blocks	**Lherzolite (Lhz) and Harzburgite (Hz)**			**Dunite (Du) and Chromitite (Chr)**		
	Cr#	**TiO_2** wt.%	**fO_2** QFM	**Cr#**	**TiO_2** wt.%	**fO_2** QFM
Aswad S & Fizh (sub-moho mantle & MTZ)	0.4-0.6	<0.15	0 to +1	0.45-0.6	0.1-0.6	+1 to +2.5
	Hz (Type 1: anhedral sp) 20 – 30% melting Transitional MOR/SSZ residue or reacted with MORB/IAT melt			**MORB or MORB/IAT**		**MORB/IAT**
				0.65-0.75	0.2-0.6	+1 to +1.5
				IAT		**IAT**
Aswad N (mid-mantle)	0.4-0.6	<0.15	-1.5 to +0.3	0.6-0.7	0.2-0.4	+1 to +1.5
	Hz (Type 1: anhedral sp) 20 – 30% melting MOR residue or trans. MOR/SSZ residue			**IAT**		**IAT**
				0.6-0.8	0.1-0.2	+0.2 to +1
				IAT/BON		**IAT/BON**
Aswad N (Banded Unit)	0.2-0.3	<0.15	0	0.55-0.9	0.1-0.2	+1 to +1.7
	Lhz (Type 1: anhedral sp) Residue 10 – 15% melting			**IAT/BON**		**IAT/BON**
	0.4-0.8	<0.15	0			
	Hz (Type 1b, 2 & 3: SI to euhedral sp) Partial reaction with IAT/BON melt					

Table 4.2: Summary of spinel data (Cr#, TiO_2 and fO_2), and its interpretation, for peridotites and chromitites from the mantle domains of the Khawr Fakkan Block and Dibba Zone.

<table>
<tr><th rowspan="2">Khawr Fakkan Block & Dibba Zone</th><th colspan="3">Lherzolite (Lhz) and Harzburgite (Hz)</th><th colspan="3">Dunite (Du) and Chromitite (Chr)</th></tr>
<tr><th>Cr#</th><th>TiO_2
wt.%</th><th>fO_2
QFM</th><th>Cr#</th><th>TiO_2
wt.%</th><th>fO_2
QFM</th></tr>
<tr><td rowspan="4">Khawr Fakkan S
(sub-moho mantle & MTZ)</td><td>0.35-0.5</td><td><0.15</td><td>0 to +0.5</td><td>0.4-0.6</td><td>0.2-0.6</td><td>+1.3 to +2</td></tr>
<tr><td colspan="3">Hz (Type 1: anhedral sp)
15 – 25% melting
Transitional MOR/SSZ residue or reacted with MORB/IAT melt</td><td colspan="2">MORB or MORB/IAT</td><td>MORB/IAT</td></tr>
<tr><td>0.6-0.7</td><td><0.1</td><td>-</td><td>0.65-0.8</td><td>0.1-0.25</td><td>+1 to +1.5</td></tr>
<tr><td colspan="3">Hz (Type 3: euhedral sp)
Partial reaction with IAT/BON melt</td><td colspan="2">IAT/BON</td><td>IAT/BON</td></tr>
<tr><td rowspan="4">Khawr Fakkan N
(mid-mantle)</td><td>0.4-0.6</td><td><0.15</td><td>-0.5 to +0.2</td><td>0.7-0.9</td><td>0 - 0.15</td><td>-1 to +1</td></tr>
<tr><td colspan="3">Hz (Type 1: anhedral sp)
20 – 30% melting
MOR residue or trans. MOR/SSZ residue</td><td colspan="2">BON
(e.g. West Zikt chr)</td><td>BON</td></tr>
<tr><td>0.6-0.8</td><td><0.1</td><td>-1 to +1</td><td>0.65-0.75</td><td>0.1-0.2</td><td>+0.5 to +1</td></tr>
<tr><td colspan="3">Cpx-poor Hz (Type 1b, 2 &3:SI-euhedral sp)
Partial reaction with BON melt</td><td colspan="2">IAT/BON
(e.g. East Zikt chr)</td><td>IAT/BON</td></tr>
<tr><td rowspan="6">Khawr Fakkan N
(Banded Unit)</td><td>0.2-0.3</td><td><0.15</td><td>-0.5 to +0.3</td><td>0.65-0.8</td><td>0.1-0.2</td><td>+0.5 to +1.5</td></tr>
<tr><td colspan="3">Lhz/Cpx-rich Hz (Type 1:anhedral sp)
10 – 15% melting
MOR residue or trans. MOR/SSZ residue</td><td colspan="2" rowspan="5">IAT/BON</td><td rowspan="5">IAT/BON</td></tr>
<tr><td>0.4-0.6</td><td><0.15</td><td>-0.5 to +0.5</td></tr>
<tr><td colspan="3">Hz (<i>Type 1:anhedral</i> sp)
20 – 30% melting
MOR residue or trans. MOR/SSZ residue</td></tr>
<tr><td>0.6-0.7</td><td><0.15</td><td>0</td></tr>
<tr><td colspan="3">Hz (Type 1b, 2 & 3: SI to euhedral sp)
Partial reaction with IAT/BON melt</td></tr>
<tr><td rowspan="4">Dibba Zone</td><td>0.4-0.6</td><td><0.2</td><td>-1.7 to -0.5</td><td>0.4-0.6</td><td><0.1</td><td>0 to + 1</td></tr>
<tr><td colspan="3" rowspan="3">Hz (Type 1: anhedral sp)
20 – 30% melting
MOR residue</td><td colspan="2">MORB or MORB/IAT</td><td>MORB</td></tr>
<tr><td>0.65-0.8</td><td>0.1-0.2</td><td>-0.5 to +0.7</td></tr>
<tr><td colspan="2">IAT/BON</td><td>IAT/BON</td></tr>
</table>

4.4 Conclusions

- Chrome-spinels from U.A.E. peridotites and chromitites have a wide variation in Cr# (e.g. 0.2 – 0.9) as a result of variable partial melting and melt-rock reaction.

- Tectonic discrimination of chrome-spinel (using Cr#, TiO_2 and fO_2) shows that the U.A.E. mantle has a complex tectonic history involving a change of tectonic setting from MOR to SSZ with time.

- The Dibba Zone peridotites share a similar history to the main ophiolite Blocks of Aswad and Khawr Fakkan.

- Harzburgites and lherzolites originally began as pre-existing mantle lithosphere formed at a MOR-type spreading ridge and were modified to various degrees by infiltration and reaction with depleted SSZ melts.

- Cr#-fO_2 cannot distinguish between residue from a 'dry' spreading ridge and a 'transitional MORB/IAT' spreading ridge but it can discriminate melt-rock reaction from these two settings.

- Melt-rock reaction trends in chrome-spinels identify five possible types of magma that infiltrated the U.A.E. mantle sequence: MORB, MORB/IAT, IAT, IAT/BON and BON.

- MORB magmas infiltrated only the mantle region of the Dibba Zone and formed dunites.

- Transitional MORB/IAT magmas infiltrated the sub-Moho mantle and MTZ to form dunites and chromitites in both the Aswad and Khawr Fakkan Blocks.

- IAT magmas infiltrated the sub-Moho mantle of only Aswad where they formed dunites and chromitites in the mantle and MTZ.

- BON magmas infiltrated the mid-mantle of Khawr Fakkan North and reacted with harzburgites to form dunites and clinopyroxene-poor harzburgites.

- IAT/BON magmas infiltrated the shear zones at the base of the ophiolite (i.e. Banded Unit) and reacted with lherzolites to form dunites and harzburgites in both the Aswad and Khawr Fakkan Blocks.

- IAT/BON magmas also infiltrated the mid-mantle of Aswad, Dibba Zone and parts of Khawr Fakkan to form dunites and chromitites.

- Some of the U.A.E peridotites are analogous to polygenetic SSZ peridotites from South Sandwich forearc and Conical Seamount, Mariana forearc.

- In the U.A.E. the residual mantle (i.e. harzburgites) and the interacting SSZ melts (i.e. dunites and chromitites) are polygenetic and this implies that the harzburgite residue was not the mantle source region for the SSZ melts.

- Melt-rock reaction was gradational in some peridotites as evidenced by (i) a change in the morphology of spinel from Type 1 (holly-leaf) to Types 2 (subidiomorphic) and 3 (euhedral) and (ii) the consumption of clinopyroxene from lherzolite – harzburgite – dunite (e.g. the Banded Unit) and from harzburgite – clinopyroxene-poor harzburgite – dunite (e.g. Khawr Fakkan North).

Chapter 5: New developments in the tectonic discrimination of chrome-spinel: analysis of gallium by Laser Ablation-ICP-MS

The most effective fingerprints for the petrogenesis and tectonic discrimination of chrome-spinels are based on occupancy of the Y (Cr, Al) site of the chrome-spinel. Co-variations between Cr# [Cr/(Cr + Al], Ti and Fe^{3+} provide sensitive indicators of the degree of melting, oxygen fugacity and melt-rock interaction as demonstrated in Chapter 4. The ferric iron (Fe^{3+}) content of chrome-spinel is dependent in part on the oxidising conditions of the mantle and is particularly useful in discriminating peridotites from MOR and SSZ settings with similar Cr# compositions (see fO_2 section, Chapter 4). However, the oxidising nature of the tectonic setting is not the only control on the Fe^{3+} content of chrome-spinel. Melt-rock reaction increases both the Fe^{3+} and Ti content of the residual chrome-spinel (e.g. Pearce et al., 2000). Also, the Fe^{3+} content of the melt can locally increase by magmatic differentiation (e.g. Arai, 1992) and thus reaction of chrome-spinel with such a melt can cause an increase in Fe^{3+} content without a change in tectonic setting, e.g. Hess Deep dunites (e.g. Allan and Dick, 1996; Arai and Matsukage, 1996).

The aim of this study is to improve the tectonic discrimination of chrome-spinel using Fe^{3+} by: 1) extending the suite of elements used in tectonic discrimination to gallium (Ga) for the first time; and 2) using Ga to monitor the local magmatic variation in Fe^{3+} so that discrimination field boundaries are not mistakenly crossed.

Ga is present in trace amounts in chrome-spinel (e.g. 10 - 120 ppm) (Kurat, 1980; McKay and Mitchell, 1980; O'Reilly et al., 1991; Griffin et al., 1993, 1994; Paktunc and Cabri, 1995; Paktunc and Hulbert, 1996). Ga was therefore analysed by laser ablation ICP-MS in this study. Modern-day peridotite samples, representative of mid-ocean ridges, passive continental margins and supra-subduction zone settings, are used to define the tectonic discrimination fields. These are then be tested mainly on peridotites from the northern Oman-U.A.E. ophiolite and the results compared to those obtained using Cr#-fO_2 plots for the same chrome-spinels (Chapter 4). This work should also further our understanding of the behaviour of Ga in chrome-spinel during mantle processes.

5.1 Rationale - why analyse Ga?

Trace elements often show larger variations than major elements during fractional crystallization or partial melting which makes them a sensitive monitor of melt-rock reaction and magmatic differentiation in spinel (e.g. Pearce et al., 2000). For example, spinels in dunites from Hess Deep have a near constant Cr# but display an increase in Ti and Fe^{3+} as a result of melt-rock reaction with a locally evolving melt (e.g. Allan and Dick, 1996; Arai and Maksukage, 1996). Furthermore, chrome-spinel phenocrysts in Mg-rich magmas record large increases in both Ti and Fe^3# [$Fe^{3+}/(Fe^{3+}+Cr+Al)$] during magmatic differentiation, and the normalisation of Ti to Fe^3# in chrome-spinel thereby discriminates MORB melts from arc melts with similar Cr# compositions (0.3 – 0.6) (Arai, 1992). The Ti-Fe^3# discrimination diagram of Arai (1992) is useful for Ti-rich chrome-spinels (> 0.4 wt.%). However, discrimination is poor for chrome-spinels with TiO_2 contents < 0.4 wt.%, which are common in peridotites.

There are two pieces of evidence that support the hypothesis that Ga could represent a proxy for the variation of Fe^{3+} during magmatic differentiation:

1) During fractional crystallization of basaltic magma, crystallizing olivine and chrome-spinel in proportion 19:1, Ga increases in the residual liquid because it is moderately incompatible (Paktunc and Cabri, 1995).

2) Ga has higher concentrations in phenocryst chrome-spinels, relative to xenocryst chrome- spinels, in kimberlites and lamproites. The positive correlation between Ga, Ti, Fe^{3+} and Ni, which increase as Mg# decreases, represents a fractional crystallization trend (Griffin et al., 1994; Griffin and Ryan, 1995).

The substitution of trace elements into the lattice site of a mineral is primarily dependent on the size of its ionic radius and valency (Goldschmidt, 1937; Onuma et al., 1968). As a trivalent cation, Ga occupies the Y (Cr, Al) site in chrome-spinel and, like Ti^{4+}, is likely to be useful for tectonic discrimination. Ga and Fe^{3+} have similar ionic radii (0.62 Å) and therefore may be expected to behave in a similar way, but only Fe^{3+} is redox-dependent. High concentrations (80 - 110 ppm) of Ga in Fe^{3+} rich minerals, such as magnetites (Burton et al., 1959), provide evidence that Ga behaves similarly to Fe^{3+} because they both have an affinity for the same minerals.

In addition, although Ga and Al have markedly different ionic radii (0.62Å and 0.51Å respectively), the chemical behaviour of Ga is closely related to that of Al, which precedes it in Group III of the periodic table. This is evident from the affinity of Ga for Al-rich mineral phases such as corundum (Al_2O_3), bauxite ($Al_2O_3.2H_2O$) and chrome-spinel $[(Mg,Fe^{2+})(Cr,Al,Fe^{3+})_2O_4]$ (Burton et al., 1959). The concentration of Ga in silicate minerals depends on the Al-content of the mineral, both elements typically decreasing in the order plagioclase > garnet > amphibole > clinopyroxene > orthopyroxene > olivine (e.g. Burton et al., 1959; Paster et al., 1974; McKay and Mitchell, 1980; O'Reilly et al., 1991; Ewart and Griffin, 1995; Paktunc and Hulbert, 1996; Glaser et al., 1999). The positive correlation between Ga and Al in chrome-spinels from continental xenoliths (Norman, 1998) indicates that Ga in chrome-spinel decreases during partial melting.

Although Ni has a positive correlation with Ga (O'Reilly, 1991; Griffin et al., 1994; Griffin and Ryan, 1995; Paktunc and Hulbert, 1995) and with Al (Stosch, 1981; Paktunc and Cabri, 1995), Ni is not likely to be as reliable as Ga in the tectonic discrimination of chrome-spinel. This is because Ni is diffusion-dependent whereas Ga is not (Roeder and Campbell, 1985; Scowen et al., 1991; Barnes, 1998). These studies demonstrated that unlike divalent cations, such as Zn and Ni, trivalent cations, such as Ga and Fe^{3+}, experience very little, if any, change during re-equilibration because of their low diffusivity in olivine. For example, chrome-spinel xenocrysts from kimberlites do not exhibit a correlation between Ga and Ni because

Ni shows a strong temperature-dependent re-equilibration between olivine and spinel (Griffin et al., 1994).

Therefore, Ga is likely to be useful in the tectonic discrimination of peridotites because:

1) Ga has a similar behaviour to both Al and Fe^{3+} during mantle and magmatic processes.
2) Unlike major cations, such as Al and Cr, Ga is likely to be a sensitive monitor of magmatic differentiation.
3) Ga is relatively diffusion-independent and has low diffusivity in olivine, unlike Ni.

5.2 Analytical methods

All the samples analysed for Ga by LA-ICP-MS were also analysed for major and minor (Fe^{3+} and TiO_2) elements by EMPA (Chapter 4). Accurate Fe^{3+} was determined using secondary (Mössbauer) spinel standards for EMPA based on 24 - 40 analyses per sample, as reported in Chapter 4 (Section 4.1.2).

The laser ablation ICP-MS used at Cardiff University comprises a New Wave UP213 laser system coupled to a Thermo X-Series ICP-MS. It has been successfully used to analyse trace elements from a variety of geological samples such as olivine-hosted melt inclusions (Jones, 2005), clinopyroxenes in gabbros from the Oman ophiolite (Lilly, 2006), clinopyroxenes and garnets in eclogites from the Roberts Victor Kimberlite, South Africa (Coggon, 2007), and the in-situ analysis of platinum-group elements in sulphides from the Bushveld Complex (McDonald, 2005; Holwell and McDonald, 2007).

A new method was developed in this study to analyse chrome-spinel by LA-ICP-MS using matrix-matched standards (i.e. chrome-spinel standards). The results have been submitted for publication to Geostandards and Geoanalytical Research and are reproduced in Appendix E. In summary, matrix-matched standards are preferred to synthetic NIST glasses, which had been used in all previous LA-ICP-MS analyses of chrome-spinel. However, because of the lack of chrome-spinel reference material, matrix-matched standards were characterised for Ga in this study by in situ microdrilling of the chrome-spinel standard followed by dissolution and conventional analysis by ICP-MS. Chromitite material, similar to that analysed for Ga by proton microprobe (Paktunc and Cabri, 1995), were then analysed by LA-ICP-MS using these matrix-matched standards. This demonstrated that the two methods produce similar values for Ga. The application of the new LA-ICP-MS method to analyse chrome-spinel in peridotites is described below.

5.2.1 Procedure for LA-ICP-MS

Chrome-spinels were analysed for Ga by LA-ICP-MS using a 213nm UV laser and well-characterised chrome-spinel standards using the methodology described in Appendix E. Ablations were carried out at 15 Hz using helium in the sealed laser cell, and the resulting vapour was combined with argon before delivery into the ICP-MS. Data were acquired in time-resolved analysis (TRA) mode using time slices of 250 milliseconds (ms). Typical acquisitions lasted 80 seconds and comprised 20 seconds measurement of the gas blank, followed by ablation of sample for approximately 60 seconds using a line 40 μm wide, 10 μm deep and approximately 250 μm long.

The ICP-MS was tuned at the start of the day using NIST612 glass to reduce low mass sensitivity while maintaining or enhancing mid to high mass sensitivity. Analytical runs consisted of a calibration block involving two measurements of three chrome-spinel standards (U.A.E.140, SD44 and ADK185) followed by NIST 612 standard and 6 - 8 unknowns, re-analysis of one chrome-spinel standard (U.A.E.140) and NIST 612 standard, 6 - 8 unknowns, re-analysis of two standards, etc. NIST612 was used to monitor instrumental performance and to correct for any drift. Chrome-spinel sample SD159, which was also analysed independently for Ga by solution ICP-MS, was analysed as an unknown to monitor inter-run variability. One run typically comprised 6 unknown samples, with 3 chrome-spinel grains analysed per sample. Two runs were commonly carried out in a day, demonstrating the high speed and ease of acquiring trace element data by LA-ICP-MS.

Following background correction of the data, the average signals were normalized to Mg, analysed for each chrome-spinel grain by electron microprobe. This was to correct for differences in the absolute amount of material that is ablated and transported during an individual analysis. The corrected average signal was then converted into a concentration by calibration against the chrome-spinel standards. The isotopes ^{24}Mg, ^{27}Al, ^{52}Cr, ^{53}Cr, ^{47}Ti and ^{51}V were measured so that the composition of the chrome-spinel could be monitored during the analysis of Ga and compared to the EMP data. Both Ga isotopes, ^{69}Ga and ^{71}Ga, were analysed to monitor interferences in the ICP-MS. The isotopes ^{44}Ca, ^{59}Co and ^{60}Ni were also measured to filter out signals from non-chrome-spinel material, such as silicates or sulphides, which commonly form mineral inclusions or infill cracks (Figure 5.1).

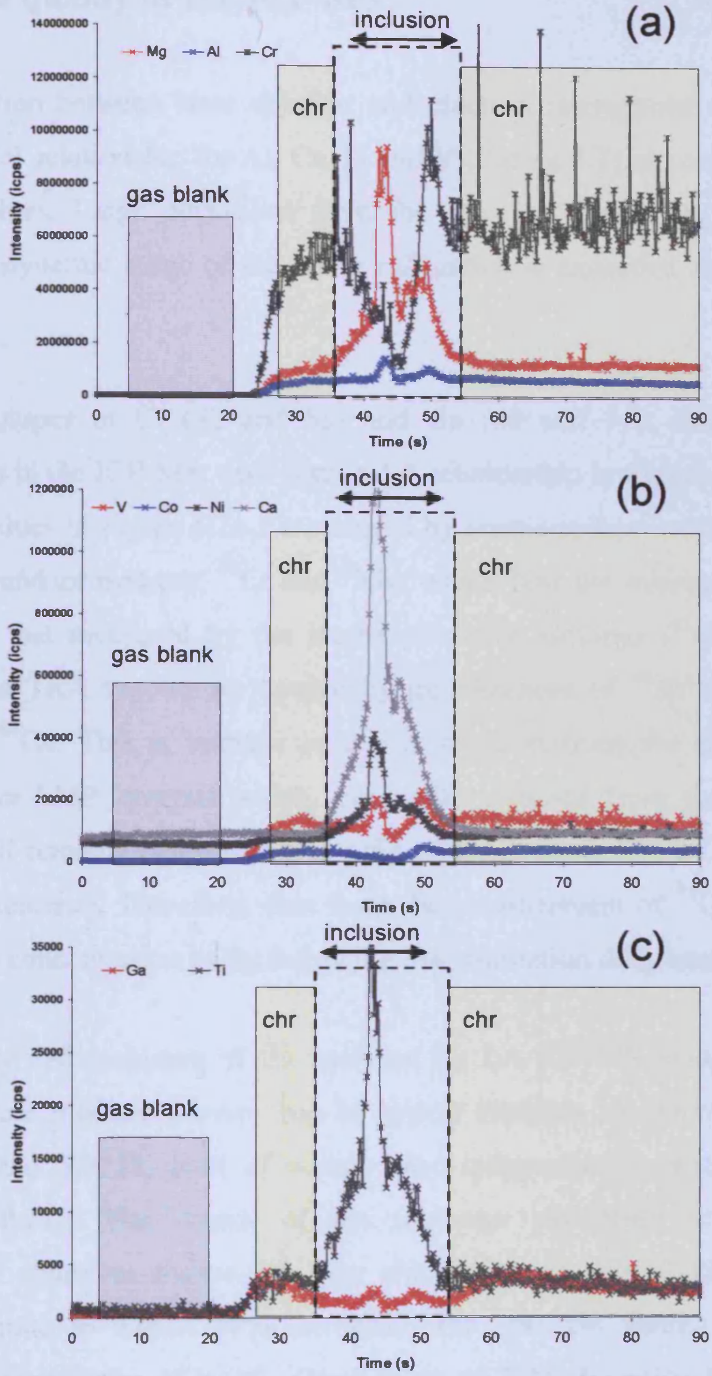

Figure 5.1: TRA spectra (Intensity of laser plotted against time (s)) for the analysis of (a) Mg, Al, Cr, (b) V, Co, Ni, Ca and (c) Ga and Ti in chrome-spinel from chromitite sample UAE140. In each diagram the gas blank (grey region), chrome-spinel (yellow region) and clinopyroxene/amphibole inclusions (white region) are marked. Ca, Ni and Ti are significantly enriched in the inclusion compared to the host spinel and were used to filter out signals from non-spinel material.

5.2.2 Data quality of LA-ICP-MS

The correlation between laser ablation and electron microprobe data has a highly significant 1:1 relationship for Al, Cr, Ti and V (Figure 5.2) although Cr and V have lower r^2 values. Large deviations from the 1:1 relationship for Cr are probably because the dynamic range of the linear calibration is exceeded at high Cr# (Figure 5.2b).

The two isotopes of Cr (52 and 53) and Ga (69 and 71), analysed to monitor interferences in the ICP-MS, each form a 1:1 relationship in Figure 5.2 e-f. However, the low r^2 values in Figure 5.2e-f are caused by erratic spikes in the TRA spectra for the more abundant isotopes, ^{52}Cr and ^{69}Ga, which bias the average signal to higher values than that measured by the interference-free isotopes (^{53}Cr and ^{71}Ga). The spikes in the TRA spectra are caused by interferences of ^{40}Ar^{12}C on ^{52}Cr and of ^{57}Fe^{12}C on ^{69}Ga. This is because carbon is remnant from the carbon coat of the samples from EMP analysis which, even after removal from the sample surface, probably still remains embedded in cracks and will randomly be incorporated into the ablated material. Therefore, data from the measurement of ^{71}Ga will be used to calculate Ga concentration in the following discrimination diagrams.

The accuracy and precision of Ga analysed by LA-ICP-MS using matrix-matched standards were monitored every run by repeat analyses of chrome-spinel samples U.A.E.140 and SD159, both of which were independently measured for Ga by solution ICP-MS. The results of the inter-run variability are shown in the performance charts in Figure 5.3. For chrome-spinel SD159 Ga, analyses were largely accurate to within 10% deviation from the Ga value, as independently determined by solution ICP-MS. There is up to 20% deviation for chrome-spinel U.A.E.140. Error bars measure one standard deviation either side of the average signal for Ga in Figure 5.3. Each analysis on Figure 5.3 fell within analytical error of the 10% deviation of the solution ICP-MS value for Ga. Therefore, Ga analysed during different runs are repeatable and comparable.

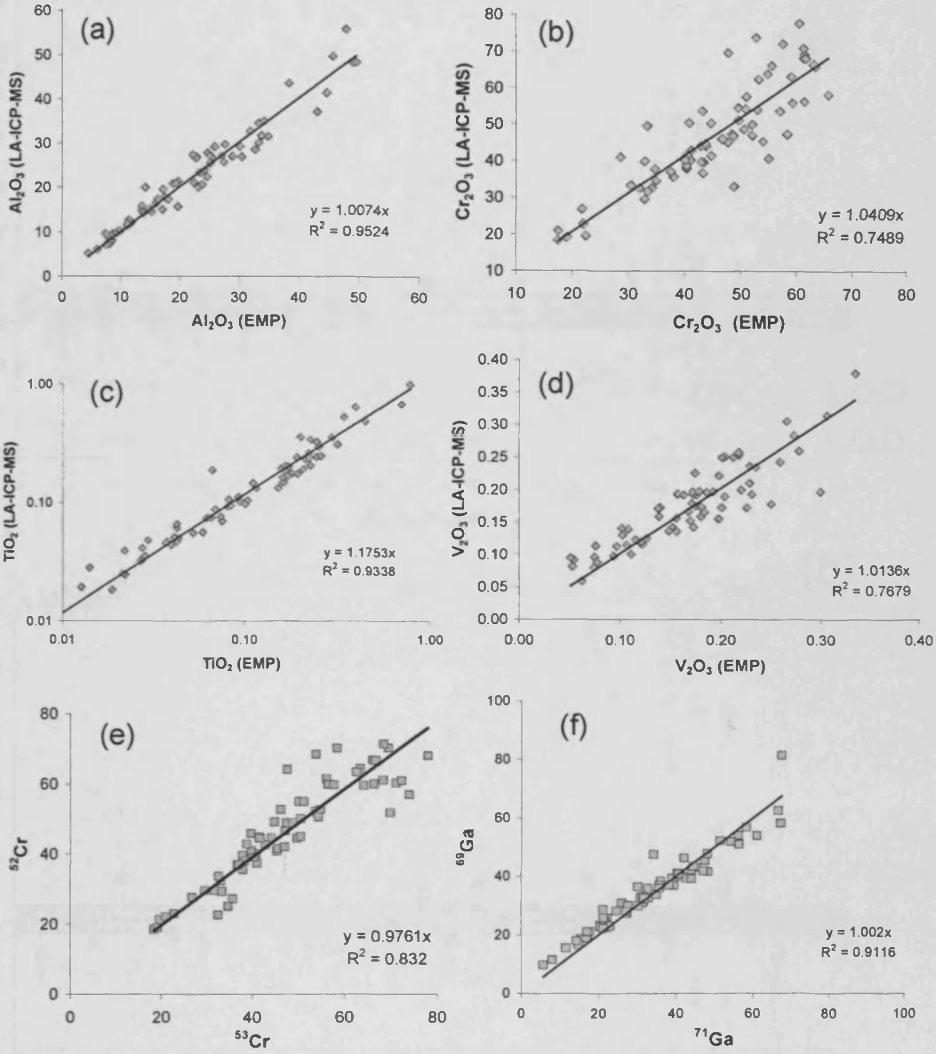

Figure 5.2: Comparison of laser-ablation ICP-MS and electron microprobe values for (a) Al_2O_3, (b) Cr_2O_3, (c) TiO_2 and (d) V_2O_3 show good agreement (1:1 relationship) between LA-ICP-MS and EMP data for chrome-spinels. Comparison between two isotopes measured simultaneously for Cr (e) and Ga (f) show good agreement (1:1) but low r^2, particularly for Cr partly because of erratic interference on ^{52}Cr.

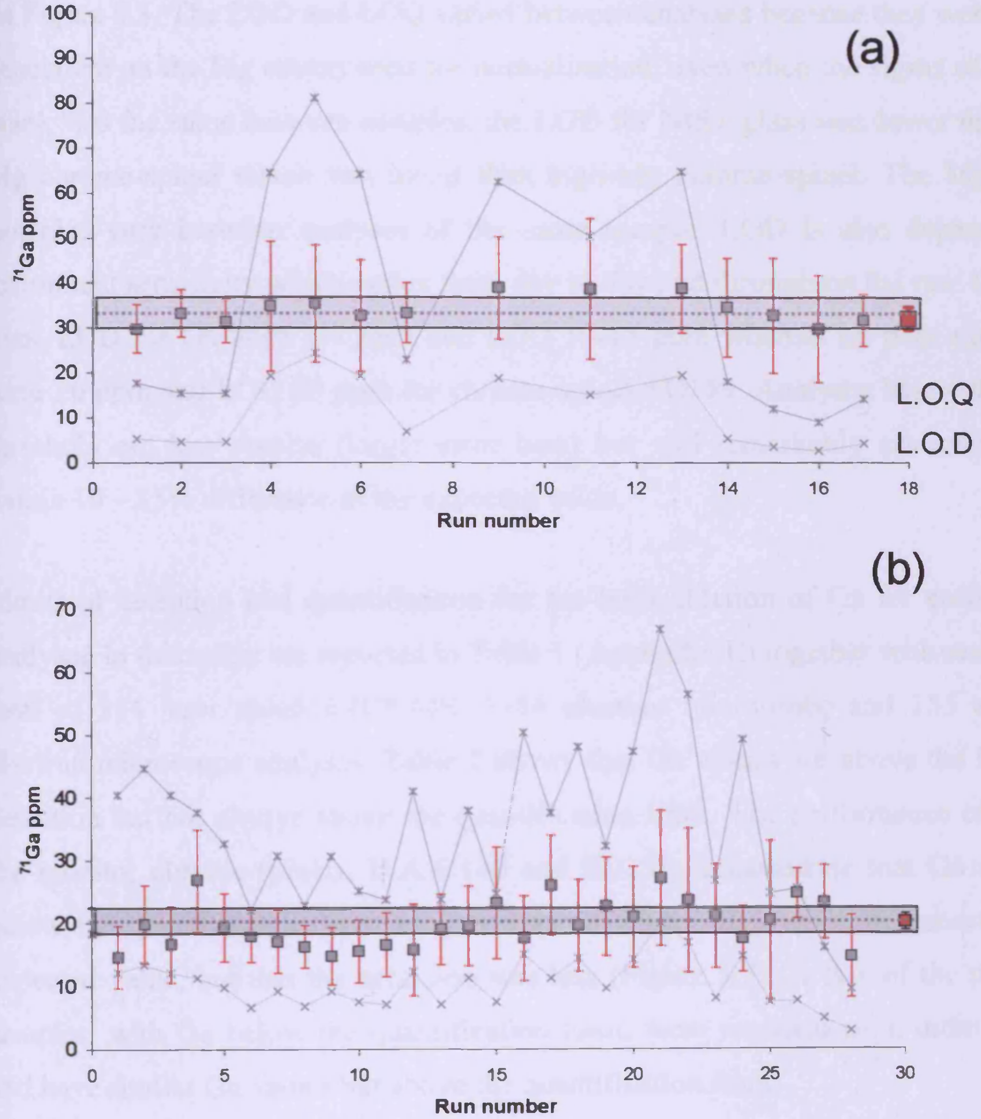

Figure 5.3: Performance charts for LA-ICP-MS analyses of Ga in chrome-spinel samples (a) SD159 and (b) UAE140 (high-Cr low Mg sample) show the inter-run variability. Grey squares represent individual analyses each run with error bars measuring 1 s.d. Average analysis for all the runs (red square) and error bars calculated from multiple standard deviations. Dashed line marks the expected Ga value, analysed by solution ICP-MS for each chrome-spinel sample, ± 10% difference (grey box). Limits of detection (L.O.D) and quantification (L.O.Q) estimated from 3 and 10 times, respectively, the standard deviation of the gas blank. Despite some analyses being below the quantification limit they are still mostly accurate to within 10 – 15% of the expected value.

The limits of detection (LOD: 3 times standard deviation of the gas blank) and quantification (LOQ: 10 times standard deviation of the gas blank) are also plotted on Figure 5.3. The LOD and LOQ varied between analyses because they were partly dependent on the Mg counts used for normalisation; even when the sigma of the gas blank was the same between samples, the LOD for NIST glass was lower than low-Mg chrome-spinel which was lower than high-Mg chrome-spinel. The Mg-counts can also vary between analyses of the same sample. LOD is also dependent on instrument sensitivity which varies from day to day and throughout the run. On good runs, LOD for Ga were 3-5 ppm and LOQ 10-15 ppm whereas on poor runs LOD were 20 ppm and LOQ 80 ppm for chrome-spinel SD159. Analyses below the LOQ threshold are less precise (larger error bars) but still remarkably accurate, i.e. to within 10 – 15% difference of the expected value.

Limits of detection and quantification for the laser-ablation of Ga for each sample analysed in this study are reported in Table 1 (Appendix E) together with results of a total of 314 laser ablation-ICP-MS, 1354 electron microprobe and 155 scanning electron microscope analyses. Table 1 shows that Ga values are above the limits of detection but not always above the quantification limit. The performance charts for the monitor chrome-spinels, U.A.E.140 and SD159, demonstrate that Ga analyses below the quantification limit are accurate to within 10 – 15% difference of the expected value, but that the precision was less (Figure 5.3). A few of the unknown samples, with Ga below the quantification limit, were repeated on a different run; and have similar Ga values but above the quantification limit.

The problem of poor precision, resulting from Ga analyses reported below quantification limit, was reduced by analysing three individual chrome-spinel grains per sample. This reduced the combined precision for the average Ga measurement. Therefore, error bars in the following Ga-Fe3# diagrams (Section 5.4.1) were calculated using the following equation:

$$[1/(n-1)]*\sqrt{(\sigma_1^2+\sigma_2^2+\sigma_3^2)}$$

where n = number of chrome-spinels measured per sample and σ = one standard deviation of Ga in the individual chrome-spinel.

Ultimately, the variation associated with analytical error described above is considerably less than the variation required for discrimination in Section 1.4. Ideally, future analyses could be improved by using wider line widths to ensure Ga signals are always above limits of quantification. However, the small areas suitable for the ablation lines of chrome-spinels in peridotites did not accommodate wider line widths easily.

5.3 Samples for analysis

5.3.1 Aims of selection

Samples were carefully selected for the analysis of Ga in order to represent the three processes which contribute to the variation of Fe^{3+} in chrome-spinel: tectonic setting, melt-rock reaction and magmatic differentiation.

Tectonic setting

The tectonic settings of interest to this study are mid-ocean ridges (MOR), supra-subduction zone (SSZ) settings and, to a lesser extent, passive continental margins (PCM). In order to develop new discrimination diagrams for Ga and Fe^{3+}, compositional fields for MOR, SSZ and PCM settings were defined by analysing modern-day peridotite samples representing each setting. Very few chrome-spinel sample analyses from the literature for modern-day oceanic settings include Ga (e.g. Ewart and Griffin, 1995; Forsythe and Allan, 1998; Denny, 1998). Instead, most previous studies analysed Ga in chrome-spinels from continental settings, e.g. mantle xenoliths, kimberlites, komatiites and layered intrusions (O'Reilly, 1991; Griffin et al., 1993; Griffin and Ryan, 1995; Paktunc and Cabri, 1995; Paktunc and Hulbert, 1996; Denny, 1998; Eggins et al., 1998; Norman, 1998; Richardson, 1999; Glaser et al., 1999; Grégoire et al., 2000; Taylor et al., 2003).

In this study, therefore, modern-day peridotite samples from PCM, MOR and SSZ settings were analysed for the first time to define oceanic tectonic fields (Section 5.3.2). Although this set of modern-day samples is relatively small (n= 21), a larger set of samples from ophiolites (n = 43), classified as having both MOR and SSZ origins by Cr#-fO_2 discrimination (see Chapter 4), were analysed to test the tectonic fields (Section 5.5).

Chromitites have not been recovered from modern-day oceans, except for a micropod (few centimetres) from Hess Deep (Maksukage and Arai, 1996). Therefore, ophiolitic chromitites have no modern analogue that can be used for their tectonic discrimination. In consequence, podiform chromitites from ophiolites analysed in this study will be tested using the tectonic fields defined by dunites from modern-day oceans.

The sample locations, rock types and the tectonic setting of each sample analysed in this Chapter are given in Table 2 (Appendix E). Sample descriptions and background geological information can be found in the references listed in Table 2.

Melt-rock reaction

Co-existing harzburgite-dunite pairs were preferentially chosen for analysis to record variations in Ga and Fe^{3+} associated with melt-rock reaction. Harzburgites represent unreacted, residual peridotites whereas Chapter 4 concluded that dunites formed by melt-rock reaction and are termed here fully 'reacted' peridotites although in reality there is a gradation between the two because harzburgites have reacted with melt to some extent (e.g. Section 4.2.2). Chromitites formed by extensive melt-rock reaction as well as some magmatic accumulation. Where available, a few lava phenocrysts were included to represent magma compositions.

Magmatic differentiation

A suite of peridotites from Hess Deep was chosen to illustrate the variation in Ga and Fe^{3+} representing interaction of peridotites with an evolving melt. Ideally, the effect of magmatic differentiation would be investigated on a suite of spinel phenocrysts, but such samples were not readily available and beyond the scope of this project.

5.3.2 Modern-day samples

Samples were carefully selected for LA-ICP-MS on the basis of their spinel chemistry (Cr#, TiO_2 and fO_2) so that they represented the full range of compositions characteristic of different tectonic settings, melt-rock reaction and magmatic differentiation. The samples were analysed in Chapter 4 and plotted on Cr#-TiO_2 and Cr#-fO_2 diagrams in Section 4.3.3 and Section 4.3.4 respectively. These plots are reproduced in this Section to aid interpretation of each sample analysed for Ga in chrome-spinel in order to fully understand how Ga behaves in Sections 5.4 and 5.5.

PCM

Two harzburgite samples from the passive continental margins of Iberia and Galicia (ODP Sites 627 and 899 respectively) represent residual, fertile mantle (Cr# 0.2 and $TiO_2 < 0.1$ wt.%). The third harzburgite sample, 637B25, has higher TiO_2 (0.2 wt.%) and higher Cr# (0.35) as a result of melt-rock reaction with a MORB-type melt (Figure 5.4a). The PCM samples plot at the low Cr#-low fO_2 region of the MOR harzburgite field in the Cr#- fO_2 diagram (Figure 5.4b).

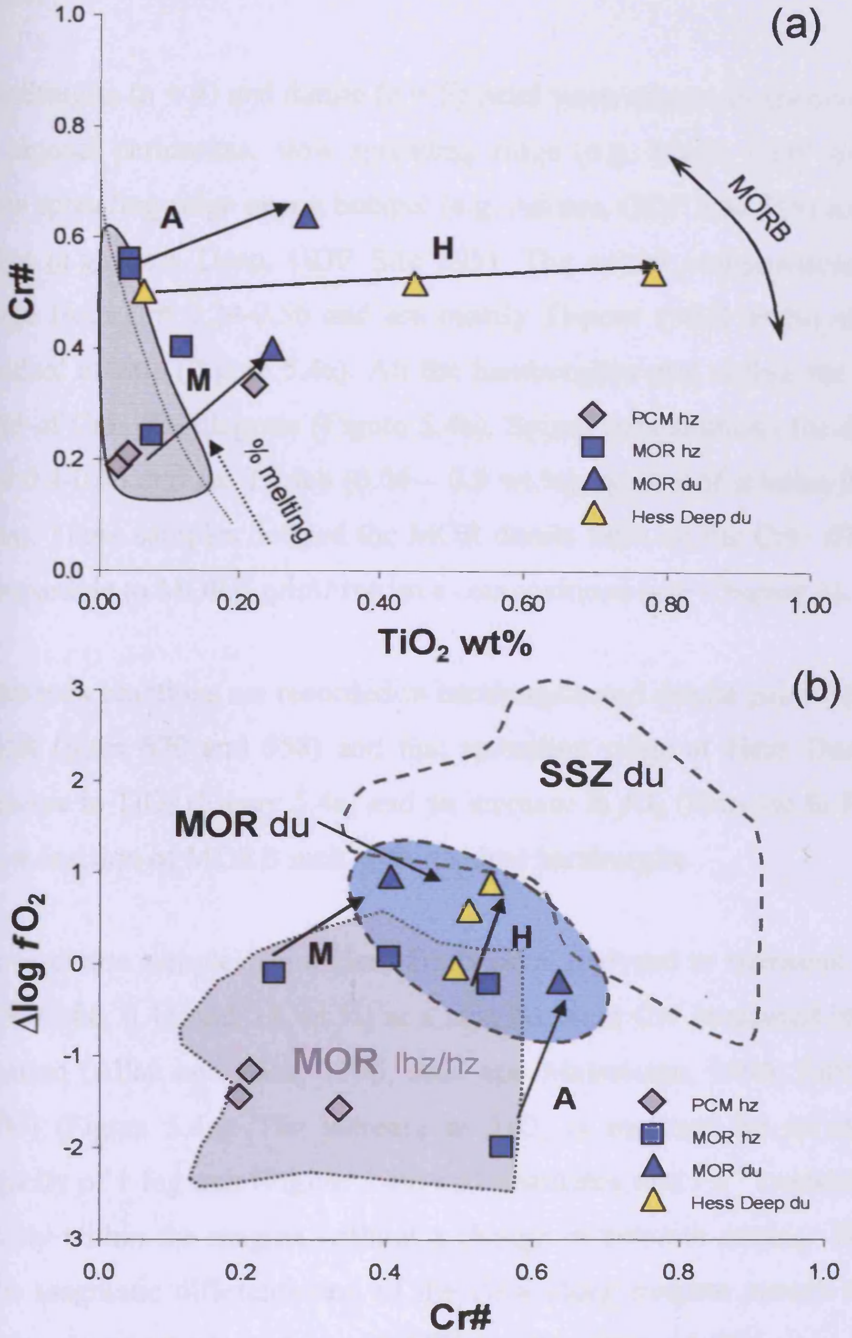

Figure 5.4: Modern-day peridotites from MOR settings plotted on spinels diagrams of (a) Cr#-TiO_2 and (b) Cr#-fO_2. Arrows mark melt-rock reaction trends between harzburgite-dunite pairs for MAR Site 670 (Trend M), Azores Site 558 (Trend A) and Hess Deep (Trend H). In (a) the grey field approximates MOR harzburgites that plot on the melting curve calculated by Pearce et al., (2000). Harzburgites and dunites that have higher TiO_2 than the melting curve have reacted with MORB melt. In (b) melt-rock reaction increases the fO_2 of spinel but fO_2 can also increase as a result of interaction with an evolving melt as exemplified by the suite of dunites from Hess Deep (Trend H).

MOR

Harzburgite (n = 4) and dunite (n = 5) pairs were chosen to encompass the full range of abyssal peridotites: slow spreading ridge (e.g. MAR, ODP sites 396 and 670), slow spreading ridge near a hotspot (e.g. Azores, ODP Site 558) and a fast spreading ridge (e.g. Hess Deep, ODP Site 895). The spinel compositions for harzburgites range from Cr# 0.24-0.56 and are mostly Ti-poor (<0.2 wt.%) and thus typical of residual mantle (Figure 5.4a). All the harzburgites plot within the MOR harzburgite field of Cr#-fO_2 diagram (Figure 5.4b). Spinel compositions for dunites range from Cr# 0.4-0.63 and are Ti-rich (0.06 – 0.8 wt.%), typical of dunites from MOR (Figure 5.4a). These samples defined the MOR dunite field on the Cr#-fO_2 diagram and are comparable to MORB primitive lava compositions (see Chapter 4).

Melt-rock reactions are recorded in harzburgite and dunite pairs from slow spreading MAR (Sites 670 and 558) and fast spreading ridge at Hess Deep. They show an increase in TiO_2 (Figure 5.4a) and an increase in fO_2 (increase in Fe^{3+}) (Figure 5.4b) upon reaction of MORB melt with residual harzburgite.

Three dunite samples from Hess Deep were analysed to represent the wide range in TiO_2 (0.06, 0.45 and 0.8 wt.%) at a near constant Cr# measured in dunites from this location (Allan and Dick, 1996; Arai and Matsukage, 1996; Edwards and Malpas, 1996) (Figure 5.4a). The increase in TiO_2 is matched by an increase in oxygen fugacity of 1 log unit (Figure 5.4b) and illustrates that Fe^{3+} content can also increase locally within the magma without a change in tectonic setting. The increase in fO_2 with magmatic differentiation of the Hess Deep magma pushes the evolved MOR dunite close to the boundary with SSZ dunites (Figure 5.4b).

SSZ

Dunites and harzburgites, representative of SSZ settings, come from the Izu-Bonin-Mariana (IBM) forearc (Parkinson and Pearce, 1998) and South Sandwich forearc (Pearce et al., 2000). The spinel compositions for harzburgites range from Cr# 0.4-0.67 and most are Ti-poor (<0.1 wt.%) except in the transitional harzburgite from South Sandwich which is relatively enriched in TiO_2 (0.17 wt.%) (Figure 5.5a). Spinel compositions for dunites range from Cr# 0.7-0.85. South Sandwich dunites (Cr# 0.7; TiO_2 0.2 – 0.25 wt.%) represent reaction with a melt of island arc tholeiite composition whereas the IBM dunite (Cr# 0.85; TiO_2 <<0.1 wt.%) represents reaction with boninitic melt (Parkinson and Pearce, 1998; Pearce et al., 2000).

Both suites of samples consist of pre-existing MOR harzburgites that have reacted with highly-depleted, SSZ melts to form transitional harzburgites and dunites (Parkinson and Pearce, 1998; Pearce et al., 2000). The melt-rock reaction is accompanied by an increase in Cr# and fO_2 and takes the harzburgites out of the MOR harzburgite field on a reaction trend towards the SSZ dunite field (Figure 5.5b).

The harzburgite sample from Torishima Forearc Seamount (Izu-Bonin forearc) represents residual SSZ mantle (Parkinson and Pearce, 1998) and plots in the SSZ field, in Figure 5.5b, defined by arc xenoliths (Parkinson and Arculus, 1999).

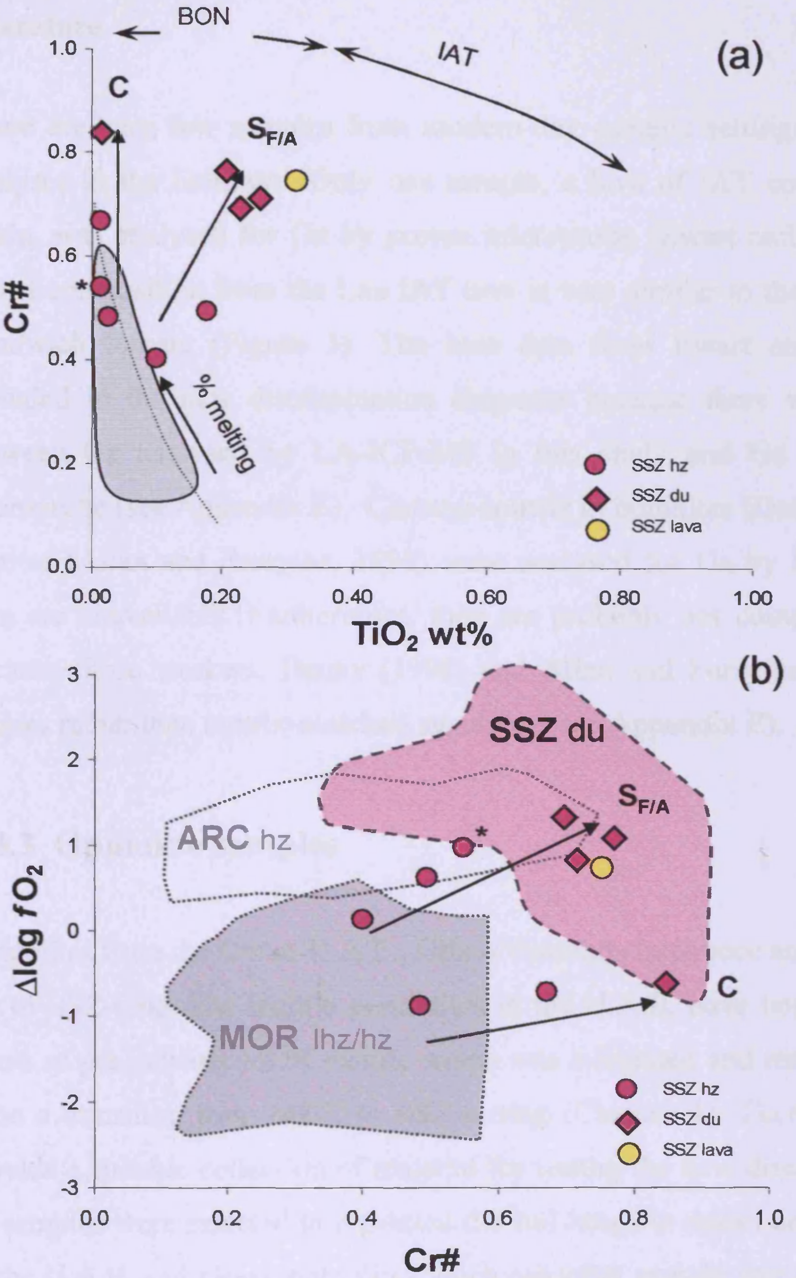

Figure 5.5: Modern-day peridotites from SSZ settings plotted on spinels diagrams of (a) Cr#-TiO_2 and (b) Cr#-fO_2. Arrows mark melt-rock reaction trends between harzburgite-dunite pairs for Conical Forearc Seamount (Trend C) and South Sandwich Forearc (Trend $S_{F/A}$). In (a) grey field approximates MOR harzburgites that follow the partial melting trend calculated by Pearce et al., (2000). Harzburgites and dunites that are displaced from the melting curve have reacted with SSZ melts such as IAT and BON. In (b) the spinel trends indicate that these SSZ peridotites formed by interaction of MOR residue with SSZ melts. * marks residual SSZ harzburgite from Torishima Forearc Seamount and plots in the SSZ (arc) hz field. Spinel data for an IAT lava is from Ewart and Griffin (1995) and plots in the SSZ dunite field.

Literature

There are very few samples from modern-day oceanic settings with published Ga analyses in the literature. Only one sample, a lava of IAT composition from Lau Basin, was analysed for Ga by proton microprobe (Ewart and Griffin, 1995). The spinel composition from the Lau IAT lava is very similar to the dunites from South Sandwich forearc (Figure 5). The lava data from Ewart and Griffin (1995) is included in the new discrimination diagrams because there was good agreement between Ga analysed by LA-ICP-MS in this study and Ga analysed by proton microprobe (see Appendix E). Chrome-spinels in boninites (Denny, 1998) and MOR picrites (Allan and Forsythe, 1998) were analysed for Ga by LA-ICP-MS, but the data are unavailable. Furthermore, they are probably not comparable to this study because those workers, Denny (1998) and Allan and Forsythe (1998), used NIST glasses rather than matrix-matched standards (see Appendix E).

5.3.3 Ophiolite samples

Ophiolites from the Oman-U.A.E., Othris/Vourinos in Greece and Troodos in Cyprus are of SSZ-type. The mantle peridotites in the U.A.E. have been interpreted in this thesis as pre-existing MOR mantle which was infiltrated and reacted with SSZ melts upon a transition from MOR to SSZ setting (Chapter 4). Therefore, these samples provide a suitable collection of material for testing the new discrimination diagrams. 43 samples were selected to represent the full range in spinel compositions recorded in the U.A.E. and Greek ophiolites. Each ophiolite sample was classified using Cr#-fO_2 diagram into an origin from the pre-existing MOR phase or the later SSZ setting phase (Chapter 4).

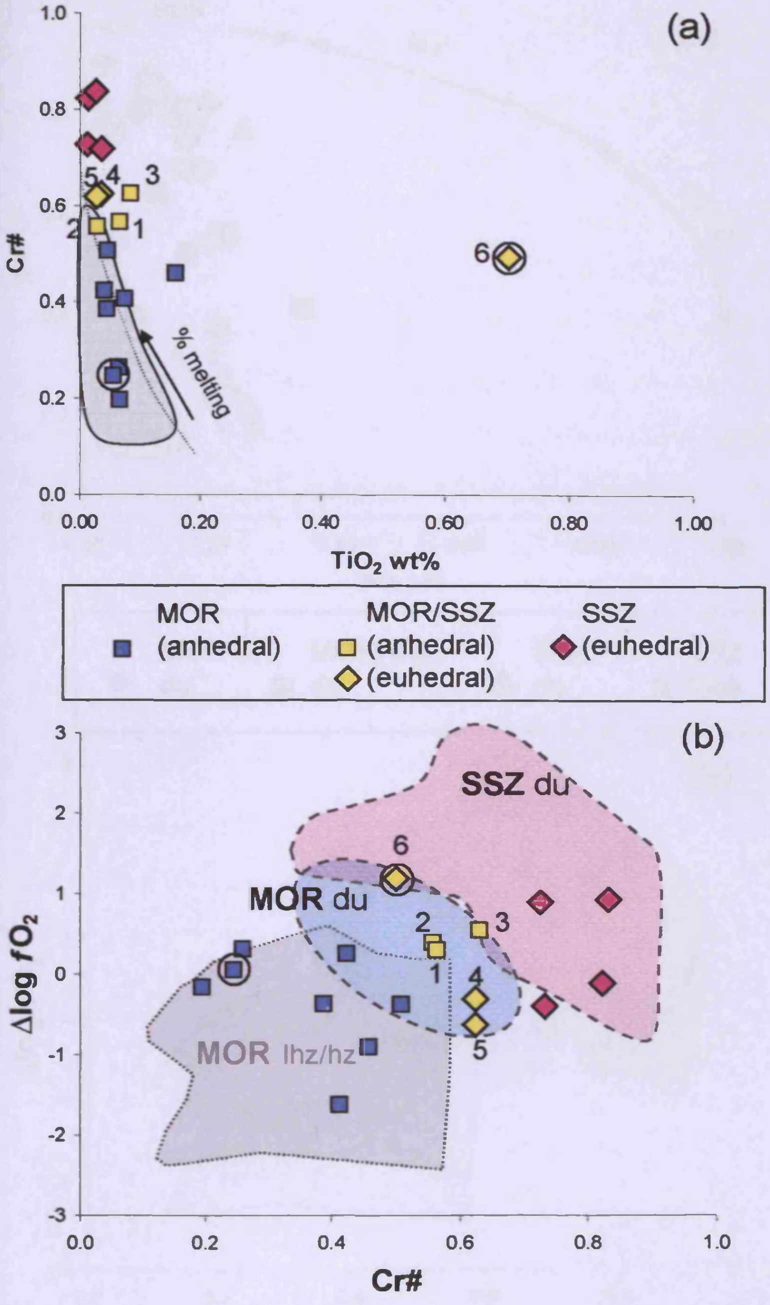

Figure 5.6: Harzburgite spinels from the U.A.E and Greek ophiolites plotted on (a) Cr#-TiO_2 and (b) Cr#-fO_2 diagrams. In (a) grey field approximates MOR harzburgites and plot on the partial melting trend calculated by Pearce et al., (2000). The Cr#-fO_2 diagram in (b) is used to classify harzburgites into MOR, MOR/SSZ and SSZ types. Anhedral spinels are characteristic of residual harzburgites and mostly plot in the MOR hz field. Euhedral spinels are characteristic of melt-rock reaction and mostly plot in the SSZ dunite field. Harzburgite spinels (marked 1-6) are ambiguously discriminated using Cr#-fO_2 diagram and classified as MOR/SSZ. Greek harzburgite spinels are circled, to distinguish them from the U.A.E. harzburgite spinels.

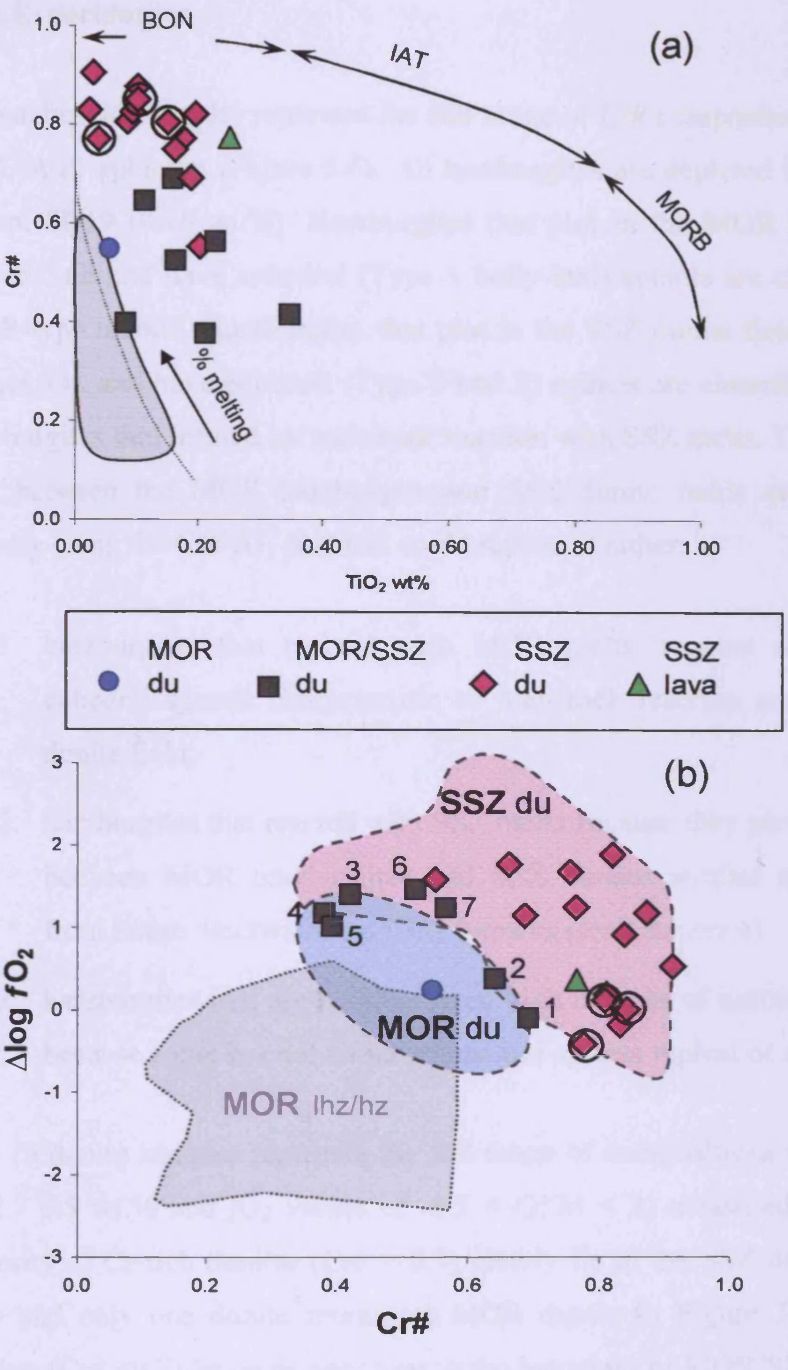

Figure 5.7: Dunites (from the U.A.E and Greek ophiolites) and a lava (Troodos ophiolite) are plotted on (a) Cr#-TiO_2 and (b) Cr#-fO_2 diagrams. In (a) grey field approximates MOR harzburgites and plot on the partial melting trend calculated by Pearce et al., (2000). The dunites and lava are displaced to higher TiO_2 than the residue trend because of melt-rock reaction. In (b) Cr#-fO_2 is used to classify dunites into MOR, MOR/SSZ and SSZ types. Dunite spinels (marked 1-7) that are ambiguously discriminated using Cr#-fO_2 diagram are classified as MOR/SSZ. Greek dunite spinels are circled, to distinguish them from the U.A.E. dunite spinels.

U.A.E. peridotites

16 harzburgite samples represent the full range of Cr# compositions (0.2 -0.85) from the U.A.E. ophiolite (Figure 5.6). All harzburgites are depleted in TiO_2 (<0.1 wt.%) except SD19 (0.16 wt.%). Harzburgites that plot in the MOR harzburgite field in Figure 5.6b and have anhedral (Type 1 holly-leaf) spinels are classified as residual MOR-type mantle. Harzburgites that plot in the SSZ dunite field at higher Cr# and higher fO_2, and have euhedral (Type 2 and 3) spinels are classified as 'reacted' SSZ harzburgites that formed by melt-rock reaction with SSZ melts. The harzburgites that plot between the MOR harzburgite and SSZ dunite fields are more difficult to classify using the Cr#-fO_2 plot and could represent either:

1. harzburgites that reacted with MOR melts because some of them have euhedral spinels characteristic of melt-rock reaction and plot in the MOR dunite field;
2. harzburgites that reacted with SSZ melts because they plot on a reaction trend between MOR harzburgites and SSZ dunites similar to SSZ harzburgites from South Sandwich and IBM forearcs (see Chapter 4);
3. harzburgites that are residual from high degrees of melting in a SSZ setting, because some but not all have anhedral spinels typical of residual peridotites.

The 19 dunite samples represent the full range of compositions (Cr# 0.4 - 0.9; TiO_2 0.02 - 0.5 wt.% and fO_2 values of $-0.5 < QFM < 2$) measured in the U.A.E. The majority of Cr-rich dunites (Cr# > 0.7) clearly lie in the SSZ dunite field in Figure 5.6b and only one dunite represents MOR dunite in Figure 5.6b. The remaining dunites (Cr# <0.7) lie on or very near to the boundary of MOR/SSZ dunites in Figure 6b). This study hopes to show that Ga-Fe^3# can improve discrimination where Cr#-fO_2 discrimination is inconclusive.

Greece peridotites and Troodos lava

Two harzburgites from the Pindos-Vourinos ophiolite were analysed; one is classified as a residual MOR harzburgite (Cr# 0.25; TiO_2 0.06 wt.%) and plots in the MOR harzburgite field in Cr#-fO_2 space (Figure 5.6). The other harzburgite, LK44, has higher fO_2, outside of the MOR harzburgite field, and plots on the MOR/SSZ boundary for dunites as well as in the arc harzburgite field (Figure 5.6). The highly enriched content of TiO_2 (0.7 wt.%) in spinel from sample LK44 implies an origin by melt-rock reaction with either a MOR or SSZ melt rather than arc mantle residue. Three dunites from the Pindos-Vourinos ophiolite and one lava (UPL olivine picrite) from the Troodos ophiolite clearly plot in the SSZ dunite field (Cr# > 0.7) (Figure 5.7).

Chromitites

Eight chromitites, from the mantle and MTZ, represent the three chemical groups found in the U.A.E. (low- and high-Cr types) shown in Chapter 4. All the chromitites plot within the SSZ dunite field although the low-Cr type (Cr# < 0.6) plots near the boundary with MOR dunite (Figure 5.8). One chromitite from Greece is high-Cr type and plots in the SSZ dunite field. Three chromitite samples from the U.A.E. have co-existing dunite pairs sampled from the dunite envelope of the ore body. The dunite envelopes have very similar spinel compositions to those in the chromitite ore body (Figure 5.8).

Literature

Few published analyses are available for comparison. Podiform chromitites from ophiolites, including the Bay of Islands Complex (Newfoundland), Thetford (Quebec) and Catalocak and Kayseri (Turkey) have a Cr# range of 0.4 – 0.9. They were analysed for Ga in chrome-spinel by proton microprobe (Paktunc and Cabri, 1995) but unfortunately no Ti values were published.

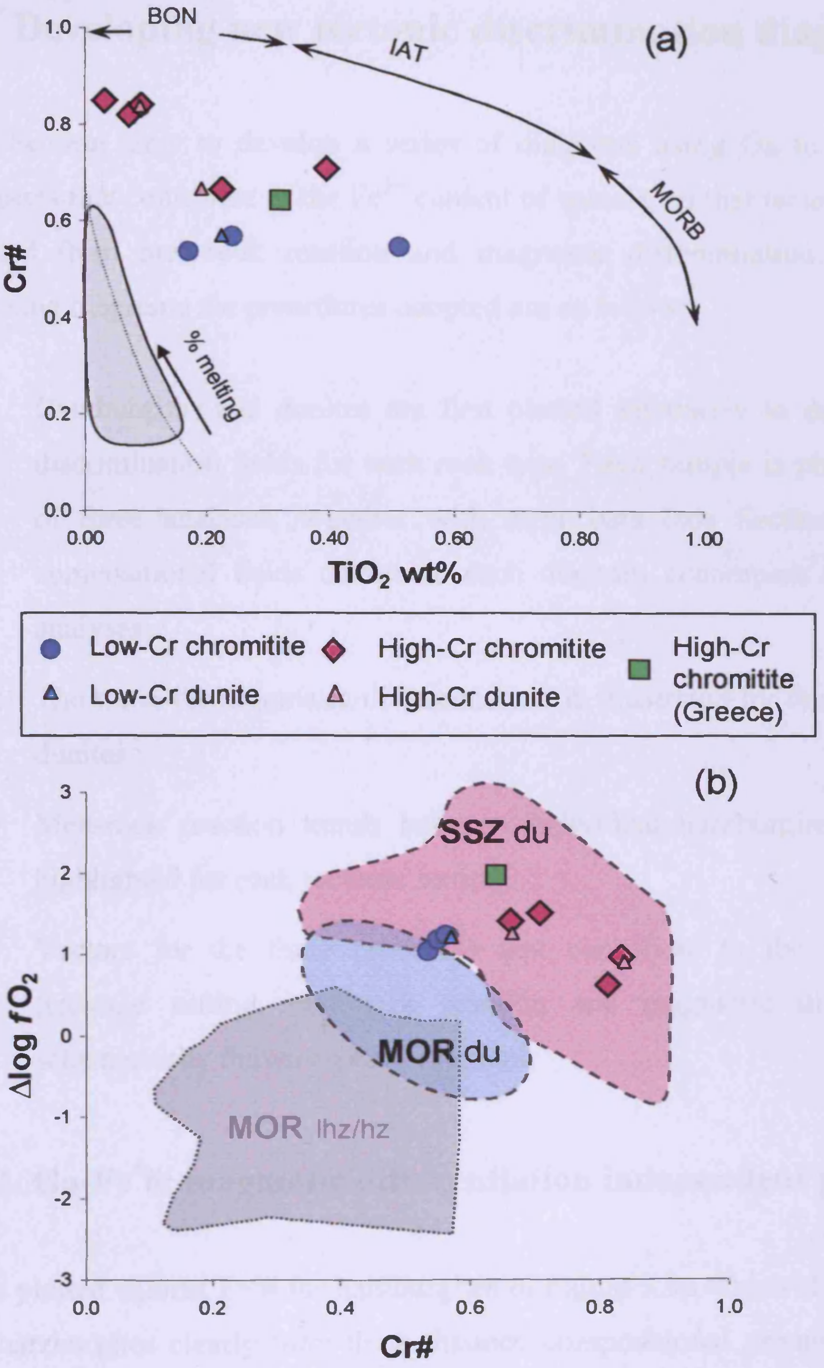

Figure 5.8: Chromitites and their co-existing dunite envelopes (from the U.A.E and Greek ophiolites) are plotted on (a) the Cr#-TiO_2 spinel diagram and (b) Cr#-fO_2 spinel diagram. In (a) the grey field approximates MOR harzburgites and plot on the partial melting trend calculated by Pearce et al., (2000). The chromitites and their dunites are displaced to higher TiO_2 than the residue trend because of melt-rock reaction. The Cr#-fO_2 diagram in (b) is used to classify chromitites and their dunites into SSZ types although the low-Cr chromitites plot on the MOR/SSZ boundary.

5.4 Developing new tectonic discrimination diagrams

This Section aims to develop a series of diagrams using Ga to resolve all three processes that contribute to the Fe^{3+} content of spinels, so that tectonic setting can be isolated from melt-rock reaction and magmatic differentiation. In each of the following diagrams the procedures adopted are as follows:

1. Harzburgites and dunites are first plotted separately to define the tectonic discrimination fields for each rock type. Each sample is plotted as the mean of three analyses, together with error bars (see Section 5.2.2), but the compositional fields drawn on each diagram encompass all the individual analyses.
2. The trend for magmatic differentiation is illustrated by the three Hess Deep dunites.
3. Melt-rock reaction trends between individual harzburgite-dunite pairs are highlighted for each tectonic setting.
4. Vectors for the three processes that contribute to the variation in Fe^{3+} (tectonic setting, melt-rock reaction and magmatic differentiation) are schematically drawn on each diagram.

5.4.1 Ga-Fe^3#: magmatic differentiation independent proxy

Ga is plotted against Fe^3# for harzburgites in Figure 5.9a which shows that modern-day harzburgites clearly form three distinct, compositional groups for PCM, MOR and SSZ tectonic settings. Ga/Fe^3# ratios, marked on Figure 5.9a, decrease in the order PCM > MOR > SSZ setting and so define boundaries between these three tectonic settings. Overlap in harzburgite compositions at the MOR-SSZ boundary arises from the two SSZ harzburgite samples which represent pre-existing MOR residues, and therefore should plot in the MOR field.

Ga is plotted against $Fe^3\#$ for dunites in Figure 5.9b. The modern-day dunites form two distinct, compositional groups for MOR and SSZ settings. A single $Ga/Fe^3\#$ ratio, marked on Figure 5.9b, defines the tectonic boundary between MOR and SSZ, and SSZ dunites have lower $Ga/Fe^3\#$ ratios than MOR dunites. Chrome-spinel from an IAT lava, analysed by proton-microprobe (Ewart and Griffin, 1995), has a low $Ga/Fe^3\#$ ratio within the SSZ dunite field. It has Ga and $Fe^3\#$ compositions very similar to those of the South Sandwich dunites; this is expected because they both have very similar Cr#, TiO_2 and fO_2 as well.

Figure 5.9 illustrates that $Ga/Fe^3\#$ ratios define tectonic boundaries. It is then important to understand how the ratios are affected by magmatic differentiation and melt-rock reaction so that tectonic boundaries are not mistakenly crossed by any processes other than a change in tectonic setting or melt-rock reaction associated with a change in tectonic setting.

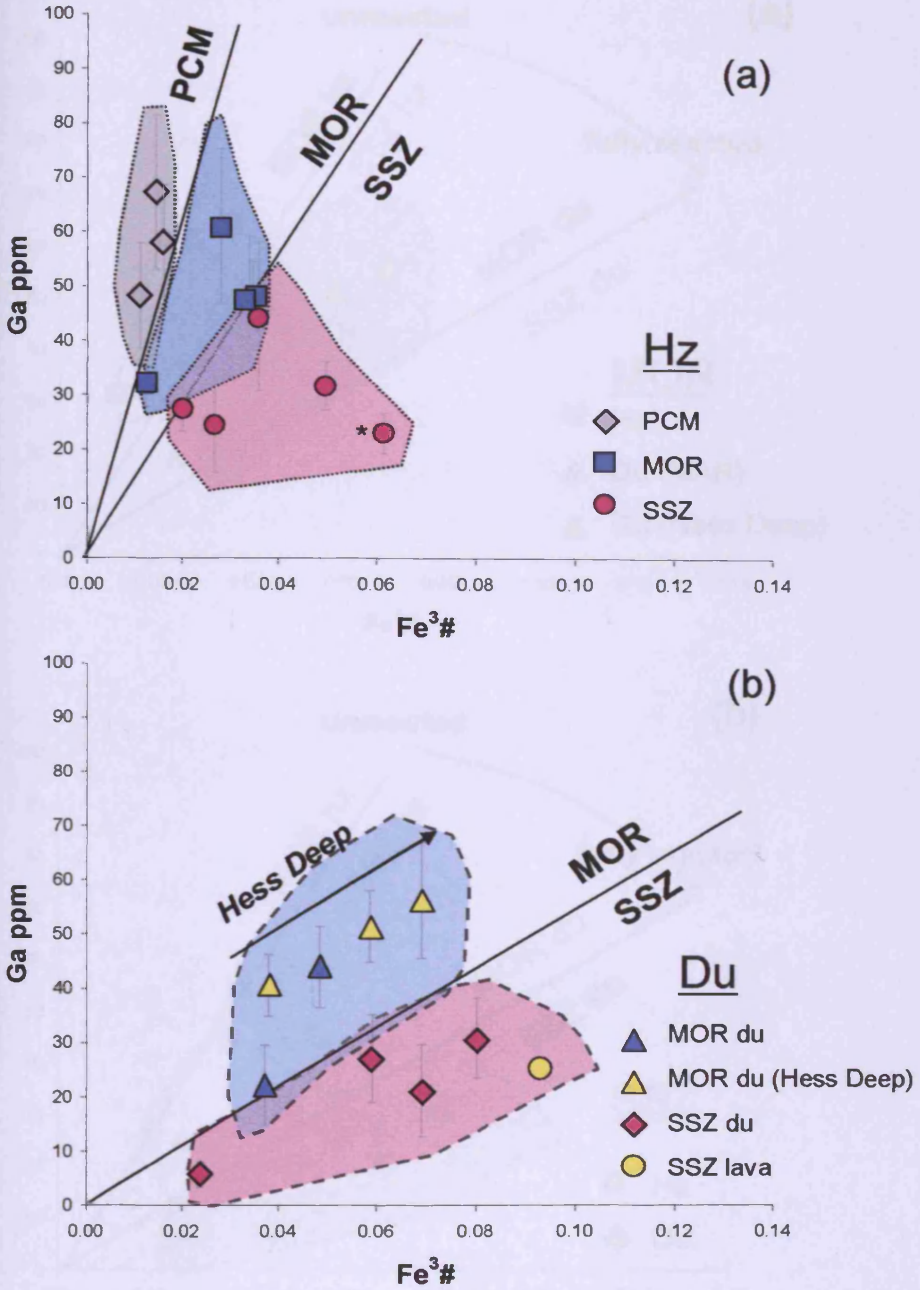

Figure 5.9: Ga vs. Fe^3# diagram defined by modern-day peridotites for the discrimination of (a) harzburgites and (b) dunites into PCM (grey field), MOR (blue field) and SSZ (pink field) settings. Solid lines represent Ga/Fe^3# ratios and define the tectonic boundaries. In (a) * marks residual SSZ harzburgite from Torishima Forearc Seamount. In (b) the arrow illustrates reaction of Hess Deep dunites with an evolving MORB melt and demonstrates that Ga/Fe^3# ratios are independent of magmatic differentiation. Spinel data from an IAT lava (Ewart and Griffin, 1995) plots in the SSZ dunite field.

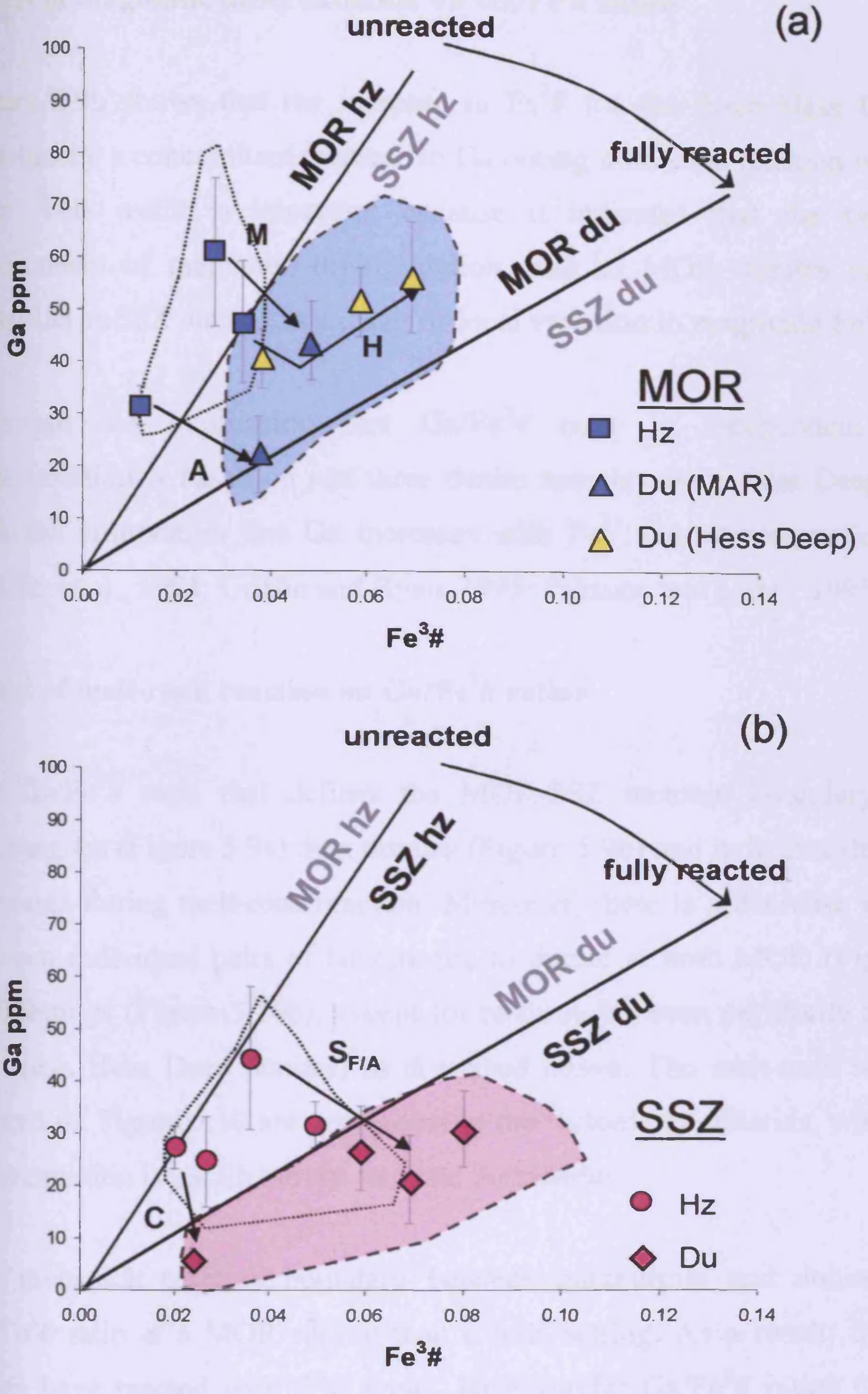

Figure 5.10: Spinel melt-rock reaction trends (arrows) between pairs of harzburgites (hz-unshaded field) and dunites (du-shaded field) in Ga-Fe^3# space at (a) MOR and (b) SSZ settings. Solid lines represent Ga/Fe^3# ratios and define the tectonic boundaries which are gradational from unreacted to fully reacted. In (a) arrows mark melt-rock reaction trends between harzburgite-dunite pairs for MAR Site 670 (Trend M), Azores Site 558 (Trend A) and Hess Deep (Trend H). In (b) arrows mark melt-rock reaction trends for peridotites from Conical Forearc Seamount (Trend C) and South Sandwich Forearc (Trend $S_{F/A}$).

Effect of magmatic differentiation on Ga/Fe^3# ratios

Figure 5.9b shows that the increase in Fe^3# for the three Hess Deep dunites is matched by a concomitant increase in Ga during melt-rock reaction with an evolving melt. This result is important because it indicates that the Ga/Fe^3# ratio is independent of magmatic differentiation, and so MOR dunites can not be mis-classified as SSZ dunites as a result of local variation in magmatic Fe^{3+}.

Although the implication that Ga/Fe^3# ratio is independent of magmatic differentiation is based on just three dunite samples from Hess Deep. It does agree with the observation that Ga increases with Fe^{3+} during magmatic differentiation (Griffin et al., 1994; Griffin and Ryan, 1995; Paktunc and Cabri; 1995).

Effect of melt-rock reaction on Ga/Fe^3# ratios

The Ga/Fe^3# ratio that defines the MOR-SSZ tectonic boundary is higher for harzburgites (Figure 5.9a) than dunites (Figure 5.9b) and indicates that Ga/Fe^3# ratio decreases during melt-rock reaction. Moreover, there is a decrease in Ga/Fe^3# ratio between individual pairs of harzburgite to dunite at both MOR (Figure 5.10a) and SSZ settings (Figure 5.10b), except for reaction between peridotite and an evolving melt (e.g. Hess Deep dunites) as described above. The melt-rock reaction tie-lines marked on Figure 5.10 are orthogonal to the tectonic boundaries, whereas magmatic differentiation is parallel to the tectonic boundaries.

The melt-rock reaction boundary between harzburgite and dunite has a higher Ga/Fe^3# ratio at a MOR setting than a SSZ setting. As a result, SSZ harburgites, which have reacted with SSZ melts, have similar Ga/Fe^3# ratios to MOR dunites (Figure 5.10). In addition, SSZ harzburgite from the Torishima Forearc Seamount, which represents residual mantle from SSZ setting has a similar Ga/Fe^3# ratio to that of SSZ dunites.

Because the tectonic boundary between MOR and SSZ is dependent on the melt-rock reaction experienced by the peridotite, it is likely to be gradational from harzburgites (unreacted) to dunites (fully reacted) (Figure 5.10). Therefore, it is important to be able to distinguish the degree of melt-rock reaction experienced by the peridotite in order to successfully discriminate the tectonic setting.

Ga/Fe^3# is plotted against Cr# in Figure 5.11 and shows that the Ga/Fe^3# ratio generally decreases with an increase in Cr# as a result of a change from PCM to MOR to SSZ setting, as well in respect to melt-rock reaction. The tectonic boundaries marked on Figure 5.10 are nearly perpendicular to the negative trend between Ga/Fe^3# and Cr# and illustrate the following points.

1. Tectonic boundaries defined by Ga/Fe^3# ratios are not fixed and the Ga-Fe^3# diagram is not sufficient to use in isolation.
2. Because Ga/Fe^3# ratios are partly dependent on Cr#, the Cr# vs. Ga/Fe^3# plot can discriminate between peridotites with similar Ga/Fe^3# ratios and with similar Cr#.
3. The compositional fields for SSZ harzburgites and MOR dunites still overlap in Cr#-Ga/Fe^3# space.

The finalised Ga-Fe^3# and Cr# vs. Ga/Fe^3# diagrams are presented in Figure 5.12 with discrimination fields labelled for each diagram. The discrimination fields which are labelled 'hz/du' represent harzburgites as well as dunites which have reacted with melt. Fields which are labelled lhz/hz represent residual peridotites which could be lherzolites as well as harzburgites. Vectors for magmatic differentiation, melt-rock reaction and tectonic setting are schematically marked on Figure 5.12 and show that Ga/Fe^3# ratio is here found to be independent of magmatic differentiation but dependent on melt-rock reaction and tectonic setting. Discrimination fields for PCM lhz/hz, MOR lhz/hz and SSZ hz/du are distinct, but there is overlap between SSZ hz and MOR du fields on both Ga-Fe^3# and Cr# vs. Ga/Fe^3# diagrams in Figure 5.12.

The Ga/Fe^3# ratio is dependent on its tectonic setting for a given amount of melt-rock reaction. Discrimination of dunites is quite clear but discrimination of harzburgites, which could experience a wide extent of melt-rock reaction, is not so well defined. Consequently, another proxy is required to assess more reliably the degree of melt-rock reaction in order to resolve tectonic discrimination when using Ga/Fe^3# ratios.

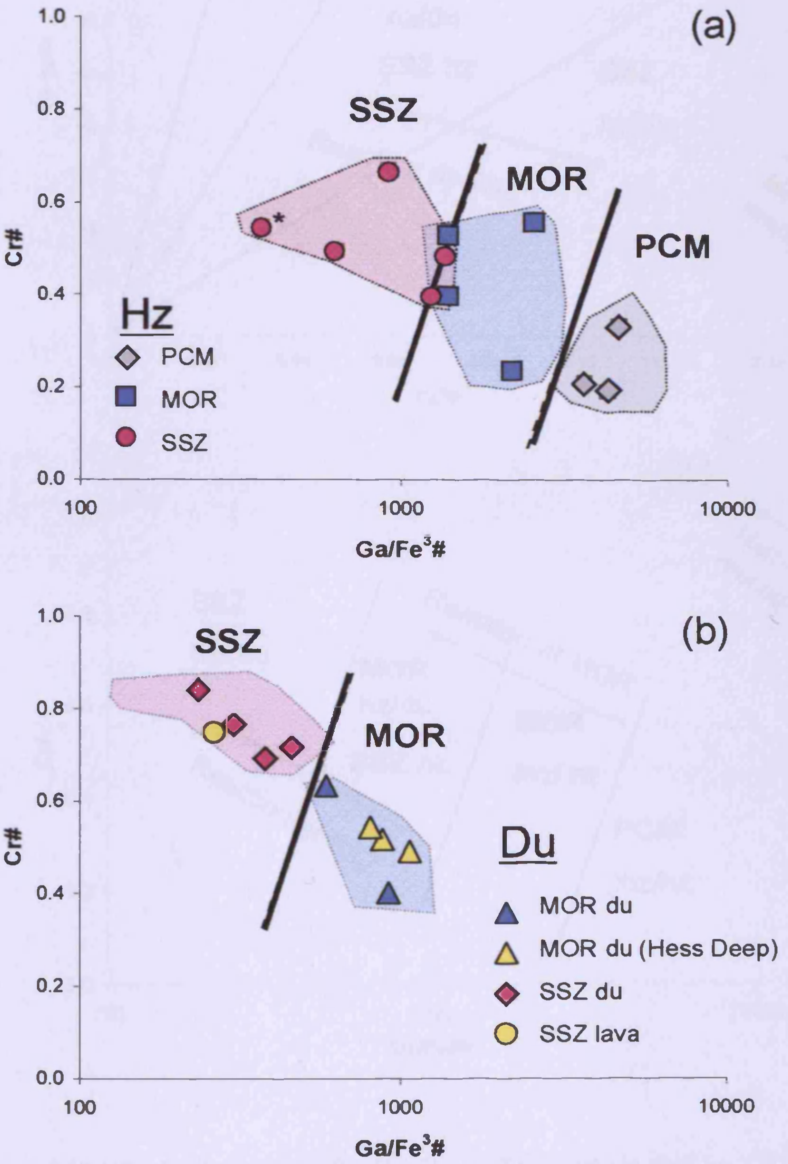

Figure 5.11: Cr# vs. Ga/Fe^3# diagram defined by modern-day peridotites for the discrimination of (a) harzburgites and (b) dunites into PCM (grey field), MOR (blue field) and SSZ (pink field) settings. Solid line marks tectonic boundaries. In (a) * marks residual SSZ harzburgite from Torishima Forearc Seamount. In (b) Ga/Fe^3# ratios independent of magmatic differentiation and thus Hess Deep dunites have near constantGa/Fe^3# ratios. Spinel data are from and IAT lava analysed by Ewart and Griffin (1995).

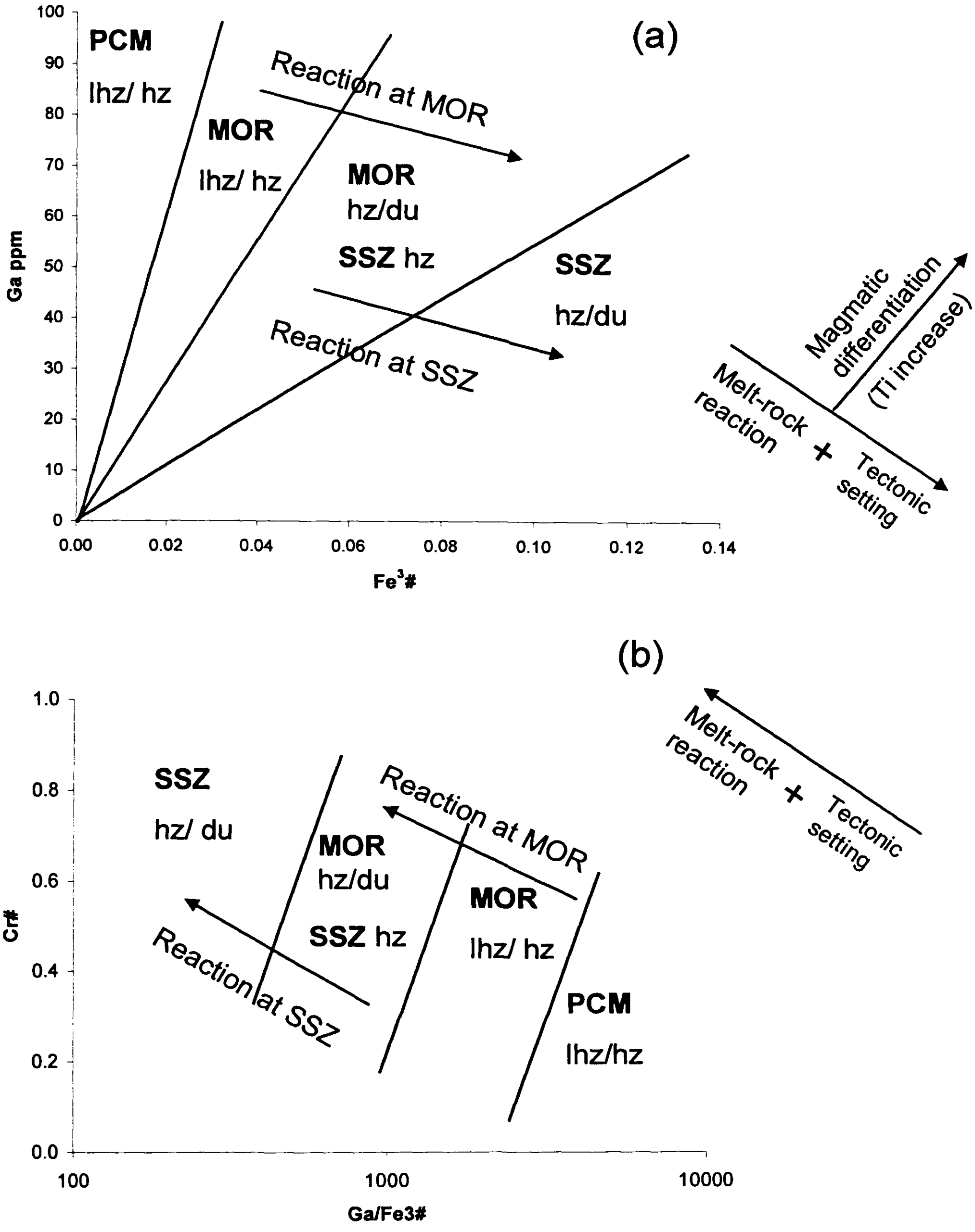

Figure 5.12: Finalised diagrams for (a) Ga vs. Fe^3# and (b) Cr# vs. Ga/Fe^3# which discriminate peridotites into four fields: PCM residual lhz/hz, MOR lhz/hz, SSZ hz/du and an overlapping field for MOR hz/du and SSZ hz. Vectors are marked schematically for tectonic setting, melt-rock reaction and magmatic differentiation. They show that Ga/Fe^3# ratios are independent of magmatic differentiation but dependent on both tectonic setting and melt-rock reaction.

5.4.2 TiO_2-Fe^3#: melt-rock reaction dependent proxy

TiO_2 is a sensitive fingerprint of melt-rock reaction because it is depleted after partial melting and enriched during interaction with a melt. As both TiO_2 and Fe^3# increase during magmatic differentiation, Arai (1992) used the TiO_2-Fe^3# diagram (Figure 5.13a) to discriminate chrome-spinel phenocrysts from MORB magmas (high Ti/Fe^3# ratios) and arc magmas (lower Ti/Fe^3# ratios) of similar Cr# compositions (0.4 – 0.6), where Ti/Fe^3# = TiO_2/Fe^3#. The MORB and arc magma fields in Figure 5.13a overlap at primitive low values of TiO_2 and Fe^3# which makes tectonic discrimination ambiguous for primitive melts.

TiO_2 plotted against Fe^3# in Figure 5.13b shows that residual harzburgites are depleted in TiO_2 and Fe^{3+}, whereas dunites plot to higher TiO_2 and Fe^3# and form a reaction trend between Ti-depleted harzburgites and Ti-enriched magmas. The mantle dunites analysed in this study plot at the low Ti-Fe^3# end of the trends defined by MORB and arc magmas (Figure 5.13a). This is to be expected for dunites that have reacted with the most primitive of melts and makes tectonic discrimination ambiguous for dunites using the TiO_2-Fe^3# diagram alone. The suite of dunites from Hess Deep, which has reacted with an evolving MORB melt, forms a reaction trend parallel to the magmatic differentiation trend of MORB magmas (Figure 5.13b).

In this study, the Ti/Fe^3# ratio is used as a proxy for melt-rock reaction for which Ti/Fe^3# increases. Residual harzburgite from SSZ settings (e.g. Torishima harzburgite, IBM forearc) has a lower Ti/Fe^3# ratio than SSZ harzburgites that have reacted with SSZ melts, because the former has spinels depleted in TiO_2 and enriched in Fe^{3+} as a result of hydrous melting. Furthermore, Ti/Fe^3# is dependent on tectonic setting: melt-rock reaction at a MOR setting causes a larger increase in Ti/Fe^3# than melt-rock reaction at a SSZ setting. The suite of harzburgites and dunites from the South Sandwich forearc illustrates that the Ti/Fe^3# ratio can remain nearly constant during melt-rock reaction with a SSZ melt.

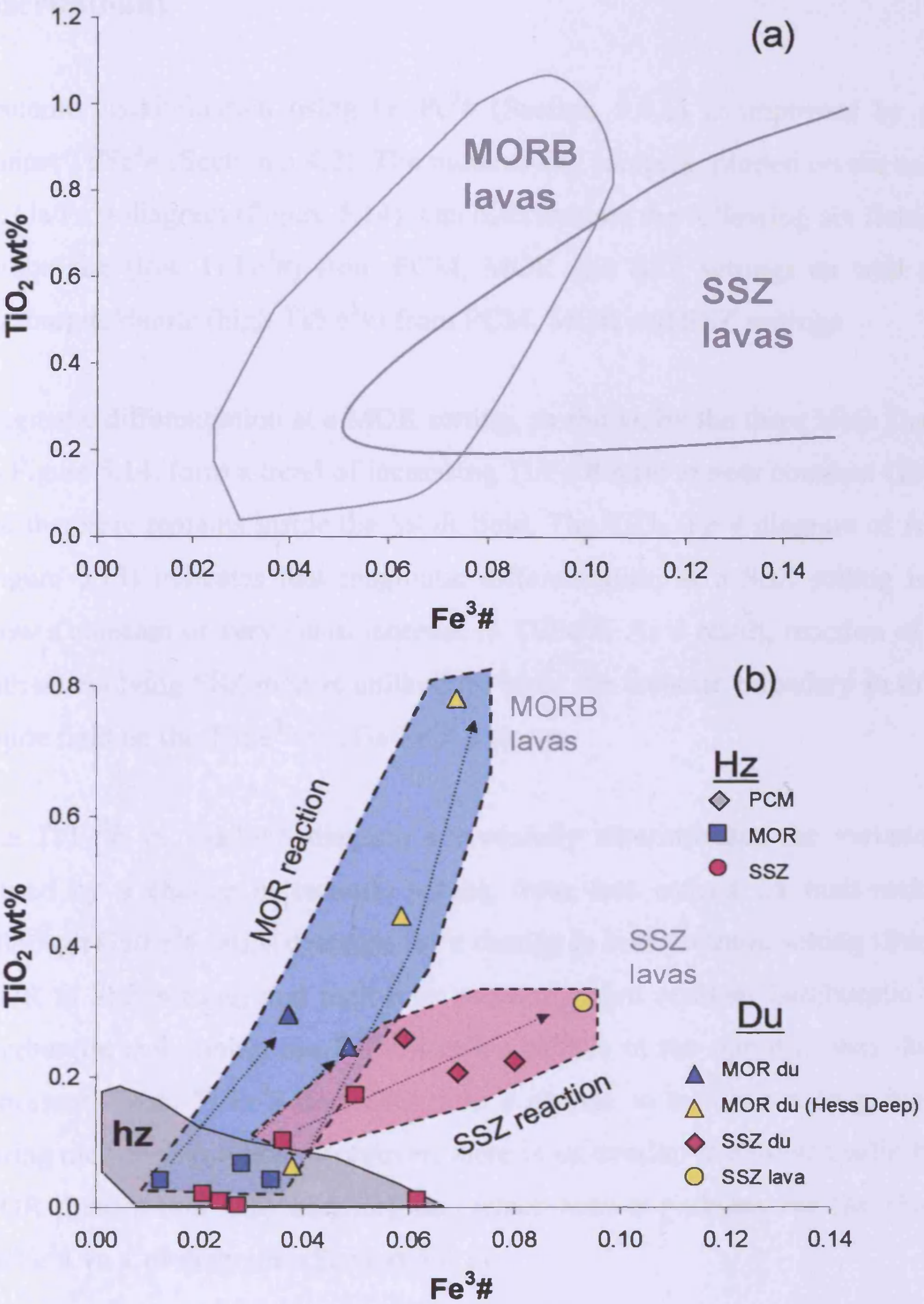

Figure 5.13: TiO_2 vs $Fe^{3}\#$ diagram for (a) the discrimination of spinel phenocrysts into MORB and SSZ lavas (discrimination fields after Arai, 1992) and (b) to show that Ti/$Fe^{3}\#$ ratios monitor melt-rock reaction at MOR and SSZ settings. In (b) the grey field approximates spinel compositions of harzburgites (Dick and Bullen, 1984; Parkinson and Pearce, 1998). Both TiO_2 and Fe^{3+} in peridotite spinel increase during melt-rock reaction and during magmatic differentiation (as shown by the suite of Hess Deep dunites)

5.4.3 Ti/Fe^3# vs. Ga/Fe^3#: a new petrogenetic and tectonic setting discriminant

Tectonic discrimination using Ga/Fe^3# (Section 5.4.1) is improved by plotting it against Ti/Fe^3# (Section 5.4.2). The modern-day samples, plotted on the new Ti/Fe^3# vs. Ga/Fe^3# diagram (Figure 5.14), can discriminate the following six fields: residual harzburgite (low Ti/Fe^3#) from PCM, MOR and SSZ settings as well as reacted harzburgite/dunite (high Ti/Fe^3#) from PCM, MOR and SSZ settings.

Magmatic differentiation at a MOR setting, as shown by the three Hess Deep dunites on Figure 5.14, form a trend of increasing Ti/Fe^3# ratio at near constant Ga/Fe^3# ratio and therefore remains inside the MOR field. The TiO_2 -Fe^3# diagram of Arai (1992) (Figure 5.13) indicates that magmatic differentiation at a SSZ setting is likely to show a constant or very small increase in Ti/Fe^3#. As a result, reaction of peridotite with an evolving SSZ melt is unlikely to cross the tectonic boundary in to the MOR dunite field on the Ti/Fe^3# vs. Ga/Fe^3# diagram.

The Ti/Fe^3# vs. Ga/Fe^3# diagram successfully discriminates the variation in Fe^{3+} caused by a change in tectonic setting from that caused by melt-rock reaction. Although Ga/Fe^3# ratios decrease for a change in both tectonic setting (from PCM to MOR to SSZ setting) and melt-rock reaction (from residual harzburgite to reacted harzburgite and dunite) the Ti/Fe^3# ratios behave in the opposite way during these processes. Thus, Ti/Fe^3# decreases with a change in tectonic setting, but increases during melt-rock reaction. Moreover, there is no overlap at similar Ga/Fe^3# ratios for MOR dunites and SSZ harzburgites, which was a problem for the Ga-Fe^3# and Ga/Fe^3# vs. Cr# diagrams (Section 5.4.1).

Tie-lines between harzburgite-dunite pairs illustrate melt-rock reaction at MOR (Figure 5.15a) and SSZ settings (Figure 5.15b). The vector for melt-rock reaction is different between MOR and SSZ settings: at a MOR setting the decrease in Ga/Fe^3# ratio is accompanied by a greater increase in Ti/Fe^3# than at a SSZ setting, which has a near constant Ti/Fe^3# during melt-rock reaction with SSZ melts.

The finalised Ti/Fe^3# vs. Ga/Fe^3# diagram is presented in Figure 5.16 with each of the six discrimination fields clearly labelled. The vectors marked on Figure 5.16 for magmatic differentiation, melt-rock reaction and tectonic setting, are clearly resolved in Ti/Fe^3# - Ga/Fe^3# space, and therefore tectonic discrimination can be tested on peridotites of different petrogenetic origin and tectonic setting.

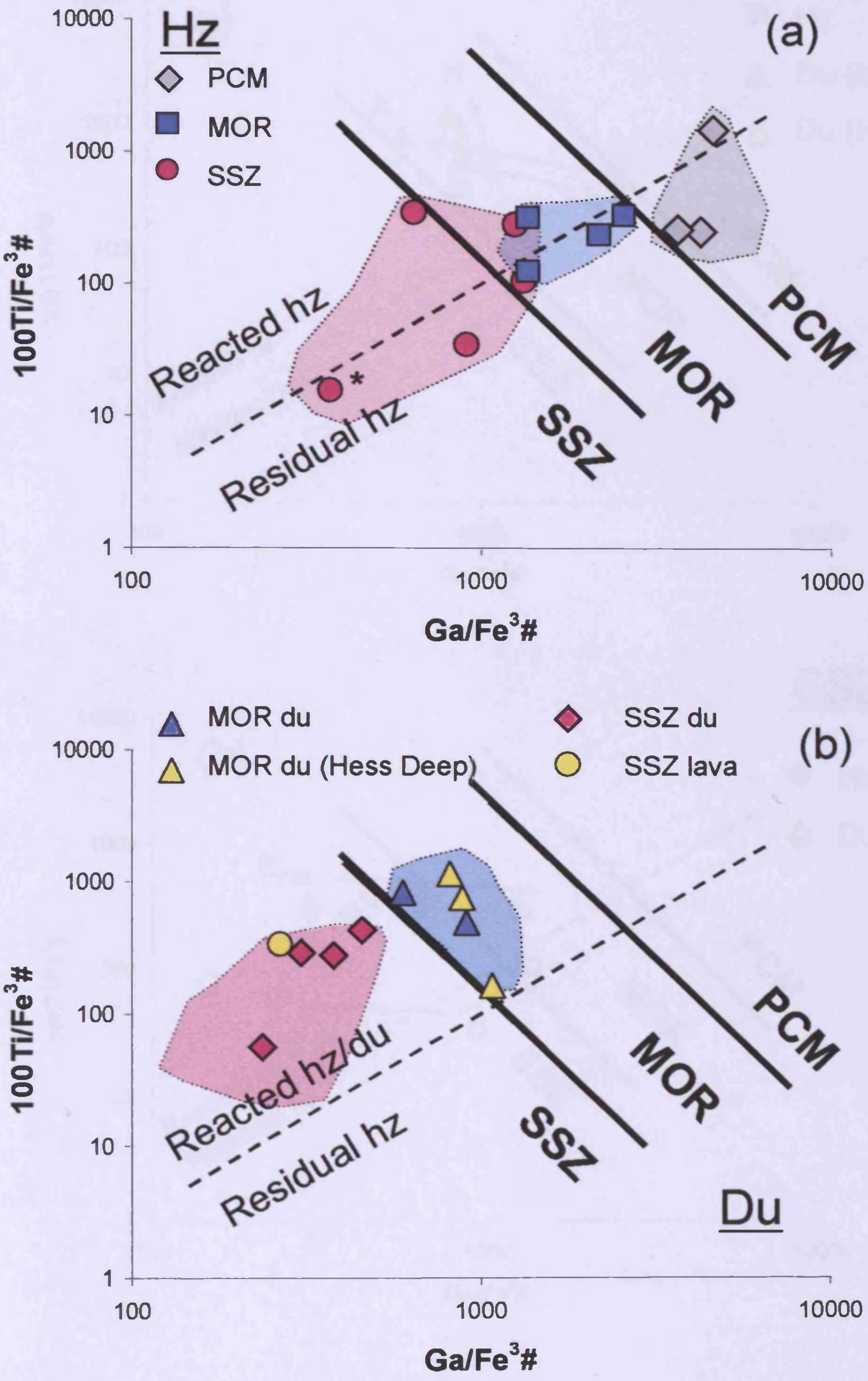

Figure 5.14: $Ti/Fe^3\#$ vs. $Ga/Fe^3\#$ defined by modern-day peridotites for the discrimination of (a) harzburgites and (b) dunites into residual and reacted peridotites at PCM (grey field), MOR (blue field) and SSZ (pink field) settings. * marks residual SSZ harzburgite from Torishima Forearc Seamount. Spinel data from an IAT lava are from Ewart and Griffin (1995).

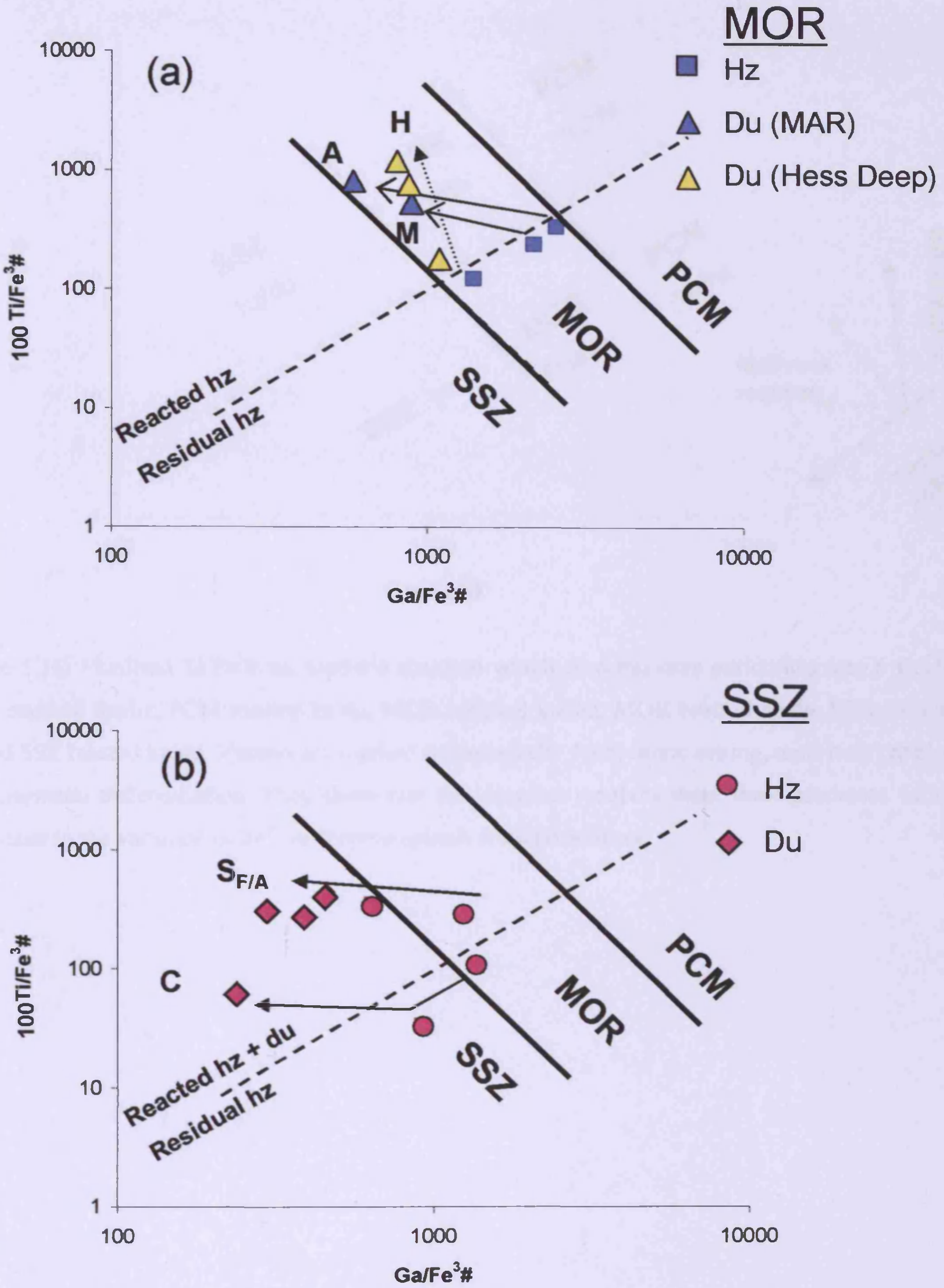

Figure 5.15: Spinel melt-rock reaction trends (arrows) between pairs of harzburgites and dunites in Ti/Fe^3# - Ga/Fe^3# space at (a) MOR and (b) SSZ settings. Solid lines define the tectonic boundaries and dashed line defines the boundary between residual and reacted peridotites. See text for further explanation. In (a) arrows mark melt-rock reaction trends between harzburgite-dunite pairs for MAR Site 670 (Trend M), Azores Site 558 (Trend A) and Hess Deep (Trend H). In (b) arrows mark melt-rock reaction trends for peridotites from Conical Forearc Seamount (Trend C) and South Sandwich Forearc (Trend S$_{F/A}$).

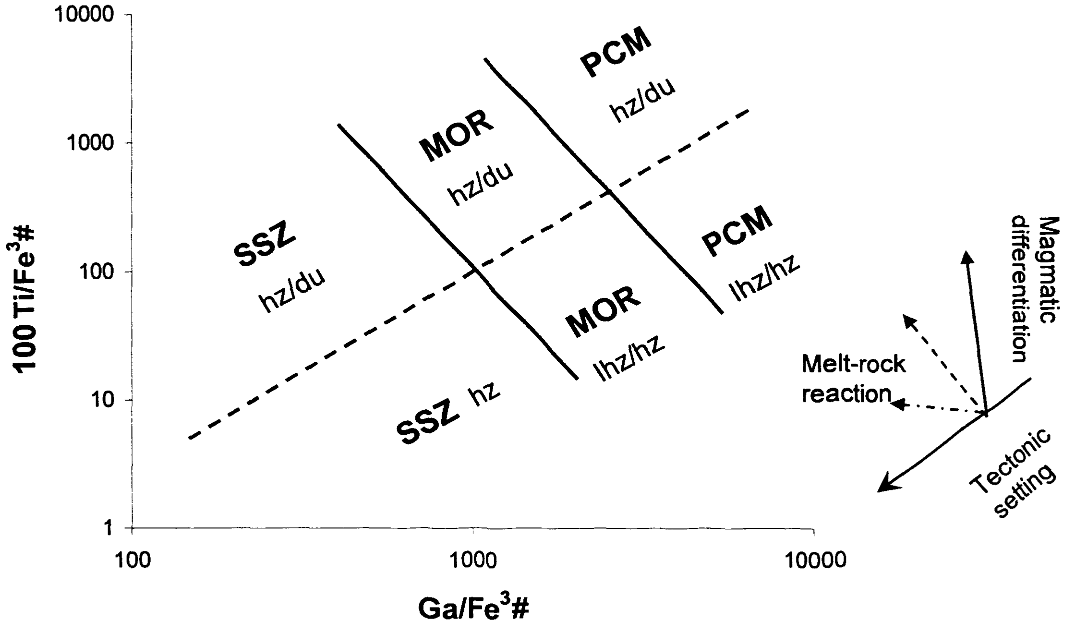

Figure 5.16: Finalised Ti/Fe^3# vs. Ga/Fe^3# diagram which discriminates peridotites into 6 fields: PCM residual lhz/hz, PCM reacted hz/du, MOR residual lhz/hz, MOR reacted hz/du, SSZ residual hz and SSZ reacted hz/du. Vectors are marked schematically for tectonic setting, melt-rock reaction and magmatic differentiation. They show that this diagram resolves these three processes which contribute to the variation of Fe^{3+} in chrome-spinels from peridotites.

5.5 Testing new tectonic discrimination diagrams on ophiolitic samples

The test consists of plotting the ophiolite samples, discriminated into MOR and SSZ tectonic origin using Cr#-fO_2 (Section 5.3.3), on the new Ti/Fe^3# vs. Ga/Fe^3# diagram to see if the samples fall in the corresponding discrimination fields established in Section 5.4.3. But first, the ophiolite samples are also plotted on the Ga-Fe^3# and. Ga/Fe^3# vs. Cr# diagrams to evaluate if the Ga data, and thus Ga/Fe^3# ratios, are comparable to that analysed for the modern-day samples.

5.5.1 Harzburgites

The ophiolitic harzburgites plot in the same region as modern-day harzburgites on the Ga-Fe^3# and Cr# vs. Ga/Fe^3# diagrams (Figure 5.17) and indicates that Ga/Fe^3# ratios are comparable between the modern-day and ophiolite samples. However, Sample 6 is clearly different from the other harzburgites, because it has a much higher Ga and Fe^3# values similar to the most evolved Hess Deep dunite (Figure 5.17a).

The U.A.E. and Greek harzburgites, which were classified into the MOR, MOR/SSZ and SSZ types in Section 5.3.3., are tested on the Ti/Fe^3# vs. Ga/Fe^3# discrimination diagram in Figure 5.18. The harzburgites fall along the boundary between residual and reacted harzburgites from MOR and SSZ settings.

The MOR ophiolitic harzburgites plot within the MOR compositional field on the Ti/Fe^3# vs. Ga/Fe^3# diagram, and close to the MOR harzburgite-dunite boundary. Sample SD19, which is enriched in TiO_2, plots clearly in the MOR dunite field, thereby indicating that it had experienced a significant melt-rock reaction with a MOR melt.

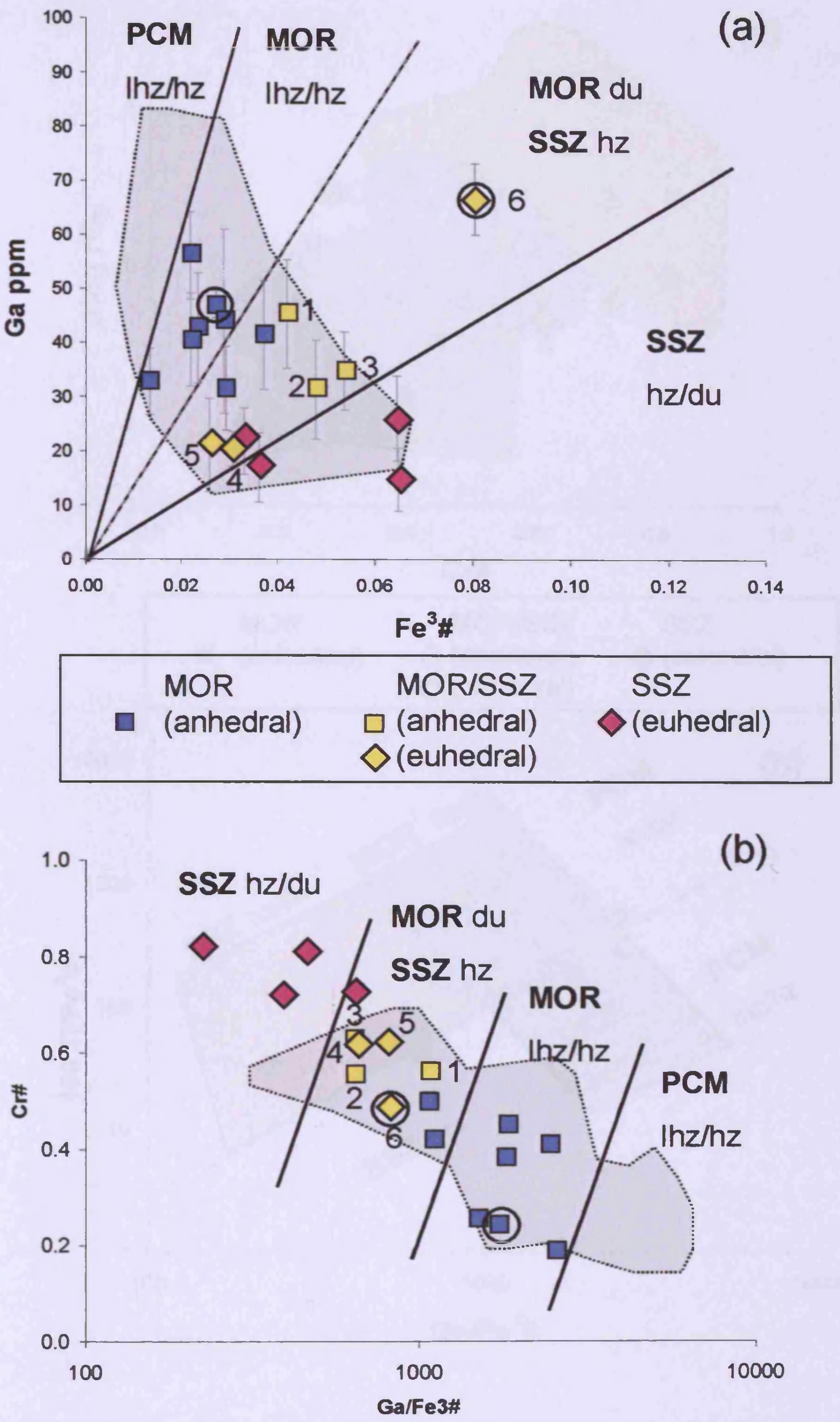

Figure 5.17: Harzburgites from the UAE and Greek ophiolites, classified as MOR, MOR/SSZ and SSZ by Cr#-fO_2, plotted on (a) Ga vs. Fe^3# and (b) Cr# vs. Ga/Fe^3# diagrams. They show that the Ga data is comparable to the range measured in modern-day samples (grey shaded fields). Greek harzburgite spinels are circled, to distinguish them from the U.A.E. harzburgite spinels.

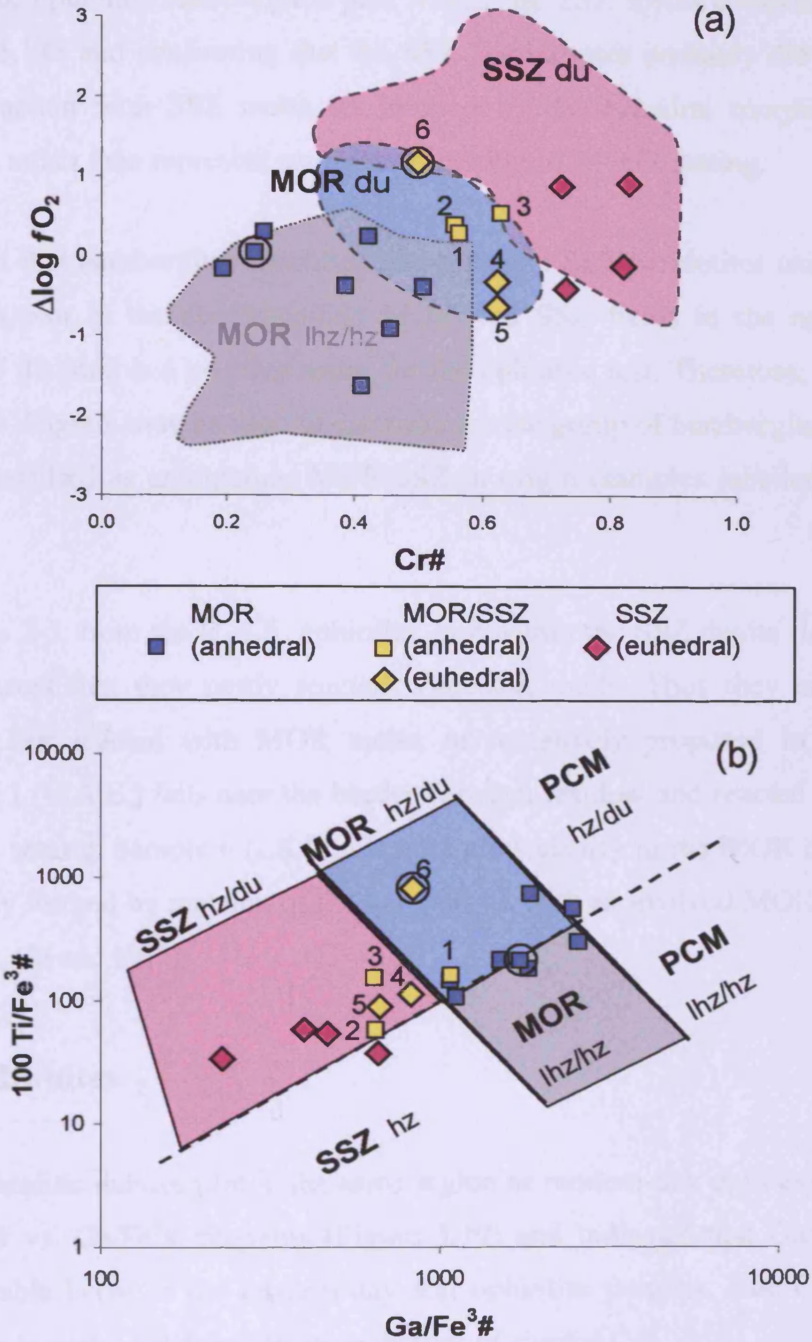

Figure 5.18: Harzburgites from the U.A.E and Greek ophiolites: (a) classified as MOR, MOR/SSZ and SSZ by the Cr#-fO_2 diagram, and (b) plotted on the Ti/Fe^3# vs. Ga/Fe^3# diagram to test the discrimination fields: MOR lhz/hz (grey), MOR reacted hz/du (blue) and SSZ reacted hz/du (pink). The MOR/SSZ harzburgites (marked 1-6) which were ambiguous on Cr#-fO_2 diagram are clearly discriminated on the Ti/Fe^3# vs. Ga/Fe^3# diagram. Greek harzburgite spinels are circled, to distinguish them from the U.A.E. harzburgite spinels.

The SSZ ophiolitic harzburgites plot within the SSZ hz/du compositional field in Figure 5.18b and confirming that the SSZ harzburgites probably did form by melt-rock reaction with SSZ melts, as implied by the euhedral morphology of their spinels, rather than represent residues of melting in an SSZ setting.

The fact that harzburgites identified as MOR and SSZ peridotites using the Cr#-fO_2 diagram plot in the corresponding MOR and SSZ fields in the new Ti/Fe^3# vs. Ga/Fe^3# diagram is a positive result for the ophiolite test. Therefore, the Ti/Fe^3# vs. Ga/Fe^3# diagram may be used to discriminate the group of harzburgites that formerly were classified as ambiguous, MOR/SSZ in origin (samples labelled 1-6 in Figure 5.18).

Samples 2-5, from the U.A.E. ophiolite, plot within the SSZ dunite field and support the concept that they partly reacted with SSZ melts. Thus they are neither SSZ residue nor reacted with MOR melts, as tentatively proposed in Section 5.3.3. Sample 1 (U.A.E.) falls near the border between residual and reacted peridotite from a MOR setting. Sample 6 (LK44, Greece) plots clearly in the MOR dunite field and probably formed by reaction of the harzburgite with an evolved MOR melt, enriched in TiO_2, Ga and Fe^{3+}.

5.5.2 Dunites

The ophiolitic dunites plot in the same region as modern-day dunites on the Ga-Fe^3# and Cr# vs. Ga/Fe^3# diagrams (Figure 5.19) and indicates that Ga/Fe^3# ratios are comparable between the modern-day and ophiolite samples. The Cr# vs. Ga/Fe^3# diagram is useful for discriminating dunites of similar Cr#.

The U.A.E. and Greek dunites, which were classified into the MOR, MOR/SSZ and SSZ types in Section 5.3.3, are tested on the Ti/Fe^3# vs. Ga/Fe^3# discrimination diagram in Figure 5.20. The dunites plot within the dunite fields from MOR and SSZ settings. The SSZ dunites and the single MOR dunite correspond to the SSZ and MOR dunite fields, respectively, in the new Ti/Fe^3# vs. Ga/Fe^3# diagram (Figure

5.20b) and the SSZ lava also plots within the SSZ dunite field. This is a positive result for the ophiolite test and highlights the potential use of the Ti/Fe^3# vs. Ga/Fe^3# diagram, however it still needs to be independently verified.

Therefore, the Ti/Fe^3# vs. Ga/Fe^3# diagram may be used to discriminate the group of dunites (samples 1-7) classified previously as ambiguous (i.e. MOR/SSZ) in origin by reference to the Cr#-fO_2 diagram (Section 5.3.3). Moreover, samples 1-4 can be now re-classified as MOR-type dunites and samples 5 – 7 as SSZ-type dunites. Some of the SSZ dunites lie on the MOR/SSZ boundary on the Ga-Fe^3# plot but plot more clearly in the SSZ field in the ratio diagram.

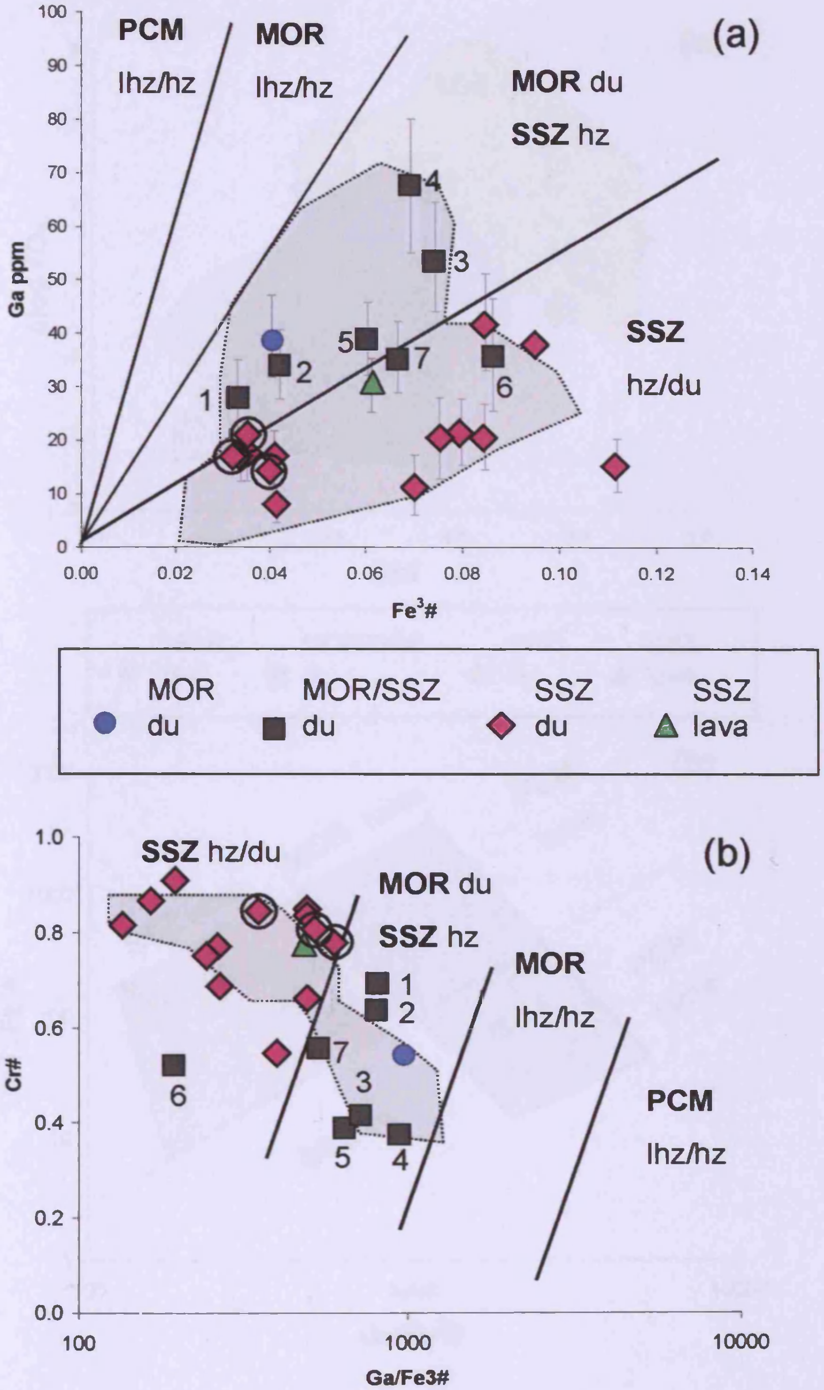

Figure 5.19: Dunites (U.A.E and Greek ophiolites) and a lava (Troodos ophiolite), classified as MOR, MOR/SSZ and SSZ by Cr#-fO_2, plotted on (a) Ga vs. Fe^3# and (b) Cr# vs. Ga/Fe^3#. They both show that the Ga data is comparable to the range measured in modern-day samples (grey shaded fields). In (b) Ga/Fe^3# ratios can discriminate dunites from MOR and SSZ settings with similar Cr# compositions. Greek dunite spinels are circled, to distinguish them from the U.A.E. dunite spinels.

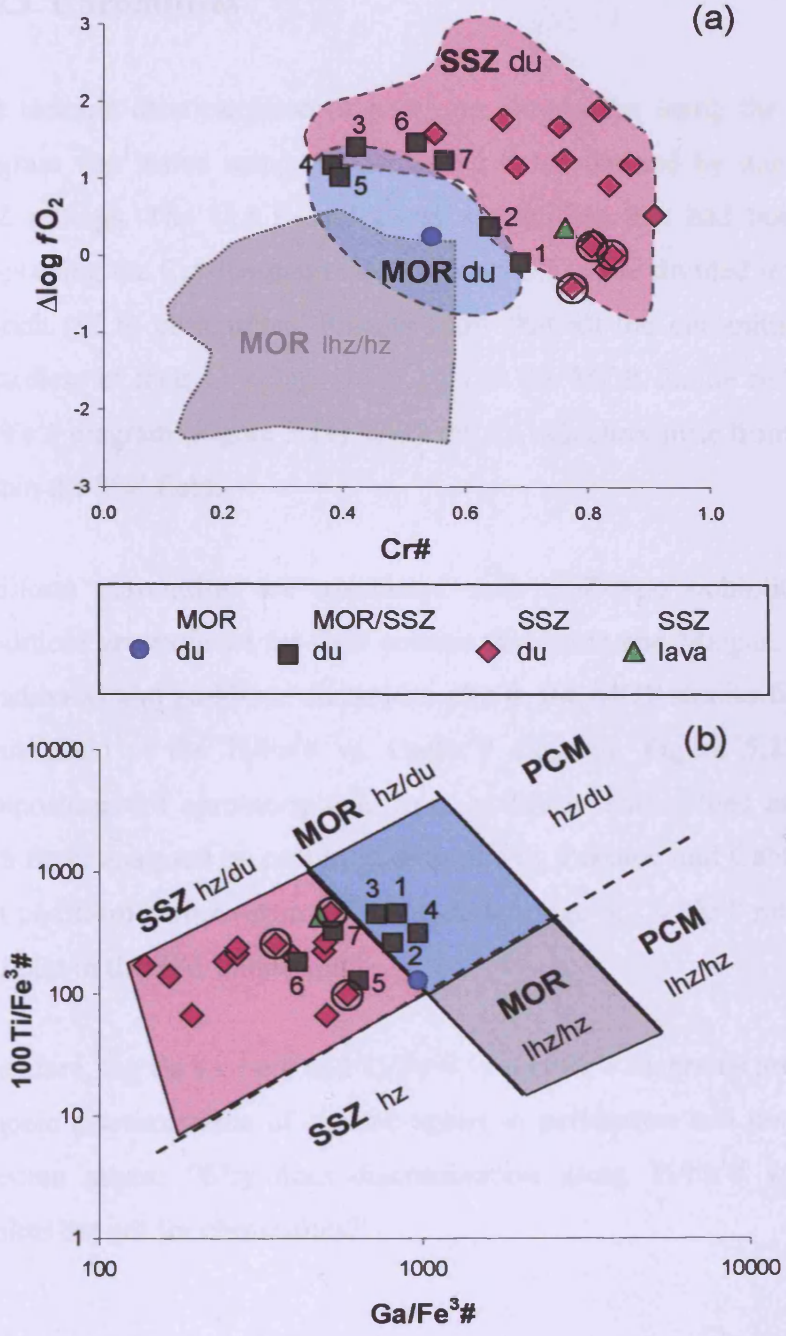

Figure 5.20: Dunites (U.A.E and Greek ophiolites) and a lava (Troodos ophiolite) classified as MOR, MOR/SSZ and SSZ by (a) Cr#-fO_2 diagram, and plotted in (b) on the $Ti/Fe^3\#$ vs. $Ga/Fe^3\#$ diagram, to test the discrimination fields; MOR lhz/hz (grey), MOR reacted hz/.du (blue) and SSZ reacted hz/du (pink). The MOR/SSZ dunites (marked 1-7), which were ambiguous on Cr#-fO_2 diagram, are clearly discriminated on $Ti/Fe^3\#$ vs. $Ga/Fe^3\#$ diagram. Greek dunite spinels are circled, to distinguish them from the U.A.E. dunite spinels.

5.5.3 Chromitites

The tectonic discrimination of podiform chromitites using the Ti/Fe^3# vs. Ga/Fe^3# diagram was tested using compositional fields defined by dunites from MOR and SSZ settings. The U.A.E. and Greek chromitites that had been classified as SSZ types using the Cr#-fO_2 diagram (Section 5.3.3) were divided into Cr-rich (>0.6) and Al-rich (<0.6) chromitites. Results show that all the chromitites from the U.A.E., regardless of their Cr-composition, plot in the MOR dunite field on the Ti/Fe^3# vs. Ga/Fe^3# diagram (Figure 5.21). Only the Cr-rich chromitite from Greece plots clearly within the SSZ field.

Podiform chromitites are associated with SSZ-type ophiolites because hydrous conditions are required for their genesis (Edwards and Malpas, 2000). It is therefore paradoxical that podiform chromitite plot in the MOR dunite field rather in the SSZ dunite field of the Ti/Fe^3# vs. Ga/Fe^3# diagram. Figure 5.22 compares Ga-Fe^3# compositions of chrome-spinels from podiform chromitites analysed in this study with those analysed by proton microprobe by Paktunc and Cabri (1995). This shows that podiform chrome-spinels have a wide range of Ga/Fe^3# ratios and that less than half plot in the SSZ dunite field.

Therefore, the Ga vs. Fe^3# and Ti/Fe^3# vs. Ga/Fe^3# diagrams are suitable only for the tectonic discrimination of chrome-spinel in peridotites and not for chromitites. The question arises: 'Why does discrimination using Ti/Fe^3# vs. Ga/Fe^3# work for dunites but not for chromitites?'

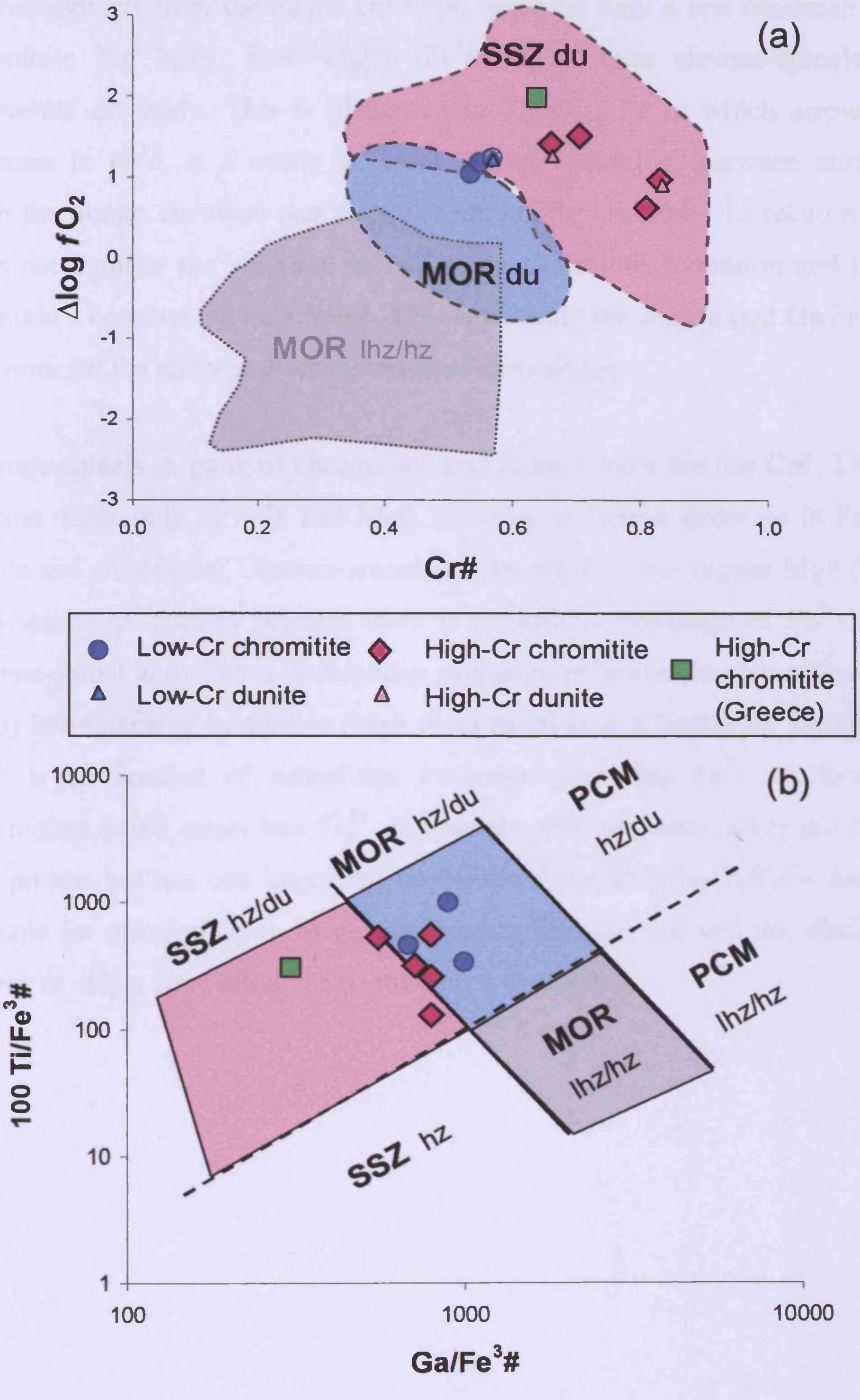

Figure 5.21: Chromitites (U.A.E and Greek ophiolites) classified as SSZ by (a) Cr#-fO_2 diagram, and (b) plotted on Ti/Fe^3# vs. Ga/Fe^3# diagram to test the discrimination fields; MOR lhz/hz (grey), MOR reacted hz/.du (blue) and SSZ reacted hz/du (pink). SSZ chromitites are classified mostly as MOR, except the Greek chromitites, using Ti/Fe^3# vs. Ga/Fe^3# diagram. Therefore, Ti/Fe^3# vs. Ga/Fe^3# diagram which works for peridotites does not work for chromitites.

Chrome-spinels from the dunite envelope, sampled only a few centimetres from the chromitite ore body, have higher Fe^3# values than chrome-spinels from the chromitite ore body. This is illustrated in Figure 5.22 in which arrows mark the decrease in Fe^3#, at a nearly constant Ga concentration, between chrome-spinels from the dunite envelope and from the chromitite ore body. In relation to this, Ga does not monitor the variation in Fe^{3+} upon chromitite formation and thus fails to maintain a constant Ga/Fe^3# value. This is possibly the reason that Ga/Fe^3# ratios do not work for the tectonic discrimination of chromitites.

Chrome-spinels in pairs of chromitites and dunites have similar Cr#, TiO_2, fO_2 and Ga and differ only in Fe^3# and Mg#. So, why is there a decrease in Fe^3# between dunite and chromitite? Chrome-spinels in chromitites have higher Mg# (lower Fe^2#) than spinels in dunites because there is subsolidus exchange of Fe^{2+}-Mg between chrome-spinel and olivine. Subsolidus exchange is limited in chromitites (low ol: sp ratio) but extensive in dunites (high ol:sp ratio) (e.g. Chapter 4). Maybe the lower Fe^3# is an artefact of subsolidus exchange involving Fe^2: i.e. lower Fe^2# in chromitites could mean less Fe^{3+}. Ultimately, this problem is beyond the scope of this project but has one important implication: the Ti/Fe^3#-Ga/Fe^3# diagram is not suitable for discrimination of detrital spinels because one can not distinguish their source of origin from either a peridotite or a chromitite.

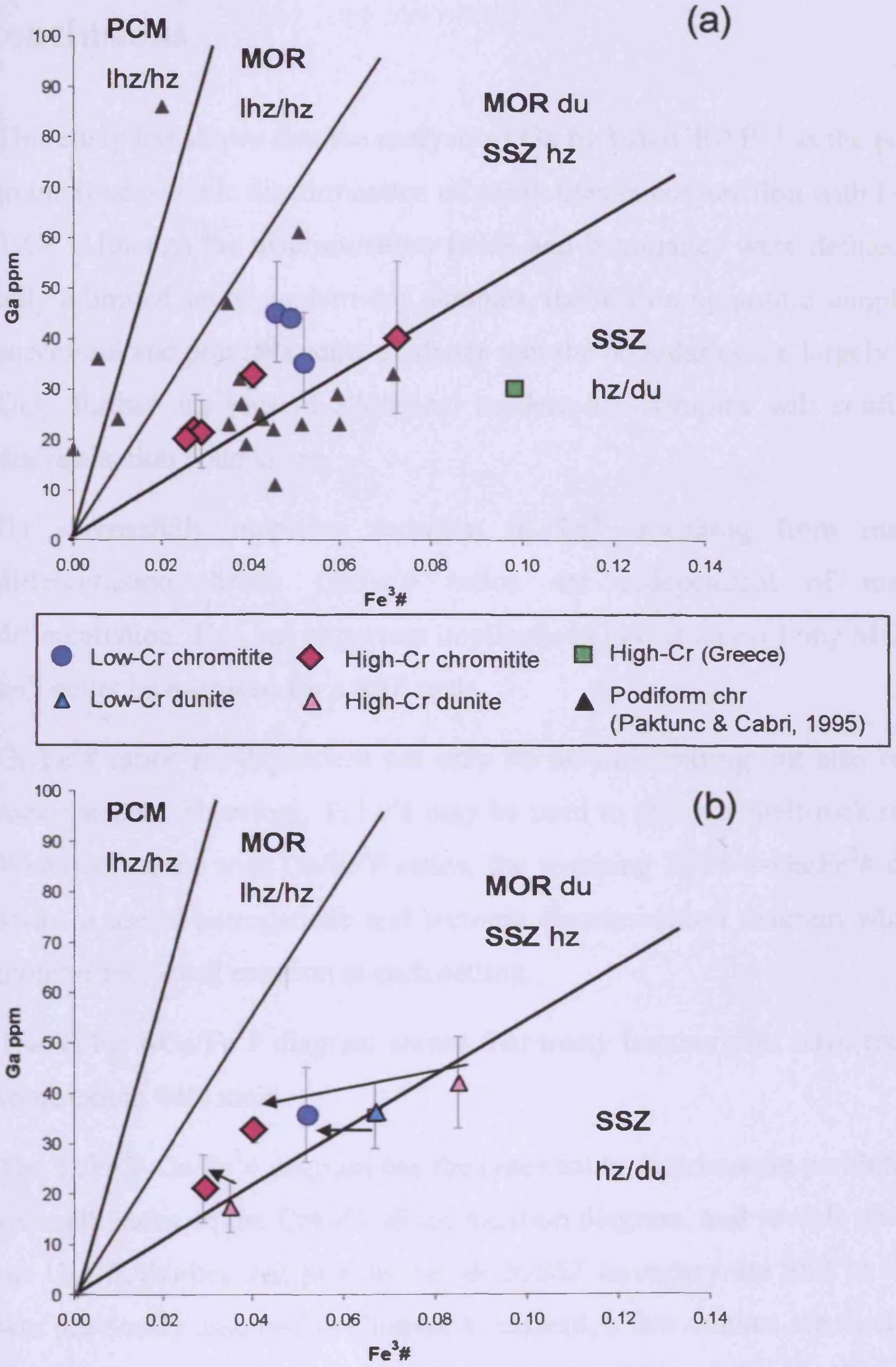

Figure 5.22: Chromitites (U.A.E and Greek ophiolites), classified as SSZ by the Cr#-fO_2 diagram, plotted on Ga vs. Fe^3# diagram in (a) and (b) to show that they plot in the MOR dunite field except for the chromitite from Greece. In (a) podiform chromitites, analysed for Ga by proton microprobe by Paktunc and Cabri, are plotted and the majority do not plot in the SSZ dunite field as expected for podiform chromitites. In (b) dunite-chromitite pairs (arrows) show that chromitites have lower Fe^3# but similar Ga to their dunite envelope resulting in lower Ga/Fe^3# ratios, but not systematically.

5.6 Conclusions

- This study has shown that the analysis of Ga by LA-ICP-MS has the potential to improve tectonic discrimination of peridotites in conjunction with Fe^{3+} and TiO_2. Although the discrimination fields and boundaries were defined using only a limited set of modern-day samples, the test on ophiolitic samples was successful and provides some evidence that the boundaries are largely robust. Only further analyses of additional modern-day samples will confirm the discrimination boundaries.
- Ga successfully monitors variation in Fe^{3+} resulting from magmatic differentiation; hence Ga/Fe^3# ratios are independent of magmatic differentiation. This has important implications in that an evolving MOR melt will never be mistaken for a SSZ melt.
- Ga/Fe^3# ratios are dependent not only on tectonic setting but also on melt-rock reaction. Therefore, Ti/Fe^3# may be used to monitor melt-rock reaction. When combined with Ga/Fe^3# ratios, the resulting Ti/Fe^3#-Ga/Fe^3# diagram forms a useful petrogenetic and tectonic discrimination diagram which can monitor melt-rock reaction at each setting.
- The Ti/Fe^3#-Ga/Fe^3# diagram shows that many harzburgites have reacted to some extent with melt.
- The Ti/Fe^3#-Ga/Fe^3# diagram has the potential to discriminate peridotites that are ambiguous on the Cr#-fO_2 discrimination diagram, and reveals that not all the U.A.E. dunites that plot on the MOR/SSZ boundary are SSZ in origin as was previously assumed in Chapter 4. Instead, a few dunites are re-classified as MORB-type dunites and the tectonic implications of this are discussed in Chapter 6.
- Unfortunately, the Ti/Fe^3#-Ga/Fe^3# diagram cannot be applied to chromitites, for reasons unknown. This implies that the Ti/Fe^3#-Ga/Fe^3# diagram is not suitable for discrimination of detrital spinels because one can not distinguish between peridotite and chromitite spinels.

- The Ti/Fe^3#-Ga/Fe^3# diagram can be applied to spinel phenocrysts and would establish whether the Ga/Fe^3# ratio really is independent of magmatic differentiation.

Chapter 6: Tectonic evolution of the northern Oman-U.A.E. ophiolite

This final Chapter provides a detailed account of the tectonic evolution of the northern Oman-U.A.E. ophiolite by combining evidence from the mantle, as presented in previous Chapters, with evidence from the crust (e.g. Lilly, 2006). As demonstrated in Chapters 4 and 5, the mantle in the U.A.E. provides strong evidence for a switch in tectonic setting from a mid-ocean ridge (MOR) to a supra-subduction zone setting (SSZ). The crustal sequence constrains the chronological order of magmatic events of the northern Oman-U.A.E ophiolite. Direct comparison between the melts that infiltrated the mantle and the magmatic history of the crustal sequence of the U.A.E. constrains the order of events in the mantle. The history of melt infiltration in the mantle is tested with field observations from Chapter 2.

Geochemical maps of the mantle domains in the U.A.E. constrain the spatial variation of SSZ magmatism that infiltrated the mantle enroute to the crust. This is especially useful where the volcanic crust is not preserved, such as in the northern parts of Khawr Fakkan and the Dibba Zone. Geochemical evidence from the U.A.E. mantle also provides new evidence for the location of the detachment of the ophiolite in relation to the subducting slab.

6.1 Magmatic evolution of the crust

The tectonic evolution of the ophiolite is well constrained by magmatic events in the crustal sequence and provides evidence for a change in tectonic setting from MOR to SSZ setting. As described in Chapter 1 the extrusive sequence of lavas in northern Oman have been subdivided into five major Units: Geotimes, Lasail, Alley, Clinopyroxene-phyric and Salahi Units (Pearce et al., 1981; Alabaster et al., 1982; Lippard et al. 1986). Subsequently Ernewein et al. (1988) and Godard et al. (2003) divided the extrusive sequence into three volcanic episodes, VI (Geotimes), V2-1 (Lasail), V2-II (Alley) and V3 (Salahi). More recently Godard et al., (2006) reverted to the original terminology proposed by Pearce et al., (1981) and Alabaster et al., (1982) as it clearly differentiates the different magmatic episodes in the Oman-U.A.E. ophiolite. Lilly (2006) extended this work into the U.A.E. and combined both nomenclatures and is summarised in Table 6.1 (after Lilly, 2006) which compares the magmatic events in Fizh, Aswad and Khawr Fakkan Blocks. These magmatic events were identified through field and geochemical investigations of the extrusive and plutonic sequence of the crust (Pearce et al., 1981; Alabaster et al., 1982; Lippard et al. 1986, Umino et al., 1990; Ishikawa et al., 2002; Lilly, 2006). In Table 6.1 each magmatic Unit of Geotimes, Lasail, Alley, Cpx-phyric and Salahi, is grouped into discrete magmatic events according to their chemistry, e.g. MORB, MORB/IAT, IAT, IAT/BON, BON for ease of comparison with the melts identified in the mantle from this study.

Table 6.1 shows that the magmatic evolution of the crust changes with time and space (i.e. between blocks). In addition, the style of the magmatism also changes with time from steady-state accretion during sea-floor spreading (V1) to localised plutonic magmatism associated with NW-SE rifting and graben formation (V2) (Alabaster et al., 1982; Lilly, 2006).

Time	**Fizh Block** Alabaster et al. (1980) Umino et al. (1990) Ishikawa et al. (2002)	**Aswad Block** Lilly (2006)	**Khawr Fakkan Block** Lilly (2006)
V3	4) **Within-plate** (Salahi Unit)	4) **Within-plate** (Salahi Unit)	5) **Within-plate** (Salahi Unit)
V2 Localised intrusions associated with rifting	3) **IAT-BON** (Alley & Cpx-phyric Units) 2) IAT (Alley Unit)	3) **IAT-BON** (Cpx-phyric Unit) 2) IAT (Alley Unit)	4) **IAT-BON** (Cpx-phyric Unit) 3) BON (Alley Unit)
V1 Sea-floor spreading	1) **MORB-IAT** (Geotimes & Lasail Units)	1) **MORB-IAT** (Geotimes & Lasail Units)	2) **MORB-IAT** (Geotimes & Lasail Units) 1) MORB

Space (North)

Table 6.1: Comparison between magmatic events in Fizh, Aswad and Khawr Fakkan Blocks identified through field and geochemical investigation of the extrusive and plutonic sections of the northern Oman-UAE ophiolite portion (Alabaster et al., 1980; Umino et al., 1990; Ishikawa et al., 2002; Lilly, 2006). Table modified from Lilly, (2006). V1- main period of crustal accretion in a marginal basin setting, V2-supra-subduction zone magmatism and V3-within-plate magmatism during emplacement on the Arabian continent. This Table demonstrates that there is a change in magma types with time and space and a change in style of magmatism from V1 to V2.

Change in magmatism with time

Table 6.1 demonstrates that in each Block the subduction-derived component of the SSZ geochemical signature of both the V1 and V2 magmatic periods increases with time. The main episodes are differentiated by the changing geochemical signature of the mantle source. V1 magmatism involves a MORB to transitional-MORB source whereas V2 magmatism comprises a SSZ source during the early stages (i.e. embryonic) of island arc development. The final stage of magmatism (V3) was associated with obduction onto the Arabian continental margin and melting of the sub-continental mantle and eruption of alkaline to transitional within-plate magmas.

The magmatic events identified in the Aswad Block (Lilly, 2006) closely match those identified in the Fizh Block by Alabaster et al., (1982). The sequence of magmatic events in the Aswad and Fizh Blocks marks an evolution from MORB/IAT to IAT to IAT/BON. This indicates progressive melting of an increasingly depleted mantle source as a result of continued volatile-induced melting above a subduction zone (e.g. Alabaster et al., 1982). Although there are some BON dykes within the Alley Unit of the Fizh Block (Ishikawa et al., 2002) the Alley Unit predominantly has an IAT chemistry (Alabaster et al., 1982). Therefore, the BON dykes from the Alley Unit are classified as IAT/BON rather than BON in Table 6.1.

In contrast, Khawr Fakkan has a distinctive magmatic history and comprises an evolution from MORB to MORB/IAT to BON to IAT/BON (Table 6.1). This sequence is unique because (i) 'true' MORB is documented for the first time in the whole of the Oman-U.A.E. ophiolite (Lilly 2006) and (ii) the V2 magmatic period starts with BON magmatism rather than IAT magmatism. This 'true' MORB magmatic event in Khawr Fakkan provides evidence for pre-existing oceanic crust that formed in a MOR setting that was not influenced by subduction.

Change in magmatism with space

Table 6.1 demonstrates that the subduction-derived component of the SSZ geochemical signature of both the V1 and V2 magmatic periods increases spatially towards the north. The blocks closest to the proposed subduction zone in the north have a more significant SSZ geochemical signature that is present earlier on. The more distal blocks exhibit a weaker SSZ geochemical signature. Therefore, the northernmost Block of Khawr Fakkan was closer to the subduction zone than the Aswad and Fizh Blocks and blocks from Southern Oman were distal from the subduction zone (Lilly, 2006).

The presence of BON and the absence of IAT magmatism in Khawr Fakkan provide evidence for the proximal location of Khawr Fakkan Block to the subduction zone (Lilly, 2006). The generation of boninites (BON) requires re-melting of a hot, shallow and depleted mantle (>1250°C at < 30km depth) in the presence of increased H_2O (Ishikawa et al., 2002). As such, boninites are associated with subduction initiation and form in close proximity to the subduction zone (Ishikawa et al., 2002).

Change in style of magmatism with time

The different magmatic periods (V1 and V2) are characterised by different methods of crustal accretion and are directly related to the evolving tectonic setting of the region (Alabaster et al., 1982; Lilly, 2006). The main crustal accretion event (V1) was associated with sea-floor spreading in a marginal basin setting. Steady-state magmatism of sea-floor spreading switched to localised plutonic magmatism (V2) associated with NW-SE rifting and graben formation in a SSZ setting. The NW-SE faulting was caused by clockwise rotation within a marginal basin setting and is discussed further in relation to the regional tectonic setting in Section 6.4. Palaeomagnetic studies on the northern part of the ophiolite (e.g. Perrin et al., 1994, 2000) provided evidence for clockwise rotation of the crust and is further supported by observations of faults and intrusive direction of dykes in the U.A.E. (Lilly, 2006).

6.2 Comparison between the mantle and crust in the U.A.E.

Chapters 4 and 5 showed that the chrome-spinel geochemistry of peridotites is useful in fingerprinting mantle lithosphere and interacting magmas. This work identified five different types of magma (e.g. MORB, MORB/IAT, IAT, IAT/BON and BON) that infiltrated the U.A.E. mantle. In this Section, the magmatic sequence in the crust (Table 6.11) of Aswad (and Fizh) and Khawr Fakkan is compared to the corresponding mantle domains to (i) confirm that the mantle and crust share the same magmatic history and (ii) constrain the sequence of melt-rock reaction in the mantle. As there is no corresponding crust for the peridotites from the Dibba Zone these peridotites are discussed separately in Section 6.4.

The spinel melt-rock reaction trends that fingerprint melt infiltration in the mantle of Aswad and Khawr Fakkan are summarised from Chapter 4 in a series of six diagrams in Figure 6.1 (Cr#-TiO_2 discrimination diagram) and Figure 6.2 (Cr#-fO_2 discrimination diagram). On each diagram ellipses approximate the spinel compositional fields of harzburgites (grey fields) and dunites/chromitites (coloured fields – see caption for details). Arrows mark reaction trends between mantle residue (harzburgite fields) and infiltrating melt (dunite fields) for each distinct magmatic event in the mantle. Each reaction trend is numbered in order of magmatic history and is determined in the following Sections 6.2.1 and 6.2.2. In these Figures the six diagrams are arranged into three rows corresponding to increasing stratigraphic depth of the mantle (i.e. sub-Moho mantle and MTZ, Mid-Mantle and Banded Unit) and two columns corresponding to the Aswad Block (left hand column) and Khawr Fakkan Block (right hand column). From this direct comparisons can be made between the blocks and between each stratigraphic depth in the mantle.

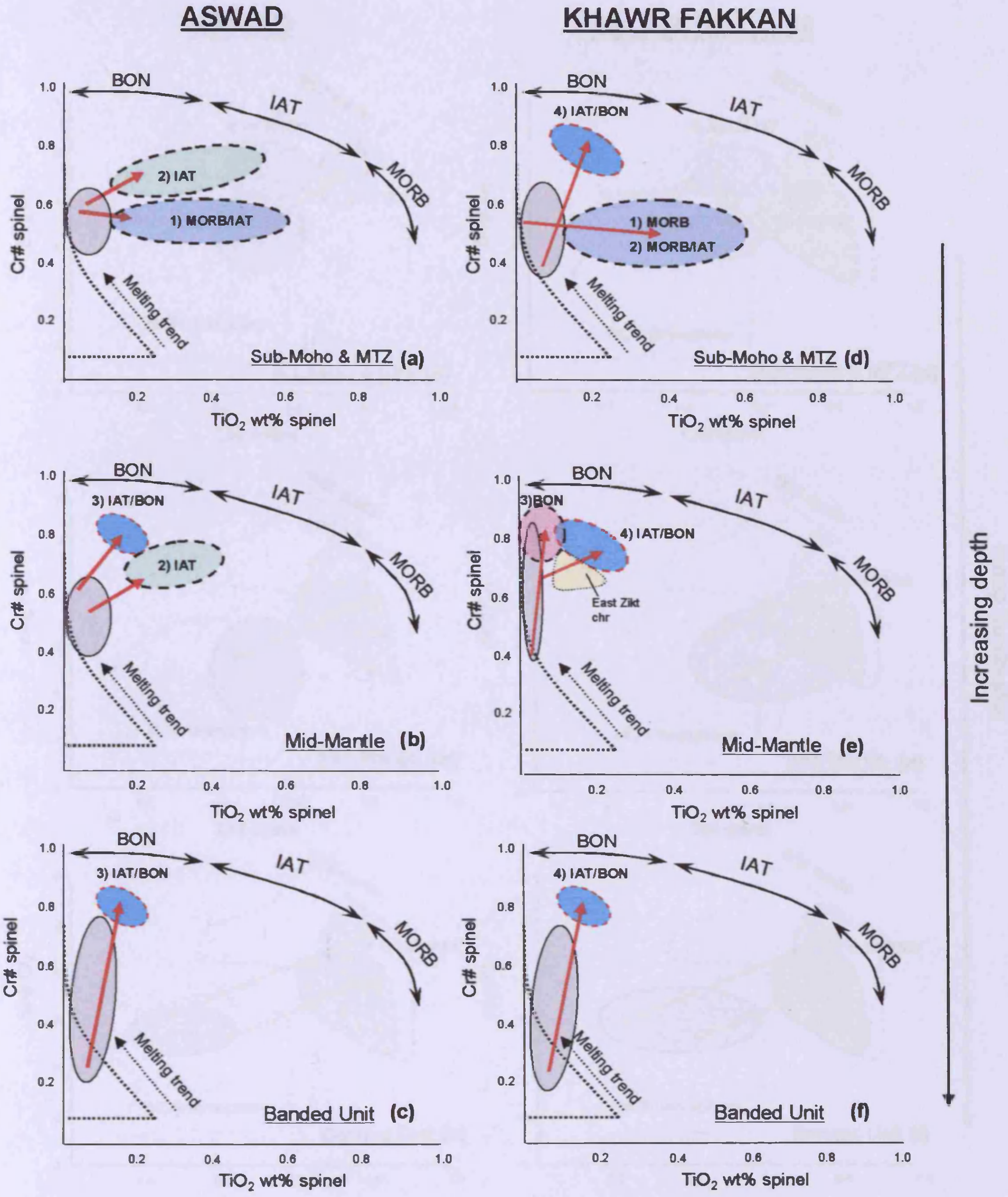

Figure 6.1: Series of Cr# vs. TiO_2 diagrams for spinels in peridotites from (a-c) Aswad Block and (d-f) Khawr Fakkan Block to summarise melt-rock reaction trends described in Section 4.3.2. Spinels from residual mantle plot on the melting trend (dotted curve) and peridotite spinels that have reacted with melt are displaced from the curve towards spinel compositions in equilibrium with the interacting magma. Spinels that crystallized from MORB, IAT and BON magmas are marked by double headed arrows for reference. Spinel fields for harzburgites (shaded grey) and dunites (dashed) and their reaction trends (red arrows) identify the types of magmas (MORB, MORB/IAT, IAT, IAT/BON and BON) that interacted with the mantle in Aswad and Khawr Fakkan. The magmatic history of the mantle is by constrained by the order of magmatic events in the crust and melt-rock reaction trends are labelled 1 – 3 in Aswad and 1 – 4 in Khawr Fakkan. This shows that the earlier melts are preferentially recorded in the shallow mantle and the later melts are preferentially recorded in the deeper mantle. Aswad has a different magmatic history to Khawr Fakkan (see text).

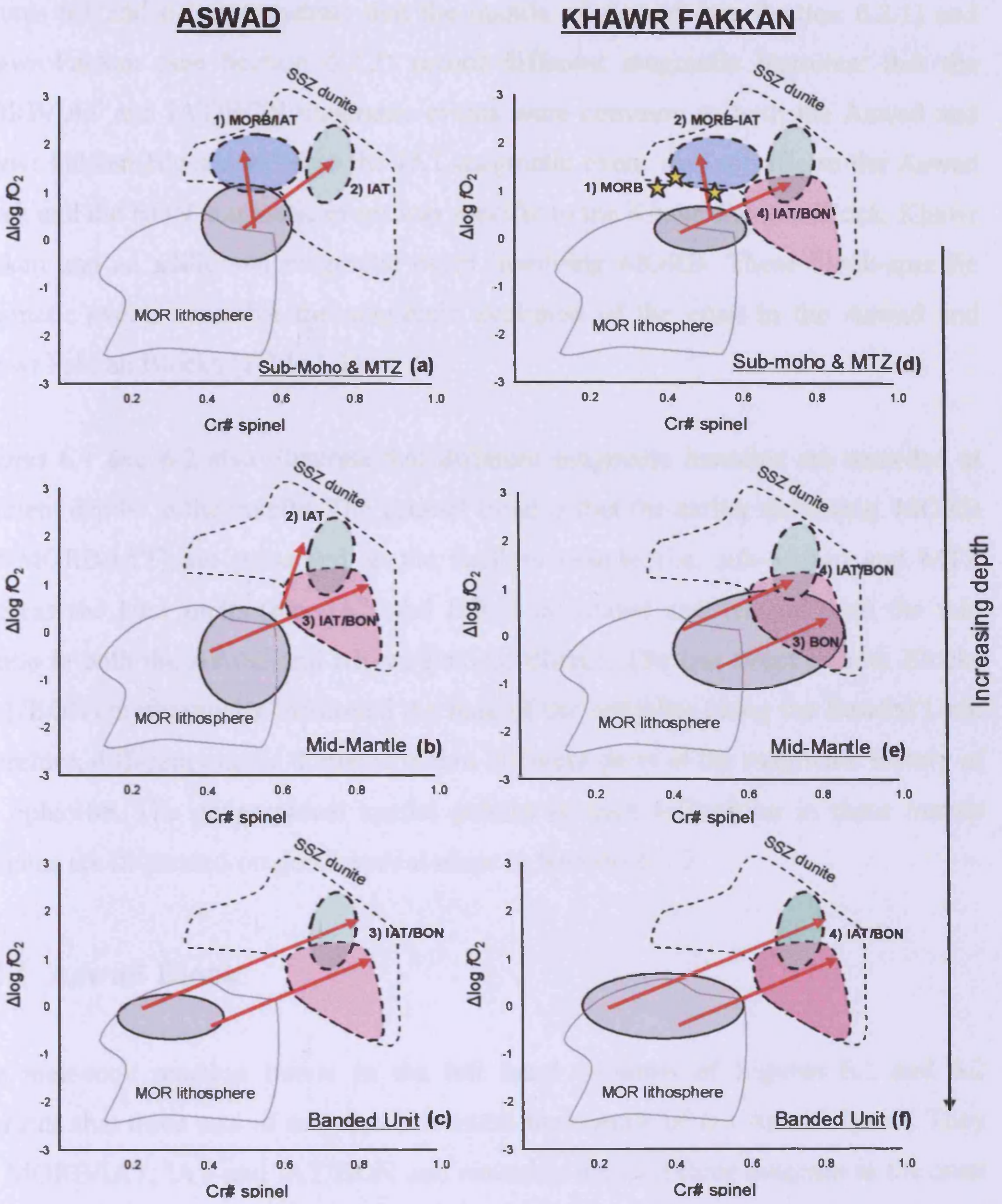

Figure 6.2: Series of Cr#-fO_2 diagrams for spinels in peridotites from (a-c) Aswad Block and (d-f) Khawr Fakkan Block to summarise melt-rock reaction trends described in Section 4.3.3. The fields for MOR lithosphere (solid line) and SSZ dunites (dashed line) are shown for reference and melt-rock reaction trends (red arrows) for UAE peridotites show interaction between MOR lithospheric protoliths and SSZ magma. Spinel fields for harzburgites (shaded grey) and dunites (MORB/IAT-blue; IAT-green; BON-pink) and their reaction trends (red arrows) identify the types of magmas (MORB, MORB/IAT, IAT, IAT/BON and BON) that interacted with the mantle in Aswad and Khawr Fakkan. Spinels formed by reaction with MORB are marked as yellow stars. The magmatic history of the mantle is by constrained by the order of magmatic events in the crust and melt-rock reaction trends are labelled 1 – 3 in Aswad and 1 – 4 in Khawr Fakkan. This shows that the earlier melts are preferentially recorded in the shallow mantle and the later melts are preferentially recorded in the deeper mantle. Aswad has a different magmatic history to Khawr Fakkan. For further explanation see text.

Figures 6.1 and 6.2 demonstrate that the mantle of Aswad (see Section 6.2.1) and Khawr Fakkan (see Section 6.2.2) record different magmatic histories: that the MORB/IAT and IAT/BON magmatic events were common to both the Aswad and Khawr Fakkan Blocks, whereas the IAT magmatic event was specific to the Aswad Block and the BON magmatic event was specific to the Khawr Fakkan Block. Khawr Fakkan had an additional magmatic event involving MORB. These block-specific magmatic events resemble the magmatic evolution of the crust in the Aswad and Khawr Fakkan Blocks (Table 6.1).

Figures 6.1 and 6.2 also illustrate that different magmatic histories are recorded at different depths in the mantle. The general trend is that the earlier melts (e.g. MORB and MORB/IAT) are preserved in the shallow mantle (i.e. sub-Moho) and MTZ whereas the later melts (e.g. IAT and BON) infiltrated and reacted with the mid mantle in both the Aswad and Khawr Fakkan Blocks. The last event in both Blocks (IAT/BON) preferentially infiltrated the base of the ophiolite along the Banded Unit. Therefore, different mantle domains record different parts of the magmatic history of the ophiolite. The geographical spatial pattern of melt infiltration in these mantle domains are illustrated on geochemical maps in Section 6.3.2.

6.2.1 Aswad Block

The melt-rock reaction trends in the left hand columns of Figures 6.1 and 6.2 illustrate that three sets of magmas infiltrated the mantle of the Aswad Block. They are MORB/IAT, IAT and IAT/BON and resemble the first three magmas in the crust of the Aswad Block (Table 6.1, Section 6.1). In the Aswad crust the order of magmatic events are 1) MORB/IAT, 2) IAT and 3) IAT/BON. This implies the following sequence of events in the mantle:

1. Peridotites (and chromitites) that reacted with MORB/IAT melts formed first during the V1 magmatic period of main crustal accretion.

2. Peridotites (and chromitites) that reacted with IAT melts formed during the early stages of the V2 magmatic period.

3. Peridotites that reacted with IAT/BON melts formed during the later stages of the V2 magmatic period.

The proposed order of magmatic events in the mantle is tested with field observations for early and late generations of dunites and chromitites (Chapter 2). Chapter 2 concluded that the early generation of magmatism formed (i) dunites from the MTZ, (ii) tabular, concordant dunites from the sub-Moho mantle and (iii) deformed chromitites from Al Hayl. In Aswad these dunites and chromitites reacted with MORB-IAT melt and confirm that this was the earliest melt in the mantle during the V1 spreading stage. In contrast, the V2 magmatic period was associated with localised intrusions associated with rifting and graben formation in the crust after the main spreading event stopped (Lilly, 2006). Late, intrusive bodies of dunite and chromitite from Wadi Mizert (Chapter 2) formed by reaction with IAT melts and this confirms that this episode of melt infiltration was later than the V1 spreading event. A few dunites from the MTZ also reacted with IAT melts indicating that not all dunites from the MTZ can be attributed to the V1 magmatic episode. Only geochemistry can distinguish later,V2 dunite bodies intruding earlier,V1 dunites in the MTZ because one dunite intruding another dunite cannot be observed in the field.

The magmas from the final event (IAT/BON) infiltrated most of the deeper mantle in Aswad and are associated exclusively with the basal shear zone of the Banded Unit. Shearing of the mantle was probably contemporaneous with the NW-SE faulting in the crust above and probably driven by clockwise rotation of the lithosphere during the V2 period of magmatism.

Peridotites from the Fizh Block show a similar history to the Aswad Block (Chapter 4) and the crustal sequence of Aswad and Fizh also share a similar magmatic evolution (Table 6.1).

6.2.2 Khawr Fakkan

The melt-rock reaction trends in the right hand columns of Figures 6.1 and 6.2 illustrate that four sets of magmas infiltrated the mantle of the Khawr Fakkan Block. These magmatic events are MORB, MORB/IAT, IAT/BON and BON and correspond to the sequence of magmas in the crust of the Khawr Fakkan Block (Table 6.1). Correlation between crust and mantle constrains the following sequence of events in the mantle:

1. Peridotites that reacted with 'true' MORB melts formed first during the initial stage of the V1 magmatic period of main crustal accretion and represent lithosphere of pre-subduction influence. Dunites that reacted with MORB were identified using the new discrimination technique in Chapter 5 (LA-ICP-MS) and are highlighted on Figure 6.2d.

2. Peridotites (and chromitites) that reacted with MORB/IAT melts formed during the later stages of the V1 magmatic period.

3. Peridotites (and chromitites) that reacted with BON melts formed during the early stages of the V2 magmatic period.

4. Peridotites (and chromitites) that reacted with IAT/BON formed during the final stage of the V2 magmatic period.

The following field observations provide some evidence to support this order of events in the mantle.

As in the Aswad Block, the early generation of dunites and chromitites described in Chapter 2 from the MTZ and sub-Moho mantle of Khawr Fakkan formed by reaction with MORB-IAT melts during the V1 magmatic period of steady state crustal accretion during seafloor spreading. A chromitite deposit from Wadi Sahana (SD102a), which was deformed by convective flow at a spreading ridge (Chapter 2), also has MORB-IAT chemistry and confirms that this episode of melt infiltration in the mantle was contemporaneous with the V1 spreading stage. In addition, there are 'true' MORB dunites in the shallow mantle of Khawr Fakkan.

Undeformed chromitites and dunites from Khawr Fakkan North, described in Chapters 2 and 3 as post-dating the spreading stage (V1), correspond to the infiltration of BON melt and the resulting melt-rock reaction. As in the Aswad Block, magmas from the last magmatic event (IAT/BON) in the Khawr Fakkan Block infiltrated the basal shear zone of the Banded Unit. In addition, this magmatic event also infiltrated the Beni Hamid Shear Zone, higher up in the mantle of Khawr Fakkan, as shown by the geochemical map (Figure 6.5) (see Section 6.3.2 for details). This influx of IAT/BON melt possibly formed undeformed chromitites in close proximity to the Beni Hamid Shear Zone, such as the East Zikt chromitite mines and in Wadi Sahana (SD106a) described in Section 2.3.3.2 (Chapter 2). The undeformed nature of these chromitites implies that there was either no further deformation along this shear zone after the chromitites formed or that deformation was localised to the shear zone and the chromitites formed distal to this deformation. IAT/BON magmas also infiltrated the MTZ in Khawr Fakkan South and formed a late body of dunite (UAE 33), which intrudes the layered gabbros (Chapter 2, Section 2.3.4) and therefore post-dates the spreading stage (V1) that formed the layered gabbros.

Despite the differences in these earlier magmatic events for the Aswad Block (e.g. IAT magmatic event) and the Khawr Fakkan Block (e.g. BON magmatic event), these two blocks share the same final magmatic event (IAT/BON). This indicates that the shear zones at the base of the Aswad and Khawr Fakkan Blocks were active at the same time and probably contemporaneous with the clockwise rotation of the lithosphere during the V2 magmatic episode.

6.3 Information from geochemical mapping of the U.A.E. mantle

A total of 234 samples (211 peridotites and 23 chromitites) analysed in Chapter 4 are plotted on the geological map of the U.A.E. using GIS (Arcview 3.2) to illustrate the regional variation in chrome-spinel geochemistry. This forms detailed 2D geochemical maps of the U.A.E. mantle, the first of their kind for the Oman-U.A.E. ophiolite. The first is a geochemical map for the variation in Cr# of harzburgites and lherzolites (Section 6.3.1) and the second is a geochemical map for melt infiltration in the mantle lithosphere (Section 6.3.2).

6.3.1 Map of Cr# in harzburgites/lherzolites

The geochemical map of spinel Cr# of harzburgites and lherzolites from the U.A.E. is contoured using GIS (Figure 6.3). All of the harzburgites are plotted on this map regardless of whether they are residual (i.e. Type 1 spinels) or formed by melt-rock reaction (i.e. Type 2 and Type 3 spinels). Additional spinel Cr# of harzburgites analysed by Monnier et al., (2006) from the northern Fizh, Aswad and Khawr Fakkan Blocks are plotted as individual data points on Figure 6.3. These data points are not used in the contouring of the Cr# spinel map because the grid references are incompatible with this study. But the Monnier et al., (2006) data points mostly agree with the Cr# contours of the map (Figure 6.3).

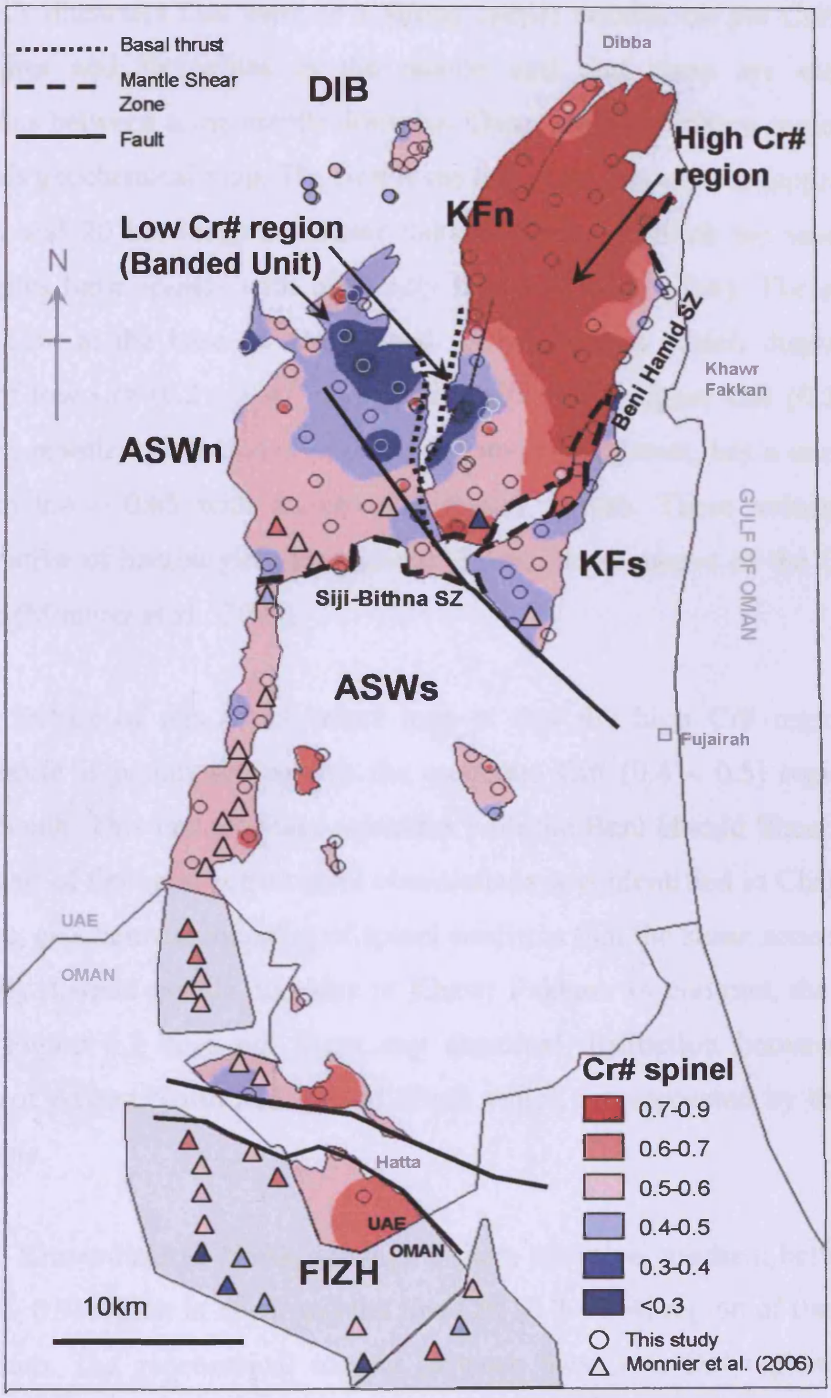

Figure 6.3: Geochemical map of spinel Cr# of harzburgites and lherzolites from the U.A.E. mantle, contoured using GIS, illustrates the strong regional variation in Cr#. There are two striking mantle regions: the high Cr# region in Khawr Fakkan North and the low Cr# region of the Banded Unit in Aswad and Khawr Fakkan. The mantle domain of Khawr Fakkan North (KFn) is chemically distinct from Khawr Fakkan South (KFs) and confirms that the Beni Hamid Shear Zone juxtaposes these two different mantle domains. Additional harzburgite spinel data from Monnier et al. (2006) are plotted as colour coded trangle symbols and confirms the spatial pattern of this map.

Figure 6.3 illustrates that there is a strong spatial control on the Cr# of spinel in harzburgites and lherzolites in the mantle and that there are clear chemical distinctions between some mantle domains. There are two striking regions that stand out on this geochemical map. The first is the large continuous area (approximately 10 km wide and 20 km long) in Khawr Fakkan North in which the vast majority of harzburgites have spinels with extremely high Cr# (0.7 – 0.9). The second is the Banded Unit at the base of Aswad and Khawr Fakkan which displays a patchy pattern of low Cr# (0.2 – 0.4) interspersed with much higher Cr# (0.5 – 0.7). The remaining mantle, not included in these two areas of interest, has a narrow range of Cr# from 0.4 – 0.65 with no obvious spatial pattern. These values of Cr# are representative of harzburgites throughout the mantle sequence of the Oman-U.A.E. ophiolite (Monnier et al., 2006).

Another feature of this geochemical map is that the high Cr# region of Khawr Fakkan north is juxtaposed against the moderate Cr# (0.4 – 0.5) region of Khawr Fakkan South. This juxtaposition coincides with the Beni Hamid Shear Zone, which on the basis of field and petrological observations was identified in Chapters 2 and 3. Therefore, geochemical mapping of spinel confirms that the shear zone separates two chemically distinct mantle domains in Khawr Fakkan. In contrast, the geochemical map in Figure 6.3 does not show any chemical distinction between the mantle domains of Aswad North and Aswad South which are separated by the Siji-Masafi Shear Zone.

In detail, Khawr Fakkan North displays a sharp chemical gradient between the high Cr# (0.7 – 0.9) region in north and the low Cr# (0.2 – 0.4) region of the Banded Unit in the south. The geochemical contact between these two Cr# regions is at a high angle to the basal thrust of the Banded Unit and the Beni Hamid Shear Zone, both of which were probably sub-parallel to the Moho. Harzburgites in the high Cr# region have Type 2 (subidiomorphic) and Type 3 (euhedral) spinels and formed by melt-rock reaction with a BON melt (Chapter 4). Therefore, this high Cr# region in Khawr Fakkan North probably resulted from a widespread influx of BON melt that intruded the mantle in a near vertical direction. The high Cr# mantle region of Khawr

Fakkan North is unique within the Oman-U.A.E. ophiolite. Section 1.4.1 described some smaller, localised areas in northern Oman that have Cr# in harzburgites as high as 0.77 (e.g. Girardeau et al., 2003; Matsukage et al., 2001; Kanke and Takazawa, 2005, 2006; Tamura and Arai, 2006). However, these areas in Oman do not compare to the high Cr# region in Khawr Fakkan North in either Cr# values (i.e. 0.7 – 0.9) or regional extent (~ 10km wide and 20km long).

In detail, the low Cr# region (0.2 – 0.4) of the Banded Unit at the base of Khawr Fakkan North and Aswad North (Figure 6.3) displays a discontinuous pattern of low Cr# spinels interspersed with much higher Cr# spinels (0.5 – 0.7). The low Cr# spinels in lherzolites represent relatively fertile mantle residue and the higher Cr# spinels in harzburgites formed by melt-rock reaction via pervasive, porous flow (Chapter 4). In some places in Aswad North, samples collected less than 1 km away from each other, or even in the same outcrop, exhibit a large difference in Cr#. The geochemical map indicates that, although the melt infiltration along the shear zones of the Banded Unit was pervasive, it was also patchy and not as regionally extensive as the episode of melt infiltration in Khawr Fakkan North.

6.3.2 Mantle map of melt infiltration

Spinels from harzburgites (i.e. Types 2 and 3), dunites and chromitites that formed by melt-rock reaction in the mantle and MTZ are plotted on Figure 6.4, termed here as the 'melt infiltration map'. Data points distinguish spinels that reacted with the following types of magma: MORB, MORB/IAT, IAT, IAT/BON and BON (Section 6.2). Figure 6.4 shows that there is a strong regional control on melt infiltration in the mantle of the U.A.E. The regional pattern of melt infiltration involves a transition from V1 magmatism (i.e. MORB/IAT) to V2 magmatism (i.e. IAT, IAT/BON and BON) from south to north. In detail, IAT magma only infiltrated the mantle of Aswad and Fizh Blocks, whereas BON magma only infiltrated the Khawr Fakkan Block. There was only infiltration of 'true' MORB melt in the northern parts of the U.A.E., i.e. in the Dibba Zone (Section 6.3.3) and in Khawr Fakkan South.

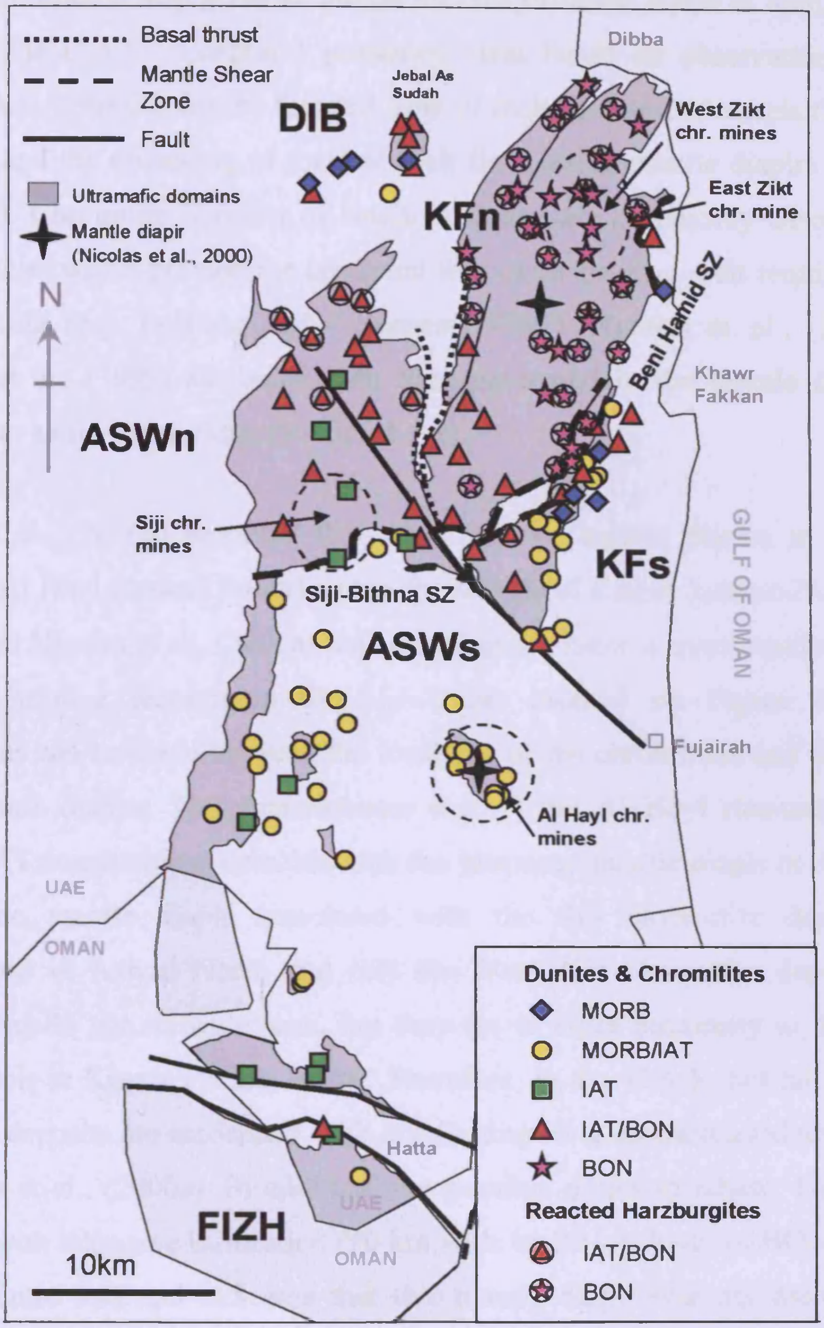

Figure 6.4: Map of the study area showing the spatial variation in the types of magmas that infiltrated the mantle lithosphere. Extensive melt-rock reaction formed dunites and chromitites and lower degrees of melt-rock reaction formed reacted harzburgites. Each ultramafic domain records a different part of the magmatic history of the ophiolite. The southern region (Aswad and Fizh blocks) has a history of increasingly depleted melts in a SSZ setting (e.g. from MORB/IAT to IAT to IAT/BON) whereas the northern region (Dibba Zone and Khawr Fakkan blocks) records subduction initiation and has a history from MOR to SSZ setting (MORB to MORB/IAT to BON to IAT/BON). The northern region of Dibba Zone and Khawr Fakkan was nearer to the subduction zone than the southern region of Aswad and Fizh.

The melt infiltration map gives an insight into the different styles of melt flow in the mantle of the U.A.E. Chapter 1 presented ideas based on observations from the Oman-U.A.E. ophiolite for the focused flow of melt in dunite channels (Kelemen et al., 1995) and the upwelling of focused melt flow inside mantle diapirs (Nicolas et al., 2000a). Chromitite deposits in southern Oman are commonly associated with mantle diapirs which provide the continual flux of Cr-bearing melt required to form such deposits (e.g. LeBlanc and Ceuleneer, 1992). Nicolas et al., (2000a) and Kelemen et al., (1995) attributed melt flow processed in the mantle of Oman to spreading at a mid-ocean ridge (Section 1.4.2).

Nicolas et al., (2000a) proposed that there are two mantle diapirs in the U.A.E. located at Al Hayl (Aswad South) and in the middle of Khawr Fakkan North (Figure 4), although Nicolas et al., (2000a) indicated that the latter is questionable. The three chromitite mining districts in the U.A.E are marked on Figure 6.4 so that comparisons can be made between the locations of the chromitites and the locations of the mantle diapirs. This demonstrates that (i) the Al Hayl chromitite deposits (MORB-IAT composition) coincide with the proposed mantle diapir of Al Hayl, (ii) there is no mantle diapir associated with the Siji chromitite deposits (IAT composition) in Aswad North and (iii) the West Zikt chromitite deposits (BON composition) do not coincide with, but they are in close proximity to, the possible mantle diapir in Khawr Fakkan North. Therefore, in the U.A.E. not all of the large chromitite deposits are associated with mantle diapirs at spreading ridges as implied by Nicolas et al., (2000a). In addition, the possible diapir in Khawr Fakkan North coincides with extensive infiltration (10 km wide by 20 km long) of BON melt in the mantle (Figure 6.4) and indicates that this mantle diapir was not associated with spreading at a mid-ocean ridge.

Figure 6.4 illustrates that the majority of dunites in the U.A.E. are not related to the focused flow of MORB or transitional MORB/IAT melt at a spreading ridge as was the case for dunites from southern Oman (Kelemen et al., 1995). Instead, the melt infiltration map demonstrates that the focusing of SSZ melts, such as IAT, IAT/BON and BON melts, into dunite channels was common in the U.A.E. mantle above a supra-subduction zone. In addition, melt infiltration was not solely constrained to dunite melt channels but melt also infiltrated the mantle between the channels modifying the harzburgite spinels by melt-rock reaction well away from the dunites. This type of widespread melt flow in the mantle indicates pervasive rather than focused, porous flow. The distribution of these modified harzburgites on Figure 6.4 indicates that there was widespread melt flow in two main regions of the mantle: in Khawr Fakkan North and the Banded Unit of Aswad North (also see Section 6.3.1). In Khawr Fakkan North BON melt reacted with spinels in dunites, chromitites and harzburgites indicating an extensive melt flux of boninitic magma into this region by focused and pervasive melt flow. As mentioned above this style of melt infiltration may be associated with a mantle diapir in this region. Some boninites are documented in the crust of Khawr Fakkan (Lilly, 2006) but this underestimates the large extent of boninitic magmatism at depth in the mantle of Khawr Fakkan North (e.g. Figures 6.3 and 6.4).

Melt flow along the basal shear zones (i.e. Banded Unit) of Aswad North and Khawr Fakkan North was also widespread with IAT/BON type magma forming dunites and reacting with spinels in some, but not all, of the basal lherzolites to form harzburgites. Section 6.2.2 concludes that IAT/BON melt also infiltrated the Beni Hamid Shear Zone and formed chromitites at East Zikt. Figure 6.4 confirms that IAT/BON melt infiltrated not only the basal shear zone but also the Beni Hamid Shear Zone in the Khawr Fakkan Block. Focused melt flow along the Beni Hamid Shear Zone is the lost likely route for the late stage IAT/BON melt to infiltrate the upper mantle of Khawr Fakkan South and to form the East Zikt chromitite deposits. This is because there is no record of IAT/BON melt infiltration in the mantle directly beneath the East Zikt chromitite deposits because only BON melt infiltrated the mantle to the west of East Zikt (Figure 6.4).

The pattern of melt infiltration in Figure 6.4 confirms the presence of the Siji-Masafi Shear Zone and the Beni Hamid Shear Zone because the mantle domains either side of these shear zone record different melt infiltration events. For example, the Siji-Masafi Shear Zone separates mantle infiltrated predominantly by IAT and

IAT/BON melts in Aswad North from mantle predominantly infiltrated by MORB/IAT and IAT melt in Aswad South.

Figure 6.5 is a schematic representation of the structural and geographical relationships between each U.A.E. mantle domain in terms of distance away from the subduction zone. This demonstrates that the Dibba Zone peridotites were closer to the subduction zone than the Khawr Fakkan Block with the Aswad and Fizh Blocks even more distal. Each mantle domain is separated by either a thrust or a shear zone that constrains the structural depth of each mantle domain in the Semail Nappe. The amount of displacement along each of the shear zones and thrusts is unknown but could be considerable in order to juxtapose mantle domains with such chemically distinct histories. The magmatic evolution of each mantle domain is summarised on Figure 6.5 and illustrates that the strong spatial control on the pattern of melt infiltration in the mantle in Figure 4 was dependent on the proximity of each mantle domain to the subduction zone. The presence of 'true' MORB and BON magmatism in Khawr Fakkan North confirms that it was closer to the subduction zone than Aswad North. The magmatic history of the Dibba Zone peridotites is described below for the first time and reveals important new information about the nature of the mantle lithosphere nearest the trench

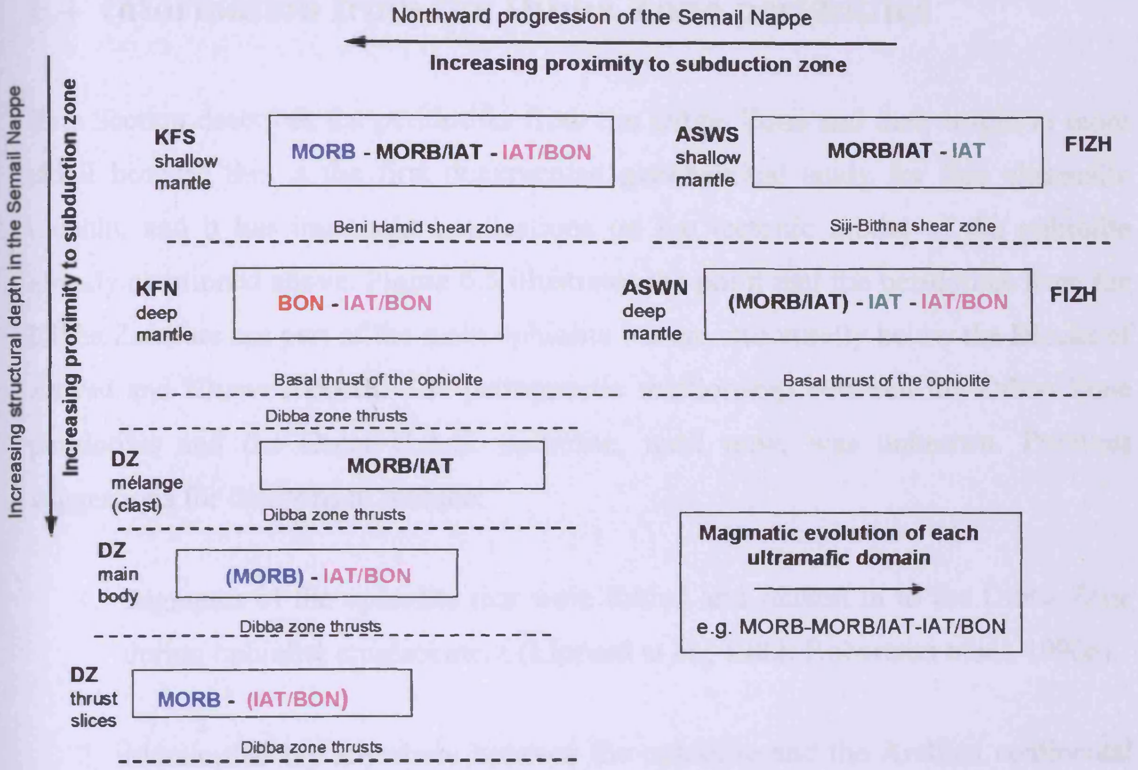

Figure 6.5: Schematic block diagram illustrating the magmatic evolution of each ultramafic domain in relation to (i) their location in the Semail Nappe and (ii) the subduction zone of the ophiolite. The ultramafic domains are (i) shallow mantle of Khawr Fakkan South (KFS) and Aswad South (ASWS), (ii) deep mantle of Khawr Fakkan North (KFN) and Aswad North (ASWN), (iii) the main body (Jebel As Sudah) of the Dibba Zone (DZ) and (iv) the serpentinized thrust slices of the Dibba Zone (DZ). Ultramafic domains that are separated by thrusts/shear zones are marked by dashed lines. This diagram indicates that the proximity of each mantle domain to the subduction zone increases in the order Fizh, Aswad, Khawr Fakkan and Dibba Zone.

6.4 Information from the Dibba Zone peridotites

This Section describes the peridotites from the Dibba Zone and their origin in more detail because this is the first documented geochemical study for this ultramafic domain, and it has important implications on the tectonic model of the ophiolite already mentioned above. Figure 6.5 illustrates the point that the peridotites from the Dibba Zone are not part of the main ophiolite but are structurally below the Blocks of Aswad and Khawr Fakkan. The petrogenetic relationship between the Dibba Zone peridotites and the Oman-U.A.E. ophiolite, until now, was unknown. Previous suggestions for their origin include:

1. Segments of the ophiolite that were folded and faulted in to the Dibba Zone during ophiolite emplacement (Lippard et al., 1982; Robertson et al., 1990a).

2. Mantle that lay anywhere between the ophiolite and the Arabian continental margin and was incorporated into the Semail Nappe during ophiolite obduction. The Dibba Zone peridotites could represent (i) Arabian continental margin, (ii) MOR lithosphere of the under-riding plate of the ophiolite, or (iii) lithosphere from between the trench of the subduction zone and the Oman-U.A.E ophiolite (Emrys Phillips (BGS) pers. comm.).

Chapter 4 concluded that the Dibba Zone peridotites are similar in part to the ophiolite peridotites because they were infiltrated by IAT/BON melts. This narrows the origin of the Dibba Zone peridotites down to either an infolded part of the ophiolite or lithosphere originating between the trench and the main ophiolite. Chapter 2 (Section 2.2.6) described the structural level of each of the three units of the Dibba Zone peridotites and this is summarised in Figure 6.5. In decreasing order below the ophiolite, and thus increasing proximity to the ophiolite, the units are Wadi Sanah Mélange, Jebal As Sudah ultramafic body and the Serpentinite Thrust Sheets (Figure 6.5).

The spinel reaction trends for the Dibba Zone peridotites from each structural unit are summarised from Chapter 4 on a series of diagrams of Cr#-TiO_2 (left column) and Cr#-fO_2 (right column) in Figure 6.6. On each diagram ellipses approximate the spinel compositional fields of harzburgites (grey fields) and dunites/chromitites (coloured fields – see caption for details). Arrows mark reaction trends between mantle residue (harzburgite fields) and infiltrating melt (dunite fields) for each distinct magmatic event in the mantle. The new discrimination technique using LA-ICP-MS (Chapter 5) played an important role in identifying MORB-type dunites in the Dibba Zone that were ambiguously discriminated using Cr#-fO_2 diagram. All of the dunite samples analysed by LA-ICP-MS are highlighted on the right hand column of Figure 6.6. In this Figure the six diagrams are arranged into three rows corresponding to increasing stratigraphic depth within the Dibba Zone (i.e. Wadi Sanah Mélange, Jebal As Sudah ultramafic body and the Serpentinite Thrust Sheets). From this direct comparisons can be made between the structural units. Because there is no accompanying crustal sequence to the Dibba Zone peridotites to constrain the sequence of events the magmatic history is assumed to resemble that of the main ophiolite, i.e. reaction with MORB predates reaction with IAT/BON.

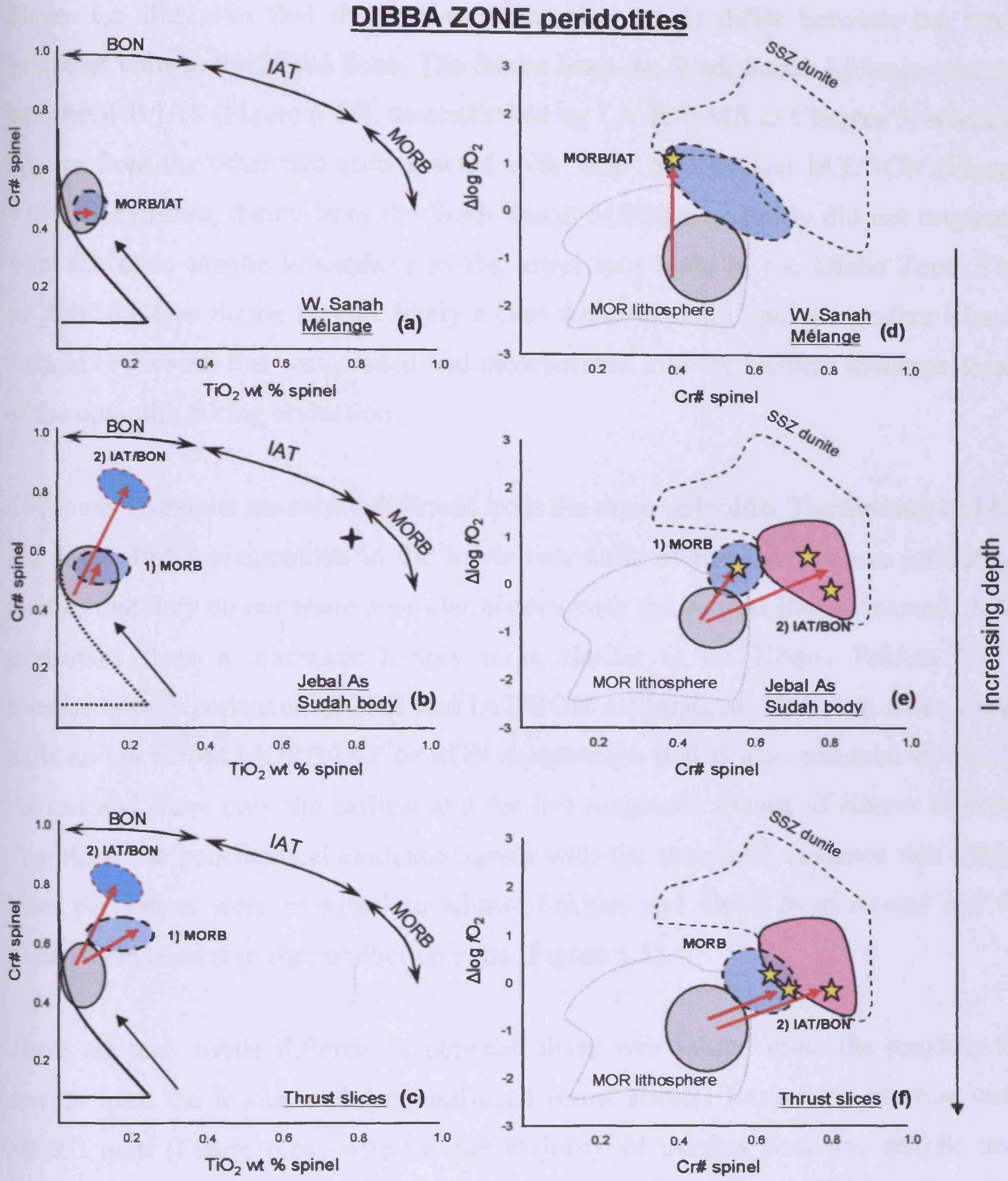

Figure 6.6: Series of spinel melt-rock reaction trends for Dibba Zone peridotites plotted on (a-c) Cr#-TiO_2 diagrams and (d-f) Cr#-fO_2 diagrams from the three different stratigraphic units. In increasing depth below the ophiolite they are (a,d) Wadi Sanah Mélange, (b,e) Jebal As Sudah main body and (c,f) serpentinized thrust slices. See Figure 6.1 and Figure 6.2 for explanation of each fields on the Cr#-TiO_2 and Cr#-fO_2 diagram, respectively. In all diagrams in this Figure spinel fields for Dibba Zone harzburgites are shade grey and the dunites (dashed ellipses) and their reaction trends (red arrows) identify the magmas (MORB, MORB/IAT and IAT/BON) that interacted with the mantle in the Dibba Zone. In the right hand column yellow stars identify the individual samples classified with the aid of Ga (LA-ICP-MS) discrimination. Peridotites from Wadi Sanah Mélange display a different trend to the lower units.

Figure 6.6 illustrates that the melt-rock reaction trends differ between the three structural units in the Dibba Zone. The dunite from the Wadi Sanah Mélange reacted with MORB/IAT (Figure 6.6d), as confirmed by LA-ICP-MS in Chapter 5, whereas dunites from the other two units reacted with 'true' MORB and IAT/BON (Figure 6.6e-f). Therefore, dunite from the Wadi Sanah Mélange probably did not originate from the same mantle lithosphere as the lower two units of the Dibba Zone. The MORB/IAT-type dunite is more likely a clast from the main ophiolite (either Khawr Fakkan or Aswad) that was eroded and incorporated into the tectonic mélange ahead of the ophiolite during obduction.

The lower two units are subtly different from the main ophiolite. The absence of IAT and MORB/IAT magmatism in the lower two units of the Dibba Zone peridotites implies that they do not share a similar history with the Aswad Block. Instead, these peridotites share a magmatic history more similar to the Khawr Fakkan Block because both experienced MORB and IAT/BON magmatism. However, these lower units do not record MORB/IAT or BON magmatism that is also common in Khawr Fakkan and share only the earliest and the last magmatic events of Khawr Fakkan. Therefore, the geochemical evidence agrees with the structural evidence that Dibba Zone peridotites were proximal to Khawr Fakkan and distal from Aswad and so places them nearest to the subduction zone (Figure 6.5).

There are also subtle differences between these two lower units: the majority of dunites from the lowest unit (serpentinized thrust sheets) formed by reaction with MORB melt (Figure 6.6e) whereas the majority of dunites from the middle unit (Jebal As Sudah ultramafic body) formed by reaction with IAT/BON melt (Figure 6.6f). This places the lowest unit furthest away from Khawr Fakkan and nearest the trench.

In summary, this study reveals that the Dibba Zone peridotites originated between the trench and Khawr Fakkan, i.e. the Dibba Zone preserves pre-existing MOR lithosphere infiltrated with 'true' MORB melts before subduction initiated. The only other record of MORB magmatism in the main ophiolite is in the shallow mantle of Khawr Fakkan South and its crust. The Dibba Zone peridotites constrain the northern limit of BON magmatism and indicate that the only pre-existing 'true' MOR lithosphere was preserved nearest the trench and that it was not affected by BON magmatism following subduction initiation. The Dibba Zone peridotites were infiltrated by IAT/BON melts during the last magmatic event that infiltrated the basal shear zone of the main ophiolite.

6.5 Tectonic implications of the mantle study

This section summarises four key points from the study of the mantle of the U.A.E.

6.5.1 Pre-existing lithosphere prior subduction initiation

The only previously documented evidence for pre-existing oceanic lithosphere before subduction started in the entire Oman-U.A.E. ophiolite was 'true' MORB dykes in the crust of Khawr Fakkan (Lilly, 2006). This study confirms that 'true' MORB melts infiltrated the mantle lithosphere in Khawr Fakkan South forming some dunites in the mantle and Moho transition zone. The Dibba Zone peridotites preserve melt-rock reaction with 'true' MORB melt and this provides the strongest evidence yet for oceanic lithosphere that formed at a spreading centre with no subduction influence. Structural evidence places the Dibba Zone peridotites closest to the trench and demonstrates that pre-subduction zone lithosphere is only preserved near the trench.

6.5.2 Melt flow above a SSZ setting

Figure 6.4 illustrates that the majority of dunites in the U.A.E. interacted with SSZ melts. Therefore, unlike southern Oman they cannot be used to study the focused flow of melt under a MOR-type spreading ridge (e.g. Kelemen et al., 1995). However, the geochemical map of melt infiltration in the U.A.E. (Figure 6.4) provides a rare insight into melt flow above a SSZ setting. This demonstrates that the flow of SZZ melt was not just focused in dunite channels, like mid-ocean ridges (e.g. Kelemen et al., 1995), but also widespread and pervasive in the mantle, away from dunite veins, so that it modified spinels in harzburgites by melt-rock reaction. The pervasive flow of SSZ melt was associated with (i) the infiltration of boninitic melt in Khawr Fakkan North centred on a possible uprising mantle diapir, and (ii) the infiltration of IAT/BON melt along the basal shear zones and possibly along the Beni Hamid shear zone.

6.5.3 Agreement between mantle and crust for the tectonic evolution of the northern Oman-U.A.E. ophiolite

The history of melt infiltration in the U.A.E. mantle, recorded by melt-rock reaction of chrome-spinels, resembles the magmatic history of the crust documented by Lilly (2006). Peridotites from the Dibba Zone and the northern region of Khawr Fakkan provide additional information for the magmatic history of these areas because the crustal sequence is absent.

Lilly (2006) proposed that the northern Oman-U.A.E. ophiolite was located in a marginal basin at <100 km north of a propagating subduction zone. Both the mantle and crust in the U.A.E. provide evidence that the northern Oman-U.A.E. ophiolite formed by a switch in tectonic setting from spreading in a marginal basin (V1) to a SSZ setting (V2). An initially MORB-like mantle source became progressively contaminated by a subduction-derived component resulting in nascent island-arc development prior to obduction on to the Arabian continental margin. This tectonic setting was first proposed by the Open University Study Group (e.g. Pearce et al., 1981, Alabaster et al., 1982; Lippard et al., 1986).

Figure 6.7 displays the proposed tectonic evolution of the Oman-U.A.E. ophiolite during the V1 and V2 magmatic periods. This figure is simplified from Lilly (2006) and the following summary is also taken from Lilly (2006) with additional reference to the mantle taken from this work.

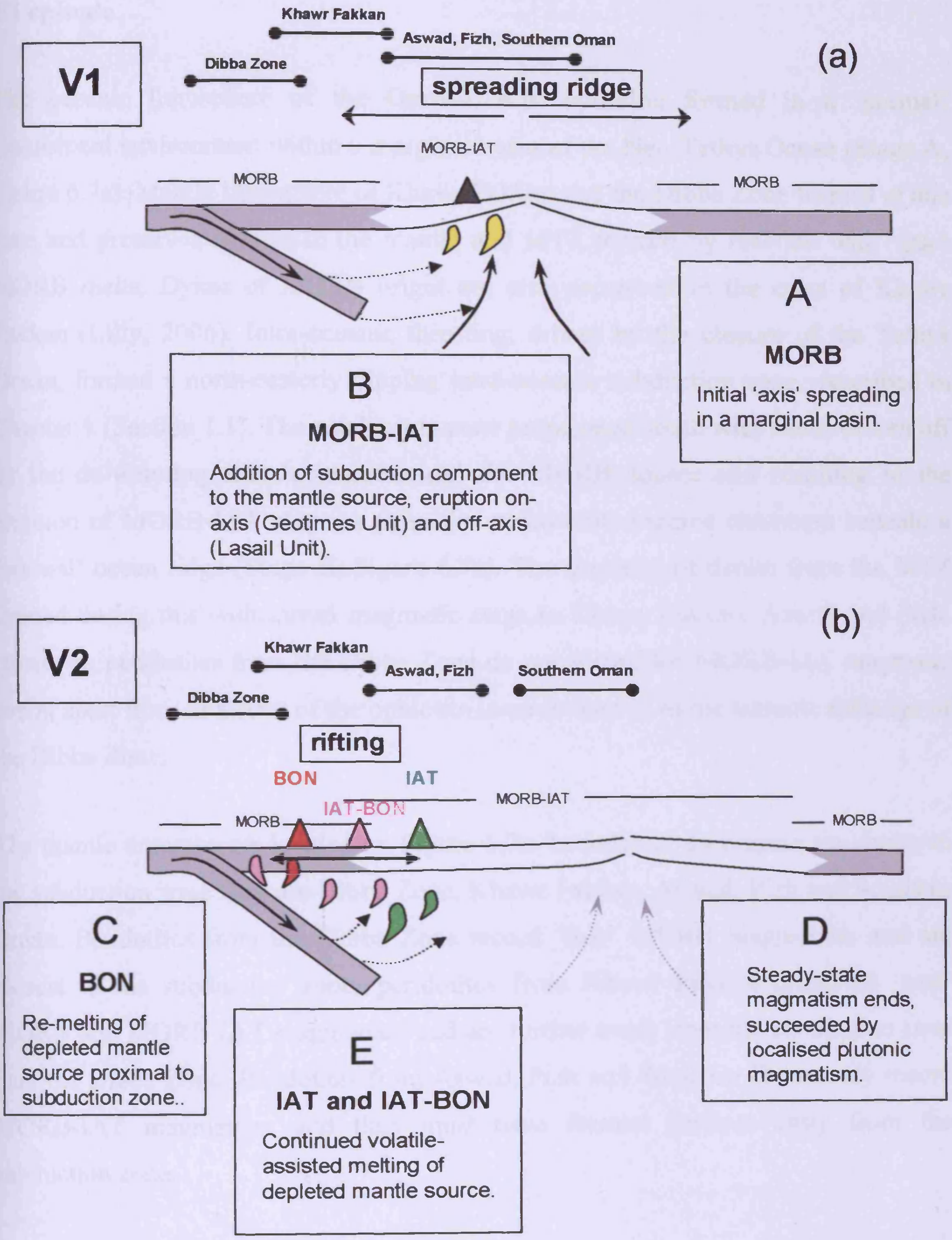

A
MORB
Initial 'axis' spreading in a marginal basin.

B
MORB-IAT
Addition of subduction component to the mantle source, eruption on-axis (Geotimes Unit) and off-axis (Lasail Unit).

C
BON
Re-melting of depleted mantle source proximal to subduction zone..

D
Steady-state magmatism ends, succeeded by localised plutonic magmatism.

E
IAT and IAT-BON
Continued volatile-assisted melting of depleted mantle source.

Figure 6.7: Cartoons illustrating the tectonic evolution of the Oman-U.A.E. ophiolite, divided into magmatic events (a) V1: Initial 'axis spreading in a marginal basin and (b) V2: magmatism in a SSZ setting associated with rifting and localised intrusions. Locations for the Dibba Zone, Khawr Fakkan, Aswad, Fizh and southern Oman blocks are marked in relation to the subduction zone. These are based on evidence for magmatic events identified in the crust (see Table 6.1) and in the peridotites (see Figure 6.5). For further explanation see text. (Adapted from Alabaster et al., 1982, Lippard et al., 1986 and Lilly, 2006).

V1 episode

The oceanic lithosphere of the Oman-U.A.E. ophiolite formed in a 'normal' extensional environment within a marginal basin of the Neo-Tethys Ocean (Stage A, Figure 6.7a). Mantle lithosphere of Khawr Fakkan and the Dibba Zone formed at this time and preserves dunites in the mantle and MTZ formed by reaction with 'true' MORB melts. Dykes of MORB origin are also preserved in the crust of Khawr Fakkan (Lilly, 2006). Intra-oceanic thrusting, driven by the closure of the Tethys Ocean, formed a north-easterly dipping intra-oceanic subduction zone, described in Chapter 1 (Section 1.1). The subduction zone propagated south with fluids driven off by the de-watering slab 'contaminating' the MORB source and resulting in the eruption of MORB-IAT magmas from the steady-state magma chambers beneath a 'normal' ocean ridge (Stage B, Figure 6.7a). The majority of dunite from the MTZ formed during this widespread magmatic stage in Khawr Fakkan, Aswad and Fizh. However, peridotites from the Dibba Zone do not record the MORB-IAT magmatic event, apart from in a clast of the ophiolite incorporated in to the tectonic mélange of the Dibba Zone.

The mantle domains are located on Figure 6.7a. In order of decreasing proximity to the subduction zone they are Dibba Zone, Khawr Fakkan, Aswad, Fizh and Southern Oman. Peridotites from the Dibba Zone record 'true' MORB magmatism and are closest to the subduction zone, peridotites from Khawr Fakkan preserves 'true' MORB and MORB-IAT magmatism and are further away from the subduction zone than the Dibba Zone. Peridotites from Aswad, Fizh and Southern Oman only record MORB-IAT magmatism and thus must have formed furthest away from the subduction zone.

V2 episode

Initiation of subduction near the spreading ridge resulted in the re-melting of the depleted, shallow mantle wedge and the generation of boninitic magma that pervasively infiltrated the mantle lithosphere of Khawr Fakkan (Stage C, Figure

6.7b). As subduction continued, steady state magmatism ended with extension accommodated by NW-SE faulting as the crust began clockwise rotation (Stage D, Figure 6.7b). Volatile-enhanced melting of increasingly depleted mantle continued above the subduction zone and generated island-arc tholeiite magmas, some with boninitic affinity (Stage E, Figure 6.7b). These melts infiltrated the mantle of the Aswad and Fizh Blocks with the last melts (i.e. IAT/BON) infiltrating along shear zones in the mantle and intruding the crust along lithospheric scale faults.

Peridotites from Khawr Fakkan reacted with BON melts whereas peridotites from Aswad and Fizh reacted with IAT melts. Therefore, Figure 6.7b illustrates that Khawr Fakkan was closer to the subduction zone than Aswad and Fizh because boninitic magmatism is typically more proximal to the subduction zone than island-arc tholeiitic magmatism (Pearce et al., 1995, 2000). Southern Oman was more distal from the subduction zone because there is no record of V2 magmatism in that region. Peridotites from the Dibba Zone were more proximal to the subduction zone than Khawr Fakkan and indicate that boninitic magmatism was not generated this close to the trench.

6.5.4 Location of detachment of the northern Oman-U.A.E. ophiolite

Figure 6.8 displays three proposed models for the obduction of the Oman-U.A.E. ophiolite in relation to the subduction zone. The first model (Figure 6.8a), introduced in Section 1.4.2, is that obduction of the ophiolite initiated at the mid-ocean ridge and induced a shallow subduction zone by underthrusting of hot, young oceanic lithosphere (e.g. Boudier et al., 1981 and 1988; Boudier and Coleman, 1981; Ishikawa et al., 2005; Arai et al., 2006). The second model (Figure 6.8b), introduced in Section 1.4.1, is that a subduction zone existed underneath the ophiolite before obduction started and that obduction initiated along the plane of the subduction zone (e.g. Searle and Malpas, 1980, 1982; Pearce et al., 1981; Lippard et al., 1986; Searle and Cox, 1999).

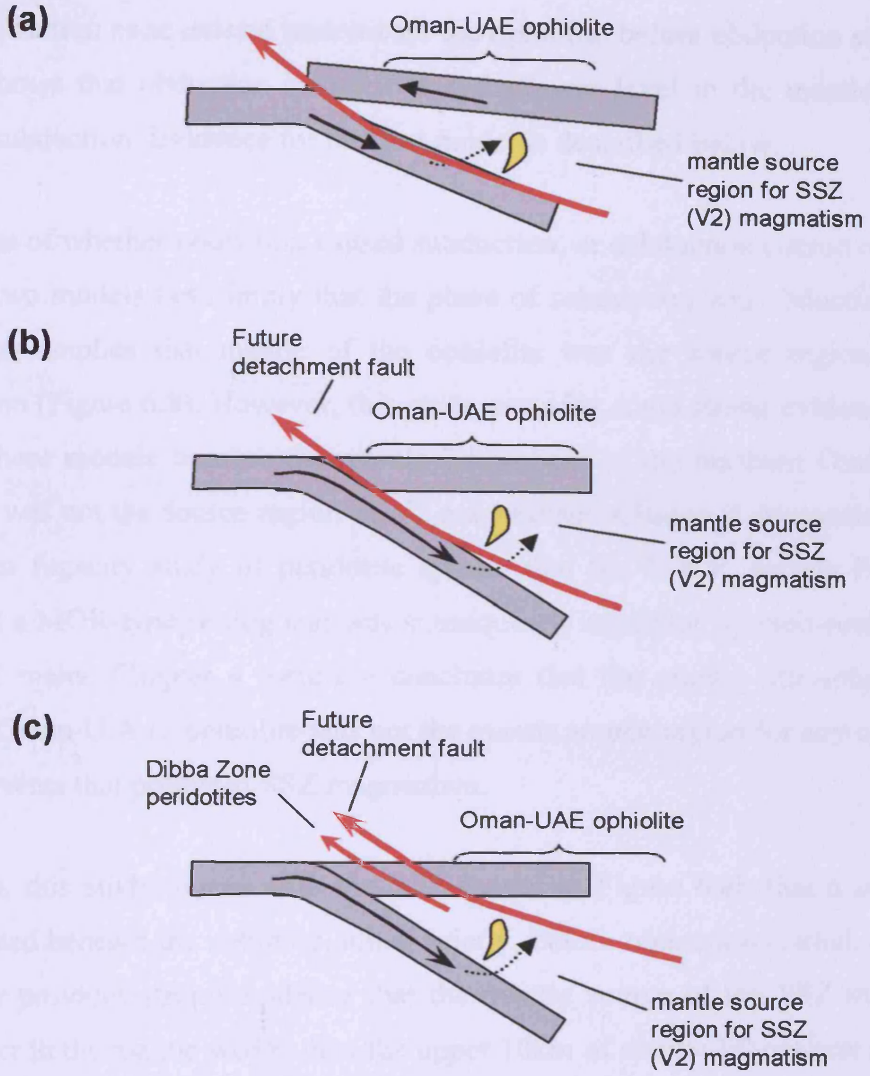

Figure 6.8: Cartoon comparing three models for the origin of the subduction zone in the Oman-UAE ophiolite, (a) obduction of the ophiolite at a mid-ocean ridge initiated subduction (e.g. Boudier et al., 1981 and 1988; Boudier and Coleman, 1981; Ishikawa et al., 2005; Arai et al., 2006), (b) the subduction zone initiated obduction along the plane of the subduction zone (Searle and Malpas, 1980, 1982; Pearce et al., 1981; Lippard et al., 1986; Searle and Cox, 1999) and (c) a subduction zone existed at a deeper level than the obduction plane of the ophiolite (this study). The red arrows mark the obduction plane of the ophiolite, i.e. the basal detachment fault of the Banded Unit. In (a) and (b) the obduction plane is the same as the subduction plane and infers that the mantle source region for the V2 magmatism (yellow upwelling) is preserved in the mantle of the Oman-UAE ophiolite. (c) This study demonstrates that the mantle source for the V2 magmatism was deeper than the mantle preserved in the Oman-UAE ophiolite and therefore the obduction plane was shallower than the subduction plane. Furthermore, mantle lithosphere nearer the trench (i.e. Dibba Zone) was incorporated underneath the ophiolite during obduction.

The third model (Figure 6.8c), proposed by this study, agrees with the second model that a subduction zone existed underneath the ophiolite before obduction started, but instead shows that obduction initiated at a shallower level in the mantle than the plane of subduction. Evidence for this last model is described below.

Regardless of whether obduction caused subduction, or subduction caused obduction, the first two models both imply that the plane of subduction and obduction are the same. This implies that mantle of the ophiolite was the source region for SSZ magmatism (Figure 6.8). However, this study provides some strong evidence against both of these models because the mantle lithosphere of the northern Oman-U.A.E. ophiolite was not the source region of V2 magmatism. Chapter 4 demonstrates from an oxygen fugacity study of peridotite spinels that the U.A.E. mantle lithosphere formed at a MOR-type setting and was subsequently modified by melt-rock reaction with SSZ melts. Chapter 4 therefore concludes that the mantle lithosphere of the northern Oman-U.A.E. ophiolite was not the mantle source region for any of the later melting events that produced SSZ magmatism.

Therefore, this study agrees with the SSZ model in Figure 6.8b that a subduction zone existed beneath the ophiolite, albeit briefly, before obduction started. However, this study provides strong evidence that the mantle source of the SSZ magmatism was deeper in the mantle wedge than the upper 10km of mantle lithosphere preserved in the ophiolite today. Therefore, the ophiolite detached at a shallower level than the plane of the subduction zone (Figure 6.8c). The detachment plane probably initiated along high-temperature mantle shear zones (i.e. Banded Unit) that were active during the clockwise rotation associated with the V2 magmatic event. Further evidence to support this obduction model is that during detachment the ophiolite incorporated slices of ultramafics between the ophiolite and the trench (i.e. Dibba Zone, see Section 6.4) as it bulldozed its way over the underlying plate and onto the continental margin. If detachment of the ophiolite initiated along the plane of the subduction zone then it could not incorporate near-trench mantle underneath it (i.e. Dibba Zone).

6.6 Conclusions

- The history of melt infiltration in the U.A.E. mantle, recorded by melt-rock reaction of chrome-spinels, resembles the magmatic history of the crust.

- Peridotites from the Dibba Zone and the northern region of Khawr Fakkan provide additional information for the magmatic history of these areas because the crustal sequence is absent.

- Both the mantle and crust in the U.A.E. provide evidence that the northern Oman-U.A.E. ophiolite formed by a switch in tectonic setting from spreading in a marginal basin (V1) to a SSZ setting (V2).

- The mantle lithosphere of the northern Oman-U.A.E. ophiolite formed during the main period of crustal accretion at a mid-ocean ridge (V1 magmatic event) in a marginal basin setting with minor influence from a subduction zone.

- The mantle lithosphere was modified by melt-rock reaction with V1 and V2 melts; geochemical maps of the mantle illustrate the regional pattern of melt infiltration and constrain the proximity of each mantle domain to the subduction zone.

- The focused flow of melt in dunite channels in the U.A.E. cannot all be attributed to the extraction of melt at a spreading ridge and its associated mantle diapirs as proposed by Nicolas et al., (2000) and Kelemen et al., (1995) for Oman.

- Geochemistry of the Dibba Zone peridotites is documented for the first time and shows that they originate from mantle lithosphere located between the trench and the main ophiolite.

- The Dibba Zone peridotites represent pre-existing mid-ocean ridge lithosphere, which was infiltrated with MORB melt prior to subduction initiation and subsequently interacted with IAT/BON melts during the final stages of V2 magmatism associated with shearing and detachment.

- Khawr Fakkan mantle provides evidence for pre-existing lithosphere formed at a mid-ocean ridge, and subsequently infiltrated with BON melts during subduction initiation which occurred proximal to the subduction zone.

- Peridotites from Aswad and Fizh provide evidence for lithosphere farther away from the subduction zone than Khawr Fakkan which formed at a spreading ridge, influenced by subduction, and interacted with increasingly depleted melts (transitional MORB, IAT, IAT/BON) as a result of volatile-enhanced melting in the mantle wedge.

- The mantle lithosphere of the northern Oman-U.A.E. ophiolite was not the source for the V2 magmatism and this indicates that the detachment of the ophiolite took place at a shallower level than the plane of the subduction zone.

- During detachment the ophiolite incorporated slices of ultramafic rocks nearer the trench (i.e. the Dibba Zone peridotites) as it bulldozed its way over the underlying plate and onto the continental margin.

- The U.A.E. region of the northern Oman-U.A.E. ophiolite provides a rare insight into the transient stage of subduction initiation.

- The SSZ (V2) magmatic period of the northern Oman-U.A.E ophiolite can be regarded as an embryonic volcanic arc which did not reach maturity before the ocean basin closed and the ophiolite was exhumed.

Chapter 7: Conclusions

The aims of this thesis as stated in Chapter 1 were:

1) To investigate the mantle processes in the U.A.E., using chrome-spinel geochemistry, associated with a switch in tectonic setting from mid-ocean ridge spreading (V1 magmatism) to a supra-subduction zone setting (V2 magmatism).

2) To relate the mantle sequence to the corresponding crustal sequence in the U.A.E. in order to investigate whether melt infiltration in the upper mantle is representative of the magmatism in the crust as documented by Lilly (2006).

The conclusions of each Chapter of thesis are summarised below and demonstrate that the aims of the thesis were achieved and more.

7.1 Summary of Chapter 2: Geology of the U.A.E. mantle and MTZ

Chapter 2 identified two possible generations of dunites and chromitites in the mantle from field observations. It hypothesised that the early generation of deformed dunites and chromitites originated from magmatism at a spreading ridge, whereas the later generation of undeformed dunites and chromitites originate from later magmatic episodes in a supra-subduction zone setting.

The BGS mapping team proposed that the Moho transition zone (MTZ) is a complex zone with massive dunite and layered gabbro forming from the early magmatic phase at the spreading ridge and wehrlite and pyroxenite intrusions of the Mixed Unit associated with the later, subduction-related magmatic phase. In addition, they identified shear zones in the upper mantle which divided both the Aswad and Khawr

Fakkan Block into shallow and deeper domains of mantle.

7.2 Summary of Chapter 3: Characterisation of the U.A.E. ultramafic rocks

Mapping peridotite microstructures confirmed the shear zones in the upper mantle of each Block. As in Oman, the U.A.E. mantle predominantly consists of harzburgite with subordinate lherzolite which is restricted to the base of the ophiolite. The close association between clinopyroxene-rich harzburgites and the mantle shear zones implies refertilisation of the shear zone by melt infiltration. A large region of Khawr Fakkan North hosts clinopyroxene-poor harzburgites which are uncommon in Oman.

Spinel textures in the U.A.E. peridotites provide important information about melt infiltration and melt-rock reaction in the mantle. Three main types of spinel were identified. Type 1 (Holly-leaf) spinels are residual from melting and characteristic of most harzburgites and lherzolites. Type 2 (subidiomorphic) and Type 3 (euhedral) spinels probably formed by melt-rock reaction and are characteristic of dunites and chromitites. However, clinopyroxene-poor harzburgites from Khawr Fakkan North and harzburgites associated with mantle shear zones also display Type 2 and Type 3 spinels. This provides evidence that melt infiltration and melt-rock reaction was common in these two areas.

Spinel morphology cannot distinguish between early and late generation of dunites and chromitites identified by Chapter 2. This is because Type 2 and Type 3 spinels in dunites and chromitites do not deform in the presence of a melt during high-temperature to low-temperature deformation of the mantle. Instead, undeformed olivine microstructures of dunites confirm field observations that large dunites in Khawr Fakkan North probably formed by later generations of melts (i.e. post spreading-ridge) in the mantle. Dunite spinels were only deformed during low-temperature emplacement of the ophiolite.

7.3 Summary of Chapter 4: Tectonic discrimination of the U.A.E. peridotites

Chapter 4 demonstrated how useful chrome-spinel geochemistry is in determining both the petrogenetic and tectonic history of peridotites. Co-variations between Cr#, Ti and Fe^{3+} provide sensitive indicators of degree of melting, oxygen fugacity and melt-rock reaction. Chrome-spinel geochemistry provides valuable information on both the nature of the mantle lithosphere and the infiltrating melts that reacted with the upper mantle and demonstrates the complex tectonic history of the northern Oman-U.A.E. ophiolite.

The chrome-spinels in peridotites have large variations in Cr# (0.2 – 0.9) and TiO_2 content (0.02 – 0.7 wt%). The Cr#-TiO_2 diagram confirmed that the majority of Type 1 spinels in harzburgites and lherzolites are residual, whereas Type 2 and Type 3 spinels in dunites and harzburgites formed by melt-rock reaction, as proposed in Chapter 3. Type 1 spinels in harzburgites have Cr# between 0.2 and 0.65 and correspond to residues from 10 -30% partial melting of a fertile mantle. Melt-rock reaction trends on the Cr#-TiO_2 diagram identified different melt compositions that reacted with the mantle. These are BON, IAT/BON, IAT, and MORB or MORB/IAT. The Cr#-TiO_2 diagram could not distinguish MORB from MORB/IAT melt-rock reaction because both form spinels with similar low Cr# (0.4 – 0.6). However, the Cr#-fO_2 diagram for spinel indicated that this melt was transitional MORB/IAT, originating from a SSZ setting, and not true MORB.

The Cr#- fO_2 diagram also demonstrated that the pre-existing mantle lithosphere formed originally at a spreading ridge and was modified to various degrees by infiltration and reaction with SSZ melts. The mantle lithosphere was cogenetic with the MORB/IAT melts that reacted with the mantle but was not cogenetic with the more depleted IAT and BON melts. The U.A.E. peridotites display similar polygenetic histories to those identified in the South Sandwich forearc and the Mariana forearc both of which formed in a SSZ setting.

7.4 Summary of Chapter 5: New developments in the tectonic discrimination of chrome-spinel: analysis of gallium by Laser Ablation-ICP-MS.

Chapter 5 developed a new method to analyse Ga in chrome-spinel by LA-ICP-MS using matrix-matched standards. This method was used to extend, for the first time, the suite of elements used in tectonic discrimination of chrome-spinel to Ga. The discrimination diagrams were set up using modern-day peridotites from passive continental margins (PCM), MOR and SSZ settings and tested on peridotites from the U.A.E. This study has shown that the analysis of Ga by LA-ICP-MS has the potential to improve tectonic discrimination of peridotites in conjunction with Fe^{3+} and TiO_2. There is some evidence that the Ga/Fe^3# ratios are independent of magmatic differentiation and thus implies that an evolving MOR melt cannot be mistaken for a SSZ melt using Ga/Fe^3# ratios. The new Ti/Fe^3#-Ga/Fe^3# diagram forms a useful petrogenetic and tectonic discrimination diagram which can monitor melt-rock reaction at each setting. The Ti/Fe^3#-Ga/Fe^3# diagram has the potential to discriminate peridotites that are ambiguous on the Cr#-fO_2 discrimination diagram, and reveals that not all the U.A.E. dunites that plot on the MOR/SSZ boundary are SSZ in origin as was assumed in Chapter 4. Instead, a few dunites are re-classified as MORB-type dunites.

Unfortunately, the Ti/Fe^3#-Ga/Fe^3# diagram cannot be applied to chromitites, for reasons unknown. This implies that the Ti/Fe^3#-Ga/Fe^3# diagram is not suitable for discrimination of detrital spinels because one can not distinguish between peridotite and chromitite spinels.

7.5 Summary of Chapter 6: Tectonic evolution of the northern Oman-U.A.E. ophiolite

Chapter 6 demonstrated that the history of melt infiltration in the U.A.E. mantle, as recorded by melt-rock reaction of chrome-spinels, resembles the magmatic history of the crust for the Aswad and Khawr Fakkan Blocks. Both the mantle and crust in the U.A.E. provide evidence that the northern Oman-U.A.E. ophiolite formed by a switch in tectonic setting from spreading in a marginal basin (V1) to a SSZ setting (V2).

Chrome-spinel geochemistry of the U.A.E. peridotites indicate that the mantle lithosphere of the northern Oman-U.A.E. ophiolite formed during the main period of crustal accretion at a mid-ocean ridge (V1 magmatic event) in a marginal basin setting with minor influence from a subduction zone. The mantle lithosphere was modified by melt-rock reaction with V1 and V2 melts. The V2 melts preferentially infiltrated the deeper mantle sections of each Block whereas the shallower mantle sections and MTZ record the earlier V1 magmatic events. Chrome-spinel chemistry confirms the hypothesis from field observations that the earlier generation of dunites and chromitites originated from the V1 spreading episode of magmatism and the later generation of dunites and chromitites formed during the V2 period of magmatism at a SSZ setting. The magmatic record of the mantle is largely representative of that in the crust. The exception is in Khawr Fakkan, where the incomplete crustal sequence underestimates the vast extent of boninitic magmatism that infiltrated the mantle in this Block.

Geochemical mapping of the mantle highlights a regional pattern to melt infiltration. The focused flow of melt in dunite channels in the U.A.E. cannot all be attributed to the extraction of melt at a spreading ridge and its associated mantle diapirs as proposed by Nicolas et al., (2000) and Kelemen et al., (1995) for Oman. The possible mantle diapir in Khawr Fakkan North is associated with extensive BON melt infiltration during subduction initiation. Geochemical mapping confirms that the shear zones in the mantle juxtapose chemically distinct mantle domains.

Geochemical mapping also constrains the proximity of each mantle domain to the subduction zone. Geochemistry of the Dibba Zone peridotites is documented for the first time and shows that they originate from mantle lithosphere located between the trench and the ophiolite. The Dibba Zone peridotites represent pre-existing mid-ocean ridge lithosphere that was infiltrated with MORB melt prior to subduction initiation, and subsequently interacted with IAT/BON melts during the final stages of V2 magmatism. Khawr Fakkan mantle provides evidence for pre-existing lithosphere formed at a mid-ocean ridge that was subsequently infiltrated with BON melts during subduction initiation. Peridotites from Aswad and Fizh formed at a spreading ridge influenced by subduction, and interacted with increasingly depleted melts (transitional MORB, IAT, IAT/BON) as a result of volatile-enhanced melting in the mantle wedge. This took place further away from the subduction zone than Khawr Fakkan. Peridotites from southern Oman provide no evidence for V2 magmatism because they were furthest away from the subduction zone.

The mantle lithosphere of the northern Oman-U.A.E. ophiolite was not the source for the V2 magmatism and indicates that the detachment of the ophiolite took place at a shallower level than the plane of the subduction zone. During detachment the ophiolite incorporated slices of ultramafic rocks near the trench (i.e. the Dibba Zone peridotites) as it bulldozed its way over the underlying plate and onto the continental margin.

7.6 Key advances

- Chrome-spinel geochemistry provides useful information on both the residual mantle and melt infiltration of the mantle via melt-rock reaction that can unravel complex tectonic histories of peridotites.

- Chrome-spinel geochemistry demonstrates that the U.A.E. peridotites have a complex tectonic history involving more than one tectonic setting: the U.A.E. mantle lithosphere formed at a MOR-type setting and was modified by melt-rock reaction with MORB-type and SSZ-type melts.

- The mantle lithosphere of the northern Oman-U.A.E. ophiolite was not the source region for the SSZ magmatism as implied by previous tectonic models.

- Instead, this study reveals that detachment of the ophiolite took place at a shallower level than the plane of the subduction zone and thus provides strong evidence for a subduction zone at a still deeper level.

- Detailed geochemical maps of the mantle highlight the spatial pattern of melt infiltration associated with a switch in tectonic setting from mid-ocean ridge to supra-subduction zone setting.

- Melt flow in dunite channels of the northern Oman-U.A.E. ophiolite cannot all be attributed to the focused flow of melt beneath a spreading ridge and its associated mantle diapirs as proposed by Nicolas et al., (2000) and Kelemen et al., (1995).

- The mantle section of the U.A.E. preserves a magmatic record comparable to that of the crust and contributes additional information where the crustal record is incomplete (e.g. Khawr Fakkan) or absent (e.g. Dibba Zone).

- The large extent of boninitic magmatism that infiltrated the mantle of the Khawr Fakkan Block during subduction initiation was previously underestimated by the crustal record.

- The results demonstrate for the first time that the Dibba Zone peridotites originate from pre-existing true MORB mantle between the trench and the Oman-U.A.E. ophiolite.

- The Dibba Zone peridotites were incorporated beneath the ophiolite during detachment as it bulldozed its way over the underlying plate and onto the continental margin.

- A new technique for the Laser Ablation-ICP-MS of chrome-spinels extends the suite of elements already used for tectonic discrimination and the resulting Ti/Fe^3# vs. Ga/ Fe^3# diagram was successfully tested on the U.A.E. peridotites.

7.7 Recommendations for future research

Laser Ablation-ICP-MS offers new opportunities to extend and improve the tectonic discrimination of chrome-spinels. This study has shown that Ga can improve discrimination using Fe^{3+} because Ga/Fe^3# ratios are potentially independent of magmatic differentiation. If this is the case, then this technique could be useful in discriminating ultramafic and mafic spinels from cumulates, such as wehrlites, pyroxenites, troctolites and gabbros from the MTZ of the northern Oman-U.A.E. ophiolite. As such, future work should aim to develop the tectonic discrimination of chrome-spinel using Ga by more LA-ICP-MS analyses of:

1) Peridotite spinels from modern-day tectonic settings to confirm the proposed tectonic boundaries on the Ti/Fe^3# vs. Ga/ Fe^3# diagram for peridotites.

2) Spinels from lavas of known tectonic settings to confirm that Ga/Fe^3# ratios are independent of magmatic differentiation.

3) Spinels from cumulates of known tectonic setting to investigate the potential of the Ti/Fe^3# vs. Ga/ Fe^3# diagram in the discrimination of cumulates from ophiolites.

Sc is also measurable in chrome-spinel by Laser Ablation-ICP-MS and could be developed in a similar manner as Ga in the discrimination of chrome-spinel.

Further work could be done with the whole rock data produced in this study and was not carried out due to time constraints. Pearce et al., (2000) showed that whole rock data can discriminate between partial melting trends and melt-mantle reaction trends in peridotites with complex tectonic histories, such as the South Sandwich forearc. This work could compliment the story of partial melting and melt-mantle reaction evidenced from chrome-spinels.

References

Adachi, Y. and Miyashita, S. (2003). Geology and petrology of the plutonic complexes in the Wadi Fizh area: Multiple magmatic events and segment structure in the northern Oman ophiolite. Geochemistry, Geophysics, Geosystems, 4, 8619, doi:10.1029/2001GC000272

Ahmed, A.H. and Arai, S. (2002). Unexpectedly high PGE-chromitite from the deeper mantle section of the northern Oman ophiolite and its tectonic implications. Contributions to Mineralogy and Petrology, 143, 263 – 278.

Al-Aabed, S. (2000). Petrogenesis of chromite and associated minerals in the upper mantle peridotite of the northern Semail Ophiolite (U.A.E). Ph.D. Thesis, Ohio State University, 639 p.

Alabaster, T., Pearce, J.A. and Maplas, J. (1982). The volcanic stratigraphy and petrogenesis of the Oman ophiolite complex. Contributions to Mineralogy and Petrology, 81, 168 - 183.

Allan, J.F., and Dick, H.J.B. (1996). Cr-rich spinel as a tracer for melt migration and melt–wall rock interaction in the mantle: Hess Deep, Leg 147. In: Mével, C., Gillis, K.M., Allan, J.F., and Meyer, P.S. (Eds.), Proceedings of the Ocean Drilling Program, Scientific Results, 147, 157–172.

Allan, J.F., Sack, R.O. and Batiza, R. (1988). Cr-rich spinels as petrogenetic indicators: MORB-type lavas from the Lamont seamount chain, eastern Pacific. American Mineralogist, 73, 741-753.

Arai S. (1992). Chemistry of chromian spinel in volcanic rocks as a potential guide to magma chemistry. Mineralogical Magazine, 56, 173-184.

Arai, S. (1994a). Characterization of spinel peridotites by olivine-spinel compositional relationships: Review and interpretation. Chemical Geology, 113, 191-204.

Arai, S., and Matsukage, K. (1996). Petrology of gabbro-troctolite-peridotite complex from Hess Deep, equatorial Pacific: implications for mantle-melt interaction within the oceanic lithosphere. In: Mével, C., Gillis, K.M., Allan, J.F., and Meyer, P.S. (Eds.), Proceedings of the Ocean Drilling Program, Scientific Results, 147, 135–155.

Arai, S., Uesugi, J and Ahmed, A.H. (2004). Upper crustal podiform chromitite from the northern Oman ophiolite as the stratigraphically shallowest chromitite in ophiolite and its implication for Cr concentration. Contributions to Mineralogy and Petrology, 147, 145-154.

Arai, S., Kadoshima, K. and Morishita,T. (2006). Widespread arc-related melting in the mantle section of the northern Oman ophiolite as inferred from detrital chromian spinels. Journal of the Geological Society, 163, 869-879.

Augé, T. (1987). Chromite deposits in the northern Oman ophiolite: mineralogical constraints. Mineralium Deposita, 22, 1- 10.

Augé, T. and Roberts, S. (1982). Petrology and geochemistry of some chromitiferous bodies within the Oman ophiolite. Ofioliti , 7.

Ballhaus, C., Berry, R.F. and Green D.H. (1991). High pressure experimental calibration of the olivine-orthopyroxene-spinel oxygen barometer: implications for the oxidation state for the upper mantle. Contributions to Mineralogy and Petrology, 107, 27-40.

Barnes S.J. and Roeder P.L. (2001). The range of spinel compositions in terrestrial mafic and ultramafic rocks. Journal of Petrology, 42, 2279-2302.

Bartholomew, I.D. (1993). The interaction and geometries of diapiric uprise centres along mid-ocean ridges-evidence from mantle fabric studies of ophioite complexes. In: Prichard, H.M., Alabaster, T., Harris, N.B.W. and Neary, C.R. (Eds.), Magmatic Processes and Plate Tectonics, Geological Society Special Publication, 76,245-256.

Benn, K., Nicolas, A., and Reuber, I. (1988). Mantle-crust transition zone and origin of wehrlitic magmas: Evidence from the Oman ophiolite. Tectonophysics, 151, 75-85.

Benoit, M., Ceuleneer, G. and Polvé, M. (1999). The remelting of hydrothermally altered peridotite at mid-ocean ridges by intruding mantle diapirs. Nature, 403, 514-518.

Blanford, W.T. (1872). Notes on Muskat and Musandam on the coast of Arabia. Records of the Geological Survey of India, 5, 75-77.

Bonatti, E. and Michael, P. J. (1989). Mantle peridotites from continental rifts to ocean basins to subduction zones. Earth and Planetary Science Letters 91, 297–311.

Boudier, F. and Coleman, R.G. (1981). Cross-section through the peridotite in the Semail ophioite, southeastern Oman mountains. Journal of Geophysical Research, 86, 307 - 326.

Boudier, F. and Nicolas, A. (1995). Nature of the Moho transition zone in the Oman ophiolite. Journal of Petrology, 36, 777–796.

Boudier, F., Ceuleneer, G. and Nicolas, A. (1988). Shear zones, thrusts and related magmatism in the Oman ophiolite: initiation of thrusting on an oceanic ridge. Tectonophysics, 151, 275-296.

Boudier, F., Godard, M. and Armbruster, C. (2000). Significance of noritic gabbros in the gabbro section of the Oman ophiolite. Marine Geophysical Researches, 21, 307 - 326 .

Boudier, F., Nicolas, A., and Ildefonse, B. (1996). Magma chambers in the Oman ophiolite: fed from the top and bottom. Earth and Planetary Science Letters, 144, 239 - 250.

Braun, M.G. and Kelemen, P.G. (2002). Dunite distribution in the Oman Ophiolite: Implications for melt flux through porous dunite conduits. Geochemistry, Geophysics, Geosystems, 3, , 8603, doi:10.1029/2001GC000289.

Brown, M.A. (1980). Textural and geochemical evidence fro the origin of some chromite deposits in the Oman ophiolite. Panayiotou, A. (Eds.), Ophiolites: Proceedings Internat. Ophiolite Symposium 1979., Geological Survey Dept. Cyprus, 714-721.

Brown, M.A. (1982). Chromite Deposits and Their Ultramafic Host Rocks in the Oman Ophiolite. Ph.D. Thesis, Open University, Milton Keynes .

Browning, P. (1982). The petrology, geochemistry, and structure of the plutonic rocks of the Oman ophiolite. Ph.D. Thesis, Open University, Milton Keynes.

Bryndzia, L. T. and Wood, B. J. (1990). Oxygen thermobarometry of abyssal spinel peridotites: the redox state and C–O–H volatile composition of the Earth's sub-oceanic upper mantle. American Journal of Science, 290, 1093-1116.

Burton, J.D., Culkin, F. and Riley, J.P. (1959). The abundances of gallium and germanium in terrestrial materials. Geochimica et Cosmochimica Acta, 16, 151-180.

Cannat, M., Mevel, C., Maia, M., Deplus, C., Durand, C., Gente, P., Agrinier, P., Belarouchi, A., Dubuisson, G., Hulmer, E. and Reynolds, J. (1995). Thin crust, ultramafic exposures, and rugged faulting patterns at the Mid Atlantic Ridge (22o-24oN). Geology, 23, 49-52.

Carter, H.J. (1850). Geological observations on the igneous rocks of Muscat and its neighbourhood, and on limestone formation at their circumference. Journal of Bombay Branch of the Royal Asiatic Society III (2), 118 - 129.

Cassard, D., Nicolas, A., Rabinovitch, M., Leblanc, M.and Prinzhofer, A. (1981). Structural classification of chromite pods in southern new Caledonia: Economic Geology, 76, 805 - 831.

Ceuleneer, G., Nicolas, A., and Boudier, F. (1988). Mantle flow paterns at an oceanic spreading centre: The Oman peridotites record. Tectonophysics, 151, 1-26.

Coggon, J. (2007). A new model for the origin of Roberts Victor ecolgites. M.Sc. Thesis, School of Earth, Ocean and Planetary Sciences, Cardiff University.

Coleman, R.G. (1971). Plate tectonic emplacement of upper mantle peridotites along continental edges. Journal of Geophysical Research, 76, 1212-1222.

Coleman, R.G. (1981). Tectonic setting of ophiolite obduction in Oman.Journal of Geophysical Research, 86, 2497-2508.

Cox, J., Searle, M.P. and Pedersen, R. (1999). The petrogenesis of leucogranitic dykes intruding the northern Semail ophiolite, United Arab Emirates: field relationshops, geochemistyr and Sr/Nd isotope systematics.Contributions to Mineralogy and Petrology, 37, 267-288.

Crawford, A.J. (1989). Boninites and related rocks. London, Unwin Hyman, 465 pp.

Denny M.B. (1998). Major and trace element discrimination of chromian spinels with particular application to the provenance of diamond indicator chromite from the Yilgarn Craton, Western Australia. Unpublished honours thesis, Department of Geology, The Australian National University.

Dewey, J.F. (1976). Ophiolite obduction. Tectonophysics, 31, 93-120.

Dewey, J.F.and Bird, J.M. (1971). Origin and emplacement of the ophiolite suite: Appalachian ophiolites in Newfoundland. In: Gillis, K., Mevel, C., Allan, J., and al., e., (Eds.), Scientific Results: College Station, TX, Ocean Drilling Program, Texas AandM University, 103-134.

Dick H.J. and Bullen T. (1984). Chromian spinel as a petrogenetic indicator in abyssal and alpine-type peridotites and spatially associated lavas. Contributions to Mineralogy and Petrology, 86, 54-76.

Dick, H. J. B., and Natland, J. H. (1996). Late stage melt evolution and transport in the shallow mantle beneath the East Pacific Rise, .In: Gillis, K., Mevel, C., Allan, J., and al., e., (Eds.), Scientific Results: College Station, TX, Ocean Drilling Program, Texas AandM University, 103-134.

Dick, H.J. (1977). Partial melting in the Josephine peridotite I, the effect on mineral composition and its consequence for geobarometry and geothermometry. American Journal of Science, 277, 801-832.

Dilek, Y. (2003). Ophiolite concept and its evolution.In: Dilek, Y and Newcomb, S. (Eds.), Ophiolite Concept and the evolution of geological thought. Geological Society of America Special Paper, 373, 1-16.

Dilek, Y., Moores, E.M. and Furnes, H. (1998). Structure of modern oceanic crust and ophiolites and implications for faulting and magmatism at oceanic spreading centres. In: Buck, R., Karson, J., Delaney, P., and Lagabrielle, Y., (Eds.), Faulting and magmatism at mid-ocean ridges: Washington, D.C., American Geophysical Union Monograph, 106, 219-266.

Edwards, S. J. and Malpas, J. (1996). Melt-peridotite interactions in shallow mantle at the East Pacific Rise: evidence from ODP Site 895 (Hess Deep). Mineralogical Magazine, 60, 191–206.

Edwards.S.J., Pearce, J.A. and Freeman, J. (2000). New insights concerning the influence of water during the formation of podiform chromitite. In: Dilek, Y., Moores, E.M., Elthon, D., and Nicolas, A., (Eds.), Ophiolites and Oceanic Crust: New Insights from Field Studies and the Ocean Drilling Program: Boulder, Colorado, Geological Society of America Special Paper 349,139-147.

Eggins S.M., Rudnick R.L. and McDonough W.F. (1998). The composition of peridotites and their minerals: a laser-ablation ICP-MS study. Earth and Planetary Science Letters, 154, 53-71.

Elburg, M.A. and Kamenetsky, V.S. (2007). Dehydration processes determine fO_2 of arc and intraplate magmas. Geochimica et Cosmochimica Acta, in press p.A252.

Ernewein, M., Pflumino, C.and Whitechurch, H. (1988). The death of an accretion zone as evidenced by the magmatic history of the Semail ophiolite (Oman). Tectonophysics, 151, 247-274.

Evans, B. W. and Frost, B. R. (1975). Chrome spinel in progressive metamorphism—a preliminary analysis. Geochimica et Cosmochimica Acta 39, 959–972.

Ewart A. and Griffin W.L. (1994). Proton-microprobe trace element study of selected Leg 135 core samples. In: Hawkins J., Parson L., Allan J., et al (Eds), Proceedings of the Ocean Drilling Program, Scientific Results, 135, 533-542.

Fabries, J. (1979). Spinel–olivine geothermometer in peridotites from ultramafic complex. Contributions to Mineralogy and Petrology, 69, 329–336.

Feig, S., Koepke, J. and Snow, J. (2006). Effect of water on tholeiitic basalt phase equilibria: An experimental study under oxidizing conditions. Contributions to Mineralogy and Petrology, 152, 611.

Gass, I.G. (1968). Is the Troodos massif of Cyprus a fragment of mesozoic ocean floor? Nature, 220, 39-42.

Gass, I.G.and Masson-Smith, D. (1963). The geology and gravity anomolies of the Troodos massif, Cyprus. Philisophical Transaction of the Royal Society of London, A 225, 417-467.

Gillespie, M.R. and Styles, M.T. (1999). BGS rock classification scheme, Volume 1: Classification of igneous rocks.British Geological Survey Research Report, (2nd edition) RR 99-06.

Girardeau, J., Monnier, C., Memee, L., and Quatrevauz, F. (2002). The Wuqbah peridotite, central Oman Ophiolite: Petrolgical characteristics of the mantle in a fossil overlapping ridge setting. Marine Geophysical Researches, 23, 43-56.

Glennie, K.W., Boeuf, M.G.A., Hughes Clark, M.W., Moody-Stuart, M., Pilaar, W.F.H and Reinhart, B.M. (1974). Geology of the Oman Mountains. Verhandelingen van het Kominklijk Nederlands geologisch mijnbouwkunding Genootschap.

Glaser S.M., Foley S.F. and Günther D. (1999). Trace element compositions of minerals in garnet and spinel peridotite xenoliths from the Vitim volcanic field, Transbaikalia, eastern Siberia. Lithos, 48, 263-285.

Gnos, E. (1992). The metamorphic rocks associated with the Oman ophiolite, Sultanate of Oman and United Arab Emirates. Ph.D. Thesis, University of Bern.

Gnos, E., Nicholas, A. (1996). Structural evolution of the northern end of the Oman ophiolite and eclosed granulites. Tectonophysics, 254, 111-137.

Godard, M., Bosch, D. and Einaudi, F. (2006). A MORB source for low-Ti magmatism in the Semail ophiolite. Chemical Geology, 234, 58-78.

Godard, M., Dautria, J-M. and Perin, M. (2003). Geochemical variability of the Oman ophiolite lavas: Relationship with spatial distribution and paleomagnetic directions. Geochemistry, Geophysics, Geosystems, 4, 8609, doi:10.1029/2002GC000452.

Godard, M., Jousselin, D. and Bodinier, J-L. (2000). Relationships between geochemistry and structure beneath a palaeo-spreading centre: a study of the mantle section in the Oman ophiolite. Earth and Planetary Science Letters, 180, 133-148.

Goldschmidt, V.M. (1937). The principles of distribution of chemical elements in minerals and rocks. Iotu Chem. Sac.655.

Grantham, G.H., Goedhart, M.L., Wipplinger, P.E., Thomas, R.J., Eglington, B.M., Harmer, R.E. and Hartzer, F.J. (2003). The geology of the Emirate of Fujairah. C.G.S. mapping report.

Greenbaum, D. (1972). Magmatic processes at ocean ridges: evidence from the Troodos Massif, Cyprus. Nature, 238, 18-21.

Greenbaum, D. (1977). The chromitiferous rocks of the Troodos ophiolite complex, Cyprus. Economic Geology and the Bulletin of the Society of Economic Geologists, Nature, 72, 1175-1194.

Grégoire M., Moine B.N., O'Reilly S.Y., Cottin J.Y. and Giret A. (2000). Trace element residence and partitioning in mantle xenoliths metasomatized by highly alkaline, silicate- and carbonate- rich melts (Kerguelen Islands, Indian Ocean). Journal of Petrology, 41, 477-509.

Griffin W.L., Sobolev N.V., Ryan C.G., Pokhilenko N.P., Win T.T. and Yefimova E.S. (1993). Trace elements in garnets and chromites: Diamond formation in the Siberian lithosphere. Lithos, 29, 235-256.

Griffin W.L., Ryan C.G., Gurney J.J., Sobolev N.V. and Win T.T. (1994). Chromite macrocrysts in kimberlites and lampriotes: geochemistry and origin. In: H.A.O. Meyer and O.H. Leonardos (Eds), Kimberlites, Related Rocks and Mantle Xenoliths. CRPM Special Publication, 1A/93, p/p/ 366 -377

Griffin W.L. and Ryan C.G. (1995). Trace element in indicator minerals: area selection and target evaluation in diamond exploration. Journal of Geochemical Exploration, 53, 311-337.

Griffin W.L., Fisher N.I., Friedman J.H. and Ryan C.G. (1997). Statistical techniques for the classification of chromites in diamond exploration samples. Journal of Geochemical Exploration, 59, 233-249.

Hacker, B.R. (1990). Simulation of the metamorphic and deformational history of the metamorphic sole of the Oman ophiolite. Journal of Geophysical Research, 95, 4895-4907.

Hacker, B.R. (1991). The role of deformation in the formation of metamorphic field gradients: ridge subduction beneath the Oman ophiolite. Tectonics, 10, 455-473.

Hacker, B.R. (1994). Rapid emplacement of young oceanic lithosphere: Argon geochronology of the Oman ophiolite. Science, 265, 1563-1565.

Hacker, B.R. and Gnos, E. (1997). The conundrum of Samail: explaining the metamorphic history. Tectonophysics, 279, 215-226.

Hacker, B.R., Mosenfelder, J.L. and Gnos,E. (1996). Rapid emplacement of the Oman ophiolite: thermal and geochronological constraints. Tectonics, 15, 1230-1247.

Hamlyn, P.R., and Bonatti, E. (1980). Petrology of mantle-derived ultramafics from the Owen fracture zone, northwest Indian Ocean: implications for the nature of the oceanic upper mantle. Earth and Planetary Science Letters, 48, 65-79.

Hellebrand, E., Snow, J.E., Dick, H.J.B., and Hofmann, A.W. (2001). Coupled major and trace elements as indicators of the extent of melting in mid-ocean-ridge peridotites. Nature, 410, 677-680.

Hess, H.H. (1955). Serpentines, orogeny and epeirogeny. In: Poldevaart, A., (ed.), Crust of the Earth (A Symposium): New York, Geological Society of America Special Paper, 62, 391-408.

Hess, H.H. (1965). Mid-ocean ridges and tectonics of the sea floor. In: Whitard, W.F., and Bradshaw, R., (Eds.), Submarine geology and geophysics: Proceedings of the 17th Symposium of the Colston Research Society: London, Butterworths, 317-334.

Hirschmann, M. (1995). Melt pathways in the mantle.Nature, 375, 737 - 738.

Holwell, D.A. and McDonald, I. (2007). Distribution of platinum-group elements in the Platreef at Overysel, northern Bushveld Copmlex: a combined PGM and LA-ICP-MS study.Contributions to Mineralogy and Petrology, DOI 10.1007/s00410-007-0185-9.

Hopson, C.A., Coleman, R.G., Gregory, R.T., Pallister, J.S. and Bailey, E.H. (1981). Geologic section through a Muscat-Ibra transect, southeastern Oman mountains. Journal of Geophysical Research, 86, 2527-2544.

Ishii, T., Robinson, P.T., Maekawa, H. and Fiske, R. (1992). Petrological studies of Peridotites from Diapiric Serpentinite Seamounts in the Izu-Ogasawara-Mariana Forearc, Leg 125. In: Fryer, P., Pearce, J.A., Stokking, L.B., et al (Eds.), Proceeding of the Ocean Drilling Program. Scientific Results, 125, 445-485.

Ishikawa, T., Fujisawa, Nagaishi, K. and Masuda, T. (2005). Trace element characteristics of the fluid liberated from amphibolite-facies slab: Inference from the metamorphic sole beneath the Oman ophiolite and implication for boninite genesis. Earth and Planetary Science Letters, 240, 355-377.

Ishikawa, T., Nagaishi, K. and Umino, S. (2002). Boninitic volcanism in the Oman ophiolite: Implications for thermal condition during transition from spreading ridge to arc. Geology, 30, 899-902

Ishiwatari, A., Yanagida, Y., Li, Y-B., Ishii, T., Haraguchi. S., Koizumi, K., Ichiyama. Y. and Umeka., M. (2006). Dredge petrology of the boninite- and adakite- bearing Hahajima Seamount of the Ogasawara (Basin) forearc: and ophiolite or a serpentinitite seamount? The Island Arc, 15, 102-118.

Jackson, E.D. (1961). Primary textures and mineral association in the ultramafic zone of the Stillwater Complex . In: Wilson, H.D.B (ed), Magmatic ore deposits, Economic Geology Monograph, 4, 41-71.

Jacques, J.L. and Green, D.H. (1980). Anhydrous melting of peridotites at 0-15kb pressure and the genesis of tholeiitic basalts. Contributions to Mineralogy and Petrology,73 287-310.

Jones, K. (2005). The laser ablation ICP-MS analysis of olivine-hosted melt inclusions from the Mull Plateau Group Lavas, Mull, Scotland. Ph.D. Thesis, School of Earth, Ocean and Planetary Sciences, Cardiff University, 273 p.

Jousselin, D. and Nicolas, A. (2000a). The Moho transition zone in the Oman ophiolite-relation with wehrlites in the crust and dunites in the mantle. Marine Geophysical Researches, 21, 229-241.

Jousselin, D. and Nicolas, A. (2000b). Oceanic ridge off-axis deep structure in the Mansah region (Sumail massif, Oman ophiolite). Marine Geophysical Researches, 21, 243-257.

Juteau, T., Ernewein, M. Reuber, I. Whitechurch, H. and Dahl, R. (1988). Duality of magmatism in the plutonic sequence of the Sumail nappe, Oman. Tectonophysics, 151, 107–135.

Kamenetsky, V.S., Crawford. A.J., and Meffre, S. (2001). Factors controlling chemistry of magmatic spinel: an empirical study of associated olivine, Cr-spinel and melt inclusions from primitive rocks. Journal of Petrology, 42, 655-671.

Kamperman,M., Danyushevsky, L.V., Taylor,W.R. and Jablonski, W. (1996). Direct oxygen measurements of Cr-rich spinel; implications for spinel stoichiometry. American Mineralogist, 81,1186-1194.

Kanke, N. and Takazawa, E. (2005). Distribution of ultra-depleted peridotites in the northern Fizh mantle section from the Oman ophiolite.Abstract for Japan Earth and Planetary Science Joint Meeting, J004 - J029.

Kanke, N. and Takazawa, E. (2006). Spatial distribution of melt conduits in the mantle beneath oceanic spreading ridges: Observations from the Ingalls and Oman ophiolites. Abstract for Japan Earth and Planetary Science Joint Meeting, K008 - K103.

Kelemen, P.B. (1990). Reaction between ultramafic rock and fractionating basaltic magma.I. Phase relations, the origin of calc-alkaline magma series, and the formation of discordant dunite. Journal of Petrology, 31, 51-98.

Kelemen, P.B., Shimizu, N., and Slaters, V.J.M. (1995). Extraction of mid-ocean-ridge basalt from the upwelling mantle by focused flow of melt in dunite channels. Nature, 375, 747 – 753.

Kelemen, P.B., Koga, K., and Shimizu, N. (1997a). Geochemistry of gabbro sills in the crust-mantle transition zone of the Oman ophiolite: implications for the origin of the oceanic lower crust.Earth and Planetary Science Letters, 146, 475-488.

Kelemen, P.B., Hirth, G., Shimizu, N., Spiegelman, M., and Dick, H.J.B. (1997b). A review of melt migration processes in the adiabatically upwelling mantle beneath oceanic spreading ridges. Philisophical Transaction of the Royal Society of London, A, 355, 283-318.

Kelemen, P. B., Braun, M. and Hirth, G. (2000). Spatial distribution of melt conduits in the mantle beneath oceanic spreading ridges: Observations from the Ingalls and Oman ophiolites. Geochemistry, Geophysics, Geosystems, 1, [Paper number 1999GC000012.

Kimball, K.L. (1990). Effects of hydrothermal alteration on the compositions of chromian spinel. Contributions to Mineralogy and Petrology, 105, 337-346.

Koepke, J., Feig, S.T., and Snow, J. (2005). Hydrous partial melting within the lower oceanic crust. Terra Nova, 17, 286–291.

Koga, K.T., Kelemen, P.B. and Shimizu, N. (2001). Petrogenesis of the crust-mantle transition zone and the origin of lower crustal wehrlite in the Oman ophiolite. Geochemistry, Geophysics, Geosystems, 2, 2000GC000132.

Korenaga, J., and Kelemen, P. B. (1997). Origin of gabbro sills in the Moho transition zone of the Oman ophiolite: Implications for magma transport in the oceanic lower crust. Journal of Geophysical Research, 102, 27,729-27,749.

Kurat G., Palme H., Spettel B. Baddenhausen H., Hofmeister H., Palme C. and Wanke H. (1980). Geochemistry of ultramafic xenoliths from Kapfenstein, Austria: evidence for a variety of upper mantle processes. Geochimica et Cosmochimia Acta, 44, 45-60.

Le Mée, L., Girardeau, J., and Monnier, C. (2004). Mantle segmentation along the Oman ophiolite fossil mid-ocean ridge.Nature, 432, 167-172.

Leblanc, M. and Ceuleneer, G. (1992). Chromite crystallization in a multicellular magma flow: Evidence from a chromitite dike in the Oman ophiolite. Lithos, 27, 231-257.

Lees, G.M. (1928). The geology and tectonics of Oman and of parts of south eastern Arabia. Quarterly Journal Geological Society of London, 110.

Lilly, R. (2006). The magmatic and crustal evolution of the northern Oman-United Arab Emirates ophiolite. PhD thesis, Cardiff University, 202pp.

Lippard, S.J., Shelton, A.W. and Gass, I.G. (1986). The Ophiolite of Northern Oman. Memoir Geological Society of London, 11, 178.

Lippard, S.J., Smewing, J.D.,Rothery, D.A., Browning, P. (1982). The geology of the Dibba zone, northern Oman mountains; a preliminary study. Journal of the Geological Society of London, 139, 59 - 66.

Lorand, J.P. and Ceuleneer, G. (1989). Silicate and base-metal sulfide inclusions in chromites from the Maqsad are (Oman ophiolite, Gulf of Oman): a model for entrapment. Lithos, 63, 161-173.

MacLeod, C.J. and Rothery, D.A. (1992). Ridge axial segmentation in the Oman ophiolite: evidence from along-stroke variations in the sheeted dyke complex. In: Parson, L.M., Murton, B.J. and Browning, P. (Eds.), Ophiolites and their modern oceanic analogues: Geological Society Special Publication, 60, 39 - 63.

MacLeod, C.J. and Yaouancq, G. (2000). A fossil melt lens in the Oman ophiolite: Implications for magma chamber processes at fast spreading ridges. Earth and Planetary Science Letters, 176, 357-373.

Matsukage, K. and Arai, S. (1996). Jadeite, Albite and Nepheline as inclusions in spinel of chromitite from Hess Deep, Equatorial Pacific: their genesis and implications for serpentinite diapir formation. Contributions to Mineralogy and Petrology, 131, 111-128.

Matsukage, K. Arai, S. Abe, N. and Yurimoto, H. (2001). Two contrasting melting styles of mantle peridotite in the northen Oman ophiolite: implications for the swich of their tectonic setting. Research Report of JSPS Grants-in Aid for Science Research, 11691121, 19-32.

McDonald, I. (2005). Development of sulphide standards for the in-situ analysis of platinum-group elements by laser ablation inductively coupled plasma-mass spectrometry (LA-ICP-MS). Extended abstract of the 10th International Platinum Symposium, 468-471.

McDonald I and Viljoen K.S. (2006). Platinum-group element geochemistry of mantle eclogites: a reconnaissance study of xenoliths from the Orapa kimberlite, Botswana. Transactions of the Institution of Mining and Metallurgy Section B-Applied Earth Science, 115, 81-93.

McKay D.B and Mitchell R.H. (1988). Abundance and distribution of gallium in some spinel and garnet lherzolites. Geochimica et Cosmochimia Acta, 52, 2867-2870.

Mellini, M., Rumori, C., Viti, C. (2005). Hydrothermally reset magmatic spinels in retrograde serpentinites: formation of "ferritchromit" rims and chlorite aureoles. Contributions to Mineralogy and Petrology, 149, 266-275.

Mercier, J-C.C. (1972). Structure des péridotites en enclaves dans quelques basaltes d'Europe et d'Hawaii. Regards sur la constitution du manteau supérieur. Thèse 3ème cycle, Univ. Nantes.

Mercier, J-C.C. and Nicolas, A. (1974). Textures and fabrics of upper-mantle peridotites as illustrated by xenoliths from basalts. Journal of Petrology, 16, 454-487.

Michael, P.J. and Bonatti, E. (1985). Peridotite composition from the North Atlantic: regional and tectonic variations and implications for partial melting. Earth and Planetary Science Letters, 73, 91-104.

Michel, J.C. (1993). Mineral occurrence and metallogenic map of the Sultanate of Oman, at scale 1:1,000,000 with Explanatory Notes. Directorate General of Minerals, Oman, pp.40.

Monnier, C., Girardeau, J., Le Mée, L. and Polvé, M. (2006). Along-ridge petrological segmentation of the mantle in the Oman ophiolite. Geochemistry, Geophysics, Geosystems, 7, Q11008, doi:10.1029/2006GC001320.

Moores, E., L. H. Kellogg, and Y. Dilek. (2000). Tethyan ophiolites, mantle convection, and tectonic ''historical contingency'': Ar esolution of the ''ophiolite conundrum''. In: Dilek, Y., Moores, E.M., Elthon, D., and Nicolas, A., (Eds.), Ophiolites and Oceanic Crust: New Insights from Field Studies and the Ocean Drilling Program: Boulder, Colorado, Geological Society of America Special Paper, 349, 3–12.

Nasir, S. (1996). Oxygen thermobarometry of the Semail harzburgite massif, Oman and United Arab Emirates. European Journal of Mineralogy, 8, 153-163.

Nell, J. and Wood, B. J. (1991). High-temperature electrical measurements and thermodynamic properties of Fe_3O_4-$FeCr_2O_4$-$MgCr_2O_4$- $FeAl_2O_4$ spinels. American Mineralogist, 76, 405-426.

Nicolas, A. (1986). A melt extraction model based on structural studies in mantle peridotites. American Mineralogist, 76, 405-426.

Nicolas, A. (1986b). Structure and petrology of peridotites: clues to their geodynamic environment. Reviews of Geophysics, 24, 875 - 895.

Nicolas, A. (1989). Structures of ophiolites and dynamics of oceanic lithosphere. Dordrecht, Netherlands, Kluwer Academic Publishers, 367 p.

Nicolas, A. and Boudier, F. (1995). Mapping oceanic ridge segments in Oman ophiolites. Journal of Geophysical Research, 100, 6179–6197.

Nicolas, A. and Prinzhofer, A. (1983) Cumulative or residual origin for the Transition Zone in ophiolites: structural evidence. Journal of Petrology, 24, 188-206.

Nicolas, A., and A. Azri, H. (1991). Chromite-rich and chromite-poor ophiolites: The Oman case. In: Peters, T.J., Nicolas, A. and Coleman,R.G. (Eds.), Ophiolite genesis and evolution of the oceanic lithosphere, 261-274. Kluwer Academic, Dordrecht, the Netherlands.

Nicolas, A., and Boudier, F. (2000). Large mantle upwellings and related variations in crustal thickness in the Oman ophiolite.In: Dilek, Y., Moores, E.M., Elthon, D., and Nicolas, A., (Eds.), Ophiolites and Oceanic Crust: New Insights from Field Studies and the Ocean Drilling Program: Boulder, Colorado, Geological Society of America Special Paper 349, 67-73.

Nicolas, A., Boudier, F., Ildefonse, B. and Ball, E. (2000a). Accretion of Oman and United Arab Emirates ophiolite – Discussion of a new structural map. Marine Geophysical Researches, 21, 147-180.

Nicolas, A., Boudier, F. Michibayashi, K. and Gerbert-Gaillard, L. (2000b). Aswad massif (United Arab Emirates): Archetype of the Oman-UAE ophiolite belt. Drilling Program: Boulder, Colorado, Geological Society of America Special Paper 349499-512.

Nicolas, A., Boudier, F., and Bouchez, J.L. (1980). Interpretation of peridotite structures from ophiolitic and oceanic environments. American Journal of Science, 280, 192-210.

Nicolas, A., Ceuleneer, G., Boudier, F., and Misseri, M. (1988). Structural mapping in the Oman ophiolite: Mantle diapirism along an oceanic ridge. Tectonophysics, 151, 27-54.

Nicolas, A., Ildefonse, B., Boudier, F., Lenoir, X., and Ben Ismail, W. (2000c). Dike distribution in the Oman-United Arab Emirates opiholite. Marine Geophysical Researches, 21, 269-287.

Nielson Pike, J.E. and Schwarzman, E.C. (1997). Classification of textures in ultramafic xenoliths. Journal of Geology, 85, 49-61.

Norman, M.D., (1998). Melting and metasomatism in the continental lithosphere: laser ablation ICPMS analysis of minerals in spinel lherzolites from eastern Australia. Contributions to Mineralogy and Petrology, 130, 240-255.

Norman M.D., Pearson N.J., Sharma A. and Griffin W.L. (1996). Quantitative analysis of trace elements in geological materials by Laser Ablation ICPMS: Instrumental operating conditions and calibration values of NIST glasses. Geostandards Newsletter, 20, 247-261.

Nonnotte, P., Ceuleneer, G., and Benoit, M. (2005). Genesis of andesitic-boninitic magams at mid-ocean ridges by melting of hydrated peridotites: Geochemical evidence from DSDP Site 334 gabbronorites. Earth and Planetary Science Letters, 236, 632-653.

Ogasawara, M., Nakagawa, M., Al-Azri, H., and Al-Araimi, M. (2002). PGE abundance in chromitites of the northern Samail ophiolite, Oman. Extended abstract of the 9th International Platinum Symposium, p. 345-348.

Ohara, Y. and Ishii, T. (1998). Peridotites from the southern Mariana forearc: Heterogeneous fluid supply in mantle wedge. The Island Arc, 7, 541-558.

Okamura, H., Arai, S., & Kim, Y.-U. (2006). Petrology of forearc peridotites from the Hahajima Seamount, the Izu Bonin arc, with special reference to chemical characteristics of chromian spinel. Mineralogical Magazine, 70, 15-26.

Onuma, N., Higuchi, H., Wakita, H. and Nagasawa, H. (1968). Trace element partition between two pyroxenes and the host lava. Earth and Planetary Science Letters, 5, 47-51.

O'Reilly, S.Y., Griffin, W.L. and Ryan, C.G. (1991). Residence of trace elements in metasomatized spinel lherzolite xenoliths: a proton microprobe study. Contributions to Mineralogy and Petrology, 109, 98-113.

Paktunc A.D. and Cabri L.J. (1995). A proton- and electron-microprobe study of gallium, nickel and zinc distribution in chromian-spinel. Lithos, 35, 261-282.

Paktunc, A.D. and Hulbert, L.J. (1996). Mineralogy of the Sturgeon Lake 01 Kimberlite, Saskatchewan: a proton microprobe study of the macrocryst phases. Exploration Mining Geology, 5, 263-279.

Pallister, J. S. and Hopson, C. A. (1981). Samail ophiolite plutonic suite: field relations, phase variation, cryptic variation and layering, and a model of a spreading ridge magma chamber. Journal of Geophysical Research, 86, 2593–2644.

Parkinson,I.J. and Arculus, R.J. (1999). The redox state of subduction zones: insights from arc-peridotites. Chemical Geology, 160, 409–423.

Parkinson I. J. and Pearce J. (1998). Peridotites from the Izu-Bonin-Mariana Forearc (ODP Leg 125): Evidence for Mantle Melting and Melt-Mantle Interaction in a Supra-Subduction Zone Setting. Journal of Petrology, 39, 1577-1618.

Paster, T.P., Schawecker, D.S. and Haskin, L.A. (1974). The behaviour of some trace elements during solidification of the Skaergaard layered series. Geochimica et Cosmochimia Acta, 38, 1549-1577.

Pearce, J.A., Alabaster, T., Shelton, A.W. and Searle, M.P. (1981). The Oman ophiolite as a Cretaceous arc-basin complex: evidence and implications. Philisophical Transaction of the Royal Society of London, A 300, 299 – 317.

Pearce, J.A., Lippard, S.J. and Roberts, S. (1984). Characteristics and tectonic significance of supra-subduction zone ophiolites. Geological Society of London, Special Publication, 16, 77-94.

Pearce, J.A. and Parkinson, I.J. (1993). Trace element models for mantle melting: application to volcanic arc petrogenesis. In: Pritchard, H.M., Alabaster, T., Harris, N.N.W., Neary, C.R. (Eds.), Magmatic Processes and Plate Tectonics, Geological Society Special Publication No. 76, 373-403.

Pearce J., Barker P.F., Edwards S.J., Parkinson I.J. and Leat, P.T. (2000). Geochemistry and tectonic significance of peridotites from the South Sandwich arc-basin system, South Atlantic. Contribution to Mineralogy and Petrology, 139, 36-53.

Penrose Conference Participants (1982). GSA Penrose field conference on ophiolite, Geotimes.

Perrin M., Plenier G., Dautria J-M., Cocuaud E. and Prévot M. (2000). Rotation of the Semail ophiolite (Oman): additional paleomagnetic data from the volcanic sequence. Marine Geophysical Researches, 21, 181- 194.

Perrin, M., Prevot, M. and Bruere, F. (1994). Rotation of the Oman ophiolite and initial location of the Ridge in the hostpot reference frame. Tectonophysics, 229, 31–42.

Peters, T. and Kambers, B.S. (1994). Peraluminous, potassium-rich granitoids in the Semail ophiolite. Contributions to Mineralogy and Petrology, 118, 229-238.

Pilgrim, G.E. (1908). The geology of the Gulf and adjoining portions of Persia and Arabia. Memoir of the Indian Geological Survey, 34, 1-77.

Python, M. and Ceuleneer,G. (2003). Nature and distribution of dykes and related melt migration structures in the mantle section of the Oman ophiolite.Geochemistry, Geophysics, Geosystems, 4, 1–34, doi:10.1029/2002GC000354.

Reinhardt, B.M. (1969). On the genesis and emplacement of ophiolites in the Oman Mountains geosyncline. Scweiz. Min. Petr. Mitt. 49.

Richardson, M. (1999). Upper mantle processes, diamond-bearing potential and stratigraphy of the mantle in the Kimberley region, Western Australia: Evidence from chromite, chromian diopside and garnet xenocryst chemistry. Unpublished honours thesis, Department of Geology, The Australian National University.

Roberts, S. (1986). The role of igneous processes in the formation of ophiolitic chromitite. Ph.D. Thesis, Department of Earth Sciences, The Open University, 250 p.

Roberts, S. and Neary, C. (1993). Petrogenesis of ophiolitic chromitite. In: Prichard, H.M., Alabaster, T., Harris, N.B.W. and Neary, C.R. (Eds.), Magmatic Processes and Plate Tectonics, Geological Society Special Publication, 76, 257-272.

Robertson, A.H.F., Blome, C.D., Cooper, D.W.J., Kemp, A.E.S., and Searle, M.P. (1990a). Evolution of the Arabian continental margin in the Dibba Zone, Northern Oman Mountains. In: Roberton, A.H.F., Searle, M.P. and Ries, A.C. (Eds.), The Geology and Tectonics of the Oman Region. Geological Society Special Publication No 49, 251-284.

Robertson, A.H.F., Kemp, A.E.S., Rex, C.D. and Blome, C.D. (1990b). Sedimentary and structural evolution of a continental margin transform lineament: the Hatta Zone, Northern Oman Mountains. In: Roberton, A.H.F., Searle, M.P. and Ries, A.C. (Eds.), The Geology and Tectonics of the Oman Region. Geological Society Special Publication No 49, 285-305.

Robertson, A.H.F., Searle, M.P. and Ries, A.C. (1990). The geology and tectonics of the Oman Region. In: Roberton, A.H.F., Searle, M.P. and Ries, A.C. (Eds.), The Geology and Tectonics of the Oman Region. Geological Society Special Publication No 49, p.845.

Roeder, P. L., Campbell, I. H. and Jamieson, H. E. (1979). A re-evaluation of the olivine-spinel geothermometer. Contributions to Mineralogy and Petrology, 68, 325-334.

Rollinson, H. (2005). Chromite in the mantle section of the Oman ophiolite: a new genetic model. The Island Arc, 14, 542-550.

Ryan C.G. (1995). The nuclear microprobe as a probe of earth structure and geological processes. Nuclear Instruments and Methods in Physics Research B, 104, 377-394.

Schiano, P., Clocchiatti, R., Lorand, J.-P. Massare, D., Deloule, E. and Chaussidon M. (1997). Primitive basaltic melts included in podiform chromites from the Oman Ophiolite. Earth and Planetary Science Letters, 146, 489-497.

Scowen, P., Roeder, P.L., and Helz, R., 1991. Reequilibration of chromite within Kilauea Iki lava lake, Hawaii. Contributions to Mineralogy and Petrology, 107, 8-20.

Searle, M. (1980). The metamorphic rocks and underlying volcanic rocks beneath the Semail Ophiolite. northern Oman mountains. Ph.D. Thesis, Open University, Milton Keynes, 213 p.

Searle, M. (1985). Sequence of thrusting and origin of culminations in the northern and central Oman mountains. Journal of Structural Geology, 7, 129-143.

Searle, M. and Cox, J. (1999). Tectonic setting, origin, and obduction fo the Oman ophiolite. Geological Society of America Bulletin, 111,104-122.

Searle, M. and Malpas, J. (1980). The structure and metamorphism of rocks beneath the Semail ophiolite of Oman, and their significance in ophiolite obduction. Royal Society of Edinburgh Philosophical Transactions, 71, 213 - 228.

Searle, M., Kames, N.P., Calonm T.J. and Smewing, J.D. (1983). Sedimentological and structural evolution of the Arabian continental margin in the Musandam Mountains and Dibba Zone, United Arab Emirates. Geological Society of American Bulletin, 94, 1381-1400.

Şengör, A.M.C. (1990). A new model for the late Palaeozoic-Mesozoic tectonic evolution of Iran and implications for Oman. In: Roberton, A.H.F., Searle, M.P. and Ries, A.C. (Eds.), The Geology and Tectonics of the Oman Region. Geological Society Special Publication No 49, 797-831.

Shervais, J.W. (2001). Birth, death, and resurrection: the life cycle of suprasubduction zone ophiolites. Geochemistry, Geophysics, Geosystems, 2, 2000GC000080.

Steinmann, G. (1927). Die ophiolitische Zonen in der mediterrananen Keltengebirgen. 14th International Geological Congree, Madrid, 2, 638-667.

Stosch H-G. (1981). Sc, Cr, Co and Ni partitioning between minerals from spinel peridotite xenoliths. Contributions to Mineralogy and Petrology, 78, 166-174.

Styles, M.T., Ellison, R.A., Arkley, S.L.B., Crowley, Q., Farrant, A., Goodenough, K.M., McKervey, J.A., Pharoah, TC., Phillips, E.R., Schofield, D. and Thomas, R.J. (2006). The geology and geophysics of the United Arab Emirates.Volume 2: Geology. Keyworth, Nottingham: British Geological Survey, 351 pp.

Suhr, G. (2003). Formation of large mantle dunites near lithospheric walls (Haylayn Massif, Oman): significance for melt transport. Geophysical Research Abstracts, 5, 07654.

Takazawa, E., Okayasu, T. and Satoh, K. (2003). Geochemistry and origin of the basal lherzolites from the northern Oman ophiolite (northern Fizh Block). Geochemistry, Geophysics, Geosystems, 2, 1021, doi:10.1029/2001GC000232.

Talkington, R. and Malpas, J. (1980). Spinel phases of the White Hills peridotite, St. Anthony Complex, Newfoundland: Part 1 occurrence and chemistry. Proceedings of the International Ophiolite Symposium, Cyprus, 607-619.

Tamura, A., and Arai, S. (2006). Harzburgite-dunite-orthopyroxenite suite as a record of supra-subduction zone setting for the Oman ophiolite mantle. Lithos, 90, 43-56.

Taylor L.W., Anand M., Promprated P., Floss C. and Sobolev N. (2003). The significance of mineral inclusions in large diamonds from Yakutia, Russia. American Mineralogist, 88, 912-920.

Thy, P. and Dilek, Y. (2003). Development of ophiolitic perspectives on spreading center magma chambers. In: Dilek, Y. and Newcomb, S. (Eds.), Ophiolite Concept and the Evolution of Geological Thought. Geological Society of America Special Paper 373, 188-226.

Tilton, G.R., Hopson, C.A. and Wright, J.E. (1981). Uranium-lead isotopic ages of the Semail ophiolite, Oman, with applications to Tethyan ocean ridge tectonics. Journal of Geophysical Research, 86, 2763 - 2775.

Umino, S., Yanai, S. , Jaman, A. R. , Nakamura, Y. , and Iiyama, J. T. (1990). The transition from spreading to subduction:Evidence from the Semail Ophiolite, northern Oman mountains. In: Malpas, J., Moores, E. M., Panayiotou, A. and Xenophontos, C. (Eds.), Ophiolites: Oceanic Crustal Analogues:Proceedings of the Symposium ``Troodos 1987",, Geol. Surv. Dep., Nicosia, Cyprus, 375-384.

Van der Voo, R., Spakman, W., and Bijwaard, H. (1999). Tethyan subducted slabs under India. Earth and Planetary Science Letters, 171, 7-20.

Varne, R., Brown, A. V., Jenner, G. A. and Falloon, T. (2000). Macquarie Island: its geology and structural history, and the timing and tectonic setting of its N-MORB to E-MORB magmatism. In: Dilek, Y., Moores, E.M., Elthon, D., and Nicolas, A., (Eds.), Ophiolites and Oceanic Crust: New Insights from Field Studies and the Ocean Drilling Program: Boulder, Colorado, Geological Society of America Special Paper, 349, 301-320.

Wakabayashi, J., and Dilek, Y. (2000). Spatial and temporal relationships between ophiolites and their metamorphic soles: a test of models of forearc ophiolite genesis. In: Dilek, Y., Moores, E.M., Elthon, D., and Nicolas, A., (Eds.), Ophiolites and Oceanic Crust: New Insights from Field Studies and the Ocean Drilling Program: Boulder, Colorado, Geological Society of America Special Paper 34953 – 34964.

Watling R.J., Herbert H.K., Barrow I.S. and Thomas A.G. (1995). Analysis of diamonds and indicator minerals for diamond exploration by laser ablation-inductively coupled plasma mass spectrometry. Analyst, 120, 1357-1364.

Wilson, H.H. (1969). Late Cretaceous eugeosynclinal sedimentation, gravity tectonics and ophiolite emplacement in the Oman Mountains, Southeast Arabia. American Association of Petroleum Geologists Bulletin, 53, 626-71.

Wood, B. J. and Virgo, D., (1989). Upper mantle oxidation state: ferric iron contents of lherzolite spinels by ^{57}Fe Mössbauer spectroscopy and resultant oxygen fugacities. Geochimica et Cosmochimica Acta , 53, 1277–1291

Zhou, M.F., Robinson, P.T. and Bai, W.J. (1994). Formation of podiform chromites by melt/rock interaction in the upper mantle. Mineralium Deposita, 29, 98-101.

Appendix A: Sample description and locality

A.1 Sample Distribution

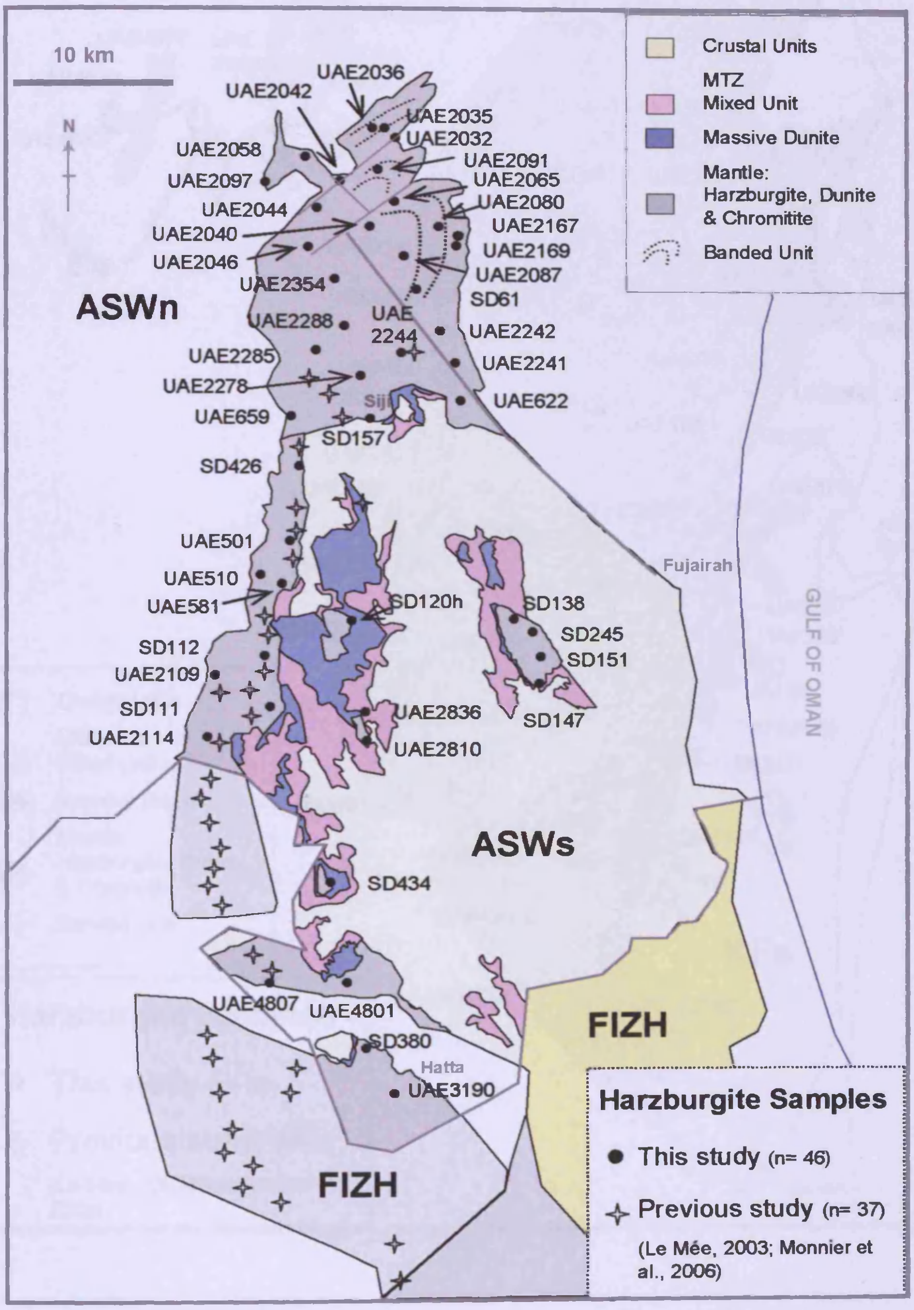

Figure A.1: Map of Aswad and Fizh Blocks displaying the spatial distribution of the harzburgite samples analysed in this study (circles), was well as the harzburgites previously analysed by Le Mée (2003) and Monnier et al., (2006) (crosses).

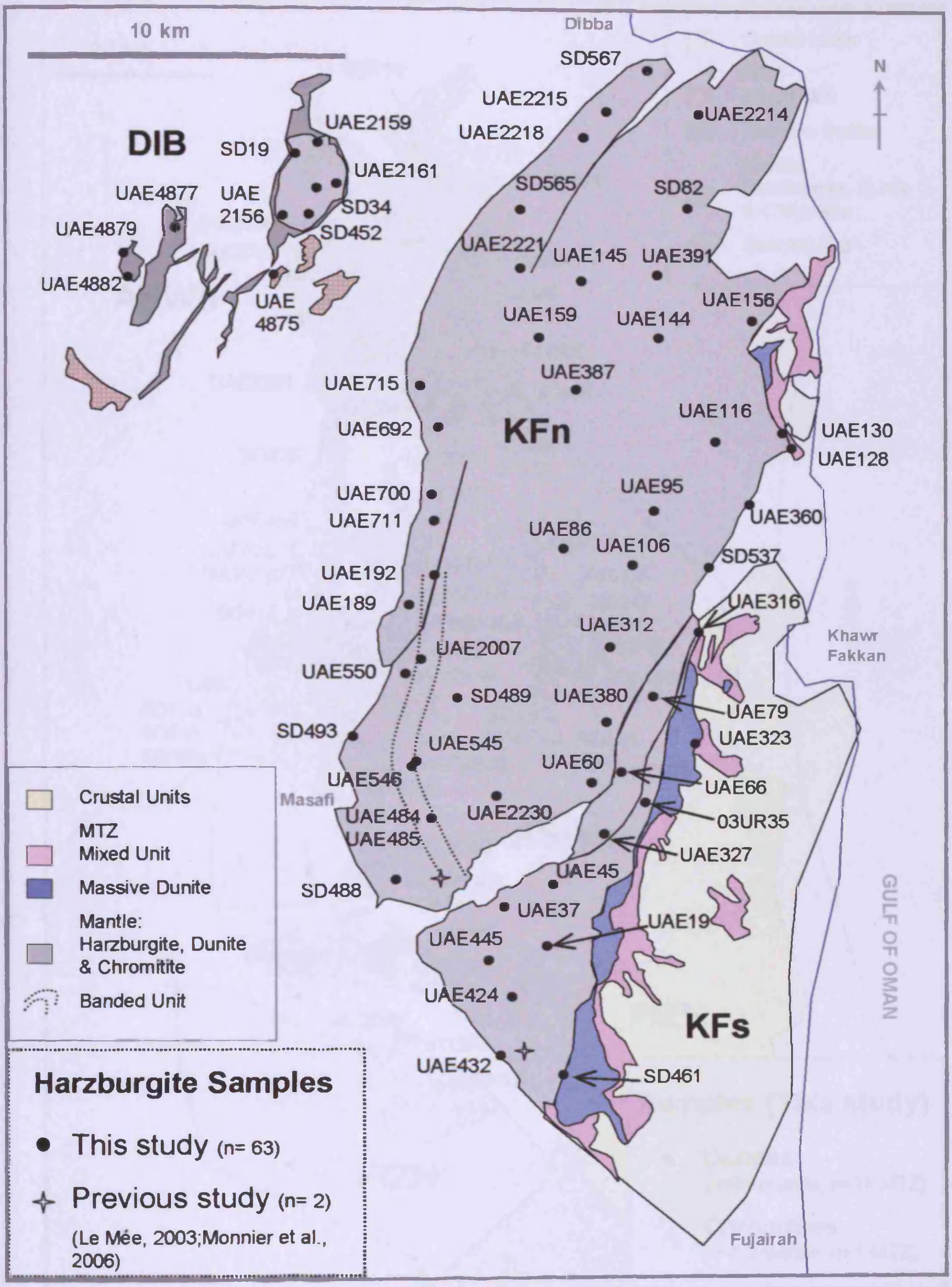

Figure A.2: Map of Khawr Fakkan Block and Dibba Zone displaying the spatial distribution of the harzburgite samples analysed in this study (circles), was well as the harzburgites previously analysed by Le Mée (2003) and Monnier et al., (2006) (crosses).

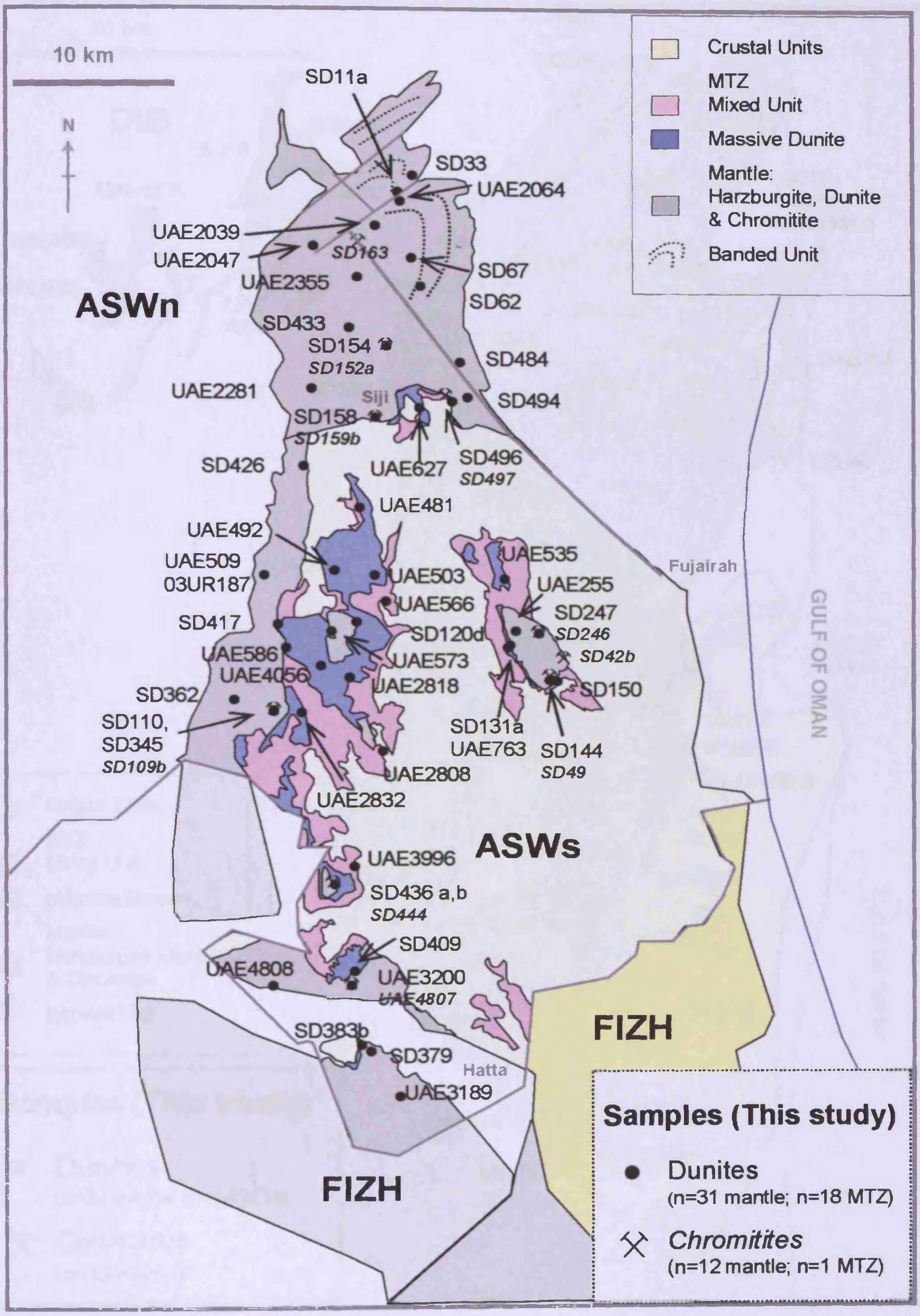

Figure A.3: Map of Aswad and Fizh Blocks displaying the spatial distribution of the dunite samples from the mantle (circles), MTZ (squares) and chromitites (crossed hammers). Chromitite sample labels italicised.

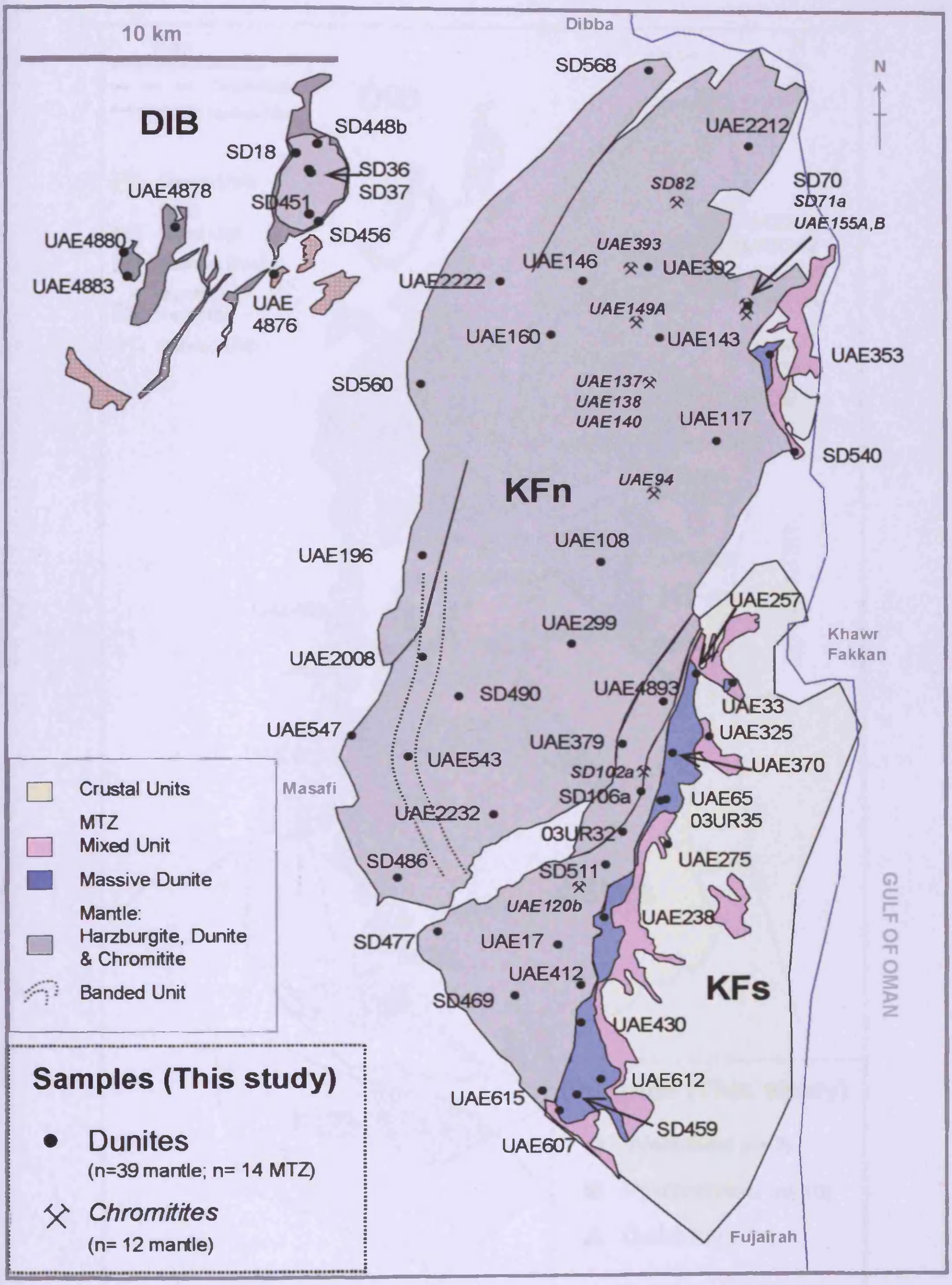

Figure A.4: Map of Khawr Fakkan Block and Dibba Zone displaying the spatial distribution of the dunite samples from the mantle (circles), MTZ (squares) and chromitites (crossed hammers). Chromitite sample labels italicised.

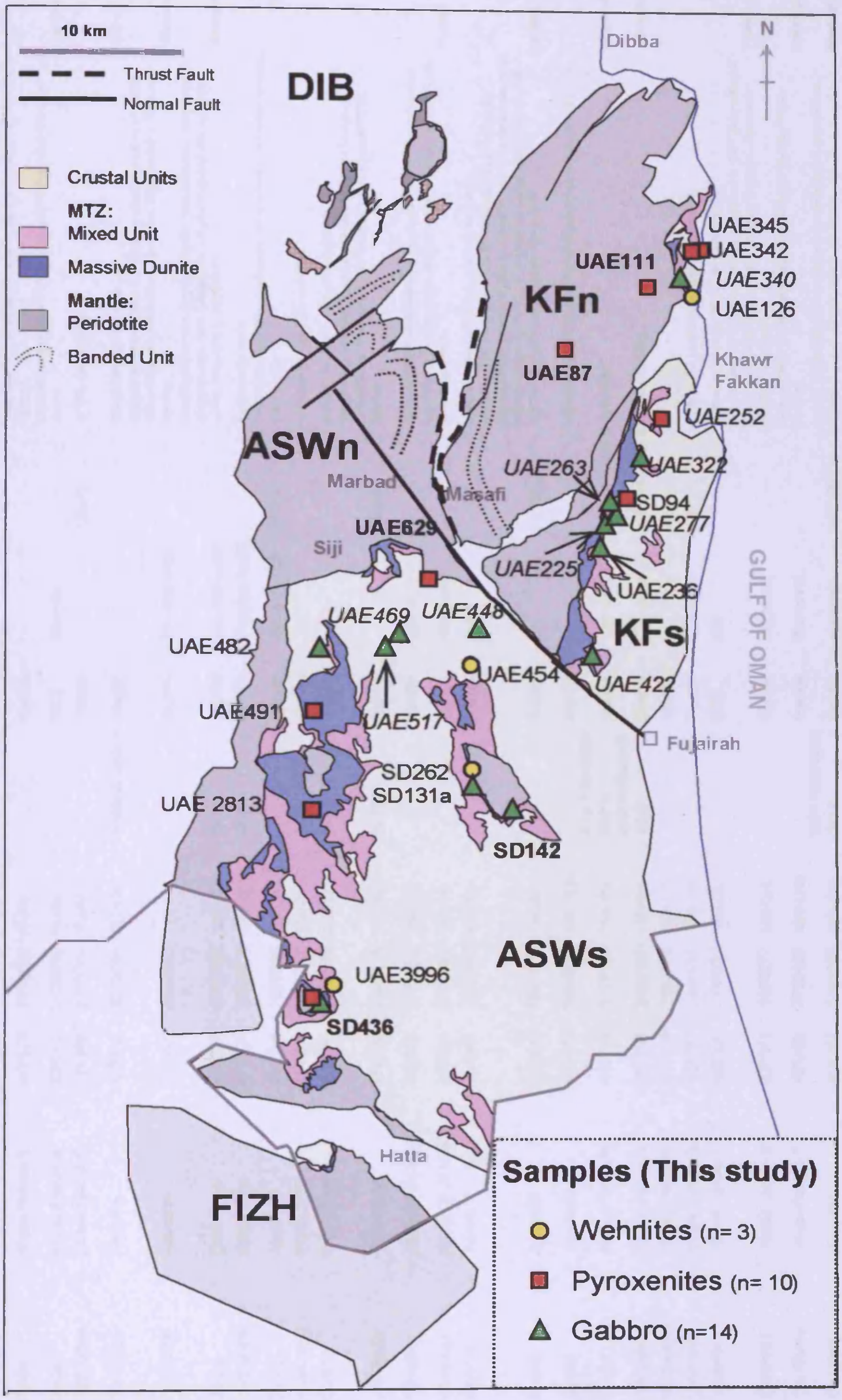

Figure A.5: Map of the study area displaying the spatial distribution of the wehrlite samples (yellow circles), pyroxenites (red squares) and gabbros (green triangles).

A2. Sample locations and field descriptions.

UAE No	Field Type	Petro Type	Region	Easting	Northing	WP	Pair	Strat Unit	Subunit	Hz foln	Dunite obs	Du dipdir/dip
03UR24	**Dunite**	Dunite	Khawr Fakkan S	427373	2796622	RLU25		Mantle			From very head of waddi, close to harzburgite, *but only traces of opx. No* hz scree	
03UR32	**Dunite**	Dunite	Khawr Fakkan S	429010	2798015	RLU34		MTZ	**msv du**		Fresh dunite from area of chromitite stringers and veins upto 10cm across	307/23NW
03UR35	**Harzburgite**	Harzburgite	Khawr Fakkan S	428395	2798069	RLU37		Mantle		126/42	nr MTZ, good foliation	
03UR187	**Dunite**	Chr-Dunite	Aswad S	400734	2779544	RLU199	UAE509, UAE510	Mantle			thin (10cms) layered hz/du	082/12E
SD11a	**Dunite**	Chr-Dunite	Aswad N	410195	2808465	1SD-22		Mantle	**Banded Unit**		interbanded dunite (30cm -8m width) w/ discontinuous interfingered layers of hz. Thin chromitite stringer <1cm thick extending 30cm ~// layering	240/40SW
SD18	**Dunite**	Dunite	Dibba Zone	413708	2826882	1SD-27	SD19	Mantle	**Banded Unit?**		thin (50cm) 2 sheets over spacing 2m. Not v extensive along strike as chopped up by faults. Maybe sub mm grains clotting into trails few ~1mm. Area siilar to banded unit	080/16ENE
SD19	**Harzburgite**	Harzburgite	Dibba Zone	413708	2826882	1SD-27	SD18	Mantle	**Banded Unit?**		hosts banded dunite	
SD33	**Dunite**	Dunite	Aswad N	411254	2809755	1SD-50		Mantle	**Banded Unit**	290/50	Thin (50cm -1m) dunite interbanded w/ hz (30cm-1.5m).Sharp contacts, 3 interbands	290/35WNW
SD34	**Harzburgite**	Harzburgite	Dibba Zone	414625	2825337	1SD-65	nr SD 36/37	Mantle			hosts thin du bands (not sampled)	
SD36	**Dunite**	Dunite	Dibba Zone	414340	2826020	1SD-67	nr SD34	Mantle			medium (4m wide) sheet w/ scattered chr	278/90
SD37	**Dunite**	Chr-Dunite	Dibba Zone	414292	2826119	1SD-68	nr SD34	Mantle		280/90	thin (1-1.5m) small red dunite irregular boundaries w/ 5 bands of chromitite made up of 1cm wide wispy strings. Concordant to hz *foliation*.	270/90
SD42b	**Chromitite**	Chromitite	Aswad S (Al Hayl)	422063	2773215	1SD-72		Mantle	**Chr mine**		small pit (10 x 10m) mostly float, plag-cpx infiltration/veining (wehrlite)	
SD49	**Chromitite**	Chromitite	Aswad S (Al Hayl)	421031	2771850	1SD-74		Mantle	**Chr mine**		only 1-2m of nodular chr exposed in small pit (5m highX 20m long). !m wide du envelope.	190/50S
SD61	**Harzburgite**	Wehrlite	Aswad N	411947	2801168	1SD-88		Mantle	**Dyke**		sampled as harzburgite, no dyke or du vein visible	
SD62	**Dunite**	Dunite	Aswad N	411835	2801318	1SD-89		Mantle		150/90	2m sheet of du + scattered chr in hz. Not planar sheet but steeply dipping folded? *Dunite- clusters of chromite, more than usual from basal* banded dunites, w/ small cm patches of possible grey opx/hz (partially dunitised?) slightly discordant diss chr + opx?	190/60S
SD67	**Dunite**	Dunite	Aswad N	411173	2803523	1SD-102b		Mantle			irregular network of du (40cm) channels leaving irregular patches of hz	
SD70	**Dunite**	Dunite	Khawr Fakkan N	432755	2820197	1SD-104	UAE156/UAE155/ SD71A	Mantle	**Chr mine**	3x5x7m deep a	du envelope	020/90; 006/80
SD71a	**Chromitite**	Chromitite	Khawr Fakkan N	432755	2820197	1SD-104	UAE156/UAE155/ SD70	Mantle	**Chr mine**	3x5x7m deep a	nodular chromitite	020/90; 006/80
SD82	**Harzburgite**	Harzburgite	Khawr Fakkan N	430219	2824508	1SD-108		Mantle				
SD89a	**Chromitite**	Chromitite	Khawr Fakkan N	429781	2824731	1SD-110		Mantle	**Chr mine**		small pit (10 x 10m) mostly float, v. weathered	
SD94	**Pyroxenite**	Cpxenite	Khawr Fakkan S	429920	2797222	1SD-112		MTZ	**mu**		ol-cpxenite intruding Gbl blocks within wehrlite	
SD102a	**Chromitite**	Chromitite	Khawr Fakkan S	428311	2799277	1SD-118		Mantle	**chr seam**		thin Pod like?msv nodules (deformed leopard ore) - 0.5-1.5cm wide and 2-4cm long, *elongate. 0.4-1m wide, 0.4-/2m long pods.* Hosted by moderate 15m dunite	115/40E; 280/55W. Lin 25/190
SD106a	**Dunite**	Chr-Dunite	Khawr Fakkan S	428159	2798425	2SD-119b		Mantle	**chr seam**		large du (30mwide) with amazing chr layers/cross bedding (10cm-1mwide)	90/70E; 262/70W; 90/90E
SD109	**Chromitite**	Chromitite	Aswad S	401457	2769387	1SD-120	SD111/SD110/SD 345	Mantle	**chr pod**	160/20SE	1x 1.5m lense/droplet of msv chr in large discordant du (part of Y du Mizert)	322/40NNW
SD110	**Dunite**	Dunite	Aswad S	401457	2769387	1SD-120	SD111/SD109	Mantle		160/20SE	large (>10m) irregular discordant du, hosting chr pod)	
SD111	**Harzburgite**	cpx-Harzburgite	Aswad S	401377	2769520	1SD-120b	SD110/SD109	Mantle		160/20SE	strong hz foliation, cm shattering (alt?)	
SD112	**Harzburgite**	Harzburgite	Aswad S	401051	2773470	1SD-121		Mantle			no du veins	
SD120d	**Dunite**	Dunite	Aswad S	407256	2776098	1SD-124	SD120h	Mantle			thin (3cm) du vein in hz (du not seen in outcrop)	
SD120h	**Harzburgite**	Harzburgite	Aswad S	407256	2776098	1SD-124	SD120d	Mantle			*host thin du vein*	
SD131a	**Dunite**	Dunite	Aswad S (Al Hayl)	418192	2774334	1SD-131		Mantle	**almost part of MTZ, but still h**		thin du (ms) patch in hz with cpx clusters/trails	
SD138	**Harzburgite**	Harzburgite	Aswad S (Al Hayl)	418864	2776156	1SD-133		Mantle			no du veins	
SD142	**Wehrlite**	Wehrlite	Aswad S (Al Hayl)	421056	2771774	1SD-135b		Mantle	**Dyke**		thin (5-10cm) nebulous ol-cpx-plag veinlets in hz	120/40ESE
SD144	**Dunite**	Dunite	Aswad S (Al Hayl)	421064	2771636	1SD-136		Mantle			thin (50cm-1m) possible channel orientation-concordant to metagb dykes?	090/20E
											10m down from contact with mu	

UAE No	Field Type	Petro Type	Region	Easting	Northing	WP	Pair	Strat Unit	Subunit	Hz foln	Dunite obs	Du dipdir/dip
SD150	Dunite	cpx-Dunite	Aswad S (Al Hayl)	421515	2771611	1SD-141		MTZ	mu		thin (1m) du layer impreg with snowflake cpx) within mu (Gbl+wehr)	
SD151	Harzburgite	Harzburgite	Aswad S (Al Hayl)	420898	2773371	1SD-142		Mantle			near MTZ	
SD152a	Chromitite	Chromitite	Aswad N	409410	2796868	1SD-143	SD154	Mantle	Chr mine		chr mine (3 x 15 x 40m)	304/52NW
SD154	Dunite	Dunite	Aswad N	409410	2796868	1SD-143	SD152a	Mantle	Chr mine		1-2m thick du envelope to chr mine (3 x 15 x 40m). actual measurement from chr stringer (1-2cm) in situ in du envelope.	304/52NW
SD157	Harzburgite	cpx-Harzburgite	Aswad N	408644	2791387	1SD-145	SD158, SD159b	Mantle	Chr mine			
SD158	Chromitite	Chromitite	Aswad N	408644	2791387	1SD-145	SD157, SD159b	Mantle	Chr mine		1m tabular seam msv chr with 50cm du envelope, small offshoots into dunite. Mine - 40m long	290/40W
SD159b	Chromitite	Chromitite	Aswad N	408644	2791387	1SD-145	SD157, SD158	Mantle	Chr mine		1m tabular seam msv chr with 50cm du envelope, small offshoots into *dunite*. Mine - 40m long	290/40W
SD163	Chromitite	Chromitite	Aswad N	407435	2804654	1SD-145		Mantle	float			
SD245	Harzburgite	Harzburgite	Aswad S (Al Hayl)	420244	2775190	2SD-28	SD247/SD246	Mantle	Chr mine		adj to pod	
SD246	Chromitite	Chromitite	Aswad S (Al Hayl)	420244	2775190	2SD-28	SD245/SD247	Mantle	Chr mine		only 1m msv chr exposed. Large mine (50m long)	040/60ENE
SD247	Dunite	Dunite	Aswad S (Al Hayl)	420244	2775190	2SD-28	SD245/SD246	Mantle	Chr mine		1m du envelope interfingering contact with chr	060/40ENE
SD255	Dunite	Dunite	Aswad S (Al Hayl)	418608	2775395	2SD-33		Mantle		000/65	thin (1.5m) discordant to hz	080/35E
SD262_chr	Chromitite	Chromitite	Aswad S (Al Hayl)	417840	2775305	2SD-35	SD262_wehr	MTZ	float mu		mu - wehrlite and du	
SD262_wehr	Wehrlite	Wehrlite	Aswad S (Al Hayl)	417840	2775305	2SD-35	SD262_chr	MTZ	float mu		mu - wehrlite and du	
SD345	Chromitite	Chromitite	Aswad S	401422	2769356	2SD-85	SD109-SD111	Mantle	chr pod	150/20SE	10-20cm thick chr seam msv with 5cm rim of more ol rich chr, 5m total length, in large discordant Y du (>30m) - irregular contact.	280/25W
SD362_chr	Dunite	Chr-Dunite	Aswad S	398592	2770155	2SD-94b	SD362_du	Mantle			Thin (40cm seen) no margins seen, low scrubby patch,	
SD362_du	Dunite	Chr-Dunite	Aswad S	398592	2770155	2SD-94b	SD362_chr	Mantle			Thin (40cm seen) no margins seen, *low scrubby patch*,	
SD379	Dunite	Dunite	Fizh	408265	2743647	2SD-101	SD380	Mantle		10/60N	thin (50cm) du vein discordant to hz	100/60E
SD380	Harzburgite	Harzburgite	Fizh	408265	2743647	2SD-101	SD379	Mantle		10/60N	host discordant du	
SD383b	Dunite	Dunite	Fizh	407615	2744102	2SD-103		MTZ	msv du		no features, contact with GbL (no mu)	
SD409_chr	Chromitite	Chromitite	Aswad S	407117	2749742	2SD-118	SD409_du	MTZ	msv du		3cm msv to diss chr layer	300/75NNW; 350/80NW; 170/80SE
SD409_du	Dunite	Dunite	Aswad S	407117	2749742	2SD-118	SD409_chr	MTZ	msv du		host to chr layers and pxenite dykes	
SD417	Dunite	Dunite	Aswad S	401738	2775837	2SD-124		Mantle			thin du vein (poor outcrop)	
SD425	Dunite	Dunite	Aswad S	403619	2787804	2SD-129	SD426	Mantle			*thin (30-40cm) rare du veins*, low scrubby hills,	100/40E
SD426	Harzburgite	Harzburgite	Aswad S	403619	2787804	2SD-129	SD425	Mantle			host du vein	
SD433	Dunite	Dunite	Aswad N	406781	2798249	2SD-134	nr UAE2288	Mantle			siji quarry local scree - no info	
SD434	Harzburgite	Harzburgite	Aswad S	405719	2756227	2SD-135	SD436	Mantle			host du and pxenite/melagb veins)	
SD436a_chr	Dunite	Chr-Dunite	Aswad S	405719	2756227	2SD-135	SD434	Mantle			1-4cm msv chr band with 1cm marin du	050/40NE
SD436a_du	Dunite	Chr-Dunite	Aswad S	405719	2756227	2SD-135	SD434	Mantle			1-4cm msv chr band with 1cm marin du	050/40NE
SD436b_chr	Dunite	Chr-Dunite	Aswad S	405719	2756227	2SD-135	SD434	Mantle			1-4*cm msv chr band with* 1cm *marin* du	050/40NE
SD436b_du	Dunite	Chr-Dunite	Aswad S	405719	2756227	2SD-135	SD434	Mantle			1-4cm msv chr band with 1cm marin du	050/40NE
SD436b_px	Pyroxenite	Pxenite	Aswad S	405719	2756227	2SD-135	*SD434*	*Mantle*			thin (5-10cm) px, ol plag (wehr/mgb) coarse margin, med centre cross *cut chr-du*	200/85SSW
SD444	Chromitite	Chromitite	Aswad S	405644	2756291	2SD-141		Mantle	Cr float		msv ore float - could be mantle or MTZ	
SD448b	Dunite	Dunite	Dibba Zone	414641	2827312	2SD-145		Mantle	banded unit?		Medium (2x10m) du bodies in hz, shattered and weathered. Some places, large cm clusters of msv chr cubes! Part of large du bands (10 - 20m)	160/40SE

UAE No	Field Type	Petro Type	Region	Easting	Northing	WP	Pair	Strat Unit	Subunit	Hz foln	Dunite obs
SD451	Dunite	Dunite	Dibba Zone	414318	2824168	2SD-147	SD452	Mantle		120/85SE	Thin (30-40cm) vein - discordant?
SD452	Harzburgite	Harzburgite	Dibba Zone	414318	2824168	2SD-147	SD451	Mantle		120/85SE	host thin du vein
SD456	Dunite	Dunite	Dibba Zone	414699	2823841	2SD-150		Mantle			Thin (1m) vein, alteration zonation
SD459	Dunite	Chr-Dunite	Khawr Fakkan S	425383	2784894	2SD-153		MTZ	Msv du		1m wide zone of msv chrtrails/layers (10-30cm wide) in msv dunite
SD461	Harzburgite	Harzburgite	Khawr Fakkan S	424909	2785938	2SD-155b		Mantle			contact with MTZ (msv du)
SD469	Dunite	Dunite	Khawr Fakkan S	422816	2789372	2SD-159	nr UAE424	Mantle			no info - scrappy outcrop
SD477	Dunite	Dunite	Khawr Fakkan S	419540	2792195	2SD-163		Mantle			Thin (0.2-0.3m) veins few chr trails
SD484	Dunite	Dunite	Aswad N	414681	2795623	2SD-169	nr UAE2241	Mantle			thin du
SD486	Dunite	Dunite	Khawr Fakkan N	417866	2794641	2SD-164	SD488	Mantle	banded unit		thin (20-50cm)du cuts px banding
SD488	Harzburgite	Harzburgite/px	Khawr Fakkan N	417866	2794641	2SD-164	SD486	Mantle	banded unit		pxenite/lhz banded with hz and du very 50cm
SD489	Harzburgite	Harzburgite	Khawr Fakkan N	420465	2802682	2SD-173	SD490	Mantle	banded unit		host du bands
SD490	Dunite	Dunite	Khawr Fakkan N	420465	2802682	2SD-173	SD489	Mantle	banded unit		Thin (20-30cm) banded dunite with 3-4 parallel 5mm wide diss chr trails
SD493	Harzburgite	Harzburgite	Khawr Fakkan N	416063	2801002	2SD-175	nr UAE543	Mantle			
SD494	Dunite	Dunite	Aswad N	415196	2792968	2SD-176	nr UAE622	Mantle			thin (2m) vein
SD496	Dunite	Dunite	Aswad N	414085	2792654	2SD-177	nr SD497	MTZ	msv du		alteration zonation
SD497	Chromitite	Chromitite	Aswad N	413611	2793059	2SD-178	nr SD496	MTZ	chr mine - msv du		large (100m) mine - no outcrop seen
SD511	Dunite	Dunite	Khawr Fakkan S	426604	2795193	2SD-184		Mantle			thin (2 - 30cm) amazing network du, *some with chr trails, conjugate* veins. Near contact iwht msv du
SD537	Harzburgite	Harzburgite	Khawr Fakkan N	431092	2808516	2SD-200		Mantle			du rare
SD540	Dunite	Dunite	Khawr Fakkan N	434743	2813608	2SD-203		MTZ	msv du		40m wide *msv du before mu and gb*
SD560	Dunite	Dunite	Khawr Fakkan N	418896	2816607	2SD-220	nr UAE715	Mantle	banded unit?		
SD565	Harzburgite	Harzburgite	Khawr Fakkan N	423158	2824447	2SD-223		Mantle			host du vein
SD567	Harzburgite	Harzburgite	Khawr Fakkan N	428530	2830706	2SD-224	SD568	Mantle			
SD568	Dunite	Dunite	Khawr Fakkan N	428530	2830706	2SD-224	SD567	Mantle	banded unit?		2-5m bands of dunite
UAE17	Dunite	Chr-Dunite	Khawr Fakkan S	424604	2791604	MTSU32		Mantle		240/75	Rxlled peridotite, chr alignemnt
UAE19	Harzburgite	Harzburgite	Khawr Fakkan S	424223	2791638	MTSU35		Mantle		030/70	good foln
UAE33	Dunite	Dunite	Khawr Fakkan S	432054	2803303	MTSU65		MTZ	mu		100m du pod within mu, cut by gb peg
UAE37	Harzburgite	Harzburgite	Khawr Fakkan S	422412	2793386	MTSU76		Mantle		135/65	
UAE45	Harzburgite	Harzburgite	Khawr Fakkan S	424522	2794375	MTSU95		Mantle		060/90	*chr alignment in du vein*
UAE60	Harzburgite	Harzburgite	Khawr Fakkan N	426106	2798966	MTSU126		Mantle		045/90	good foln
UAE65	Chromitite	Chromitite	Khawr Fakkan S	429207	2798085	MTSU132		MTZ	msv du		chr layers in loose block
UAE66	Harzburgite	Harzburgite	Khawr Fakkan N	427372	2799371	MTSU135		Mantle		066/90	few thin 3cm opxenite and 5cm anastomosing network of du veins
UAE79	Harzburgite	Harzburgite	Khawr Fakkan N	428696	2802744	MTSU158		Mantle		245/80	*no veins*
UAE86	Harzburgite	Harzburgite	Khawr Fakkan N	424975	2809392	MTSU183	UAE87opx	Mantle		020/90	narrow du veins and px+chr veins
UAE87	Pyroxenite	Ol-Opxenite	Khawr Fakkan N	424975	2809392	MTSU183	UAE86	Mantle			Px vein in harzburgitre
UAE94	Chromitite	Chromitite	Khawr Fakkan N	428755	2811733	MTSU199		Mantle	float		chr layer in dunite float
UAE95	Harzburgite	Harzburgite	Khawr Fakkan N	428748	2811056	MTSU197		Mantle		100/85	
UAE106	Harzburgite	Harzburgite	Khawr Fakkan N	427882	2808644	MTSU225		Mantle		065/90	large du pod 10m x 100m nearby (wp223-224)
UAE108	Dunite	Dunite	Khawr Fakkan N	426487	2808707	MTSU227		Mantle		320/20	many veins of dunite
UAE111	Pyroxenite	Ol-Opxenite	Khawr Fakkan N	431429	2814449	MTSU241		Mantle		050/90	many du veins cut by opxenite
UAE116	Harzburgite	Harzburgite	Khawr Fakkan N	431417	2814142	MTSU247	UAE117	Mantle		060/90	
UAE117	Dunite	Dunite	Khawr Fakkan N	431417	2814142	MTSU247	UAE116	Mantle		060/90	
UAE120b	Chromitite	Chromitite	Khawr Fakkan S	425573	2794091	MTSU254		Mantle	float		
UAE126	Wehrlite	Wehrlite	Khawr Fakkan N	434800	2813774	MTSU269		MTZ	top mu/gbl		thin werhlite layers in GbL // to gb layering

UAE No	Field Type	Petro Type	Region	Easting	Northing	WP	Pair	Strat Unit	Subunit	Hz foln	Dunite obs	Du dipdir/dip
UAE130	Harzburgite	cpx-Harzburgite	Khawr Fakkan N	434245	2814536	MTSU276		Mantle			med granular recryst hz	
UAE137	Chromitite	Chromitite	Khawr Fakkan N	428594	2816679	MTSU319	UAE138, 140	Mantle	Chr mine	310/90, 75/80,	thin (1m) du envelope	225/80
UAE138	Chromitite	Chromitite	Khawr Fakkan N	428594	2816679	MTSU319	UAE137, 140	Mantle	Chr mine	pod 3m x 5m:	outer zone chr-du	225/80
UAE140	Chromitite	Chromitite	Khawr Fakkan N	428594	2816679	MTSU319	UAE137, 138	Mantle	Chr mine	pod 3m x 5m:	core msv chr ore	225/80
UAE143	Dunite	Dunite	Khawr Fakkan N	428986	2818758	MTSU311	UAE144	Mantle			Thin (2m thick x 10m long)du. Pre and post wp - large du pods 50m (wp309) and 100mlongx20mthick (wp313) and 20-30m (wp314), 60m x 10 (wp 325); 100x20 (wp321). Also smaller anastomosing veins	
UAE144	Harzburgite	Harzburgite	Khawr Fakkan N	428986	2818758	MTSU311	UAE143	Mantle		115/70; 095/60	no foln	
UAE145	Harzburgite	Harzburgite	Khawr Fakkan N	425714	2821233	MTSU330	UAE146	Mantle			pods of du in hz with scattered cr	
UAE146	Dunite	Dunite	Khawr Fakkan N	425714	2821233	MTSU330	UAE145	Mantle			pods du in hz with scattered Cr; pxenite near by	
UAE149A	Chromitite	Chromitite	Khawr Fakkan N	428025	2819346	MTSU320		Mantle	Chr mine		msv cr ore	310/90; 230/90
UAE155A	Chromitite	Chromitite	Khawr Fakkan N	432727	2819730	MTSU348	UAE156, SD70, SD71A	Mantle	Chr mine	3x5x7m deep a	addit follows du vein w/ stringer and small pods Cr (ore body 095/55)	020/90; 006/80
UAE155B	Chromitite	Chromitite	Khawr Fakkan N	432727	2819730	MTSU348	UAE156, SD70, SD71A	Mantle	Chr mine	3x5x7m deep a	addit follows du vein w/ stringer and small pods Cr (ore body 095/55)	020/90; 006/80
UAE156	Harzburgite	Harzburgite	Khawr Fakkan N	432951	2819524	MTSU350		Mantle		360/90	*du veins - no data*	
UAE159	Harzburgite	Harzburgite	Khawr Fakkan N	423956	2818740	MTSU354	nr UAE160	Mantle		140/80	abundant du veins upto 1m with some prominent chr	140/80
UAE160	Dunite	Dunite	Khawr Fakkan N	424396	2818834	MTSU353	nr UAE159	Mantle		275-90	large du pod 100m long, 50m high up cliff. Surrounded by numerous *anastomosing du*	240
UAE189	Harzburgite	cpx-Harzburgite	Khawr Fakkan N	418925	2804412	MTSU403		Mantle		200/70	strongly foliated rc perid mylonite with interleaved blocks of much coarser hz	
UAE192	Harzburgite	Harzburgite	Khawr Fakkan N	419482	2808217	MTSU417		Mantle		130/70	*foliated hz*	
UAE196	Dunite	Chr-Dunite	Khawr Fakkan N	418970	2808966	MTSU437		Mantle			thin du layers upto 3-5m	090/40
UAE225	Wehrlite	Wehrlite	Khawr Fakkan S	428056	2794945	KGU086					?Recrystallised harzburgite	
UAE236	Wehrlite	Wehrlite	Khawr Fakkan S	427716	2793229	KGU103		MTZ	mu		Wehrlite	
UAE238	Dunite	Chr-Dunite	Khawr Fakkan S	426591	2792800	KGU109		MTZ	msv du			
UAE252	Pyroxenite	ol-cpxenite	Khawr Fakkan S	432401	2803725	KGU137		MTZ	mu		Pyroxene-rich ?wehrlite	
UAE257	Dunite	Dunite	Khawr Fakkan S	430489	2803731	KGU167		MTZ	msv du			
UAE263	Gabbro	Ol-Gb	Khawr Fakkan S	428444	2796989	KGU186		MTZ	mu		Gabbro from sheet in wehrlite/dunite	
UAE275	Dunite	Dunite	Khawr Fakkan S	429293	2796083	KGU225		MTZ	mu		dunite sheet intruding gabbro.	
UAE277	Wehrlite	Wehrlite	Khawr Fakkan S	429102	2795818	KGU229		MTZ	mu		?wehrlite from adjacent to contact with gabbro sheet	
UAE299	Dunite	Dunite	Khawr Fakkan N	425237	2805070	KGU348		Mantle			abundant dunite veins, some very chromite rich	
UAE312	Harzburgite	Harzburgite	Khawr Fakkan N	426893	2804983	KGU412		Mantle			Adjacent to tonalitic intrusion	
UAE316	Harzburgite	Harzburgite	Khawr Fakkan S	430659	2805652	KGU427		Mantle			Close to a contact with wehrlite	
UAE322	Gabbro	Ol-Gb	Khawr Fakkan S	430855	2800670	KGU440		MTZ	mu		Gabbro from gabbro sheet within wehrlites of the MTZ	
UAE323	Harzburgite	Harzburgite	Khawr Fakkan S	430491	2800672	KGU443		MTZ			harzburgite. Cut by some opx pegmatites.	
UAE325	Dunite	Dunite	Khawr Fakkan S	431046	2800890	KGU448		MTZ	mu		?dunite from pod within feldspathic wehrlite in MTZ	
UAE327	Harzburgite	cpx-Harzburgite	Khawr Fakkan S	426631	2796668	KGU457		Mantle				
UAE340	Gabbro	Ol-Gb	Khawr Fakkan S	433874	2815360	KGU506		MTZ	mu		Layered Gabbro from a sheet in wehrlite	
UAE342	Pyroxenite	websterite	Khawr Fakkan S	435469	2817530	KGU509		MTZ	mu/wehr		Mapped as large Wehrlite area (no du or gbl), but mostly pxenite	
UAE345	Pyroxenite	Websterite	Khawr Fakkan S	434891	2817384	KGU515		MTZ	mu/wehr		Olivine pyroxenite - no du or gbl of normal mu	
UAE353	Dunite	Dunite	Khawr Fakkan S	433722	2818005	KGU547		MTZ	msv du		Dunite with some chr stringers	
UAE360	Harzburgite	cpx-Harzburgite	Khawr Fakkan N	432843	2811319	KGU568		Mantle				
UAE370	Dunite	cpx-Dunite	Khawr Fakkan S	429514	2800177	KGU605		MTZ	msv du			

UAE No	Field Type	Petro Type	Region	Easting	Northing	WP	Pair	Strat Unit	Subunit	Hz foln	Dunite obs	Du dipdir/dip
UAE379	Dunite	Dunite	Khawr Fakkan N	427353	2800548	KGU641		Mantle			Major pod of dunite over 100 m across.	
UAE380	Harzburgite	Harzburgite	Khawr Fakkan N	426765	2801628	KGU648		Mantle				
UAE387	Harzburgite	Harzburgite	Khawr Fakkan N	425517	2816418	KGU677		Mantle			Hz with anastomosing dunite veins, cut by major shear zone	
UAE391	Harzburgite	Harzburgite	Khawr Fakkan N	428936	2821566	KGU701		Mantle			Hz contains dunite sheets up to 1 m thick	
UAE392	Dunite	Dunite	Khawr Fakkan N	428484	2821889	KGU703		Mantle			Outcrop largely composed of dunite sheets > 1m thick with some harzburgite, dunite sheets have patches that are chromite-rich	
UAE393	Chromitite	Chromitite	Khawr Fakkan N	427821	2821744	KGU708		Mantle	Chr mine		Chromitite from old chromite mine, excavated along vein ~ 1m wide	290/45
UAE412	Dunite	Dunite	Khawr Fakkan S	425545	2789817	RTU103		Mantle			just du	
UAE422	Wehrlite	Wehrlite	Khawr Fakkan S	427217	2784308	RTU128		MTZ	mu		slightly fspathic wehrlite, within GbL	
UAE424	Harzburgite	cpx-Harzburgite	Khawr Fakkan S	422781	2789390	RTU212		Mantle			no folian	
UAE430	Dunite	cpx-Dunite	Khawr Fakkan S	425564	2788141	RTU234		MTZ	msv du		dunite (near rxllised hz?)	
UAE432	Harzburgite	Harzburgite	Khawr Fakkan S	422241	2786793	RTU242		Mantle			fractured rc hz	
UAE445	Harzburgite	Harzburgite	Khawr Fakkan S	421756	2791011	RTU302		Mantle			no fabric	
UAE448	Gabbro	Troctolite	Aswad S	418376	2786649	RTU315		GbL			layered gabbro with some thin wehrlite sills	294/62
UAE454	Wehrlite	Wehrlite	Aswad S	417767	2783884	RTU390					hz faulted to gb - no fabric but passes into foliated hz	
UAE469	Pyroxenite	cpxenite	Aswad S	412258	2786038	RTU492					structureless coarse wehrlite pod within varitextured gb	
UAE481	Wehrlite	Wehrlite	Aswad S	407468	2784622	RTU652		MTZ	mu		du and wehrlite within tab gb-l blocks, cut by gb peg	
UAE482	Gabbro	Troctolite	Aswad S	406163	2785178	RTU667		MTZ	mu		msv wehr = du with 10s-100m blocks of layered gb	
UAE484	Harzburgite	Harzburgite	Khawr Fakkan N	419332	2797356	RTU720	UAE485	Mantle		122/38	foliated hz with layers of larger msv du	
UAE485	Harzburgite	Harzburgite	Khawr Fakkan N	419332	2797356	RTU720	UAE484	Mantle			dunite layer	
UAE491	Pyroxenite	Ol-cpxenite	Aswad S	405678	2779935	RTU770		MTZ	msv du		Du contain 10m pod of coarse pxenite	
UAE492	Dunite	cpx-Dunite	Aswad S	405678	2779935	RTU770		MTZ	msv du_cpximpreg du		Blebby dunite with elongate cm scale cpx blebs aligned	018/80
UAE501	Harzburgite	Harzburgite	Aswad S	402881	2782138	RTU820		Mantle	mu		px-peridotite and dunite nr u/m + gb blocks	
UAE503	Wehrlite	Wehrlite	Aswad S	408545	2779606	RTU835		MTZ	msv du_cpximpreg du		msv du with cpx oiks locally forming veins and blebs 'wehrlite'	038/35
UAE509	Dunite	Dunite	Aswad S	400740	2779547	RTU872	UAE510, 03UR187	Mantle			thin (10cms) layered hz/du	097/10
UAE510	Harzburgite	Harzburgite	Aswad S	400740	2779547	RTU872	UAE509, 03UR187	Mantle			thin (10cms) layered hz/du	
UAE517	Gabbro	Gb bithna	Aswad S	411114	2785117	RTU945					peg patches and veins	
UAE535	Dunite	Dunite	Aswad S (Al Hayl)	417811	2779289	RTU1127		MTZ	msv du		featureless msv du	
UAE543	Dunite	Chr-Dunite	Khawr Fakkan N	418331	2799989	RTY1235		Mantle			du with chr layers, some several cm thick, discontinuous in hz	165/20
UAE545	Harzburgite	Harzburgite	Khawr Fakkan N	418743	2799884	RTU1236	nr U543	Mantle			2-20cm du layers	158/10
UAE546	Harzburgite	Harzburgite	Khawr Fakkan N	418530	2799677	RTU1237		Mantle		275/85	hz an dthin du veins	168/12
UAE547	Dunite	Dunite	Khawr Fakkan N	415986	2800947	RTU1246		Mantle			irregular body not layered, no fabric	
UAE550	Harzburgite	cpx-Harzburgite	Khawr Fakkan N	418249	2803741	RTU1279		Mantle		155/55	good se layerin opx	
UAE566	Dunite	cpx-Dunite	Aswad S	409373	2777585	RTU1423		MTZ	mu		Cpx-blebby dunite within msv du (mu in map)	
UAE573	Dunite	Dunite	Aswad S	405536	2775365	RTU1519		MTZ	msv du		featureless msv du	
UAE581	Harzburgite	Harzburgite	Aswad S	402352	2778847	RTU1645		Mantle			no du mo fabric	
UAE586	Dunite	Dunite	Aswad S	402296	2774061	RTU1722		MTZ	msv du		msv du no fabric	
UAE607	Dunite	Dunite	Khawr Fakkan S	424669	2784184	JNU179		MTZ	msv du		Dunite with spinel foliation	
UAE612	Dunite	Plag-dunite	Khawr Fakkan S	426402	2785570	JNU188		MTZ	msv du		?Dunite	
UAE615	Dunite	Dunite	Khawr Fakkan S	423938	2785081	JNU208		Mantle				
UAE622	Harzburgite	Harzburgite	Aswad N	415132	2792794	JNU272		Mantle				

UAE No	Field Type	Petro Type	Region	Easting	Northing	WP	Pair	Strat Unit	Subunit	Hz foln	Dunite obs	Du dipdir/dip
UAE627	Wehrlite	Wehrlite	Aswad S	411821	2792125	JNU312		MTZ	mu		?Harzburgite	
UAE629	Pyroxenite	Websterite	Aswad N	414531	2790803	JNU325		Mantle				
UAE659	Harzburgite	Harzburgite	Aswad N	402954	2791559	DST164		Mantle				
UAE692	Harzburgite	Harzburgite	Khawr Fakkan N	419667	2814760	DST422		Mantle				
UAE700	Harzburgite	Harzburgite	Khawr Fakkan N	419412	2811809	DST461		Mantle				
UAE711	Harzburgite	Harzburgite	Khawr Fakkan N	419508	2810579	DST493		Mantle				
UAE715	Harzburgite	Harzburgite	Khawr Fakkan N	418945	2816627	DST504		Mantle				
UAE763	Dunite	Dunite	Aswad S (Al Hayl)	418042	2774093	DISU335		MTZ	msv du		du with some wehrlite patches and hz (nrSD revit)	
UAE2007	Harzburgite	Harzburgite	Khawr Fakkan N	418925	2804412	MTSU463	UAE2008	Mantle			banded du-hz // to flat lying shears	
UAE2008	Dunite	Dunite	Khawr Fakkan N	418925	2804412	MTSU463		Mantle		090/40; 090/75	Banded hz-du (10cm to 7-8m)	080/25
UAE2032	Harzburgite	Harzburgite	Aswad N	410531	2812713	MTSU537		Mantle			well foliated rc pd	
UAE2035	Harzburgite	Harzburgite	Aswad N	409722	2813371	MTSU544		Mantle		310/10	good foln	
UAE2036	Harzburgite	Harzburgite	Aswad N	408830	2813401	MTSU545		Mantle		240/30	-	
UAE2039	Dunite	Dunite	Aswad N	408643	2805990	MTSU553	UAE2040	Mantle			2m du with cr stringer roughly // to edge	340/80
UAE2040	Harzburgite	Lherzolite	Aswad N	408643	2805990	MTSU553	U2039	Mantle		300/90	part rc	
UAE2042	Harzburgite	Harzburgite	Aswad N	406526	2809365	MTSU564		Mantle		050/60	with thin du veins	
UAE2044	Harzburgite	Harzburgite	Aswad N	404858	2807298	MTSU569		Mantle			mostly du (rc perid)?	
UAE2046	Harzburgite	cpx-Harzburgite	Aswad N	404280	2804418	MTSU576	UAE2047	Mantle			lots of du veins with few small cr stringers	
UAE2047	Dunite	Chr-Dunite	Aswad N	404280	2804418	MTSU576	UAE2046	Mantle			lots of du veins, 1-2m	310/90
UAE2058	Harzburgite	Harzburgite	Aswad N	404087	2811214	MTSU602		Mantle				
UAE2064	Dunite	Dunite	Aswad N	410443	2807803	MTSU630/1SD-:	UAE2065	Mantle	Banded Unit	100/60?	thin band of dunite	
UAE2065	Harzburgite	cpx-Harzburgite	Aswad N	410443	2807803	MTSU630/1SD-:	UAE2064	Mantle	Banded Unit	100/60	host banded dunite	
UAE2080	Harzburgite	Harzburgite	Aswad N	413502	2805918	MTSU666		Mantle	Banded Unit	240/20	banded du-hz 1-2-5m	260/20
UAE2087	Harzburgite	cpx-Harzburgite	Aswad N	411074	2803665	MTSU685		Mantle	Banded Unit		40cm layers du	180/80?
UAE2091	Harzburgite	Harzburgite	Aswad N	409229	2810249	MTSU696		Mantle	Banded Unit		banded du 1-2m thick	280/30
UAE2097	Harzburgite	Lherzolite	Aswad N	401124	2809254	MTSU707		Mantle				
UAE2109	Harzburgite	cpx-Harzburgite	Aswad S	397433	2771932	MTSU773		Mantle				
UAE2114	Harzburgite	Harzburgite	Aswad S	396788	2767312	MTSU791		Mantle			no foln	
UAE2156	Harzburgite	Harzburgite	Dibba Zone	413144	2824105	MTSU869		Mantle			du veins 120/80	120/80SE
UAE2159	Harzburgite	Harzburgite	Dibba Zone	414670	2827352	MTSU872		Mantle	Banded Unit		lots of du upto 30m thick	105/70)
UAE2161	Harzburgite	cpx-Harzburgite	Dibba Zone	415453	2825500	MTSU875		Mantle		045/90	few thin du	
UAE2167	Dunite	Dunite	Aswad N	414667	2804669	MTSU882	nr UAE2169	Mantle	Banded Unit		banded du upto 20m thick, most smaller	315/40
UAE2169	Harzburgite	Lherzolite	Aswad N	414821	2804435	MTSU881	nr UAE2167	Mantle	Banded Unit	265/60		
UAE2212	Dunite	Dunite	Khawr Fakkan N	432796	2827335	KGU793		Mantle			abundant dunite veins up to 1m across, dunite has abundant scattered crystals and stringers of chromite.	
UAE2214	Harzburgite	Harzburgite	Khawr Fakkan N	430720	2828702	KGU812		Mantle			Hz with dunite veins	
UAE2215	Harzburgite	cpx-Harzburgite	Khawr Fakkan N	426811	2828823	KGU821		Mantle			Hz with dunite veins, sample taken from dunite vein	
UAE2218	Harzburgite	Harzburgite	Khawr Fakkan N	425868	2827672	KGU839		Mantle			Hz with dunite veins	
UAE2221	Harzburgite	Harzburgite	Khawr Fakkan N	423132	2821821	KGU852		Mantle			Hz with dunite veins, dunite contains moderately abundant scattered chromite	
UAE2222	Dunite	Dunite	Khawr Fakkan N	422241	2821210	KTU877		Mantle			abundant dunite veins up to 2m across, chromite in dunite veins defines a foliation.	
UAE2230	Harzburgite	Harzburgite	Khawr Fakkan N	422114	2798325	KGU905		Mantle			Fabric defined by parallel dunite bands	
UAE2232	Dunite	Chr-Dunite	Khawr Fakkan N	421923	2797410	KGU915		Mantle			Pod or layer of dunite in harzburgite (3D shape not clear at outcrop), with abundant N-S trending stringers of chromitite	

UAE No	Field Type	Petro Type	Region	Easting	Northing	WP	Pair	Strat Unit	Subunit	Hz foln	Dunite obs	Du dipdir/dip
UAE2241	Harzburgite	Harzburgite	Aswad N	414722	2795569	KG963		Mantle				
UAE2242	Harzburgite	Harzburgite	Aswad N	413624	2797992	KG969		Mantle			Harzburgite from 10 m wide mylonite zone	
UAE2244	Harzburgite	cpx-Harzburgite	Aswad N	410942	2796350	KG978		Mantle		288/20	1-2 cm thick, parallel dunite bands are // to pyroxene foliation	
UAE2278	Harzburgite	Harzburgite	Aswad N	407948	2794653	KG1201		Mantle			Rare, thin dunite veins	|
UAE2281	Dunite	Dunite	Aswad N	404204	2793643	KGU1226		Mantle			abundant dunite veins	
UAE2285	Harzburgite	Harzburgite	Aswad N	404712	2796555	KG1253		Mantle			No dunite veins	
UAE2288	Harzburgite	Harzburgite	Aswad N	406814	2798390	KG1275		Mantle				
UAE2354	Harzburgite	Harzburgite	Aswad N	406066	2801894	KG1796		Mantle			Some irregular dunite veins	
UAE2355	Chromitite	Chromitite	Aswad N	407409	2801988	KGU1800		Mantle			Dunite veins in harzburgite with fairly high chromite concentrations	
UAE2808	Dunite	Dunite	Aswad S	409180	2766275	RTU1918		MTZ	mu		large pod of amorphous du within mu of wehrlite dominated, cpxenite mu with gb-l	
UAE2810	Harzburgite	Harzburgite	Aswad S	408386	2767011	RTU1923		Mantle		no fabric	no du	
UAE2814	Dunite	cpx-Dunite	Aswad S	406835	2771853	RTU1935		MTZ	msv du		featureless du	
UAE2832	Dunite	Dunite	Aswad S	403352	2769202	RTU2113		MTZ	msv du		featureless du with cpxenite veins	
UAE2836	Harzburgite	Harzburgite	Aswad S	408228	2769129	RTU2139		Mantle		no fabric	no du	
UAE3189	Dunite	Dunite	Fizh	410270	2740243	MTSU1548/2SD	UAE3190	Mantle		320/80NW	thin (1m) tabular du - cpx stringer	320/50
UAE3190	Harzburgite	Harzburgite	Fizh	410270	2740243	MTSU1548/2SD	UAE3189	Mantle		320/80NW	host du and pxenite vein	
UAE3200	Dunite	Dunite	Aswad S	406883	2748636	MTSU1558/2SD	UAE4801	Mantle		270/60W	Thin (50cm) du band in hz, cut by px peg (webst?)	060/80; 070/40
UAE3996a_chr	Chromitite	Chromitite	Aswad S	407121	2757646	RTU2986	UAE3996a_wehr	MTZ	mu	similar to alhayl	Dunite contains stratiform cr (2cm msv layer and sidd cr, cut by gb peg) in du dominated mu-du+wehr+gb no olcpx.	
UAE3996a_we	Wehrlite	Wehrlite	Aswad S	407121	2757646	RTU2986	UAE3996a_chr	MTZ	mu	similar to alhayl	Dunite contains stratiform cr (2cm msv layer and sidd cr, cut by gb peg) in du dominated mu-du+wehr+gb no olcpx.	
UAE4056	Chromitite	Chromitite	Aswad S	404711	2772743	RTU3785		MTZ	msv du		Dunite with chromite. Msv du with cpxenite bodies, almost base of mu	
UAE4801	Harzburgite	Harzburgite	Aswad S	406883	2748636	MTSU1558/2SD	UAE3200	Mantle		270/60W	host thin du vein	
UAE4803	Chromitite	Chromitite	Aswad S	406883	2748636	MTSU1555/2SD	nr UAE3200/UAE4801	Mantle	float			
UAE4807	Harzburgite	Harzburgite	Aswad S	401289	2748610	MTSU1561/2SD	UAE4808	Mantle			host band of thin dunite	
UAE4808	Dunite	Dunite	Aswad S	401289	2748610	MTSU1561/2SD	UAE4807	Mantle			thin (2-3m thick) du bands in hz	290/35
UAE4875	Harzburgite	Serp - Harzburgite	Dibba Zone	412757	2821493	MTSU1771/2SD	UAE4876	Mantle	Serp Sanah Melange		serp hz hosting du veins, clast in melange	
UAE4876	Dunite	Serp - Dunite	Dibba Zone	412757	2821493	MTSU1771/2SD	UAE4875	Mantle	Serp Sanah Me	350/40	thin (20-50cm) du veins in hz	
UAE4877	Harzburgite	Harzburgite	Dibba Zone	408553	2823573	MTSU1772/2SD	UAE4878	Mantle	Serp Thrust slice		fresh recrystallized hz kernel in serpentinite	
UAE4878	Dunite	Dunite	Dibba Zone	408553	2823573	MTSU1772/2SD	UAE4877	Mantle	Serp Thrust slice		thin (40cm?) du in very serp hz	200/90
UAE4879	Harzburgite	Harzburgite	Dibba Zone	406340	2822447	MTSU1773/2SD	UAE4880	Mantle	Serp Thrust slice		freshish hz with du veins	
UAE4880	Dunite	Serp - Dunite	Dibba Zone	406340	2822447	MTSU1773/2SD	UAE4879	Mantle	Serp Thrust slice		thin (1.5m) du vein with 3mm sized chr grains	
UAE4882	Harzburgite	Harzburgite	Dibba Zone	406525	2821379	MTSU1774/2SD	UAE4883	Mantle	Serp Thrust slice		fresh 'mini blob' hz with several du veins	
UAE4883	Dunite	Serp - Dunite	Dibba Zone	406525	2821379	MTSU1774/2SD	UAE4882	Mantle	Serp Thrust sli	340/45	thin (30-50cm) du veins // foln, with 3mm chr grains	340/45
UAE4893	Dunite	Dunite	Khawr Fakkan N	429106	2802492	MTSU1804		Mantle			thin (0.5m) irregular body	250/30

Appendix B: Petrography

B.1 Alteration

The igneous mineral assemblage of olivine, orthopyroxene, clinopyroxene and chrome-spinel in peridotites remains stable at high temperatures (>1000°C ~ granulite facies) even in the presence of fluids. However, below 1000°C the ultramafic minerals undergo alteration via metamorphic reactions in the presence of fluids which post-dates the formation of MT/LT peridotite deformation (1100-1000°C /1000-900°C) (e.g. Gnos et al., 1996). As the ophiolite cools, hydrothermal alteration causes retrograde hydration reactions in the peridotite mineral assemblage over a wide range of temperatures (Evans and Trommsdorff, 1970; Frost, 1974; Evans and Frost, 1975).

The metamorphic history of alteration in the peridotites ranges from medium-temperature alteration in the amphibolite facies above 450°C to low-temperature alteration below 450°C in the greenschist facies and the prehnite-pumpellyite facies.

Medium-temperature alteration

Medium-temperature alteration, typically at 500-800°C, results in the transformation of clinopyroxene into tremolite (Ca-rich amphibole), orthopyroxene into cummingtonite (Ca-poor amphibole) and talc, and chrome spinel into ferrit-chromite, magnetite and chlorite. Olivine remained unchanged during medium-temperature alteration. Ferritchromit progressively replaces magmatic spinels by a dissolution-recrystallization process during hydrothermal alteration (Evans and Frost, 1975; Kimball, 1990; Mellini et al., 2005).

The fluids involved in MT alteration could come from a variety of sources: seawater that infiltrated into the mantle along shear zone during obduction; fluids derived from a subduction zone, e.g. hydration of peridotites from the South Mariana Forearc (Ohara and Ishii, 1998); and water derived from of the adjacent metamorphic rocks. Gnos and Nicolas (1996) proposed that prograde dehydration of the metamorphic rocks of Beni Hamid in the Khawr Fakkan Block could be a source for fluids in the surrounding peridotites. However, the BGS mapping team demonstrates that the Beni Hamid Metamorphics were already dry granulites, with peak metamorphism pre-dating incorporation with the ophiolite, and thus could not be a source for fluids (see BGS report, 2006).

There is evidence for some MT alteration of the U.A.E. peridotites from the presence of talc, amphibole (e.g. Figure B.1) and ferritchromit (e.g. Figure B.2) in some samples

Amphibole

U.A.E. opx-bearing peridotites can contain up to 3% amphibole, which commonly forms an alteration rim of clinopyroxene (Figure B.1b) or colourless, fine-grained needles (Figure B.1c). One sample (U.A.E.189), classified as an amphibole-peridotite (60% ol, 15% opx, 35% amph and 1% chr), contained euhedral amphibole grains (Figure B.1). The amphibole needles represent alteration under static conditions, whereas euhedral amphiboles represent alteration and recrystallisation during deformation.

The composition of calcic-amphibole changes with temperature: upon cooling, the alkalis (Na + K) decrease, whereas Al decreases so that Si increases (Evans, 1977). This is demonstrated by Leake's plot of Na+K vs Si (Figure B.3), which illustrates that pargasite forms at magmatic conditions (e.g. Hess Deep) but edenite/hornblende and tremolite form by hydration during cooling (e.g. peridotite from Izu Bonin Mariana forearc (Ishii et al., 1992; Okamura and Arai, 2006).

The few amphiboles analysed in this study are calcic-amphiboles, specifically tremolites (Mg# > 0.9) (Figure B.3). The amphiboles display a small range in composition, ranging from magnesio-hornblende (U.A.E.692) to end-member tremolite. This variation is a result from cooling upon hydration, as found in amphiboles from IBM forearc peridotites (Ishii et al., 1992; Okamura and Arai, 2006). The composition of amphiboles varies from grain to grain within each sample, demonstrating that they continued to grow over a range of temperatures.

Ferritchromit

Ferritchromit consists of a nanometric association of Cr-magnetite, chlorite and lizardite. Mg and Al, released during the spinel to ferritchromit replacement, interact with mesh-textured serpentine, giving rise to chloritic aureoles (i.e. intergrown chlorite, lizardite and "septochlorite") (Mellini et al., 2005).

Hydrothermally-altered spinels may be differentiated from unreacted, magmatic spinel in thin section. The relict, magmatic spinels are coloured in plane-polarised light and have a 'ceramic' texture in reflected light on a polished probe section (e.g. unaltered core of spinel in Figure B.2a-b). In contrast, the altered spinels have an opaque rim of fine-grained ferritchromit, which is brown in reflected light (Figure B.2a-b), and a colourless aureole of Fe-poor chlorite (Figure B.2c). A back-scattered electron image of a partly-altered spinel (Figure B.2d) demonstrates the visible difference between the relict, magmatic core (grey) and the altered ferritchromit rim (bright). The alteration is progressive, starting from the rim and the cracks until the whole spinel grain is replaced as in Figure B.2e-f.

The majority of samples from the study have unaltered chrome-spinels, whereas some (7%) had narrow ferritchromit rims and chlorite aureoles. Only a few samples (10%) contain largely altered chrome-spinels but, even in these samples, a few relict magmatic spinels were preserved in the core or larger grains. Only one sample (U.A.E.189) out of the 109 studied had no analysable magmatic spinel.

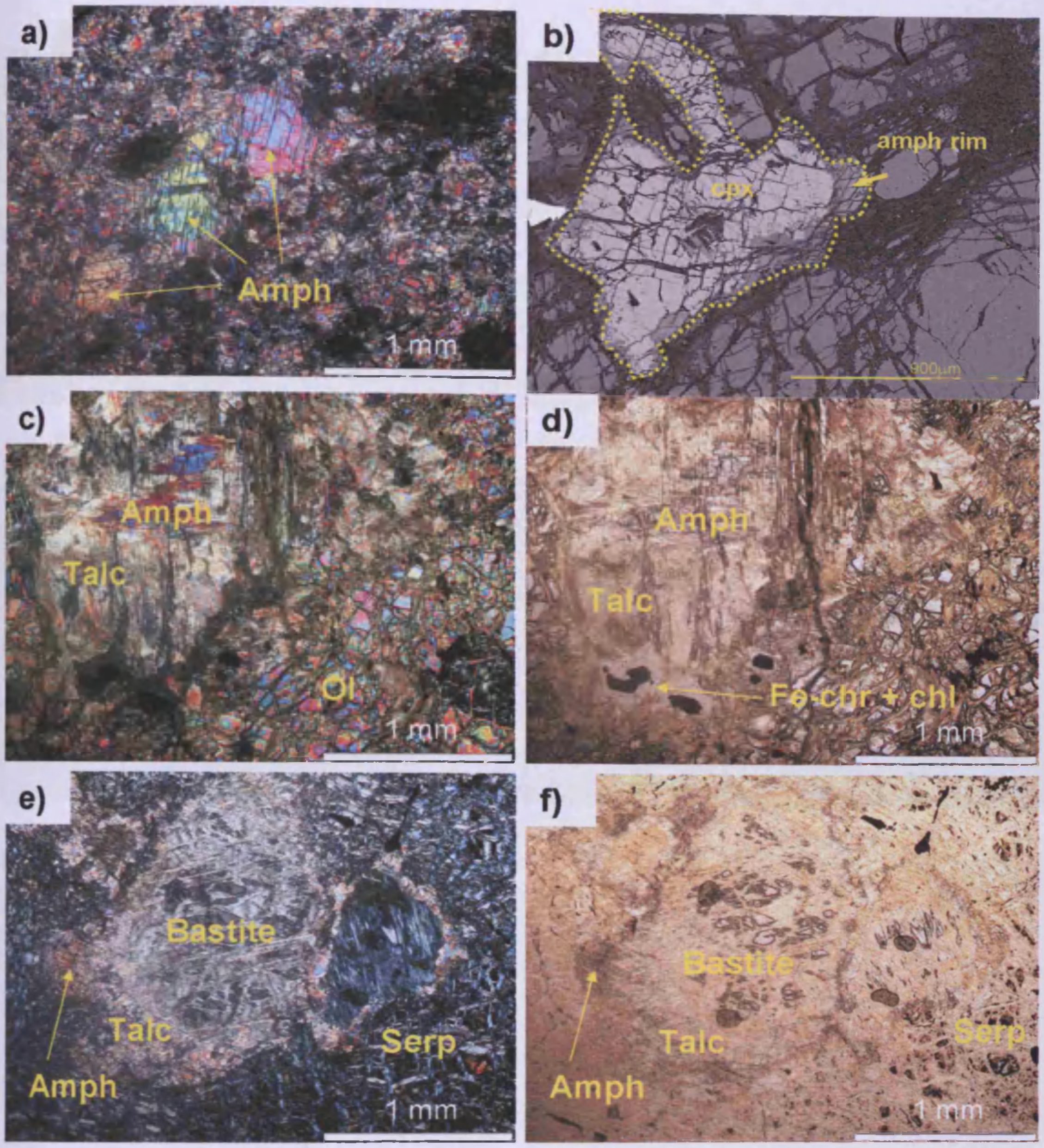

Figure B.1: **Medium Temperature hydrothermal alteration** of orthopyroxene (opx)-bearing peridotites. (a) LT (fg-porph) Amphibole-peridotite with magnetite and chlorite after spinel. Amphibole (amph) recrystallised to euhedral shape during LT deformation (UAE189). (b) Alteration rim of amphibole (tremolite) on clinopyroxene grain (UAE327). (c-d) MT (cg-porph) harzburgite with talc and needles of amphibole, after opx, and ferritchromit and chlorite aureoles, after spinel (UAE550). Olivine has few serpentine veins. (e-f) HT (cg-gran) harzburgite with talc and amphibole altered rim and bastite core after opx. Olivine altered to a serpentine mesh texture (SD426).

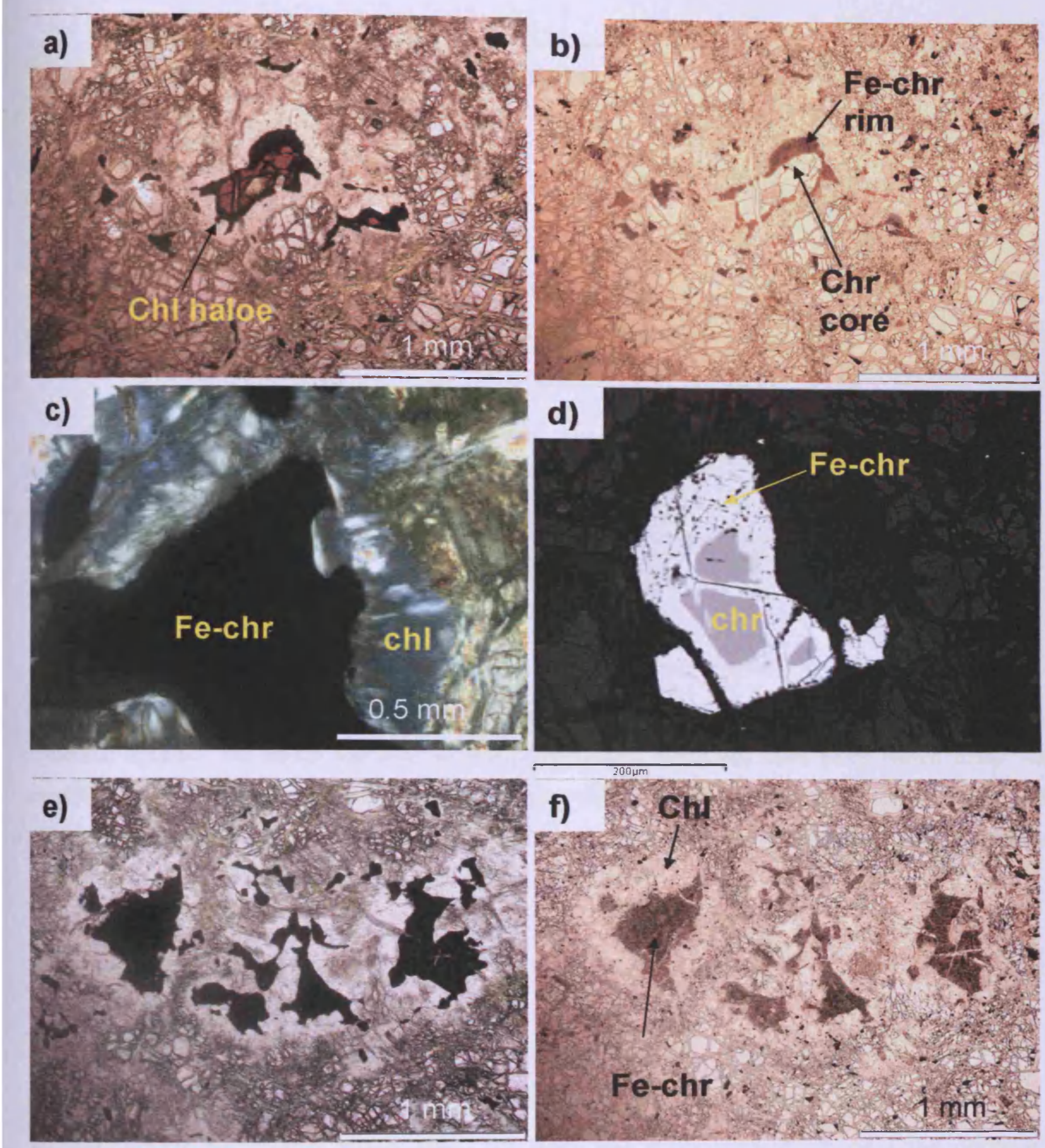

Figure B.2: Alteration, of varying degrees, of chrome-spinel (chr) to ferritchromit (Fe-Chr) and Mg-rich, colourless chlorite (Chl) aureoles. (a) Fresh spinel (brown) with black, altered rim (Fe-chr) and colourless chlorite aureole in ppl (UAE2080), (b) Fresh core has ceramic texture, in reflected light, whereas altered rim has a brown, fine-grained texture (UAE2080). (c) close up of chlorite-aureole in xpl (UAE2097). (d) Back scattered electron image of fresh, grey chr and white rim of Fe-chr. Alteration progresses along cracks (UAE550). (e-f) Ferritchromit pseudomorphs after completely altered spinels (UAE2080): (e) black Fe-chr with chl aureole in ppl; (f) Brown, fine-grained texture of Fe-chr in reflected light.

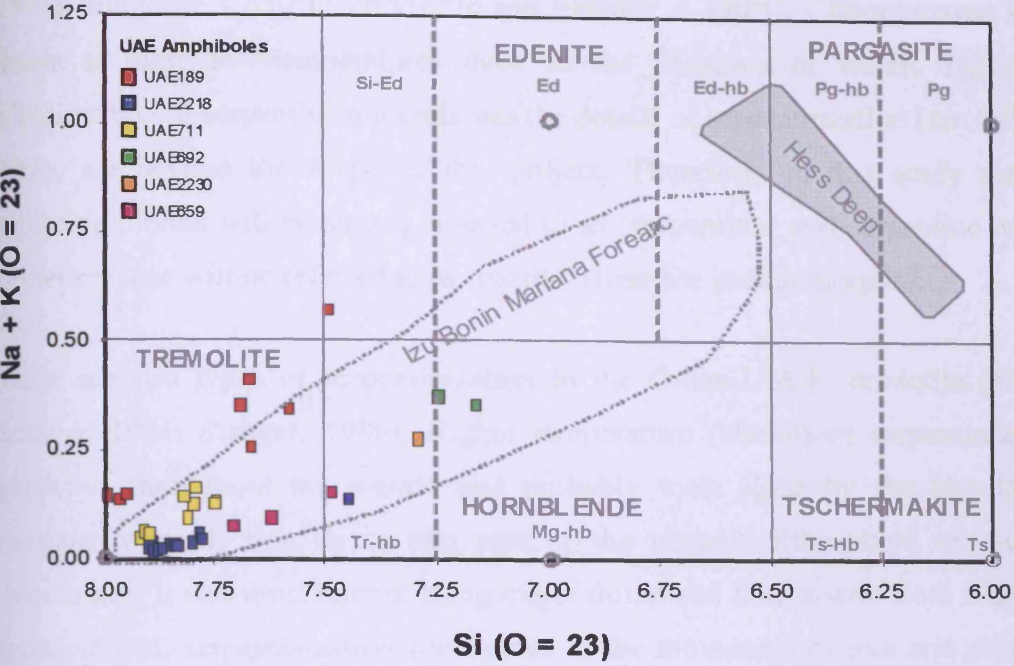

Figure B.3: Compositional variations of Ca-amphiboles (Leake, 1978) in peridotites from this study (coloured squares), Izu Bonin Mariana forearc (IBM) (open field) and Hess Deep (filled field). All amphiboles from Hess Deep (Arai and Matsukage, 1996; Matsukage and Arai, 1998) are high-T magmatic amphiboles (pargasite) whereas amphiboles from IBM record cooling with hydration. (Okamura, et al., 2006; Ishii et al., 1992; Ohara and Ishii, 2006).

Regional variation of MT alteration

MT alteration is greatest within the shear zones, marked by HT and LT microstructures. The basal detachment thrust hosts completely altered spinels and the amphibole-peridotite. Many samples from the Beni Hamid Shear Zone contain amphibole, which was only active at HT conditions. Although the BHSZ was not reactivated during emplacement, fluids did permeate preferentially along the pre-existing shear zone, resulting in MT alteration.

Low-temperature alteration

Low-temperature alteration results in the conversion of olivine and orthopyroxene to the serpentine minerals. These are stable over a range of temperatures (Evans, 1977): antigorite < 550°C, chrysotile and lizardite < 350°C. Clinopyroxene remains stable at these low-temperatures even in the presence of water. The detailed identification of serpentine minerals and the details of serpentinzation (see O'Hanley, 1996) are beyond the scope of this project. Therefore, in this study serpentine replacing olivine will be simply referred to as 'serpentine' and serpentine replacing orthopyroxene will be referred to as 'bastite' (lizardite pseudomorphs).

There are two types of serpentinization in the Oman-U.A.E. ophiolite (Neal and Stanger, 1984; Stanger, 1986). Higher temperature (alteration) serpentinization is pervasive throughout the mantle and probably took place by the circulation of seawater when it was an in situ part of the oceanic lithosphere or during its detachment. It was most intense along major thrust and fault zones. Low temperature (precipitation) serpentinization was related to the movement of past and present day meteoric waters (< 50°C) through the rocks upon post-emplacement exposure (Dunlop and Fouillac, 1984).

All U.A.E. peridotites are serpentinized to varying degrees with olivine commonly displaying a mesh texture and trails of magnetite and/or haematite and bastite pseudomorphs replacing some of the orthopyroxenes (e.g. Figure B.4). Magnetite (LT alteration) can also intergrow with the chlorite aureole (MT alteration) of spinel (Figure B.4f).

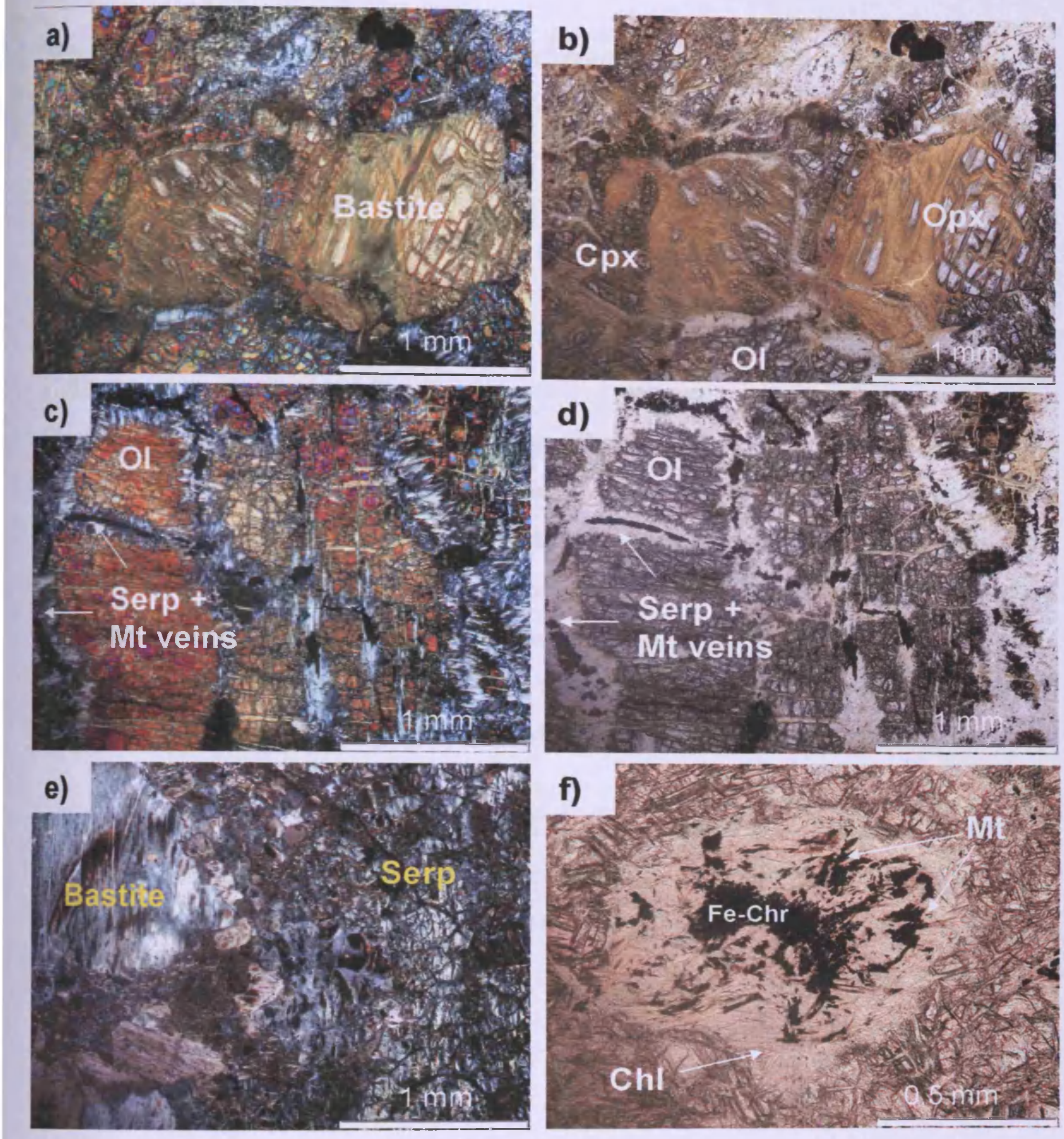

Figure B.4: **Low-temperature hydrothermal alteration/serpentinization** of orthopyroxene (opx)-bearing peridotites. (a-b) Bastite pseudomorphs with relict opx, relatively fresh cores of olivine and fresh clinopyroxene (UAE2042). (c-d) Veins of serpentine (antigorite) and magnetite along grains boundaries of olivine (UAE2040). (e) Complete serpentinization to bastite pseudomorphs, after orthopyroxene porphyroclasts, and serpentine mesh texture, after olivine. No relicts remaining (UAE4875). (f) Magnetite (low-T alteration) intergrown with chlorite aureole around ferritchromit (Fe-Chr) (Medium-T alteration of chrome-spinel).

Regional variation of low-T alteration

The spatial distribution of serpentinzation represents a regional, rather than a local, variation, as the freshest sample possible was collected from each outcrop. The majority of samples (85%) had less than 60% serpentinization. The more extensively serpentinized samples were observed along the western, desert border of Aswad south (Figure B.5a), in close proximity to the Wadi Ham faults in Aswad North (Figure B.5b), and in the serpentinites of the Dibba Zone.

Unlike the distribution of MT alteration, which was restricted to shear zones only, low degrees of high-temperature serpentinzation are pervasive through the mantle. Intense serpentinization, which was observed as bleached serpentinite along the Wadi Ham fault (Figure B.5b), probably resulted from focused flow of serpentinized fluids at higher temperatures. On an outcrop scale, the degree of serpentinization is high along all fractures because of low-temperature serpentinization from meteoric waters. Serpentinized peridotites from the Dibba Zone also formed at higher temperatures as they were highly deformed during obduction.

Extensive regional serpentinization along the western desert border probably resulted from low-temperature serpentinzation associated with tropical weathering and groundwater alteration that formed Listwaenite deposits on the Tertiary erosion surface (see Chapter 1, Section 1.1.6).

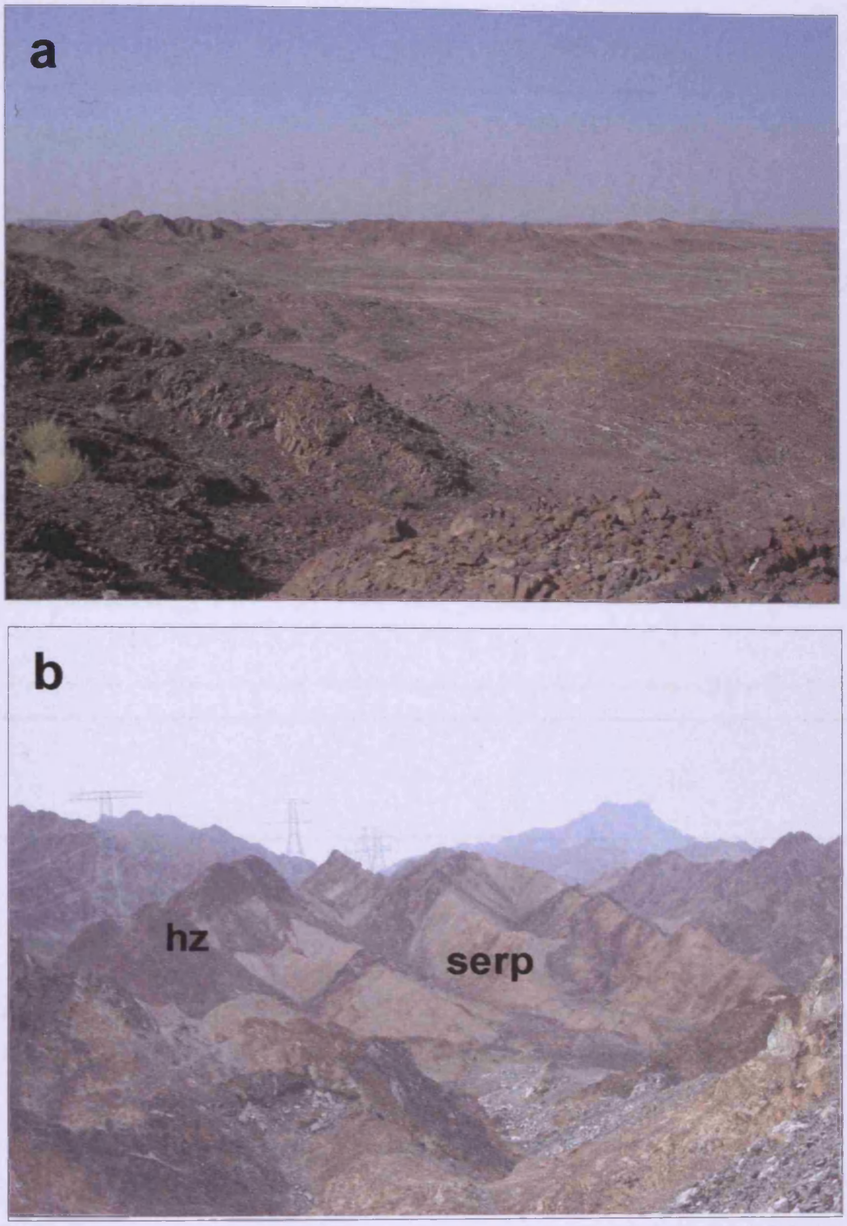

Figure B.5: Highly serpentinized regions: (a) desert border along western margin of Aswad south forming low crumbly hills. (b) Bleached-serpentinite (serp), among darker, more resistant, harzburgites (hz), along the Wadi Ham Fault zone in Aswad North near Masafi.

B.2 Petrographic classification of samples

Sample	Rock Type		OL		OPX		CPX		PLAG		SPINEL		Spinel Type		Silicate Inclusions	Microstructure Type		AMPH	%serp alt	Alteration
			Actual	[Original]	Actual	[Original]	Actual	[Original]	Actual	Origina	Actual	[Original]								
03UR35	Harzburgite	**Harzburgite**	65	78	15	20	1	1			1	1	HL			HT	mg-gran		18	serp
SD111	Harzburgite	**Harzburgite**	45	82	3	15	1	1			2	2	HL			HT	mg-gran		51	serp (+ talc)
SD112	Harzburgite	**Harzburgite**	20	83	5	15		1			<0.5	<0.5	HL			HT	cg-gran		74	serp
SD120_hz	Harzburgite	**Harzburgite**	55	84	5	15					1	1	HL	fabric		HT	cg-gran		39	serp + talc
SD138	Harzburgite	**Harzburgite**	45	78	15	20		1			<1	1	HL			HT	cg-gran		39	serp (+ talc + mt)
SD147	Harzburgite	**Cpx-Harzburgite**	60	80	14	15	3	3			2	2	HL			HT-rc	mg-fg gran		22	serp
SD151	Harzburgite	**Harzburgite**	65	82	14	15	2	2			1	1	HL	fabric		HT	mg-gran		19	serp
SD157	Harzburgite	**Harzburgite**	45	76	17	20	2	2			2	2	HL			HT	cg-gran		35	serp
SD19	Harzburgite	**Harzburgite**	50	80	17	20					0.5	0.5	HL			HT	cg-gran		33	serp
SD245	Harzburgite	**Harzburgite**	40	79	5	20					1	1	HL			HT	cg-gran		55	serp + talc
SD34	Harzburgite	**Harzburgite**	60	83	14	15		<1			1	1	HL			HT	cg-mg gran		24	serp
SD380	Harzburgite	**Harzburgite**	45	78	15	20	1	1			1	1	HL			HT	cg-gran		39	serp + talc
SD426	Harzburgite	**Harzburgite**	10	79	10	20					1	1	HL			HT	cg-gran		80	serp + talc
SD434	Harzburgite	**Harzburgite**	60	83	14	15	<0.5	<0.5			1	1	HL			HT	mg-gran		24	serp
SD452	Harzburgite	**Harzburgite**	55	77	15	20		<1			2	2	HL	fabric		MT	cg-porph		28	serp + talc
SD461	Harzburgite	**Harzburgite**	50	83	12	15	<1	<1			1	1	HL	fabric		HT	mg-gran		37	serp
SD488	Harzburgite	**Harzburgite**	45	69	30	30		?			1	1	SI	fabric		HT	mg-gran		24	serp
SD489	Harzburgite	**Harzburgite**	30	83	12	15	<1	<1			1	1	HL+SI			MT	cg-porph		57	serp (+ talc)
SD493	Harzburgite	**Cpx-Harzburgite**	40	75	20	20	4	4			1	1	HL	fabric		MT	cg-porph		37	serp
SD537	Harzburgite	**Cpx-Harzburgite**	40	80	5	15	2	3			2	2	SI		yes	HT	cg-gran	1	53	serp + talc
SD565	Harzburgite	**Harzburgite**	40	87	5	10	0	2			1	1	SI	some Eu	yes	MT	cg-porph	2	54	serp
SD567	Harzburgite	**Harzburgite**	30	77	15	20	2	2			1	1	EU	occluded		MT	cg-porph		54	serp
SD61	Harzburgite	**Lherzolite**	45	67	15	20	12	12			1	1	HL			MT	cg-porph		31	serp (+ talc + mt)
SD82	Harzburgite	**Harzburgite**	45	84	5	15					1	1	EU	occluded		HT	cg-gran		49	serp
UAE106	Harzburgite	**cpx-poor Harzburgite**	45	78	18	20	1	1			1	1	EU	pellet	yes	HT	cg-gran		36	serp
UAE116	Harzburgite	**cpx-poor Harzburgite**	55	89	5	10		<0.1			1	1	EU	occluded	-	HT	cg-gran	1	39	serp (+ talc)
UAE128	Harzburgite	**Harzburgite**	75	83	14	15	1	1			1	1	HL+SI			HT-rc	mg-fg gran		9	serp
UAE130	Harzburgite	**Cpx-Harzburgite**	78	81	14	15	2	3			1	1	HL+SI			HT-rc	mg-fg gran	2	4	serp
UAE144	Harzburgite	**cpx-poor Harzburgite**	45	88	3	10	0	1			1	1	EU		yes	HT	cg-gran	1	51	serp (+ talc)
UAE145	Harzburgite	**cpx-poor Harzburgite**	55	79	15	20		<0.1			1	1	EU	occluded		MT	cg-porph		29	serp + talc
UAE156	Harzburgite	**cpx-poor Harzburgite**	55	73	22	25	1	1			1	1	EU	occluded		HT	cg-gran		21	serp
UAE159	Harzburgite	**cpx-poor Harzburgite**	50	78	17	20	<1	<1			1	1	EU	occluded	yes	MT	cg-porph		32	serp (+ talc)
UAE189	Harzburgite	**Lherzolite (Amph-peridotite)**	35	83	5	15		?			0	2	HL			LT	fg-porph	35	59	serp + talc
UAE19	Harzburgite	**Harzburgite**	30	83	14	15	1	1			1	1	HL	fabric		HT-rc	mg-fg gran		55	serp
UAE192	Harzburgite	**Harzburgite**	50	83	5	15		<1			0.5	1	HL			MT	cg-porph		44	serp + talc
UAE2007	Harzburgite	**Harzburgite**	40	83	2	15	0	1			0.2	1	HL			MT	cg-porph	1	57	serp + talc
UAE2032	Harzburgite	**Harzburgite**	80	89	10	10					1	1	SI			LT	fg-porph		9	serp
UAE2035	Harzburgite	**Lherzolite**	60	69	18	20	8	10			<0.5	<0.5	HL			MT	cg-porph	1	12	serp
UAE2036	Harzburgite	**Harzburgite**	60	84	10	15					1	1	SI			LT	fg-porph	1	29	serp
UAE2040	Harzburgite	**Harzburgite**	40	83	0	15		1			0.5	1	HL			HT	mg-gran		59	serp (+ talc + mt)
UAE2042	Harzburgite	**Harzburgite**	15	77	2	20	2	2			1	1	EU	poik		MT	cg-porph		82	serp
UAE2044	Harzburgite	**Harzburgite**	5	83	1	15		1			1	1	SI		occluded	HT-rc	mg-fg-gran		94	serp
UAE2046	Harzburgite	**Cpx-Harzburgite**	35	80	10	15	3	3			2	2	HL			MT	cg-porph		53	serp (+ talc)
UAE2058	Harzburgite	**Cpx-Harzburgite**	35	71	20	25		3			1	1	SI			MT	cg-porph	1	43	serp (+ talc)
UAE2065	Harzburgite	**Lherzolite**	40	65	20	20	13	13			2	2	HL	fabric		MT	cg-porph		29	serp
UAE2080	Harzburgite	**Harzburgite**	35	82	5	15	1	1			0.5	2	HL			HT-rc	mg-fg-gran	1	59	serp + talc
UAE2087	Harzburgite	**Harzburgite**	50	78	18	20	1	1			1	1	HL+SI			HT	cg-gran		31	serp
UAE2091	Harzburgite	**Cpx-Harzburgite**	55	71	23	25	2	3			1	1	HL	fabric		HT	cg-gran	1	19	serp
UAE2097	Harzburgite	**Lherzolite**	55	63	28	30	6	6			0.5	<1	HL			HT-rc	mg-fg-gran		11	serp (+ talc)
UAE2109	Harzburgite	**Harzburgite**	35	63	33	35	1	1			1	1	HL			HT	mg-gran		31	serp
UAE2114	Harzburgite	**Harzburgite**	20	80	8	20					0.5	0.5	HL			HT	cg-gran		72	serp
UAE2156	Harzburgite	**Harzburgite**	50	68	28	30		1			<1	<1	HL			HT	mg-gran		20	serp (+ talc)

Sample	Rock Type		OL		OPX		CPX		PLAG		SPINEL		Spinel Type		Silicate Inclusions	Microstructure Type		AMPH	%serp alt	Alteration
			Actual	[Original]	Actual	[Original]	Actual	[Original]	Actual	Origina	Actual	[Original]								
UAE2159	Harzburgite	**Harzburgite**	5	83	0	15	0	1				1	HL			MT	cg-porph	1	95	serp + talc
UAE2161	Harzburgite	**Cpx-Harzburgite**	45	70	25	25	3	3			2	2	HL	fabric		HT-rc	mg-fg gran	1	26	serp
UAE2169	Harzburgite	**Cpx-Harzburgite**	45	76	15	20	2	3			<0.25	<0.5	HL			MT	cg-porph	2	38	serp
UAE2214	Harzburgite	**cpx-poor Harzburgite**	35	89	7	10					1	1	SI		yes	MT	cg-porph		58	serp
UAE2215	Harzburgite	**cpx-poor Harzburgite**	45	88	8	10	1	1			1	1	EU	occluded		MT	cg-porph	1	46	serp (+ talc)
UAE2218	Harzburgite	**cpx-poor Harzburgite**	30	83	13	15					2	2	EU	occluded	yes	MT	cg-porph	3	56	serp
UAE2221	Harzburgite	**cpx-poor Harzburgite**	40	83	12	15	<1	1			1	1	EU	occluded	yes	MT	cg-porph	1	47	serp
UAE2230	Harzburgite	**Harzburgite**	60	84	12	15					1	1	HL			MT	cg-porph		27	serp
UAE2241	Harzburgite	**Cpx-Harzburgite**	75	80	13	15	4	4			0.5	1	HL			MT	cg-porph		7	serp
UAE2242	Harzburgite	**Harzburgite**	0	84	0	15		?			1	1	HL	fabric		LT-myl	mylonite		100	serp + mt
UAE2244	Harzburgite	**Cpx-Harzburgite**	25	76	18	20	3	3			<1	<1	HL			HT	mg-gran		55	serp
UAE2278	Harzburgite	**Harzburgite**	40	78	18	20		<1			1	1	HL			HT	cg-gran		41	serp
UAE2285	Harzburgite	**Harzburgite**	55	78	5	20		<1			1	1	HL			HT-rc	mg-fg gran		39	serp + talc
UAE2288	Harzburgite	**Harzburgite**	10	83	12	15		<1			1	1	HL			MT	cg-porph		78	serp
UAE2354	Harzburgite	**Harzburgite**	40	81	14	15		3			2	2	HL	fabric		MT	cg-porph		43	serp
UAE2810	Harzburgite	**Harzburgite**	45	72	20	25		2			1	1	HL	fabric		HT-rc	mg-fg gran		33	serp
UAE2836	Harzburgite	**Cpx-Harzburgite**	55	76	18	20	3	3			1	1	HL	fabric		HT	mg-gran		24	serp
UAE312	Harzburgite	**Harzburgite**	75	84	14	15					1	1	EU	occluded		MT	cg-porph		10	serp
UAE316	Harzburgite	**Harzburgite**	65	83	10	15	1	2			0.25	0.5	HL			HT	cg -mg gran	1	23	serp (+ talc)
UAE3190	Harzburgite	**Harzburgite**	25	72	22	25		<1			1	1	HL			MT	cg-porph		52	serp
UAE327	Harzburgite	**Cpx-Harzburgite**	62	80	12	15	3	4			1	1	SI		yes	HT	cg-gran	1	22	serp (+ talc)
UAE360	Harzburgite	**Cpx-Harzburgite**	65	81	10	15	1	3			1	1	HL			HT	mg-gran	2	22	serp (+ talc)
UAE37	Harzburgite	**Harzburgite**	60	88	8	10		<1			<1	<1	SI			HT-rc	mg-fg-gran		31	serp (+ talc)
UAE380	Harzburgite	**cpx-poor Harzburgite**	75	83	14	15					2	2	SI		-	HT-rc	cg-fg-gran		9	serp
UAE387	Harzburgite	**cpx-poor Harzburgite**	60	79	5	20					1	1	EU	occluded		HT	mg-gran		34	serp + talc
UAE391	Harzburgite	**cpx-poor Harzburgite**	55	78	17	20	1	1			1	1	EU	occluded		HT	cg-gran		27	serp (+ talc)
UAE424	Harzburgite	**Harzburgite**	70	82	13	15	1	2			<1	<1	HL			HT	mg-gran		14	serp
UAE432	Harzburgite	**Cpx-Harzburgite**	40	83	14	15		1			1	1	HL+SI		yes	LT-myl	mylonite		45	serp
UAE445	Harzburgite	**Harzburgite**	60	78	*15*	*20*	*1*	*1*				1	HL			HT	cg-mg gran		23	serp
UAE45	Harzburgite	**Harzburgite**	50	81	5	15	2	2			2	2	HL	fabric		HT-rc	mg-fg gran		43	serp + talc
UAE4801	Harzburgite	**Harzburgite**	50	73	20	25	<0.5	<0.5			1	1	HL+SI		some	MT	cg-porph		29	serp
UAE4807	Harzburgite	**Harzburgite**	55	73	20	25	<1	<1			1	1	HL			MT	cg-porph		23	serp
UAE484	Harzburgite	**Harzburgite**	65	84	12	15					1	1	EU	occluded	yes	MT	cg-porph		22	serp
UAE485	Harzburgite	**Harzburgite**	60	84	5	15					1	1	EU		-	HT-rc	mg-fg gran	2	34	serp + talc
UAE501	Harzburgite	**Harzburgite**	0	84	0	15					<1	<1	HL		-	HT	cg-gran		100	serp
UAE510	Harzburgite	**Harzburgite**	0	84	0	15					<0.5	<0.5	SI			-	-		100	serp
UAE545	Harzburgite	**Harzburgite**	55	88	0	10					2	2	HL		seive	MT	cg-porph	1	44	serp + talc
UAE546	Harzburgite	**Harzburgite**	45	78	10	20	1	1			1	1	HL	fabric		MT	cg-porph		44	serp
UAE550	Harzburgite	**Harzburgite**	50	83	0	15		?			0.2	2	HL	fabric		MT	cg-porph	1	49	serp + talc
UAE581bgs	Harzburgite	**Harzburgite**	35	83	10	15	1	1			1	1	HL			HT	mg-gran		54	serp (+ talc)
UAE60	Harzburgite	**Harzburgite**	50	78	12	20	1	1			1	1	SI		yes	HT-rc	cg-fg gran	1	37	serp (+ talc)
UAE622	Harzburgite	**Harzburgite**	45	82	12	15	2	2			<1	<1	HL			HT-rc	mg-fg gran		41	serp (+ talc)
UAE659	Harzburgite	**Harzburgite**	40	89	5	10					<1	<1	HL		-	HT	cg-gran	2	55	serp
UAE66	Harzburgite	**Harzburgite**	45	78	15	20		1			1	1	EU	occluded + HL		HT	mg-gran	2	39	serp (+ talc)
UAE692	Harzburgite	**cpx-poor Harzburgite**	50	88	1	10	<1	<1			1	1	EU	pellet		MT	cg-porph	1	48	serp + talc
UAE700	Harzburgite	**Harzburgite**	45	82	8	15		<1			2	2	SI			MT	cg-porph		45	serp + talc
UAE711	Harzburgite	**Harzburgite**	70	84	1	15					1	1	HL			MT	cg-porph	1	28	serp (+ talc + mt)
UAE715	Harzburgite	**Harzburgite**	40	79	10	20					1	1	EU	occluded		MT	cg-porph		49	serp + talc
UAE79	Harzburgite	**Harzburgite**	40	77	*15*	*20*	2	2			1	1	EU	occluded		HT	cg-gran		43	serp
UAE86	Harzburgite	**cpx-poor Harzburgite**	65	84	14	15					1	1	EU	occluded		HT	cg-gran		20	serp
UAE95	Harzburgite	**cpx-poor Harzburgite**	50	78	18	20	1	1			1	1	EU	occluded		HT	cg-mg gran	2	31	serp (+ talc)
UAE323	Harzburgite	**Harzburgite**	65	88	8	10		1			1	1	HL	fabric		HT-rc	fg-gran		26	serp (+ talc)
UAE4875	Harzburgite	**Harzburgite**	0	84	0	15					1	1	HL			MT	cg-porph		100	serp

Sample	Rock Type		OL		OPX		CPX		PLAG		SPINEL		Spinel Type		Silicate Inclusions	Microstructure Type		AMPH	%serp alt	Alteration
			Actual	[Original]	Actual	[Original]	Actual	[Original]	Actual	Original	Actual	[Original]								
UAE4877	Harzburgite	**Cpx-Harzburgite**	70	76	20	20	3	3			1	1	HL			LT	fg-porph		6	serp
UAE4879	Harzburgite	**Harzburgite**	10	76	18	20	3	3			1	1	HL			MT	cg-porph		71	serp
UAE4882	Harzburgite	**Cpx-Harzburgite**	35	75	15	20	4	4			1	1	HL			LT	fg-porph		47	serp
03UR187	Dunite	**Chr-Dunite**	0	90							10	10	*SI/cuspate*		*poikilitic*	-	-		100	ol=dol
SD106a	Dunite	**Chr-Dunite**	20	78							22	22	SI/EU	trail + partia	poikilitic	HT	cg-gran		74	
UAE3189	Dunite	***Dunite***	60	98							2	2	HL			MT	peg-porph	1	39	
SD11a	Dunite	**Chr-Dunite**	5	88							12	12	HL	fabric		-	-		94	
SD110	Dunite	**Dunite**	15	98							2	2	SI	trail	poikilitic	-	-		85	
SD120_du	Dunite	**Dunite**	65	96	0	3					<1	<1	SI	*fabric*		HT	cg-mg gran		34	serp (+talc)
SD144	Dunite	**Dunite**	70	96			0	1			3	3	SI/cuspate		poikilitic	HT-rc	mg-fg gran		27	
SD158_chr	Chromitite	**Chromitite**	0	5							95	95	SI/cuspate	full chain	poikilitic	-	-			
SD154	Dunite	**Dunite**	55	99							1	1	SI		poikilitic	HT	cg-mg gran		44	
SD158_du	Dunite	**Dunite**	15	97							3	3	SI/EU	fabric/elongate		HT	cg-gran		85	
SD18	Dunite	**Dunite**	60	99							<1	<1	EU		poikilitic	HT	cg-gran		39	
SD247	Dunite	**Dunite**	65	98							2	2	SI	weak fabric	poikilitic	HT-rc	mg-gran		34	
SD255	Dunite	***Dunite***	75	97							3	3	SI/cuspate		poikilitic	HT-rc	mg-gran		23	
SD345	Dunite	**Chr-Dunite**	0	60							40	40	EU	chain	poikilitic	-	-		100	
SD33	Dunite	**Dunite**	55	100							0.5	0.5	HL	fabric/elongate		LT	mg-fg granoblast		45	
SD362_chr	Chromitite	**Chromitite**	0	15							85	85	*SI/cuspate*	*partial chair*	*poikilitic (dohnut)*	-	-			
SD36	Dunite	**Dunite**	70	99							1	1	SI/cuspate			HT-rc	mg-gran		29	
SD37	*Dunite*	***Chr-Dunite***	10	94	0	1					6	6	SI/cuspate		poikilitic	HT-rc	mg-gran		89	
SD362_du	Dunite	**Dunite**	10	97	0	2					1	1	SI/cuspate		poikilitic	-	-		90	
SD379	Dunite	**Dunite**	0	99							1	1	SI/EU		poikilitic	-	-		100	
SD417	Dunite	**Dunite**	15	98							2	2	*SI/cuspate*	*fabric*	*poikilitic*	*HT-rc*	*mg-gran*		85	
SD425	Dunite	**Dunite**	3	99							<1	<1	SI			-	-		97	
SD436a_chr	Chromitite	**Chromitite**	0	5							95	95	SI/cuspate	partial chair	poikilitic (dohnut)	-	-			
SD433	Dunite	**Dunite**	10	98	<1	<1					1	1	SI		poikilitic	-	-		89	
SD436b_chr	Chromitite	**Chromitite**	0	5							95	95	SI/cuspate	partial chair	poikilitic (dohnut)	-	-			
SD436a_du	Dunite	**Dunite**	45	96			3	3			1	1	*SI/cuspate*		*poikilitic*	*HT-rc*	*mg-gran*		53	
SD436b_du	Dunite	**Dunite**		99								1	SI			HT	cg-mg gran		100	
SD448b	Dunite	**Dunite**	0	99							<1	<1	SI			-	-		100	
SD451	Dunite	**Dunite**	60	97							3	3	SI/cuspate		poikilitic (inclusions)	HT-rc	mg-gran		38	
SD456	Dunite	**Dunite**	0	99							1	1	HL	fabric		-	-		100	
SD469	Dunite	**Dunite**	75	98			1	1			1	1	SI	chain	*poikilitic*	HT	*cg-mg gran*		23	
SD477	Dunite	**Dunite**	0	99							1	1	SI/cuspate		poikilitic	-	-		100	
SD484	Dunite	**Dunite**	1	99							1	1	EU			-	-		99	
SD490	Dunite	**Chr-dunite**	50	90							10	10	SI/cuspate	trail /elongate		MT	mg-porph		44	
SD486	Dunite	**Dunite**	0	99							1	1	SI			-	-		100	
SD511	Dunite	**Chr-Dunite**	75	92							8	8	*SI/cuspate*		*poikilitic*	*HT-rc*	*mg-gran*		18	
SD494	Dunite	**Dunite**	55	99							<1	1	SI			HT-rc	mg-gran		44	
SD560	Dunite	**Dunite**	55	100							<0.5	<0.5	EU			MT	cg-porph		45	
SD568	Dunite	**Dunite**	45	98							2	2	EU			MT	peg-porph		54	
SD62	Dunite	**Dunite**	55	97			2	2			1	1	SI/EU	fabric/elong	poikilitic	MT	cg-porph		43	
SD67	Dunite	**Dunite**	60	98							2	2	EU			MT	cg-porph		39	
SD71a	Dunite	**Chr-Dunite**	40	70							30	30	SI/cuspate	net	poikilitic (inclusions)	HT-rc	mg-gran		43	
SD70	Dunite	***Dunite***	60	98			<1	<1			1	1	EU		poikilitic	HT	peg		39	
UAE117	Dunite	**Chr-Dunite**	55	95							5	5	SI/cuspate		poikilitic	HT	cg-gran	2	42	
UAE138-du	Dunite	**Chr-Dunite**	50	90							10	10	SI	trail // conta	inclusion trails	MT	peg-porph		44	
UAE138-chr	Chromitite	**Chromitite**	10	25							75	75	SI/EU	partial chair	poikilitic (incl)	HT	mg-gran			
UAE108	Dunite	**Dunite**	15	97							3	3	SI	trail		HT	peg		85	
UAE143	Dunite	**Dunite**	30	98							2	2	EU			MT	peg-porph	<1	69	
UAE146	Dunite	**Dunite**	65	99							1	1	EU			MT	cg-porph	<1	34	
UAE17	Dunite	**Chr-Dunite**	70	94				<1			6	6	SI/cuspate	fabric/elong	poikilitic	HT-rc	mg-fg gran	<1	26	

Sample	Rock Type		OL		OPX		CPX		PLAG		SPINEL		Spinel Type		Silicate Inclusions	Microstructure Type		AMPH	%serp alt	Alteration
			Actual	[Original]	Actual	[Original]	Actual	[Original]	Actual	Origina	Actual	[Original]								
UAE196	Dunite	**Chr-Dunite**	0	80							20	20	SI/cuspate			-	-		100	
UAE160	Dunite	**Dunite**	60	99							1	1	EU			HT	peg	<1	39	
UAE2008	Dunite	**Dunite**	35	99							1	1	SI	elongate		MT	cg-porph		65	
UAE2039	Dunite	**Dunite**	30	99							1	1	SI/EU		poikilitic	HT-rc	mg-fg gran		70	
UAE2047	Dunite	**Dunite**	60	96							4	4	HL	fabric/elongate		MT	cg-porph		38	
UAE2167	Harzburgite	**Harzburgite**	50	94	5	5	<1	<1			0.5	0.5	SI/EU			HT-rc	fg-gran		44	serp
UAE2212	Dunite	**Chr-Dunite**	40	95							5	5	SI/cuspate			HT	cg-gran		58	
UAE2064	Dunite	**Dunite**	60	98			<1	<1			1	1	SI			MT	peg-porph		39	
UAE2232	Dunite	**Chr-Dunite**	25	70							30	30	SI/cuspate	trail cut ol fa	poikilitic	LT	mg granoblast		64	
UAE2222	Dunite	**Dunite**	40	97			1	1			2	2	EU			HT	peg		59	
UAE2355	Dunite	**Chr-dunite**	5	55							45	45	SI/cuspate	banded	poikilitic	-	-		91	
UAE2281	Dunite	**Dunite**	60	99							<1	<1	SI			MT	cg-porph		39	
UAE299	Dunite	**Dunite**	60	98							2	2	EU	c-cuspate		MT	peg-porph		39	
UAE3200	Dunite	**Dunite**	20	99							1	1	SI/EU		poikilitic	HT	cg-gran		80	
UAE379	Dunite	**Dunite**	60	99							1	1	SI/EU		poikilitic	HT	peg		39	
UAE392	Dunite	**Dunite**	35	99							1	1	SI			HT	peg	<1	65	
UAE412	Dunite	**Dunite**	50	97			<1	<1			2	2	SI			HT	cg-mg gran		48	
UAE4808	Dunite	**Dunite**	45	99			1	1			1	1	EU		poikilitic	HT-rc	mg-gran		54	
UAE4893	Dunite	**Dunite**	70	97			2	2			1	1	SI/EU		poikilitic	HT	cg-gran		28	
UAE509	Dunite	**Dunite**	2	99							1	1	SI/cuspate	fabric		-	-		98	
UAE543	Dunite	**Chr-Dunite**	35	90							10	10	HL	fabric/elong	poikilitic	LT	mg-fg granoblast		61	
UAE547	Dunite	**Dunite**	40	99							<0.5	<0.5	SI			LT	mg-fg granoblast		60	
UAE615	Dunite	**Dunite**	65	98			<1	<1			1	1	SI/EU	fabric/elong	poikilitic	HT	cg-mg gran		34	
03UR24	Dunite	**Plag-Dunite**	80	91			2	2	0	8	1	1	SI		poikilitic	HT-rc	mg-gran		12	pl=clay + chl
03UR32	Dunite	**Dunite**	55	97			1	1			2	2	SI			HT	cg-mg gran		43	
SD131a_du	Dunite	**Dunite**	70	98			1	1	0	1	1	1	SI			HT-rc	mg-gran		29	
SD131a_gb	Gabbro	**Ol-Gb**	35	54			25	25	0	20	1	1	SI			HT-rc	mg-gran		35	
SD150	Dunite	**Cpx-Dunite**	65	94			5	5			1	1	SI/cuspate	fabric // cpx	poikilitic	HT-rc	mg-fg gran		31	
SD383b	Dunite	**Chr-Dunite**	0	93							7	7	EU		poikilitic	-	-		100	
SD409_du	Dunite	**Chr-Dunite**	10	85							15	15	SI/EU	partial chair	poikilitic	HT-rc	mg-gran		88	
SD459	Dunite	**Chr-dunite**	60	90							10	10	SI/EU	trail + chain	poikilitic	HT-rc	mg-gran		33	
SD496	Dunite	**Dunite**	35	99							1	1	SI		poikilitic	HT-rc	mg-fg gran		65	
SD540	Dunite	**Dunite**	0	98			<1	<1			1	1	SI			-	-		100	
UAE238	Dunite	**Dunite**	85	97							3	3	SI/cuspate	partial chair	poikilitic	HT-rc	mg-fg gran		12	
UAE257	Dunite	**Dunite**	40	99							1	1	SI/cuspate	elongate	poikilitic	HT-rc	mg-gran		60	
UAE275	Dunite	**Dunite**	85	98			1	1			1	1	SI			HT-rc	mg-gran		13	
UAE2808	Dunite	**Dunite**	15	100							0.5	0.5	SI			HT-rc	fg gran		85	
UAE2814	Dunite	**Cpx-Dunite**	75	94			5	5			<1	<1	SI			HT-rc	mg-gran		20	
UAE2832	Dunite	**Dunite**	75	98			1	1			1	1	SI			HT-rc	mg-gran		23	
UAE325	Dunite	**Dunite**	0	99							0	1	SI			-	-		100	
UAE33	Dunite	**Dunite**	80	97			1	2			1	1	SI			HT-rc	mg-fg gran		18	
UAE353	Dunite	**Dunite**	85	96			1	1	??		3	3	SI/EU	partial chair	poikilitic	HT	cg-mg gran		11	
UAE370	Dunite	**Plag-Dunite**	70	93			1	1	0	4	2	2	SI	elongate	poikilitic	HT-rc	mg-gran		25	
UAE3996a_crdu	Wehrlite	**Chr-Wehr**	50	60			20	20			20	20	EU	partial chair	poikilitic	HT-rc	mg-fg gran			
UAE4056	Dunite	**cpx-chr-du**	5	53			7	7			40	40	EU	partial chair	poikilitic	HT-rc	mg-fg gran		91	
UAE430	Dunite	**Dunite**	70	98			<1	<1			1	1	SI			HT-rc	mg-gran		29	
UAE481	Dunite	**Plag-dunite**	15	92					0	7	1	1	SI		poikilitic	HT-rc	mg-fg gran		84	plag alt
UAE503	Dunite	**Cpx-Dunite**	30	89			10	10		?	1	1	SI			HT-rc	mg-gran		66	
UAE535	Dunite	**Dunite**	70	97			2	2			1	1	SI			HT-rc	mg-fg gran		28	
UAE566	Dunite	**Cpx-Dunite**	50	91			8	8			1	1	SI			HT-rc	mg-fg gran		45	
UAE573	Dunite	**Dunite**	30	98							2	2	SI	fabric	poikilitic	HT	cg-mg gran		69	
UAE586	Dunite	**Dunite**	15	99							1	1	SI/EU		poikilitic	HT-rc	mg-gran		85	
UAE607	Dunite	**Dunite**	70	99							1	1	SI		poikilitic	HT-rc	mg-fg gran		29	

Sample	Rock Type		OL		OPX		CPX		PLAG		SPINEL		Spinel Type		Silicate Inclusions	Microstructure Type		AMPH	%serp alt	Alteration
			Actual	[Original]	Actual	[Original]	Actual	[Original]	Actual	Original	Actual	[Original]								
UAE612	*Dunite*	**Cpx-Dunite**	40	91			2	8			1	1	SI		poikilitic	HT-rc	mg-gran		56	cpx/plag alter
UAE627	Dunite	**Cpx-Dunite**	80	92			7	7			1	1	SI			HT-rc	mg-gran		13	
UAE65_chr	Chromitite	**Chromitite**	5	15			??	??			80	80	SI/EU	chain, occluded	poikilitic (incl)	HT	mg-gran		serp + Ca	
UAE65_du	Dunite	**Cpx-Dunite**	80	90			8	8			2	2	SI/EU			HT-rc	mg-gran		11	
UAE763	Dunite	**Dunite**	70	98				<1			1	1	SI		poikilitic	HT-rc	mg-gran		29	
UAE4876	Dunite	**Dunite**	0	99							<1	<1	SI			-	-		100	
UAE4878	Dunite	**Dunite**	0	99							<0.5	<0.5	HL	fabric/elongate		-	-		100	
UAE4880	Dunite	**Dunite**	0	99							<0.5	<0.5	HL			-	-		100	
UAE4883	Dunite	**Dunite**	0	97							2	2	SI	fabric/elongate		-	-		100	
SD102a	Dunite	**chr-dunite**	15	60							40	40	SI/cuspate	partial chain	poikilitic (dohnut)	HT	cg-mg gran			
SD109	Chromitite	**Chromitite**	0	0			0	5			95	95	SI/EU	*full chain*	poikilitic (dohnut)	-	-	5	Ca veins	
SD152a	Chromitite	**Chromitite**	25	42	<1	1	1	1			55	55	SI/cuspate	shear fabric, pa	poikilitic (dohnut)	HT	cg-gran			
SD159b	Chromitite	**Chromitite**	0	2							98	98	EU	full chain	poikilitic (incl)	-	-		Ca veins	
SD163	Chromitite	**Chromitite**	3	10			2	5			85	85	SI/EU	full chain	poikilitic (incl)	-	-		Ca veins	
SD246	Chromitite	**Chromitite**	2	5			3	10			85	85	EU	full chain	poikilitic (incl)	HT	fg-gran			
SD42b	Chromitite	**Chromitite**	5	27			0	3			70	70	SI/EU	partial chain	poikilitic (incl)	HT	mg-gran			
SD49	Chromitite	**Chromitite**	10	40							60	60	SI/cuspate	partial chain	poikilitic (incl)	HT	mg-gran			
SD89a	Chromitite	**Chromitite**	0	15							85	85	EU	full chain	poikilitic (dohnut)	-	-			
UAE120bCh	romitite	**Chromitite**	15	25			5	5			70	70	SI/cuspate	partial chain	poikilitic	HT	cg-mg gran			
UAE140	Chromitite	**Chromitite**	0	0	5	5	4	5			90	90	EU	full chain	poikilitic (dohnut)	MT	mg-porph			
UAE155B	Chromitite	**Chromitite**	0	30							70	70	SI/cuspate	partial chain	*poikilitic*	-	-			
UAE393	Chromitite	**Chromitite**	5	25			<1	<1			65	65	SI/cuspate	partial chain	poikilitic (incl)	HT	mg-gran			
UAE4803	Chromitite	**Chromitite**	1	5							95	95	SI/cuspate	full chain	poikilitic (incl)	-	-			
UAE94	Chromitite	**Chromitite**	10	35							65	65	SI/cuspate	full chain	poikilitic (dohnut)	MT	cg porph			
SD262_chr	*Chromitite*	***Chromitite***	0	15			2	3			80	85	SI/EU	full chain	poikilitic (incl)	-	-	1		
SD409_chr	Chromitite	**Chromitite**	0	20							80	80	SI/cuspate	full chain	*poikilitic (dohnut)*	-	-			
SD444	Chromitite	**Chromitite**	8	13			1	2			85	85	SI/cuspate	*full chain:settlin*	poikilitic (incl)	HT	fg-gran			
SD497	Chromitite	**Chromitite**	5	5			5	5			90	90	EU	full chain:settlin	poikilitic (incl)	-	-			
SD436b_px	Pyroxenite	**Ol-Cpxenite**	7	10	*10*	*10*	80	80					SI			HT	mg-gran			
SD436b_gb	Gabbro	**Gb**			3	3	12	12	0	85						HT	fg-gran			
UAE111	Pyroxenite	**Ol-Opxenite**			5	95	2	4			1	1	SI/EU			HT	peg gran	2	*cpx/amph fg inte* talc	
UAE629	Pyroxenite	**Websterite**	5	5	30	30	65	65			< 1	< 1	SI			HT-rc	mg-fg gran			
UAE87	Pyroxenite	**Ol-Opxenite**	20	25	66	72	2	2			1	1	SI			MT	peg/cg-porph			
SD94	Pyroxenite	**Cpxenite**	3	4	4	4	*80*	88	1	2	1	1	SI/EU			HT	peg gran		*ol + pl interstital fg*	
UAE252	Pyroxenite	**Cpxenite**	5	5	5	5	88	88	1	1	< 1	< 1	SI			HT	cg-gran		*opx often poik interstitial*	
UAE2813	Pyroxenite	**Ol-websterite**	15	15	15	15	70	70			<<0.5	<<0.5	SI			HT	mg-gran			
UAE342	Pyroxenite	**opxenite**			95	95	5	5			<<0.5	<<0.5	SI			HT	cg-gran			
UAE345	Pyroxenite	**Websterite**			35	35	65	65			<<0.5	<<0.5	SI			HT	mg-gran			
UAE469	Gabbro	**Ol-Gb**	25	35	2	2	43	43	18	20	< 1	< 1	SI			HT	cg-gran		*px poik and gran*	
UAE491	Pyroxenite	**Ol-Cpxenite**	30	40			59	59	0	1	<<0.5	<<0.5	SI			HT	cg-porph			
SD142	Gabbro	**Ol-Gb**	30	50	10	10	25	25	1	15	< 1	< 1	SI			HT	mg-gran		*poik plg-cpx, px fg network*	
SD262_wehr	Wehrlite	**Wehrlite**	40	67			30	30			1	1	SI		poikilitic (dohnuts)	HT-rc	mg-gran		*cpx gran, strained*	
UAE126	Wehrlite	**Wehrlite**	<1	60			40	40			<1	<1	SI			-	-		*cpx cg gran, part poik*	
UAE225	Gabbro	**Ol-Gb**	50	64			20	20	15	15	1	1	SI			HT-rc	mg-fg gran		*cpx gran*	
UAE236	Gabbro	**Troctolite**	60	74			7	7	3	15	4	4	SI/cuspat	partial chain	poikilitic (dohnuts)	HT-rc	mg-fg gran		*cpx gran, plag interstital*	
UAE277	Gabbro	**Ol-Gb**	15	58			25	25	4	15	2	2	HL			HT-rc	mg-fg gran		*cpx gran/poik*	
UAE3996a_wehr	Wehrlite	**Wehrlite**	60	74			25	25			1	1	SI		poikilitic (dohnuts)	HT-rc	mg-gran		*strained poik*	
UAE422	Gabbro	**Ol-Gb**	50	71	3	3	15	15	3	10	1	1	SI		poikilitic (dohnuts)	HT-rc	fg gran		*cpx gran/poik*	
UAE492	Dunite	**plag-cpx-dunite**	65	93			3	3	0	3	1	1	SI		poikilitic (dohnuts)	HT-rc	fg gran			
UAE263	Gabbro	**Ol-Gb**																		
UAE322	Gabbro	**Ol-Gb**																		
UAE340	Gabbro	**Ol-Gb**																		
UAE448	Gabbro	**Troctolite**																		
UAE482	Gabbro	**Troctolite**	35	58					0	40	2	2	SI			HT	mg-gran			
UAE517	Gabbro	**Gb bithna**																		

Appendix C: Whole rock analyses

C.1 Method for whole rock analysis by Inductively-Coupled Plasma (ICP) Optical Emission Spectrometry (OES) and ICP-Mass Spectrometry (MS)

Sample preparation of powders

Rock samples collected in the field were prepared following the standard procedures of the geochemical facilities at Cardiff University during 2004-2005. Hand specimens were first cut to size, weighing between 100 – 150g, and ground on a diamond saw to remove weathered surfaces and alteration veins. The hand specimens were reduced to chips in a clean jaw crusher, and then reduced to a fine powder using an agate ball mill. The resulting powders were transferred to clean plastic bags for storage.

Loss on Ignition (LOI) analysis

Approximately 2.0g of each sample powder was accurately weighed into clean ceramic vials and heated in a muffle furnace at 900°C for 2 hours to release H_2O, CO_2 and other volatiles. After cooling, the mass of the ignited residue was determined and loss on ignition (LOI) calculated. The ignited powders were stored in sealed plastic bags within a dessicator prior to analysis. All iron was oxidised from Fe^{2+} to Fe^{3+} and therefore reported as Fe_2O_3 in the analysis.

Sample preparation for dissolution of peridotites by $LiBO_2$ fusion:

1. 0.040g (± 0.003g) of the ignited powder (Section C1.2) was mixed with 0.600 g (± 0.005g) of lithium metaborate flux (Alfa Aesar Spectroflux 100B) in acid-washed platinum-rhodium crucibles;

2. 10-15 drops of lithium iodide wetting agent (20% vol LiI) was added to the sample/flux mixture, which was then fused at 900°C over a propane burner on a Claisse FLUXY automated fusion system;

3. After fusion the melt was poured into a 250ml Teflon beaker containing 30ml of 10% HNO_3 and 20ml 18.2MΩ deionised water;
4. The solution was stirred on a hotplate using a magnetic stirrer until all of the quenched glass fragments had dissolved;
5. After dissolution, the clear solution was spiked with 1ml of 100ppm Rh solution as an internal standard and made up to 100ml with deionised water.

Certified reference materials used for calibration and monitoring data quality were prepared in the same manner as above, as were blanks but with omitting the sample material.

Analysis of fusion solutions on ICP-OES

The abundance of major elements i.e. Si, Ti, Al, Fe, Mn, Mg, Ca, K, Na and P (reported as oxides) and some minor elements i.e. Sc, V, Cr, Co, Ni, Cu, Sr, Zr, Y, and Ba (reported as elements in ppm) were measured by the Jobin Yvon Horiba ULTIMA 2 ICP-OES instrument at Cardiff University in 2005/2006, operated by Ms E. De Vos and Dr. I. McDonald.

Calibration was performed using a procedural blank and solutions of the international certified reference materials W2, BIR-1, MRG-1, JA2, JP-1, DTS-1, and a mix of DTS-1 and MRG-1 in varying proportions (10-30; 20-20; and 30-10) to cover high Mg concentrations. 1ppm Rh spike in the fusion solution was used an internal standard to correct for drift over the course of the run. Analysis of JB1-a solution was repeated every 6 unknowns as an external check on instrumental drift and corrected by interpolation.

Each analysis of a solution was the average of 3 repeat measurements of intensity from which the standard deviation was used to calculate limits of detection and quantification (see Section C.3). Accuracy was assessed by routine analysis of certified reference materials JB1a (basalt) and JP-1, PCC-1 and DTS-1 (peridotites) as unknowns. Results of the ICP-OES analyses are given in full in Section C.3.

Analysis of fusion solutions on ICP-MS

The abundance of rare earth elements (REE), Ti, V, Cr, Mn, Co, Fe, Ni, Cu, Zn, Ga, Rb, Sr, Y, Zr, Nb, Ba, Hf, Ta, Pb, Th and U were analysed on the Thermo Elemental X Series (X7) ICP-MS system in 2005/2006 at Cardiff University, operated by Dr I. McDonald.

The same rock solutions, including standards and blanks used in calibration and monitoring, that were used for the ICP-OES were diluted for the ICP-MS in the following way; 1ml of x ppb In-Th spike was added as an internal standard to 1ml of rock solution to correct for instrumental drift at high masses. This was diluted with 8ml of 2% HNO3 to produce a working volume of 10ml. Calibration was performed using the procedural blank and W2-, BIR-1, MRG-1, JA-2 and DTS-1.

Analysis of W-2 solution was repeated every 6 unknowns as an external check on instrumental drift. Each analysis of a solution was the average of 4 repeat measurements of counts per second from which the standard deviation was used to calculate limits of detection and quantification. Accuracy was assessed by routine analysis of certified reference materials JB1a (basalt) and JP-1, PCC-1 and DTS-1 (peridotites) as unknowns. Results of the ICP-MS by fusion analysis are given in full in Section C.3.

Sample preparation for the dissolution of peridotites by HF-HNO_3 method

Dried sample powders were prepared by following the standard acid digestion method of Cardiff University:

1. 0.1g (± 0.005g) of sample powder was weighed into a clean Nalgene vial;
2. 0.5ml concentrated HNO_3 was added to the powder in the vial and after any reaction had ceased 4ml of HF was carefully added. The vials were then heated for at least 24 hours on a hot plate at 1250°C;
3. After cooling the solution was evaporated from the vials still on the hotplate until a clear fluid with a plastic consistency remained;

4. 1ml of concentrated HNO_3 was then added to the vials, and a resulting solution evaporated. This procedure was carried out twice, with care taken not to burn the samples;
5. After evaporating for a second time, 5ml of 5M HNO_3 was added to the vials to dissolve and residue;
6. The resulting solution was spiked with 1ml 2500ppb mixed Rh-Re standard solution, and made up to 50ml volume with deionised water.

Certified reference materials used for calibration and monitoring data quality were prepared in the same manner as above, as were procedural blanks but with omitting the sample material. Acid blanks for each reagent were prepared as follows: 1ml concentrated HNO_3 with 0.2ml Rh-Re spike made up to 50ml with deionised water; 1ml 5M HNO_3 with 0.2ml Rh-Re spike made up to 50ml with deionised water and 0.25ml HF with 0.2ml Rh-Re spike made up to 50ml with deionised water.

The standard procedure described above was modified for dissolution of peridotites in the following manner:

1. Extra care was taken to ensure thorough cleaning of the Nalgene vials by dishwasher, heating with 0.5ml HNO_3 - 4ml HF mix for 72 hours to dissolve any previous particles followed by with rinsing by deionised water. Vials and volumetric flasks used for preparation of the enriched standards were kept separate from those used for depleted peridotites and the blanks. Ultra-pure acids were used. This minimised blank contribution.
2. Chrome-spinel does not fully dissolve during HF-HNO_3 digestion and so the samples were heated for much longer than standard procedure (minimum of 72 hours and up to 2 weeks). The sample powders were also reground in a clean agate pestle and mortar, to break up the chrome spinel into a very fine grain size to increase digestion. Any solutions that still contained un-dissolved black chrome-spinel were filtered out.

Analysis of HF solutions on ICP-MS

The abundance of rare earth elements (REE), Ca, Sc, Ti, V, Cr, Zn, Ga, Rb, Sr, Y, Zr, Nb, Cs and Ba, were analysed on the Thermo Elemental X Series (X7) ICP-MS system in 2005/2006 at Cardiff University, operated by Dr I. McDonald.

2ml of the initial rock solution was diluted with 8ml 2% HNO_3 for analysis on the ICP-MS. Calibration was performed using the procedural blank and W-2, BHVO-1, X108, MRG-1 and ENDV. Elements with low abundances were given long count times e.g. 80ms for the REE and Nb, 50ms for Y and Zr and 20ms for the rest apart from 10s for Ca and 5ms for Cr. Analysis of W-2 solution was repeated every 6 unknowns as an external check on instrumental drift. Acid blanks were analysed to check baseline contamination in the instrument's tubing and each reagent. Each analysis of a solution was the average of 4 repeat measurements of counts per second. Accuracy was assessed by routine analysis of certified reference materials JB1a, BIR-1 and BCR-1 (basalt) and PCC-1 and DTS-1 (peridotites) as unknowns (Section C.2). Results of the ICP-MS by HF-HNO_3 analysis are given in full in Section C.3.

Limits of detection (LOD) and quantification (LOQ) were calculated from 3s and 10s, respectively, where s is 1 standard deviation of the sample intensities of repeat measurements (n= 4 and 10) of the procedural blank. The standard deviation was then converted into concentration from the calibration gradient. The highest values for LOD and LOQ, compiled from three to six different procedural blank solutions, are given for each element in Table C.1, together with the average procedural blank level.

Table C.1: Analytical masses, detection limits, quantification limits and blank level. Values are in ppm. s is 1 standard deviation.

Analytical mass	Detection limit (3s)	Quantification limit (10s)	Procedure blank level
89Y	0.0017	0.0056	0.0043
139La	0.0013	0.0043	0.0118
140Ce	0.0111	0.0369	0.1774
141Pr	0.0006	0.0021	0.0023
146Nd	0.0023	0.0076	0.0083
147Sm	0.0013	0.0042	0.0025
153Eu	0.0008	0.0026	-
157Gd	0.0022	0.0075	0.0235
159Tb	0.0002	0.0007	0.0002
163Dy	0.0008	0.0027	0.0013
165Ho	0.0002	0.0005	0.0004
166Er	0.0005	0.0016	0.0009
169Tm	0.0001	0.0005	0.0002
172Yb	0.0005	0.0018	0.0012
175Lu	0.0001	0.0004	0.0002

C.2 Data quality of Y and REE by HF-HNO_3 digestion

Estimation of precision and accuracy

Precision and accuracy for each analytical technique were estimated from repeat analyses of peridotite CRMs (certified reference materials), such as PCC-1 (Table C.2a) and JP-1 (Table C.2b). Precision was estimated from %RSD (Relative Standard Deviation which is defined as: 1s/mean * 100) of multiple preparations of each peridotite CRM. This includes errors from sample preparation as well as instrument precision. A %RSD value below 5% is considered to be a conservative estimate of instrument precision for most elements. The peridotite standards were prepared many times to assess any heterogeneity arisen from multiple sampling of a coarse-grained peridotite as well as instrument precision at depleted values.

Accuracy was estimated from the % difference between the average CRM value determined in this study compared with the CRM value published in the literature (%Diff = (cert-average analysis)/ cert *100). A % difference value within ± 10% of the certified value is considered to be accurate. Trace elements from peridotites are difficult to analyse accurately due to their low abundance and poorly constrained certified values. Published values for PCC-1 and JP-1, compiled from the literature in Table C.2, are plotted as a field on the chrondrite-normalised REE graph in Figure

C.1. The average CRM values from this study plot within the range of compiled literature values (Figure C.1), although the % differences between this study and the 'average' literature values for each element are greater (10 – 40% diff; Table C.2) .

Table C.2a: Comparison of Y and REE data (this study, n=12) with compiled literature values for PCC-1.

PCC-1	this study n=12	1s	%RSD	%Diff	lit. av. n=15	1s	1	2	3	4	5
Y	**0.0740**	0.013	17	-18	**0.0898**	0.018	*0.1				0.1300
La	**0.0274**	0.011	42	-30	**0.0392**	0.008	0.0520	0.0520	0.0380	0.0390	0.0399
Ce	**0.0551**	0.013	23	-15	**0.0651**	0.017	0.1000	0.1000		0.0570	0.0497
Pr	**0.0058**	0.002	28	-36	**0.0091**	0.002	0.0130	0.0130	0.0140	0.0085	
Nd	**0.0239**	0.005	19	-25	**0.0318**	0.001	0.0420	0.0420	0.0520	0.0300	0.0230
Sm	**0.0043**	0.001	28	-35	**0.0066**	0.001	0.0066	0.0066	0.0064	0.0080	*0.05
Eu	**0.0008**	0.000	45	-47	**0.0015**	0.001	0.0018	0.0018		0.0018	*0.007
Gd	**0.0053**	0.002	32	-34	**0.0080**	0.003	*0.014	0.0140		0.0080	
Tb	**0.0011**	0.000	21	-18	**0.0014**	0.000	0.0015	0.0015		0.0015	
Dy	**0.0082**	0.001	9	-23	**0.0107**	0.002	0.0100	0.0100		*0.0013	
Ho	**0.0025**	0.000	12	-15	**0.0029**	0.000	0.0025	0.0025		0.0038	
Er	**0.0100**	0.001	10	-18	**0.0122**	0.001	*0.012	0.0120	*0.0056	0.0123	
Tm	**0.0022**	0.000	8	-16	**0.0027**	0.000	0.0027	0.0027		0.0025	
Yb	**0.0201**	0.002	12	-10	**0.0223**	0.002	0.0240	0.0240	0.0180	0.0215	0.0217
Lu	**0.0043**	0.000	11	-15	**0.0051**	0.001	0.0057	0.0057	0.0057	0.0049	

PCC-1	6	7	8	9	10	11	12	13	14	15
Y	0.0860	0.0790		0.0784				0.0870	0.0790	0.0790
La	0.0288	0.0320	0.0376	0.0501	0.04800	.0330	0.0290	0.0290	0.0460	0.0340
Ce	0.0555	0.0570	0.0562	0.0822	0.07100	.0600	0.0560	0.0530	0.0528	0.0610
Pr	0.0068	0.0080	0.0076	0.0088	0.00980	.0076	0.0072	0.0068	0.0076	0.0091
Nd	0.0258	0.0280	0.0295	0.0321	0.03200	.0260	0.0280	0.0250	0.0260	0.0350
Sm	0.0059	0.0070	0.0076	0.0060	0.00700	.0049	0.0051	0.0050	0.0070	0.0095
Eu	0.0012	0.0020	0.0021	0.0010	0.00200	.0009	0.0010	0.0011	0.0009	0.0024
Gd	0.0067	0.0080	0.0095	0.0053	0.00760	.0053	0.0059	0.0061	0.0059	0.1300
Tb	0.0012	0.0020	0.0014	0.0011	0.00160	.0010	0.0011	0.0012	0.0011	0.0014
Dy	0.0097	0.0120	0.0121	0.0096	0.01200	.0085	0.0094	0.0087	0.0110	0.0160
Ho	0.0029	0.0030	0.0031	0.0028	0.00310	.0023	0.0027	0.0027	0.0030	0.0034
Er	0.0121	0.0130	0.0135	0.0111	0.01200	.0100	0.0113	0.0113	0.0117	0.0160
Tm		0.0030	0.0029	0.0024	0.00270	.0020	0.0024		0.0028	0.0032
Yb	0.0215	0.0220	0.0235	0.0217	0.02300	.0200	0.0221	0.0213	0.0227	0.0280
Lu	0.0048	0.0060	0.0054	0.0044	0.00500	.0045	0.0047	0.0046	0.0047	0.0054

s = standard deviation, %RSD = relative standard deviation, %Diff = percentage difference between literature average value (lit. av.) and average from this study. (1) USGS, (2) Govindaraju, (1994), (3) Jochum et al., (), (4) Ionov et al. (1992), (5) Parkinson (1992), (6) Parkinson and Pearce (1998), (7) Niu and Hekinian (1997b), (8) Godard et al (2000), (9) Qi et al. (2005), (10) Olive et al., 2001, (11) and (12) Jain et al., (2000), (13) Eggins et al. (1997), (14) Robinson et al. (1999) and (15) Makishima and Nakamura (1997). * outliers not used in average for literature values.

Table C.2b: Comparison of Y and REE data (this study, n = 6) with compiled literature values for JP-1

JP-1	this study n=6	1s	%RSD	%Diff	lit. av. n=5	1s	1	2	3	4	5
Y	**0.0796**	0.005	49	-10	**0.0882**		0.1080	0.1000	-	-	0.0882
La	**0.0263**	0.006	23	-21	**0.0334**	0.005	0.0280	0.0300	0.0400	0.0380	0.0308
Ce	**0.0454**	0.002	5	-24	**0.0594**	0.007	0.0630	0.0540	*0.2	0.0670	0.0536
Pr	**0.0074**	0.001	17	-17	**0.0089**	0.002	0.0089	0.0071	*0.02	0.0120	0.0077
Nd	**0.0314**	0.006	18	-7	**0.0339**	0.004	0.0340	0.0330	*0.07	0.0390	0.0297
Sm	**0.0080**	0.001	16	-42	**0.0139**	0.005	0.0100	0.0130	0.0200	0.0190	0.0077
Eu	**0.0030**	0.001	27	0	**0.0030**	0.001	0.0030	0.0031	0.0030	0.0046	0.0011
Gd	**0.0090**	0.001	15	-33	**0.0135**	0.005	0.0120	0.0130	0.0200	0.0160	0.0064
Tb	**0.0018**	0.000	7	-30	**0.0025**	0.000	0.0026	0.0026	0.0030	0.0027	0.0017
Dy	**0.0119**	0.001	5	-31	**0.0172**	0.003	0.0150	0.0180	0.0200	0.0200	0.0130
Ho	**0.0030**	0.000	11	-27	**0.0041**	0.001	0.0039	0.0043	-	0.0052	0.0031
Er	**0.0100**	0.001	7	-32	**0.0146**	0.004	0.0120	0.0140	0.0200	0.0160	0.0111
Tm	**0.0021**	0.000	7	-21	**0.0027**	0.001	-	0.0210	-	0.0033	0.0021
Yb	**0.0173**	0.001	4	-15	**0.0202**	0.002	0.0190	*0.0047	0.0200	0.0230	0.0188
Lu	**0.0037**	0.000	5	-11	**0.0042**	0.001	0.0042	*0.12	-	0.0050	0.0034

s = standard deviation, %RSD = relative standard deviation, %Diff = percentage difference between literature average value (lit. av.) and average from this study. (1) Takazawa et al., (2003). (2) literature compiled by Takazawa et al., (2003) (e.g. Imai et al., (1995); Takazawa et al., (2000); Eggins et al., (1997); Makishima and Nakamura, (1997, 1999)), (3) Govindaraju, (1994). (4) Ionov et al., (1992) and (5) Qi et al., (2005). * outliers not used in average for literature values.

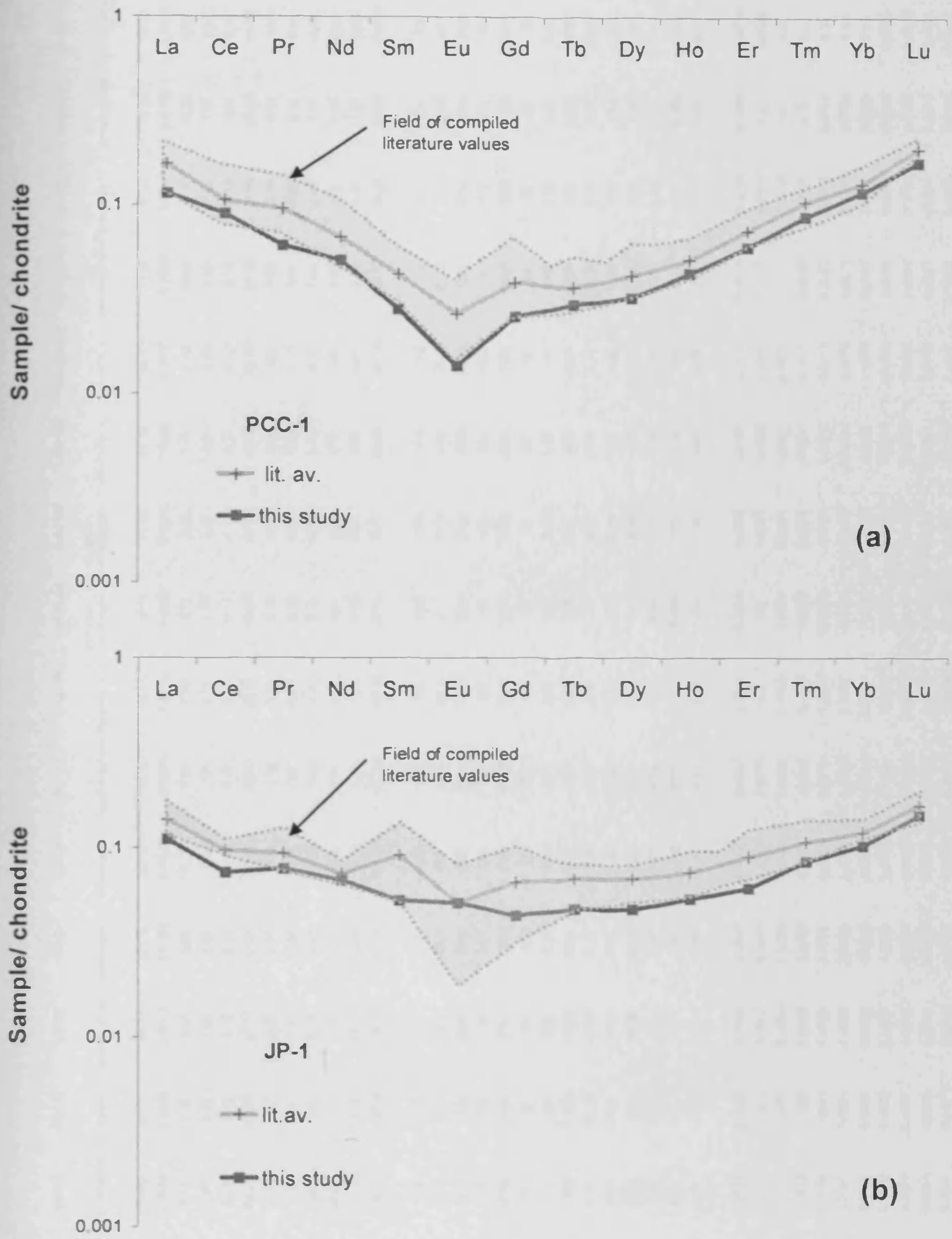

Figure C.1: chondrite-normalised (Sun and McDonough, 1989) REE profiles for Y and REE whole rock data determined in this study and compared with literature values for (a) PCC-1 and (b) JP-1 peridotite CRMs. The grey field in each graph represents the range in compiled literature values (given in Tables C.2a and b) and the literature average (lit. av.) marked as grey solid line. This study Y and REE values (black line and square symbols) plot at the lower end of the range of values compiled from the literature.

C.3 Table of results for whole rock analyses

					03UR35	SD111	SD151	SD157	SD19	SD426	SD493	UAE130	UAE144	UAE159	UAE189	UAE2035	UAE2046	UAE2065	UAE2087	UAE2159
			LOD	LOQ	Harzburgite	Cpx-Harzburgite	Harzburgite	Cpx-Harzburgite	Harzburgite	Harzburgite	Cpx-Harzburgite	Harzburgite	Cpx-poor Harzburgite	Cpx-poor Harzburgite	Lherzolite	Lherzolite	Cpx-Harzburgite	Lherzolite	Cpx-Harzburgite	Cpx-Harzburgite
SiO2	wt%	OES	0 01	0 02	39.53	39.85	38.92	40.71	38.70	39.65	42.50	42.14	39.44	40.62	40.90	43.47	39.23	41.55	39.22	36.62
TiO2	wt%	MS	0 0004	0 0013	0.0101	0.0025	0.0022	0.0044	0.0153	0.0043	0.0206	0.0103	0.0030	0.0073	0.0208	0.0537	0.0046	0.0419	0.0106	0.0036
Al2O3	wt%	OES	0 00	0 02	0.82	0.45	0.46	0.44	0.62	0.78	1.29	0.78	0.15	0.23	1.75	2.40	0.48	1.82	0.72	0.57
Fe2O3	wt%	OES	0 00	0 00	8.10	7.88	8.02	7.96	8.07	7.09	7.51	8.14	7.67	7.56	7.21	8.20	8.10	7.62	7.77	7.26
MnO	wt%	OES	0 00	0 00	0.12	0.12	0.12	0.12	0.12	0.10	0.11	0.13	0.11	0.11	0.11	0.12	0.12	0.12	0.11	0.11
MgO	wt%	OES	0 00	0 00	42.45	40.28	42.95	42.78	42.32	40.09	40.67	42.86	40.47	41.17	40.36	39.93	41.46	39.13	43.15	39.24
CaO	wt%	OES	0 00	0 01	0.69	0.55	0.57	0.50	0.37	0.68	1.13	0.99	0.19	0.40	1.62	2.3	0.90	2.04	0.64	0.19
Na2O	wt%	OES	0 021	0 069	n.d.	n.d.	n.d.	n.d.	*0.03*	0.03	0.02	*0.02*	*0.03*	0.00	0.14	0.13	0.01	*0.05*	*0.02*	*0.03*
K2O	wt%	OES	0 008	0 027	n.d.	*0.02*	n.d.	*0.03*	*0.01*	0.02	0.02	n.d.	*0.03*	0.04	0.02	0.01	0.02	*0.02*	*0.01*	0.05
P2O5	wt%	OES	0 014	0 047	0.02	*0.02*	n.d.	n.d.	n.d.	0.02	0.00	*0.02*	n.d.	0.01	0.02	0.02	0.01	n.d.	*0.02*	0.09
LOI	wt%	OES			7.85	11.74	9.38	10.22	9.79	12.65	9.12	7.24	9.85	9.47	6.85	3.91	9.37	6.76	7.92	16.06
Total	wt%	OES			99.58	100.91	100.42	102.76	100.04	101.13	102.37	102.32	97.93	99.62	99.00	100.55	99.71	99.15	99.59	100.23
Sc	ppm	OES			6.8	7.0	7.79	7.5	4.2	10.76	9.3	8.2	3.89	7.05	10.3	12.8	10.4	8.3	7.0	6.0
V	ppm	_HF	0.11	0.37	*33.5*	31.3	37.4	*19.5*	20.1	38.7	34.5	*28.1*	22.7	22.21	39.6	51.3	31.74	*54.5*	33.0	24.7
Cr	ppm	OES			*2694*	*2217*	2591	*2987*	2006	2867	2603	3088	*3322*	2423	2823	2926	2984	2834	2524	2640
Co	ppm	OES			105	113	116	116	111	102	106	115	115	106	104	108	117	111	111	104
Ni	ppm	OES			2030	2048	2188	2707	2081	1798	2126	2247	2313	2439	2042	1942	2368	1995	2250	2096
Zn	ppm	OES			43	60	43	60	52	31	34	50	42	25	32	43	34	48	52	46
Ga	ppm	MS	0.03	0.09	1.32	0.62	0.64	0.61	0.75	0.98	1.28	0.98	0.53	0.76	1.59	2	1.08	1.81	1.06	0.56
Rb	ppm	HF			0.015	0.016	0.008	0.019	0.03	0.03	0.02	0.03	0.03	0.01	0.35	0.27	0.03	0.35	0.016	0.03
Sr	ppm	HF			0.74	9.59	11.67	6.13	6.30	10.55	4.21	3.3	2.1	8.22	6.73	1.75	26.19	2.28	3.41	2.05
Y	ppm	HF			0.15	0.04	0.04	0.07	0.10	0.06	0.62	0.16	0.02	0.03	1.05	1.96	0.06	1.26	0.15	0.03
Zr	ppm	HF			0.10	0.17	0.09	0.15	*0.14*	0.07	0.11	0.13	0.15	0.08	0.30	0.70	0.06	0.36	0.12	*0.14*
Nb	ppm	HF			0.23	0.32	0.30	0.32	0.40	0.13	0.15	0.19	0.48	0.15	0.18	0.14	0.14	0.32	0.15	0.15
Cs	ppm	HF			0.001	n.d.	n.d.	0.019	n.d.	0.002	0.01	*0.007*	0.003	0.002	0.36	0.09	0.01	0.11	0.005	0.003
Ba	ppm	HF			n.d.	n.d.	n.d.	n.d.	0.09	0.67	0.11	*0.18*	0.30	1.89	3.94	0.75	0.87	0.55	n.d.	*0.17*
La	ppm	HF			0.0007	0.0045	0.0053	0.0053	0.0036	0.0050	0.0082	0.0054	0.0043	0.0037	0.0190	0.0028	0.0034	0.0090	0.0016	0.0016
Ce	ppm	HF			n.d.	0.0655	0.1244	0.0543	0.0480	0.1316	0.0008	n.d	n.d	0.0067	0.1360	0.0157	0.0122	0.0704	n.d.	0.0023
Pr	ppm	HF			n.d.	0.0001	0.0002	0.0002	0.0000	0.0001	0.0016	0.0001	0.0004	0.0001	0.0057	0.0100		0.0034	n.d.	n.d.
Nd	ppm	HF			n.d.	0.0013	0.0008	0.0026	0.0008	0.0011	0.0092	0.0015	0.0036	0.0015	0.0391	0.1112	0.0008	0.0391	n.d.	n.d.
Sm	ppm	HF			n.d.	0.0003	0.0009	0.0010	0.0003	0.0007	0.0116	0.0014	0.0014	0.0004	0.0271	0.0819	0.0002	0.0391	0.0004	n.d.
Eu	ppm	HF			0.0000	0.0001	0.0001	0.0005	0.0000	0.0005	0.0055	0.0011	0.0008	0.0004	0.0136	0.0370	0.0001	0.0182	0.0004	n.d.
Gd	ppm	HF			n.d.	0.0005	0.0009	0.0032	0.0007	0.0014	0.0332	0.0064	0.0030	0.0014	0.0623	0.1585	0.0008	0.0931	0.0029	n.d.
Tb	ppm	HF			0.0010	0.0002	0.0002	0.0007	0.0006	0.0003	0.0091	0.0016	0.0003	0.0002	0.0159	0.0363	0.0003	0.0227	0.0015	0.0001
Dy	ppm	HF			0.0134	0.0021	0.0037	0.0068	0.0087	0.0034	0.0790	0.0174	0.0019	0.0020	0.1270	0.2678	0.0047	0.1763	0.0165	0.0018
Ho	ppm	HF			0.0050	0.0010	0.0014	0.0023	0.0036	0.0018	0.0209	0.0056	0.0006	0.0007	0.0333	0.0637	0.0017	0.0441	0.0057	0.0009
Er	ppm	HF			0.0217	0.0051	0.0071	0.0098	0.0152	0.0100	0.0707	0.0218	0.0020	0.0035	0.1098	0.1947	0.0091	0.1376	0.0225	0.0047
Tm	ppm	HF			0.0048	0.0016	0.0018	0.0022	0.0035	0.0027	0.0133	0.0046	0.0004	0.0008	0.0198	0.0339	0.0024	0.0238	0.0048	0.0014
Yb	ppm	HF			0.0411	0.0160	0.0190	0.0205	0.0303	0.0267	0.0960	0.0367	0.0031	0.0089	0.1379	0.2253	0.0216	0.1615	0.0390	0.0149
Lu	ppm	HF			0.0082	0.0039	0.0042	0.0042	0.0060	0.0060	0.0170	0.0073	0.0009	0.0021	0.0236	0.0378	0.0048	0.0275	0.0075	0.0037
Hf	ppm	HF			0.0009	0.0024	0.0017	0.0022	0.0016			0.0036	n.d					0.0202	0.0019	0.0009
Ta	ppm	HF			0.0053	0.0033	0.0038	0.0030	0.0031			0.0051	0.0043					0.0043	0.0075	0.0034
Pb	ppm	HF			n.d.	0.0395	n.d.	0.2180	0.1210			n.d	n.d					n.d.	n.d.	n.d.
Th	ppm	HF			n.d.	0.0007	0.0009	0.0007	0.0003			n.d	n.d					n.d.	n.d.	n.d.
U	ppm	HF			0.0009	0.0019	0.0012	0.0012	0.0019			0.0034	n.d					n.d.	n.d.	0.0056

	UAE2221	UAE2230	UAE2241	UAE2288	UAE312	UAE316	UAE3190	UAE327	UAE391	UAE424	UAE432	UAE45	UAE4807	UAE484	UAE545	UAE546	UAE659	UAE2064	SD67
	Cpx-poor Harzburgite	Harzburgite	Cpx-Harzburgite	Harzburgite	Cpx-poor Harzburgite	Cpx-poor Harzburgite	Harzburgite	Cpx-Harzburgite	Cpx-poor Harzburgite	Cpx-Harzburgite	Harzburgite	Harzburgite	Harzburgite	Harzburgite	Harzburgite	Harzburgite	Harzburgite	Dunite	Dunite
SiO2	38.20	39.25	40.94	39.34	41.28	42.11	40.70	39.21	40.56	41.33	41.15	40.42	39.95	40.97	39.09	39.76	40.04	32.59	35.06
TiO2	0.0043	0.0039	0.0085	0.0064	0.0052	0.0161	0.0041	0.0031	0.00125	0.0078	0.0079	0.0021	0.0039	0.0041	0.0057	0.0105	0.0064	0.0053	0.0053
Al2O3	0.18	0.44	0.97	0.52	0.29	0.79	0.47	0.29	0.21	0.94	0.76	0.66	0.81	0.48	0.53	0.64	0.53	0.06	0.04
Fe2O3	7.42	7.83	7.84	7.58	8.83	8.62	7.99	8.60	8.56	8.03	7.96	8.20	7.54	7.99	8.43	7.49	7.93	8.15	7.59
MnO	0.11	0.12	0.12	0.12	0.13	0.12	0.12	0.12	0.12	0.12	0.13	0.11	0.11	0.11	0.12	0.12	0.10	0.13	0.11
MgO	43.81	44.74	41.99	40.18	44.69	40.86	40.50	41.97	43.25	41.67	41.17	41.89	42.04	42.71	42.29	39.92	39.55	46.87	46.05
CaO	0.21	0.47	0.98	0.57	0.44	0.79	0.75	0.39	0.39	0.88	0.89	0.75	0.79	0.51	0.41	0.62	0.45	0.08	0.04
Na2O	0.01	n.d.	*0.04*	n.d.	*0.03*	*0.04*	*0.02*	*0.03*	*0.03*	*0.02*	*0.03*	0.01	0.02	0.03	*0.05*	*0.04*	0.04	n.d.	n.d.
K2O	0.00	n.d.	*0.02*	*0.01*	*0.03*	n.d.	*0.01*	0.04	n.d.	*0.01*	n.d.	0.01	0.03	0.00	n.d.	n.d.	-0.01	*0.01*	*0.01*
P2O5	0.01	*0.00*	n.d.	n.d.	*0.03*	*0.02*	*0.02*	*0.02*	n.d.	n.d.	*0.02*	0.00	0.02	0.01	*0.02*	n.d.	0.01	n.d.	n.d.
LOI	10.02	7.47	6.23	12.05	5.01	6.16	10.28	8.68	7.10	6.78	9.15	8.48	9.53	8.78	10.17	10.12	12.22	12.05	11.99
Total	99.99	100.31	99.14	100.38	100.75	99.53	100.88	99.30	100.22	99.79	101.26	100.54	100.84	101.60	101.11	98.71	100.88	99.94	100.89
Sc	5.6	*7.3*	10.7	7.3	6.4	7.5	8.2	7.1	6.16	8.9	8.6	8.7	7.9	7.4	5.20	7.45	7.64	3.7	4.0
V	11.6	*22.3*	41.3	34.3	26.8	40.3	*27.9*	29.4	40.2	39.0	38.0	35.35	28.5	28.2	37.4	30.3	34.0	11.1	8.0
Cr	2162	*2480*	2967	2783	*2981*	2346	*2549*	*2317*	*2563*	*3311*	2753	2624	2593	2641	*2259*	2524	2160	*3343*	*2376*
Co	107	116	113	109	124	110	106	115	120	116	103	109	105	106	109	113	100	116	116
Ni	2345	2551	2107	2027	2663	1786	2084	2306	2243	2133	1919	2186	2063	2404	2109	1748	2099	2635	2629
Zn	25	31	47	45	28	46	39	45	33	38	50	34	38	34	35	44	37	44	35
Ga	0.58	0.59	1.13	0.79	0.66	0.93	0.66	0.62	0.38	0.84	0.86	0.79	0.77	0.55	0.71	0.74	0.67	0.41	0.45
Rb	0.01	0	1.16	0.04	0.01	0.08	0.02	0.04	0.02	0.016	0.03	0.09	0.02	0.50	0.008	0.03	0.03	0.02	0.01
Sr	0.17	1.95	1.58	15.53	0.87	8.36	13.28	3.49	6.5	2.90	1.26	0.47	11.63	0.49	3.57	0.75	8.40	0.87	0.30
Y	0.02	0.04	0.19	0.08	0.34	0.21	0.06	0.03	0.07	0.13	0.12	0.08	0.04	0.11	0.11	0.16	0.08	0.02	0.01
Zr	0.06	0.12	*0.17*	0.34	1.00	*0.17*	0.10	0.13	0.36	0.13	*0.14*	0.06	0.06	0.16	*0.15*	n.d.	0.15	0.18	0.15
Nb	0.16	0.27	0.41	0.42	0.29	0.18	0.21	0.25	0.48	0.17	0.15	0.14	0.14	0.16	0.24	0.22	0.15	0.29	0.39
Cs	0.000	0.005	1.77	0.014	0.003	0.006	0.0144	0.01	n.d	n.d.	0.003	0.01		0.003	n.d.	n.d.	0.000	0.003	0.00
Ba	0.93	n.d.	1.15	n.d.	n.d	n.d.	0.38	0.24	n.d	n.d.		0.05	0.35	0.79	n.d.	n.d.	0.80	*0.38*	0.01
La	0.0071	0.0055		0.0027	0.0025	0.0017	0.0038	0.0038	*0.0021*	0.0030	0.0056	0.0032	0.0038	0.0132	0.0027	0.0046	0.0095	0.0039	0.0013
Ce	0.1545	0.0076		n.d.	n.d	0.0016	0.0840	0.0106	n.d	0.0027	n.d.	n.d.	0.0840	0.0062	0.0404	n.d.	0.0097	0.0135	n.d.
Pr	0.0003	0.0008		0.0001	0.0002	n.d.	n.d.	0.0002	n.d	n.d.	0.0004	n.d.	n.d	0.0023	0.0000	0.0005	0.0013	0.0002	n.d.
Nd	0.0021	0.0026	0.0030	0.0013	0.0008	0.0012	n.d.	0.0010	*0.0009*	0.0008	0.0031	n.d.	n.d	0.0109	0.0008	0.0021	0.0064	0.0016	0.0008
Sm	0.0001	0.0007	0.0004	0.0008	0.0008	0.0011	n.d.	0.0000	*0.0001*	0.0005	0.0006	n.d.	n.d	0.0030	0.0009	0.0015	0.0012	0.0004	0.0003
Eu	n.d.	0.0003	0.0002	0.0003	0.0003	0.0005	n.d.	0.0001	*0.0003*	0.0005	0.0004	0.0001	n.d	0.0010	0.0003	0.0007	0.0004	0.0001	0.0001
Gd	0.0003	0.0013	0.0057	0.0061	0.0012	0.0028	n.d.	0.0003	*0.0013*	0.0016	0.0014	0.0002	n.d	0.0051	0.0021	0.0044	0.0011	0.0008	0.0001
Tb	0.0001	0.0002	0.0015	0.0006	0.0002	0.0022	0.0001	0.0001	*0.0000*	0.0012	0.0009	0.0003	0.0001	0.0013	0.0012	0.0018	0.0007	0.0001	0.0001
Dy	0.0013	0.0026	0.0184	0.0072	0.0013	0.0220	0.0027	0.0020	*0.0005*	0.0117	0.0116	0.0055	0.0027	0.0112	0.0131	0.0181	0.0071	0.0013	0.0008
Ho	0.0005	0.0011	0.0062	0.0026	0.0006	0.0072	0.0012	0.0009	*0.0001*	0.0040	0.0042	0.0024	0.0012	0.0032	0.0039	0.0054	0.0025	0.0004	0.0003
Er	0.0025	0.0060	0.0265	0.0120	0.0027	0.0279	0.0066	0.0050	*0.0007*	0.0174	0.0181	0.0111	0.0066	0.0126	0.0152	0.0207	0.0116	0.0022	0.0013
Tm	0.0007	0.0016	0.0058	0.0029	0.0007	0.0060	0.0019	0.0015	*0.0003*	0.0039	0.0043	0.0028	0.0019	0.0027	0.0033	0.0043	0.0029	0.0005	0.0004
Yb	0.0069	0.0162	0.0488	0.0279	0.0080	0.0481	0.0184	0.0154	0.0030	0.0338	0.0375	0.0268	0.0184	0.0232	0.0267	0.0353	0.0253	0.0059	0.0038
Lu	0.0016	0.0038	0.0098	0.0059	0.0019	0.0092	0.0044	0.0036	0.0010	0.0069	0.0077	0.0059	0.0044	0.0047	0.0055	0.0071	0.0057	0.0014	0.0010
Hf		0.0019	0.0019	0.0024	0.0159	0.0024	0.0012		0.0049	0.0024	0.0016				0.0017	0.0039		0.0032	0.0019
Ta		0.0040	0.0060	0.0060	0.0040	0.0028	0.0020		0.0060	0.0050	0.0035				0.0035	0.0040		0.0043	0.0093
Pb		n.d.	0.0638	n.d.	n.d	n.d.	n.d.		n.d	0.1363	n.d.				n.d.	n.d.		1.1873	0.2110
Th		0.0014	0.0007	n.d.	n.d	0.0002	0.0007		n.d	0.0012	0.0009				0.0004	0.0002		0.0014	0.0024
U		n.d.	0.0019	0.0014	n.d	0.0024	0.0052		n.d	0.0029	0.0066				0.0034	0.0032		0.0027	0.0002

	SD433	SD18	SD33	UAE392	SD265	SD425	UAE160	UAE2047	UAE2222	UAE3189	UAE4808	UAE543	UAE547	SD362U	AE509	UAE275	UAE33	SD383	UAE2808
	Dunite	Dunite	Dunite	Dunite	Dunite	Dunite	Dunite	Chr-Dunite	Dunite	Dunite	Dunite	Dunite	Dunite	Dunite	Dunite	Dunite	Dunite	Dunite	Dunite
SiO_2	35.77	36.50	36.40	38.03	37.35	35.49	36.82	35.84	38.14	36.77	35.55	36.28	36.78	36.43	36.18	41.94	39.25	34.30	36.40
TiO_2	0.0072	0.0058	0.0087	0.0013	0.0065	0.0046	0.0022	0.0050	0.0011	0.0021	0.0077	0.0027	0.0021	0.0225	0.0019	0.0069	0.0030	0.0130	0.0130
Al_2O_3	0.09	0.06	0.21	0.19	0.46	0.08	0.05	0.15	0.13	0.04	0.25	0.17	0.07	0.37	0.17	0.62	0.28	0.50	0.60
Fe_2O_3	8.13	8.31	8.44	7.90	9.88	8.68	6.59	8.02	8.16	9.42	8.73	7.67	7.25	10.19	9.34	12.31	9.69	9.52	8.96
MnO	0.12	0.12	0.11	0.11	0.13	0.09	0.10	0.10	0.11	0.12	0.12	0.10	0.09	0.12	0.10	0.17	0.13	0.13	0.13
MgO	41.29	43.18	41.09	41.25	43.13	40.78	44.80	43.38	43.00	42.25	41.28	43.55	43.01	39.30	38.34	38.54	42.59	36.16	42.48
CaO	0.69	0.45	0.84	0.34	0.46	0.75	0.10	0.02	0.23	0.23	0.05	0.13	0.14	0.28	1.11	0.40	0.15	3.14	0.02
Na_2O	*0.03*	n.d.	*0.02*	n.d.	0.02	0.05	0.05	0.01	0.03	0.01	0.00	0.02	0.05	0.04	0.01	0.08	n.d.	0.02	0.01
K_2O	*0.02*	*0.02*	*0.01*	n.d.	0.01	0.02	0.02	0.01	-0.01	0.01	0.01	-0.01	-0.01	0.04	0.01	n.d.	0.00	0.03	0.00
P_2O_5	n.d.	*0.02*	n.d.	*0.02*	0.03	0.01	0.03	0.00	0.02	0.01	0.01	0.01	0.01	0.01	0.00	0.04	0.01	0.03	0.01
LOI	13.71	13.29	13.11	11.45	9.90	13.87	11.43	11.84	10.15	11.58	14.42	11.06	13.42	13.29	14.86	6.48	6.57	16.02	14.51
Total	99.86	101.96	100.25	99.29	101.37	99.84	100.00	99.38	99.95	100.45	100.40	98.98	100.81	100.09	100.10	100.57	98.69	99.87	103.12
Sc	4.2	3.8	3.9	3.1	4.4	3.3	2.51	3.94	4.34	5.21	4.21	3.33	3.34	5.42	4.45	5.64	4.22	4.44	4.86
V	12.7	12.8	*14.6*	13.1	22.9	9.4	12	18	20.3	9.66	19.5	16.6	6.97	39.3	20.36	26.6	32.9	44.9	24.6
Cr	*2782*	*2893*	*2820*	*5822*	4826	820	3490	3228	2383	604	5564	3026	695	3729	1707	4391	5601	13128	5918
Co	120	122	116	121	126	125	115	116	117	126	119	114	110	121	127		126	125	125
Ni	2600	2660	2701	2444	2319	2763	2589	2576	2395	2580	2434	2365	2334	2252	2254	1399	1379	2166	2295
Zn	46	42	60	29	42	39	25	33	26	44	33	22	39		38	52	22	44	40
Ga	0.57	0.52	0.55	0.39	1.00	0.40	0.38	0.68	0.31	0.36	0.92	0.49	0.20	1	0.40	1.10	0.48	1.53	1.50
Rb	0.01	0.02	0.01	0.01	0.021	0.02	0.01	0.01	0.01	0.01	0.02	0.01	0.02	0.02	0.01	0.01	0.05	0.03	0.01
Sr	88.31	40	222.67	48.23	109.5	49.03	13.82	2.76	6.43	16.81	3.96	0.77	8.16	17.76	62.78	4.06	6.27	69.10	0.59
Y	0.03	0.03	0.10	0.01	0.05	0.04	0.03	0.03	0.03	0.03	0.05	0.07	0.04	0.24	0.04	0.09	0.06	0.06	0.08
Zr	0.13	*0.16*	0.14	*0.12*	0.10	0.07	0.08	0.07	0.06	0.05	0.10	0.13	0.12	0.40	0.11	0.08	0.10	0.16	0.16
Nb	0.26	*0.29*	0.26	*0.27*	0.16	0.14	0.16	0.15	0.16	0.14	0.13	0.18	0.17	0.14	0.13	0.18	0.16	0.12	0.15
Cs	n.d.	*0.000*	0.00	*0.000*	0.003	0.001	0.00	0.004	0.000	0.001	0.002	0.001	0.000	0.001	0.000	0.001	0.002	0.001	n.d.
Ba	1.23	2.51	1.34	1.43	1.31	0.78	1.58	0.26	0.09	0.71	0.76	n.d	0.06	0.57	1.56	0.14	0.18	5.87	n.d.
La	0.0031	0.0069	0.0035	0.0019	0.0043	0.0039	0.0075	0.0043	0.0047	0.0007	0.0034	0.0030	0.0032	0.0161	0.0048	0.0048	0.0129	0.0105	0.0065
Ce	0.0057	0.0222	0.0518	n.d.	0.0399	n.d	0.0596	0.0469	0.0566	n.d	n.d	n.d	0.0043	0.1369	0.0345	0.0631	0.0002	0.0987	0.1094
Pr	n.d.	0.0007	n.d.	n.d.	n.d	0.0000	0.0013	0.0001	n.d	n.d	0.0003	0.0001	n.d	0.0045	0.0002	0.0003	0.0019	0.0012	0.0009
Nd	0.0008	0.0041	0.0026	0.0008	0.0008	0.0012	0.0069	0.0008	0.0008	n.d	0.0023	0.0012	n.d	0.0238	0.0021	0.0039	0.0073	0.0064	0.0059
Sm	0.0001	0.0008	0.0033	n.d.	0.0003	0.0004	0.0021	0.0010	n.d	n.d	0.0005	0.0011	0.0004	0.0088	0.0001	0.0022	0.0020	0.0015	0.0023
Eu	0.0001	0.0005	0.0013	0.0004	0.0006	0.0010	0.0008	0.0001	n.d	n.d	0.0003	0.0002	n.d	0.0031	0.0002	0.0012	0.0008	0.0016	0.0008
Gd	n.d.	0.0000	0.0057	n.d.	0.0067	0.0029	0.0023	0.0000	n.d	n.d	0.0015	0.0016	0.0006	0.0140	0.0018	0.0044	0.0041	0.0027	0.0035
Tb	0.0002	0.0002	0.0016	0.0000	0.0004	0.0002	0.0005	0.0002	0.0002	0.0001	0.0005	0.0007	0.0004	0.0034	0.0003	0.0012	0.0009	0.0008	0.0011
Dy	0.0023	0.0025	0.0122	0.0004	0.0041	0.0026	0.0034	0.0021	0.0021	0.0016	0.0047	0.0076	0.0043	0.0268	0.0025	0.0093	0.0064	0.0060	0.0092
Ho	0.0007	0.0008	0.0032	0.0002	0.0015	0.0011	0.0008	0.0007	0.0008	0.0008	0.0015	0.0022	0.0013	0.0072	0.0008	0.0026	0.0018	0.0017	0.0025
Er	0.0040	0.0036	0.0111	0.0014	0.0072	0.0053	0.0026	0.0039	0.0038	0.0042	0.0059	0.0083	0.0052	0.0273	0.0036	0.0098	0.0066	0.0061	0.0108
Tm	0.0011	0.0008	0.0021	0.0005	0.0018	0.0014	0.0006	0.0010	0.0010	0.0012	0.0016	0.0018	0.0011	0.0058	0.0009	0.0020	0.0014	0.0014	0.0024
Yb	0.0106	0.0080	0.0174	0.0060	0.0177	0.0133	0.0045	0.0101	0.0100	0.0117	0.0157	0.0154	0.0104	0.0483	0.0087	0.0179	0.0126	0.0121	0.0215
Lu	0.0024	0.0021	0.0036	0.0017	0.0043	0.0034	0.0010	0.0024	0.0025	0.0030	0.0034	0.0034	0.0023	0.0097	0.0023	0.0039	0.0026	0.0028	0.0045
Hf	0.0022	0.0019	0.0034	0.0009			0.0035	0.0284											
Ta	0.0038	0.0033	0.0040	0.0028			0.0217	0.0072											
Pb	0.1275	n.d.	0.0430	n.d.			n.d	n.d											
Th	0.0007	0.0014	0.0007	0.0012			0.0088	0.0095											
U	0.0029	0.0104	0.0019	0.0007			0.0065	0.0371											

	UAE325	UAE353	UAE607	SD131A	UAE481	UAE108	UAE627	UAE482	UAE454
	Dunite	Dunite	Dunite	Ol-gb	Plag-Dunite	Dunite	Wehrlite	Troctolite	Wehrlite
SiO2	33.57	38.40	37.93	33.75	36.99	37.18	38.14	41.54	50.18
TiO2	0.0090	0.0101	0.0060	0.0238	0.0253	0.0027	0.0166	0.0462	0.0822
Al2O3	0.07	0.62	0.22	0.50	1.36	0.31	0.50	10.10	1.49
Fe2O3	17.15	7.11	8.52	9.81	8.43	8.83	11.45	7.64	7.86
MnO	0.19	0.10	0.11	0.14	0.11	0.11	0.16	0.10	0.16
MgO	38.69	45.02	41.22	44.60	38.68	39.08	40.99	29.47	31.12
CaO	0.18	0.06	0.05	0.49	0.42	0.16	0.63	3.45	2.13
Na2O	0.07	0.03	0.02	0.00	0.05	0.01	0.03	0.06	0.23
K2O	n.d.	0.01	n.d.	0.04	0.00	0.01	0.02	0.01	0.01
P2O5	0.03	0.03	0.01	0.02	0.02	0.01	0.02	0.01	0.03
LOI	11.87	9.31	10.47	9.14	13.95	14.56	8.74	8.41	5.81
Total	101.81	100.71	98.57	98.51	100.04	100.28	98.72	100.84	99.10
Sc	6.65	3.01	3.42	5.27	4.47	4.40	6.84	4.05	15.34
V	10.3	23.3	22.3	30.32	96.4	28.7	35.3	134.7	149.3
Cr	191	14071	5190	4234	4607	5039	3564	5679	2029
Co	165	119	130	124	122	130	137	102	81
Ni	812	3288	2068	1997	1535	2630	1950	1472	434
Zn	83	15	23	41	24	31	45	30	14
Ga	0.71	1.60	0.56	2.08	1.43	0.74	1.13	5.90	1.49
Rb	0.01	0.04	0.02	0.02	0.01	0.02	0.02	0.02	0.05
Sr	0.14	4.49	2.39	8.57	112.46	14.36	3.78	44.86	10.05
Y	0.14	0.08	0.04	0.21	0.51	0.008	0.39	0.77	2.16
Zr	0.10	0.17	0.10	0.22	0.41	0.078	0.42	0.90	3.68
Nb	0.12	0.20	0.19	0.18	0.20	0.13	0.20	0.22	0.21
Cs	n.d.	0.004	0.001	0.00	0.00	0.001	0.002	0.002	0.002
Ba	0.01	0.06	0.14	0.73	0.47	2.70	0.23	1.08	1.69
La	0.0066	0.0457	0.0035	0.0034	0.0028	0.0054	0.0110	0.1270	0.1428
Ce	0.1270	0.1822		n.d.	n.d.	0.1009		0.2278	0.4494
Pr	0.0008	0.0096	0.0001	0.0014	0.0035	0.0001	0.0038	0.0195	0.0155
Nd	0.0052	0.0328	0.0015	0.0119	0.0305	0.0008	0.0271	0.1195	0.0993
Sm	0.0021	0.0056	0.0010	0.0062	0.0151	0.0001	0.0140	0.0338	0.0335
Eu	0.0013	0.0014	0.0005	0.0025	0.0089	0.0003	0.0052	0.0335	0.0124
Gd	0.0029	0.0060	0.0001	0.0100	0.0227	n.d.	0.0210	0.0381	0.0496
Tb	0.0012	0.0012	0.0002	0.0026	0.0056	0.0000	0.0055	0.0081	0.0146
Dy	0.0116	0.0086	0.0025	0.0213	0.0425	0.0003	0.0396	0.0563	0.1293
Ho	0.0039	0.0022	0.0011	0.0058	0.0120	0.0001	0.0101	0.0165	0.0447
Er	0.0176	0.0076	0.0050	0.0195	0.0343	0.0008	0.0293	0.0464	0.1304
Tm	0.0047	0.0016	0.0013	0.0036	0.0051	0.0002	0.0043	0.0062	0.0150
Yb	0.0455	0.0143	0.0119	0.0278	0.0362	0.0032	0.0289	0.0494	0.1114
Lu	0.0109	0.0029	0.0030	0.0055	0.0067	0.0012	0.0053	0.0088	0.0176
Hf									
Ta				0.0143					
Pb									
Th				0.0153					
U				0.0256					

Appendix D: Chrome-spinel analyses by electron microprobe

Sample	**UAE106**	**UAE116**	**UAE144**	**UAE145**	**UAE156**	**UAE156**	**UAE159**	**UAE2214**	**UAE2215**
Groups	Harzburgite	Harzburgite	Harzburgite	Harzburgite	Harzburgite	Harzburgite	Harzburgite	Harzburgite	Harzburgite
Rock Type	**Cpx-poor**	**Cpx-poor**	**Cpx-poor**	**Cpx-poor**	**Cpx-poor**	**Cpx-poor**	**Cpx-poor**	**Cpx-poor**	**Cpx-poor**
Region	KFN	KFN	KFN	KFN	KFN	KFN	KFN	KFN	KFN
Region	Mantle	Mantle	Mantle	Mantle	Mantle	Mantle	Mantle	Mantle	Mantle
Spinel shape	EU	EU	EU	EU	EU	EU	EU	SI	EU
Cal	**new cal**	old cal	**new cal**	old cal	old cal	**new cal**	**new cal**	**new cal**	old cal
n=	4	6	24	4	4	18	4	4	4
SiO2	0.02	0.06	0.02	0.02	0.04	0.04	0.03	0.03	0.02
TiO2	0.01	0.01	0.02	0.03	0.03	0.04	0.03	0.02	0.05
Al2O3	7.96	12.06	8.63	13.10	13.72	13.74	12.76	11.54	21.17
V2O3	0.36	0.35	0.31	0.29	0.26	0.27	0.22	0.25	0.23
Cr2O3	59.46	55.55	59.23	55.75	53.60	54.76	57.03	57.29	46.85
Fe2O3	3.07	1.65	1.64	0.66	1.04	1.22	1.01	0.99	1.14
MgO	8.34	9.37	8.42	9.86	9.50	9.65	9.54	9.36	12.06
MnO	0.31	0.34	0.27	0.21	0.22	0.25	0.25	0.31	0.18
FeO	19.95	18.48	19.58	18.14	18.39	18.73	19.22	18.70	15.99
NiO	0.06	0.05	0.02	0.06	0.05	0.06	0.04	0.07	0.02
ZnO	0.19	0.21	0.19	0.19	0.20	0.19	0.20	0.23	0.17
Total	99.73	98.14	98.33	98.31	97.05	98.96	100.34	98.80	97.87
Mg#	0.427	0.474	0.434	0.492	0.479	0.479	0.470	0.472	0.573
Cr#	**0.834**	**0.755**	**0.822**	**0.741**	**0.724**	**0.728**	**0.750**	**0.769**	**0.597**
Fe^3# (corr)	0.056	0.020	0.036	0.009	0.013	0.029	0.027	0.027	0.014
Fe^3/SumFe (pr)	0.122	0.072	0.070	0.033	0.049	0.056	0.047	0.048	0.060
Fe^3/SumFe (corr)	0.178	0.072	0.122	0.033	0.049	0.108	0.100	0.100	0.060
Fa (Ol)	0.088	0.088	0.086	0.087	0.087	0.087	0.089	0.083	0.085
T°C (Balhaus)	708	689	693	692	669	686	692	691	689
fO_2 (FMQ)	**0.63**	**-1.15**	**-0.09**	**-2.63**	**-1.82**	**-0.47**	**-0.63**	**-0.54**	**-1.68**

Sample	**UAE2221**	**UAE380**	**UAE387**	**UAE391**	**UAE692**	**UAE86**	**UAE95**	**03UR35**	**SD111**
Groups	Harzburgite	Harzburgite	Harzburgite	Harzburgite	Harzburgite	Harzburgite	Harzburgite	Harzburgite	Harzburgite
Rock Type	**Cpx-poor**	**Cpx-poor**	**Cpx-poor**	**Cpx-poor**	**Cpx-poor**	**Cpx-poor**	**Cpx-poor**	**Hz**	**Hz**
Region	KFN	KFN	KFN	KFN	KFN	KFN	KFN	KFN	ASWS
Region	Mantle	Mantle	Mantle	Mantle	Mantle	Mantle	Mantle	Mantle	Mantle
Spinel shape	EU	SI	EU	EU	EU	EU	EU	HL	HL
Cal	old cal	old cal	old cal	**new cal**	old cal	old cal	old cal	old cal	**new cal**
n=	6	6	3	40	4	4	4	4	4
SiO2	0.03	0.02	0.03	0.03	0.01	0.02	0.03	0.02	0.04
TiO2	0.08	0.04	0.03	0.01	0.03	0.03	0.02	0.071	0.03
Al2O3	9.39	10.51	11.14	13.54	9.06	7.40	15.73	32.33	19.98
V2O3	0.11	0.26	0.22	0.34	0.30	0.37	0.27	0.16	0.25
Cr2O3	58.69	54.23	55.68	55.10	56.51	57.22	50.47	32.81	46.51
Fe2O3	1.59	4.35	1.73	1.89	4.64	4.33	2.37	2.67	3.79
MgO	9.50	8.41	9.11	9.67	8.00	8.22	10.43	14.05	11.09
MnO	0.29	0.26	0.24	0.30	0.31	0.28	0.28	0.22	0.30
FeO	17.99	19.82	18.53	18.92	20.85	19.31	17.18	14.35	17.76
NiO	0.02	0.04	0.03	0.04	0.05	0.05	0.04	0.13	0.05
ZnO	0.11	0.19	0.18	0.21		0.09	0.15	0.26	0.17
Total	97.81	98.12	96.92	100.05	99.75	97.31	96.96	97.07	99.98
Mg#	0.485	0.431	0.467	0.477	0.407	0.431	0.519	0.638	0.527
Cr#	**0.807**	**0.776**	**0.770**	**0.732**	**0.807**	**0.838**	**0.683**	**0.405**	**0.610**
Fe^3# (corr)	0.020	0.056	0.022	0.033	0.060	0.056	0.029	0.032	0.054
Fe^3/SumFe (pr)	0.074	0.166	0.078	0.082	0.168	0.165	0.110	0.152	0.161
Fe^3/SumFe (corr)	0.074	0.166	0.078	0.118	0.168	0.165	0.110	0.152	0.195
Fa (Ol)	0.081	0.085	0.088	0.093	0.090	0.086	0.092	0.093	0.093
T°C (Balhaus)	715	664	692	701	671	701	710	678	694
fO_2 (FMQ)	**-1.04**	**0.71**	**-0.99**	**-0.37**	**0.71**	**0.65**	**-0.55**	**-0.04**	**0.58**

Appendix D: Chrome-spinel analyses by electron microprobe

Sample	SD120h	SD138	SD151	SD157	SD19	SD245	SD34	SD380	SD426
Groups	Harzburgite	Harzburgite	Harzburgite	Harzburgite	Harzburgite	Harzburgite	Harzburgite	Harzburgite	Harzburgite
Rock Type	**Hz**	**Hz**	**Hz**	**Hz**	**Hz**	**Hz**	**Hz**	**Hz**	**Hz**
Region	ASWS	ASWS	ASWS	ASWN	DIBBA	ASWS	DIBBA	FIZH	ASWS
Region	Mantle	Mantle	Mantle	Mantle	Mantle	Mantle	Mantle	Mantle	Mantle
Spinel shape	HL	HL	HL	HL	HL	HL	HL	HL	HL
Cal	old cal	old cal	old cal	new cal	new cal	new cal	old cal	new cal	new cal
n=	4	4	4	34	40	4	4	4	4
SiO_2	0.03	0.14	0.02	0.02	0.04	0.02	0.03	0.01	0.03
TiO_2	0.11	0.05	0.04	0.08	0.16	0.05	0.04	0.12	0.03
Al_2O_3	19.57	21.27	23.13	18.82	30.42	20.02	25.91	23.69	23.11
V_2O_3	0.22	0.25	0.24	0.20	0.16	0.22	0.20	0.17	0.22
Cr_2O_3	45.51	43.71	43.04	47.69	38.01	45.53	40.78	43.54	43.30
Fe_2O_3	3.43	3.65	3.45	4.04	1.54	4.27	1.63	2.94	3.32
MgO	10.48	11.74	12.46	10.67	14.14	11.16	13.03	13.12	12.33
MnO	0.20	0.21	0.21	0.25	0.16	0.21	0.13	0.20	0.19
FeO	18.17	16.26	15.85	18.50	15.02	17.54	14.97	15.23	16.12
NiO	0.11	0.10	0.07	0.08	0.11	0.13	0.11	0.08	0.13
ZnO	0.21	0.08	0.18	0.21	0.24	0.16	0.18	0.20	0.23
Total	98.04	97.46	98.70	100.57	99.99	99.32	97.01	99.30	99.00
Mg#	0.508	0.560	0.584	0.506	0.628	0.532	0.609	0.607	0.578
Cr#	**0.609**	**0.580**	**0.555**	**0.630**	**0.456**	**0.604**	**0.514**	**0.552**	**0.557**
Fe^{3}# (corr)	0.043	0.042	0.041	0.054	0.022	0.063	0.020	0.041	0.048
Fe^{3}/SumFe (pr)	0.149	0.158	0.166	0.162	0.091	0.183	0.093	0.153	0.161
Fe^{3}/SumFe (corr)	0.149	0.158	0.166	0.185	0.108	0.224	0.093	0.177	0.194
Fa (Ol)	0.092	0.092	0.091	0.093	0.097	0.090	0.094	0.091	0.092
T°C (Balhaus)	661	699	713	682	712	696	710	748	716
$f\text{O}_2$ (FMQ)	**0.21**	**0.15**	**0.15**	**0.56**	**-0.90**	**0.90**	**-1.10**	**0.10**	**0.41**

Sample	SD434	SD452	SD461	SD488	SD489	SD565	SD567	SD82	UAE128
Groups	Harzburgite	Harzburgite	Harzburgite	Harzburgite	Harzburgite	Harzburgite	Harzburgite	Harzburgite	Harzburgite
Rock Type	**Hz**	**Hz**	**Hz**	**Hz**	**Hz**	**Hz**	**Hz**	**Hz**	**Hz**
Region	ASWS	DIBBA	KFS	KFN	KFN	KFN	KFN	KFN	KFN
Region	Mantle	Mantle	Mantle	Mantle	Mantle	Mantle	Mantle	Mantle	Mantle
Spinel shape	HL	HL	HL	SI	HL+SI	SI	EU	EU	HL+SI
Cal	new cal	new cal	new caln	ew cal	new cal	new cal	new cal	new cal	old cal
n=	4	35	4	4	40	4	4	4	4
SiO_2	0.04	0.03	0.04	0.05	0.03	0.03	0.01	0.03	0.04
TiO_2	0.07	0.04	0.11	0.05	0.03	0.02	0.03	0.02	0.06
Al_2O_3	24.63	27.07	25.63	12.73	19.68	6.41	19.66	13.72	29.19
V_2O_3	0.16	0.17	0.21	0.28	0.28	0.22	0.26	0.31	0.16
Cr_2O_3	41.42	41.20	39.42	54.35	48.44	62.86	48.76	55.46	34.72
Fe_2O_3	3.51	2.02	3.95	2.86	1.56	1.09	1.28	0.88	3.54
MgO	12.30	13.95	11.61	8.69	10.23	7.48	10.55	10.03	13.82
MnO	0.24	0.16	0.22	0.30	0.24	0.36	0.23	0.28	0.22
FeO	16.49	14.50	17.76	20.23	19.03	21.07	18.49	18.14	14.75
NiO	0.08	0.11	0.07	0.03	0.05	0.03	0.03	0.04	0.09
ZnO	0.20	0.17	0.21	0.19	0.24	0.23	0.23	0.23	0.25
Total	99.15	99.43	99.24	99.75	99.81	99.79	99.55	99.13	96.84
Mg#	0.571	0.633	0.539	0.433	0.490	0.388	0.505	0.497	0.637
Cr#	**0.530**	**0.505**	**0.508**	**0.741**	**0.623**	**0.868**	**0.625**	**0.731**	**0.444**
Fe^{3}# (corr)	0.047	0.029	0.051	0.047	0.031	0.031	0.026	0.025	0.050
Fe^{3}/SumFe (pr)	0.163	0.116	0.169	0.111	0.070	0.047	0.061	0.043	0.217
Fe^{3}/SumFe (corr)	0.186	0.143	0.184	0.151	0.114	0.098	0.100	0.098	0.217
Fa (Ol)	0.088	0.089	0.096	0.090	0.090	0.080	0.090	0.090	0.089
T°C (Balhaus)	675	734	644	660	638	656	652	714	708
$f\text{O}_2$ (FMQ)	**0.54**	**-0.35**	**0.60**	**0.34**	**-0.30**	**-0.24**	**-0.62**	**-0.81**	**0.67**

Appendix D: Chrome-spinel analyses by electron microprobe

Sample	UAE19	UAE192	UAE2007	UAE2032	UAE2036	UAE2040	UAE2042	UAE2044	UAE2080
Groups	Harzburgite	Harzburgite	Harzburgite	Harzburgite	Harzburgite	Harzburgite	Harzburgite	Harzburgite	Harzburgite
Rock Type	Hz	Hz	Hz	Hz	Hz	Hz	Hz	Hz	Hz
Region	KFS	KFN	KFN	ASWN	ASWN	ASWN	ASWS	ASWN	ASWN
Region	Mantle	Mantle	Mantle	Mantle	Mantle	Mantle	Mantle	Mantle	Mantle
Spinel shape	HL	HL	HL	SI	SI	HL	EU	SI	HL
Cal	new cal	new cal	new cal	old cal	old cal	old cal	new cal	old cal	old cal
n=	4	4	5	5	4	4	4	4	4
SiO2	0.01	0.02	0.03	0.04	0.02	0.02	0.03	0.02	0.02
TiO2	0.07	0.09	0.06	0.05	0.07	0.08	0.10	0.07	0.06
Al2O3	21.09	29.90	43.06	25.44	11.63	28.47	25.13	25.06	43.99
V2O3	0.18	0.16	0.11	0.19	0.16	0.19	0.22	0.23	0.08
Cr2O3	46.49	36.08	22.39	41.62	52.34	38.10	41.79	40.05	21.07
Fe2O3	2.17	3.19	2.26	1.96	3.87	1.82	2.55	2.84	2.05
MgO	10.92	12.94	15.93	11.97	8.42	12.42	12.27	12.10	16.94
MnO	0.21	0.20	0.12	0.24	0.38	0.22	0.25	0.23	0.09
FeO	18.26	16.46	13.53	16.99	19.41	16.67	16.66	16.20	11.72
NiO	0.08	0.10	0.24	0.06	0.04	0.08	0.06	0.06	0.22
ZnO	0.24	0.25	0.26	0.21	0.13	0.25	0.23	0.25	0.23
Total	99.73	99.38	98.00	98.76	96.49	98.34	99.28	97.12	96.47
Mg#	0.518	0.585	0.681	0.557	0.436	0.572	0.569	0.572	0.724
Cr#	**0.597**	**0.447**	**0.259**	**0.523**	**0.751**	**0.473**	**0.527**	**0.517**	**0.243**
Fe^{3}# (corr)	0.038	0.043	0.029	0.024	0.050	0.022	0.034	0.035	0.025
Fe^{3}/SumFe (pr)	0.102	0.155	0.145	0.097	0.153	0.095	0.124	0.141	0.153
Fe^{3}/SumFe (corr)	0.145	0.178	0.157	0.097	0.153	0.095	0.141	0.141	0.153
Fa (Ol)	0.092	0.093	0.091	0.090	0.091	0.094	0.092	0.093	0.090
T°C (Balhaus)	663	647	611	638	669	632	672	669	669
fO_2 (FMQ)	**0.05**	**0.46**	**0.31**	**-0.65**	**0.41**	**-0.71**	**-0.08**	**-0.05**	**-0.06**

Sample	UAE2087	UAE2109	UAE2114	UAE2156	UAE2159	UAE2167	UAE2230	UAE2242	UAE2278
Groups	Harzburgite	Harzburgite	Harzburgite	Harzburgite	Harzburgite	Harzburgite	Harzburgite	Harzburgite	Harzburgite
Rock Type	Hz	Hz	Hz	Hz	Hz	Hz	Hz	Hz	Hz
Region	ASWN	ASWS	ASWS	DIBBA	DIBBA	ASWN	KFN	ASWN	ASWN
Region	Mantle	Mantle	Mantle	Mantle	Mantle	Mantle	Mantle	Mantle	Mantle
Spinel shape	HL+SI	HL	HL	HL	HL	SI/EU	HL	HL	HL
Cal	new cal	old cal	old cal	old cal	new cal	old cal	new cal	new cal	old cal
n=	32	4	4	5	4	4	42	4	4
SiO2	0.03	0.02	0.02	0.03	0.07	0.03	0.03	0.02	0.03
TiO2	0.08	0.03	0.02	0.04	0.02	0.10	0.04	0.07	0.03
Al2O3	31.00	23.24	27.12	22.46	24.22	9.50	20.71	20.53	25.75
V2O3	0.17	0.18	0.13	0.21	0.19	0.15	0.20	0.21	0.17
Cr2O3	35.93	42.61	40.72	44.16	44.22	54.34	46.09	48.17	40.91
Fe2O3	1.94	2.97	1.73	2.24	1.40	3.59	2.80	1.29	2.40
MgO	13.50	11.79	14.38	12.24	12.10	7.15	11.19	11.37	12.94
MnO	0.17	0.19	0.18	0.24	0.14	0.39	0.20	0.23	0.16
FeO	15.60	16.70	13.36	15.72	16.92	21.05	17.57	17.44	15.39
NiO	0.11	0.08	0.11	0.12	0.13	0.01	0.07	0.10	0.08
ZnO	0.25	0.29	0.15	0.19	0.16	0.29	0.21	0.23	0.22
Total	98.77	98.08	97.91	97.66	99.57	96.60	99.10	99.64	98.07
Mg#	0.609	0.559	0.659	0.582	0.560	0.378	0.532	0.539	0.601
Cr#	**0.439**	**0.551**	**0.502**	**0.569**	**0.551**	**0.793**	**0.599**	**0.612**	**0.516**
Fe^{3}# (corr)	0.028	0.037	0.021	0.028	0.025	0.049	0.043	0.026	0.029
Fe^{3}/SumFe (pr)	0.107	0.145	0.110	0.118	0.070	0.136	0.129	0.068	0.128
Fe^{3}/SumFe (corr)	0.131	0.145	0.110	0.118	0.109	0.136	0.163	0.105	0.128
Fa (Ol)	0.087	0.092	0.081	0.092	0.082	0.081	0.082	0.090	0.088
T°C (Balhaus)	637	674	732	713	641	608	653	683	687
fO_2 (FMQ)	**-0.11**	**0.01**	**-0.81**	**-0.58**	**-0.40**	**0.60**	**0.45**	**-0.66**	**-0.32**

Appendix D: Chrome-spinel analyses by electron microprobe

Sample	UAE2285	UAE2288	UAE2354	UAE2810	UAE312	UAE316	UAE3190	UAE37	UAE424
Groups	Harzburgite	Harzburgite	Harzburgite	Harzburgite	Harzburgite	Harzburgite	Harzburgite	Harzburgite	Harzburgite
Rock Type	Hz	Hz	Hz	Hz	Hz	Hz	Hz	Hz	Hz
Region	ASWN	ASWN	ASWN	ASWS	KFN	KFS	FIZH	KFS	KFS
Region	Mantle	Mantle	Mantle	Mantle	Mantle	Mantle	Mantle	Mantle	Mantle
Spinel shape	HL	HL	HL	HL	EU	HL	HL	SI	HL
Cal	old cal	new cal	old cal	old cal	new cal	old cal	new cal	old cal	new cal
n=	4	20	4	4	24	4	4	4	40
SiO2	0.01	0.03	0.03	0.03	0.03	0.02	0.04	0.02	0.03
TiO2	0.03	0.07	0.04	0.03	0.04	0.08	0.05	0.05	0.04
Al2O3	21.93	22.79	28.17	24.62	13.50	33.87	19.77	21.99	31.88
V2O3	0.25	0.25	0.17	0.20	0.27	0.16	0.28	0.22	0.18
Cr2O3	43.23	43.89	38.85	40.09	53.05	30.20	47.86	43.46	34.67
Fe2O3	3.55	2.80	2.31	3.39	4.13	2.96	2.62	3.28	2.97
MgO	11.22	11.92	13.61	11.81	9.21	14.36	11.12	10.85	13.45
MnO	0.22	0.20	0.20	0.23	0.26	0.16	0.18	0.19	0.21
FeO	17.31	16.73	14.87	16.61	19.84	13.87	17.81	18.08	16.08
NiO	0.07	0.09	0.11	0.05	0.06	0.10	0.10	0.05	0.12
ZnO	0.20	0.20	0.19	0.23	0.20	0.27	0.14	0.23	0.29
Total	98.04	98.95	98.57	97.28	100.58	96.04	99.96	98.43	99.92
Mg#	0.537	0.560	0.621	0.560	0.453	0.651	0.527	0.518	0.601
Cr#	**0.569**	**0.564**	**0.481**	**0.522**	**0.725**	**0.374**	**0.619**	**0.570**	**0.422**
Fe^3# (corr)	0.044	0.042	0.028	0.041	0.065	0.035	0.040	0.040	0.037
Fe^3/SumFe (pr)	0.159	0.133	0.128	0.158	0.158	0.169	0.116	0.144	0.151
Fe^3/SumFe (corr)	0.159	0.168	0.128	0.158	0.203	0.169	0.152	0.144	0.160
Fa (Ol)	0.091	0.087	0.089	0.092	0.088	0.095	0.090	0.094	0.093
T°C (Balhaus)	664	679	692	660	677	682	682	647	639
fO_2 (FMQ)	**0.29**	**0.31**	**-0.38**	**0.24**	**0.92**	**0.15**	**0.13**	**0.13**	**0.27**

Sample	UAE445	UAE45	UAE4801	UAE4807	UAE484	UAE485	UAE501	UAE510	UAE545
Groups	Harzburgite	Harzburgite	Harzburgite	Harzburgite	Harzburgite	Harzburgite	Harzburgite	Harzburgite	Harzburgite
Rock Type	Hz	Hz	Hz	Hz	Hz	Hz	Hz	Hz	Hz
Region	KFS	KFS	ASWS	ASWS	KFN	KFN	ASWS	ASWS	KFN
Region	Mantle	Mantle	Mantle	Mantle	Mantle	Mantle	Mantle	Mantle	Mantle
Spinel shape	HL	HL	HL+SI	HL	EU	EU	HL	SI	HL
Cal	old cal	new cal	new cal	new cal	old cal	old cal	old cal	new cal	new cal
n=	3	4	3	4	6	6	10	3	3
SiO2	0.02	0.01	0.04	0.05	0.02	0.11	0.04	0.04	0.04
TiO2	0.05	0.01	0.06	0.01	0.06	0.08	0.03	0.10	0.09
Al2O3	28.62	28.07	19.69	27.92	21.29	20.63	25.33	27.57	23.91
V2O3	0.20	0.20	0.28	0.14	0.18	0.17	0.17	0.18	0.17
Cr2O3	37.41	38.94	47.37	39.20	46.31	47.06	38.16	36.69	42.61
Fe2O3	2.38	3.09	3.18	2.83	1.54	1.24	4.84	4.18	2.65
MgO	13.27	13.06	10.93	13.32	11.65	11.65	12.37	11.16	10.46
MnO	0.22	0.20	0.26	0.19	0.28	0.24	0.21	0.23	0.31
FeO	15.15	16.11	18.05	15.57	16.65	16.46	15.85	18.70	19.38
NiO	0.08	0.11	0.06	0.12	0.05	0.04	0.11	0.09	0.04
ZnO	0.14	0.27	0.20	0.21	0.22	0.25	0.18	0.35	0.38
Total	97.53	100.09	100.12	99.56	98.23	97.94	97.31	99.30	100.02
Mg#	0.610	0.593	0.519	0.605	0.556	0.557	0.583	0.517	0.492
Cr#	**0.467**	**0.482**	**0.617**	**0.485**	**0.593**	**0.605**	**0.503**	**0.472**	**0.545**
Fe^3# (corr)	0.028	0.044	0.047	0.039	0.019	0.014	0.058	0.052	0.043
Fe^3/SumFe (pr)	0.126	0.155	0.137	0.145	0.081	0.060	0.219	0.174	0.116
Fe^3/SumFe (corr)	0.126	0.188	0.170	0.170	0.081	0.060	0.219	0.179	0.153
Fa (Ol)	0.092	0.090	0.092	0.086	0.083	0.081		0.092	0.088
T°C (Balhaus)	674	672	683	671	661	660		585	593
fO_2 (FMQ)	**-0.35**	**0.48**	**0.34**	**0.31**	**-0.98**	**-1.49**		**0.86**	**0.49**

Appendix D: Chrome-spinel analyses by electron microprobe

Sample	**UAE546**	**UAE550**	**UAE581**	**UAE60**	**UAE622**	**UAE659**	**UAE66**	**UAE700**	**UAE711**
Groups	Harzburgite	Harzburgite	Harzburgite	Harzburgite	Harzburgite	Harzburgite	Harzburgite	Harzburgite	Harzburgite
Rock Type	Hz	Hz	Hz	Hz	Hz	Hz	Hz	Hz	Hz
Region	KFN	KFN	ASWS	KFN	ASWN	ASWN	KFN	KFN	KFN
Region	Mantle	Mantle	Mantle	Mantle	Mantle	Mantle	Mantle	Mantle	Mantle
Spinel shape	HL	HL	HL	SI	HL	HL	EU	SI	HL
Cal	**new cal**	**new cal**	old cal	old cal	old cal	old cal	**new cal**	**new cal**	old cal
n=	4	4	4	4	4	10	4	4	10
SiO2	0.04	0.16	0.02	0.02	0.02	0.03	0.04	0.04	0.03
TiO2	0.09	0.09	0.03	0.05	0.06	0.05	0.06	0.04	0.03
Al2O3	27.71	46.39	22.16	21.02	24.26	27.71	16.38	7.34	21.90
V2O3	0.15	0.09	0.20	0.21	0.21	0.23	0.32	0.20	0.24
Cr2O3	40.39	20.43	41.92	44.34	39.42	38.32	48.85	59.18	44.87
Fe2O3	1.30	2.33	4.66	3.03	3.59	2.48	3.96	4.06	2.10
MgO	12.62	16.42	11.87	10.64	12.39	11.75	8.61	7.70	10.29
MnO	0.21	0.16	0.21	0.24	0.20	0.23	0.30	0.32	0.29
FeO	16.66	14.13	16.22	18.03	15.19	17.67	20.86	21.00	19.00
NiO	0.05	0.16	0.11	0.07	0.09	0.05	0.06	0.02	0.04
ZnO	0.27	0.29	0.19	0.35	0.14	0.41	0.23	0.18	0.30
Total	99.49	100.64	97.59	98.02	95.58	98.93	99.66	100.08	99.11
Mg#	0.576	0.674	0.567	0.515	0.593	0.545	0.424	0.395	0.492
Cr#	**0.494**	**0.228**	**0.559**	**0.586**	**0.522**	**0.481**	**0.667**	**0.844**	**0.579**
Fe^3# (corr)	0.023	0.026	0.057	0.039	0.044	0.031	0.065	0.073	0.026
Fe^3/SumFe (pr)	0.070	0.129	0.210	0.138	0.178	0.120	0.146	0.148	0.094
Fe^3/SumFe (corr)	0.104	0.138	0.210	0.138	0.178	0.120	0.196	0.213	0.094
Fa (Ol)	0.089	0.098	0.092	0.092	0.090	0.092	0.090	0.086	0.089
T°C (Balhaus)	640	592	706	648	700	603	617	684	602
fO_2 (FMQ)	**-0.58**	**0.14**	**0.71**	**0.07**	**0.34**	**-0.08**	**0.99**	**1.16**	**-0.48**

Sample	**UAE715**	**UAE79**	**SD147**	**SD493**	**SD537**	**UAE130**	**UAE2046**	**UAE2058**	**UAE2091**
Groups	Harzburgite	Harzburgite	Harzburgite	Harzburgite	Harzburgite	Harzburgite	Harzburgite	Harzburgite	Harzburgite
Rock Type	Hz	Hz	Cpx-rich	Cpx-rich	Cpx-rich	Cpx-rich	Cpx-rich	Cpx-rich	Cpx-rich
Region	KFN	KFN	ASWS	KFN	KFN	KFN	ASWN	ASWN	ASWN
Region	Mantle	Mantle	Mantle	Mantle	Mantle	Mantle	Mantle	Mantle	Mantle
Spinel shape	EU	EU	HL	HL	SI	HL+SI	HL	SI	HL
Cal	**new cal**	old cal	old cal	**new cal**	**new cal**	**new cal**	old cal	old cal	old cal
n=	4	4	4	4	4	40	4	4	4
SiO2	0.03	0.01	0.04	0.02	0.02	0.03	0.03	0.04	0.02
TiO2	0.02	0.02	0.04	0.07	0.04	0.06	0.06	0.12	0.10
Al2O3	7.97	13.55	29.77	43.43	9.10	30.71	19.50	23.02	45.08
V2O3	0.23	0.34	0.18	0.11	0.30	0.17	0.27	0.18	0.08
Cr2O3	58.41	51.85	36.63	24.18	58.76	36.02	45.30	41.22	20.77
Fe2O3	3.60	3.67	2.58	1.55	2.65	2.53	3.06	3.49	2.32
MgO	7.74	9.21	14.14	16.50	7.66	13.45	10.59	11.29	16.94
MnO	0.30	0.27	0.19	0.14	0.34	0.16	0.24	0.26	0.12
FeO	20.79	19.07	14.14	13.31	21.45	15.78	17.51	17.10	12.50
NiO	0.03	0.04	0.11	0.19	0.05	0.12	0.05	0.13	0.24
ZnO	0.22	0.24	0.20	0.20	0.24	0.24	0.18	0.22	0.26
Total	99.34	98.26	98.01	99.70	100.61	99.26	96.78	97.07	98.42
Mg#	0.399	0.463	0.642	0.691	0.389	0.605	0.519	0.542	0.711
Cr#	**0.831**	**0.720**	**0.452**	**0.272**	**0.812**	**0.440**	**0.609**	**0.546**	**0.236**
Fe^3# (corr)	0.065	0.047	0.030	0.020	0.044	0.036	0.038	0.043	0.027
Fe^3/SumFe (pr)	0.136	0.150	0.145	0.106	0.102	0.133	0.136	0.160	0.160
Fe^3/SumFe (corr)	0.192	0.150	0.145	0.119	0.132	0.160	0.136	0.160	0.160
Fa (Ol)	0.086	0.090	0.096	0.092	0.089	0.092	0.097	0.087	0.097
T°C (Balhaus)	677	673	729	635	651	656	680	642	670
fO_2 (FMQ)	**0.94**	**0.31**	**-0.36**	**-0.41**	**0.23**	**0.17**	**-0.11**	**0.43**	**0.02**

Appendix D: Chrome-spinel analyses by electron microprobe

Sample	UAE2161	UAE2169	UAE2241	UAE2244	UAE2836	UAE327	UAE360	UAE432	SD61	UAE2035	UAE2065	UAE2097
Groups	Harzburgite	Harzburgite	Harzburgite	Harzburgite	Harzburgite	Harzburgite	Harzburgite	Harzburgite	Harzburgite	Harzburgite	Harzburgite	Harzburgite
Rock Type	Cpx-rich	Cpx-rich	Cpx-rich	Cpx-rich	Cpx-rich	Cpx-rich	Cpx-rich	Cpx-rich	Lhz	Lhz	Lhz	Lhz
Region	DIBBA	ASWN	ASWNA	SWN	ASWS	KFS	KFS	KFS	ASWNA	SWN	ASWN	ASWN
Region	Mantle	Mantle	Mantle	Mantle	Mantle	Mantle	Mantle	Mantle	Mantle	Mantle	Mantle	Mantle
Spinel shape	HL	HL	HL	HL	HL	SI	HL	HL+SI	HL	HL	HL	HL
Cal	old cal	old cal	new cal	old cal	new cal	old cal	new cal	old cal	old cal	old cal	new cal	old cal
n=	4	4	38	4	4	4	4	4	4	4	24	4
SiO2	0.03	0.04	0.04	0.02	0.03	0.03	0.02	0.03	0.09	0.03	0.04	0.02
TiO2	0.03	0.08	0.04	0.05	0.04	0.054	0.04	0.06	0.08	0.06	0.07	0.05
Al2O3	25.79	42.05	35.02	24.06	25.98	16.25	30.90	27.23	38.57	45.01	49.02	38.70
V2O3	0.21	0.09	0.16	0.20	0.19	0.32	0.20	0.18	0.14	0.09	0.09	0.14
Cr2O3	40.59	21.55	32.83	42.78	39.24	47.19	37.06	38.51	26.18	20.34	17.46	26.61
Fe2O3	1.77	2.75	1.53	2.30	4.02	4.29	1.88	1.81	2.39	2.48	1.88	2.45
MgO	13.03	16.20	14.53	11.97	12.08	8.84	13.71	12.03	15.09	16.81	17.88	15.11
MnO	0.23	0.11	0.15	0.19	0.22	0.23	0.20	0.20	0.13	0.14	0.12	0.15
FeO	14.74	12.22	14.91	16.78	16.99	19.80	15.58	16.66	13.76	12.45	11.78	13.96
NiO	0.08	0.24	0.11	0.10	0.09	0.05	0.09	0.07	0.16	0.26	0.29	0.21
ZnO	0.15	0.27	0.24	0.28	0.22	0.21	0.25	0.24	0.24	0.19	0.15	0.22
Total	96.64	95.59	99.55	98.72	99.09	97.27	99.93	97.01	96.83	97.87	98.79	97.60
Mg#	0.612	0.707	0.635	0.562	0.560	0.443	0.612	0.564	0.662	0.710	0.733	0.662
Cr#	**0.514**	**0.256**	**0.387**	**0.544**	**0.503**	**0.661**	**0.446**	**0.487**	**0.313**	**0.233**	**0.193**	**0.316**
Fe^3# (corr)	0.021	0.033	0.023	0.029	0.050	0.054	0.028	0.022	0.027	0.029	0.022	0.029
Fe^3/SumFe (pr)	0.099	0.184	0.095	0.117	0.180	0.163	0.104	0.094	0.138	0.166	0.140	0.148
Fe^3/SumFe (corr)	0.099	0.184	0.117	0.117	0.187	0.163	0.132	0.094	0.138	0.166	0.142	0.148
Fa (Ol)	0.098	0.091	0.088	0.091	0.093	0.096	0.093	0.092	0.092	0.095	0.095	0.100
T°C (Balhaus)	732	662	631	663	656	637	667	623	630	653	656	657
fO_2 (FMQ)	**-1.10**	**0.39**	**-0.35**	**-0.39**	**0.61**	**0.53**	**-0.31**	**-0.67**	**-0.02**	**0.18**	**-0.16**	**-0.08**

Sample	SD110	SD120d	SD144	SD154	SD158_du	SD18	SD247	SD255	SD33
Groups	Dunite	Dunite	Dunite	Dunite	Dunite	Dunite	Dunite	Dunite	Dunite
Rock Type	Du	Du	Du	Du	Du	Du	Du	Du	Du
Region	ASWS	ASWS	ASWS	ASWN	ASWN	DIBBA	ASWS	ASWS	ASWN
Region	Mantle	Mantle	Mantle	Mantle	Mantle	Mantle	Mantle	Mantle	Mantle
Spinel shape	SI	SI	SI/cusp	SI	SI/EU	EU	SI	SI/cusp	HL
Cal	new cal	old cal	new cal	old cal	new cal	new cal	new caln	ew cal	old cal
n=	4	4	4	4	14	38	4	4	4
SiO2	0.02	0.02	0.02	0.03	0.02	0.04	0.03	0.03	0.01
TiO2	0.31	0.14	0.26	0.36	0.19	0.08	0.15	0.20	0.168
Al2O3	12.30	17.29	23.16	18.42	16.28	9.31	21.71	22.36	22.74
V2O3	0.15	0.22	0.15	0.13	0.12	0.19	0.16	0.17	0.20
Cr2O3	50.19	46.63	42.90	44.10	47.83	59.42	37.99	41.05	42.07
Fe2O3	7.01	4.20	4.78	5.42	6.02	2.03	9.21	7.13	3.52
MgO	8.95	9.58	11.88	11.09	10.72	9.85	10.11	11.55	10.89
MnO	0.31	0.22	0.20	0.28	0.24	0.26	0.24	0.24	0.21
FeO	19.83	19.08	17.84	16.85	17.78	17.89	19.42	17.91	18.17
NiO	0.07	0.09	0.11	0.08	0.13	0.05	0.11	0.12	0.03
ZnO	0.17	0.24	0.13	0.17	0.08	0.13	0.16	0.16	0.24
Total	99.31	97.70	101.45	96.92	99.41	99.26	99.29	100.91	98.24
Mg#	0.447	0.473	0.544	0.541	0.519	0.495	0.482	0.536	0.518
Cr#	**0.732**	**0.644**	**0.554**	**0.616**	**0.663**	**0.811**	**0.540**	**0.552**	**0.554**
Fe^3# (corr)	0.104	0.053	0.067	0.068	0.085	0.041	0.124	0.095	0.043
Fe^3/SumFe (pr)	0.244	0.169	0.197	0.227	0.236	0.092	0.301	0.266	0.153
Fe^3/SumFe (corr)	0.286	0.169	0.236	0.227	0.273	0.150	0.338	0.305	0.153
Fa (Ol)	0.085	0.092	0.088	0.097	0.073	0.081	0.093	0.094	0.087
T°C (Balhaus)	693	650	676	743	679	746	649	704	622
fO_2 (FMQ)	**1.80**	**0.59**	**1.13**	**0.85**	**1.76**	**0.17**	**2.16**	**1.60**	**0.45**

Appendix D: Chrome-spinel analyses by electron microprobe

Sample	**SD36**	**SD362_du**	**SD379**	**SD417**	**SD425**	**SD433**	**SD436a_du**	**SD436b_du**	**SD448b**
Groups	Dunite	Dunite	Dunite	Dunite	Dunite	Dunite	Dunite	Dunite	Dunite
Rock Type	**Du**	**Du**	**Du**	**Du**	**Du**	**Du**	**Du**	**Du**	**Du**
Region	DIBBA	ASWS	FIZH	ASWS	ASWS	ASWN	ASWS	ASWS	DIBBA
Region	Mantle	Mantle	Mantle	Mantle	Mantle	Mantle	Mantle	Mantle	Mantle
Spinel shape	SI/cusp	SI/cusp	SI/EU	SI/cusp	SI	SI	SI/cusp	SI	SI
Cal	old cal	old cal	**new cal**	**new cal**	**new cal**	**new cal**	old cal	**new cal**	**new cal**
n=	4	4	6	4	2	4	3	3	5
SiO2	0.01	0.04	0.02	0.03	0.01	0.04	0.05	0.03	0.04
TiO2	0.08	0.58	0.18	0.21	0.18	0.13	0.37	0.61	0.11
Al2O3	14.43	20.62	15.62	21.18	24.40	13.64	19.55	20.69	11.24
V2O3	0.19	0.36	0.20	0.21	0.15	0.21	0.21	0.26	0.17
Cr2O3	52.86	40.75	47.43	42.35	40.24	54.17	41.69	40.03	58.11
Fe2O3	2.40	5.68	7.39	6.15	6.49	2.87	6.32	7.32	1.85
MgO	10.85	9.65	10.50	10.51	13.19	8.94	9.68	9.08	9.70
MnO	0.25	0.26	0.25	0.27	0.19	0.26	0.29	0.27	0.33
FeO	16.79	19.92	18.12	19.08	15.74	20.54	19.44	21.42	18.81
NiO	0.04	0.15	0.13	0.15	0.14	0.03	0.13	0.13	0.08
ZnO	0.15	0.27	0.11	0.19	0.19	0.24	0.13	0.18	0.16
Total	98.05	98.29	99.94	100.34	100.93	101.09	97.85	100.03	100.59
Mg#	0.536	0.464	0.509	0.497	0.601	0.437	0.470	0.431	0.479
Cr#	**0.711**	**0.570**	**0.671**	**0.573**	**0.525**	**0.727**	**0.589**	**0.565**	**0.776**
Fe^{3}# (corr)	0.030	0.071	0.099	0.078	0.085	0.052	0.078	0.104	0.040
Fe^{3}/SumFe (pr)	0.116	0.207	0.271	0.228	0.277	0.113	0.227	0.237	0.083
Fe^{3}/SumFe (corr)	0.116	0.207	0.296	0.241	0.313	0.168	0.227	0.277	0.142
Fa (Ol)	0.080	0.104	0.099	0.098	0.089	0.085	0.097	0.115	0.090
T°C (Balhaus)	714	645	761	667	751	650	647	656	734
fO_2 (FMQ)	**-0.30**	**0.99**	**1.41**	**1.20**	**1.46**	**0.64**	**1.23**	**1.49**	**-0.05**

Sample	**SD568**	**SD62**	**SD67**	**SD70**	**UAE108**	**UAE143**	**UAE146**	**UAE160**	**UAE2008**
Groups	Dunite	Dunite	Dunite	Dunite	Dunite	Dunite	Dunite	Dunite	Dunite
Rock Type	**Du**	**Du**	**Du**	**Du**	**Du**	**Du**	**Du**	**Du**	**Du**
Region	KFN	ASWN	ASWN	KFN	KFN	KFN	KFN	KFN	KFN
Region	Mantle	Mantle	Mantle	Mantle	Mantle	Mantle	Mantle	Mantle	Mantle
Spinel shape	EU	SI/EU	EU	EU	SI	EU	EU	EU	SI
Cal	**new cal**	old cal	**new cal**	**new cal**	old cal	**new cal**	old cal	**new cal**	**new cal**
n=	5	4	24	4	6	24	4	4	24
SiO2	0.03	0.04	0.03	0.04	0.03	0.03	0.04	0.04	0.04
TiO2	0.06	0.17	0.10	0.11	0.02	0.02	0.05	0.03	0.16
Al2O3	13.14	18.16	5.98	12.24	17.77	8.39	11.11	4.45	11.61
V2O3	0.20	0.20	0.12	0.18	0.19	0.27	0.22	0.07	0.16
Cr2O3	56.76	48.98	60.66	56.26	45.65	61.37	56.67	65.87	53.27
Fe2O3	1.24	2.36	3.79	1.98	5.48	1.31	1.63	1.71	4.68
MgO	9.72	11.17	7.04	9.47	10.26	8.68	9.20	8.74	7.91
MnO	0.30	0.24	0.33	0.30	0.28	0.27	0.23	0.30	0.32
FeO	19.12	17.18	21.88	19.12	18.03	19.81	18.81	19.20	21.34
NiO	0.06	0.06	0.04	0.05	0.08	0.03	0.05	0.03	0.05
ZnO	0.21	0.17	0.20	0.20	0.12	0.18	0.23	0.23	0.31
Total	100.82	98.72	100.17	99.95	97.91	100.36	98.22	100.67	99.84
Mg#	0.476	0.537	0.365	0.469	0.504	0.439	0.466	0.449	0.399
Cr#	**0.743**	**0.644**	**0.872**	**0.755**	**0.633**	**0.831**	**0.774**	**0.909**	**0.755**
Fe^{3}# (corr)	0.031	0.029	0.070	0.037	0.068	0.034	0.021	0.041	0.085
Fe^{3}/SumFe (pr)	0.057	0.110	0.137	0.087	0.215	0.056	0.074	0.077	0.169
Fe^{3}/SumFe (corr)	0.113	0.110	0.197	0.131	0.215	0.117	0.074	0.143	0.242
Fa (Ol)	0.080	0.079	0.082	0.084	0.086	0.085	0.080	0.069	0.077
T°C (Balhaus)	672	668	658	688	667	701	668	712	626
fO_2 (FMQ)	**-0.21**	**-0.26**	**1.19**	**0.02**	**1.09**	**-0.19**	**-0.89**	**0.52**	**1.69**

Appendix D: Chrome-spinel analyses by electron microprobe

Sample	UAE2039	UAE2047	UAE2064	UAE2222	UAE2281	UAE299	UAE3189	UAE3200	UAE379
Groups	Dunite	Dunite	Dunite	Dunite	Dunite	Dunite	Dunite	Dunite	Dunite
Rock Type	Du	Du	Du	Du	Du	Du	Du	Du	Du
Region	ASWN	ASWN	ASWN	KFN	ASWN	KFN	FIZH	ASWS	KFN
Region	Mantle	Mantle	Mantle	Mantle	Mantle	Mantle	Mantle	Mantle	Mantle
Spinel shape	SI/EU	HL	SI	EU	SI	EU	HL	SI/EU	SI/EU
Cal	old cal	old cal	new cal	old cal	old cal	new cal	new cal	new cal	old cal
n=	4	4	24	4	4	24	40	4	6
SiO_2	0.02	0.03	0.03	0.03	0.02	0.02	0.03	0.04	0.03
TiO_2	0.37	0.12	0.19	0.04	0.11	0.05	0.10	0.22	0.07
Al_2O_3	14.32	13.52	8.10	13.03	10.37	7.05	20.12	11.61	8.53
V_2O_3	0.09	0.17	0.07	0.24	0.17	0.17	0.40	0.16	0.18
Cr_2O_3	49.28	50.53	54.92	54.77	50.64	59.06	36.87	53.51	56.08
Fe_2O_3	4.94	5.52	7.70	1.58	7.12	4.85	12.26	5.28	5.32
MgO	10.10	10.17	7.60	10.12	7.36	8.02	9.50	9.52	8.26
MnO	0.29	0.26	0.37	0.25	0.36	0.35	0.24	0.28	0.34
FeO	17.98	17.72	21.55	17.55	21.16	20.50	20.13	18.99	19.98
NiO	0.08	0.09	0.07	0.05	0.03	0.03	0.19	0.08	0.06
ZnO	0.17	0.13	0.20	0.22	0.31	0.14	0.28	0.23	0.18
Total	97.66	98.26	100.80	97.88	97.65	100.24	100.12	99.92	99.03
Mg#	0.502	0.506	0.387	0.508	0.384	0.411	0.458	0.473	0.425
Cr#	**0.698**	**0.715**	**0.820**	**0.738**	**0.766**	**0.849**	**0.551**	**0.756**	**0.815**
Fe^3# (corr)	0.064	0.070	0.112	0.020	0.095	0.074	0.163	0.084	0.069
Fe^3/SumFe (pr)	0.203	0.220	0.247	0.077	0.237	0.176	0.357	0.203	0.195
Fe^3/SumFe (corr)	0.203	0.220	0.281	0.077	0.237	0.212	0.395	0.257	0.195
Fa (Ol)	0.086	0.083	0.086	0.082	0.081	0.088	0.099	0.083	0.080
T°C (Balhaus)	710	713	679	697	621	707	670	716	672
fO_2 (FMQ)	**0.92**	**1.11**	**1.91**	**-1.01**	**1.76**	**1.10**	**2.49**	**1.44**	**1.18**

Sample	UAE392	UAE4808	UAE4893	UAE509	UAE547	UAE615
Groups	Dunite	Dunite	Dunite	Dunite	Dunite	Dunite
Rock Type	Du	Du	Du	Du	Du	Du
Region	KFN	ASWS	KFN	ASWS	KFN	KFS
Region	Mantle	Mantle	Mantle	Mantle	Mantle	Mantle
Spinel shape	SI	EU	SI/EU	SI/cusp	SI	SI/EU
Cal	new cal	new cal	old cal	old cal	old cal	new cal
n=	4	4	5	4	6	4
SiO_2	0.04	0.04	0.03	0.04	0.02	0.02
TiO_2	0.08	0.25	0.13	0.06	0.15	0.48
Al_2O_3	9.36	13.65	12.24	19.15	16.64	24.98
V_2O_3	0.12	0.14	0.18	0.27	0.24	0.16
Cr_2O_3	60.09	50.56	48.49	43.04	45.91	36.04
Fe_2O_3	1.40	5.41	7.70	6.75	5.80	8.49
MgO	9.52	8.57	8.58	10.58	8.36	10.84
MnO	0.21	0.32	0.28	0.25	0.31	0.22
FeO	18.58	20.78	19.68	18.51	21.09	19.79
NiO	0.03	0.10	0.10	0.13	0.07	0.22
ZnO	0.08	0.18	0.18	0.15	0.63	0.20
Total	99.51	100.01	97.58	98.93	99.21	101.44
Mg#	0.477	0.424	0.438	0.511	0.417	0.496
Cr#	**0.812**	**0.713**	**0.727**	**0.601**	**0.649**	**0.492**
Fe^3# (corr)	0.032	0.080	0.100	0.088	0.076	0.112
Fe^3/SumFe (pr)	0.062	0.192	0.263	0.266	0.210	0.285
Fe^3/SumFe (corr)	0.116	0.227	0.263	0.266	0.210	0.318
Fa (Ol)	0.076	0.093	0.088		0.076	0.099
T°C (Balhaus)	702	663	676		569	649
fO_2 (FMQ)	**-0.10**	**1.23**	**1.68**		**1.64**	**1.96**

Appendix D: Chrome-spinel analyses by electron microprobe

Sample	03UR187	SD102a	SD106a	SD11a	SD345	SD37	SD490	SD71a	UAE117	UAE138_du
Groups	Dunite	Dunite	Dunite	Dunite	Dunite	Dunite	Dunite	Dunite	Dunite	Dunite
Rock Type	Chr-Du	Chr-Du	Chr-Du	Chr-Du	Chr-Du	Chr-Du	Chr-Du	Chr-Du	Chr-Du	Chr-Du
Region	ASWS	KFS	KFS	ASWN	ASWS	DIBBA	KFN	KFN	KFN	KFN
Region	Mantle	Mantle	Mantle	Mantle	Mantle	Mantle	Mantle	Mantle	Mantle	Mantle
Spinel shape	Sl/cusp	Sl/cusp	Sl/EU	HL	EU	Sl/cusp	Sl/cusp	Sl/cusp	Sl/cusp	Sl
Cal	new cal	old cal	new cal	old cal	new cal	old cal	new cal	new cal	old cal	new cal
n=	4	4	4	4	3	6	2	20	6	4
SiO2	0.02	0.02	0.03	0.03	0.02	0.04	0.03	0.03	0.02	0.02
TiO2	0.07	0.29	0.12	0.18	0.40	0.17	0.21	0.13	0.07	0.09
Al2O3	21.92	20.20	8.51	14.05	14.10	17.36	12.99	15.21	8.76	8.26
V2O3	0.20	0.12	0.09	0.10	0.17	0.09	0.11	0.08	0.17	0.05
Cr2O3	42.92	42.07	59.88	50.49	50.91	50.47	54.30	52.38	58.95	63.17
Fe2O3	5.78	8.73	3.41	4.13	4.90	0.74	3.05	3.57	2.17	1.82
MgO	11.02	15.27	10.35	12.55	10.65	12.61	9.63	12.31	8.51	12.16
MnO	0.27	0.23	0.24	0.22	0.24	0.20	0.34	0.22	0.32	0.16
FeO	18.55	11.13	17.36	14.18	17.71	14.35	19.06	15.15	19.66	14.84
NiO	0.10	0.15	0.07	0.07	0.09	0.07	0.02	0.08	0.04	0.10
ZnO	0.16	0.10	0.04	0.07	0.08	0.06	0.15	0.08	0.14	0.04
Total	101.01	98.29	100.11	96.06	99.27	96.16	99.88	99.25	98.81	100.70
Mg#	0.515	0.711	0.536	0.621	0.518	0.613	0.474	0.592	0.436	0.594
Cr#	**0.568**	**0.583**	**0.826**	**0.707**	**0.708**	**0.661**	**0.737**	**0.698**	**0.819**	**0.837**
Fe^3# (corr)	0.076	0.104	0.057	0.059	0.073	0.011	0.045	0.055	0.028	0.035
Fe^3/SumFe (pr)	0.221	0.418	0.151	0.238	0.200	0.056	0.126	0.177	0.091	0.102
Fe^3/SumFe (corr)	0.246	0.418	0.211	0.238	0.241	0.056	0.151	0.226	0.091	0.158
Fa (Ol)	0.091	0.050	0.052	0.073	0.070	0.081	0.078	0.062	0.086	0.047
T°C (Balhaus)	662	786	690	818	691	780	669	724	684	720
fO_2 (FMQ)	**1.28**	**2.66**	**1.60**	**0.94**	**1.53**	**-2.06**	**0.49**	**1.20**	**-0.54**	**0.90**

Sample	UAE17	UAE196	UAE2212	UAE2232	UAE2355	UAE543
Groups	Dunite	Dunite	Dunite	Dunite	Dunite	Dunite
Rock Type	Chr-Du	Chr-Du	Chr-Du	Chr-Du	Chr-Du	Chr-Du
Region	KFS	KFN	KFN	KFN	ASWN	KFN
Region	Mantle	Mantle	Mantle	Mantle	Mantle	Mantle
Spinel shape	Sl/cusp	Sl/cusp	Sl/cusp	Sl/cusp	Sl/cusp	HL
Cal	new cal	old cal	old cal	new cal	old cal	new cal
n=	24	4	4	4	4	4
SiO2	0.03	0.03	0.03	0.03	0.01	0.02
TiO2	0.22	0.19	0.06	0.08	0.24	0.19
Al2O3	27.14	12.58	10.57	11.21	14.68	14.90
V2O3	0.12	0.07	0.12	0.12	0.08	0.14
Cr2O3	37.71	54.29	56.91	57.73	52.08	51.48
Fe2O3	5.09	2.54	1.52	2.05	3.39	3.75
MgO	13.04	11.20	10.41	10.90	13.65	10.53
MnO	0.21	0.23	0.31	0.26	0.20	0.32
FeO	16.19	15.82	16.26	16.57	13.29	17.76
NiO	0.15	0.06	0.04	0.04	0.10	0.04
ZnO	0.13	0.06	0.08	0.05	0.04	0.11
Total	100.02	97.06	96.31	99.03	97.77	99.25
Mg#	0.591	0.558	0.533	0.539	0.658	0.514
Cr#	**0.482**	**0.743**	**0.783**	**0.776**	**0.704**	**0.699**
Fe^3# (corr)	0.067	0.032	0.019	0.038	0.050	0.056
Fe^3/SumFe (pr)	0.226	0.127	0.077	0.099	0.226	0.160
Fe^3/SumFe (corr)	0.254	0.127	0.077	0.151	0.226	0.194
Fa (Ol)	0.079		0.072	0.061	0.060	0.074
T°C (Balhaus)	656		720	695	801	682
fO_2 (FMQ)	**1.41**		**-0.91**	**0.59**	**1.01**	**0.95**

Appendix D: Chrome-spinel analyses by electron microprobe

Sample	SD109	SD152a	SD158_chr	SD159b	SD163	SD246	SD362_chr	SD42b	SD436a_chr	SD436b_chr
Groups	Chromitite	Chromitite	Chromitite	Chromitite	Chromitite	Chromitite	Chromitite	Chromitite	Chromitite	Chromitite
Rock Type	Chr	Chr	Chr	Chr	Chr	Chr	Chr	Chr	Chr	Chr
Region	ASWS	ASWN	ASWN	ASWN	ASWN	ASWS	ASWS	ASWS	ASWS	ASWS
Region	Mantle	Mantle	Mantle	Mantle	Mantle	Mantle	Mantle	Mantle	Mantle	Mantle
Spinel shape	SI/EU	SI/cusp	SI/cusp	EU	SI/EU	EU	SI/cusp	SI/EU	SI/cusp	SI/cusp
Cal	old cal	**new cal**	**new cal**	**new cal**	old cal	**new cal**	old cal	old cal	old cal	old cal
n=	4	4	9	23	3	4	4	4	4	2
SiO2	0.01	0.03	0.03	0.02	0.02	0.02	0.03	0.02	0.04	0.02
TiO2	0.41	0.21	0.21	0.23	0.14	0.33	0.75	0.31	0.43	0.53
Al2O3	11.94	17.10	17.78	17.39	13.40	22.27	20.45	24.51	19.79	20.60
V2O3	0.20	0.15	0.09	0.12	0.16	0.17	0.35	0.13	0.20	0.18
Cr2O3	51.76	49.80	49.89	50.59	54.97	43.36	41.59	42.30	43.82	44.63
Fe2O3	5.11	3.00	3.35	2.88	2.70	4.82	5.82	3.61	5.54	5.13
MgO	11.00	12.91	13.03	13.04	13.28	13.54	11.20	15.58	12.34	11.98
MnO	0.23	0.22	0.20	0.20	0.18	0.16	0.23	0.20	0.20	0.25
FeO	16.07	14.09	14.57	14.43	13.04	14.67	17.85	12.53	15.73	17.27
NiO	0.13	0.14	0.08	0.13	0.12	0.14	0.17	0.15	0.12	0.13
ZnO	0.09	0.07	0.05	0.07	0.13	0.05	0.14	0.06	0.13	0.06
Total	96.95	97.73	99.28	99.11	98.13	99.54	98.57	99.39	98.33	100.77
Mg#	0.550	0.621	0.615	0.618	0.646	0.622	0.528	0.703	0.584	0.553
Cr#	**0.744**	**0.661**	**0.653**	**0.661**	**0.734**	**0.566**	**0.577**	**0.537**	**0.598**	**0.592**
Fe^3# (corr)	0.066	0.037	0.048	0.041	0.034	0.066	0.072	0.051	0.067	0.061
Fe^3/SumFe (pr)	0.225	0.163	0.172	0.155	0.162	0.230	0.228	0.255	0.242	0.212
Fe^3/SumFe (corr)	0.225	0.163	0.209	0.180	0.162	0.268	0.228	0.255	0.242	0.212
Fa (Ol)		0.074	0.050	0.044	0.042	0.067		0.061		
T°C (Balhaus)		778	657	625	682	709		770		
fO_2 (FMQ)		**0.14**	**1.46**	**1.43**	**1.08**	**1.50**		**1.13**		

Sample	SD49	SD89a	UAE120b	UAE138_chr	UAE140	UAE155B	UAE393	UAE4803	UAE94
Groups	Chromitite	Chromitite	Chromitite	Chromitite	Chromitite	Chromitite	Chromitite	Chromitite	Chromitite
Rock Type	Chr	Chr	Chr	Chr	Chr	Chr	Chr	Chr	Chr
Region	ASWS	KFN	KFS	KFN	KFN	KFN	KFN	ASWS	KFN
Region	Mantle	Mantle	Mantle	Mantle	Mantle	Mantle	Mantle	Mantle	Mantle
Spinel shape	SI/cusp	EU	SI/cusp	SI/EU	EU	SI/cusp	SI/cusp	SI/cusp	SI/cusp
Cal	**new cal**	**new cal**	old cal	**new cal**	old cal	**new cal**	**new cal**	**new cal**	old cal
n=	24	17	4	4	22	5	24	4	4
SiO2	0.02	0.02	0.02	0.03	0.03	0.03	0.02	0.04	0.03
TiO2	0.17	0.04	0.39	0.09	0.03	0.15	0.08	0.43	0.09
Al2O3	25.31	7.92	22.82	8.54	7.94	17.53	9.63	17.69	9.12
V2O3	0.17	0.18	0.15	0.05	0.21	0.08	0.08	0.06	0.07
Cr2O3	42.92	62.43	43.37	63.53	60.42	52.01	61.53	50.59	57.63
Fe2O3	3.46	1.14	3.16	1.55	2.37	2.93	1.70	3.14	2.61
MgO	14.54	10.66	14.23	13.59	9.20	14.42	12.90	14.17	10.43
MnO	0.18	0.23	0.21	0.15	0.26	0.13	0.18	0.17	0.29
FeO	13.88	16.44	13.14	12.54	18.62	12.69	13.60	13.13	16.14
NiO	0.13	0.07	0.12	0.07	0.05	0.13	0.08	0.19	0.02
ZnO	0.05	0.09	0.03	0.00	0.16	0.03	0.05	0.09	0.10
Total	100.84	99.23	97.62	100.13	99.29	100.14	99.83	99.69	96.53
Mg#	0.652	0.536	0.659	0.659	0.6124	0.670	0.628	0.660	0.535
Cr#	**0.532**	**0.841**	**0.560**	**0.833**	**0.852**	**0.666**	**0.811**	**0.657**	**0.809**
Fe^3# (corr)	0.046	0.026	0.038	0.029	0.0259	0.044	0.028	0.048	0.034
Fe^3/SumFe (pr)	0.185	0.059	0.179	0.099	0.0748	0.174	0.102	0.183	0.127
Fe^3/SumFe (corr)	0.217	0.109	0.179	0.155	0.1253	0.221	0.136	0.229	0.127
Fa (Ol)	0.063	0.050	0.064	0.037		0.046	0.044	0.060	0.070
T°C (Balhaus)	686	672	720	725		708	717	781	738
fO_2 (FMQ)	**1.04**	**0.33**	**0.58**	**0.98**		**1.35**	**0.61**	**0.97**	**0.09**

Appendix D: Chrome-spinel analyses by electron microprobe

Sample	**UAE323**	**03UR32**	**SD496**	**SD540**	**UAE238**	**UAE257**	**UAE275**	**UAE2808**	**UAE2832**
Groups	Harzburgite	Dunite	Dunite	Dunite	Dunite	Dunite	Dunite	Dunite	Dunite
Rock Type	**Hz**	**Du**	**Du**	**Du**	**Du**	**Du**	**Du**	**Du**	**Du**
Region	KFS	KFS	ASWN	KFN	KFS	KFS	KFS	ASWS	ASWS
Region	MTZ	MTZ	MTZ	MTZ	MTZ	MTZ	MTZ	MTZ	MTZ
Spinel shape	HL	SI	SI	SI	SI/cuspate	SI/cuspate	SI	SI	SI
Cal	old cal	old cal	**new cal**	**new cal**	old cal	**new cal**	old cal	old cal	old cal
n=	4	4	10	24	4	4	4	4	4
SiO2	0.03	0.03	0.07	0.03	0.19	0.04	0.02	0.04	0.03
TiO2	0.10	0.26	0.24	0.21	0.45	0.23	0.22	0.34	0.39
Al2O3	24.59	19.81	12.03	33.32	23.04	23.86	25.56	24.52	17.44
V2O3	0.25	0.12	0.17	0.17	0.16	0.15	0.13	0.14	0.12
Cr2O3	40.93	44.06	50.72	30.46	34.14	39.58	31.80	32.68	43.51
Fe2O3	1.54	5.17	7.10	5.62	9.56	5.50	9.81	8.99	7.39
MgO	11.07	11.31	7.35	12.98	10.39	10.70	9.32	11.20	9.99
MnO	0.18	0.28	0.32	0.21	0.22	0.24	0.25	0.28	0.27
FeO	17.64	17.15	22.66	17.45	18.75	19.10	20.98	17.83	18.80
NiO	0.11	0.09	0.04	0.13	0.15	0.12	0.11	0.14	0.10
ZnO	0.22	0.17	0.18	0.22	0.12	0.17	0.18	0.14	0.11
Total	96.64	98.44	100.88	100.80	97.17	99.67	98.36	96.31	98.13
Mg#	0.529	0.541	0.366	0.572	0.494	0.508	0.443	0.536	0.487
Cr#	**0.528**	**0.599**	**0.739**	**0.380**	**0.499**	**0.527**	**0.455**	**0.472**	**0.626**
Fe^3# (corr)	0.020	0.064	0.110	0.070	0.115	0.062	0.119	0.116	0.092
Fe^3/SumFe (pr)	0.077	0.217	0.219	0.230	0.307	0.174	0.300	0.332	0.263
Fe^3/SumFe (corr)	0.077	0.217	0.275	0.252	0.307	0.210	0.300	0.332	0.263
Fa (Ol)	0.101	0.077	0.102	0.110	0.107	0.100	0.118	0.091	0.092
T°C (Balhaus)	634	663	654	651	671	645	603	658	684
***f*O$_2$ (FMQ)**	**-1.14**	**1.21**	**1.64**	**1.15**	**1.81**	**0.88**	**1.89**	**2.15**	**1.53**

Sample	**UAE325**	**UAE33**	**UAE353**	**UAE412**	**UAE430**	**UAE535**	**UAE573**	**UAE586**	**UAE607**	**UAE763**
Groups	Dunite	Dunite	Dunite	Dunite	Dunite	Dunite	Dunite	Dunite	Dunite	Dunite
Rock Type	**Du**	**Du**	**Du**	**Du**	**Du**	**Du**	**Du**	**Du**	**Du**	**Du**
Region	KFS	KFS	KFN	KFS	KFS	ASWS	ASWS	ASWS	KFS	ASWS
Region	MTZ	MTZ	MTZ	MTZ	MTZ	MTZ	MTZ	MTZ	MTZ	MTZ
Spinel shape	SI	SI	SI/EU	SI	SI	SI	SI	SI/EU	SI	SI
Cal	old cal	**new cal**	old cal	old cal	old cal	**new cal**	old cal	old cal	old cal	old cal
n=	5	4	6	4	10	4	4	4	4	4
SiO2	0.18	0.03	0.03	0.01	0.02	0.03	0.02	0.02	0.03	0.02
TiO2	1.89	0.18	0.21	0.47	0.36	0.32	0.37	0.40	0.25	0.29
Al2O3	3.56	15.13	14.74	23.33	26.99	24.88	22.36	15.67	12.85	23.14
V2O3	0.34	0.18	0.08	0.16		0.12	0.13	0.10	0.10	0.19
Cr2O3	13.78	49.56	53.28	38.96	33.25	36.25	41.88	43.03	47.78	36.42
Fe2O3	46.05	4.94	2.74	4.50	7.64	7.37	4.80	8.64	7.20	8.09
MgO	1.33	8.75	10.90	10.47	11.22	11.38	13.48	8.44	8.61	10.87
MnO	0.62	0.30	0.30	0.27	0.49	0.28	0.20	0.34	0.26	0.24
FeO	30.14	20.74	17.44	18.80	18.33	17.99	14.13	20.61	19.71	18.07
NiO	0.21	0.04	0.08	0.10		0.12	0.17	0.08	0.13	0.15
ZnO	0.18	0.21	0.10	0.21		0.15	0.13	0.19	0.13	0.18
Total	98.29	100.06	99.91	97.29	98.32	98.90	97.68	97.52	97.05	97.64
Mg#	0.073	0.430	0.528	0.500	0.521	0.531	0.632	0.423	0.439	0.519
Cr#	**0.722**	**0.687**	**0.708**	**0.528**	**0.452**	**0.494**	**0.557**	**0.648**	**0.714**	**0.514**
Fe^3# (corr)	0.696	0.076	0.034	0.056	0.090	0.098	0.059	0.111	0.094	0.099
Fe^3/SumFe (pr)	0.577	0.178	0.126	0.182	0.272	0.273	0.241	0.278	0.250	0.291
Fe^3/SumFe (corr)	0.577	0.221	0.126	0.182	0.272	0.306	0.241	0.278	0.250	0.291
Fa (Ol)		0.095	0.065	0.090		0.101	0.079	0.091	0.082	0.110
T°C (Balhaus)		657	654	609		684	761	637	652	701
***f*O$_2$ (FMQ)**		**1.11**	**0.34**	**0.93**		**1.64**	**0.95**	**1.92**	**1.73**	**1.45**

Appendix D: Chrome-spinel analyses by electron microprobe

Sample	**SD262_chr**	**SD409_chr**	**SD444**	**SD497**	**UAE65_chr**	**SD383b**	**SD409_du**	**SD459**	**UAE4056**
Groups	Chromitite	Chromitite	Chromitite	Chromitite	Chromitite	Dunite	Dunite	Dunite	Dunite
Rock Type	**Chr**	**Chr**	**Chr**	**Chr**	**Chr**	**Chr-Du**	**Chr-Du**	**Chr-Du**	**cpx-chr-du**
Region	ASWS	ASWS	ASWS	ASWN	KFS	FIZH	ASWS	KFS	ASWS
Region	MTZ	MTZ	MTZ	MTZ	MTZ	MTZ	MTZ	MTZ	MTZ
Spinel shape	SI/EU	SI/cuspate	SI/cuspate	EU	SI/EU	EU	SI/EU	SI/EU	EU
Cal	old cal	old cal	**new cal**	**new cal**	**new cal**	**new cal**	old cal	**new cal**	**new cal**
n=	**4**	**4**	23	5	3	5	**4**	**4**	**4**
SiO2	0.03	0.02	0.02	0.02	0.03	0.05	0.03	0.03	0.01
TiO2	0.49	0.28	0.51	0.26	0.25	0.17	0.27	0.20	0.34
Al2O3	23.00	12.45	23.53	23.35	22.70	13.45	12.14	19.90	14.67
V2O3	0.19	0.10	0.11	0.08	0.10	0.18	0.11	0.11	0.15
Cr2O3	41.86	53.80	42.78	43.99	44.81	54.82	53.80	45.55	50.53
Fe2O3	3.67	4.94	3.59	3.46	3.76	3.22	5.10	4.97	4.16
MgO	12.72	12.67	14.11	15.14	14.06	10.41	11.52	11.63	10.39
MnO	0.21	0.23	0.18	0.21	0.16	0.29	0.23	0.28	0.21
FeO	15.65	14.11	14.02	12.07	14.10	18.30	16.00	17.14	17.98
NiO	0.09	0.09	0.15	0.16	0.07	0.03	0.08	0.06	0.06
ZnO	0.06	0.06	0.07	0.05	0.06	0.12	0.08	0.15	0.11
Total	97.97	98.75	99.08	98.79	100.10	101.04	99.35	100.02	98.60
Mg#	0.592	0.616	0.643	0.692	0.640	0.503	0.562	0.548	0.508
Cr#	**0.550**	**0.744**	**0.549**	**0.558**	**0.570**	**0.732**	**0.748**	**0.606**	**0.698**
Fe^3# (corr)	0.044	0.061	0.049	0.049	0.052	0.054	0.063	0.066	0.067
Fe^3/SumFe (pr)	0.174	0.241	0.191	0.211	0.194	0.134	0.223	0.209	0.174
Fe^3/SumFe (corr)	0.174	0.241	0.221	0.250	0.233	0.189	0.223	0.231	0.226
Fa (Ol)			0.061	0.050	0.061	0.100	0.068	0.082	0.077
T°C (Balhaus)			690	700	697	773	745	695	696
fO_2 (FMQ)			**1.19**	**1.46**	**1.24**	**0.28**	**1.25**	**1.12**	**1.22**

Sample	**SD150**	**UAE2814**	**UAE503**	**UAE566**	**UAE612**	**UAE627**	**UAE65_du**	**UAE492**	**03UR24**
Groups	Dunite	Dunite	Dunite	Dunite	Dunite	Dunite	Dunite	Dunite	Dunite
Rock Type	**Cpx-Du**	**Cpx-Du**	**Cpx-Du**	**Cpx-Du**	**Cpx-Du**	**Cpx-Du**	**Cpx-Du**	**Plag-cpx-Du**	**Plag-Du**
Region	ASWS	ASWS	ASWS	ASWS	KFS	ASWN	KFS	ASWS	KFS
Region	MTZ	MTZ	MTZ	MTZ	MTZ	MTZ	MTZ	MTZ	MTZ
Spinel shape	SI/cuspate	SI	SI	SI	SI	SI	SI/EU	SI	SI
Cal	old cal	old cal	old cal	old cal	**new cal**	old cal	**new cal**	old cal	old cal
n=	**4**	**4**	**4**	**6**	**4**	**4**	**4**	10	**4**
SiO2	0.03	0.03	0.03	0.03	0.21	0.03	0.02	0.03	0.02
TiO2	0.53	0.30	0.32	0.25	0.34	0.37	0.23	0.219	0.11
Al2O3	20.41	22.78	20.07	21.05	29.61	24.35	22.20	24.41	35.20
V2O3	0.20	0.24	0.18	0.20	0.14	0.23	0.12		0.11
Cr2O3	34.61	37.34	42.63	42.52	34.45	36.47	43.41	37.08	29.69
Fe2O3	11.22	7.08	5.17	4.86	4.53	7.93	4.79	6.16	2.90
MgO	9.35	9.86	11.10	10.43	12.95	8.21	11.82	10.46	13.45
MnO	0.30	0.30	0.22	0.27	0.23	0.318	0.28	0.55	0.19
FeO	19.78	19.55	17.88	18.70	16.50	20.82	17.38	18.69	16.19
NiO	0.17	0.10	0.17	0.06	0.18	0.15	0.09		0.13
ZnO	0.14	0.23	0.14	0.16	0.23		0.07		0.26
Total	96.74	97.81	97.90	98.52	99.37	98.87	100.38	97.62	98.25
Mg#	0.458	0.474	0.533	0.499	0.572	0.391	0.548	0.499	0.599
Cr#	**0.532**	**0.524**	**0.588**	**0.575**	**0.438**	**0.501**	**0.567**	**0.505**	**0.361**
Fe^3# (corr)	0.142	0.087	0.070	0.059	0.073	0.070	0.067	0.073	0.034
Fe^3/SumFe (pr)	0.340	0.249	0.230	0.190	0.231	0.186	0.200	0.227	0.147
Fe^3/SumFe (corr)	0.340	0.249	0.230	0.190	0.260	0.186	0.240	0.227	0.147
Fa (Ol)	0.128	0.120	0.104	0.105	0.088	0.133	0.081		0.104
T°C (Balhaus)	715	665	735	675	640	568	670		621
fO_2 (FMQ)	**1.80**	**1.14**	**0.82**	**0.59**	**1.50**	**0.80**	**1.26**		**0.11**

Appendix D: Chrome-spinel analyses by electron microprobe

Sample	**UAE370**	**UAE481**	**UAE236**	**UAE448**	**UAE482**	**UAE517**	**SD131a**	**UAE225**	**UAE263**
Groups	Dunite	Dunite	Gabbro	Gabbro	Gabbro	Gabbro	Gabbro	Gabbro	Gabbro
Rock Type	**Plag-Du**	**Plag-Du**	**Troctolite**	**Troctolite**	**Troctolite**	**Ol-Gabbro**	**Ol-Gabbro**	**Ol-Gabbro**	**Ol-Gabbro**
Region	KFS	ASWS	KFS	ASWS	ASWS	ASWS	ASWS	KFS	KFS
Region	MTZ	MTZ	MTZ	MTZ	MTZ	MTZ	MTZ	MTZ	MTZ
Spinel shape	SI	SI							
Cal	old cal	old cal	old cal	old cal	**new cal**	old cal	old cal	old cal	old cal
n=	4	4	4	10	23	1	4	10	8
SiO_2	0.03	0.02	0.05	0.03	0.03	0.04	0.03	0.02	0.01
TiO_2	0.13	0.44	0.26	1.05	0.58	2.17	0.37	0.14	0.07
Al_2O_3	34.62	27.07	24.75	16.76	36.18	13.44	23.32	29.83	28.26
V_2O_3	0.12	0.13	0.19		0.22		0.24		
Cr_2O_3	28.71	38.27	36.47	34.22	26.48	27.36	38.03	33.13	34.63
Fe_2O_3	3.91	2.82	4.64	15.34	5.78	21.72	4.99	3.02	4.72
MgO	12.89	13.85	9.54	6.92	14.24	3.01	10.68	10.12	10.16
MnO	0.23	0.16	0.23	0.68	0.21	0.59	0.23	0.56	0.52
FeO	16.75	14.37	20.00	23.75	16.03	30.12	18.04	19.69	19.89
NiO	0.13	0.12	0.11		0.21		0.10		
ZnO	0.21	0.17	0.18		0.14		0.17		
Total	97.73	97.42	96.43	98.77	100.11	98.51	96.20	96.52	98.26
Mg#	0.580	0.634	0.460	0.341	0.614	0.151	0.514	0.478	0.476
Cr#	**0.357**	**0.487**	**0.497**	**0.578**	**0.329**	**0.577**	**0.522**	**0.427**	**0.451**
Fe^3# (corr)	0.046	0.034	0.057	0.197	0.067	0.303	0.062	0.035	0.055
Fe^3/SumFe (pr)	0.179	0.156	0.174	0.366	0.249	0.392	0.201	0.120	0.175
Fe^3/SumFe (corr)	0.179	0.156	0.174	0.366	0.2581	0.392	0.201	0.120	0.175
Fa (Ol)	0.100	0.089	0.111	0.151	0.090	0.219	0.105	0.131	0.128
T°C (Balhaus)	593	735	589	683	620	561	663	575	602
fO_2 (FMQ)	**0.73**	**-0.07**	**0.69**	**2.12**	**1.58**	**2.47**	**0.75**	**-0.22**	**0.46**

Sample	**UAE277**	**UAE322**	**UAE340**	**UAE422**	**UAE469**	**UAE3996a_chr**	**SD262_wehr**	**UAE126**	**UAE3996a_wehr**
Groups	Gabbro	Gabbro	Gabbro	Gabbro	Gabbro	Wehrlite	Wehrlite	Wehrlite	Wehrlite
Rock Type	**Ol-Gabbro**	**Ol-Gabbro**	**Ol-Gabbro**	**Ol-Gabbro**	**Ol-Gabbro**	**chr-wehr**	**Wehrlite**	**Wehrlite**	**Wehrlite**
Region	KFS	KFS	KFN	KFS	ASWS	ASWS	ASWS	KFN	ASWS
Region	MTZ	MTZ	MTZ	MTZ	MTZ	MTZ	MTZ	MTZ	MTZ
Spinel shape									
Cal	old cal	old cal	old cal	old cal	old cal	**new cal**	old cal	**new cal**	old cal
n=	10	1	9	9	9	3	3	4	4
SiO_2	0.02	0.02	0.03	0.03	0.05	0.03	0.02	0.03	0.02
TiO_2	0.26	0.00	0.27	0.89	5.31	0.46	0.37	0.06	0.42
Al_2O_3	28.61	31.62	28.17	22.64	6.73	24.02	24.52	34.50	23.09
V_2O_3						0.15	0.18	0.12	0.18
Cr_2O_3	34.96	31.20	32.88	36.27	15.00	41.48	38.23	30.76	40.19
Fe_2O_3	3.89	4.68	6.14	6.83	35.52	4.80	4.24	3.74	6.04
MgO	11.30	9.76	9.03	9.72	2.02	12.42	10.38	13.16	10.41
MnO	0.55	0.43	0.50	0.56	0.37	0.22	0.26	0.18	0.27
FeO	18.21	21.31	22.05	19.90	33.39	17.16	19.17	17.00	19.90
NiO						0.14	0.05	0.02	0.13
ZnO						0.05	0.18	0.20	0.14
Total	97.81	99.08	99.12	96.93	98.41	100.92	97.60	99.77	100.79
Mg#	0.525	0.449	0.421	0.465	0.097	0.564	0.492	0.580	0.483
Cr#	**0.450**	**0.398**	**0.439**	**0.518**	**0.599**	**0.537**	**0.511**	**0.374**	**0.539**
Fe^3# (corr)	0.045	0.053	0.072	0.084	0.574	0.066	0.052	0.048	0.084
Fe^3/SumFe (pr)	0.159	0.164	0.199	0.234	0.488	0.202	0.168	0.167	0.217
Fe^3/SumFe (corr)	0.159	0.164	0.199	0.234	0.488	0.239	0.168	0.193	0.255
Fa (Ol)	0.114	0.170	0.156	0.113	0.236	0.084		0.119	0.104
T°C (Balhaus)	628	586	589	650	672	682		655	655
fO_2 (FMQ)	**0.25**	**0.16**	**0.69**	**1.22**	**3.31**	**1.19**		**0.41**	**1.31**

Appendix D: Chrome-spinel analyses by electron microprobe

Sample	**UAE491**	**SD94**	**UAE252**	**UAE342**	**UAE345**	**SD142**	**SD436b_px**	**UAE111**	**UAE87**	**UAE629**
Groups	Pyroxenite	Pyroxenite	Pyroxenite	Pyroxenite	Pyroxenite	Gabbro	Pyroxenite	Pyroxenite	Pyroxenite	Pyroxenite
Rock Type	**Ol-cpxenite**	**Cpxenite**	**Cpxenite**	**Opxenite**	**Websterite**	**Ol-Gabbro**	**ol-Cpxenite**	**Ol-Opxenite**	**Ol-Opxenite**	**Websterite**
Region	ASWS	KFS	KFS	KFN	KFN	ASWS	ASWS	KFN	KFN	ASWN
Region	MTZ	MTZ	MTZ	MTZ	MTZ	Mantle	Mantle	Mantle	Mantle	Mantle
Spinel shape										
Cal	**new cal**	**new cal**	old cal	old cal	old cal	old cal	**new cal**	old cal	**new cal**	old cal
n=	2	4	9	4	4	4	5	4	5	4
SiO2	0.03	0.03	0.03	0.02	0.06	0.03	0.03	0.03	0.01	0.05
TiO2	0.23	0.18	0.14	0.17	0.18	0.24	0.29	0.09	0.03	0.31
Al2O3	29.75	27.18	28.90	15.28	19.18	23.12	28.21	6.27	8.45	17.88
V2O3	0.22	0.28			0.44	0.28	0.21	0.34	0.24	0.46
Cr2O3	33.09	30.83	28.28	43.92	39.66	40.22	34.51	60.58	57.93	38.00
Fe2O3	3.63	9.29	8.38	7.13	7.69	4.32	5.36	2.39	4.43	10.07
MgO	9.75	8.19	8.38	7.02	6.21	10.26	10.69	7.00	8.11	5.01
MnO	0.32	0.38	0.53	0.68	0.31	0.27	0.23	0.32	0.33	0.44
FeO	20.95	23.24	22.27	21.84	24.66	19.10	19.83	21.48	20.58	26.27
NiO	0.09	0.05			0.05	0.13	0.09	0.03	0.05	0.04
ZnO	0.39	0.12			0.50	0.24	0.24	0.10	0.18	0.24
Total	98.45	99.75	96.94	96.07	98.93	98.20	99.69	98.63	100.35	98.77
Mg#	0.455	0.385	0.401	0.364	0.311	0.490	0.491	0.367	0.413	0.253
Cr#	**0.346**	**0.432**	**0.396**	**0.658**	**0.581**	**0.539**	**0.451**	**0.866**	**0.821**	**0.588**
Fe^{3}# (corr)	0.054	0.121	0.100	0.092	0.113	0.053	0.072	0.030	0.075	0.128
Fe^{3}/SumFe (pr)	0.142	0.264	0.252	0.226	0.222	0.173	0.199	0.088	0.1637	0.255
Fe^{3}/SumFe (corr)	0.171	0.293	0.252	0.226	0.262	0.173	0.228	0.088	0.2189	0.255
Fa (Ol)	0.118	0.143	0.157			0.108	0.130		0.087	0.151
T°C (Balhaus)	550	568	558			641	646		693	525
fO_2 (FMQ)	**0.72**	**1.75**	**1.38**			**0.46**	**0.85**		**1.15**	**1.55**

Appendix E: Analysis of Ga in chrome-spinel by LA-ICP-MS

E.1 Method

A new method was developed in this study to analyse chrome-spinel by LA-ICP-MS using matrix-matched standards. The results have been submitted for publication to Geostandards and Geoanalytical Research and the manuscript is reproduced below. In summary, matrix-matched standards are preferred to synthetic NIST glasses, which had been used in all previous LA-ICP-MS analyses of chrome-spinel. However, because of the lack of chrome-spinel reference material, matrix-matched standards were characterised for Ga in this study by in situ microdrilling of the chrome-spinel standard followed by dissolution and conventional analysis by ICP-MS. Chromitite samples, which had been analysed for Ga by proton microprobe (Paktunc and Cabri, 1995), were then analysed by LA-ICP-MS using these matrix-matched standards. This demonstrated that the two methods produce similar values for Ga.

The application of the new LA-ICP-MS method to analyse chrome-spinel in peridotites is described in Chapter 5, and the accompanying results is given in Section E.2 together with the sample descriptions in Section E.3.

'Quantitative analysis of trace elements in chrome-spinel by Laser Ablation ICP-MS using matrix-matched standards: are NIST glasses suitable for accurate calibration of chromites?'

S. A. S. Dare[1], I. McDonald[1], J. A. Pearce 1 and M. T. Styles[2]

[1] School of Earth, Ocean and Planetary Sciences, Cardiff University, Cardiff, CF10 3YE, U.K. (DareSA@cf.ac.uk)

[2] British Geological Survey, Keyworth, Nottingham, NG12 5GG, U.K.

1 Abstract

Laser ablation inductively coupled plasma mass spectrometry (LA-ICP-MS) is widely used for rapid in situ analyses of trace elements in chromites, particularly for the discrimination of diamond indicator chromites. Quantification of trace elements has previously utilised synthetic glasses (NIST CRM 612/610) to calibrate chromites. Matrix-matched standards, characterised in this study by electron microprobe, ion microprobe and solution ICP-MS analyses, demonstrate that chrome-spinels and NIST glasses still ablate differently for many of the elements. Inter-element fractionation effects due to different ablation rates of various elements produce inaccurate values for many trace elements in chromite when using NIST glasses as an external standard. The degree of inaccuracy varies with laser frequency, composition of NIST glass used and the element chosen as an internal standard, all of which have varied from study to study in the past.

The analysis of chrome-spinel by laser Ablation-ICP-MS using matrix-matched standards eliminates inter-element fractionation effects and produces accurately quantified Ti, V Mn, Zn, Ni, Co, Ga and Sc concentrations in chromites from podiform and stratiform chromitites, with detection limits < 1μg g $^{-1}$ for Ga and Sc. Therefore, this study confirms the need to develop good international chromite standards and replace NIST glasses in the calibration of trace elements in chromites by LA-ICP-MS analysis. Until then, serious problems will remain when comparing

chromite data between studies that have utilised different calibration conditions. This could be particularly important when using trace elements in chromites as diamond indicators and could lead to the misidentification of potentially diamondiferous chromites.

2 Introduction

Trace elements in chrome-spinel (chromite) have a range of important applications: (a) to determine mineral-mineral partition coefficients of natural chromites (Griffin et al. 1993, Ewart and Griffin 1994, Eggins et al. 1998, Norman 1998, Glaser et al. 1999, Grégoire et al. 2000) (b) to determine mineral-melt partition coefficients of experimentally doped spinel (Horn et al. 1994), (c) to improve the discrimination of chromites in the exploration for diamonds (e.g. Griffin et al. 1993, Denny 1998, Richardson 1999), (d) the tectonic discrimination of mafic-ultramafic rocks (e.g. Dick and Bullen 1984, Arai 1992, Parkinson and Pearce 1998, Pearce et al. 2000, Barnes and Roeder 2001, Dare et al. 2007) and (e) comparative planetary mineralogy of basalts (Papike et al. 2002, 2004, 2005, Karner et al. 2005).

Chromites typically contain a limited set of trace elements that are measurable by high-quality EMP analysis using longer counting times than for routine-major element analysis, for example, Mn, Co, Ni, Zn, Ti and V. EMP systems provide rapid and efficient mineral identification and major element analysis, but with detection limits around 100 ppm they provide little scope for trace elements studies. Trace elements, such as Sc and Ga are measurable in chromite separates using neutron activation analysis (NAA), particle-induced X-ray emission (PIXE) and energy dispersive X-ray fluorescence (EDXRF) (Kurat et al. 1980, Stosch 1981, McKay and Mitchell 1988, Potts et al. 1992, Nayak and Vijayan 2006). However, bulk-rock sampling of trace elements are often compromised by the presence of trace silicate impurities in the opaque spinel separates despite ultra-clean mineral separates (Eggins et al. 1998).

Microbeam analytical techniques, with detection limits around 1 ppm, are especially well-suited for the in situ measurement of trace-elements due to their high spatial resolution and their ability to avoid inclusions that can compromise the trace-element compositions of mineral separates (Foley et al. 1996, Eggins et al. 1998).

Microbeam techniques have measured Sc, Ga, Y, Zr and Nb in chromite by proton microprobes (O'Reilly et al. 1991, Griffin et al. 1993, Ewart and Griffin 1994, Griffin and Ryan 1995, Paktunc and Cabri 1995, Paktunc and Hulbert 1996), ion microprobes (Papike et al. 2002, Taylor et al. 2003) and laser ablation-ICP-MS (LA-ICP-MS) (Horn et al. 1994, Watling et al. 1995, Chen et al. 1997, Forsythe and Allan 1998, Eggins et al. 1998, Norman 1998, Denny 1998, Richardson 1999, Glaser et al. 1999, Grégoire et al. 2000). LA-ICP-MS is the principal method for rapid in situ trace element analysis (1 – 2 minutes for analyse an area 40 μm diameter by 250 μm long) compared to much longer analysis times for proton microprobe (6 – 8 minutes on average but up to 22 minutes for an area 30 um diameter (Griffin et al. 1994, Paktunc and Cabri 1995)). LA-ICP-MS instruments have also become more widely accessible than proton microprobes, e.g. Ryan (1995) reported only 18 laboratories worldwide which run proton microprobes.

Quantitative analysis relies on well-characterised external standards and, to date, in situ trace element analyses of chromites using LA-ICP-MS have relied on NIST glasses as a certified reference material (CRM) (summarized by Pearce et al. 1997). The relatively low concentrations of Fe, Mg, Ti and Cr limit the usefulness of NIST glasses as external standards for chromite (Norman et al. 1996). More importantly the ablation behaviour during LA-ICP-MS analysis is matrix-dependent and matrix-matched calibration standards lead to the most accurate determinations (Jackson 2001). Unfortunately, there is still a lack of international chromite standards for in situ trace element work and the EMPA chromite standards UCB396 and USNM 117075 are only certified for a limited number of minor elements (Jarosewich et al. 1980).

The aim of this study is: 1) to characterise a selected suite of trace elements in matrix-matched standards for the LA-ICP-MS analysis of chromite; 2) to determine which of these selected suite of trace elements in chromites are measurable by LA-ICP-MS using a UV 213 nm laser; 3) to assess the accuracy of calibrating chromites using NIST glass standards and 4) to assess the accuracy and quality of data of calibrating chromites using matrix-matched standards.

The trace elements selected for analysis in this study are trivalent cations Sc^{3+}, Ga^{3+} and Y^{3+} because trivalent cations, which occupy the Y (Cr, Al) site of chromite, are most useful for petrogenetic and tectonic discrimination (e.g. Cr# [Cr/ (Cr + Al)], V, Ti and Fe^{3+}/ Total Fe) (e.g. Dick and Bullen 1984, Arai 1992, Parkinson and Pearce 1998, Pearce et al. 2000, Barnes and Roeder 2001, Papike et al. 2002, 2004, 2005). Ni^{2+} was included among the suite of trivalent elements for LA-ICP-MS analysis because of its similar behaviour to Al^{3+} and Ga^{3+} in chromites (O'Reilly et al. 1991, Paktunc and Hulbert 1996). In addition, the suite of elements was extended to include Mn^{2+}, Co^{2+} and Zn^{2+} to test the accuracy of calibration of chromites using NIST glasses over the range of LA-ICP-MS operating conditions commonly employed in previous studies.

3 Analytical methods and experimental-set up

3.1 Analysis of chromite standards

3.1.1 Samples

Chromite grains used in this study are samples from podiform and stratiform chromitite ores taken from a variety of locations and chosen to represent a wide range of compositions. Podiform chromitites are from (i) the northernmost part of the Oman-U.A.E. ophiolite (UAE140, SD444 and SD159) and (ii) from the Jurassic Pindos-Vourinos ophiolites in northern Greece (79d, XM2, AR90-28). They cover a wide range in chromite compositions from depleted oceanic settings. Stratiform chromitites are from (i) the Proterozoic mafic-ultramafic intrusive complexes of Andohankiranomena, Madagascar (ADK185), (ii) the Upper Critical Zone of the Bushveld Complex, South Africa (UG-2) and (iii) the Great Dyke, Zimbabwe (GD4). All samples, except UG-2, contain coarse-grained chromite and are all massive chromitites (> 80% chr) except for XM-2 and AR90-28 which are chromitiferous dunites. The chromites are chemically homogeneous, except 79d, with very little alteration to ferritchromit at their rims. Silicate inclusions of olivine, clinopyroxene and amphibole, up to 10 μm in size, commonly form trails in some chromitite samples.

3.1.2 Major element determination

Major and minor elements of the chromites were characterised by in situ microbeam techniques. Chromite samples ADK185, GD4 and UG2 were analysed at Cardiff University using a Cambridge Instruments (ZEISS SMT) S360 scanning electron microscope (SEM), coupled to an Oxford Instruments INCA energy plus which included both energy dispersive (ED) and wave dispersive (WD) X-ray analysis system. Chromites were analysed with a 20 kV accelerating voltage, 20 nA beam current and a fixed beam size (approximately 10-15nm) with a live-time of 50 s for EDX. Ti and V were analysed by WDX with count times of 20 s plus 5 s background. Calibration was carried out on metals for all elements except MgO (for Mg) and wollastonite (for Ca).

Chromite samples UAE140, SD444, SD159, 79d, XM2 and AR90-28 were analysed using a fully automated Cameca SX-50 electron microprobe equipped with three wavelength-dispersive crystal spectrometers at the British Geological Survey. The EMP analytical conditions employed an accelerating voltage of 15 kV, with 20 nA beam current, a fixed beam size (approximately 1 μm), and standard PAP procedures. Calibration was carried out on metals (Ti, V, Mn, Ni and Zn), synthetic oxides (Al_2O_3, Cr_2O_3 and Fe_2O_3) and natural materials (forsterite and wollastonite). Counting times on peaks were 10 – 30s for Si, Fe, Mg, Cr, Ni, Mn, Zn, 40s for Al and V and 120s for Ti; backgrounds were counted on both the high and low wavelength sides of each peak for a total of 30s.

Multiple analyses, between 20 and 45 replicates, were acquired for precise quantification of each chromite grain by EMP and SEM analyses. The mean values of the major and trace elements compositions of the chromites are given in Table 1 and 2. Error, calculated from the standard deviation of multiple analyses ($1/(n-1)\sqrt{(n_1^2+n_2^2+n_3^2+n_4^2)}$), and precision, measured by the 1σ relative standard deviation (RSD %), is given in Table 1 along with limits of detection and quantification. The detection and quantification limits are defined as three times and ten times the standard deviation on the background counts, respectively. Precision was good (i.e. <10% RSD) for the major and minor elements analysed by the electron microprobe except where the minor elements, e.g. Si, Mn, Ni, Zn and Ti, were near detection limits.

3.1.3 Trace element determination

3.1.3.1 Ion microprobe

A Cameca ims-4f ion microprobe of the University of Edinburgh/NERC was used to analyses masses ^{26}Mg, ^{30}Si, ^{40}Ca, ^{45}Sc, ^{49}Ti, ^{51}V, ^{53}Cr, ^{54}Fe, ^{55}Mn, ^{59}Co, ^{60}Ni, ^{64}Zn, ^{71}Ga and ^{89}Y in chromitite samples 79d, XM2 and AR90-28 (and peridotite samples L90-35, LK44 and BT6B). Polished thin sections were bombarded with a primary beam of 15 keV 16O- ions focussed into a 5 – 30 um spot and a primary beam current of 5-6 nA. Backgrounds were measured at mass 130.5. Analytical and data reduction methods follow Zinner and Crozaz (1986). Ion microprobe intensities were normalised using the relationships of trace element/ ^{26}Mg ratios (normalised to known chromite MgO content determined from electron microprobe).

The ionprobe and electron microprobe analyses of the chromite samples agreed well, to within ± 10% difference for most elements, which is well within the combined analytical uncertainties of both methods (Figure 1, Table 2). The range of values determined by ion probe for the trace elements in chromite are as follows: Ca (28 – 150 μg g^{-1} element), Ga (103 – 392 μg g^{-1} element), Sc (0.6 – 12.9 μg g^{-1} element) and Y (0.004 – 0.021 μg g^{-1} element). Ga concentrations determined by the ion microprobe are much higher than those previously determined for unmetasomatised chromites (10-90 μg g^{-1}, e.g., Kurat et al. 1980, McKay and Mitchell 1988, Potts et al. 1992, Griffin et al. 1993, Ewart and Griffin 1994, Chen et al. 1997, Norman 1998, Eggins et al. 1998, Glaser et al. 1999) and indicate that the IE extrapolation for the calibration of Ga was invalid. Furthermore, Ga was not reported in ion microprobe analyses of chromites (Taylor et al. 2003).

However, the Sc concentrations determined by the ion microprobe are similar to the range previously determined for chromites (0.1 to 7 μg g^{-1}) (Kurat et al. 1980, McKay and Mitchell 1988, Potts et al. 1992, Griffin et al. 1993, Norman 1998, Eggins et al. 1998, Glaser et al. 1999, Grégoire et al. 2000, Taylor et al. 2003). Ca and Y concentrations determined by the ion microprobe in this study have similar values (17 – 307 and 0.008 – 0.034 μg g^{-1} respectively) to those determined in chromites by ion microprobe by Taylor et al. (2003).

3.1.3.2 Dissolution ICP-MS and ICP-OES

Chromitite samples UAE140, SD444, ADK185 and SD159, representative of the wide range in chromite compositions, were selected for trace element analysis of Ga and Sc by dissolution of chromite in lithium metaborate flux at Cardiff University. Unfortunately the chromite samples 79d, XM2 and AR90-28, which had previously been ion probed, were unsuitable for dissolution because the chromite grains were not large enough for microdrilling and massive chromitite 79d was compositionally inhomogeneous (e.g. Al_2O_3: 15.6 – 18.8 wt%).

Large (2-4 mm) chromite grains were hand-picked from coarsely-crushed chromitite samples UAE140, SD444 and ADK185 and mounted in polished blocks, from which approximately 2 mg of each sample was micro-drilled. However, SD159 was prepared by crushing 100 g of massive chromitite and reduced to a fine powder using an agate ball mill. Because chromite is a dissolution-resistant mineral (e.g. Merkle et al. 2004) the normal dissolution procedure (McDonald and Viljoen 2006) was modified by adding pure silica to the chromite powder to produce a composition more like that of a silicate rock that could be dissolved more easily.

Thus approximately 2 mg of each chromite sample were weighed accurately and mixed with 0.05 g of pure silica powder and 0.6 g of Li metaborate flux (Alfa Aesar Spectroflux 100B). Approximately 0.5 mL of a solution of 20% (weight/volume) lithium iodide (Alfa Aesar) was added as a non-wetting agent. The mixture was fused over a propane burner on a Claisse Fluxy automated fusion system. After fusion, the melt was automatically poured into a 250 mL Teflon beaker containing 10 mL of 10% HNO_3 and 15 mL of 18.2 MΩ deionised water and the solution was stirred using a magnetic stirrer until all of the glass fragments had dissolved. After dissolution, the solution was made up to 50 mL with 18.2 MΩ deionised water. Blanks were prepared in the same manner as above, but omitting the sample material.

Solutions were then analysed for Mg, Fe, Al (reported as oxides) and Sc (reported as elements in $\mu g\ g^{-1}$) using a JY Horiba ULTIMA2 ICP-OES system. 9.9 mL of the rock solution was spiked with 0.1 mL of a 100 $\mu g\ mL^{-1}$ Rh spike solution as an internal standard, producing a spiked rock solution in 2% HNO_3 for analysis on the ICP-OES. Typical instrumental parameters and limits of merit are given in McDonald and Viljoen (2006). Calibration was performed using blanks and solutions of the international certified reference material (CRMs) DTS-1, BIR 1, MRG1 and JA2, prepared as in McDonald and Viljoen (2006). Accuracy, assessed by analysis of CRM W2, prepared as an unknown and limits of detection and quantification are also given in Table 1.

Analyses for Mg, Fe, Ti (reported as oxides) and V and Ga (reported as elements in µg g^{-1}) were carried out by ICP-MS using the same unspiked solutions as prepared for the ICP-OES, except that the original rock solution was diluted 10 times with 2% HNO_3 and spiked with 1 mL of 5 ng mL^{-1} of In and Tl internal standards to correct for instrumental drift at low mid and high masses respectively. Analyses were performed using a Thermoelemental X series (X7) ICP-MS system. Typical instrumental parameters are those reported in McDonald and Viljoen (2006) with dwell time for Ga of 30s. Calibration was performed using blanks and solutions of CRMs W2, BIR 1, MRG1 and JA2, prepared as in McDonald and Viljoen (2006). Accuracy checks were assessed by analysis of CRM JB1-a and STM-1 prepared as unknowns and limits of detection and quantification are also given in Table 1.

Precision was good (<10% RSD) for the elements determined by solution except for Sc by ICP-OES (> 20%). Accuracy checks using CRMs during solution analysis demonstrated that they were accurate within 6% Relative Difference (%RD) of the certified concentrations.

Overall, the solution and electron microprobe analyses of the chromite standards agreed well, to within ± 10% difference for most elements, which is well within the combined analytical uncertainties of both methods (Figure 2, Table 1). There are larger deviations for V reflecting proximity to its detection limit. The high correlation for Fe in particular, between electron microprobe and solution analyses, demonstrated that the dissolution of chromite using Li metaborate flux was complete.

Ga concentrations in the chromite ICP-MS solutions varied from 20 to 60 µg g^{-1} and fell within the range (10-90 µg g^{-1}) previously determined for unmetasomatised chromites (Kurat et al. 1980, McKay and Mitchell 1988, Potts et al. 1992, Griffin et al. 1993, Ewart and Griffin 1994, Chen et al. 1997, Norman 1998, Eggins et al. 1998, Glaser et al. 1999). However, Sc concentrations in the chromite ICP-OES solutions, which varied from 5 to 45 µg g^{-1}, were much higher than previously published (0.1 to 7 µg g^{-1}) (Kurat et al. 1980, McKay and Mitchell 1988, Potts et al. 1992, Griffin et al.

1993, Norman 1998, Eggins et al. 1998, Glaser et al. 1999, Grégoire et al. 2000, Taylor et al. 2003) and was probably caused by silicate inclusions incorporated in the microdrilling of the chromites.

In summary, the Sc, Ca and Y were determined successfully in chromites 79d, XM2 and AR90-28 by ion microprobe whereas Ga (± Sc) were determined successfully in chromites UAE140, SD444, ADK185 and SD159by solution ICP-MS. These chromite samples were used to detect Ga, Sc, Ca and Y by LA-ICP-MS.

3.2 Method development of LA-ICP-MS

3.2.1 LA-ICP-MS Instrumentation

Recent developments in laser ablation systems have significantly improved ablation performance and the Nd:YAG UV (213 nm) laser produces a finer particle distribution, an increase in transport efficiency of the aerosol, better sensitivities, stable signals and reduced spalling (e.g. Jackson 2001). The laser ablation ICP-MS used at Cardiff University comprises a New Wave Research UP213 laser system coupled to a Thermo X Series ICP-MS.

Typical operating conditions for laser ablation analyses were based on the procedure of McDonald (2005) and are summarised in Table 3. Ablations were carried out under helium in the sealed laser cell, and the resulting vapour combined with argon before delivery into the ICP-MS. The ICP-MS was tuned using NIST612 glass to reduce low mass sensitivity while maintaining or enhancing mid to high mass sensitivity. Data were acquired in time-resolved analysis (TRA) mode using time slices of 250 milliseconds (ms). Typical acquisitions lasted 80 seconds and comprised 20 seconds measurement of the gas blank, followed by ablation of sample for approximately 60 seconds using a line 10 μm deep and approximately 250 μm long. A line was produced by moving the sample (at a fixed speed) while the laser beam is repetitively pulsed in a scanning (raster) mode. A scanning line reduces time dependent variations in the signal intensity which are related to crater formation of a single-spot and improves signal stability (Gonázlez et al. 2004). Changing the sampling strategy from a scanning line to a single spot reported no significant differences for inter-element fractionation or matrix dependency on NIST 610 and 612 glasses (Gonzalez et al. 2004).

Following background correction of the data, average signals obtained during laser sampling were normalized to an internal standard, usually a refractory, major element determined independently by electron microprobe (Fryer et al. 1995). Normalization by an internal standard corrected for differences in the absolute amount of material that was ablated and transported during an individual analysis and therefore must behave similarly to the elements under investigation (Norman et al. 1996, Chen et al. 1997). During a long run, the ICP-MS sensitivity can change and matrix effects can cause both signal enhancement and depression of analyte signals, and this was corrected by frequent recalibration and drift correction using a NIST glass.

Calibration lines are necessary to define the ICP-MS response over a range of concentrations and are constructed using a series of geochemical reference standards of similar composition to the unknown materials. The corrected average signal is then converted to a concentration value by calibration against the following external standards: (a) NIST 610 and NIST 612 and (b) matrix-matched chromite standards.

Limits of detection are a function of the background noise (gas blank) and sensitivity (Longerich et al. 1996). The detection and quantification limits were defined as three times and ten times the standard deviation of the gas blank, respectively, for each individual ablation run.

3.2.2 Operating conditions

Ga, Sc and Y were detected in chromite by ion microprobe and therefore, LA-ICP-MS experiments were carried out to optimise the operating conditions for the detection and quantification of these selected trace elements, by varying the line width (40 to 100 µm), the frequency of the laser (4 to 20 Hz) and the carrier gas (He + Ar or Ar only), the results of which are summarised in Table 4. Counting times were 60 s for Ga, 68 s for Y and 69 s for Sc.

Ga was quantified under all experimental conditions whereas Y was always below the detection limit. The quantification of Sc depended on experimental conditions with signal intensity optimised using helium gas, maximum laser frequency (20 Hz) and maximum line width (100 μm). At a fixed frequency and fixed line width, the signal intensity decreased six-fold when using argon only as the gas carrier as observed by Eggins et al. (1998), Jackson (2001) and Horn and Günther (2003). Therefore, when using argon Sc was only analysed above the quantification limit at maximum operating conditions (20 Hz, 100 μm) yet under helium gas Sc was quantified using lower frequencies and narrower line widths.

Higher frequencies (15 – 20 Hz) of the laser improved the signal intensity and thus quantification of trace elements. Moreover, at higher frequencies spatial resolution was improved because trace elements were still detected even when using narrower lines (< 50 μm), which were required for fine-grained chromites which are commonly found as accessory minerals in ultramafic rocks (e.g. Dare et al. 2007). Ga and Sc were chosen for calibration using NIST glasses and matrix matched standards at optimal conditions suitable for coarse-grained chromites (20 Hz, 100 μm) and fine-grained chromites (15 Hz, 40 μm).

For the extended suite of trace elements in chromite Ti, V, Mn, Co, Ni and Zn were quantified at all laser frequencies and line widths in helium gas. Counting times were 8 s for V, 10 s for Ni, 13 s for Ti, 15 s for Co and Mn and 32 s for Zn. Ca (counting time of 30 s) was never detected using argon and only detected, but below the quantification limit, using maximum operating conditions when using helium (Table 4).

3.2.3 Laser ablation characteristics of chromite and NIST glass

3.2.3.1 Ejecta deposits

In chromite, varying the carrier gas and the frequency of the laser has visible effects on the amount of fallout ejecta (material which is not fully vaporised) from the ablated lines. Helium, rather than pure argon, minimises deposition of ablation products around ablation sites and also improving sample transport efficiency (e.g. Eggins et al. 1998, Jackson 2001, Horn and Günther 2003). In this study, the amount of ejecta and the distance it was deposited away from the laser line increased dramatically when using helium gas; from very little ejecta at 4 Hz to widespread ejecta at 20 Hz, up to a distance of 200 μm (Figure 3a). The ejecta deposit increased along the ablation line. The fraction of ejecta redeposited using argon gas was much greater and its dispersion much greater (up to 500 μm) when compared to using helium gas. Cleavage spalling resulted in cubic-shaped indentations in the pit-wall and particles that were not vaporised but ejected out of the laser pit (Figure 3b). Therefore, it is important, especially at high laser frequencies and using argon gas, to ensure that the element chosen for the internal standard ablates in a similar way to the other elements in the vapour in order to correct for varying ablation yields due to ejecta fallout and cleavage spalling in chromite. In this study, ejecta fallout was minimal during the ablation of NIST glasses.

3.2.3.2 Signal stability of NIST glass

The effect on signal stability of changing the operating conditions was evaluated in this study by comparing time-resolved signal intensities over an ablation time-period of 30 s. The change in signal stability, and thus the ablation yield, with time can be quantified by an 'ablation yield index', i.e. the ratio of the mean signal intensity in the second half of the time-spectrum to the mean signal intensity of the first half of the time-spectrum, without normalisation by an internal standard. Comparing the ablation yield index for different elements can demonstrate whether or not these elements behave in the same way during ablation, which is crucial for normalising the data to an internal standard.

The ablation of NIST glass produces a flat, stable signal (equivalent to an ablation yield index of 1.0) for all elements throughout the time-spectrum, independent of laser frequency or gas carrier (e.g. Figure 4a and b). Therefore, there was no inter-element fractionation during the 30 s ablation of NIST glass in this study. In contrast, inter-element fractionation (elemental fractionation) was reported for NIST glass during longer ablation time-periods in which there is an increasing signal intensity for volatile elements (e.g. Si, Ga and Zn) compared to refractory elements (e.g. Ca, Al and Sc), which remained essentially constant over the 4 minute ablation time-period (Fryer et al. 1995, Norman et al. 1996). Fryer et al. (1995) defined an elemental fractionation index, using a 266 nm Nd:YAG laser system, whereby intensity ratios (analyte/Ca) of the second two minutes were divided by the intensity ratio of the first two minutes of a 4-minute ablation sequence of NIST 610. The using helium in this study, even at high frequencies such as 20 Hz. This is in contrast to previous LA-ICP-MS studies of chromites which used helium gas and low laser frequencies (4 – 10Hz) to minimise inter-element fractionation (Eggins et al. 1998; Glaser et al. 1999), and thus could not optimise the laser operating conditions to quantify trace elements.

In this study, only a few analyses of the Cr-rich chromite (UAE 140) at 20 Hz displayed inter-element fractionation using helium because the ablation yield indices of Mg (1.19), Sc (1.18) and Ga (1.23) were higher than those of Al (1.13) and Ca (1.09) (Table 5). On this basis therefore, Mg was chosen as the internal standard because Mg ablates at the same rate as Sc and Ga when inter-element fractionation rarely occurs during the ablation of chromite. For this case the fractionation index, using Mg as an internal standard, was 1.0 ± 0.05 for Al, Sc and Ga whereas the refractory element Ca was 0.9 relative to Mg.

It is well documented that helium gives a more stable signal than pure argon (e.g. Eggins et al. 1998, Jackson 2001, Horn and Günther 2003) and previous LA-ICP-MS studies of chromites which used argon have used low frequencies (4 – 10 Hz) to minimise inter-element fractionation (Norman et al. 1996, Norman 1998, Grégoire et al. 2000). In this study the unstable chromite signal was more pronounced using argon gas than helium gas, and not all the elements ablated in the same way e.g., Sc had a flat, constant signal whereas Al, and Mg more so, had increasingly unstable signals (Figure 5). Thus the ablation yield index in chromites varied among elements e.g. Sc (0.99 – 1.05), Al (1.11 – 1.22) and Mg (1.15 to 1.35) resulting in inter-element fractionation for all chromites when using argon gas at 20 Hz (Table 5). In this case, Mg or Al could not be used as an internal standard for Sc in chromites when using argon.

3.2.4 Verification of selected trace elements in matrix matched standards by LA-ICP-MS

Before using the matrix matched standards to test the accuracy of the NIST glass calibration their major element concentrations, determined by EMP and SEM analyses, and trace element concentrations, determined by solution ICP-MS and ion microprobe, must be verified by the signal response of LA-ICP-MS, which was normalised using Mg as an internal standard. The laser response forms a good correlation with the electron microprobe concentrations ($R^2 > 0.9$) for Al, Ti, Cr and Ni (Figure 8). The correlation coefficient is lower for V ($R^2 = 0.5$) but improves ($R^2 = 0.97$) when more chromite samples are added and indicates that the V concentration determined by the electron microprobe is less accurate when near its detection limit (Figure 8).

Importantly the laser response has a good correlation with the solution ICP-MS concentrations determined for Ga ($R^2 = 0.97$) but not for Sc (Figure 9). However, there is a good correlation between laser response and ion microprobe values for Sc in chromite samples XM-2, 79d and AR90-28 ($R^2 = 9.3$). Moreover, chromite solution SD159 lies on the ionprobe trend, SD444 lies within the limit of error, whereas UAE140 and ADK185 have much higher Sc in the ICP-OES solution than in the actual chromite.

For example, laser ablation of chromite and small inclusions of clinopyroxene and amphibole, which are commonly 10 µm diameter, show that the inclusions are enriched in Sc, Y and Ca but depleted in Mg, Al and Ga compared to chromite (Figure 10). During microdrilling of the chromite, in preparation for solution ICP-MS, the accidental incorporation of just a few inclusions contaminated the resulting 2 mg of chromite powder with additional Sc, Y and Ca, thus overestimating their true concentrations in chromite, as was the case for solutions SD444, UAE140 and ADK185. However, solution SD159 was not compromised by additional Sc, Y and Ca because it probably contained less clinopyroxene/ amphibole inclusions than did the other chromites.

The good correlation between laser response and pre-determined trace element concentrations verifies that Ga, determined by solution ICP-MS, and Sc, determined by ion probe, represent relative concentrations in the chromite; whereas Sc determined by solution ICP-MS is sometimes compromised by silicate inclusions in the chromite.

3.2.5 Calibration of chromites using NIST glass

NIST glasses (NIST 612 and NIST 610) were tested for their accuracy in the calibration of a Ga and Sc measured by LA-ICP-MS at optimal operating conditions

(20 Hz, 100 um) in the chromite standards UAE140, SD444, SD159 and ADK 185 (Ga measured independently by solution ICP-MS) and 79d, XM2, AR90-28 (Sc measured independently by ion microprobe). Mg was used as the internal standard and the results of the calibration are given in Table 7. Sc was underestimated by 10 to 40 % relative difference in chromites using NIST glasses for calibration. Ga was sometimes overestimated by 10 to 40% using NIST 610 and generally underestimated by 20 to 35% using NIST 612. Al was commonly overestimated by 10 to 25% using both NIST glasses.

NIST glasses (NIST 612 and NIST 610) were tested for their accuracy in the calibration of a Al, Ti, V, Cr, Ni, Ga and Sc measured by LA-ICP-MS in the chromite sample SD159, for which Ga was independently measured by solution ICP-MS. SD159 was used to monitor inter-run variability for the LA-ICP-MS analyses of Ga in chromites from peridotites, for which the most suitable operating conditions were 15 Hz and 40 um line width (Dare et al. 2007). The ratio of the observed concentration, average of 8 to 12 LA-ICP-MS analyses calibrated using NIST glass, divided by the expected concentration, determined independently by EMP an solution ICP-MS, demonstrates that calibration of chromite using NIST glass is inaccurate (> 10% relative difference) for the majority of elements (Figure 11). When normalised to Mg, Al was overestimated by 10 to 25% whereas Ti, V, and Cr was underestimated by 10 to 60%. Ni, Ga and Sc were underestimated by 12 to 40% using NIST 612, but within 10 to 20% accuracy using NIST 610. The inaccuracy of the calibration is dependent on which NIST glass is used, and NIST 610 gives LA-ICP-MS results closer to the expected values in chromite than NIST 612.

Using Al or Ti as an internal standard amplifies the inaccuracy of the NIST calibration: when Al is used all the other elements are greatly underestimated, typically between 20 and 60%, whereas normalising to Ti overestimates most other elements, typically by 20 to 80% (Figure 11). Therefore, Mg is the most appropriate internal standard for NIST calibration because the majority of trace elements are closer to the expected values of trace elements in chromite.

Similar inaccuracies using NIST 612 to calibrate USGS basaltic glass BCR-2G were reported by Jackson (2001), which were explained by inter-matrix differences between the external standard and the unknown analyte in the basaltic glass (see later).

3.2.6 Calibration using matrix-matched standards

The calibration for Ga employed matrix-matched standards SD444, UAE140, and ADK185, with values determined independently by solution ICP-MS, whereas the calibration for Sc employed ion microprobe values for 79d and AR90-28. Results for the calibration of chromites not used in the calibration lines are given in Table 8.

Sc calibration using matrix-matched standards produced more accurate concentrations (between 10 – 20%) for XM2 and SD159 (Table 8) than using NIST (Table 7). Also the low concentrations observed for SD444, UAE140 and ADK185 (4 – 8 μm g^{-1}) using matrix-matched calibration confirms that the solution ICP-MS concentrations (13 – 45 μm g^{-1}) were compromised for Sc by silicate inclusions. Calibration of chromites using matrix matched standards produced accurate concentrations (within 10% relative difference) for Ga and Al. Multiple analyses of the monitor chromite, SD159, analysed every run for a suite of peridotites (Dare et al. 2007) showed improved accuracy (< 10% relative difference) for Al, Ti, V, Cr, Ni and Ga (Figure 12) compared to NIST glass (Figure 11). Therefore, Mg, Al or Ti could equally be used as an internal standard, however, Mg is preferred because if any inter-element fractionation occurs during the chromite ablation Mg behaves most similar to Sc and Ga.

4 Results of matrix-matched calibration

In this study, LA-ICP-MS analyses of chromites, using helium gas and a UV 213nm laser, measured Ga and Sc, with detection limits < 1 μg g^{-1} at optimal conditions (20 Hz, 100um). Detection limits are compromised slightly when using 15 Hz and 40 μm (3-10 μg g^{-1}). The detection limit for Ga is typically 6 μg g^{-1} for a proton microprobe (Griffin et al. 1994).

CRM NIST glasses can not confidently assess the precision and accuracy of the chromite calibration using matrix-matched standards, although NIST glasses sometimes produce accurate results for Ga when normalised to Mg (Table 7, Figure 11). As yet, there are no international chromite CRMs available to verify the accuracy of the Ga and Sc determined in the matrix-matched chromite standards developed in this study. However, chromitite samples from layered intrusions of the Bushveld Complex (UG2) and the Great Dyke, Zimbabwe (GD4) analysed in this study have also been analysed for Ga by proton microprobe (Paktunc and Cabri, 1995). The Ga contents analysed by LA-ICP-MS using matrix-matched standards in this study are similar to the Ga contents analysed previously by proton microprobe and verifies the matrix-matched standards developed for the first time in this study (Table 9). The variation in Ga between samples analysed is probably due to the natural variation within the layered intrusion caused by fractional crystallisation, as seen by the variable major compositions (Table 9).

The calibration of Ga in chromites, using the matrix-matched standards developed in this study, was applied to peridotites and podiform chromitites from the Oman-U.A.E. ophiolite (Dare et al. 2007). The agreement between laser ablation and electron microprobe data is generally good and shows a 1:1 relationship for Al, Ti, V and Ni (Figure 13). Ga analysed by LA-ICP-MS using matrix-matched standards plot along the Ga-Ni trend for podiform chromitites and mantle xenoliths analysed by proton microprobe O'Reilly et al. 1991, Ewart and Griffin 1994, Paktunc and Cabri 1995, Paktunc and Hulbert 1996) which also verifies the data (Figure 14).

5 Are NIST glasses suitable for calibration of chromites?

5.1 Matrix-dependent ablation behaviour

Figure 11 demonstrated that calibrations of chromites using NIST glasses are inaccurate for many elements. The difference in signal stability between NIST glass (stable) and chromites (unstable) indicates that chromites ablate differently from NIST. Furthermore, the signal response to an increase in frequency from 4 to 20 Hz, keeping line width and carrier gas constant, is much greater for chromite (five- to six-fold increase in signal intensity) compared to NIST glass (only a two- to three-fold increase in signal intensity). In contrast, at fixed frequency the signal response to an increase in the width of the line from 40 μm to 100 μm, keeping laser frequency and carrier gas constant, was the same for both chromite and NIST glass samples. Thus, the signal response to changes in ablation frequency of the laser is matrix-dependent but the signal response to changes in ablation line width is matrix-independent.

The ablation rate was quantified by the counts per wt% element whereby the counts were the mean signal intensity (intensity counts per second (icps)) from the LA-ICP-MS and wt% element were determined from the electron microprobe. Under fixed conditions chromites ablate at the same rate (as measured by counts per wt% MgO and Al_2O_3) independent of chromite composition (Figure 6) which vary in Cr# (Cr/ (Cr + Al)) from 0.2 to 0.8 in chromites ablated in peridotites (Dare et al. 2007). The scatter observed for chromites in Figure 6 is caused by differences in the absolute amount of material that is ablated and transported during an individual analysis, caused by matrix effects, changes in laser sampling yield and transport efficiency and demonstrates the need for normalisation of each analysis to an internal standard (Fryer et al. 1995, Norman et al. 1996, Chen et al. 1997). Laser sampling yields can vary from one sample to another and from laser firing to firing because of different sample compositions and surface structures (Jackson 2001).

The ablation rate of chromite is slower than the ablation rate of NIST glass for all the elements (Figure 6 c and d). This is expected because the oxide structure of chromite has stronger bonds than the solid solution structure of synthetic NIST glass. Thus chromites absorb more energy from the laser so that less ablated aerosol reaches the ICP-MS than the ablation of NIST. However, the difference in ablation rates between chromite and NIST glass is element-dependent and varies from only 7% slower (e.g. Al) to 90% slower (e.g. Co) in chromite than NIST glass (Table 6). Therefore, inter-matrix differences between chromite and NIST glasses cause inter-element fractionation when comparing the ablation of chromite and NIST (e.g. Figure 7) even though inter-element fractionation was not observed for each individual ablation. The degree of inter-element fractionation is dependent on the frequency of the laser and the composition of the NIST glass used although the fractionation pattern remains the same shape (Table 6, Figure 7). The differential ablation rates between chromites and NIST glass is less for NIST 610 than NIST 612 and can differ by up to 20% (Figure 7a). Decreasing the frequency from 20 Hz to 4 Hz minimises the difference in ablation rates between chromites and NIST glass by up to 20% for most elements (Figure 7b and c).

The ratios of chromite and NIST glass ablation rates are normalised to Mg in Figure 7 to demonstrate the importance in selecting a suitable internal standard when using NIST glass as external standards for the ablation of chromites. For example, the ablation rates of chromite and NIST 610 are similar for Ga and Ni when normalised to Mg at 15Hz (Figure 7 b), however, Ti or V is more appropriate than Mg as an internal standard for Ni and Ga when using NIST 612 (Figure 7 c).

5.2 Limitations of NIST glass

Calibration using a single CRM, as was common practise in previous chromite analyses, can only be attempted if the calibration lines are linear and pass through the origin, and if the CRM and the samples have similar compositions (Stix et al. 1995). Although CRM NIST glasses (e.g. NIST 612 and NIST 610) are well documented for a wide variety of trace elements (Pearce et al. 2000) they have much lower compositional ranges than chromites for Mg, Al, Fe, Cr, Ti, V, Ni and Zn and only have similar compositions for Co, Ga and Sc.

Using NIST glasses to calibrate chromite samples causes inter-element fractionation and inaccurate trace element quantification if the wrong internal standard is chosen (as described above). Successful quantification of elements with fractionation factors dissimilar from the internal standard thus requires careful matching with internal standards with similar behaviour during ablation, or by the development of procedures that minimize inter-element fractionation such as using matrix-matched standards (see below). This study demonstrates that vigorous testing of ablation rates, for all elements under investigation, between NIST glass and matrix-matched chromites standards is required to correctly select internal standards for accurate trace element determination of chromite using NIST glass. Just one internal standard (e.g. Mg, Ti, V or Al) as has been used in the past, is probably insufficient to match ablation behaviours of all the trace elements (Figure 7). Furthermore, it is difficult to predict from fractionation index of Fryer et al. (1995) alone which elements will behave the same during matrix-dependent fractionation.

Even having correctly identified internal standards for one set of operating conditions and CRM NIST glass, they may not be correct when used at different operating conditions because behaviour (ablation rates) among elements is dependent on operating conditions and NIST glass composition used. The resulting inaccuracies are particularly important when considering the small range in variation of low abundance elements such as Ga and Sc (Table 8).

The problem of miss-matched standards (e.g. using NIST glass to calibrate chromites) is insignificant for an internally consistent data set analysed under a fixed set of operating conditions. It becomes important, however, when comparing chromite data between laboratories that have used different laser wavelengths and operating conditions. Some trace elements in chromites previously measured using NIST glasses are therefore, probably inconsistently inaccurate owing to the dependency of inter-element fractionation on the laser operating conditions, which have varied in previous studies, as follows: using helium (Eggins et al. 1998, Glaser et al. 1999) or argon gas (Chen et al. 1997, Norman 1998, Grégoire et al. 2000); calibration against NIST 610 (Norman 1998, Glaser et al. 1999, Grégoire et al. 2000) or NIST 612 (Chen et al. 1997, Eggins et al. 1998, Glaser et al. 1999); spot widths ranging from 30 and 200 μm wide; laser frequencies (4-10 Hz).

The degree of inter-element fractionation also changes with laser wavelength (e.g. Jackson 2001) which has varied among previous chromite studies; e.g. 1064 nm (Chen et al. 1994, Watling et al. 1995), 266 nm (Norman 1998), 213 nm (Dare et al. 2007) and 913 nm (Eggins et al. 1998, Denny 1998, Richardson 1999, Glaser et al. 1999). Fractionation effects have prevented quantification without matrix-matched standards with 1064 nm (e.g. Watling et al. 1995). Fractionation effects have been reduced but not eliminated using Nd:YAG lasers with shorter UV wavelengths (e.g. 266 nm and 213 nm) (Jackson 2001). The absorption of 213 nm radiation is substantially more matrix-independent, compared to 266 nm lasers, and reduces inter-matrix differences in elemental fractionation for the rare-earth elements but not for the transition elements, such as Ti, V, Zn and Ga, which are common in chromite (Figure 3.11, Jackson 2001). Inter-element fractionation in silicates was insignificant for Eximer lasers (193 nm) for frequencies < 20 Hz, because their ablation rates were largely matrix-independent amongst NIST 612, hornblende, augite, garnet and zircon (Günther et al. 1997). However, but the question remains whether ablation rates are matrix-independent amongst NIST and chromites when using Eximer lasers (193 nm) for the quantification of trace elements in chromite (e.g. Eggins et al. 1998, Denny 1998, Richardson 1999, Glaser et al. 1999).

5.3 Limitations of matrix matched standards

The matrix–matched standards, as characterised in this study, eliminated inter-element fractionation between external standard and unknown chromite and accurately determined a limited, selected set of trace elements in chromite. Limitations of using natural chromites as matrix-matched standards are that they are not as homogeneous as synthetically prepared CRMs and also commonly contain silicate inclusions, which can compromise trace element determinations by bulk rock methods especially for elements incompatible in chromite such as Sc. Natural chromites have a limited selection of trace elements compared to NIST glasses and their composition is strongly controlled by geological setting. For example, Zr and Nb are essentially absent (< 6 μg g $^{-1}$) in chromites from layered intrusions and ophiolites (Griffin and Ryan 1995, Denny 1998, Richardson 1999) but Zr and Nb are enriched (e.g. Zr: 6 -40 μg g $^{-1}$ and Nb: 6 – 20 μg g $^{-1}$) in metasomatised spinels that have resided in and reacted with a highly alkaline magma (such as a kimberlite, lamproite or ultramafic lamprophyre) (Griffin and Ryan 1995, Norman 1998, Denny 1998, Eggins et al. 1998, Richardson 1999, Glaser et al. 1999, Grégoire et al. 2000). It was, therefore, not possible to determine the accuracy of NIST calibration for measuring Nb and Zr in chromite using the matrix-matched standards developed in this study. This problem must be considered in the future for diamond exploration dependent upon chromite trace elements detected by LA-ICP-MS analysis.

The way forward is to develop homogeneous, synthetic chromites doped to appropriate levels of trace elements found in natural spinels (e.g. Horn et al. 1994), which can then be analysed by bulk rock analysis and microbeam techniques such as proton microprobe.

6 CONCLUSIONS

1) Trace elements in chromites were characterised independently by high-quality electron microprobe and scanning electron microprobe analyses (for Ti, V, Ni, Mn, Zn and Co), ion microprobe (for Sc) and by solution ICP-MS analysis using lithium metaborate flux (for Ga and Sc), to test the accuracy of synthetic glasses (NIST CRM 612/610) in the calibration and quantification of trace elements in chromites.

2) Ga and Sc were measured above quantification limits over a wide range of laser operating conditions using helium, whereas Sc was only quantifiable at maximum conditions (e.g. 20 Hz, 100 um) using argon gas. Ca was mostly below quantification and Y always below detection limits.

3) In spite of chromites displaying unstable signals at high frequencies, the combination of helium gas and a UV 213 nm laser eliminated inter-element fractionation for an individual chromite analysis and thus higher frequencies (e.g. 20Hz) can be employed to optimise trace element quantification. However, the UV 213 nm laser did not eliminate inter-element fractionation for argon gas as a gas carrier.

4) NIST glasses and chromites ablate differently for many of the elements using a UV 213 nm laser. Inter-element fractionation effects due to different ablation rates of various elements result in the inaccuracy of many trace elements in chromite using NIST glasses as an external standard.

5) The degree of inaccuracy varies with laser frequency, the composition of NIST glass used, and with the element chosen as an internal standard; all of which have varied between earlier studies.

6) In this study, characterisation of matrix-matched standards eliminated inter-element fractionation effects. They also accurately quantified Ti, V Mn, Zn, Ni, Co, Ga and Sc in chromites from podiform and stratiform chromitites, with detection limits < 1μg g $^{-1}$ for Ga and Sc.

7) Therefore, this study identifies the need to develop good international chromite standards to replace NIST glasses in the calibration of trace elements in chromites by LA-ICP-MS analysis.

8) These results have important implications for comparing chromite trace element analyses among previous studies which used NIST glass as external standards. Until then, it will remain difficult to confidently compare chromite data between studies that have utilised different calibration conditions. This could be particularly important when using trace elements in chromites as diamond indicators and could lead to the misidentification of diamondiferous chromites.

9) Moreover, the development of trace elements in chromites for petrogenetic and tectonic discrimination by LA-ICP-MS in the future should involve a standard procedure for calibration of chromites using matrix-matched standards.

ACKNOWLEDGEMENTS

This work was carried out under Departmental PhD funding at Cardiff University. The authors would like to thank Hazel Prichard for supplying the chromitite samples UG-2 and GD-4 and Pete Fisher for his assistance with the SEM analyses and Edinburgh Ion Microprobe Facility/NERC for assistance with ion microprobe analyses.

TABLES for paper

Table 1: Major and trace element compositions of chromite standards by electron microprobe analysis (EMPA), scanning electron microscope (SEM), and dissolution by Li metaborate flux using the ICPS-OES and ICP-MS. Limits of merit are limits of detection (LOD), limits of quantification (LOQ), error based on multiple analyses (n) and relative standard deviation (RSD%). Accuracy monitored by relative difference (%Rel Diff) of certified reference materials W2 and JB1-a.

c			EMP LOD	EMP LOQU	AE140	Error	RSD (%)	SD444	Error	RSD (%)	SD159	Error	RSD (%)	ADK185*	Error	RSD (%)	SEM* LOD	SEM* LOQ
EMP/SEM*																		
SiO_2		%	0.04	0.12	0.04	0.02	43	0.03	0.01	49	0.03	0.01	27	NA				
TiO_2		%	0.02	0.07	0.034	0.01	25	0.515	0.01	3	0.227	0.01	3	0.63	0.04	6.1	0.01 ^{WD}	0.04 ^{WD}
Al_2O_3		%			7.44	0.11	2	23.53	0.17	1	17.39	0.08	0	17.06	0.09	0.5		
V_2O_3		%	0.04	0.13	0.085	0.01	13	0.112	0.01	10	0.121	0.01	9	0.192	0.02	12.3	0.04 ^{WD}	0.12 ^{WD}
Cr_2O_3		%			64.07	0.29	0	42.78	0.23	1	50.59	0.07	0	39.58	0.13	0.3		
FeO*		%			15.06	0.18	1	17.25	0.24	1	17.02	0.15	1	35.95	0.13	0.4		
MgO		%			12.35	0.12	1	14.11	0.08	1	13.04	0.05	0	5.15	0.06	1.2		
MnO		%	0.12	0.39	0.17	0.06	34	0.18	0.03	15	0.20	0.02	9	0.49	0.04	10.2	0.15	0.48
CoO		%			NA			NA			NA			0.34	0.10	30.3	0.15	0.48
NiO		%	0.10	0.32	0.10	0.05	51	0.15	0.06	39	0.13	0.02	12	<d.l.			0.11	0.37
ZnO		%	0.10	0.34	0.06	0.04	66	0.08	0.04	51	0.13	0.02	12	0.52	0.06	13.1	0.16	0.51
Total		%			99.42			98.73			98.88			99.47				
n			*44*	*44*	*21*			*23*			*23*			*45*				
ICP-OES																		
	Line																W2	%Rel Diff
MgO	279.553 nm	%			11.77	0.14	1	12.19	0.20	2	13.07	0.07	1	4.20	0.09	2.0	6.6	3.3
FeO*	259.940 nm	%			16.45	0.43	3	17.20	0.30	2	17.94	0.45	2	34.66	0.72	2.1	11.4	6.2
Al_2O_3	308.215 nm	%			12.78	0.34	3	25.34	0.59	2	20.76	0.36	2	17.69	0.46	2.6	15.1	-1.4
Sc	361.384 nm	ppm	0.77	2.56	37.6	16.8	45	13.6	7.8	57	5.5	5.8	104	45.4	9.4	20.7	36.9	5.0
n					*2*			*2*			*2*			*2*			*1*	
ICP-MS																		
	Isotope																JB1-a	%Rel Diff
MgO	24	%			12.78	0.10	1	13.58	0.07	1	13.84	0.26	2	4.70	0.06	1.2	8.03	3.6
FeO*	56	%			15.52	0.10	1	16.43	0.09	1	16.35	0.2	1	34.12	0.21	0.6	9.24	1.5
TiO_2	49	%	0.0004	0.0012	< d.l.			0.21	0.01	6	0.10	0.01	14	0.55	0.02	3.0	1.32	1.4
V_2O_3	51	%	0.0000	0.0001	0.133	0.001	1	0.126	0.001	1	0.120	0.002	1	0.160	0.002	1.4	0.03	-2.7
V	51	ppm	0.237	0.789	902	6.38	1	857	6.24	1	819	11.06	1	1088	15.18	1.4	200	-2.7
Ga	71	ppm	0.014	0.045	20.4	0.37	2	44.1	0.45	1	33.3	0.60	2	60.6	0.42	0.7	18.2	2.4
n					5			5			3			3			*4*	

Operating conditions of EMP: Count times on peaks are Cr, Mn, Ni (10s), Mg, Si, Zn (20s), V, Fe (30s), Al (40s), Ti (50s)
Operating conditions of SEM: Livetime 50s on peaks for EDX and count time of 40s for V by wave dispersive (WD)
FeO* represent total Fe reported as FeO.
< d.l. = below detection limit
n = number of replicates

Appendix E: Analysis of Ga in chrome-spinel by LA-ICP-MS

Table 2: Major and trace element compositions of chromite standards by electron microprobe analysis (EMPA) and ion microprobe.

	L35-90	**AR90-28**	**LK44**	**79d**	**XM2**	**BT6B**
	Hz	**Chr-du**	**Hz**	**Chr**	**Chr-du**	**Du**
EMP (SD)						
SiO2	0.03	0.03	0.03	0.02	0.01	0.04
TiO2	0.06	0.04	0.70	0.32	0.15	0.10
Al2O3	44.68	11.06	25.01	16.99	9.84	7.56
V2O3	0.11	0.16	0.30	0.23	0.06	0.20
Cr2O3	21.93	57.70	37.54	44.75	61.37	61.75
FeOT	14.56	19.08	22.04	26.38	16.23	21.14
MgO	17.02	10.28	12.60	9.27	12.34	8.87
MnO	0.13	0.24	0.24	0.26	0.22	0.29
NiO	0.24	0.04	0.12	0.06	0.05	0.03
ZnO	0.17	0.14	0.16	0.09	0.07	0.14
Total	98.93	98.76	98.74	98.36	100.33	100.12
EMP (JAP)						
SiO2	0.02	0.05	0.02	0.18		0.02
TiO2	0.03	0.06	0.51	0.32		0.10
Al2O3						
V2O3	0.15		0.35	0.28	0.09	0.27
Cr2O3	18.40	63.28	39.20	44.82	61.79	62.11
FeOT	14.70			25.68	15.95	22.49
MgO	17.21	9.95	12.03	9.32	12.12	8.13
MnO	0.15	0.32	0.29	0.35		0.43
NiO	0.27	0.08	0.17	0.07	0.00	0.06
ZnO	0.19		0.21	0.08	0.06	0.19
CoO	0.09		0.08	0.07		0.11
SIMS (ave)						
Cr2O3	13.80	55.43	34.05	42.91	61.43	52.31
FeOT	18.44			29.18	16.63	19.04
TiO2	0.03	0.04	0.58	0.30	0.15	0.09
V2O3	0.10	0.21	0.29	0.30	0.10	0.24
CaO	0.01	0.01	0.03	0.01	0.01	0.01
Ga (ppm)	216	120	392	243	128	103
Sc (ppm)	0.57	12.87	0.64	7.74	7.38	6.27
Y (ppm)	0.037	0.004	0.021	0.007	0.007	0.007

Appendix E: Analysis of Ga in chrome-spinel by LA-ICP-MS

Table 3: Summary of laser ablation system and ICP-MS operating conditions.

Laser Ablation	
Laser ablation device	New Wave UP213
Laser type	Nd-YAG
Wavelength	213 nm
Mode	Q-switched
Power	65% power
Frequency	4, 10, 15 and 20 Hz
Energy	~ 10 J cm^{-2}
Line width	40, 80 and 100 μm
Line depth	10 μm
Line length	~ 250 to 400 μm
ICP-MS	
Instrument	Thermo Electron X Series
Plasma conditions	
Helium carrier gas flow	0.7 L/min
Argon make up gas flow	0.56 - 0.65 L/min
Cones	Nickel
Data Acquisition parameters	
Scanning mode	Peak hopping
Dwell time	200 ms
Background acquisition time	20 s
Signal acquistion time	60 s
Elements scanned	^{24}Mg, ^{27}Al, ^{44}Ca, ^{45}Sc, ^{47}Ti, ^{51}V, ^{53}Cr, ^{55}Mn, ^{59}Co, ^{60}Ni, ^{64}Zn, ^{71}Ga,

Appendix E: Analysis of Ga in chrome-spinel by LA-ICP-MS

Table 4: Experimental results for trace element detection and quantification in chromite upon varying the gas carrier, frequency of the laser and line width.

Gas Carrier	**Frequency**	**Line width**	**> q.l.**	**< q.l.**	**< d.l.**
Argon	20 Hz	100 µm	Ga, Sc		Ca, Y
Argon	20 Hz	80 µm	Ga	Sc	Ca, Y
Argon	20 Hz	40 µm	Ga		Ca, Y, Sc
Argon	15 Hz	100 µm	Ga	Sc	Ca, Y
Argon	4 Hz	100 µm	Ga	Sc	Ca, Y
Helium	20 Hz	100 µm	Ga, Sc	Ca	Y
Helium	20 Hz	80 µm	Ga, Sc	Ca	Y
Helium	20 Hz	40 µm	Ga, Sc		Ca, Y
Helium	15 Hz	100 µm	Ga, Sc	Ca	Y
Helium	15 Hz	80 µm	Ga, Sc		Ca, Y
Helium	15 Hz	40 µm	Ga, Sc	(Sc)	Ca, Y
Helium	4 Hz	100 µm	Ga, Sc		Ca, Y

Dwell times 30 ms for Ca, 60 ms for Ga, 68 ms for Y and 69 ms for Sc
q.l. is the quantification limit, defined as 10 times the standard deviation of the gas blank
d.l. is the detection limit, defined as 3 times the standard deviation of the gas blank
(Sc) a few samples have Sc < q.l. but the majority of samples are quantifiable

Appendix E: Analysis of Ga in chrome-spinel by LA-ICP-MS

Table 5: Ablation yield index (see text) for each element analysed over a range of frequencies (4, 10, 15 and 20Hz) and in helium gas and argon gas only for chromites (UAE 140, Mdgcr, SD159 and SD444) and NIST glasses (612 and 610).

Experiment A	**24Mg**	**27Al**	**44Ca**	**47Ti**	**51V**	**53Cr**	**55Mn**	**59Co**	**60Ni**	**66Zn**	**71Ga**
4Hz											
UAE140	1.06	1.03		1.09	1.07	1.05	1.11	1.10	1.05	1.08	1.15
Mdgcr	1.00	0.98		0.96	0.98	0.97	0.98	1.00	0.95	1.00	1.02
NIST612	0.97	0.99	0.99	0.95	1.00	1.05	1.00	0.96	0.99	1.01	0.99
NIST610	1.08	1.02	1.05	1.03	1.05	1.08	1.04	1.03	1.03	1.00	1.00
10Hz											
UAE140	1.06	1.06		1.04	1.06	1.04	1.04	1.06	1.02	1.05	1.04
Mdgcr	1.09	1.08		1.08	1.09	1.09	1.07	1.06	1.08	1.07	1.08
NIST612	0.86	1.02	1.02	1.15	1.02	1.00	1.04	1.00	0.98	0.98	1.01
NIST610	1.05	1.05	1.00	1.01	1.01	0.99	1.01	0.98	0.99	0.99	1.00
15Hz											
UAE140	1.09	1.11		1.09	1.12	1.08	1.10	1.09	1.08	1.09	1.09
Mdgcr	1.12	1.12		1.20	1.12	1.13	1.13	1.11	1.12	1.10	1.11
NIST612	1.02	1.00	1.01	1.01	1.00	1.10	1.02	1.01	0.99	0.97	1.01
NIST610	0.94	0.94	0.97	0.97	0.99	0.98	0.97	0.98	0.99	0.99	0.99
20Hz											
UAE140	1.13	1.11		1.12	1.11	1.09	1.11	1.09	1.10	1.09	1.11
Mdgcr	1.02	1.03		1.00	0.98	1.00	1.01	0.99	0.91	1.01	1.00
NIST612	0.99	1.06	1.04	1.13	1.07	0.86	1.02	1.06	1.05	1.04	1.04
NIST610	1.01	1.00	1.00	1.02	1.00	0.97	1.00	1.00	0.99	1.00	1.00

Experiment B	**24Mg**	**27Al**	**44Ca**	**45Sc**	**71Ga**	**Experiment C**	**25Mg**	**27Al**	**45Sc**
Helium						**Argon**			
UAE140*	1.19	1.13	1.09	1.18	1.23		1.32	1.22	1.05
Mdgcr	1.02	1.02	1.03	1.06	1.05		1.15	1.11	0.99
SD159	1.04	1.02	1.04	1.02	1.04		1.32	1.15	1.04
SD444	1.03	1.03	1.04	1.04	1.04		1.35	1.18	1.05
NIST612	1.01	1.04	1.03	1.02	1.02		0.97	0.98	1.00
NIST610	1.01	1.00	1.01	1.00	0.99		0.97	1.00	1.01

Operating Conditions:

Experiment A- helium gas, 40um line width, Dwell times: 2s (Cr), 4s (Mg, Al), 8s (V), 10s (Ni), 12s (Ca), 13s (Ti), 15s (Co, Mn), 32s (Zn), 60s (Ga)

Experiment B- helium gas, 20Hz, 100um line width, Dwell times: 4s (Mg, Al), 30s (Ca), 69s (Sc), 60s (Ga)

Experiment C- argon gas, 20Hz, 100um line width, Dwell times: 15s (Mg, Al) and 69s (Sc).

Appendix E: Analysis of Ga in chrome-spinel by LA-ICP-MS

Table 6: Ratio of ablation rates (counts per wt% element) of chromite (chr) to NIST 610 and NIST 612 for each element at 4, 15 and 20 Hz.

Element	Chr/ NIST 610			Chr/ NIST 612		
	20Hz	15Hz	4Hz	20Hz	15Hz	4Hz
Mg	0.66	0.34	0.32	0.71	0.30	0.21
Al	0.84	0.44	0.43	0.93	0.43	0.45
Ti	0.57	0.29	0.27	0.45	0.20	0.18
V	0.56	0.31	0.31	0.51	0.23	0.21
Cr	0.45	0.24	0.26	0.37	0.18	0.16
Mn	0.44	0.26	0.26	0.42	0.21	0.19
Co	0.09	0.06	0.06	0.08	0.05	0.04
Ni	0.58	0.33	0.33	0.39	0.22	0.18
Zn	0.38	0.23	0.22	0.21	0.08	0.05
Ga	0.55	0.32	0.34	0.50	0.25	0.24
Sc	0.37			0.44		

Appendix E: Analysis of Ga in chrome-spinel by LA-ICP-MS

Table 7: Calibration of chromites using NIST 612 and NIST 610 glasses by LA-ICP-MS compared to concentrations (C) expected by independent analyses by ion microprobe, solution ICP-OES/MS and electron microprobe (EMP). % Relative Difference (%RD) measures the accuracy of the NIST calibration relative to expected concentration. Typical range for precision given by 1 σ. Sc, Ga and Al measured by LA-ICP-MS at 20 Hz, 100 um line width in helium gas and using Mg as an internal standard.

Chromite	Method	C expected	**NIST 612 cal**		**NIST 610 cal**	
		Sc µg g^{-1}	LA-ICP-MS	%R.D.	LA-ICP-MS	%R.D.
79d	Ionprobe	**7.7**	5.5	-28	4.8	-37
XM2	Ionprobe	**7.4**	6.3	-15	5.5	-26
AR9028	Ionprobe	**12.9**	10.2	-21	8.9	-31
SD159	sol-ICP-OES	**5.5**	5.0	-9	4.4	-21
		s	0.1-0.5		0.1-0.5	
		Ga µg g^{-1}				
SD159	sol-ICP-MS	**33.3**	26.4	-21	37.2	12
U140	sol-ICP-MS	**20.4**	13.4	-34	18.9	-8
ADK185	sol-ICP-MS	**60.6**	59.6	-2	84.0	39
SD444	sol-ICP-MS	**44.1**	34.8	-21	49.0	11
		s	1.3 - 3.2		1.8-4.5	
		Al$_2$O$_3$ wt %				
SD159	EMP	**17.4**	21.2	22	21.0	21
UG2	EMP	**16.4**	19.3	18	19.1	16
GD4	EMP	**10.5**	13.2	26	13.0	24
XM2	EMP	**9.8**	12.2	24	12.0	22
AR9028	EMP	**11.1**	12.0	8	11.8	7
UAE140	EMP	**7.4**	8.2	10	8.1	9
ADK185	EMP	**17.1**	21.8	28	21.5	26
SD444	EMP	**23.5**	28.5	21	28.2	20
		s	0.4-1.6		0.4-1.6	

Table 8: Calibration of chromites using matrix matched standards for LA-ICP-MS compared to concentrations (C) expected by independent analyses by ion microprobe, solution ICP-OES/MS and electron microprobe (EMP). % Relative Difference (%RD) measures the accuracy of the NIST calibration relative to expected concentration. Typical range for precision given by 1 σ. Sc, Ga and Al measured by LA-ICP-MS at 20 Hz, 100 um line width in helium gas and using Mg as an internal standard.

Chromite	Method	C expected	**chromite cal**	
		Sc µg g^{-1}	LA-ICP-MS	%R.D.
XM2	Ionprobe	**7.4**	8.1	10
SD159	sol-ICP-OES	**5.5**	6.5	18
U140	sol-ICP-OES	**38.6**	6.0	-85
ADK185	sol-ICP-OES	**45.4**	4.1	-91
SD444	sol-ICP-OES	**13.6**	7.7	-43
		s	0.2-0.7	
		Ga µg g^{-1}		
SD159	sol-ICP-MS	**33.3**	29.9	-10
		s	1.5	
		Al_2O_3 wt %		
SD159	EMP	**17.4**	17.4	0
UG2	EMP	**16.4**	15.9	-4
GD4	EMP	**10.5**	10.8	3
XM2	EMP	**9.8**	10.0	1
AR9028	EMP	**11.1**	9.8	-11
		s	0.6-1.9	

Appendix E: Analysis of Ga in chrome-spinel by LA-ICP-MS

Table 9: Calibration of Ga in UG2 (Bushveld Layered Intrusion) and GD4 (Great Dyke Layered Intrusion) using matrix matched standards for LA-ICP-MS compared to concentrations determined on similar samples by proton microprobe (Paktunc and Cabri 1995). Ga measured by LA-ICP-MS at 20 Hz, 100 um line width in helium gas and using Mg as an internal standard. Major elements determined by electron microprobe (EMP) in both studies.

	UG-2, Bushveld			**Great Dyke, Zimbabwe**		
	UG2	**UG2-1**	**UG2-11**	**GD4**	**GrDy**	**Zimb**
	LA-ICP-MS	PMP	PMP	LA-ICP-MS	PMP	PMP
Ga	58	73	70	28	43	35
EMP						
Al_2O_3	16.4	9.5	12.0	10.5	11.6	11.2
Cr#	0.64	0.69	0.71	0.78	0.76	0.78
Mg#	0.43	0.20	0.37	0.56	0.51	0.64

FIGURES for paper

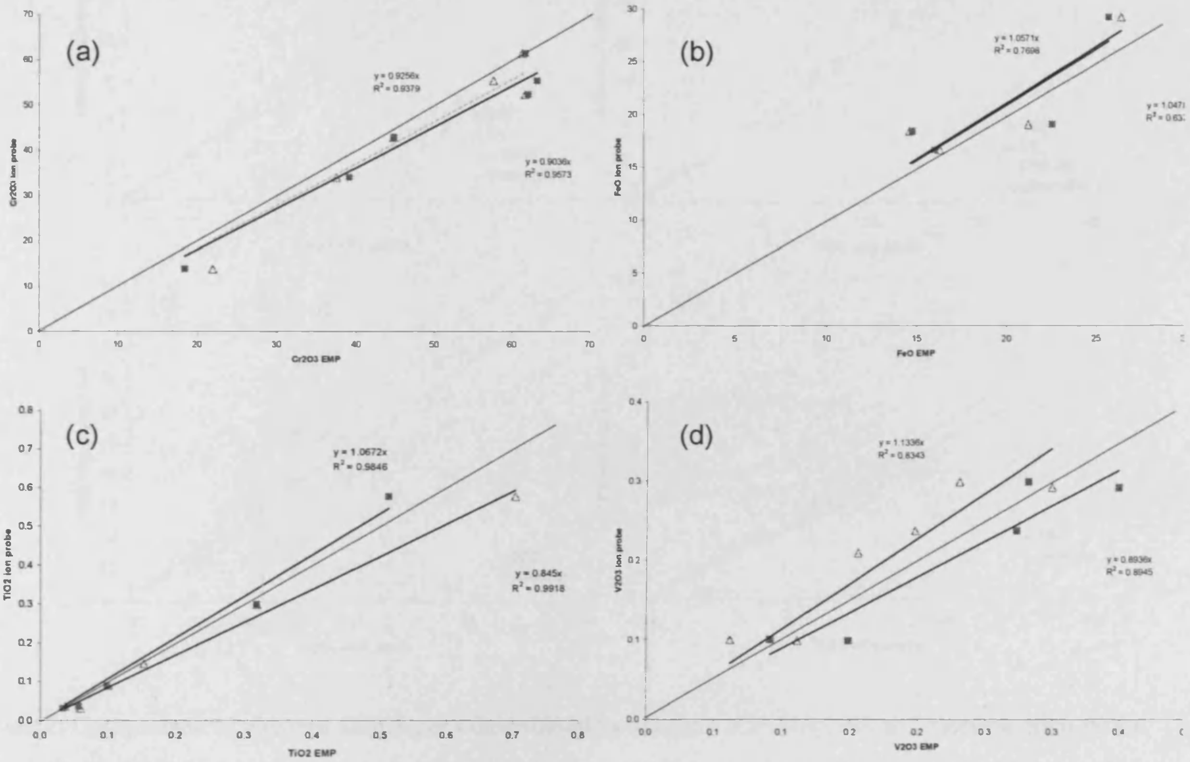

Figure 1: Comparison of element abundances determined by electron microprobe (triangle analysed by SD, square analysed by JAP) and ion probe for (a) Cr_2O_3, (b) FeO, (c) TiO_2 and (d) V_2O_3. Solid line marks 1:1 correlation line.

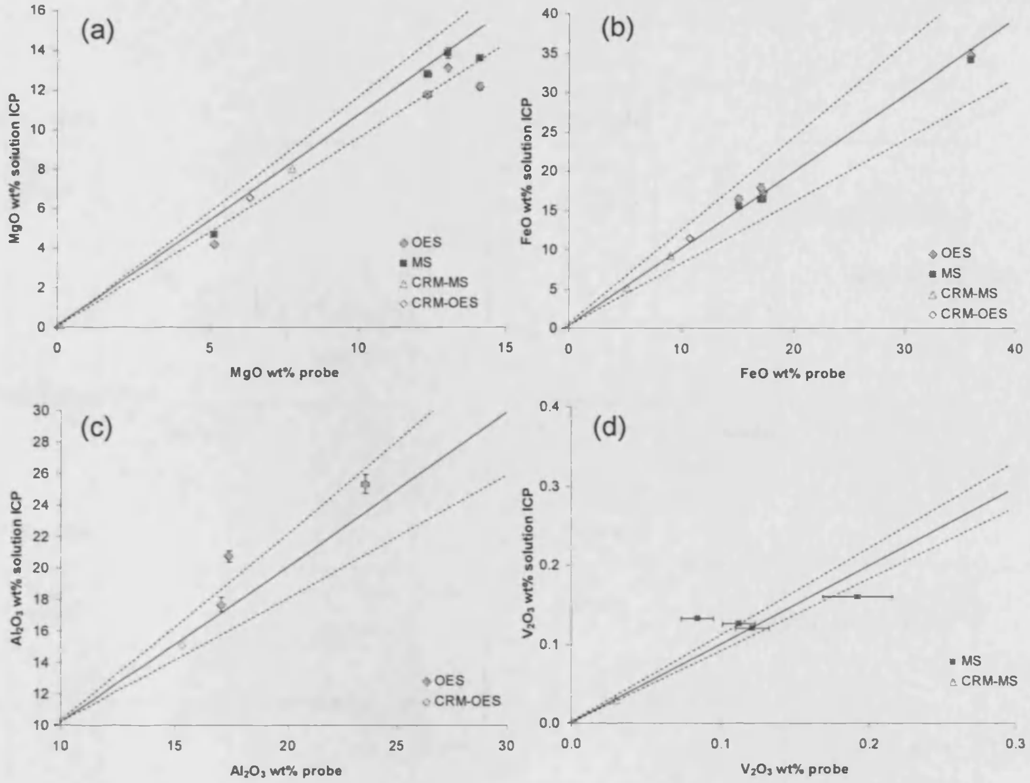

Figure 2: Comparison of element abundances determined by solution ICP-MS/OES and electron microprobe for (a) MgO, (b) FeO, (c) Al_2O_3 and (d) V_2O_3. Solid line marks 1:1 correlation line and dashed lines mark ± 10% relative difference.

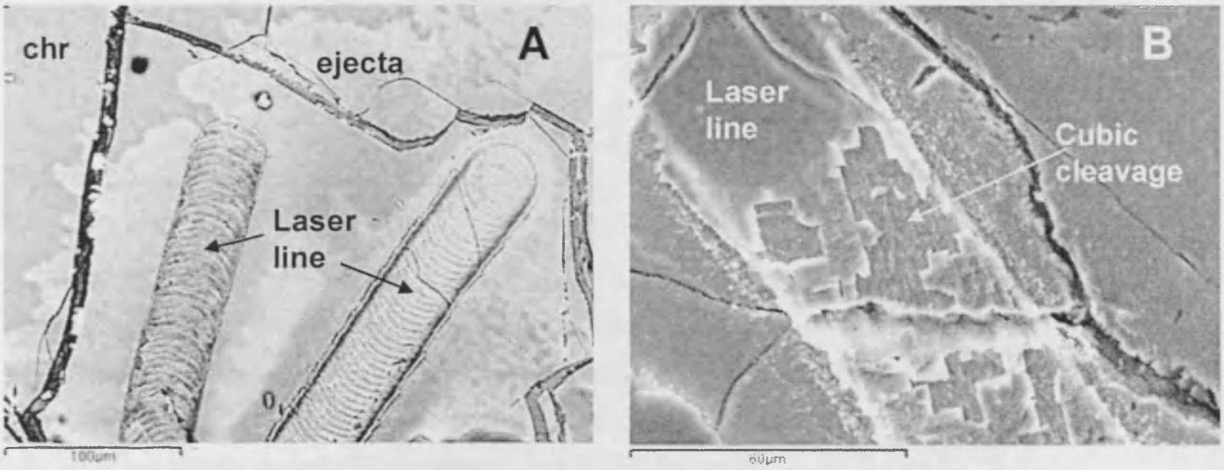

Figure 3: Backscattered SEM images of chromites. Characteristics of ablations lines in chrome-spinel: Ejecta fallout (pale grey) deposited on chromite surface (darker grey) (a), and cubic-shaped cleavage spalling in the pit wall (b).

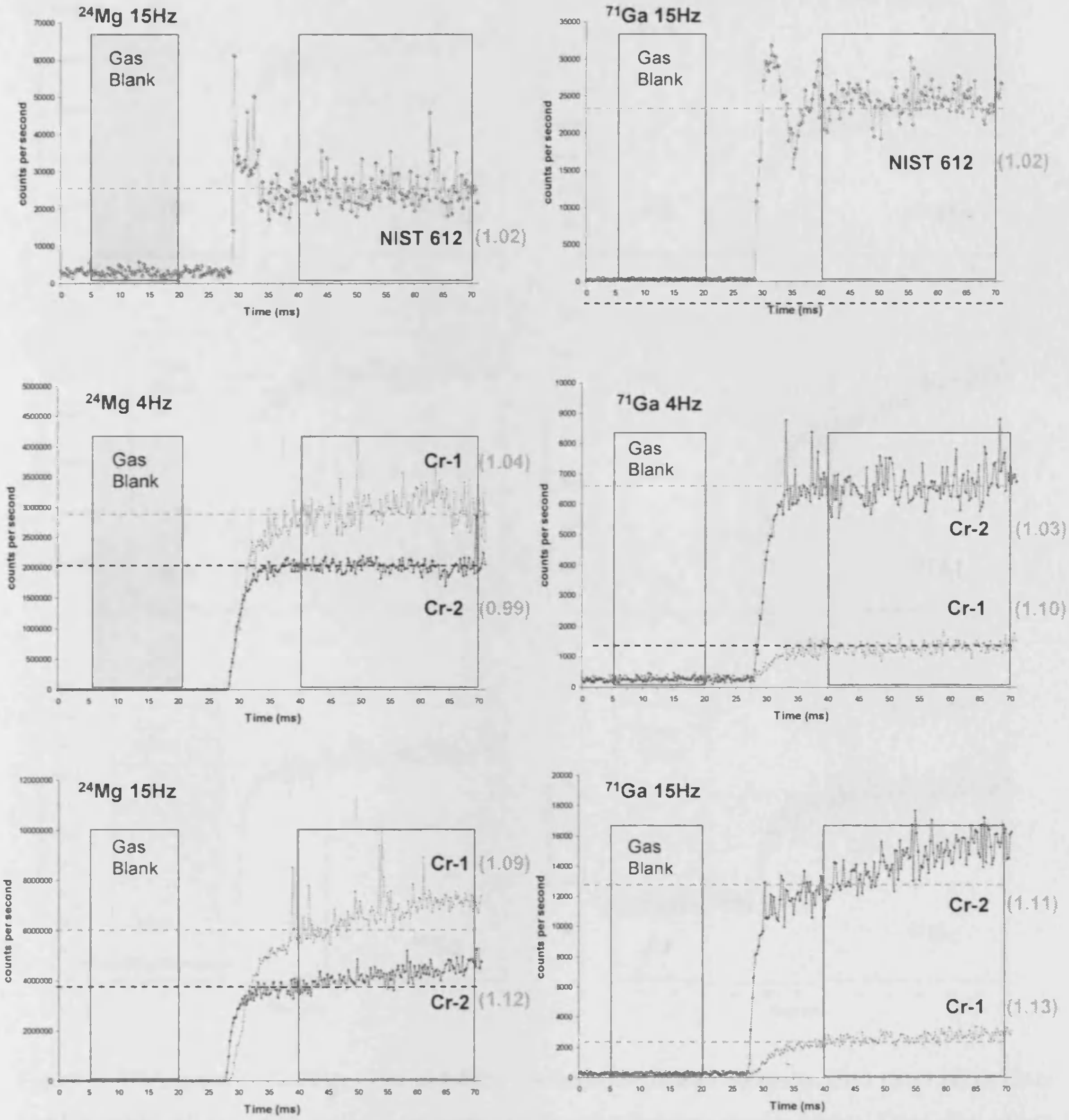

Figure 4: TRA spectra of 24Mg and 71Ga for laser ablation of NIST612 (a and b) and chromites, Cr-1 (UAE140) and Cr-2 (SD444) (c - f) at 4Hz and 15Hz. Line width 40 um and He gas carrier. Time-slice of gas blank from 5 – 20s (grey region) and time-slice of sample from 40 to 70s (yellow region). Ablation yield index (see text) is bracketed next to signal profile. Dashed line marks the average signal intensity at the start of the sample time-slice for comparison with end of time-slice.

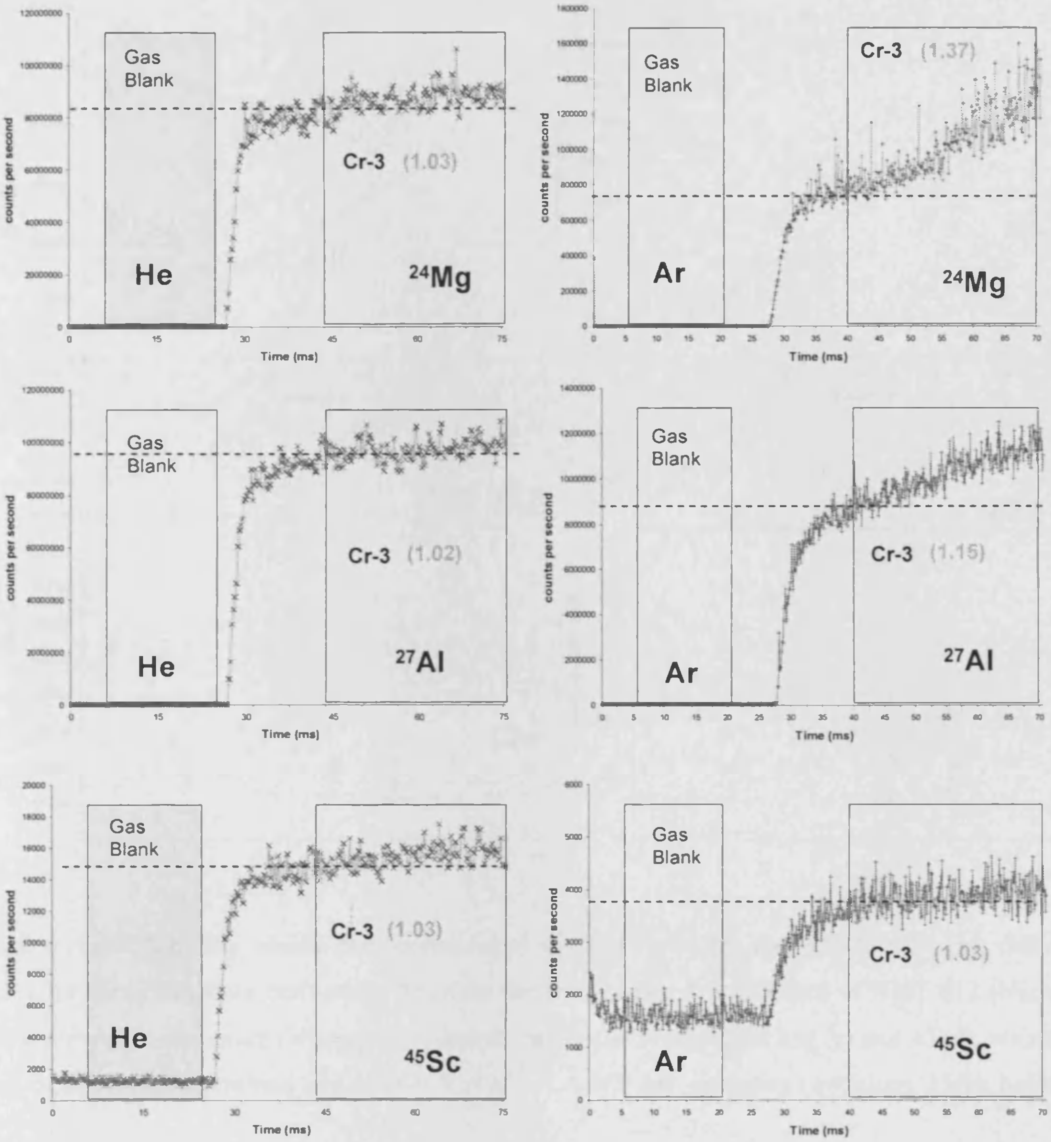

Figure 5: TRA spectra of 24Mg, 17Al and 45Sc for laser ablation of chromite, Cr-3 (SD159) at 20Hz and line width 40 um using Helium gas carrier (left) and Argon gas carrier (right). Time-slice of gas blank from 5 – 20s (grey region) and time-slice of sample from 40 to 70s (yellow region). Ablation yield index (see text) is bracketed next to signal profile. Dashed line marks the average signal intensity at the start of the sample time-slice for comparison with end of time-slice.

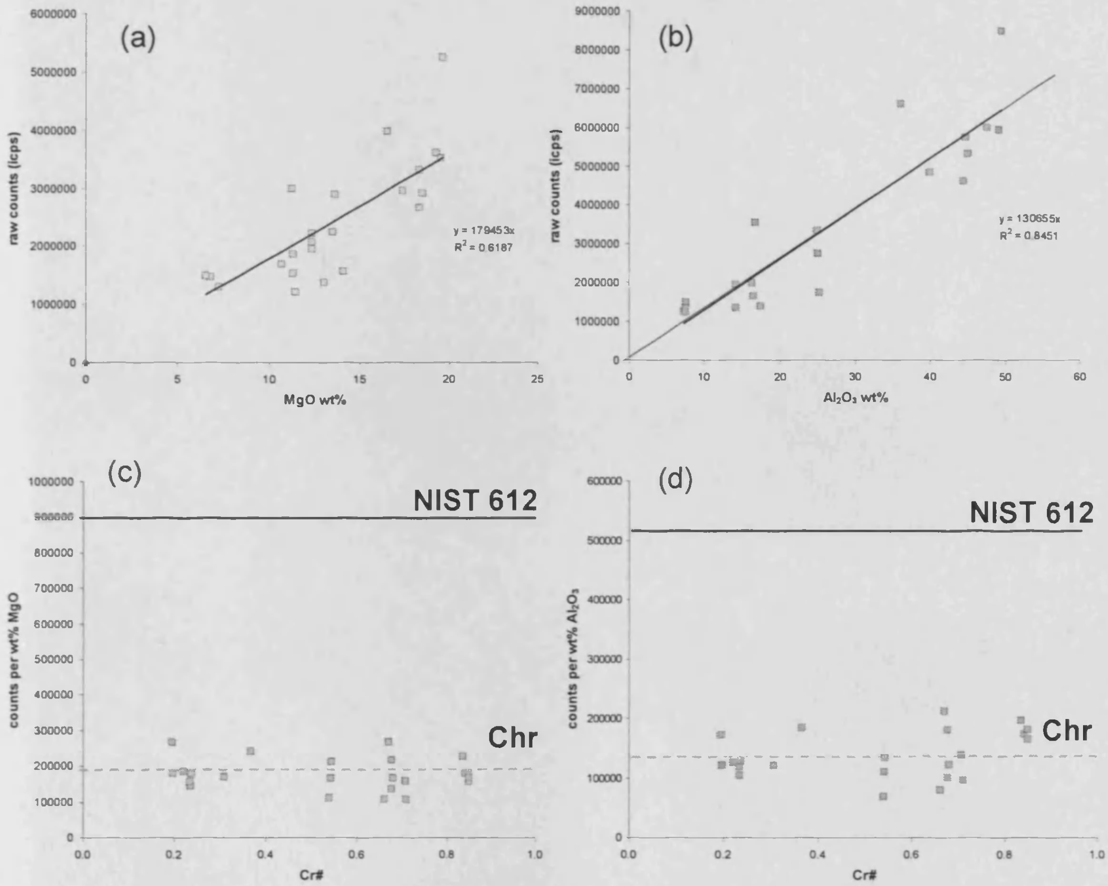

Figure 6: Laser intensity counts per second (icps) vs. MgO wt% (a) and Al2O3 wt% (b), defined by EMPA for chromites from peridotites. Ablation rate (counts per wt% element) of NIST 612 (black solid line) compared to chromites (chr- squares, dashed line marks average) for Mg (c) and Al (d), with a wide range compositions quantified by Cr# (Cr/ (Cr+Al)). LA-ICP-MS operating conditions: 15Hz, helium, 40 µm.

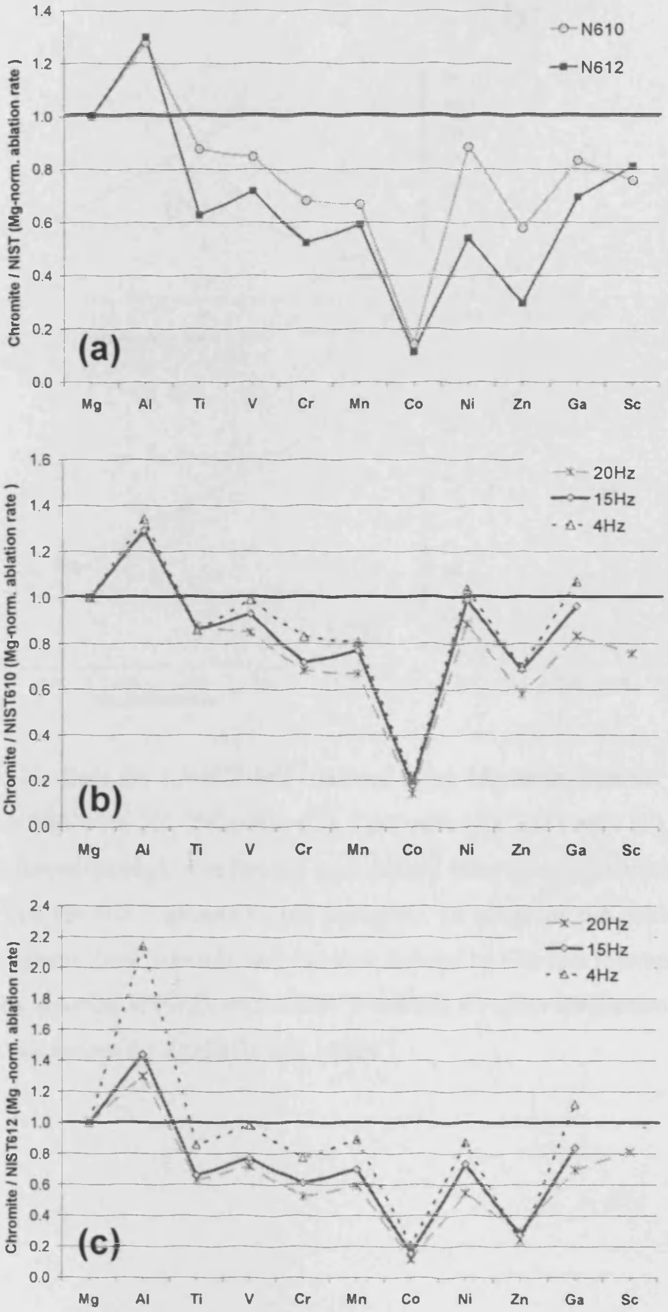

Figure 7: Variation in the ratio of chromite and NIST glass ablation rates relative to Mg (a) with NIST glass standard at 20 Hz, (b) with frequency for NIST 612 and (c) with frequency for NIST 610. Operating conditions: Helium gas and 100 µm line width.

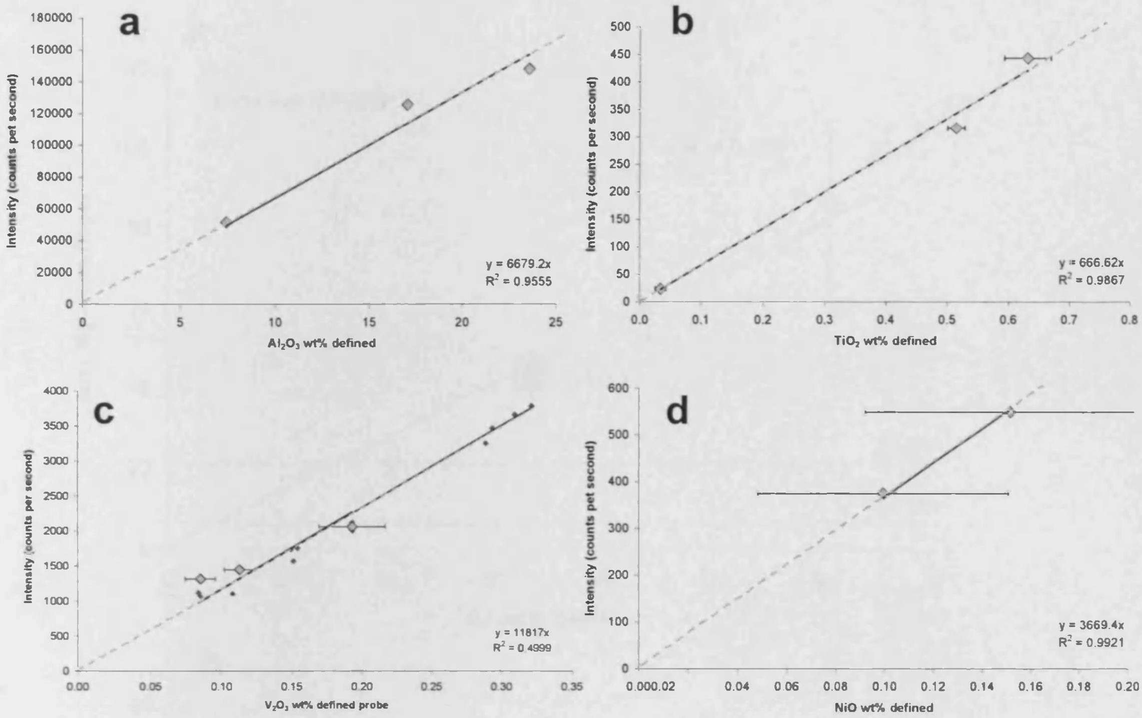

Figure 8: Calibration lines for LA-ICP-MS analyses using Mg as an internal standard for Al2O3 wt% (A), TiO2 wt% (B) , V2O3 wt% (C), NiO wt% (D), CoO wt% (E), ZnO wt% (F), Ga ppm (G) and Sc ppm (H). Calibration lines, forced through zero for, are grey dashed lines for matrix matched standards (grey diamonds) and black solid line for NIST glasses (black triangles). Gradient of the calibration line and the correlation coefficient (R2) between laser intensity and element defined by electron microprobe for all elements except Ga and Sc (defined by solution ICP-MS and --OES) is marked for each calibration. Operating conditions: Helium gas, 15Hz and 40um except for Sc (20Hz and 100um).

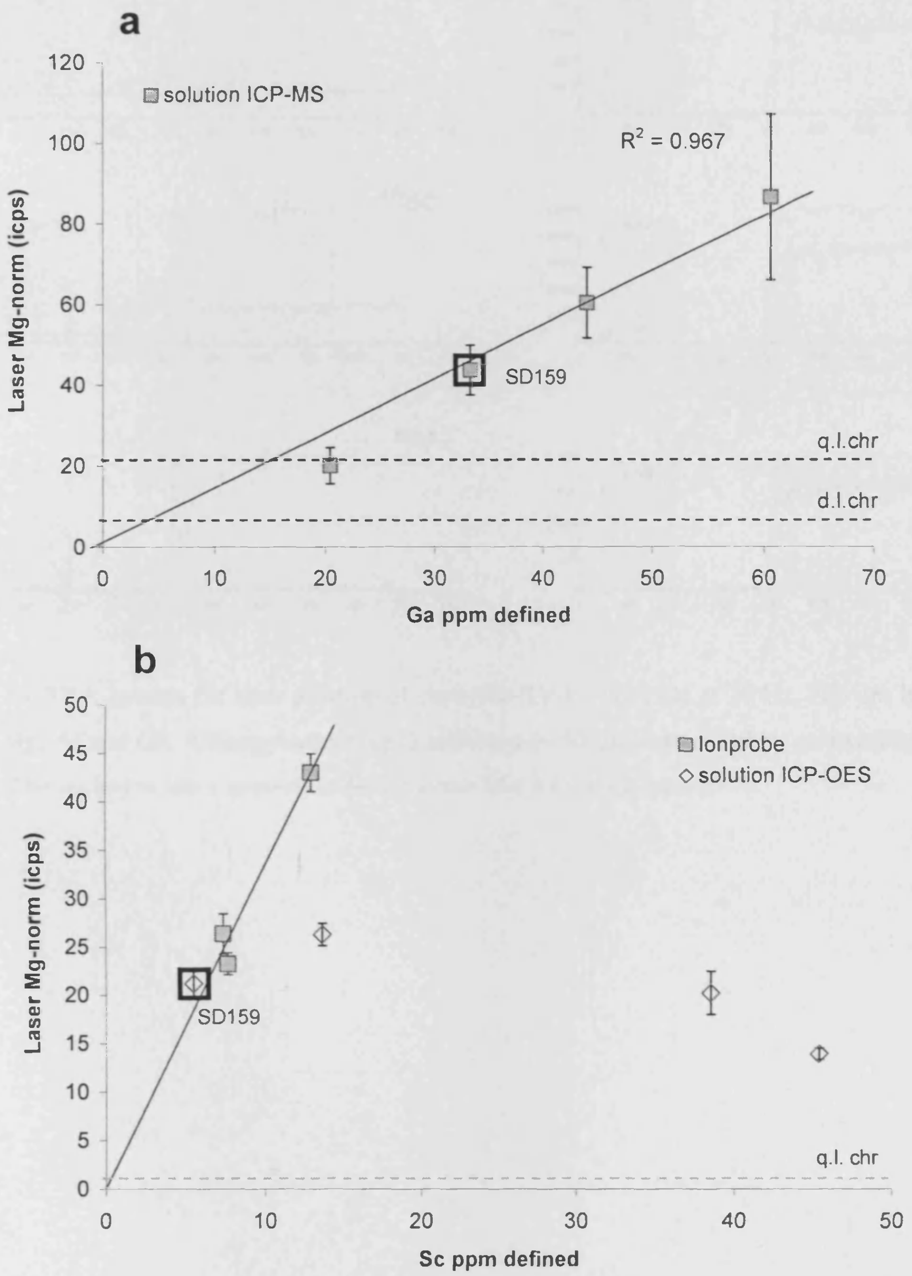

Figure 9: Signal intensity of the laser (intensity counts per second-icps) normalised to Mg against concentration of Ga (at 15Hz, 40 μm), defined by solution ICP-MS, and Sc (at 20 Hz, 100 μm) defined by ICP-OES and ionprobe. Solution prepared from bulk-rock powder (SD159) highlighted by open square whereas solutions prepared from microdrilled powder not highlighted. R2 - correlation coefficient, D.L- detection limit and Q.L.- quantification limit.

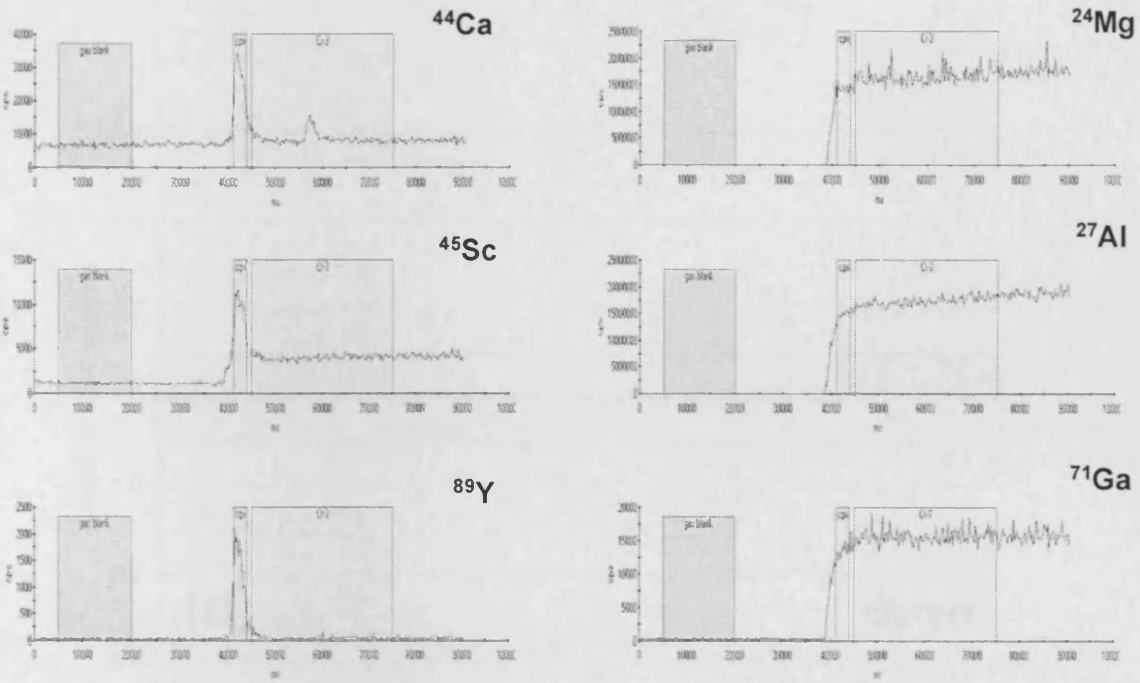

Figure 10: TRA spectra for laser ablation of chromite (Cr-3 = SD159) at 20 Hz, 100 µm line width for Ca, Sc, Y, Mg, Al and Ga. Clinopyroxene (cpx) inclusion (~ 10 µm) identified by co-existing peaks in Ca, Sc and Y. The inclusion has a negligible deficit in the Mg, Al and Ga intensities.

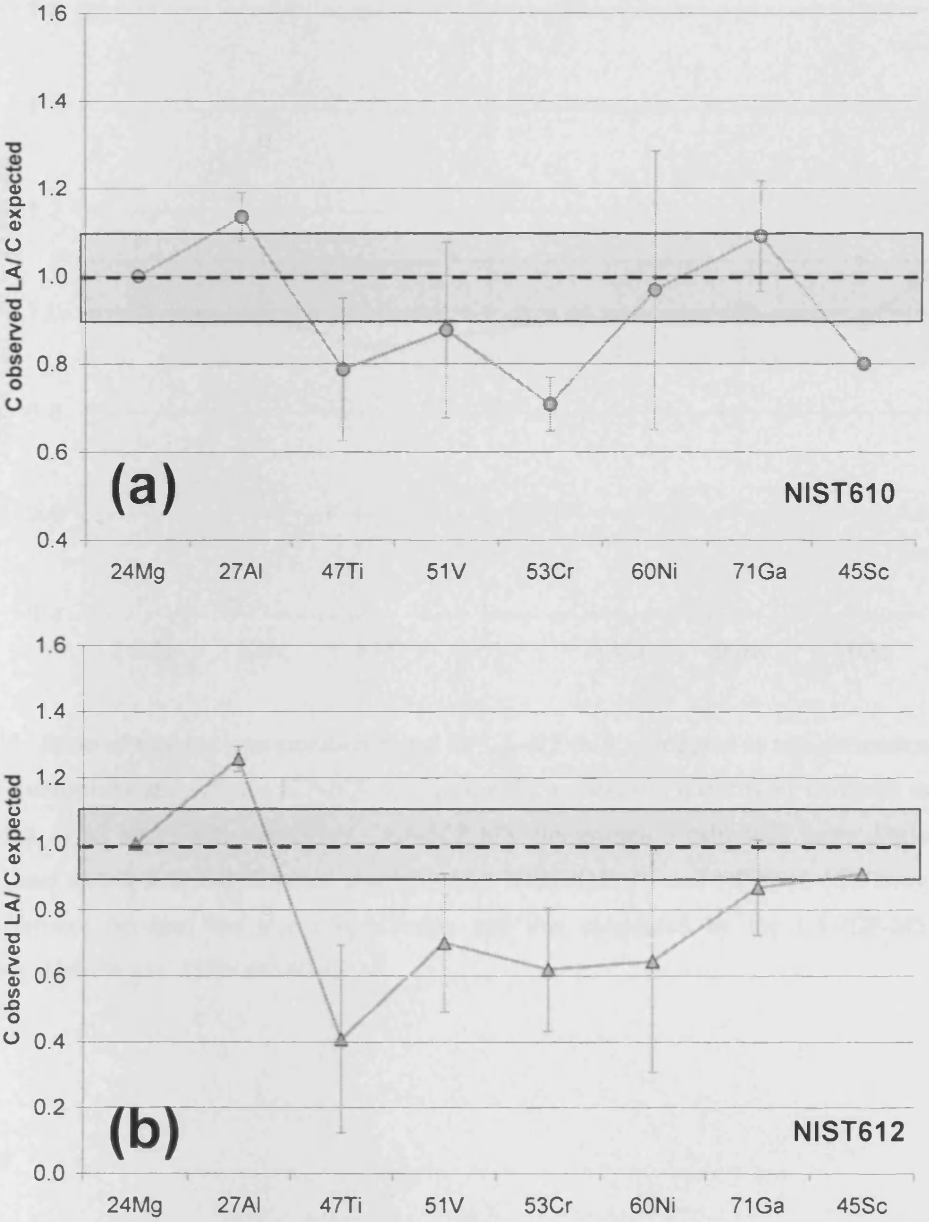

Figure 11: Ratio of element concentration found by LA-ICP-MS, compared to true concentration found by electron microprobe and solution ICP-MS to measure the accuracy in quantifying chromite sample SD159, analysed 8 to 12 times with error bars. LA-ICP-MS concentration calibrated using Mg as an internal standard and matrix-matched chromite standards (A), NIST 610 (B) and NIST612 (C). Grey box marks ± 10% difference between the true concentration and that calculated by the LA-ICP-MS . Operating conditions: Helium gas, 15Hz and 40um.

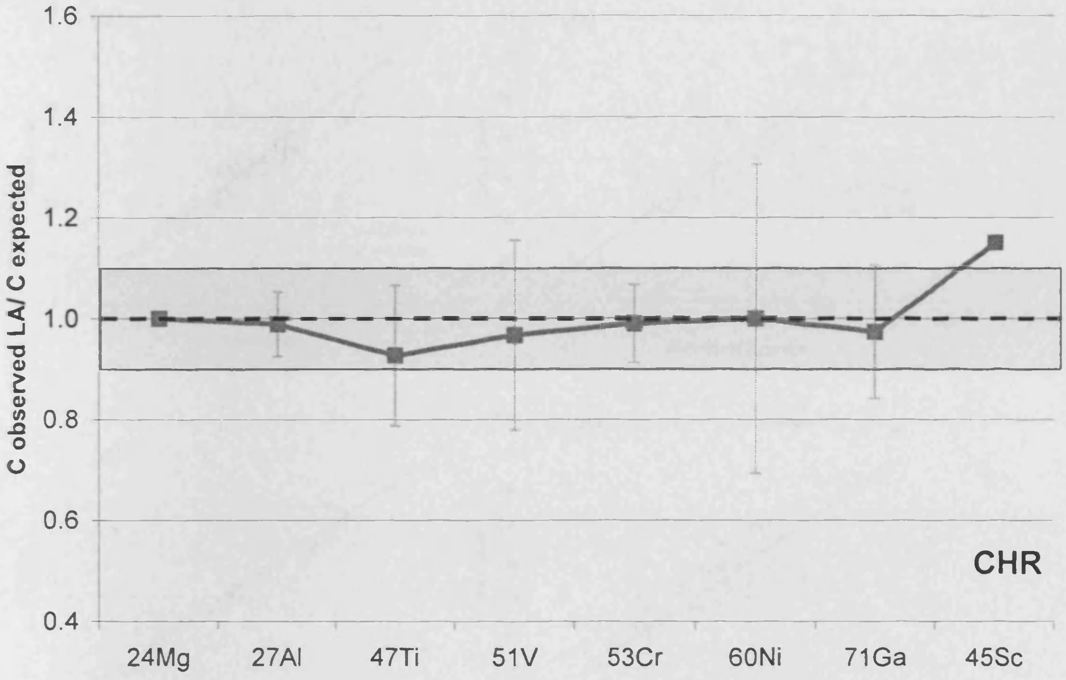

Figure 12: Ratio of element concentration found by LA-ICP-MS, compared to true concentration found by electron microprobe and solution ICP-MS to measure the accuracy in quantifying chromite sample SD159, analysed 8 to 12 times with error bars. LA-ICP-MS concentration calibrated using Mg as an internal standard and matrix-matched chromite standards (A), NIST 610 (B) and NIST612 (C). Grey box marks ± 10% difference between the true concentration and that calculated by the LA-ICP-MS . Operating conditions: Helium gas, 15Hz and 40um.

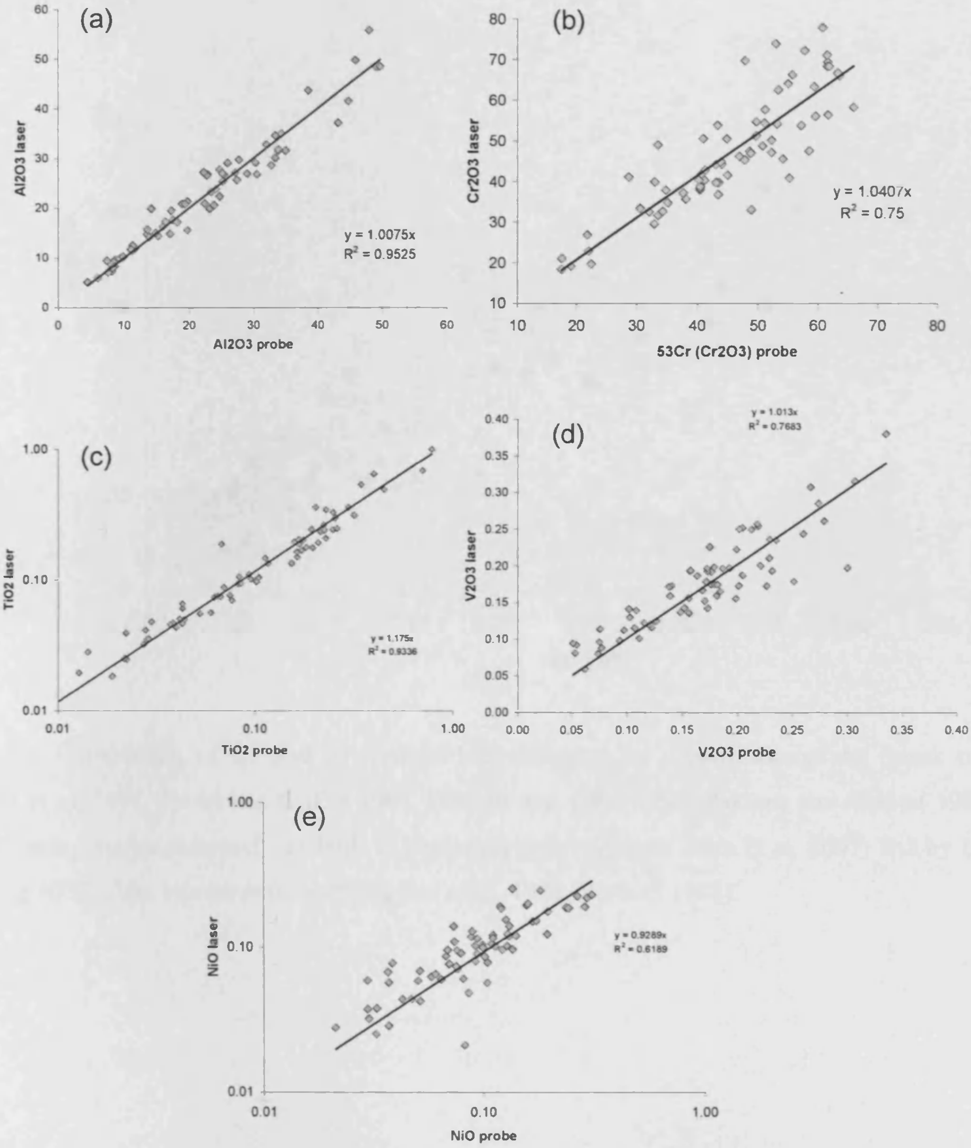

Figure 13: Comparison of laser-ablation ICP-MS and electron microprobe data for Al_2O_3 (a), Cr_2O_3 (b), TiO_2 (d), V_2O_3 (e) and NiO (f). R^2 = correlation coefficient.

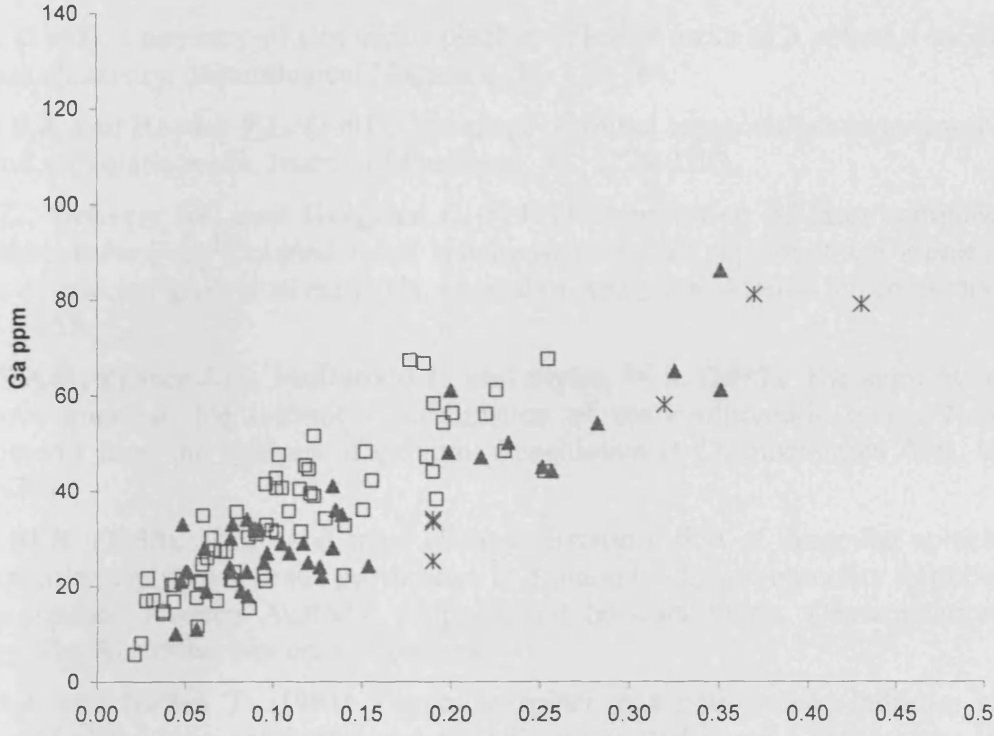

Figure 14: Comparison of Ga and Ni measured in chromites by proton microprobe (black triangles: O'Reilly et al. 1991, Ewart and Griffin 1994, Paktunc and Cabri 1995, Paktunc and Hulbert 1996), LA-ICP-MS using matrix-matched standards in chromites (open squares: Dare et al. 2007) and by LA-ICP-MS using NIST glass standards (crosses: Eggins et al., 1998, Norman 1998).

REFERENCES

Arai S. (1992). Chemistry of chromian spinel in volcanic rocks as a potential guide to magma chemistry. Mineralogical Magazine, 56, 173-184.

Barnes S.J. and Roeder P.L. (2001). The range of spinel compositions in terrestrial mafic and ultramafic rocks. Journal of Petrology, 42, 2279-2302.

Chen Z., Doherty W. and Grégoire C. (1997). Application of laser sampling microprobe inductively coupled mass spectrometry to the in situ trace element analysis of selected geological materials. Journal of Analytical Atomic Spectrometry, 12, 653 – 659.

Dares S.A.S., Pearce J.A., McDonald I., and Styles, M.S. (2007). The application of chrome-spinel in the tectonic discrimination of mafic-ultramafic rocks: New developments from the analysis of gallium. Geochimica et Cosmochimica Acta, in press, A201.

Denny M.B. (1998). Major and trace element discrimination of chromian spinels with particular application to the provenance of diamond indicator chromite from the Yilgarn Craton, Western Australia. Unpublished honours thesis, Department of Geology, The Australian National University.

Dick H.J. and Bullen T. (1984). Chromian spinel as a petrogenetic indicator in abyssal and alpine-type peridotites and spatially associated lavas. Contributions to Mineralogy and Petrology, 86, 54-76.

Eggins S.M., Rudnick R.L. and McDonough W.F. (1998). The composition of peridotites and their minerals: a laser-ablation ICP-MS study. Earth and Planetary Science Letters, 154, 53-71.

Ewart A. and Griffin W.L. (1994). Proton-microprobe trace element study of selected Leg 135 core samples. In: Hawkins J., Parson L., Allan J., et al (eds), Proceedings of the Ocean Drilling Program, Scientific Results, 135, 533-542.

Fryer B.J., Jackson S.E. and Longerich H.P. (1995). The design, operation and role of the Laser-Ablation Microprobe coupled with an inductively coupled plasma-mass spectrometer (LAM-ICP-MS) in the earth sciences. The Canadian Mineralogist, 33, 303-312.

Gao S., Liu X., Yuan H., Hattendorf B., Günther D., Chen L. and Hu S. (2002). Determination of forty two major and trace elements in USGS and NIST SRM glasses by laser ablation-inductively coupled plasma-mass spectrometry. Geostandards Newsletter, 26, 181- 196.

Glaser S.M., Foley S.F. and Günther D. (1999). Trace element compositions of minerals in garnet and spinel peridotite xemoliths from the Vitim volcanic field, Transbaikalia, eastern Siberia. Lithos, 48, 263-285.

Gonzälez J.J., Fernändez A., Mao X. and Rusoo R.E. (2004). Scanning vs. single spot laser ablation (λ = 213 nm) inductively coupled plasma mass spectrometry. Spectrochimica Acta Part B, 59, 369-374.

Grégoire M., Moine B.N., O'Reilly S.Y., Cottin J.Y. and Giret A. (2000). Trace element residence and partitioning in mantle xenoliths metasomatized by highly alkaline, silicate- and carbonate- rich melts (Kerguelen Islands, Indian Ocean). Journal of Petrology, 41, 477-509.

Griffin W.L., Sobolev N.V., Ryan C.G., Pokhilenko N.P., Win T.T. and Yefimova E.S. (1993). Trace elements in garnets and chromites: Diamond formation in the Siberian lithosphere. Lithos, 29, 235-256.

Griffin W.L., Ryan C.G., Gurney J.J., Sobolev N.V. and Win T.T. (1994). Chromite macrocrysts in kimberlites and lampriotes: geochemistry and origin. In: H.A.O. Meyer and O.H. Leonardos (Eds), Kimberlites, Related Rocks and Mantle Xenoliths. CRPM Special Publication, 1A/93, p/p/ 366 -377

Griffin W.L. and Ryan C.G. (1995). Trace element in indicator minerals: area selection and target evaluation in diamond exploration. Journal of Geochemical Exploration, 53, 311-337.

Griffin W.L., Fisher N.I., Friedman J.H. and Ryan C.G. (1997). Statistical techniques for the classification of chromites in diamond exploration samples. Journal of Geochemical Exploration, 59, 233-249.

Günther D., Frischknecht R., Heinrich C.A. and Kahlert H-J. (1997). Capabilities of an Argon Fluoride 193 nm Excimer laser for laser ablation inductively coupled plasma mass spectrometry microanalysis of geological materials. Journal of Analytical Atomic Spectrometry, 12, 939 – 944.

Günther D. and Hattendorf B. (2001). Elemental fractionation in LA-ICP-MS. In: Sylvestor P. (eds), Laser-ablation-ICPMS in the earth sciences: principles and applications, Mineralogical Association of Canada., 29, 83 – 91.

Horn I., Foley F., Jackson S.E. and Jenner G.A. (1994). Experimentally determined partitioning of high field strength- and selected transition elements between spinel and basaltic melt. Chemical Geology, 117, 193-218.

Horn I. and Günther D. (2003). The influence of ablation carrier gasses Ar, He and Ne on the particle size distribution and transport efficiencies of laser ablation-induced aerosols: implications for LA-ICP-MS. Applied Surface Science, 207, 144 - 157.

Jackson S.E. (2001). The application of Nd:YAG lasers in LA-ICP-MS. In: Sylvestor P. (eds), Laser-ablation-ICPMS in the earth sciences: principles and applications, Mineralogical Association of Canada., 29, 29 – 45.

Jarosewich E., Nelen J.A. and Norberg J.A. (1980). Reference samples for electron microprobe analysis. Geostandards Newsletter, 4, 43-47.

Kurat G., Palme H., Spettel B. Baddenhausen H., Hofmeister H., Palme C. and Wanke H. (1980). Geochemistry of ultramafic xenoliths from Kapfenstein, Austria: evidence for a variety of upper mantle processes. Geochimica et Cosmochimia Acta, 44, 45-60.

Lilly, R. (2006). The magmatic and crustal evolution of the northern Oman-United Arab Emirates ophiolite. PhD thesis, Cardiff University, 202pp.

McDonald, I. (2005). Development of sulphide standards for the in-situ analysis of platinum-group elements by laser ablation inductively coupled plasma-mass spectrometry (LA-ICP-MS). Extended abstract of the 10th International Platinum Symposium, 468-471.

McDonald I and Viljoen K.S. (2006). Platinum-group element geochemistry of mantle eclogites: a reconnaissance study of xenoliths from the Orapa kimberlite, Botswana. Transactions of the Institution of Mining and Metallurgy Section B-Applied Earth Science, 115, 81-93.

McKay D.B and Mitchell R.H. (1988). Abundance and distribution of gallium in some spinel and garnet lherzolites. Geochimica et Cosmochimia Acta, 52, 2867-2870.

Merkle R.L., Lubser M. and Gräser P.P.H. (2004). Incongruent dissolution of chromite in lithium tetraborate flux. X-Ray Spectrometry, 33, 222-224.

Nayak P.K. and Vijayan V. (2006). Complementary PIGE, PIXE, EDXRF and y-ray spectroscopic investigation on natural chromites. Nuclear Instruments and Methods in Physics Research B, 245, 505-510.

Norman M.D., Pearson N.J., Sharma A. and Griffin W.L. (1996). Quantitative analysis of trace elements in geological materials by Laser Ablation ICPMS: Instrumental operating conditions and calibration values of NIST glasses. Geostandards Newsletter, 20, 247-261.

Paktunc A.D. and Cabri L.J. (1995). A proton- and electron-microprobe study of gallium, nickel and zinc distribution in chromian-spinel. Lithos, 35, 261-282.

Parkinson I. J. and Pearce J. (1998). Peridotites from the Izu-Bonin-Mariana Forearc (ODP Leg 125): Evidence for Mantle Melting and Melt-Mantle Interaction in a Supra-Subduction Zone Setting. Journal of Petrology, 39, 1577-1618.

Pearce J., Barker P.F., Edwards S.J., Parkinson I.J. & Leat P.T. (2000). Geochemistry and tectonic significance of peridotites from the South Sandwich arc-basin system, South Atlantic. Contribution to Mineralogy and Petrology, 139, 36-53.

Pearce N.J.G., Perkins W.T., Westgate J.A., Gorton M.P., Jackson S.E., Neal C.R. and Chenery S.P. (1997). A compilation of new and published major and trace element data for NIST SRM 610 and NIST SRM 612 glass reference materials. Geostandards Newsletter, 21, 115 – 144.

Potts P.J., Gowing C.J.B. and Govindaraju K. (1992). Preparation, homogeneity evaluation and cooperative study of two new chromitite reference samples CHR-PT+ and CHR-BKG. Geostandards Newsletter, 16, 81 – 108.

Richardson, M. (1999). Upper mantle processes, diamond-bearing potential and stratigraphy of the mantle in the Kimberley region, Western Australia: Evidence from chromite, chromian diopside and garnet xenocryst chemistry. Unpublished honours thesis, Department of Geology, The Australian National University.

Ryan C.G. (1995). The nuclear microprobe as a probe of earth structure and geological processes. Nuclear Instruments and Methods in Physics Research B, 104, 377-394.

Stix J., Gauthier G., and Ludden J. (1995). A critical look at quantitative laser-ablation ICP-MS analysis of natural and synthetic glasses. The Canadian Mineralogist, 33, 435 – 444.

Stosch H-G. (1981). Sc, Cr, Co and Ni partitioning between minerals from spinel peridotite xenoliths. Contributions to Mineralogy and Petrology, 78, 166-174.

Taylor L.W., Anand M., Promprated P., Floss C. and Sobolev N. (2003). The significance of mineral inclusions in large diamonds from Yakutia, Russia. American Mineralogist, 88, 912-920.

Watling R.J., Herbert H.K., Barrow I.S. and Thomas A.G. (1995). Analysis of diamonds and indicator minerals for diamond exploration by laser ablation-inductively coupled plasma mass spectrometry. Analyst, 120, 1357-1364.

E.2 Table 1: Results from LA-ICP-MS of chrome-spinel in peridotites

The mean results of the analysis of chrome-spinel in peridotites and chromitites by the electron microprobe (EMP) and LA-ICP-MS are presented below They are divided by Setting, i.e. Passive Continental Margin (PCM), Mid-Ocean Ridge (MOR), Supra-Subduction Zone (SSZ), and ophiolites (northern Oman-U.A.E.; Pindos-Vourinos, Northern Greece; Troodos, Cyprus). Oxides are given in compound wt% and Ga is given in ppm. The limits of detection and quantification for Ga and its 1.s.d are given for each sample.

Additional data is included from the EMP analysis for Cr#, Mg#, Fe^3#, Fe^3/Sum Fe, Fa (olivine), T °C and fO_2 (FMQ). Ferric iron was measured using secondary EMP standards described in Section 4.1.2 and T°C and fO_2 (FMQ) calculated using Ballhaus et al., (1991). Ratios of 100Ti/Fe^3# (where Ti = TiO_2 measured by EMP) and Ga/Fe^3#, used for the tectonic discrimination diagrams are also given.

Appendix E: Analysis of Ga in chrome-spinel by LA-ICP-MS

Sample No.	637A25	637A23	899B27	670A8	670A5 core	670A5 alt	395-18	558-43	558D43	895D3B
Rock Type	Hz	Hz	Hz	Hz	Du	Du	Hz	Hz	Du	Hz
Spinel Type										
Setting	Pass.Marg	Pass.Marg	Pass.Marg	MOR	MOR	MOR	MOR	MOR	MOR	MOR
EMP (n=)	16	11	14	15	17	2	18	21	20	19
SiO_2	0.04	0.02	0.03	0.03	0.02	5.10	0.03	0.04	0.05	0.06
TiO_2	0.22	0.04	0.03	0.07	0.25	0.24	0.12	0.04	0.30	0.04
Al_2O_3	38.35	47.88	49.56	45.71	33.34	1.00	34.24	24.68	19.31	25.13
V_2O_3	0.14	0.08	0.05	0.10	0.15	0.07	0.15	0.20	0.18	0.20
Cr_2O_3	28.64	19.04	17.52	21.71	33.28	24.64	34.18	46.76	49.56	43.72
FeO	14.60	12.01	12.25	13.95	17.74	54.85	16.45	15.31	21.37	17.38
MnO	0.17	0.12	0.12	0.13	0.16	2.48	0.14	0.06	0.14	0.18
MgO	16.09	18.68	18.49	17.84	15.06	5.97	15.45	13.91	10.66	13.55
ZnO	0.18	0.20	0.17	0.15	0.13	0.27	0.14	0.15	0.17	0.15
NiO	0.20	0.29	0.31	0.27	0.16	0.06	0.17	0.09	0.07	0.10
Total	98.62	98.36	98.54	99.96	100.30	94.69	101.06	101.36	101.88	100.50
Cr#	0.334	0.211	0.192	0.242	0.401	0.943	0.401	0.560	0.633	0.539
Mg#	0.691	0.769	0.756	0.733	0.653	0.290	0.664	0.625	0.495	0.613
Fe^3#	0.015	0.016	0.011	0.028	0.047	0.570	0.035	0.012	0.037	0.034
Fe^{3+}/SumFe	0.082	0.116	0.081	0.176	0.217	0.597	0.176	0.065	0.134	0.156
Fa (ol)	0.105	0.100	0.095	0.097	0.080	0.0803	0.090	0.090	0.100	0.092
T°C	738	792	695	727	670	777	711	755	687	744
fO_2 (FMQ)	-1.57	-1.17	-1.43	-0.08	0.88	5.00	0.11	-1.97	-0.19	-0.21
LA-ICP-MS										
$^{27}Al_2O_3$	43.70	55.88	48.52	49.83	32.62	4.89	35.04	27.79	20.90	25.40
$^{47}TiO_2$	0.26	0.05	0.04	0.09	0.262	0.502	0.134	0.047	0.356	0.07
$^{51}V_2O_3$	0.16	0.09	0.08	0.13	0.228	0.302	0.137	0.222	0.175	0.25
$^{52}Cr_2O_3$	37.38	18.93	22.08	27.64	51.98	85.2	33.70	52.68	55.06	49.18
$^{53}Cr_2O_3$	41.06	19.23	21.04	26.87	52.94	75.7	32.65	46.21	51.24	44.86
^{60}NiO	0.18	0.19	0.23	0.23	0.300	0.603	0.15	0.09	0.14	0.10
^{69}Ga	58.35	56.87	41.75	54.10	55.6	19.3	47.89	33.01	22.53	45.53
^{71}Ga	**67.23**	**58.21**	**48.29**	**61.00**	**53.4**	**9.9**	**48.18**	**31.60**	**22.20**	**47.52**
Ga 1sd	18.88	10.32	9.61	14.24	10.1	6.9	6.30	3.71	7.34	11.67
Ga LOD	16.39	3.18	15.06	20.43	30.4	40.8	4.11	2.66	12.90	21.25
Ga LOQ	54.65	10.59	50.20	68.11	101.2	135.9	13.70	8.85	43.01	70.83
100Ti/Fe^3#	1530.0	256.3	252.0	243.8	532.9	41.3	333.2	342.9	798.5	124.7
Ga/Fe^3#	4618.1	3623.4	4270.5	2166.0	1143.9	17.4	1387.8	2545.3	595.0	1396.6

Sample No.	895D10	895E1Du	895E8Du	779A11	779A14	780C18	783A18	DR53.3	DR52.5	DR52.6
Rock Type	Du	Du	Du	Hz	Du	Hz	Hz	Du	Du	Du
Spinel Type										
Setting	MOR	MOR	MOR	SSZ	SSZ	SSZ	SSZ	SSZ	SSZ	SSZ
EMP (n=)	20	19	44	21	9	18	45	18	17	14
SiO_2	0.03	0.04	0.04	0.05	0.14	0.03	0.03	0.04	0.02	0.04
TiO_2	0.78	0.06	0.45	0.01	0.01	0.02	0.01	0.21	0.22	0.26
Al_2O_3	23.36	27.60	25.88	17.18	7.42	28.87	23.78	11.30	14.79	13.81
V_2O_3	0.21	0.18	0.19	0.22	0.20	0.18	0.23	0.23	0.14	0.13
Cr_2O_3	40.82	40.48	40.35	52.05	61.52	40.35	42.97	55.67	51.06	52.05
FeO	21.86	18.28	20.56	18.58	23.91	17.60	22.55	24.90	24.05	24.72
MnO	0.22	0.18	0.11	0.25	0.81	0.19	0.23	0.33	0.27	0.28
MgO	12.32	13.47	13.08	11.01	6.85	13.03	11.36	8.35	9.98	9.36
ZnO	0.14	0.16	0.15	0.15	0.28	0.21	0.23	0.22	0.14	0.18
NiO	0.16	0.09	0.13	0.06	0.08	0.08	0.10	0.07	0.08	0.07
Total	99.91	100.55	101.06	99.56	101.20	100.56	101.49	101.33	100.75	100.91
Cr#	0.540	0.496	0.511	0.670	0.529	0.484	0.548	0.768	0.698	0.717
Mg#	0.561	0.604	0.584	0.530	0.355	0.585	0.522	0.412	0.480	0.454
Fe^3#	0.069	0.038	0.059	0.027	0.024	0.020	0.062	0.069	0.080	0.059
Fe^{3+}/SumFe	0.243	0.167	0.226	0.109	0.070	0.092	0.215	0.204	0.250	0.175
Fa (ol)	0.102	0.097	0.104	0.090	0.078	0.090	0.091	0.085	0.086	0.084
T°C	749	719	750	713	597	643	646	657	698	656
fO_2 (FMQ)	0.88	-0.02	0.59	-0.67	-0.59	-0.86	0.98	1.12	1.34	0.86
LA-ICP-MS										
$^{27}Al_2O_3$	23.34	29.74	29.19	19.53	9.65	27.01	20.66	12.57	15.07	14.20
$^{47}TiO_2$	1.002	0.075	0.489	0.02	0.03	0.025	0.009	0.193	0.240	0.248
$^{51}V_2O_3$	0.250	0.198	0.197	0.26	0.19	0.166	0.173	0.236	0.172	0.125
$^{52}Cr_2O_3$	50.11	44.63	42.91	55.03	59.96	38.14	41.03	60.05	59.84	46.54
$^{53}Cr_2O_3$	50.51	41.69	38.85	50.14	56.53	38.36	39.78	66.37	57.76	47.14
^{60}NiO	0.20	0.10	0.12	0.06	0.02	0.07	0.08	0.08	0.09	0.07
^{69}Ga	51.07	40.83	52.28	28.08	9.78	27.29	23.03	25.87	32.82	28.06
^{71}Ga	**56.24**	**40.59**	**51.47**	**24.59**	**5.70**	**27.37**	**23.02**	**21.26**	**30.92**	**27.25**
Ga 1sd	10.65	5.64	6.62	8.68	2.32	4.11	3.68	8.49	7.31	8.06
Ga LOD	12.84	3.39	3.49	16.91	9.48	3.30	4.21	16.36	12.85	4.90
Ga LOQ	42.81	11.30	11.64	56.35	31.60	10.99	14.03	54.53	42.84	16.34
100Ti/Fe^3#	1133.1	167.6	764.5	33.6	59.1	107.3	16.5	299.9	278.8	438.8
Ga/Fe^3#	814.0	1066.2	877.5	917.7	238.8	1362.4	374.3	307.5	385.7	460.6

Appendix E: Analysis of Ga in chrome-spinel by LA-ICP-MS

Sample No.	**D52.8**	**D52.11**	**UAE2065**	**UAE2241**	**SD157**	**UAE2288**	**SD426**	**UAE4875**	**SD452**	**SD19**
Rock Type	**Hz**	**Hz**	**Lhz**	**Hz**	**Hz**	**Hz**	**Hz**	**Hz**	**Hz**	**Hz**
Spinel Type			**HL**	**HL**	**HL**	**HL**	**HL**	**HL**	**HL**	**HL**
Setting	SSZ	SSZ	UAE	UAE	UAE	UAE	UAE	UAE	UAE	UAE
EMP (n=)	16	41	23	38	34	20	4	6	35	40
SiO_2	0.04	0.04	0.04	0.04	0.02	0.03	0.03	0.03	0.03	0.04
TiO_2	0.17	0.10	0.07	0.04	0.08	0.07	0.03	0.07	0.04	0.16
Al_2O_3	27.35	33.77	49.02	34.88	18.82	22.79	23.11	33.82	27.07	30.42
V_2O_3	0.17	0.20	0.09	0.16	0.20	0.25	0.22	0.11	0.17	0.16
Cr_2O_3	40.10	33.42	17.46	32.85	47.69	43.89	43.30	34.97	41.20	38.01
FeO	20.71	18.33	13.48	16.39	22.14	19.24	19.10	13.58	16.32	16.40
MnO	0.21	0.18	0.12	0.17	0.25	0.20	0.19	0.15	0.16	0.16
MgO	12.62	14.00	17.88	14.48	10.67	11.92	12.33	15.65	13.95	14.14
ZnO	0.25	0.20	0.15	0.24	0.00	0.20	0.23	0.12	0.17	0.24
NiO	0.10	0.14	0.29	0.11	0.08	0.09	0.13	0.13	0.11	0.11
Total	101.74	100.38	98.60	99.37	100.1798.	67	98.66	98.64	99.22	99.83
Cr#	0.496	0.399	0.193	0.387	0.630	0.564	0.557	0.410	0.505	0.456
Mg#	0.564	0.613	0.733	0.635	0.506	0.560	0.578	0.686	0.633	0.628
Fe^3#	0.050	0.036	0.022	0.023	0.054	0.042	0.048	0.013	0.029	0.022
Fe^{3+}/SumFe	0.193	0.162	0.142	0.117	0.185	0.168	0.194	0.081	0.143	0.108
Fa (ol)	0.092	0.097	0.095	0.088	0.093	0.087	0.092	0.090	0.089	0.097
T°C	658	653	656	631	682	679	716	737	734	712
fO_2 (FMQ)	0.65	0.17	-0.16	-0.35	0.56	0.31	0.41	-1.60	-0.37	-0.90
LA-ICP-MS										
$^{27}Al_2O_3$	25.72	31.81	48.46	31.59	20.88	26.87	19.95	31.57	27.21	26.91
$^{47}TiO_2$	0.203	0.104	0.074	0.061	0.106	0.19	0.041	0.076	0.050	0.15
$^{51}V_2O_3$	0.143	0.173	0.10	0.194	0.252	0.18	0.254	0.115	0.167	0.14
$^{52}Cr_2O_3$	39.11	29.58	18.48	29.56	40.83	44.70	36.99	25.00	42.67	27.19
$^{53}Cr_2O_3$	40.31	31.70	18.44	29.60	45.33	44.21	36.81	34.76	42.91	35.70
^{60}NiO	0.10	0.12	0.22	0.10	0.06	0.12	0.10	0.10	0.12	0.11
^{69}Ga	32.34	43.47	54.04	39.28	33.85	43.02	30.82	32.63	31.50	41.09
^{71}Ga	**31.76**	**44.47**	**56.08**	**42.66**	**34.84**	**45.28**	**31.30**	**32.83**	**31.50**	**40.56**
Ga 1sd	4.41	13.70	8.11	10.17	7.21	10.00	9.11	6.12	7.74	8.58
Ga LOD	3.76	4.24	12.9	20.14	13.93	17.16	10.50	8.52	12.16	13.2
Ga LOQ	12.53	14.15	43.0	67.15	46.43	57.20	16.35	28.40	40.53	44.0
100Ti/Fe^3#	349.6	287.7	301.8	181.5	152.3	158.0	57.2	550.5	147.3	737.4
Ga/Fe^3#	638.3	1233.0	2557.7	1819.3	645.5	1076.9	651.5	2448.1	1072.1	1841.4

Sample No.	**UAE144**	**SD489**	**UAE312**	**UAE715**	**UAE391**	**UAE2007**	**SD567**	**UAE424**	**UAE2064**	**SD67**
Rock Type	**Hz**	**Hz**	**Hz**	**Hz**	**Hz**	**Hz**	**Hz**	**Hz**	**Du**	**Du**
Spinel Type	**EU**	**HL+SI**	**EU**	**EU**	**EU**	**HL**	**EU**	**HL**	**SI**	**EU**
Setting	UAE	UAE	UAE	UAE	UAE	UAE	UAE	UAE	UAE	UAE
EMP (n=)	24	40	24	4	40	5	4	40	24	24
SiO_2	0.02	0.03	0.03	0.03	0.03	0.03	0.01	0.03	0.03	0.03
TiO_2	0.02	0.03	0.04	0.02	0.01	0.06	0.03	0.04	0.19	0.10
Al_2O_3	8.63	19.68	13.50	7.97	13.54	43.06	19.66	31.88	8.10	5.98
V_2O_3	0.31	0.28	0.27	0.23	0.34	0.11	0.26	0.18	0.07	0.12
Cr_2O_3	59.23	48.44	53.05	58.41	55.10	22.39	48.76	34.67	54.92	60.66
FeO	21.06	20.43	23.55	24.03	20.62	15.56	19.64	18.76	28.48	25.29
MnO	0.27	0.24	0.26	0.30	0.30	0.12	0.23	0.21	0.37	0.33
MgO	8.42	10.23	9.21	7.74	9.67	15.93	10.55	13.45	7.60	7.04
ZnO	0.19	0.24	0.20	0.22	0.21	0.26	0.23	0.29	0.20	0.20
NiO	0.02	0.05	0.06	0.03	0.04	0.24	0.03	0.12	0.07	0.04
Total	98.16	99.65	100.17	98.98	100.0597.	77	99.42	99.62	100.0299	.79
Cr#	0.822	0.623	0.725	0.831	0.732	0.259	0.625	0.422	0.820	0.872
Mg#	0.434	0.490	0.453	0.399	0.477	0.681	0.505	0.601	0.387	0.365
Fe^3#	0.036	0.031	0.065	0.065	0.033	0.029	0.026	0.037	0.112	0.070
Fe^{3+}/SumFe	0.122	0.114	0.203	0.192	0.118	0.157	0.100	0.160	0.281	0.197
Fa (ol)	0.086	0.090	0.088	0.086	0.093	0.091	0.090	0.093	0.086	0.082
T°C	693	638	677	677	701	611	652	639	679	658
fO_2 (FMQ)	-0.09	-0.30	0.92	0.94	-0.37	0.31	-0.62	0.27	1.91	1.19
LA-ICP-MS										
$^{27}Al_2O_3$	9.66	21.39	14.79	8.83	15.83	37.22	15.62	32.81	7.39	5.97
$^{47}TiO_2$	0.018	0.03	0.05	0.039	0.019	0.074	0.048	0.04	0.176	0.100
$^{51}V_2O_3$	0.32	0.26	0.29	0.235	0.380	0.139	0.244	0.19	0.080	0.116
$^{52}Cr_2O_3$	64.46	48.93	51.92	64.20	40.04	21.28	32.21	39.60	59.70	68.21
$^{53}Cr_2O_3$	63.40	47.47	54.18	47.57	40.87	19.67	33.12	37.93	64.10	77.96
^{60}NiO	0.03	0.04	0.06	0.04	0.03	0.19	0.06	0.10	0.09	0.06
^{69}Ga	19.13	23.22	30.90	16.60	23.39	39.23	23.36	39.98	18.66	15.63
^{71}Ga	**16.97**	**20.30**	**26.00**	**14.76**	**21.76**	**43.94**	**21.09**	**41.41**	**15.38**	**11.60**
Ga 1sd	6.40	3.21	7.88	5.79	6.16	17.06	8.54	10.01	4.97	5.58
Ga LOD	17.5	12.60	16.62	11.44	13.57	16.84	26.85	17.86	10.20	10.67
Ga LOQ	58.3	41.99	55.40	38.13	45.23	56.15	59.36	59.53	34.02	35.56
100Ti/Fe^3#	51.8	87.8	58.6	33.9	38.4	212.7	114.0	106.1	172.8	141.4
Ga/Fe^3#	467.8	661.7	402.5	227.6	657.5	1512.2	814.8	1112.01	37.1	164.8

Appendix E: Analysis of Ga in chrome-spinel by LA-ICP-MS

Sample No.	SD158	SD159b	SD494	SD484	SD255	SD425	SD451	UAE4876	UAE4878	SD18
Rock Type	Du	Chr	Du	Du	Du	Du	Du	Du	Du	Du
Spinel Type	SIEU		SI	EU	SI	SI	SI	SI	HL	EU
Setting	UAE	UAE	UAE	UAE	UAE	UAE	UAE	UAE	UAE	UAE
EMP (n=)	14	23	10	4	4	2	27	6	4	38
SiO_2	0.02	0.02	0.03	0.02	0.03	0.01	0.04	0.03	0.03	0.04
TiO_2	0.19	0.23	0.17	0.11	0.20	0.17	0.05	0.08	0.16	0.08
Al_2O_3	16.28	17.39	11.11	18.04	22.36	24.62	24.13	32.71	15.89	9.31
V_2O_3	0.12	0.12	0.18	0.22	0.17	0.14	0.17	0.23	0.15	0.19
Cr_2O_3	47.83	50.59	54.02	48.66	41.05	40.36	43.18	31.97	52.86	59.42
FeO	23.20	17.02	26.49	21.86	24.32	21.68	16.65	17.84	18.48	19.71
MnO	0.24	0.20	0.34	0.35	0.24	0.13	0.17	0.18	0.26	0.26
MgO	10.72	13.04	7.36	9.79	11.55	13.36	13.81	15.14	11.50	9.85
ZnO	0.08	0.07	0.22	0.21	0.16	0.24	0.13	0.20	0.17	0.13
NiO	0.13	0.13	0.09	0.09	0.12	0.17	0.11	0.19	0.04	0.05
Total	98.81	98.82	100.029	9.33	100.20	100.87	98.45	98.57	99.54	99.05
Cr#	0.663	0.661	0.765	0.644	0.552	0.524	0.546	0.396	0.691	0.811
Mg#	0.519	0.618	0.371	0.475	0.536	0.605	0.637	0.671	0.552	0.495
Fe^3#	0.085	0.041	0.080	0.042	0.095	0.087	0.040	0.061	0.033	0.041
Fe^{3+}/SumFe	0.273	0.180	0.219	0.144	0.305	0.319	0.189	0.276	0.135	0.150
Fa (ol)	0.073	0.044	0.094	0.084	0.094	0.089	0.082	0.090	0.081	0.081
T°C	679	625	641	627	704	756	752	744	732	746
fO_2 (FMQ)	1.76	1.43	1.22	0.35	1.60	1.48	0.26	1.01	-0.15	0.17
LA-ICP-MS										
$^{27}Al_2O_3$	17.34	17.75	11.51	17.22	21.02	22.41	23.93	28.59	16.34	9.88
$^{47}TiO_2$	0.243	0.21	0.168	0.147	0.358	0.20	0.06	0.093	0.194	0.094
$^{51}V_2O_3$	0.121	0.12	0.159	0.200	0.193	0.17	0.23	0.211	0.142	0.197
$^{52}Cr_2O_3$	51.83	48.94	41.54	42.03	40.24	35.57	52.38	22.61	57.06	61.59
$^{53}Cr_2O_3$	69.85	48.79	45.55	46.99	40.37	37.96	53.79	32.54	73.95	56.13
^{60}NiO	0.16	0.14	0.05	0.13	0.19	0.15	0.12	0.12	0.07	0.04
^{69}Ga	46.24	35.89	24.32	47.61	37.06	38.49	36.86	39.35	29.99	18.90
^{71}Ga	**42.13**	**32.74**	**21.55**	**34.19**	**38.23**	**35.98**	**39.44**	**38.93**	**27.62**	**16.77**
Ga 1sd	9.08	2.4	6.21	6.47	9.45	10.44	7.64	6.82	7.45	5.01
Ga LOD	14.36	12.79	11.04	10.60	11.42	15.53	11.41	10.55	13.71	8.15
Ga LOQ	47.86	42.62	36.80	35.33	38.08	51.76	38.04	35.16	45.71	27.17
100Ti/Fe^3#	225.1	559.7	213.9	265.2	210.6	190.4	129.6	133.9	472.1	205.5
Ga/Fe^3#	494.9	806.6	268.9	811.4	400.6	415.3	976.1	642.1	830.4	409.8

Sample No.	UAE2008	UAE143	UAE160	UAE138	UAE138	SD540	SD511	UAE33	UAE65du	UAE65cr
Rock Type	Du	Du	Du	Du	Chr	Du	Du	Du	Du	Chr
Spinel Type	SI	EU	EU	SI		SI	SI	SI	SIEU	
Setting	UAE	UAE	UAE	UAE	UAE	UAE	UAE	UAE	UAE	UAE
EMP (n=)	24	24	4	4	4	24	24	4	4	3
SiO_2	0.04	0.03	0.04	0.02	0.03	0.03	0.03	0.03	0.02	0.03
TiO_2	0.16	0.02	0.03	0.09	0.09	0.21	0.34	0.18	0.23	0.25
Al_2O_3	11.61	8.39	4.45	8.26	8.54	33.32	30.19	15.13	22.20	22.70
V_2O_3	0.16	0.27	0.07	0.05	0.05	0.17	0.18	0.18	0.12	0.10
Cr_2O_3	53.27	61.37	65.87	63.17	63.53	30.46	32.90	49.56	43.41	44.81
FeO	25.55	20.99	20.74	16.48	13.93	22.51	22.65	25.19	21.68	17.49
MnO	0.32	0.27	0.30	0.16	0.15	0.21	0.23	0.30	0.28	0.16
MgO	7.91	8.68	8.74	12.16	13.59	12.98	12.82	8.75	11.82	14.06
ZnO	0.31	0.18	0.23	0.04	0.00	0.22	0.13	0.21	0.07	0.06
NiO	0.05	0.03	0.03	0.10	0.07	0.13	0.16	0.04	0.09	0.07
Total	99.37	100.23	100.50	100.52	99.98	100.23	99.64	99.57	99.90	99.72
Cr#	0.755	0.831	0.909	0.837	0.833	0.380	0.422	0.687	0.567	0.570
Mg#	0.399	0.439	0.449	0.594	0.659	0.572	0.573	0.430	0.548	0.640
Fe^3#	0.085	0.034	0.041	0.035	0.029	0.070	0.075	0.076	0.067	0.052
Fe^{3+}/SumFe	0.242	0.117	0.143	0.158	0.155	0.252	0.263	0.221	0.240	0.233
Fa (ol)	0.077	0.085	0.069	0.047	0.037	0.110	0.096	0.095	0.081	0.061
T°C	626	701	712	720	725	651	653	657	670	697
fO_2 (FMQ)	1.69	-0.19	0.52	0.90	0.98	1.15	1.40	1.11	1.26	1.24
LA-ICP-MS										
$^{27}Al_2O_3$	11.99	9.19	5.16	8.06	8.25	30.20	29.22	14.44	27.29	26.64
$^{47}TiO_2$	0.16	0.02	0.035	0.111	0.101	0.233	0.532	0.177	0.343	0.327
$^{51}V_2O_3$	0.19	0.31	0.096	0.095	0.092	0.152	0.175	0.175	0.123	0.113
$^{52}Cr_2O_3$	63.53	71.57	70.30	66.81	66.92	29.28	40.31	52.76	45.92	44.94
$^{53}Cr_2O_3$	62.63	68.43	58.37	66.72	66.13	33.36	39.91	54.75	39.73	41.59
^{60}NiO	0.06	0.03	0.03	0.06	0.10	0.25	0.20	0.04	0.08	0.11
^{69}Ga	22.60	19.93	11.61	21.15	28.57	81.68	51.91	22.85	36.03	36.94
^{71}Ga	**20.72**	**17.13**	**8.04**	**17.61**	**21.12**	**67.55**	**54.25**	**20.35**	**35.55**	**35.70**
Ga 1sd	6.10	4.80	3.40	5.14	6.74	12.51	10.26	7.59	6.59	9.39
Ga LOD	13.75	11.47	8.21	10.31	11.12	15.08	11.04	14.36	5.14	5.34
Ga LOQ	45.83	38.24	27.37	40.78	52.18	50.26	36.80	47.88	17.14	17.79
100Ti/Fe^3#	190.6	65.5	67.5	262.8	324.1	306.9	461.0	238.4	340.6	474.8
Ga/Fe^3#	244.4	505.2	193.7	500.5	725.5	969.6	725.8	269.1	530.6	686.2

Appendix E: Analysis of Ga in chrome-spinel by LA-ICP-MS

Sample No.	**UAE393**	**UAE140**	**SD444**	**SD49**	**SD345**	**L35-90**	**LK44**	**AR90-28**	**XM-2**	**BT6B**	**79d**	**Tr1**
Rock Type	**Chr**	**Chr**	**Chr**	**Chr**	**Chr**	**Hz**	**Hz**	**Du**	**Du**	**Du**	**Chr**	**Lava**
Spinel Type												
Setting	UAE	UAE	UAE	UAE	UAE	Greece	Greece	Greece	Greece	Greece	Greece	Troodos
EMP (*n*=)	24	21	23	24	3	16	5	32	10	12	49	20
SiO_2	0.02	0.04	0.02	0.02	0.02	0.03	0.03	0.03	0.01	0.04	0.02	0.08
TiO_2	0.08	0.03	0.51	0.17	0.40	0.06	0.70	0.04	0.15	0.10	0.32	0.25
Al_2O_3	9.63	7.44	23.53	25.31	14.10	44.68	25.01	11.06	9.84	7.56	16.99	11.69
V_2O_3	0.08	0.08	0.11	0.17	0.17	0.11	0.30	0.16	0.06	0.20	0.23	0.10
Cr_2O_3	61.53	64.07	42.78	42.92	50.91	21.93	37.54	57.70	61.37	61.75	44.75	57.10
FeO	15.12	15.06	17.25	16.99	22.11	14.56	22.04	19.08	16.23	21.14	26.38	16.36
MnO	0.18	0.17	0.18	0.18	0.24	0.13	0.24	0.24	0.22	0.29	0.26	0.17
MgO	12.90	12.35	14.11	14.54	10.65	17.02	12.60	10.28	12.34	8.87	9.27	14.05
ZnO	0.05	0.04	0.07	0.05	0.08	0.17	0.16	0.14	0.07	0.14	0.09	0.05
NiO	0.08	0.10	0.15	0.13	0.09	0.24	0.12	0.04	0.05	0.03	0.06	0.10
Total	99.83	99.39	98.72	100.4998.	78	98.93	98.74	98.76	100.33	100.129	8.36	99.95
Cr#	0.811	0.750	0.549	0.532	0.708	0.248	0.502	0.778	0.807	0.846	0.639	0.766
Mg#	0.628	0.612	0.643	0.652	0.518	0.711	0.575	0.513	0.599	0.448	0.451	0.667
Fe^3#	0.028	0.026	0.049	0.046	0.073	0.027	0.081	0.035	0.032	0.040	0.099	0.061
Fe^{3+}/SumFe	0.136	0.124	0.221	0.217	0.241	0.162	0.281	0.134	0.147	0.136	0.275	0.282
Fa (ol)	0.044		0.061	0.063	0.070	0.093	0.100	0.095	0.061	0.086	0.079	0.094
T°C	717		690	686	691	663	743	785	787	728	624	1084
fO_2 (FMQ)	0.61		1.19	1.04	1.53	0.07	1.23	-0.40	0.19	0.05	1.98	0.33
LA-ICP-MS												
$^{27}Al_2O_3$	10.11			26.87	19.98	41.57	27.10	11.81	10.29	7.12	14.89	12.18
$^{47}TiO_2$	0.07			0.19	0.644	0.06	0.68	0.05	0.13	0.097	0.31	0.30
$^{51}V_2O_3$	0.11			0.18	0.197	0.10	0.20	0.16	0.06	0.155	0.19	0.14
$^{52}Cr_2O_3$	70.39			44.70	50.62	22.93	37.03	61.05	60.41	61.16	45.01	68.55
$^{53}Cr_2O_3$	69.43			44.21	54.41	22.84	37.19	72.35	71.16	68.33	50.51	53.85
^{60}NiO	0.09			0.12	0.12	0.19	0.18	0.08	0.07	0.04	0.07	0.09
^{69}Ga	25.74	20.43	44.06	43.02	41.12	41.92	62.74	22.15	21.12	17.99	36.42	29.88
^{71}Ga	**22.23**	**20.43**	**44.06**	**45.28**	**40.34**	**47.08**	**66.61**	**21.27**	**16.96**	**14.26**	**30.16**	**30.25**
Ga 1sd	6.63	0.37	0.45	10.00	15.12	2.52	6.65	2.00	0.12	3.53	1.56	5.03
Ga LOD	15.16			17.16	26.60	5.62	7.92	3.08	3.24	5.89	3.06	9.93
Ga LOQ	50.55			57.20	88.65	18.74	26.40	10.26	10.81	19.64	10.19	33.11
100Ti/Fe^3#	271.9	133.0	1044.7	360.2	547.9	216.0	871.6	105.2	474.0	252.5	322.1	412.7
Ga/Fe^3#	799.6	796.9	894.4	983.0	555.3	1721.7	826.5	606.5	527.5	357.1	305.7	493.0

E.3 Sample Descriptions

Table 2: Description of samples analysed for Ga in chrome-spinel in Chapter 5.

Sample No.	Location	Setting	Rock Type	Additional Info	References	Sp %	Spinel Type
637A25	Galicia, Atlantic Margin	PCM	**Harzburgite**	Leg 103, Site 637A 25R-2 90-95	Boillot et al., 1980; Evans & Girardeau, 1988	<3	
637A23	Galicia, Atlantic Margin	PCM	**Harzburgite**	Leg 103, Site 637A 23R-3 64-68	Boillot et al., 1980; Evans & Girardeau, 1988	<3	
899B27	Iberia, Atlantic Margin	PCM	**Harzburgite**	Leg 149, Site 899B 27R-1	Cornen et al., 1996; Seifert & Brunotte, 1996	<3	
670A8	Mid-Atlantic Ridge (MAR)	MOR	**Harzburgite**	Leg 109, Site 670A 8R-1 18-24	Fuji, 1990; Juteau et al., 1990	<3	
670A5	Mid-Atlantic Ridge (MAR)	MOR	**Dunite**	Leg 109, Site 670A 5R-1 72-77	Fuji, 1990; Juteau et al., 1990	<3	
395-18	Mid-Atlantic Ridge (MAR)	MOR	**Harzburgite**	Leg 45, Site 395 18R-2 109-114	Arai & Fuji., 1979	<3	
558-43	Azores, MAR	MOR	**Harzburgite**	Leg 82, Site 558 43R-1 84-89	Michael & Bonatti et al., 1985	<3	
558D43	Azores, MAR	MOR	**Dunite**	Leg 82, Site 558 43R-1 18-23	Michael & Bonatti et al., 1985	<3	
895D3B	Hess Deep, East Pacific Rise	MOR	**Harzburgite**	Leg 147, Site 895D 3R-1 15B	Matsukage, 1996; Edwards & Malpas, 1996	<3	
895D3A	Hess Deep, East Pacific Rise	MOR	**Harzburgite**	Leg 147, Site 895D 3R-1 15A	Allan & Dick, 1996; Arai & Matsukage, 1996; Edwards & Malpas, 1996	<3	
895D10	Hess Deep, East Pacific Rise	MOR	**Dunite**	Leg 147, Site 895D 10W-1	Matsukage, 1996; Edwards & Malpas, 1996	<3	
895E7Hz	Hess Deep, East Pacific Rise	MOR	**Harzburgite**	Leg 147, Site 895E 7R-2 10	Matsukage, 1996; Edwards & Malpas, 1996	<3	
895E1Du	Hess Deep, East Pacific Rise	MOR	**Dunite**	Leg 147, Site 895E 1R-3 3D	Matsukage, 1996; Edwards & Malpas, 1996	<3	
895E8Du	Hess Deep, East Pacific Rise	MOR	**Dunite**	Leg 147, Site 895E 8R-1 103-105	Matsukage, 1996; Edwards & Malpas, 1996	<3	
779A11	Conical Seamount, Maiana Forearc	SSZ	**Harzburgite**	Leg 125, Site 779A 11R-1 16-23	Ishii et al., 1992; Parkinson & Pearce, 1998	<3	
779A14	Conical Seamount, Maiana Forearc	SSZ	**Dunite**	Leg 125, Site 779A 14R-2 18-25	Parkinson & Pearce, 1998	<3	
780C18	Conical Seamount, Maiana Forearc	SSZ	**Harzburgite**	Leg 125, Site 780C 18R-1 51-55	Parkinson & Pearce, 1998	<3	
783A18	Torishima Seamount, Izu-Bonin Forearc	SSZ	**Harzburgite**	Leg 125, Site 783A 18R-1 96-99	Parkinson & Pearce, 1998	<3	
DR53.3	South Sandwich Forearc, Scotia Sea	SSZ	**Dunite**		Pearce et al., 2000	<3	Eu
DR52.5	South Sandwich Forearc, Scotia Sea	SSZ	**Dunite**		Pearce et al., 2000	<3	Eu
DR52.6	South Sandwich Forearc, Scotia Sea	SSZ	**Dunite**		Pearce et al., 2000	<3	Eu
DR52.8	South Sandwich Forearc, Scotia Sea	SSZ	**Harzburgite**	Transitional harzburgite	Pearce et al., 2000	<3	Eu
DR52.11	South Sandwich Forearc, Scotia Sea	SSZ	**Harzburgite**		Pearce et al., 2000	<3	An
UAE2065	ASWN, northern Oman-U.A.E.	ophiolite	**Lherzolite**		This study	<3	An
UAE2241	ASWN, northern Oman-U.A.E.	ophiolite	**Harzburgite**		This study	<3	An
SD157	ASWN, northern Oman-U.A.E.	ophiolite	**Harzburgite**	label 3) on hz plots	This study	<3	An
UAE2288	ASWN, northern Oman-U.A.E.	ophiolite	**Harzburgite**	label 1) on hz plots	This study	<3	An
SD426	ASWS, northern Oman-U.A.E.	ophiolite	**Harzburgite**	label 2) on hz plots	This study	<3	An
UAE4875	DIBBA, northern Oman-U.A.E.	ophiolite	**Harzburgite**		This study	<3	An
SD452	DIBBA, northern Oman-U.A.E.	ophiolite	**Harzburgite**		This study	<3	An
SD19	DIBBA, northern Oman-U.A.E.	ophiolite	**Harzburgite**		This study	<3	An
UAE144	KFN, northern Oman-U.A.E.	ophiolite	**Harzburgite**		This study	<3	Eu
SD489	KFN, northern Oman-U.A.E.	ophiolite	**Harzburgite**	label 4) on hz plots	This study	<3	Eu
UAE312	KFN, northern Oman-U.A.E.	ophiolite	**Harzburgite**		This study	<3	Eu
UAE715	KFN, northern Oman-U.A.E.	ophiolite	**Harzburgite**		This study	<3	Eu
UAE391	KFN, northern Oman-U.A.E.	ophiolite	**Harzburgite**		This study	<3	Eu
UAE2007	KFN, northern Oman-U.A.E.	ophiolite	**Harzburgite**		This study	<3	An
SD567	KFN, northern Oman-U.A.E.	ophiolite	**Harzburgite**	label 5) on hz plots	This study	<3	Eu
UAE424	KFS, northern Oman-U.A.E.	ophiolite	**Harzburgite**		This study	<3	An
UAE2064	ASWN, northern Oman-U.A.E.	ophiolite	**Dunite**		This study	<3	Eu
SD67	ASWN, northern Oman-U.A.E.	ophiolite	**Dunite**		This study	<3	Eu
SD158	ASWN, northern Oman-U.A.E.	ophiolite	**Dunite**		This study	<3	Eu
SD159b	ASWN, northern Oman-U.A.E.	ophiolite	**Chromitite**		This study	98	Eu
SD494	ASWN, northern Oman-U.A.E.	ophiolite	**Dunite**		This study	<3	Eu
SD484	ASWN, northern Oman-U.A.E.	ophiolite	**Dunite**	label 2) on du plots	This study	<3	Eu
SD255	ASWS, northern Oman-U.A.E.	ophiolite	**Dunite**		This study	<3	Eu
SD425	ASWS, northern Oman-U.A.E.	ophiolite	**Dunite**	label 6) on du plots	This study	<3	Eu
SD451	DIBBA, northern Oman-U.A.E.	ophiolite	**Dunite**		This study	<3	Eu
UAE4876	DIBBA, northern Oman-U.A.E.	ophiolite	**Dunite**	label 5) on du plots	This study	<3	Eu
UAE4878	DIBBA, northern Oman-U.A.E.	ophiolite	**Dunite**	label 1) on du plots	This study	<3	An
SD18	DIBBA, northern Oman-U.A.E.	ophiolite	**Dunite**		This study	<3	Eu
UAE2008	KFN, northern Oman-U.A.E.	ophiolite	**Dunite**		This study	<3	Eu
UAE143	KFN, northern Oman-U.A.E.	ophiolite	**Dunite**		This study	<3	Eu
UAE160	KFN, northern Oman-U.A.E.	ophiolite	**Dunite**		This study	<3	Eu

Table 2 continued: Description of samples analysed for Ga in chrome-spinel in Chapter 5.

Sample No.	Location	Setting	Rock Type	Additional Info.	References	Sp %	Spinel Type
UAE138	KFN, northern Oman-U.A.E.	ophiolite	**Chr-Dunite**		This study	10	Eu
UAE138	KFN, northern Oman-U.A.E.	ophiolite	**Chromitite**		This study	75	Eu
SD540	KFS, northern Oman-U.A.E.	ophiolite	**Dunite**	MTZ; label 4) on du plots	This study	<3	Eu
SD511	KFS, northern Oman-U.A.E.	ophiolite	**Chr-Dunite**	label 3) on du plots	This study	8	Eu
UAE33	KFS, northern Oman-U.A.E.	ophiolite	**Dunite**	MTZ	This study	<3	Eu
UAE65du	KFS, northern Oman-U.A.E.	ophiolite	**Cpx-Dunite**	MTZ; label 7) on du plots	This study	<3	Eu
UAE65cr	KFS, northern Oman-U.A.E.	ophiolite	**Chromitite**	MTZ	This study	80	Eu
UAE393	KFN, northern Oman-U.A.E.	ophiolite	**Chromitite**		This study	65	Eu
UAE140	KFN, northern Oman-U.A.E.	ophiolite	**Chromitite**		This study	90	Eu
SD444	ASWS, northern Oman-U.A.E.	ophiolite	**Chromitite**	MTZ	This study	85	Eu
SD49	ASWS, northern Oman-U.A.E.	ophiolite	**Chromitite**		This study	60	Eu
SD345	ASWS, northern Oman-U.A.E.	ophiolite	**Chr-Dunite**		This study	40	Eu
L35-90	Pindos-Vourinos, northern Greece	ophiolite	**Harzburgite**	label 7) on hz plots	sample from J.A.Pearce	<3	An
LK44	Pindos-Vourinos, northern Greece	ophiolite	**Harzburgite**	label 6) on hz plots	sample from J.A.Pearce	<3	An
AR90-28	Pindos-Vourinos, northern Greece	ophiolite	**Dunite**	label 10) on du plots	sample from J.A.Pearce	<3	Eu
XM-2	Pindos-Vourinos, northern Greece	ophiolite	**Chr-Dunite**	label 9) on du plots	sample from J.A.Pearce		Eu
BT6B	Pindos-Vourinos, northern Greece	ophiolite	**Chr-Dunite**	label 8) on du plots	sample from J.A.Pearce		Eu
79d	Pindos-Vourinos, northern Greece	ophiolite	**Chromitite**	label 1) on Fig 2	sample from J.A.Pearce		Eu
Tr1	northern Troodos, Cyprus	ophiolite	**ol-picrite lava**	Upper Pillow Lava	sample from H.Prichard	<3	Eu